Numerical Simulation of Walls and Seismic Design Recommendations for Walled Buildings

Joshua S. Pugh

A dissertation submitted in partial fulfillment
of the requirements for the degree of

Doctor of Philosophy

University of Washington

2012

Reading Committee:

Laura Lowes, Chair

Dawn Lehman

Marc Eberhard

John Stanton

Program Authorized to Offer Degree:
Civil & Environmental Engineering

University of Washington

Abstract

Numerical Simulation of Walls and
Seismic Design Recommendations for Walled Buildings

Joshua S. Pugh

Chair of the Supervisory Committee:
Professor Laura Lowes
Civil & Environmental Engineering

Structural walls are a commonly used lateral force-resisting system in low, medium and high-rise building construction in seismically active regions throughout the world. The stiffness and strength provided by structural walls are ideal for resisting service level seismic events; additionally, walls that are capacity designed to suppress shear failure are expected to perform well in design level seismic events by dissipating energy through ductile inelastic flexural response. To achieve this objective, seismic design procedures for walls are required that 1) adequately estimate shear demands expected to develop in walls yielding in flexure and 2) limit inelastic flexural demands to levels which ensure an acceptable collapse risk can be achieved. Validation of such procedures for walls can be aided by the use of numerical tools such as finite element analysis; however such tools must be capable of accurately simulating inelastic wall response, including deteriorating flexural response and loss of lateral load-carrying capacity.

The research presented discusses development of a recommended modeling approach for simulating inelastic wall response and the use of the proposed simulation method to evaluate existing US seismic design procedures for slender walls. The recommended modeling approach utilizes material energy regularization to allow for mesh-independent prediction of post-peak behavior and accurate simulation of wall ductility (in terms of system drift) using fiber-type distributed-plasticity line elements. Material energy recommenda-

tions for both confined and unconfined wall regions were developed using an experimental dataset of 21 cyclically loaded wall test specimens.

Existing US seismic design procedures were evaluated in terms of collapse risk and assessment was performed using inelastic time history analysis (ITHA) and incremental dynamic analysis (IDA) in accordance with the Federal Emergency Management Agencys (FEMA) P695 methodology. Preliminary assessment using P695 identified that current US design procedures, which do not include capacity design provisions for wall shear, significantly underestimate wall shear demands when compared to shear demands predicted for building models subjected to design level ground motion records and that walls designed using current US procedures may be unable to develop the assumed flexural mechanism. To address this problem, a modified modal response spectrum analysis, which is verified by P695 analysis to adequately suppress shear failure and allow fully development of the desired flexural mechanism, was developed. Results of P695 analyses are used to establish recommended flexural force reduction factors and design envelopes for slender walls.

TABLE OF CONTENTS

LIST OF FIGURES

LIST OF TABLES

ACKNOWLEDGMENTS

The financial support for this research was provided by the National Science Foundation. Specifically, funding was provided for by NSF Grant CMMI-0829978 (Seismic Response of Reinforced Concrete Walls) and NSF Grant CMMI-0421577 (Seismic Behavior, Analysis and Design of Complex Wall Systems).

I would like to express my gratitude to my advisors Professors Laura Lowes and Dawn Lehman for their guidance and advice over the course of this research. Thanks to Professors Marc Eberhard and John Stanton for serving on my committee and their suggestions that helped improve this dissertation. I would also like to thank my Graduate Student Representative, Professor Duane Storti. Additional thanks to Professors Peter Mackenzie, Nathan Kutz and Greg Miller for their guidance and enthusiasm along the way as well.

I'm very grateful to have been helped along the way with good friends and co-workers. Friendships with Joe Uceda, Josef Taylor and Tyler Winkley have made work seem a lot less like it. Beating down Jordan Hague and Jake Turgeon in fantasy football helped too. I'm also very fortunate to have worked with thoughtful and talented professional mentors; special thanks to Richard Dusang and Bob Heron for encouraging me to pursue my education. Finally, being able to work with fellow doctoral students who could relate to the pains of returning to school after experiencing the so-called 'real' world helped me out a ton; special thanks to David Webster, David Lattanzi, Keith Palmer and Mohammad Malakoutian.

I could not have done this without the love and support of my family. It was a tough few years and your ongoing support, patience and love helped more than you know. Thank you to my parents for always providing the perfect blend of encouragement, high expectations and love. Special thanks to my brother, Jake, for commiserating when that blend seemed skewed, and for being a superb Rock Band bandmate and pop culture conversationalist.

DEDICATION

To my dad, Julian Lee Pugh Jr. You encouraged me to embark on a fun, challenging and unique path; I miss you.

To my mom, Carolyn Pugh. Thank you for always being willing to listen and for helping keep me focused; your support helps more than you know.

To my patient and supportive Bri. And to think, I thought a doctorate would be the best thing I found in Seattle.

Chapter 1
INTRODUCTION

Reinforced concrete walls are a common seismic lateral force resisting system used throughout the western United States. They are expected to sustain inelastic deformations under large earthquakes, so numerical simulation tools are needed that are capable of accurately simulating nonlinear wall response. Additionally, seismic design procedures for walls are required that ensure that:

1. inelastic response occurs only in ductile response mechanisms

2. shear demands in walls remain below acceptable levels during seismic events

3. inelastic response mechanisms are sufficiently ductile to sustain expected inelastic deformations.

For walls, current seismic design procedures are intended to limit inelastic response to flexural yielding in wall regions detailed to promote enhanced inelastic flexural deformation capacity while suppressing shear failure mechanisms.

Numerical tools such as the finite element analysis are needed to validate current seismic design procedures for walls. In particular, they need to be able to simulate deterioration in flexural response and the consequent loss of lateral strength. However many finite element tools in widespread use today are unable to do this well. Accurate simulation of strength deterioration is important both for:

1. ensuring walls can safely sustain design level inelastic demands and

2. determining the margin of safety provided for seismic events that exceed the design level.

The development of finite element models capable of simulating the complete inelastic performance of reinforced concrete walls would lead to improvements in current seismic design procedures and promote the use of performance-based design for wall buildings.

The research presented in this thesis addresses analysis and design of slender walls that respond inelastically primarily through flexural yielding.

1.1 Research Objectives

The primary objectives of the research presented in this thesis are:

1. To develop modeling recommendations that provide accurate simulation of cyclic response, including loss of lateral strength for slender walls responding primarily in flexure.

2. To evaluate US seismic design procedures for walls by conducting inelastic time history analyses (ITHA) using the above modeling recommendations.

3. To develop improved seismic design procedures that ensure that slender walls develop the desired flexural response mechanism and can sustain expected inelastic flexural deformations.

1.2 Overview

The current research focuses on the development of a method for accurately simulating cyclic response of slender concrete walls and the application of this method to evaluate and advance current design procedures for walled buildings. The research comprises

1. the development of a regularized distributed-plasticity beam-column element that accurately simulates cyclic wall response

2. the validation of the model through comparison of simulated and measured response for walls of varying cross section shape

3. the use of the regularized beam column element element to develop capacity design recommendations for shear design and recommended force reduction factors (i.e. - R factors) for slender walls.

Chapters 2 and 3 present the development of the regularized beam column element that enables accurate simulation of deteriorating flexural response of cyclically loaded wall specimens. Chapter 2 demonstrates that conventional,i.e. unregularized, distributed-plasticity and plane stress finite element models can not accurately simulate strength deterioration and that drift capacity determined using conventional models is highly mesh sensitive.

In Chapter 3, material regularization techniques are applied to distributed-plasticity beam column elements. Post-yield material energy values, which are required for material regularization, are determined for concrete using experimental data from wall tests and for steel using experimental data from material tests. Relationships for post-yield material energy are shown to provide accurate simulation of strength deterioration for walls observed in the laboratory to exhibit softening response prior to failure.

Chapters 4 and 5 use the regularized distributed-plasticity element to assess both current US wall seismic design procedures and also various capacity design procedures for walls used throughout the world. In Chapter 4, a preliminary assessment of core wall buildings ranging in height between 16 and 30 stories demonstrates that current US seismic design procedures can significantly underestimate shear demands in slender walls responding inelastically in flexure. In Chapter 5, current shear capacity design recommendations used in building code documents outside the US for walls are assessed. Current capacity design recommendations were assessed by performing inelastic time history analysis (ITHA) of 64 walled building models. Results presented in Chapter 5 demonstrate that current wall shear recommendations do not accurately predict shear demands determined to develop in the walls using ITHA for walls designed considering a range of building heights, initial fundamental periods and force reduction factors.

In Chapter 6, ITHA results are used to develop a modified Modal Response Spectrum Analysis (MRSA) method for capacity design of shear in slender walls. The modified

MRSA method is demonstrated to adequately limit shear demands to acceptable levels for slenders wall models subjected to both design level and maximum considered earthquake demands.

In Chapter 7, recommendations for flexural force reduction factors for slender walls are developed that limit the amount of wall flexural damage to acceptable levels for buildings subjected to maximum considered earthquake demands.

Chapter 8 summarizes the research presented in the thesis, identifies important conclusions and makes recommendations for future work to advance nonlinear analysis and seismic design procedures for slender concrete walls.

Chapter 2

NUMERICAL SIMULATION OF SLENDER WALL RESPONSE USING CONVENTIONAL MODELING APPROACHES

2.1 Introduction

The research presented in this chapter focuses on assessing the ability of two finite element modeling tools, currently in widespread use by both the design and reserach structural engineering communities, to accurately simulate the response of 21 previously tested slender wall specimens observed to dissipate energy primarily through flexural yielding and limited in drift capacity by deteriorating flexural response. Both fiber section distributed-plasticity beam colum element models and Modified Compression Field Theory-based plane stress element models are assessed. Results of the assessment demonstrate that both models are capable of simulating peak strength and yield stiffness of wall specimens, however neither model can accurately simulate the observed drift capacity or the onset of deteriorating flexural response. Investigation of element behavior for both modeling approaches identifies that inaccuracies in simulating drift capacity are due to the localization of inelastic deformations which begin once strength loss ocurs in the numerical simulation. This localization affects the accuracy of the simulated response while also rendering the simulation of strength degredation to be highly mesh dependent.

A summary background on previous numerical simulations of walls and available modeling tools is provided in Section 2.2. Background on the 21 experimental specimens used as the basis for assessing simulated response quantities is provided in Section 2.4. Numerical simulation results using fiber section distributed-plasticity beam column elements are presented in Section 2.5. Plane stress element simulation results are presented in Section 2.6.

2.2 Background on Numerical Simulation and Modeling of Slender Walls

Currently, nonlinear analysis of walls responding in flexure may be accomplished using models of varying sophistication and complexity. The simplest and most basic approach is likely a lumped-plasticity model in which a flexural hinge is located at the critical section of the wall and the remainder of the wall is simulated using elastic elements. The most commonly used model is likely the multi-linear moment-rotation backbone curve for walls responding in flexure that is presented in ASCE 41 Supplement 1 (2007). The basic form of this curve was established using data from laboratory tests of walls with varying design characteristics. The curve is defined for a specific wall using the nominal flexural capacity, the axial load and shear demands developed, and the longitudinal reinforcement ratio of the wall. A hinge length of half the length of the wall is implicitly assumed. ASCE 41 does not provide recommendations for defining response under cyclic loading, and varying approaches are used in practice. While this model is computationally efficient and numerically robust, it provides an extremely simplified representation of cyclic response. Rotation capacities defined in ASCE 41 are average values determined from experimental tests and must be considered to have a high level of uncertainty. Since the moment-rotation response of the hinge is defined prior to the analysis, the model cannot account for the impact on response of variation in axial or shear load. Additionally, beyond the simplified representation of response, since nonlinear response is limited to the location of the lumped-plasticity hinge, multiple analyses may be required in which additional hinges are introduced or hinges are moved to accurately simulate the distributed nonlinearity within the wall. The simplicity, computational efficiency and robustness of the model do, however, make the model attractive for use in research addressing earthquake design and response of walls (Panneton et al. 2006, Calugaru and Panagiotou 2012, Rejec et al. 2011).

More sophisticated lumped-plastic models employ fiber-type section models to define the moment-curvature response of the critical wall section and a plastic-hinge length to transform moment-curvature response to moment-rotation response. Here the fiber-type discretization of the section comprises concrete and steel fibers for which stress-strain response is defined by one-dimensional constitutive models. The curvature and axial

strain imposed on the section determine the axial strain of individual fibers and the moment and axial load carried by the section is computed from the fiber stresses and areas. Fiber-section models are available in most nonlinear software including SAP2000 (http://www.csi.berkeley.edu) and OpenSees (Mazzoni et al, 2006). In comparison with an ASCE 41-type model, these models enable simulation of the impact of axial load on flexural response and provide objective simulation of cyclic response, if cyclic material constitutive models are employed. However, these models employ the assumption that plane sections remain plane, which may introduce error for some wall configurations and cannot simulate the impact of shear on flexural response. The fiber-section lumped-plasticity model also requires the choice of a hinge-length over which nonlinear action occurs; this length must be defined using laboratory data, and this limits the accuracy of the model for general application. Finally, multiple analyses with new models may be required to accurately simulate the distribution of nonlinearity within the wall. Thus, while this model is computational efficient and robust and can provide an accurate representation of the nonlinear flexural response of a wall section, simulation of nonlinear response at multiple sections up the height of the wall requires multiple analyses and input for the user.

Typically, the fiber-type section model described above is employed within a finite element to simulate the nonlinear response of a reinforced concrete component such as a wall. For example within the OpenSees analysis platform, fiber-type sections can be incorporated into distributed-plasticity displacement-based beam-column elements as well as distributed-plasticity and lumped-plasticity force-based beam-column elements. In this context, displacement-based elements employ the assumptions of a linear curvature field and constant axial deformation field along the length of the element, force-based elements employ the assumptions of a linear moment and constant axial force distribution along the length of the element, distributed-plasticity elements include multiple nonlinear fiber-type sections along the length of the element, and lumped-plastic element include nonlinear fiber sections at the ends of the element. This approach enables simulation of nonlinear action at multiple locations up the height of the wall. Additionally, the beam-column element formulation is typically quite numerically robust; although, if section strength loss is rapid, convergence problems can arise in the intra-element solution that is required for the

force-based element formulation.

The primarily limitations of these models for simulating the response of slender reinforced concrete walls are i) the fundamental assumption that plane sections remain plane, which can results in inaccurate simulation of fiber strains and thus inaccurate simulate of the strength and/or deformation capacity, ii) the decoupling of flexure and shear response that follows from the plane-sections-remain-plane assumption, and ii) the difficulty of using two-node beam-column line elements to model three-dimensional walls with complex configurations within three-dimensional structures. Additionally, the research presented in this chapter shows that for many wall designs employed in practice, loss of lateral load carrying capacity results from concrete crushing and reinforcement buckling; as a result, in the numerical model deformation localizes at a critical section and accurate, mesh-objective simulation of drift capacity requires regularization of material response. Additionally, while line-element models may not be ideal for simulation of buildings with complex configurations, they are ideal for simulation of buildings with regular configurations and/or simulation using idealized models as they provide computational efficiency, numerical robustness and accurate results. For example, Boivin and Paultre (2012) employ the fiber-section distributed-plasticity force-based beam-column element implemented in OpenSees to investigate shear and moment demands in slender walls subjected to earthquake loading.

Multiple variations of the fiber-section hinge model and the fiber-section distributed-plasticity beam-column element have been employed and implemented in research and commercial software to simulate wall response. For example, Orakcal et al. (2004) employ the multiple-vertical-line-element model (MVLEM) proposed by Vulcano et al. (1988) to simulate the nonlinear flexural response of slender walls. The MVLEM is essentially a finite-length fiber-section model combined with a horizontal spring that simulates the shear flexibility of the wall; Orakcal et al. employ standard one-dimensional cyclic constitutive models to define the response of concrete and steel fibers and an elastic shear-response model. Orakcal and Wallace (2006) show that the MVLEM can provide accurate simulation of wall response for walls for which the assumptions of plane sections remain plane, elastic shear response, and decoupling of flexure and shear response are valid. Ghobarah et al. (2004) and Galal (2007) simulated the response of a five-story wall subjected to dynamic

shake-table loading (CAE 2002) using a model in which fiber-type sections were placed between elastic two-dimensional plane-stress elements (a plane-sections-remain-plane constraint was imposed at the interface between the fiber-section and the plane-stress elements); the model provided reasonably accurate simulation of strength and hysteretic response under dynamic loading. Finally, the fiber shell wall element implemented in Perform (http://www.csi.berkeley.edu) may be considered a variation of the fiber-type section model as flexural response is determined by the stress-strain response of vertical fibers with shear response determined by an independent one-dimensional shear model.

While slender walls respond primarily in flexure, shear deformation is not insignificant (Lowes et al. 2012), shear stiffness reduces with increasing flexural and shear demand (Lowes et al. 2012), and high shear demand may reduce drift capacity (Birely 2012) . Thus, improved simulation of wall response can, potentially, be achieved using models that simulate nonlinear shear response and flexure-shear interaction. Several researchers have extended the fiber-section model to simulate these. In these models, fiber response is typically defined by a two-dimensional strain field, the assumption that fibers are in a state of plane stress, and a two-dimensional constitutive model. Examples of this type of model include that proposed by Jiang and Kurama (2010) and by Petrangeli et al. (1999), both of which use the microplane model (Bazant and Oh 1985, Bazant and Prat 1988; Bazant and Ozbolt 1990; Ozbolt and Bazant 1992) to define multi-dimensional concrete response. Response 2000 (Bentz 2000) employs a similar approach with multi-dimensional concrete response defined using the Modified Compression Field Theory (Vecchio and Collins 1986). Jiang and Kurama (2010) show that this modeling approach enables simulation of nonlinear shear response, interaction of flexure and shear mechanism and reasonably accurate simulation of observed response for a limited number of wall specimens. However, while these models provide the potential for improved simulation of response, the flexure-shear fiber-section elements are more computationally demanding and less numerically robust than the models in which flexure and shear response are decoupled. Further, this approach is still limited by the difficulty of using two-node beam-column line elements to model three-dimensional walls with complex configurations within three-dimensional structures for some formulations, and, for some formulations, by the assumption that plane-

sections-remain-plane (though not perpendicular to the neutral axis).

Analysis using continuum element offers the greatest potential for accurate simulation of nonlinear response, including nonlinear flexure, shear and torsional response, as well as the greatest flexibility for simulation of complex wall configurations and three-dimensional building systems. For planar walls and some non-planar walls, analyses using two-dimensional plane-stress elements and concrete constitutive models can provide accurate results. For non-planar walls, fiber shell elements (here fibers are two-dimensional and concrete fiber response is determined using a two-dimensional plane-stress concrete constitutive model) or three-dimensional brick elements can provide accurate simulation of response. Analysis using continuum-type elements is extremely computationally demanding, and typically analyses are done using implicit solution algorithms, which are often plagued by convergence issues, especially when solutions are sought beyond the point at which strength loss initiates. Additionally, accurate and mesh-objective simulation of response requires regularization of material response, often requires consideration of initial conditions, and may, for walls exhibiting tension-controlled response, require that an empirically calibrated reinforcing steel constitutive model be employed to capture bar buckling and rupture. Palermo and Vechhio (2007) employed VecTor2 with two-dimensional plane stress elements and a variant of the two-dimensional MCFT or DSFM (disturbed stress field model) reinforced concrete constitutive model to simulate the response of I-shaped walls tested by Palermo (2002); accurate simulation of initial stiffness was achieved by pre-cracking the concrete elements to simulate shrinkage cracking observed in the laboratory and accurate simulation of drift capacity was achieved by Palermo.

2.3 Selected Tools Used for Numerical Simulation of Slender Walls

As both beam column elements and continuum elements are used extensively by the design and research communities, both models were investigated to determine the extent which current modeling approaches can be used to simulate cyclic response of slender walls. Beam column element models are advantageous because they are significantly less computationally demanding than continuum element models. Continuum element models

are much more computational demanding and complex 2- and 3-dimensional models can become impractical for non-research applications. However, continuum element models are free from restrictions (i.e. - 1D material models, plane section kinematics) which are inherent to currently available beam column element models.

For simulation results presented in this chapter, both beam column and continuum element models were used to assess numerical simulation of slender walls. Beam column element simulations were performed using fiber-type distributed-plasticity beam column elements available in the OpenSees open-source software platform (Mazzoni, et al., 2006). Continuum element simulations were performed using modified compression field theory-based plane stress elements available in the VecTor2 commercial finite element package (Wong and Vecchio, 2002).

Both modeling approaches were assessed by comparing simulated cyclic wall response quantities to experimental data for 21 laboratory tested wall specimens. Details on the experimental dataset used for model evaluation is provided in Section 2.4. Simulation results for beam column element models and continuum element models are discussed in Section 2.5 and Section 2.6, respectively.

2.4 Experimental Specimens Used to Assess Simulated Wall Response

Previously tested slender wall specimens were used to evaluate beam column and continuum element wall simulations discussed in this chapter. For evaluations discussed in this chapter, the available specimens were limited to cyclically loaded planar (rectangular) wall specimens in which specimen failure was initiated by deteriorating flexural response (Table 2.1). Although slender wall specimens with other cross-section configurations (i.e. - barbell, C-shaped, T-shaped) have been tested, the largest experimental dataset exists for planar walls. Simulation of non-planar walls were also performed and results of these simulations are provided in Chapter 3.

To assemble the data set, previous laboratory tests of reinforced concrete wall subassemblages subjected to quasi-static lateral loading were reviewed. A test specimen was included in the data set if four criteria were met. First, specimens were included if they ex-

hibited flexure-controlled response with loss of lateral load carrying capacity resulting from tensile rupture of longitudinal reinforcement (prior to or following buckling) or crushing of boundary element concrete. Second, specimens were sufficiently thick, at least 76.2 mm (3 in.), to ensure that wall thickness would not adversely affect response. Third, sufficient data were available in the literature to fully define a numerical model; data deemed necessary included concrete compressive strength, data defining reinforcing steel stress-strain response, specimen geometry and reinforcement layout, and test specimen boundary conditions in the laboratory. Fourth, sufficient data were provided to enable evaluation of simulation results; data deemed necessary included global load-displacement response as well as the observed failure mechanism. Information regarding configuration, design and loading of the experimental specimens used for validation are provided in Table 2.1 and Figures 2.1 to 2.5. A detailed review of the wall specimens is presented in Appendix A. Data presented also includes derived quantities that could be expected to affect specimen performance. Quantities in Table 2.1 and Figures 2.1 to 2.5 are defined as follows:

- l_w = wall length
- t = wall thickness
- $\rho_{long,g}$ = gross longitudinal reinforcement ratio computed using the gross wall area and total area of longitudinal reinforcement.
- $\rho_{long,w}$ = longitudinal reinforcement ratio within the wall web.
- $\rho_{long,be}$ = longitudinal reinforcement ratio within confined boundary elements near the wall ends.
- ρ_t = horizontal (transverse) reinforcement ratio within the web of the wall.
- ρ_{vol} = volumetric reinforcement ratio for confined boundary elements.
- scale = t/12 inches

- l_w/t = wall aspect ratio

- f'$_c$ = concrete compressive strength

- $M_b/(V_b l_w)$ = shear span ratio, where M_b and V_b are the moment and shear force developed at the base of the wall, respectively.

- λ_n = axial load ratio ($P/A_g f'_c$), where P is the axial load at the base of the wall and A_g is the gross wall area.

- α_v = shear demand ratio ($V_{b,max}/(A_{cv}(f'_c)^{0.5})$) where $V_{b,max}$ is the maximum base shear developed during the test and A_{cv} is the gross web area.

- $V_{b,max}/V_n$ = shear demand-capacity ratio where V_n is the nominal shear strength computer per ACI 318 (2011) using actual concrete and steel strengths.

- $M_{b,max}/M_n$ = flexural strength ratio where $M_{b,max}$ is the maximum base moment developed during the test and M_n is the nominal flexural strength of the wall computed per ACI 318 (2011) using actual concrete and steel strengths.

- ϵ_t = extreme layer tensile strain when wall section reaches the nominal flexural strength defined by ACI 318 (2011). Nominal flexural strength is the flexural capacity when the extreme compression fiber strain reaches -0.003 using reported specimen material strengths.

- Tension Controlled(Y/N) indicates whether the calculated extreme layer tensile strain, determined by moment curvature analysis, when the section reaches an extreme compression fiber strain of -0.003 exceeds the tension-controlled limit of 0.005 prescribed by ACI 318 (2011) Section 10.3.4.

- Δ_y = yield drift ($\%$), calculated as the drift measured at the top of the specimen when the base moment reaches the theoretical yield moment.

- Δ_u = drift capacity ($\%$), the drift measured at the top of the specimen when the lateral load carrying capacity of the specimen dropped to 80$\%$ of the historic maximum, for drift demands in excess of historical drift demands.

- Loading Type indicates the manner in which lateral loading was applied; monotonic (M), unidirectional-cyclic (UC) or bidirectional-cyclic (BC)

- Failure Mode indicates the primary mechanism causing lossof lateral load carrying capacity: concrete crushing and buckling of longitudinal steel (CB) or rupture of longitudinal steel before of after significant buckling of longitudinal reinforcement (BR).

Table 2.1: Specimen Database

Specimen ID	Author	Load Type	l_w/t	M/(Vl_w)	λ_n^1	α_v^2	V$_{max}$/V$_n$	Δ_y (%)	Δ_u (%)	Tension Controlled(Y/N)	Failure Mode
WSH1	Dazio, et al.	UC	13.3	2.28	0.055	2.01	0.44	0.24	1.04	Y	BR
WSH2	Dazio, et al.	UC	13.3	2.28	0.063	2.27	0.53	0.27	1.75	Y	BR
WSH3	Dazio, et al.	UC	13.3	2.28	0.064	2.92	0.67	0.32	2.07	Y	BR
WSH4	Dazio, et al.	UC	13.3	2.28	0.063	2.77	0.62	0.29	1.60	Y	CB
WSH5	Dazio, et al.	UC	13.3	2.28	0.137	2.81	0.59	0.20	1.52	Y	BR
WSH6	Dazio, et al.	UC	13.3	2.26	0.114	3.58	0.83	0.31	2.04	Y	CB
W1	Liu	UC	6.07	3.13	0.077	2.31	0.46	0.64	2.98	Y	CB
W2	Liu	UC	6.07	3.13	0.036	1.67	0.37	0.55	2.91	Y	BR
PW1	Lowes, et al.	UC	20.0	2.84	0.099	3.51	0.71	0.38	1.53	Y	BR
PW2	Lowes, et al.	UC	20.0	2.08	0.133	5.31	1.11	0.45	1.50	Y	CB
PW3	Lowes, et al.	UC	20.0	2.00	0.104	4.41	0.88	0.24	1.22	Y	CB
PW4	Lowes, et al.	UC	20.0	2.00	0.122	4.63	0.88	0.40	1.01	Y	CB
RW1	Thomsen, et al.	UC	12.0	3.13	0.105	2.57	0.50	0.48	2.26	Y	BR
RW2	Thomsen, et al.	UC	12.0	3.13	0.092	2.65	0.52	0.55	2.35	Y	CB
R1	Oesterle, et al.	UC	18.8	2.35	0.004	1.14	0.23	0.15	2.30	Y	BR
R2	Oesterle, et al.	UC	18.8	2.35	0.004	2.05	0.42	0.34	2.89	Y	BR
S5	Vallenas, et al.	M	21.2	1.60	0.048	6.81	0.85	0.31	1.47	Y	CB
S6	Vallenas, et al.	UC	21.2	1.60	0.048	6.42	0.80	0.32	1.65	Y	CB
WR20	Oh, et al.	UC	7.50	2.00	0.104	3.00	0.76	0.35	2.82	Y	CB
WR10	Oh, et al.	UC	7.50	2.00	0.098	2.87	0.65	0.47	2.82	Y	CB
WR0	Oh, et al.	UC	7.50	2.00	0.108	2.97	0.74	0.52	2.14	Y	CB

[1] Axial Load Ratio Including Self-Weight (P/(A$_g$f'$_c$)

[2] Shear Demand (V$_{max}$ = α_v(A$_{cv}\sqrt{f_c'(psi)}$))

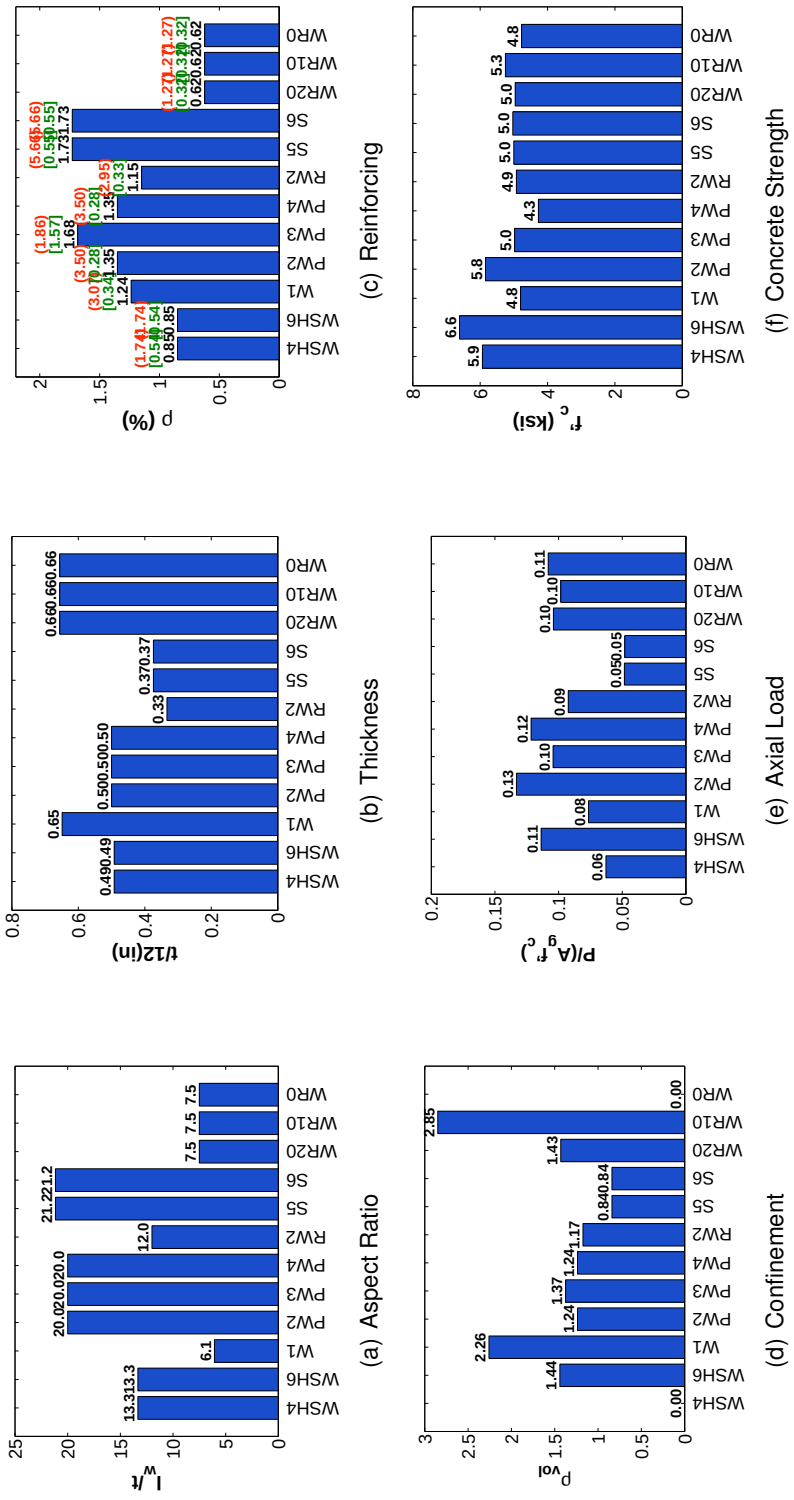

Figure 2.1: Specimen Parameters (CB Specimens)

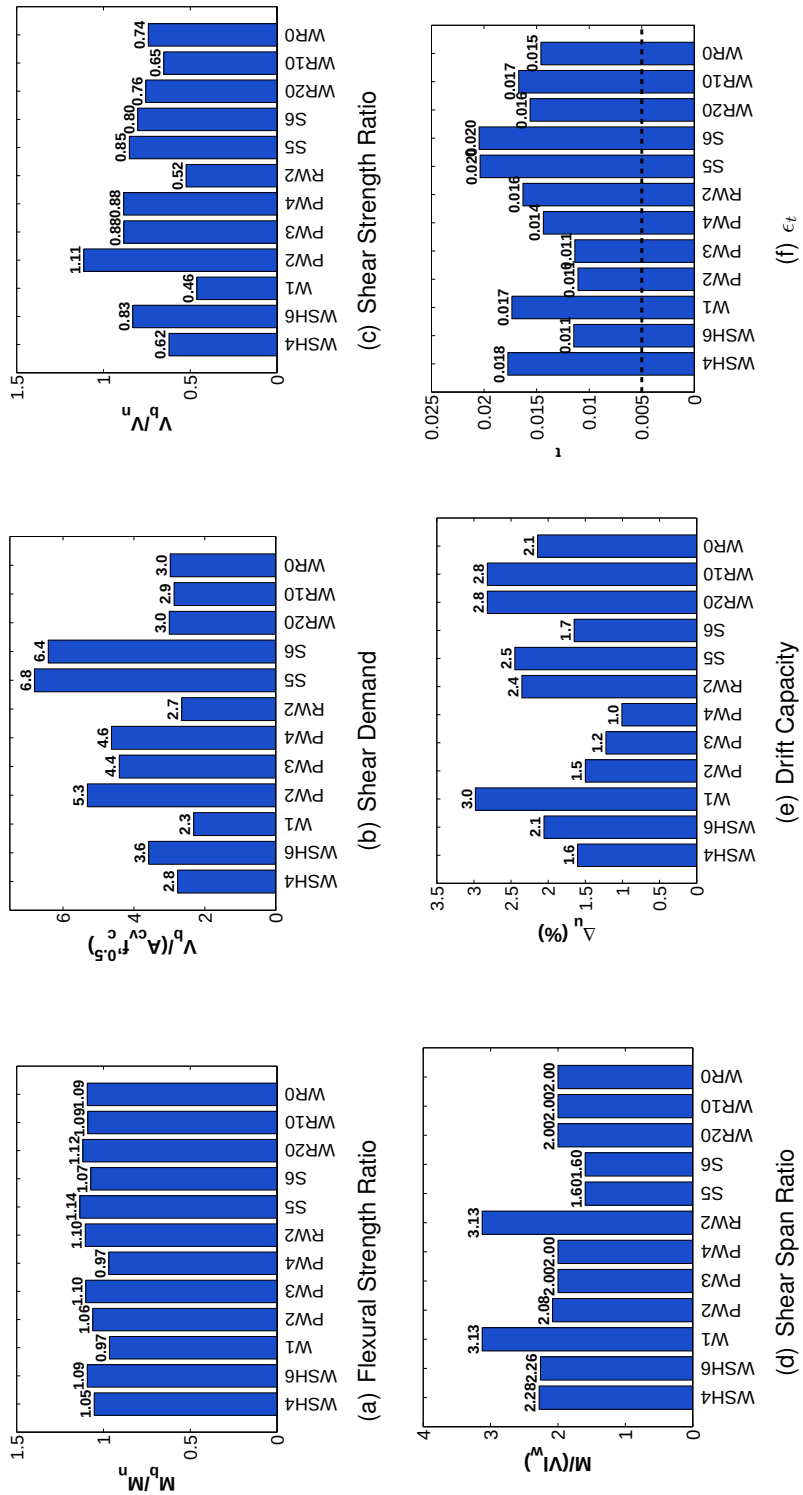

Figure 2.2: Specimen Parameters (CB Specimens)

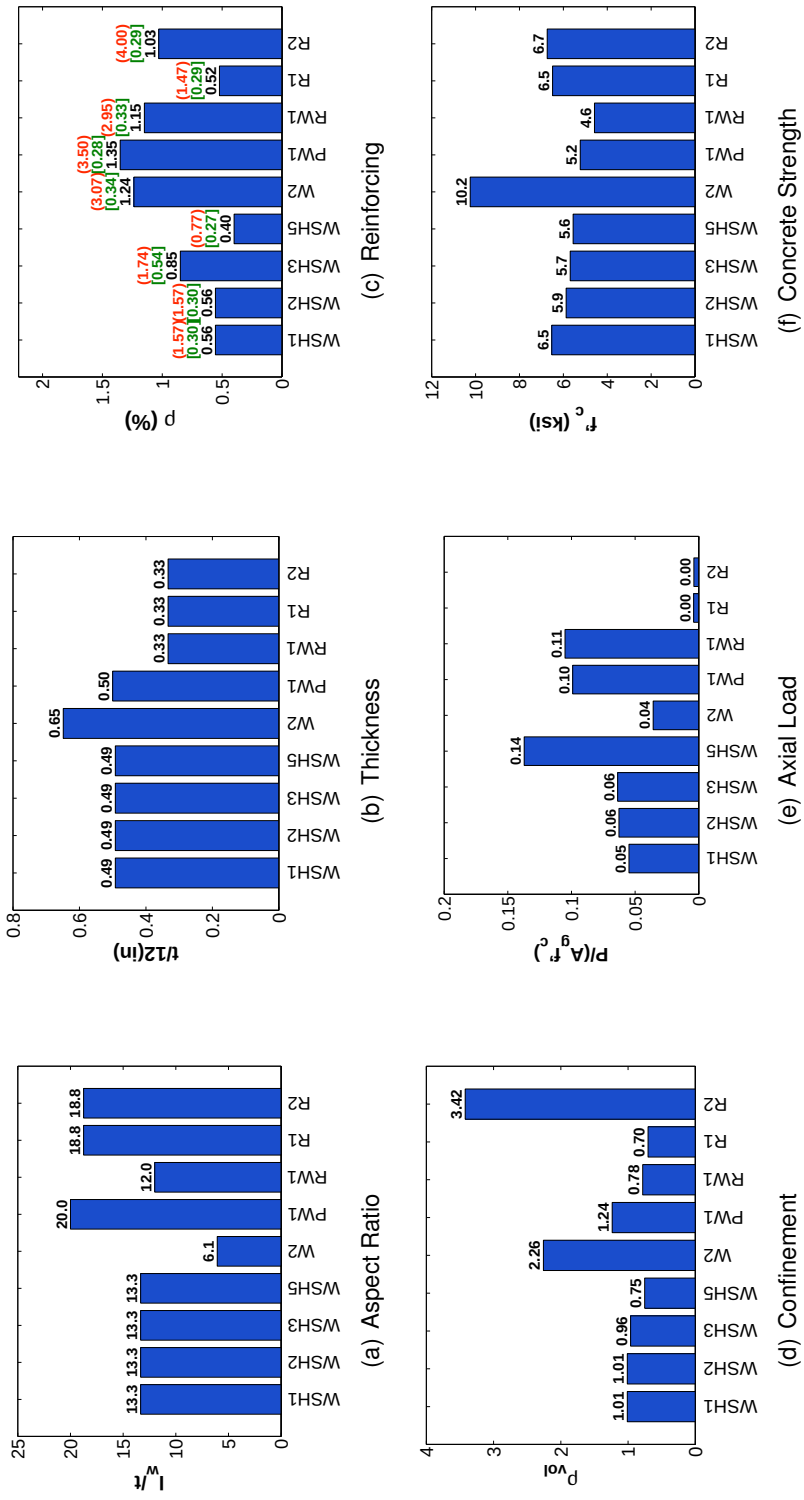

Figure 2.3: Specimen Parameters (BR Specimens)

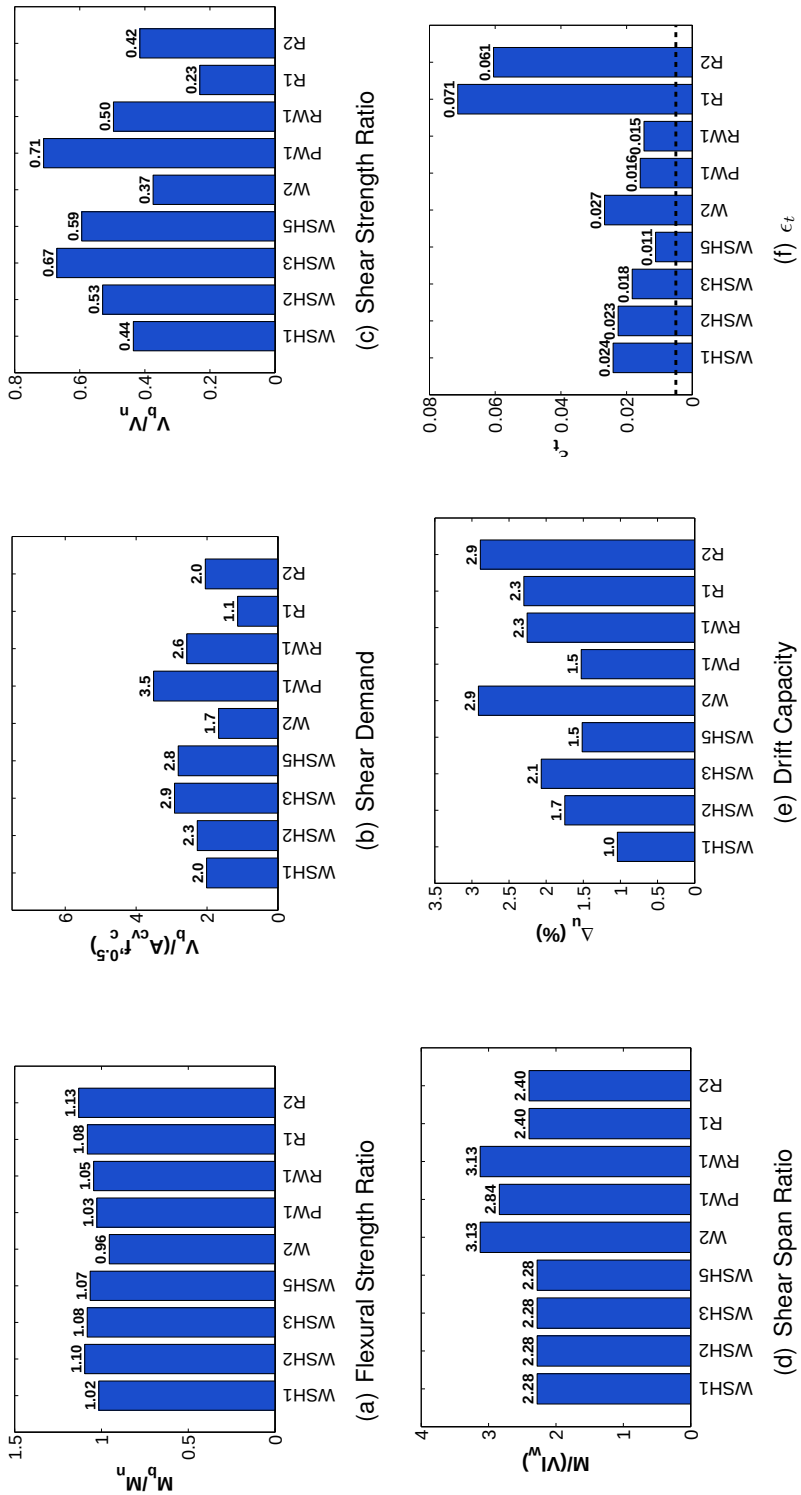

Figure 2.4: Specimen Parameters (BR Specimens)

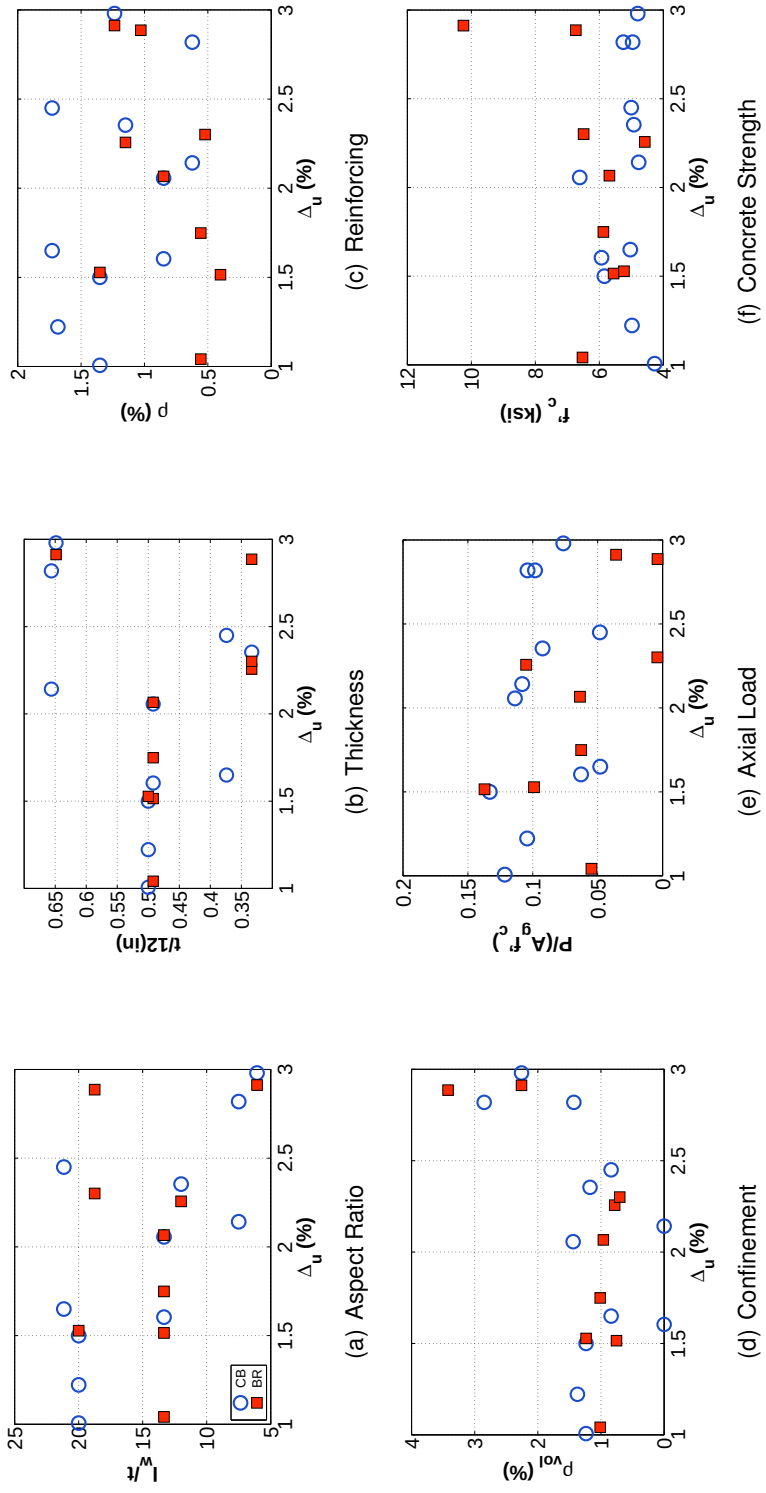

Figure 2.5: Specimen Trend Comparison

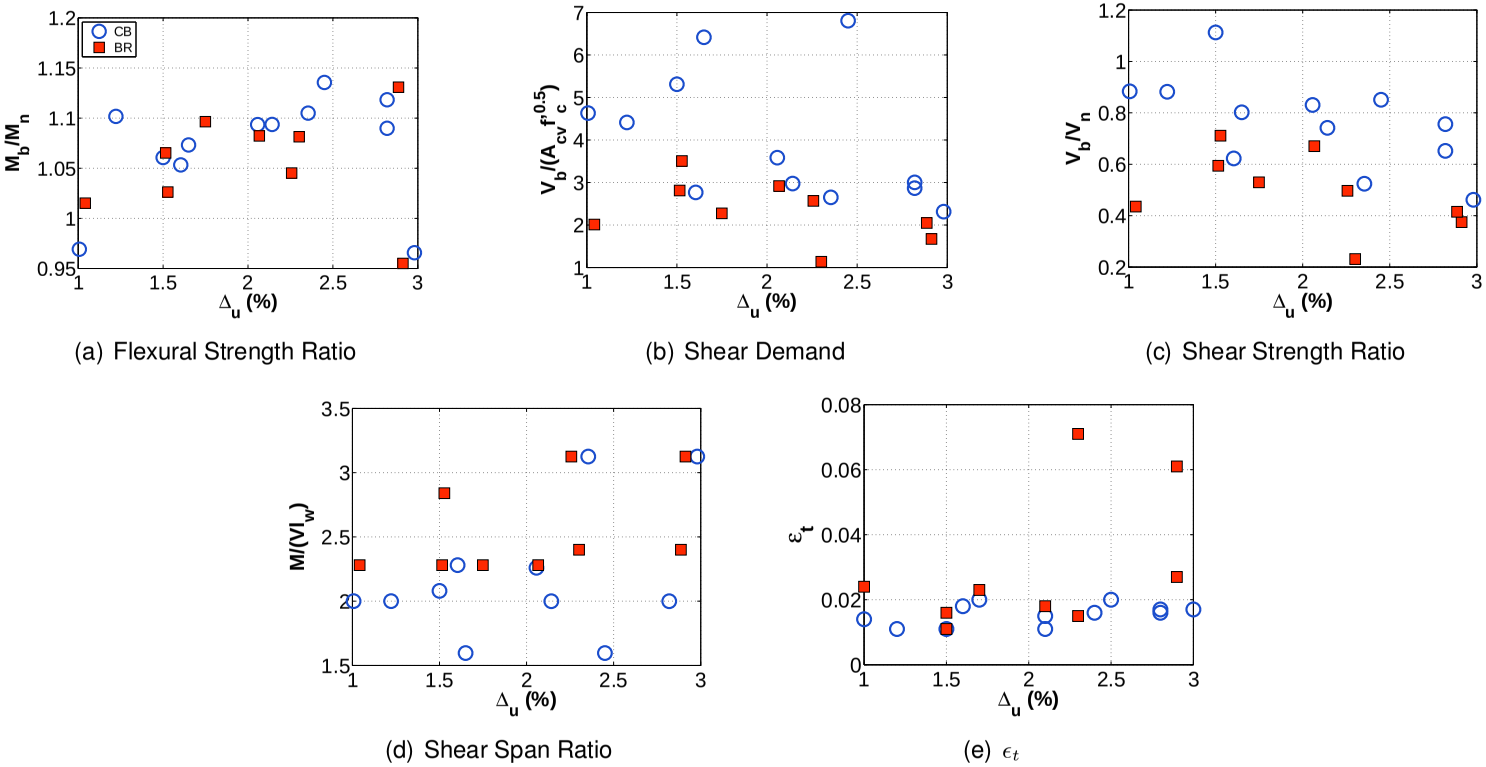

(a) Flexural Strength Ratio (b) Shear Demand (c) Shear Strength Ratio

(d) Shear Span Ratio (e) ϵ_t

Figure 2.6: Specimen Trend Comparison

2.4.1 Comments on Experimental Specimen Database

Review of the specimen data provide the following observations:

1. All slender wall specimens would be classified as tension-controlled per ACI 318 (2011). However, 12 of the 21 specimens were observed to fail in compression rather than tension even though the minimum tensile strain, ϵ_t, calculated for any specimen (0.11) was greater than twice the tension controlled limit suggested by ACI 318 (0.005).

2. Comparison of design parameters for specimens failing in compression and tensile suggests that increased shear demands may contribute to compression failures in slender walls (Figures 2.5(b) and (c)). All slender wall specimens subjected to shear demands greater than $4\sqrt{f'_c(psi)}A_{cv}$ failed due to flexural compression; 5 of the 12 compression controlled specimens were subjected to shear demands greater than $4\sqrt{f'_c}A_{cv}$. All slender walls subjected to shear demand-capacity ratios greater than 0.75 failed due to flexural compression; 8 of the 12 compression controlled specimens were subjected to shear demand-capacity ratios greater than 0.75. Four of the 12 compression controlled specimens were subjected to shear demand less than $4\sqrt{f'_c}A_{cv}$ and a demand-capacity ratio less than 0.75.

2.5 Simulating Wall Response Using Basic Fiber-Type Distributed-Plasticity Beam Column Elements

This section presents wall simulation results generated using basic, i.e - unregularized, distributed-plasticity beam column elements. Discussion of model development is provided in Section 2.5.1. Simulation results for both displacement-based and force-based element models are provided in Section 2.5.2.

2.5.1 Nonlinear Model Details

Distributed-plasticity beam column element wall modeling was performed using the open-source OpenSees software platform (Mazzoni et al, 2006) considering two available ele-

ment formulations:

1. The force-based distributed-plasticity fiber-section beam column elements (*forceBeamColumn*) by Spacone et al. (1992). The force-based element employs the assumptions of a linear moment and constant axial force distribution along the length of the element. For wall specimens loaded laterally by concentrated loads, the internal force distribution used by the force-based element can satisfy equilibrium with a low-level of mesh refinement. An additional internal solution algorithm is required for the force-based element, because element stiffness matrices and resisting force vectors are not directly available using a flexibility-based element formulation.

2. The displacement-based distributed-plasticity fiber-section beam column elements (*dispBeamColumn*) by Scott (2001). The displacement-based element employs the assumptions of a linear curvature field and constant axial deformation along the length of the element. For simulation of inelastic wall systems, the linear curvature field can not accurately simulate the spread of inelasticity. To improve accuracy using displacement-based elements, high levels of mesh refinement may be required.

All specimen models were meshed to represent a single cantilever extending vertically above a fixed base using several beam column elements connected in series. The fixed base of each model was taken at the interface between the wall specimen and the base reaction block. The element mesh extended to the top of the wall specimen (Figure 2.7). Two load patterns were applied to each specimen model, 1) an axial load case and 2) a lateral load case. For each specimen model, the axial load case consisted of a single concentrated vertical load applied to the top of the specimen. The magnitude of the axial load was equal to the sum of the external axial load applied to the specimen (either from actuator loads or post-tensioning) and the self-weight, including top reaction block, of the specimen. Lateral loads consisting of a horizontal shear force and in-plane bending moment were applied to each specimen. The applied shear force represented the concentrated external actuator loading applied to each specimen and the bending moment accounted for the difference between the top of the specimen and the height at which the actuator actually

contacted the specimen. This loading pattern exactly matched the internal distribution of shear and bending forces for 15 of the 21 specimens. For the other six specimens,PW1-PW4 and S5-S6, small distributed shear forces were applied along the specimen height in addition to the primary shear force applied at the top of the specimens. The simulated load pattern, which lumped the entire lateral shear force to the top of the specimen, was found to overestimate elastic flexural specimen demands near the wall base by less than 0.25%, which was deemed sufficiently accurate for the current study. The lateral load pattern was applied to each specimen to match the cyclic drift history applied to the specimen in the laboratory. Specifics of the number of elements and the number of fiber sections used are provided in Section 2.5.2 for both force-based element and displacement-based element models. The co-rotational formulation (de Souza, 2000) was used to simulate geometric nonlinearity.

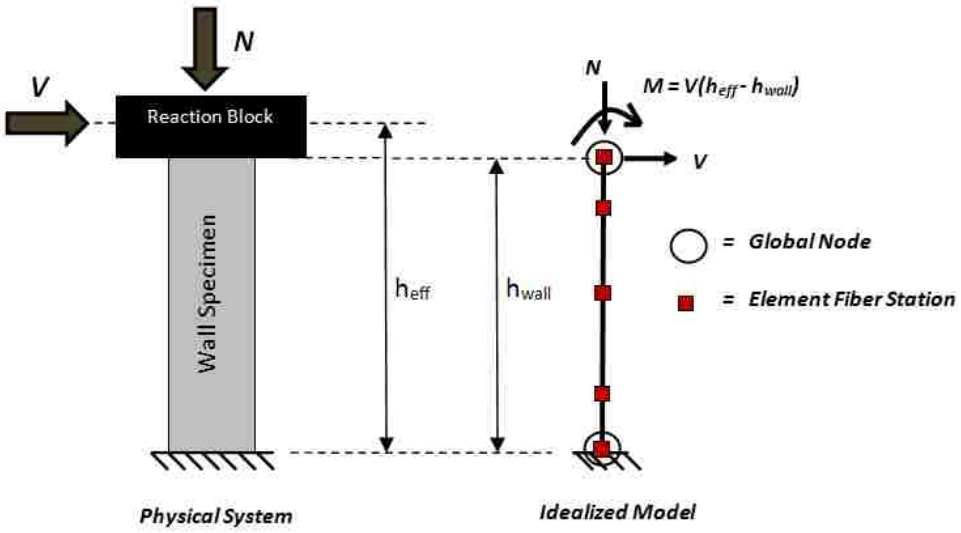

Figure 2.7: Typical Wall Specimen Line Element Model

2.5.1.1 Flexural Response

Wall flexural response was simulated using a fiber-type section model to represent the wall specimen cross-section. Fiber section geometry, including bar locations, confined boundary element regions and cover dimensions, were defined using data reported in the literature. Fiber sections were discretized using 32 fibers across the length of the boundary element, a consistent fiber thickness throughout the web region and a single fiber across the thickness direction. Fiber section discretization studies, used to establish a preferred level of mesh refinement, are presented in Appendix A. The studies confrimed the provided discretization was sufficiently refined to enable accurate and converged simulation of cyclic response.

The OpenSees Concrete02 uniaxial material model was used to model both confined and unconfined concrete fibers. Strength and ductility enhancement of confined concrete fibers were determined using the model developed by Saatcioglu and Razvi (1992). For both unconfined and confined concrete fibers, the strain at peak strength was determined such that the initial material modulus, E_c, was equal to $57000\sqrt{f'_c}$(psi). The Concrete02 model, which defines pre-peak compressive stress-strain response using the Hognestad parabolic relationship:

$$f_c = f'_c(\frac{2\epsilon}{\epsilon_0} - (\frac{\epsilon}{\epsilon_0})^2) \tag{2.1}$$

and, therefore

$$E_c = 2\frac{f'_c}{\epsilon_0} \tag{2.2}$$

yields the following expressions for determining ϵ_0 given an initial modulus, Ec = $57000\sqrt{f'_c}$:

$$\epsilon_{0u} = \frac{2f'_c}{57000\sqrt{f'_c}} \tag{2.3}$$

$$\epsilon_{0c} = \frac{2K_c f'_c}{57000\sqrt{K_c f'_c}} \tag{2.4}$$

where ϵ_{0u} is the strain associated with peak unconfined concrete compressive strength, ϵ_{0c} is the strain associated with peak confined compressive strength, f'$_c$ is the unconfined compressive strength and K$_c$ is the confined concrete strength enhancement factor determined using the Saatcioglu and Razvi model. Concrete tensile strength was taken as $4\sqrt{f'_c}$ (psi) per recommendations by Wong and Vecchio (2006) and tensile stiffness, E$_t$, was taken equal to the initial compressive stiffness, E$_c$. Per recommendations by Yassin (1994), the post-peak tension slope was defined as E$_t$/20. For unconfined fibers, the strain associated with 80% strength loss, ϵ_{20u}, was assumed to be 0.008. For confined fibers, ϵ_{20c} was determined using the softening slope determined by the Saatcioglu and Razvi (1992) confinement model. Compressive strength as reported in the literature was used to define concrete material models. When available, day-of-test compressive strength was used. If day-of-test data was unavailable, reported 28-day strength was used instead. A summary of how Concrete02 material model parameters were defined is provided in Table 2.2.

Table 2.2: Concreteo2 Material Model Parameters

Mat'l Param.	Unconfined	Confined
f$_p$	f'$_c$	K$_c$f'$_c$
ϵ_0	Equation 2.3	Equation 2.4
f$_{20}$	0.20f'$_c$	0.20K$_c$f'$_c$
ϵ_{20}	0.008	Saat. & Razvi Eqn. 14-15
K$_c$	N/A	Saat. & Razvi Eqns. 6-11
f$_t$	$4\sqrt{f'_c}$	$4\sqrt{f'_c}$
E$_t$	E$_c$	E$_c$
E$_{ts}$	0.05E$_t$	0.05E$_t$

The OpenSees Steel02 uniaxial material model was used to model reinforcing steel fibers. This model includes a bi-linear stress-strain envelope with Menegotto-Pinto curves

used to define unloading and reloading cycles; the Menegotto-Pinto curves enable simulation of the Bauschinger effect. Reported yield strength, ultimate strength and rupture strain were used to define initial and post-yield hardening and an elastic modulus of 29000 ksi was assumed. Post-yield hardening was defined as a line through the yield point and a point passing through the stress-strain pair (ϵ_u, f_u), where ϵ_u is the rupture strain of the material and f_u is the tensile strength of material. Although the rupture strain and tensile strength do not occur simultaneously during material testing, this approximation was required due to the bi-linear formulation of the Steel02 model. Default cyclic material model parameters were used for all specimen models. Tensile rupture and compression buckling of the reinforcing were simulated using the OpenSees MinMax wrapper material. When reinforcing tensile strains reached the rupture strain, steel tensile strength was reduced to zero. Likewise for compression, strength loss due to buckling was assumed to occur when compressive strains corresponding to 80$\%$ loss of concrete strength, ϵ_{20}, were reached.

2.5.1.2 Shear Response

A linear effective shear stiffness model was used to simulate the response of the wall in shear. The effective shear stiffness was defined using a reduced shear modulus, G_{eff}, equal to 10$\%$ of the elastic shear modulus, G_c, per the recommendations of Oyen (2006). Shear deformations were included in the force-based element models through the use of the 'section aggregator' function available in OpenSees. The section aggregator enables 'aggregation' of a shear section and flexural section; the aggregated section is then incorporated in the force-based element response. Shear strains at each fiber section are integrated along the element length to determine the shearing deformations within the element. Shear strains were determined using the shear force vs. shear strain relationship:

$$V_s = G_{eff} k_s A_{web} \tag{2.5}$$

Where V_s is the element shear force, k_s is the shear form factor taken as 5/6 for planar specimens and 1.0 for flanged specimens and A_{web} is the specimen web area (Roark and

Young, 1975). Although shear and flexural responses are aggregated using the force-based element, the aggregation merely superposes flexure and shear response and no interaction is considered at the section or element level.

The displacement-based beam column element in OpenSees cannot simulate shear response by using the section aggregator function. For this model, a zero-length shear-spring element was added at the base of the wall specimen to simulate shear deformations in the wall. The use of a single spring was deemed appropriate for the specimen models, because internal shear force is constant along the specimen height for all the model simulations. Shear spring response was determined using the shear force vs. shear deformation relationship:

$$V_s = \frac{G_{eff} k_s A_{web}}{H_{wall}} \tag{2.6}$$

Where all quantities are as defined previously and H_{wall} is the height of the wall specimen.

2.5.1.3 Nonlinear Solution Technique

In conducting analysis of the wall test specimens, a nonlinear solution for each time step was initially attempted using the Newton-Raphson algorithm. A global convergence tolerance on the Relative Energy Increment was assigned a value of 1e-5 and the global convergence tolerance of the force-based element internal solution was assigned a value of 1e-8. If convergence was not achieved during a time step, a solution strategy developed by the author modified solution parameters (nonlinear solver, monitored convergence quantity, global tolerance) until convergence was achieved.

2.5.2 Wall Simulation Results

Wall simulations using beam column elements were performed for each wall specimen using the force-based and displacement-based element models and several meshes for

each model were considered. Improved accuracy for force-based element models, which for most specimens exactly represent the moment distribution up the height of the wall specimens using a single element, is gained by increasing the number of fiber sections along the element length. To study the effects of mesh refinement on force-based element models, a single element mesh was used to model the specimens and 3, 5 and 7 fiber sections, i.e. integration points, were used over the height of the element. Because the accuracy of the displacement-based element model is limited by the assumption of a linear curvature field over the height of the element, an increased number of elements is required to improve simulation of inelastic response and the nonlinear curvature field that develops in regions of inelasticity. To study the effects of mesh refinement on displacement-based element models, element meshes of 2, 4, 8 and 16 elements were analyzed. Five fiber sections were used for each displacement-based element.

Model simulation results are presented in Tables 2.3 - 2.5. In Tables 2.3 - 2.5, ratios of simulated to measured specimen response quantities are reported for both force-based and displacement-based models. Response quantities compared were

1. Model stiffness as determined by the secant stiffness to yield. System yield was defined as the point in the load-displacement response when the theoretical yield moment was achieved at the wall base. The theoretical yield moment was determined using moment-curvature analysis and reported material strengths. The theoretical yield moment was defined as the flexural strength when the extreme tensile layer of reinforcement reached the reported yield stress.

2. Peak strength in terms of maximum simulated base shear.

3. Ultimate drift, defined as the drift level at which the lateral load carrying capacity of the wall dropped to 80% of the historic maximum, for drift demands in excess of historic drift demands.

Tables 2.3 - 2.5 present response quantity ratios for wall specimens separated by failure type. Tables 2.3 - 2.4 present results for tension-controlled walls with simulation results for

the two specimens which failed due to tension rupture provided in Table 2.3 and simulation results for the 7 specimens which failed due to tension rupture occurring after significant buckling had occurred. Table 2.5 provides simulation results for the 12 specimens which were compression-controlled and failed due to concrete crushing or buckling of longitudinal reinforcement.

Data from Tables 2.3 - 2.5 demonstrate that:

1. Accurate simulation of wall specimen stiffness was achieved by both force-based and displacement-based models and the simulation accuracy was unaffected by the selected mesh. For all 21 specimens, a mean simulated stiffness ratio of 1.01 (coefficient of variation = 0.12) was calculated for displacement-based models and a mean simulated stiffness ratio of 0.99 (COV = 0.11) was calculated using force-based models.

2. Accurate simulation of wall specimen strength was achieved by both force-based and displacement-based models, although the simulated strength of displacement-based models was affected by the selected mesh. Strength ratios of 1.06, 1.03 and 1.01 were calculated for displacement-based models using 4, 8 and 16 element models. Force based element models were unaffected by the selected mesh with strength ratios of 0.97, 0.99 and 0.99 calculated for 3, 5 and 7 fiber section models.

3. Drift capacity was most accurately simulated for the two specimens failing due to tensile rupture, prior to singificant buckling, using force-based models and seven fiber sections. For these two specimens, the mean simulated to observed drift capacity ratio was 1.00 with a coefficient of variation = 0.29. For the seven fiber section model, drift capacity of the WSH1 specimen was underpredicted by 20% while being overpredicted by 20% for the WSH1 specimen. Three and five fiber section model mean drift capacity ratios for these two specimens were 2.39 (COV = 0.10) and 1.20 (COV = 0.14), respectively. Simulated to observed drift capacity ratios for the displacement-based element models were 3.12, 1.95 and 1.46 for 4, 8 and 16 element models, respectively.

4. For the seven tension-controlled wall specimens which failed due to steel rupture after significant buckling occurred, mean drift capacity was overpredicted by both force-based and displacement-based models. The most accurate simulation of drift capacity was provided by the seven fiber section force-based model, for which mean drift capacity was overpredicted by 54% (COV = 0.64). For force-based element models, significant mesh dependency was observed with mean drift capacity ratios of 2.63 and 1.62 determined for three and five fiber section models, respectively. Similarly, displacement-based element drift capacity simulation results were sensitive to the selected mesh, with mean drift ratios of 3.01, 2.35 and 1.93 determined for element meshes of 4, 8 and 16, respectively. For both force-based and displacement-based models, the coefficient of variation increased significantly as the selected mesh increased. For force-based elements, coefficients of variation increased from 0.21 to 0.64 for three and seven fiber section models; an increase from 0.25 to 0.50 was calculated for displacement-based models. It is suspected that the overprediction of drift capacity for specimens failing in tension after buckling (mean ratio = 1.54) compared to simulations for specimens failing in tension prior to significant buckling (mean ratio = 1.00) is due to the fact that reinforcing strength and ductility deterioration due to buckling was not accounted for in any of the simulation models.

5. For the 12 compression-controlled wall specimens, mean drift capacity was overpredicted by both force-based and displacement-based models but not as severly as for rupture/buckling specimens. The most accurate simulation of drift capacity for the compression-controlled specimens was provided by the seven fiber section force-based model, for which mean specimen drift capacity was overpredicted by 24%. However, the coefficient of variation for these simulations was approximately 0.70, indicating a significant scatter in the simulated drift capacity. Specifically, drift capacity of specimen PW2 was accurately simulated (drift capacity ratio = 1.00), but drift capacity ratios less than 0.65 were calculated for 5 of the 12 specimens. Load displacement plots for the PW2 and WSH4 specimens are provided in Figure 2.8. Displacement-based models simulate higher drift capacity for

the compression-controlled specimens than the force-based models. Displacement-based model mean simulated to observed drift capacity ratios were calculated to be 2.79, 2.00 and 1.57 for 4, 8 and 16 element models, respectively.

6. Drift capacity for the specimens appears to slowly converge, with significant mesh dependency existing even for 7-section force-based element models and 16-element displacement-based element models. However, the inability of the models to simulate drift capacity accurately for the specimens is not due to the slow convergence of the model. This can be demonstrated by the fact that for 10 of the 21 specimens, the most refined models considered in this study simulated a drift capacity less than observed experimentally. For 5 of the 21 specimens, the simulated drift capacity was less than 45% of the experimentally determined drift capacity. Further mesh refinement for these models would be expected to either maintain or increase errors in simulated drift capacity for these specimens.

7. Comparison of wall simulation results with cyclic moment-curvature analyses performed for each specimen base section identified the trend that wall sections that experience strength loss prior to failure, i.e. - strength loss occurs gradually due to deteriorating compressive response rather than suddenly due to tensile rupture, exhibit a larger mesh dependency and significantly underpredict specimen drift capacity. For the 10 sections exhibiting softening prior to failure, increasing the force-based element mesh from 5- to 7-fiber section decreased mean simulated drift capacity by 25%. For the 11 sections which hardening prior to failure, increasing the mesh from 5- to 7-sections decreased mean simulated drift capacity by 1.3%. The mean simulated to observed drift capacity ratio for softening sections was 0.64 (COV = 0.48), which confirms that drift capacity was underpredicted for these specimens. The mean simulated to observed drift capacity ratio for hardening sections was calculated to be 2.03 (COV = 0.63). These results suggest that the basic distributed-plasticity model can not accurately simulate drift capacity for both softening and hardening sections. Cyclic moment-curvature results for the wall specimens are provided in Appendix A.

In addition to tabular data, Figure 2.9 provides cyclic load displacement results for four specimens exhibiting different failure modes. Figures 2.9(a) and (d) present load displacement curves for two specimens observed to fail due to crushing/buckling. For these specimens, the provided plots demonstrate that model refinement significantly reduces the simulated drift capacity; for these specimens, the 3IP overestimated the observed specimen drift capacity while both 5IP and 7IP meshes severely underestimated the observed drift capacity. Figure 2.9(b) presents simulated load displacement curves for a specimen observed to fail due to steel rupture prior to buckling. For this specimen, the 3IP mesh overestimated the observed drift capacity by approximately 240%. However, the 5IP mesh accurately simulated the observed drift capacity while the 7IP mesh underestimates the observed drift capacity by 20%. These results indicate that mesh dependency exists for the distributed-plasticity element model even for simulation of tension-controlled wall specimens. However, simulation of these specimens appear to be less sensitive to the selected mesh when at least 5 integration points are used to define the mesh. Finally, Figure 2.9(c) presents load displacement results for a specimen observed to fail due to steel rupture after significant buckling has occurred. For this specimen, the 5IP model significantly overestimated drift capacity while both 5IP and 7IP meshes simulated drift capacity within 10% of the observed drift capacity. These results also suggest that simulation of BR specimens can be improved as long as a minimum of 5 integration points are used for the model. However, as demonstrated in Table 2.4, the use of at least 5 integration points does not always guarantee that accurate simulation of drift capacity can be obtained for wall specimens observed to buckle then rupture.

Table 2.3: Basic Model Simulation Results (Rupture Failures)

Specimen	Displacement-Based									Force-Based								
	$\frac{k_{y,sim}}{k_{y,obs}}$			$\frac{V_{bm,sim}}{V_{bm,obs}}$			$\frac{\Delta_{u,sim}}{\Delta_{u,obs}}$			$\frac{k_{y,sim}}{k_{y,obs}}$			$\frac{V_{bm,sim}}{V_{bm,obs}}$			$\frac{\Delta_{u,sim}}{\Delta_{u,obs}}$		
	4 EL	8 EL	16 EL	4 EL	8 EL	16 EL	4 EL	8 EL	16 EL	3 IP	5 IP	7 IP	3 IP	5 IP	7 IP	3 IP	5 IP	7 IP
WSH1	1.00	1.00	1.00	1.05	1.01	1.00	3.36	1.95	1.39	0.98	0.99	1.00	0.94	0.97	0.97	2.56	1.08	0.79
PW1	0.99	0.99	0.99	1.06	1.04	1.03	2.88	1.95	1.53	0.98	0.99	0.99	1.00	1.01	1.01	2.22	1.31	1.20
Mean	0.99	1.00	0.99	1.06	1.02	1.01	3.12	1.95	1.46	0.98	0.99	0.99	0.97	0.99	0.99	2.39	1.20	1.00
COV	0.00	0.01	0.00	0.00	0.02	0.02	0.11	0.00	0.07	0.00	0.00	0.00	0.04	0.03	0.03	0.10	0.14	0.29

Table 2.4: Basic Model Simulation Results (BR Failures)

Specimen	Displacement-Based									Force-Based								
	$\frac{k_{y,sim}}{k_{y,obs}}$			$\frac{V_{bm,sim}}{V_{bm,obs}}$			$\frac{\Delta_{u,sim}}{\Delta_{u,obs}}$			$\frac{k_{y,sim}}{k_{y,obs}}$			$\frac{V_{bm,sim}}{V_{bm,obs}}$			$\frac{\Delta_{u,sim}}{\Delta_{u,obs}}$		
	4 EL	8 EL	16 EL	4 EL	8 EL	16 EL	4 EL	8 EL	16 EL	3 IP	5 IP	7 IP	3 IP	5 IP	7 IP	3 IP	5 IP	7 IP
WSH2	1.00	1.00	1.00	0.98	0.95	0.94	3.42	2.00	1.40	1.00	0.98	1.00	0.88	0.93	0.93	2.57	0.98	0.84
WSH3	0.97	0.96	0.96	1.00	0.96	0.95	2.67	1.70	1.20	0.99	0.95	0.95	0.90	0.93	0.94	2.42	0.92	0.72
WSH5	0.82	0.81	0.81	1.01	0.96	0.94	1.75	1.14	0.72	0.78	0.80	0.80	0.90	0.91	0.91	1.66	0.66	0.47
W2	1.20	1.16	1.14	1.10	1.07	1.07	4.12	3.38	2.71	1.08	1.11	1.12	0.98	1.07	1.06	2.75	2.01	2.11
RW1	1.12	1.11	1.10	1.02	0.99	0.99	2.85	1.98	1.48	1.06	1.08	1.09	0.91	0.98	0.97	2.76	1.11	1.10
R1	0.96	0.97	0.96	1.13	1.10	1.09	3.48	3.48	3.22	0.88	1.00	0.94	1.04	1.05	1.05	3.47	2.93	2.82
R2	1.17	1.14	1.13	1.17	1.14	1.14	2.77	2.77	2.77	1.09	1.11	1.12	1.10	1.11	1.11	2.77	2.71	2.68
Mean	1.03	1.02	1.01	1.06	1.03	1.02	3.01	2.35	1.93	0.98	1.00	1.00	0.96	1.00	1.00	2.63	1.62	1.54
COV	0.13	0.12	0.12	0.07	0.07	0.08	0.25	0.38	0.50	0.12	0.11	0.12	0.09	0.08	0.08	0.21	0.57	0.64

Table 2.5: Basic Model Simulation Results (CB Failures)

Specimen	Displacement-Based									Force-Based								
	$\frac{k_{y,sim}}{k_{y,obs}}$			$\frac{V_{bm,sim}}{V_{bm,obs}}$			$\frac{\Delta_{u,sim}}{\Delta_{u,obs}}$			$\frac{k_{y,sim}}{k_{y,obs}}$			$\frac{V_{bm,sim}}{V_{bm,obs}}$			$\frac{\Delta_{u,sim}}{\Delta_{u,obs}}$		
	4 EL	8 EL	16 EL	4 EL	8 EL	16 EL	4 EL	8 EL	16 EL	3 IP	5 IP	7 IP	3 IP	5 IP	7 IP	3 IP	5 IP	7 IP
WSH4	0.98	0.98	0.97	1.05	1.00	0.97	1.54	0.94	0.62	0.99	0.97	0.97	0.93	0.94	0.94	1.27	0.57	0.44
WSH6	0.89	0.89	0.89	0.98	0.95	0.93	2.68	1.74	1.19	0.88	0.89	0.89	0.89	0.91	0.91	2.58	0.95	0.65
W1	1.22	1.18	1.17	1.11	1.06	1.05	3.86	2.69	2.18	1.12	1.16	1.17	0.98	1.05	1.04	2.69	1.62	1.64
PW2	1.01	1.00	1.00	1.04	1.01	0.99	3.00	1.89	1.38	0.99	1.00	1.00	0.96	0.98	0.98	2.33	1.13	1.00
PW3	0.87	0.87	0.87	1.02	1.00	0.99	4.51	3.43	2.87	0.87	0.87	0.87	0.96	0.98	0.98	4.10	2.46	2.36
PW4	1.05	1.05	1.05	1.28	1.24	1.23	4.93	3.77	3.24	1.04	1.04	1.04	1.20	1.20	1.21	3.48	2.88	2.81
RW2	1.17	1.13	1.12	0.94	0.92	0.92	3.19	2.25	1.76	1.06	1.10	1.11	0.84	0.92	0.91	3.07	1.38	1.38
S5	0.84	0.84	0.84	1.12	1.09	1.07	2.25	1.78	1.53	0.84	0.84	0.84	1.05	1.05	1.06	1.77	1.44	1.43
S6	0.88	0.88	0.88	1.18	1.15	1.14	3.34	2.66	2.26	0.88	0.88	0.88	1.11	1.11	1.12	2.62	2.13	2.13
WR20	1.05	1.01	1.01	0.97	0.93	0.92	1.37	0.80	0.52	1.01	1.00	1.01	0.89	0.90	0.90	1.25	0.47	0.31
WR10	1.15	1.09	1.09	0.99	0.95	0.94	1.93	1.35	0.80	1.06	1.08	1.08	0.91	0.92	0.92	1.86	0.79	0.46
WR0	1.18	1.16	1.12	0.99	0.96	0.94	0.92	0.56	0.39	1.09	1.11	1.10	0.91	0.92	0.92	0.76	0.34	0.27
Mean	1.03	1.01	1.00	1.06	1.02	1.01	2.79	1.99	1.57	0.99	0.99	0.99	0.97	0.99	0.99	2.31	1.35	1.24
COV	0.13	0.12	0.11	0.09	0.09	0.09	0.45	0.51	0.60	0.10	0.11	0.11	0.11	0.10	0.10	0.42	0.60	0.70

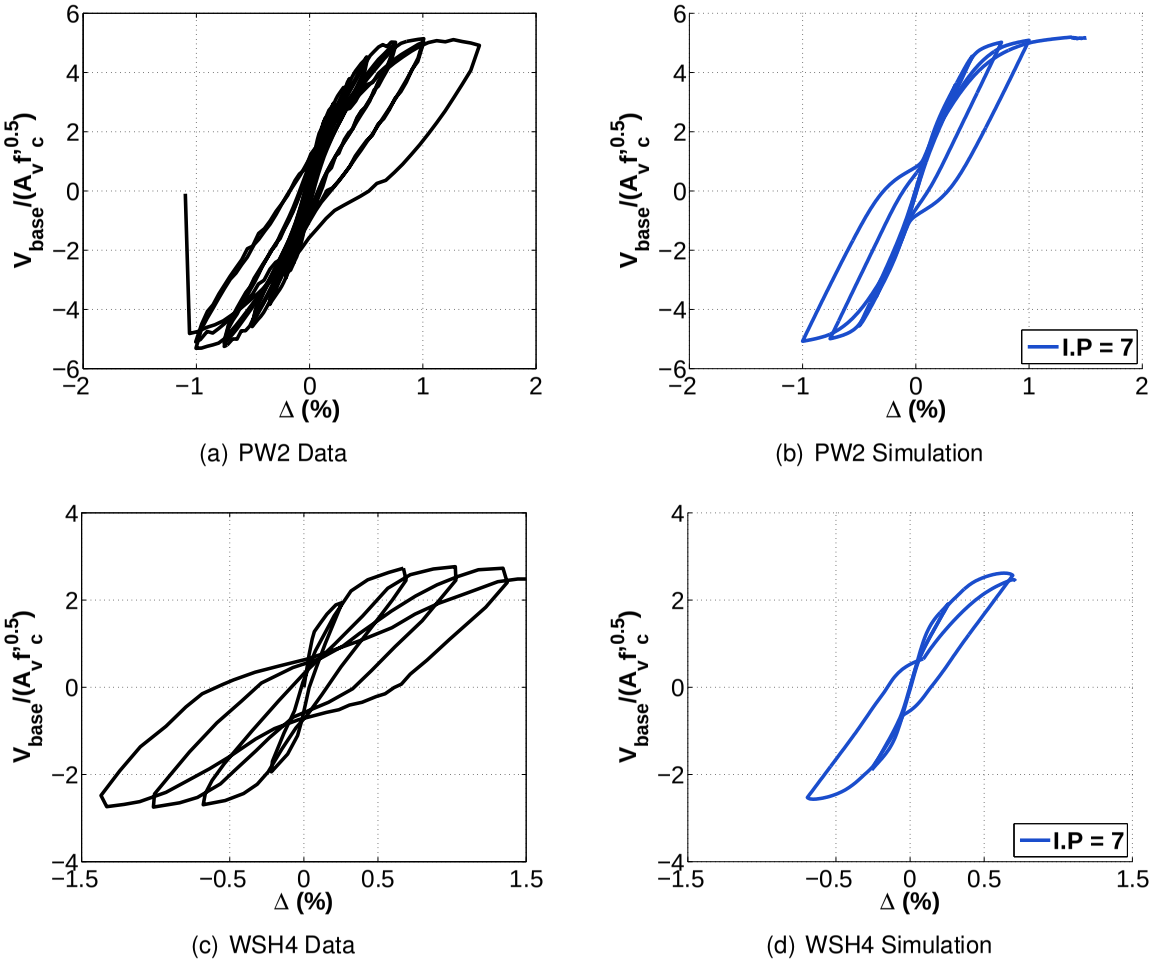

(a) PW2 Data (b) PW2 Simulation

(c) WSH4 Data (d) WSH4 Simulation

Figure 2.8: Force-Based Simulation Results (7-section)

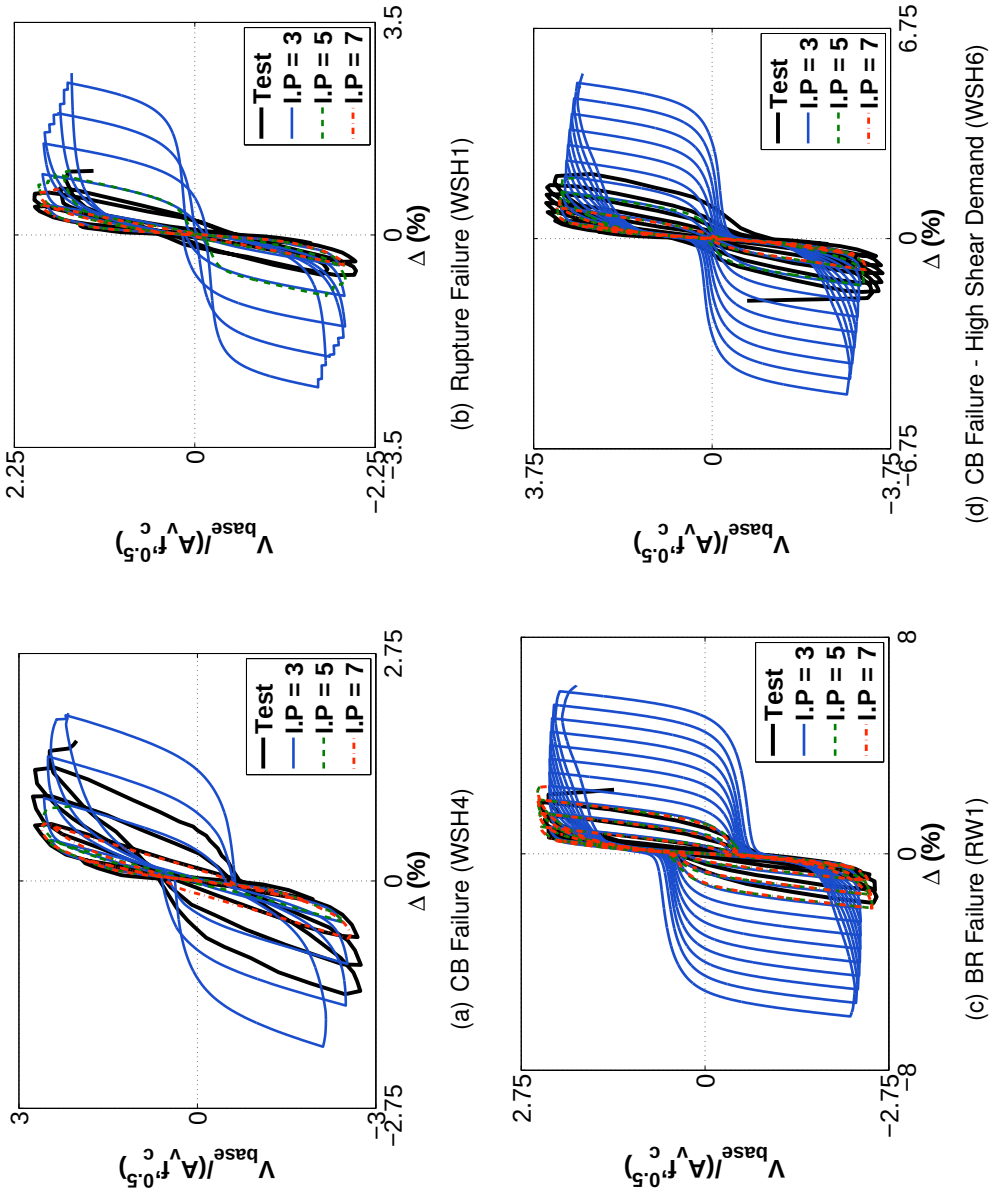

(a) CB Failure (WSH4)

(b) Rupture Failure (WSH1)

(c) BR Failure (RW1)

(d) CB Failure - High Shear Demand (WSH6)

Figure 2.9: Specimen Load Displacement Curves

2.5.2.1 Comments on Basic Model Simulation Results

Simulated to observed response comparison identified that wall stiffness and strength can be accurately predicted using both force-based and displacement-based element models but the models exhibit significantly larger variability for simulating drift capacity for both tension-controlled and compression-controlled specimens, depending on whether critical section behavior exhibits gradual softening or hardens prior to failure. To investigate this behavior, Figure 2.10 shows, for the force-based element model, the simulated curvature profiles up the height of the wall at two drift demand levels for wall specimen WSH4:

1. Δ = 0.30% (Just beyond yield of the longitudinal reinforcement in all three models)

2. Δ = 1.73% (Just following the onset of strength loss in the 3-section model)

The data in Figure 2.10 shows that mesh sensitivity in simulated drift capacity results from localization of deformations at the wall base critical section. This behavior can be identified by comparing the simulated curvature distributions at the two drift levels shown in Figure 2.10. In Figure 2.10, curvature diagrams are normalized by the base curvature demand simulated using the 7-fiber section model, i.e. the most highly refined mesh considered in the current study. At a drift of 0.30% (Figure 2.10(a)), the base curvature demand was found to be nearly identical for all three meshes. Slightly larger demands were predicted for the 3-section model, but this difference is due to the coarse sampling of fiber sections; when additional sections are added base curvature demands converge, which can be seen by comparing base curvature demands results for the 5- and 7-section models. At the onset of softening in the 3-section model (Figure 2.10(b)), it can be seen that severe localization has occurred for the 5- and 7-section models. Comparison of drift histories ((Figure 2.10(c) and (d)) confirms the localization of nonlinear response is associated with softening behavior. The localization occurs because the 5- and 7-fiber section models simulate a significantly more rapid strength loss and both models failed prior to achieving the drift level (1.73%) achieved by the 3-section model.

This localization of deformation is unique to softening systems and occurs because strength loss at a single critical section results in increased deformation at the softening

section and elastic unloading, and thus reduced deformation, at the other sections. Increased deformations at the softening section are linked to global system displacements by the integration weight (length) associated with the critical section. This length is defined by the mesh. Increased mesh density leads to a reduction in the integration length attributed to the critical section; reduction in the critical integration length causes larger curvature demands to develop at the softening section and the rapid accumulation of inelastic curvature demands at the critical section causes increasingly brittle softening response simulated by the model. Regularization methods discussed previously by Coleman and Spacone (2001) address this behavior by defining the softening portion of the material stress-strain curve using a mesh-dependent element characteristic length used commonly in continuum mechanics. For beam column line elements, this length is the integration weight of the fiber section. Regularization methods were applied to the distributed-plasticity element wall models and results of these analyses are discussed in Chapter 3.

For hardening systems increased deformation at the critical section is accompanied by increased strength, which results in the spread of yielding and increased load and deformation at other sections. Thus, regularization techniques are not needed for systems that harden until failure, such as steel beams and columns and concrete beams). However, as noted in Table 2.1, a significant number of tested concrete wall specimens exhibit a softening-type response at larger drift demands because response at these drift levels is determined by concrete crushing.

The potential for distributed plasticity beam-column elements to exhibit mesh-sensitivity due to localization of deformations at a single softening section has been identified previously (Coleman and Spacone, 2001). However, to date, distributed plasticity elements have been used primarily to simulate the response of concrete and steel beams and columns that exhibit a hardening-type response out to large drift demands. Typically, failure of these components is either not simulated, with system failure defined via post-processing of analysis results (Berry 2006), or is simulated via steel fracture in tension, in which case the critical section exhibits catastophic strength loss and further tracking of the softened response is immaterial. Figure 2.11 shows simulated response histories for a reinforced concrete column tested by Tanaka et al. (1990) exhibiting a tension-controlled flexural

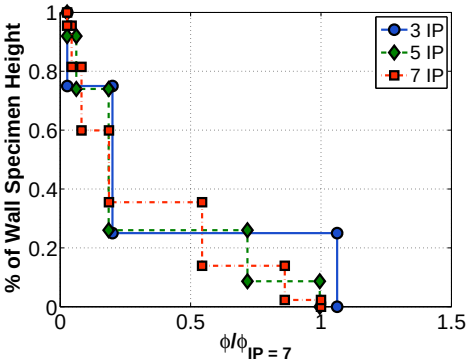

(a) ϕ Diagram (Δ = 0.30%)

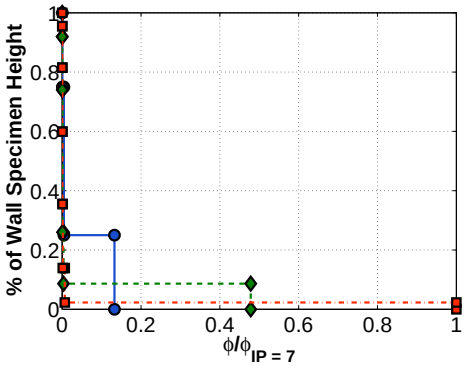

(b) ϕ Diagram (Δ = 1.73%)

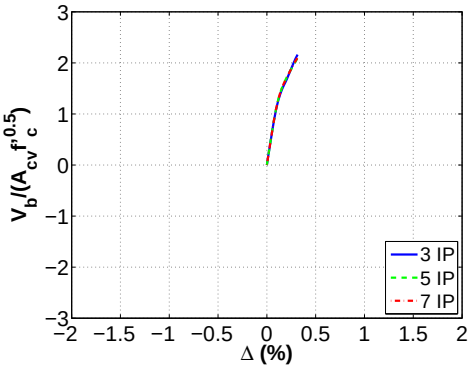

(c) Drift History (Δ = 0.30%)

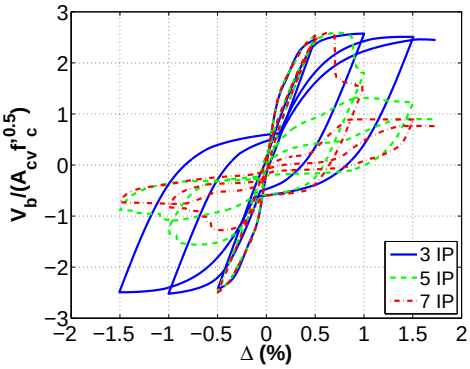

(d) Drift History (Δ = 1.73%)

Figure 2.10: Local Demand Profiles (WSH4 Specimen Model)

response; strength loss results from fracture of the longitudinal reinforcement and no significant mesh-sensitivity in the simulated results was observed.

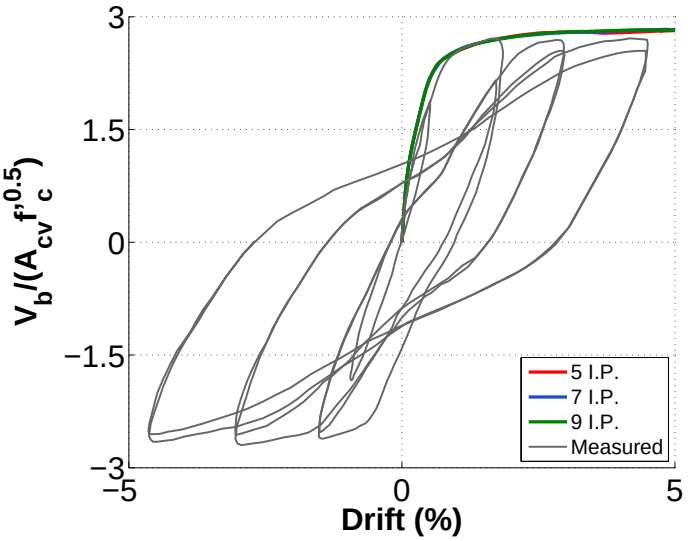

Figure 2.11: Hardening Column Specimen (Specimen S5, Tanaka et al.)

Beyond showing mesh-sensitive drift capacity results, the data in Tables 2.3 - 2.5 also show that maximum strength predicted using the displacement-based converges slowly and requires a significant number of elements to accurately simulate laboratory results. This is unexpected given that model strength is defined by the fiber-section flexural response which is identical for all model meshes considered. A closer look at the results reveals the extreme variability in the axial load distribution within the displacement-based element model (Figure 2.12). These data show that at a low level of mesh refinement (4 elements) simulated axial load at a section that varies between 40% and 160% of the applied constant axial load and that even for a highly refined mesh (32 elements) simulated axial load at a section varies between 75% and 110% of the applied constant axial load. For the displacement-based element formulation, this variation in axial load at the section occurs despite the fact that the resultant axial load for the element is equal (within the solution tolerance) to the globally applied axial load. This is due to the fact the displacement-based element formulation assumes a constant axial strain at each section along the length of the

element and that equilibrium is satisfied on average within the element. Since axial load at the section level affects the flexural strength of the section, the variation in axial load along the length of the element results in variation in element flexural and shear strength. While increasing the number of elements reduces the section-level variation in axial load, axial load variation for practical levels of mesh refinement (i.e. - 12 to 16 elements) was found to be sufficiently large that it affected modeling recommendations and simulation results discussed in Chapter 3.

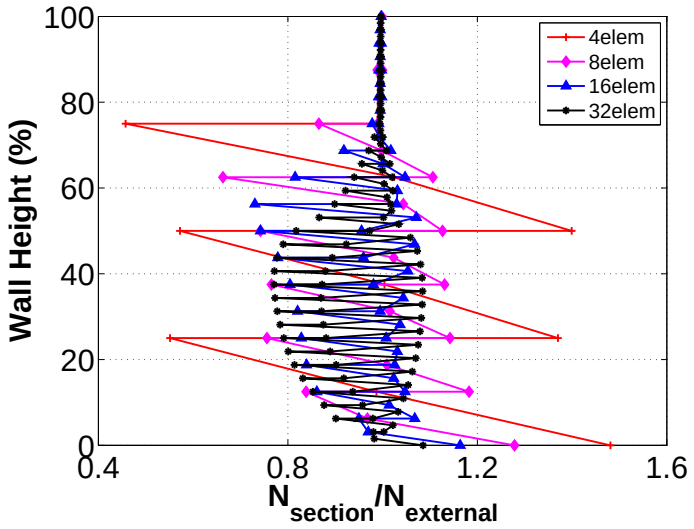

Figure 2.12: Ratio of Simulated Section Axial Load to Constant Applied Axial Load

2.6 Simulating Wall Response Using Plane Stress Elements and the Modified Compression Field Theory

In this section, the wall specimens previously used to assess line element models are used to assess the accuracy which the VecTor2 software program, which uses plane stress elements and constitutive relationships based on the Modified Compression Field Theory (MCFT), simulate measured wall response. The use of the VecTor2 software allows simulation of wall response that is free from kinematic and constitutive limitations inherent in line element models. Such limitations include 1) the use of plane-section kinematics, 2)

the uncoupling of flexure and shear response and 3) the use of uniaxial material models. In contrast, the VecTor2 software uses 1) rectangular plane-stress elements which account for transverse, longitudinal and shearing strain components, 2) MCFT constitutive relationships which account for smeared cracking and re-orientation of principal stress and strain directions due to shearing deformations and 3) material models for concrete which account for enhanced strength and ductility due to both bi-axial and tri-axial strain states.

To develop plane stress element models using VecTor2, all specimen models were meshed to represent a single cantilever extending vertically above a fixed base using an orthogonal grid of rectangular plane stress elements. Horizontal and longitudinal reinforcement were modeled as smeared throughout the plane stress element mesh (i.e. - bars were not modeled as discrete elements). Smeared out-of-plane reinforcement was assigned to the edge wall elements to account for beneficial confinement effects expected to develop in the well-confined boundary element regions. Specimen foundation and top reaction blocks were modeled using elastic plane stress elements and the foundation base was assigned full fixity. Two load cases were applied to each specimen: 1) axial load comprising the external axial load applied to the specimen as well as self-weight and 2) a horizontal shear force applied at the specimen effective loading height. Axial load was applied as a uniform pressure load distributed equally to the row of nodes located at the top of the specimen. The uniform axial pressure load was applied prior to the application of lateral loading and the axial load remained constant for the duration of the analysis. The horizontal shear force was applied as a uniform displacement boundary condition applied to the row of nodes located at the top of the specimen. For monotonic analysis, increasing horizontal displacement was prescribed to the top boundary nodes until failure of the specimen occurred. For cyclic analyses, the displacement boundary condition was varied cyclically to match the drift history applied experimentally to each wall specimen. Pre-defined cyclic load history patterns can be defined using VecTor2 model input files, however these patterns were typically incapable of exactly matching the drift histories applied to the specimens. To overcome this limitation, MATLAB scripts developed by the author were used to drive the VecTor2 solution and ensure the desired displacement history was applied to the specimens. For the VecTor2 model assessment discussed in this chapter, several levels of

mesh refinement were considered. For each mesh, element aspect ratios were maintained as close to one as possible. For each specimen, meshes of 2, 3 and 4 plane stress elements across the length of the heavily reinforced and/or well-confined boundary element region were considered (Figure 2.13). A mesh of 2 elements across the boundary element length generally satisfied shear wall meshing recommendations provided by the VecTor2 development group (Palermo and Vecchio, 2009). Increasingly denser meshes were considered to investigate the impact that the selected model mesh and element size has on the simulated response quantities for cyclically loaded slender walls.

Addition modeling parameters required to completely define the specimen models are provided in Table 2.6. The parameters selected represent either 1) recommended parameters for shear modeling provided by the VecTor2 development group (Palermo and Vecchio, 2009) or 2) VecTor2 program default values (Wong and Vecchio, 2006). Brief definitions for the modeling parameters listed in Table 2.6 are

- Pre-peak curve = envelope curve defining the pre-peak concrete compressive response.

- Post-peak curve = envelope curve defining the post-peak concrete compressive response.

- Compression Softening Model = relationship used to define the influence of tensile strain perpendicular to the principal compressive strain direction on concrete compressive response.

- Confinement - relationship used to determine principal concrete compressive strength and strain enhancement due to co-existing bi-axial and tri-axial strain states.

- Concrete cyclic model - relationship used to determined unloading and reloading rules for concrete and transition curves between concrete reloading from tension to compressive.

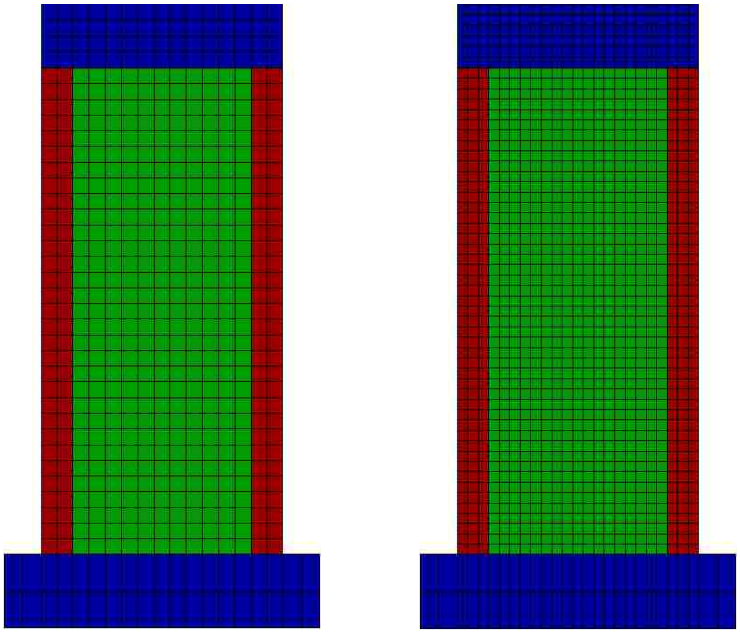

(a) 2 Elem per BE

(b) 3 Elem per BE

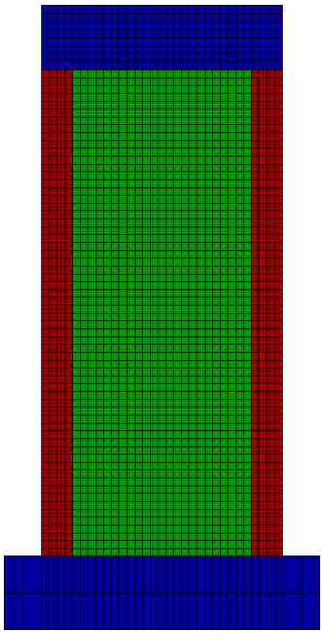

(c) 4 Elem per BE

Figure 2.13: VecTor2 Mesh Refinement (WSH4 Specimen)

- Tension Stiffening - relationship defining the post-cracking tensile response of concrete including the influence of smeared reinforcing bars.

- Tension Softening - relationship defininining the post-cracking energy for concrete tensile response based on fracture energy regularization.

- Cracking criterion - relationship defining the strain state at which concrete cracking occurs.

- Tension Splitting - relationship for concrete exhibiting a splitting failure at the bar interface. Requires explicit modeling of reinforcing bars; not compatible with smeared reinforcing.

- Dilatation - relationship for lateral expansion based on the existing two-dimensional strain state within the element.

- Steel Modeling - selection for either modeling steel as smeared within the concrete elements or modeled explicitly as truss elements between concrete elements. Smeared steel modeling was used for all models discussed in this thesis.

- Cyclic steel model - relationship used to determined unloading and reloading rules for reinforcing steel.

- Buckling - relationship used to simulate buckling of explicitly modeled steel reinforcing.

- Dowel Action - relationship used to define dowel strength of reinforcing and rate of slip deformation.

- Bond Model - relationship defining the development of bond stress between concrete and explicitly model reinforcing steel bars.

- MCFT/DSFM - user can select use of disturbed stress field model instead of classic MCFT kinematics. DSFM allows for calculation of additional shearing deformations due to slip along crack surfaces.

- Crack Shear - check used in MCFT to ensure equilibrium can be maintained along cracked concrete surfaces within concrete elements with smeared reinforcement.

- Crack Width - relationship used to define shear transfer strength along crack surfaces. Shear stress transferred along the crack surface decreases as crack width increases.

- NL Geometry - allows the inclusion of geometric nonlinearities. Only allowed for quadrilateral element meshes.

- Step Averaging - defines the weighting of current and previous solution steps which determine advancement of the explicit solution technique used by VecTor2.

- Convergence - criteria used to determine whether the current solution step has converged.

2.6.1 Wall Simulation Results

Simulation results for the VecTor2 models are provided in Tables 2.7 - 2.9. In Tables 2.7 - 2.9, ratios of simulated to measured specimen response quantities are compared for models using increasingly denser element meshes. As for the line element, the response quantities compared were

1. Model stiffness as determined by the secant stiffness to yield. System yield was defined as the point in the load-displacement response when the theoretical yield moment was achieved at the wall base. The theoretical yield moment was determined using moment-curvature analysis and reported material strengths. The theoretical yield moment was defined as the flexural strength when the extreme tensile layer of reinforcement reached the reported yield stress.

Table 2.6: VecTor2 Modeling Parameters

Concrete Constitutive Model			Steel Constitutive Model			General Modeling Options		
Parameter	Option Selected	Default (Y/N)	Parameter	Option Selected	Default (Y/N)	Parameter	Option Selected	Default (Y/N)
Pre-Peak Curve	Hognestad	Y	Steel Modeling	Smeared	Y	MCFT/DSFM	MCFT	Y
Post-Peak Curve	Mod. Park-Kent	Y	Cyclic Model	Seckin	Y	Crack Shear	Vecchio-Collins (1986)	Y
Comp. Softening	Vecchio (1992-A)	Y	Buckling	N/A[1]	Y	Crack Width	100% of Agg. Size	Y
Confinement	Kupfer/Richart	Y	Dowel Action	N/A[2]	Y	NL Geometry	Not Considered	Y
Cyclic Model	Decay (Palermo)	N	Bond Model	N/A[1]	Y	Step Averaging	0.500	Y
Tension Stiffening	Mod. Bentz (2003)	Y				Convergence	Weighted Disp.	Y
Tension Softening	Linear	Y						
Cracking Criterion	Uniaxial	Y						
Tension Splitting	N/A[1]	Y						
Dilatation	Variable-Kupfer	Y						

[1] Requires discrete bar modeling

[2] Requires DSFM

2. Peak strength in terms of maximum simulated base shear.

3. Ultimate drift, defined as the drift level at which the lateral load carrying capacity of the wall dropped to 80% of the historic maximum, for drift demands in excess of historic drift demands.

Tables 2.7 - 2.9 present statistics for simulated response quantities for the 21 specimens, for three levels of mesh refinement and separated by the observed specimen failure type. Tables 2.7 - 2.8 present results for tension-controlled walls with simulation results for the two specimens which failed due to tension rupture provided in Table 2.7 and simulation results for the 7 specimens which failed due to tension rupture occurring after significant buckling had occurred. Table 2.9 provides simulation results for the 12 specimens which were compression-controlled and failed due to concrete crushing or buckling of longitudinal reinforcement. Data from Tables 2.3- 2.5 demonstrate that

1. The VecTor2 models adequately simulated maximum strength with mean ratio of observed strength ranging from 1.08 for the coarse mesh to 1.01 for the fine mesh and coefficients of variation of 0.10 and 0.06, respectively. For specimens exhibiting tension-controlled failures, increasing the element size from 2-elements per boundary element to 4-elements per boundary element improved the mean strength ratio from 1.12 (COV = 0.12) to 1.03 (COV = 0.06).

2. Simulated stiffness was generally higher than measured experimentally. For all 21 specimens, the mean ratio of simulated to observed stiffness was 1.12 with a coefficient of variation of 0.08. Stiffness statistics were essentially independent of the selected element size. It should be noted that in a previous study by Palermo (2006) in which VecTor2 was used to simulate wall response, models were ‘pre-cracked’ to simulate shrinkage cracking in the laboratory. The pre-cracking allowed improved estimates of yield stiffness although no rationale for the amount of pre-cracking applied to each model was provided by Palermo.

3. Drift capacity simulation results were found to be significantly dependent on the selected element size. For tension-controlled walls, simulated to observed drift capacity ratios ranged from 2.73 to 2.03 for 2-element and 4-element meshes. For compression-controlled walls, drift capacity ratios ranged from 1.82 to 1.38 for 2-element and 4-element meshes. Increasingly refined element meshes (i.e. - smaller element sizes) predicted reduced drift capacity with more rapid strength loss. This general behavior is shown for two of the wall specimens in Figure 2.14. Similar behavior was found for 15 of the 21 slender wall specimens considered, the other four specimens exhibited similar trends when comparing 2-element and 3-element results but 4-element simulations resulted in a higher simulated drift capacity. Simulated load-displacement plots for all specimen models are provided in Appendix B.

4. Full cyclic analyses of several specimens were performed to compare simulated drift capacity, for a given element size, with experimental observed drift capacity and to assess the impact that cyclic loading has on the simulated yield drift. Figure 2.15 presents cyclic analysis results for two specimens that exhibited compression controlled (crushing) flexural failures, PW2 and RW2, considering a mesh generated using 3 elements across the boundary element. VecTor2 cyclic analyses were unable to accurately simulate strength loss at a drift level consistent with the experimental data. VecTor2 analysis overpredicted the drift capacity of PW2 by approximately 50$\%$. Cyclic analysis of RW2 was stopped at a drift approximately equal to 180$\%$ of the experimentally determined drift capacity. Similar results were determined for other specimens suggesting significant uncertainty in using the VecTor2 program to accurately detect strength loss of slender walls. Comparison of yield stiffness from montonic and cyclic simulations indicated that cyclic loading did not signficantly affect the simulated stiffness for drift values near the theoretical yield point.

Table 2.7: VecTor2 Model Simulation Results (Rupture Failures)

Specimen	VecTor2 (MCFT)								
	$\frac{k_{y,sim}}{k_{y,obs}}$			$\frac{V_{bm,sim}}{V_{bm,obs}}$			$\frac{\Delta_{u,sim}}{\Delta_{u,obs}}$		
	2 EL	3 EL	4 EL	2 EL	3 EL	4 EL	2 EL	3 EL	4 EL
WSH1	1.17	1.17	1.09	1.03	1.02	1.01	0.82	0.69	0.75
PW1	1.19	1.17	1.16	1.11	1.08	1.03	4.63	4.76	4.90
Mean	1.18	1.17	1.13	1.07	1.05	1.02	2.73	2.73	2.82
COV	0.01	0.00	0.04	0.05	0.04	0.01	0.98	1.05	1.04

Table 2.8: VecTor2 Model Simulation Results (BR Failures)

Specimen	VecTor2 (MCFT)								
	$\frac{k_{y,sim}}{k_{y,obs}}$			$\frac{V_{bm,sim}}{V_{bm,obs}}$			$\frac{\Delta_{u,sim}}{\Delta_{u,obs}}$		
	2 EL	3 EL	4 EL	2 EL	3 EL	4 EL	2 EL	3 EL	4 EL
WSH2	1.10	1.10	1.00	1.02	0.99	0.98	2.82	1.81	1.47
WSH3	1.11	1.11	1.03	1.07	1.02	1.00	2.12	1.41	1.24
WSH5	1.03	1.04	0.94	1.04	1.02	1.01	2.04	1.34	1.32
W2	1.18	1.17	1.17	1.49	1.28	1.21	4.53	4.07	4.23
RW1	1.22	1.22	1.14	1.16	1.08	1.04	2.05	1.73	1.37
R1	1.08	1.08	1.08	1.09	1.02	1.01	2.50	2.50	2.50
R2	1.12	1.12	1.12	1.07	1.03	0.98	2.50	2.50	2.08
Mean	1.12	1.12	1.08	1.13	1.06	1.03	2.65	2.19	2.03
COV	0.06	0.05	0.08	0.14	0.09	0.08	0.33	0.43	0.53

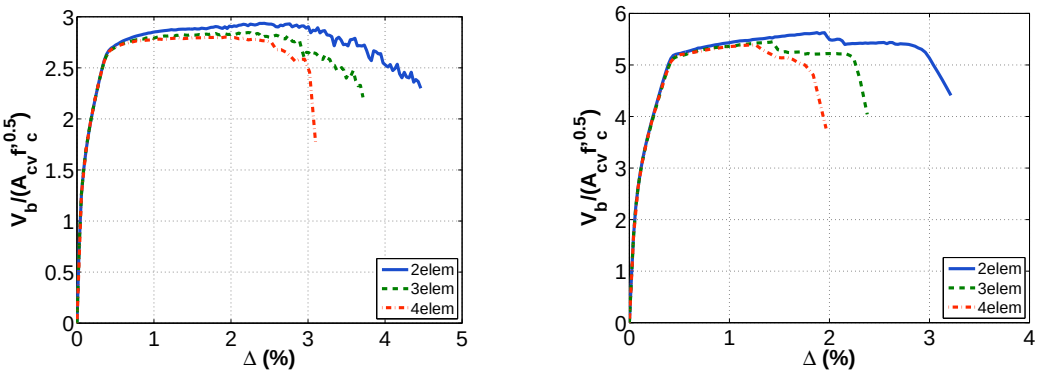

(a) WSH4 Specimen (b) PW2 Specimen

Figure 2.14: VecTor2 Mesh Dependency

Table 2.9: VecTor2 Model Simulation Results (CB Failures)

Specimen	VecTor2 (MCFT)								
	$\frac{k_{y,sim}}{k_{y,obs}}$			$\frac{V_{bm,sim}}{V_{bm,obs}}$			$\frac{\Delta_{u,sim}}{\Delta_{u,obs}}$		
	2 EL	3 EL	4 EL	2 EL	3 EL	4 EL	2 EL	3 EL	4 EL
WSH4	1.14	1.14	1.14	1.06	1.03	1.01	2.76	2.29	1.88
WSH6	1.07	1.06	0.98	1.08	1.03	1.00	1.76	2.02	1.46
W1	1.25	1.24	1.16	1.29	1.16	1.15	2.25	1.63	2.00
PW2	1.18	1.16	1.17	1.06	1.03	1.01	2.11	1.54	1.23
PW3	1.23	1.22	1.21	1.11	1.07	1.04	3.02	3.03	2.80
PW4	1.23	1.22	1.22	1.17	1.14	1.11	2.47	2.25	1.54
RW2	1.17	1.16	1.09	1.05	1.01	0.97	2.13	2.32	1.57
S5	1.13	1.18	1.18	0.94	0.92	0.91	0.69	0.51	0.44
S6	1.24	1.23	1.23	1.00	0.97	0.96	0.99	0.81	0.65
WR20	1.04	1.03	1.03	1.00	0.96	0.95	0.88	0.78	0.71
WR10	1.20	1.18	1.04	1.02	1.00	1.00	0.93	0.86	0.96
WR0	1.11	1.09	0.99	0.99	0.97	0.96	1.80	0.92	1.35
Mean	1.17	1.16	1.12	1.06	1.02	1.00	1.82	1.58	1.38
COV	0.06	0.06	0.08	0.09	0.07	0.07	0.43	0.51	0.48

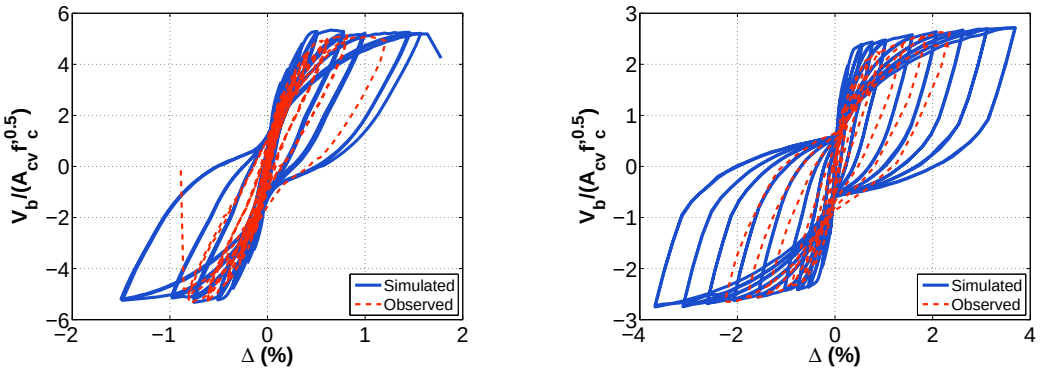

(a) WSH2 Specimen (b) RW2 Specimen

Figure 2.15: VecTor2 Cyclic Response Comparison

2.6.1.1 Comments on VecTor2 Simulation Results

The dependency of simulated softening response on element size suggests that softening localization, previously identified to occur in distributed-plasticity beam column elements, also affects continuum element models when such models are used to simulate strength loss of compression controlled concrete components. Plots of localized compression damage for the WSH4 specimen are provided in Figure 2.16. In Figure 2.16, the principal compressive stress field for the specimen is presented for the three meshes at a drift of 3%. 3% drift corresponds to the drift when strength loss began in the most coarsely meshed model. For all three meshes, maximum principal compressive strains occur at the wall toe, are nearly vertical at the wall edge, and become rotated for adjacent interior elements. The magnitude of the compressive strain is indicated by the length of the red line representing the principal strain and it can be seen that the magnitude of compressive strain increases significantly as the element size is reduced. Comparison of the strain plots with the load-displacement response simulated for these models in Figure 2.14(a) suggests that the increased accumulation of compression damage at the wall toe reduced the simulated specimen drift capacity and that the rate of accumulated compression damage is dependent on the selected mesh and critical element size.

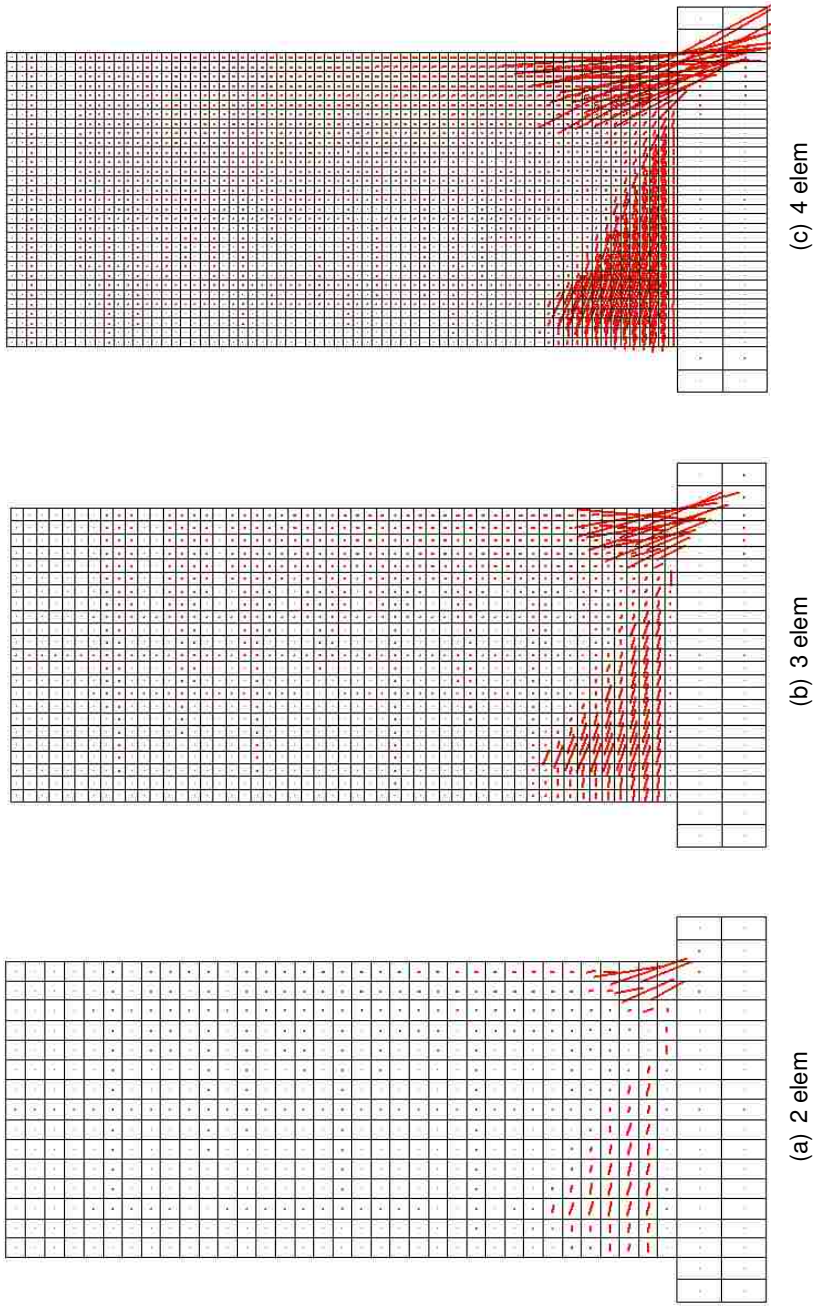

Figure 2.16: Principal Compressive Strain at Δ = 3.00% (WSH4)

To further investigate mesh dependency in VecTor2, a three-element mesh of plain concrete elements was constructed and subjected to monotonically increasing uniaxial tension and compression was considered (Figure 2.17). The middle element of the mesh comprised concrete that was 10% weaker in tension and compression than the other elements, with the objective that inelastic deformations would localize in the middle element. A 12 inch total bar length was used and the length of the middle element was varied from 4 to 8 inches in 2 inch increments. The bar was assigned an axial area of 9 in^2 (3 in. by 3 in. square).

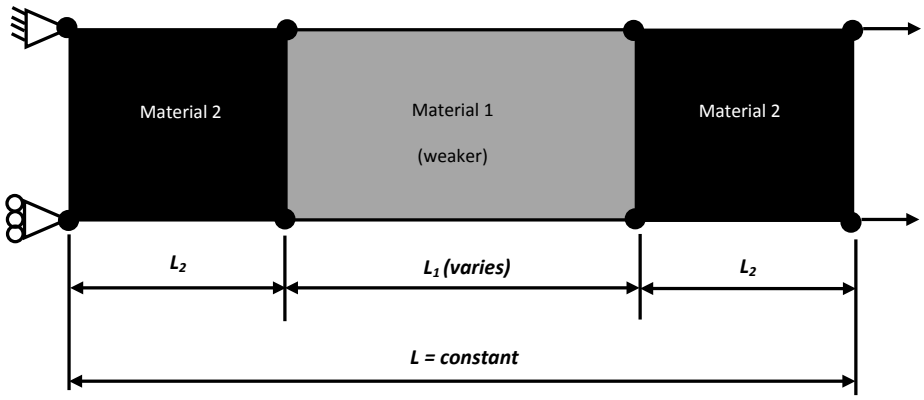

Figure 2.17: Three-Element Bar Model

Results considering monotonically increasing axial tension at both the global level (stress vs displacement) and material level (stress vs strain) are shown in Figure 2.18(a) and (b), respectively. Similar plots for monotonically increasing axial compression are shown in Figure 2.18(c) and (d). The data presented in Figure 2.18 show global tensile softening response is essentially unaffected by the selected element size while global compression softening response becomes increasingly brittle as element size decreases. Tensile response is independent of the element size because the VecTor2 tension softening model

regularizes tension response using an element size-dependent characteristic length. The regularization modifies the post-cracking stress-strain response to account for the element length and enables the global response to be determined objectively and rapidly converge with decreasing element size. Regularization has not been implemented for softening in compression, thus global response that is determined by compression softening cannot be determined objectively.

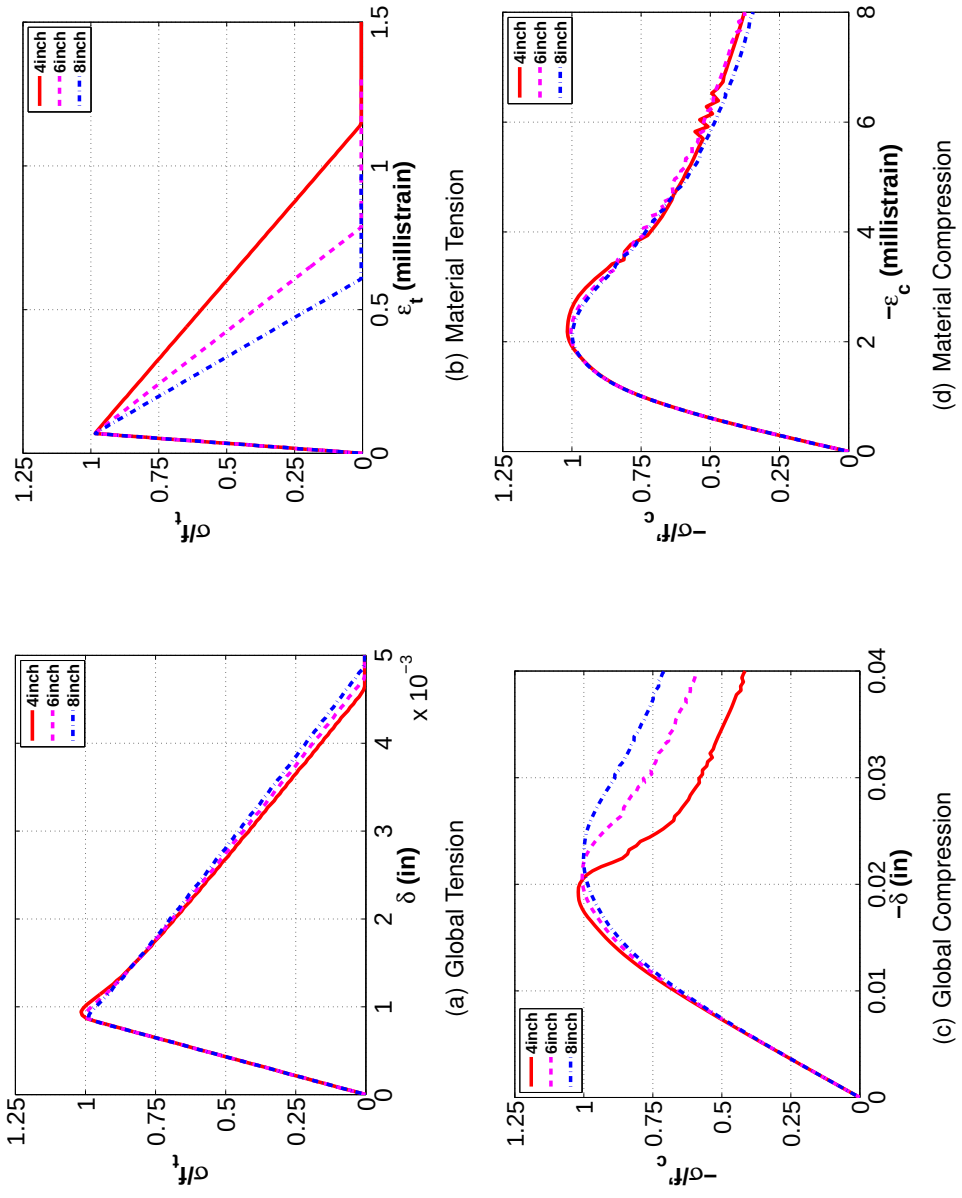

Figure 2.18: Axial Bar Response

2.7 Conclusions

Numerical models of 21 walls tested in the laboratory were developed using force-based and displacement-based distributed-plasticity beam column element models and 2D continuum elements employing the modified compression field theory. Results for these specimens presented in this chapter show that both types of models can adequately simulate strength and stiffness of slender walls; however neither model is capable of accurately simulating observed specimen drift capacity.

It was demonstrated that the inability of current models to simulate strength loss is due to the localization of inelastic deformation that occurs when system softening begins. For beam-column elements with fiber-type secion models, inelastic deformation localizes at the critical section, with the severity of localization increasing as the length of the critical fiber section decreases. For plane stress elements, the severity of softening was found to depend on the selected element size, with increasingly brittle response simulated for increasingly refined meshes.

Studies performed using simple VecTor2 element models suggest that objective global response can be achieved when deformations localize due to material softening by regularizing material response. VecTor2 tension softening response regularizes material behavior by determining mesh-dependent tensile stress-strain response based on element size. This regularization was shown to virtually eliminate mesh depedency compared to similar studies of unregularized compression response. Regularization of distributed-plasticity beam column elements is discussed extensively in Chapter 3. Regularization of compression models in VecTor2 is limited by the closed-source nature of the commercial software and could not be accomplished by the current research.

Chapter 3

RECOMMENDATIONS FOR NONLINEAR MODELING OF SLENDER WALLS USING REGULARIZED DISTRIBUTED-PLASTICITY BEAM COLUMN ELEMENTS

3.1 Introduction

The research presented in this chapter focuses on developing recommendations for modeling slender walls, which dissipate energy primarily through flexural yielding, using computationally efficient beam-column elements. Slender walls are used commonly in design of mid- and high-rise buildings in seismic regions; however, robust performance-based numerical modeling recommendations for these components do not exist.

Research presented in this chapter shows that complete cyclic response of slender walls responding in flexure, including loss of lateral load carrying capacity, can be simulated using beam-column elements in which nonlinear flexural response is predicted by a fiber-type cross-sectional model.

However, accurate prediction of response requires that the 1D concrete and steel material models used to simulate section response are 'regularized' using a mesh-dependent characteristic length and material-dependent post-yield energy. Results presented in this chapter demonstrate that fiber section material regularization significantly reduces the limitations in predicting complete cyclic response of slender walls using basic (i.e. - unregularized) distributed-plasticity beam column elements identified in Chapter 2.

To develop the proposed regularization technique for distributed-plasticity beam-column elements, techniques developed by previous research were extended. Post-yield energy values for plain and confined concrete and a post-yield energy for reinforcing steel were determined to enable accurate prediction of drift capacity for reinforced concrete walls.

Background on distributed-plasticity elements and damage localization is provided in Section 3.2. Damage localization concepts lead directly to the inclusion of post-yield mate-

rial energy regularization in the numerical simulations. Recommended values for material energy are developed using available planar wall specimen data in Section 3.3. Section 3.4 discusses the accuracy of line element planar wall simuatlions using the material recommendations developed in Section 3.3. Regularization of hardening sections is discussed in Section 3.5. Additional validation of the proposed method using non-planar wall specimen data is provided in Section 3.6.

3.2 Background on Fiber Beam-Column Elements

Distributed-plasticity fiber section beam-column element models are used throughout this chapter to develop recommendations for numerical modeling of slender walls that dissipate energy primarily through flexural yielding. Both displacement-based and force-based elements are evaluated using an extensive set of recently tested slender wall specimens. Background on these element formulations are provided in Sections 3.2.1 and 3.2.2. Additional discussion of fiber-type flexural sections is provided in Section 3.2.3.

3.2.1 Distributed-Plasticity Beam-Column Elements

Distributed-plasticity (DP) beam-column elements use multiple fiber sections at pre-assigned locations along the element length with total element response determined by numerically integrating the fiber section responses. Gauss-Lobatto integration is typically selected because it permits fiber station locations at element end points, which is useful for nonlinear analysis of structures subjected to earthquake loading because inelastic response of structures subjected to seismic loads typically concentrates at member ends.

In general, there are two primary classes of DP elements implemented and available in commercial software including:

1. Displacement-Based Distributed Plasticity Beam Column (DBBC) Elements

2. Force-Based Distributed Plasticity Beam Column (FBBC) Elements

3.2.1.1 Displacement-Based Elements

The displacement-based beam column (DBBC) element formulation uses assumed displacement fields to relate element deformations to nodal displacements. Such displacement fields are commonly approximated using standard frame element shape functions which assume constant axial strain and linear curvature distribution along the element length. For wall locations expected to experience significant flexural yielding, the use of many DBBC elements may be required to reasonably approximate the associated nonlinear curvature distribution.

3.2.1.2 Force-Based Elements

The force-based beam column (FBBC) element formulation is based on assumed internal force distributions of constant axial load and linearly varying bending moment within the element. An internal force distribution satisfying equilibrium assuming no distributed frame loads are applied is most common, however modifications to be used for certain cases of distributed loads are available (Spacone, 1991). The use of FBBC elements capable of automatically satisfying modeled load patterns and boundary conditions can allow for significant computational savings compared to similar DBBC element models. However the FBBC element solution is based on a flexibility formulation and an requires additional numerical solution at the element level to be compatible with typical displacement-based finite element programs (Spacone 2005).

3.2.2 Damage Localization in DP Elements

Coleman and Spacone (2001) found that under some circumstances DP elements exhibit mesh sensitivity due to damage localization at critical fiber section locations. Both DBBC and FBBC elements exhibit such sensitivity; however DBBC element models localize damage in a critical element while FBBC element models localize damage at a single critical fiber section. The extent of this sensitivity greatly depends on the response of the critical fiber section:

- Hardening Section Behavior - Both element global (force-deformation) and local (moment-curvature, peak strains) response quantities can be predicted objectively (mesh-independent).

- Elastic Perfectly Plastic (EPP) Section Behavior - Element global quantities can be predicted objectively; local response quantities depend on the selected mesh.

- Softening Section Behavior - Both element global quantities and local response quantities depend on the selected mesh.

Coleman and Spacone (2001) provide a simple demonstration of the localization problem. Consider the case of an isolated cantilevered wall loaded laterally at the free end and modeled using a single FBBC element with EPP fiber section behavior (Figure 3.1). For this system, peak strength is reached when the base fiber section reaches the plastic moment capacity, M_p. At this point, only the base fiber section (which has reached the plastic limit) will deform inelastically if further tip displacement is imposed, and further displacement can increase without an increase in the applied load. For a given tip displacement, the three meshes shown in Figure 3.1 will develop different curvature demands at the critical section. This is because the increase in mesh (fiber section) reduces the characteristic length assigned to the base fiber section by the numerical integration scheme used to determine total element response. As the characteristic length assigned to the base section decreases, the curvature demand must increase for the prescribed tip displacement to be achieved. The global load-diplacement response for the three systems is identical because each system has the same peak strength, M_p, and each system reaches the same prescribed tip displacement. However, the local response quantities (i.e., curvature demand) depend on the selected mesh.

Similar behavior occurs for system softening however both global and local response quantities are affected (Figure 3.2). Once peak system strength is reached, global response predictions become increasingly brittle as the selected mesh increases. The localized inelastic demands which occur after peak strength is reached leads to more rapid

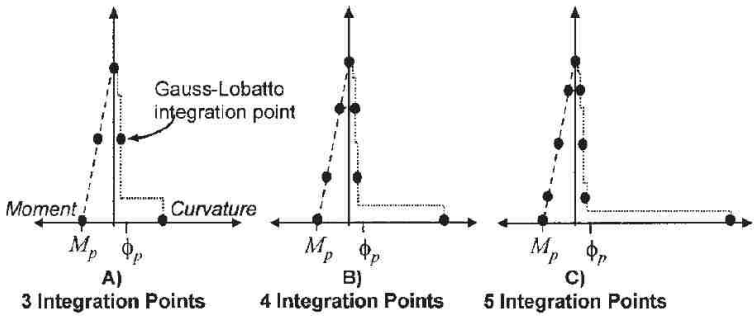

Figure 3.1: EPP Cantilever Wall Behavior (Coleman and Spacone, 2001)

system strength loss as the characeristic length associated with the critical section (or critical element for DBBC elements) decreases (i.e. - five integration points (IP) vs 3 integration points (IP)).

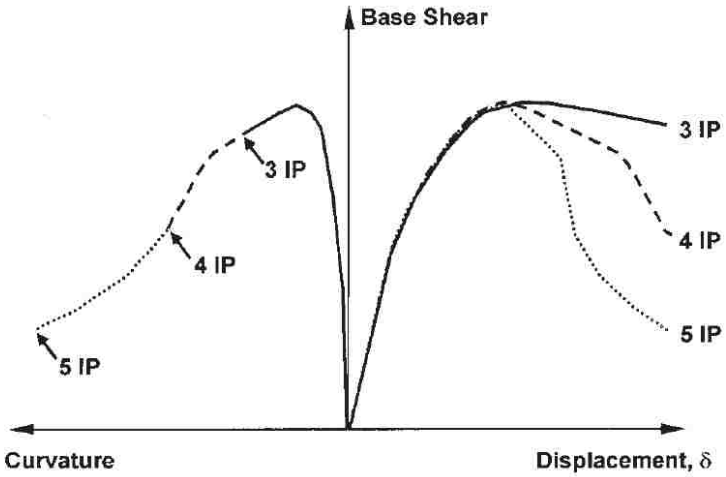

Figure 3.2: Softening Cantilever Wall Behavior (Coleman and Spacone, 2001)

To alleviate global load-displacement mesh dependency due to damage localization, Coleman and Spacone (2001) proposed a material regularization technique. The proposed material regularization method is based on the observation that compression failure in con-

crete cylinder tests is a localized phenomenon and experimental evidence that the energy dissipated by concrete during compression failure is essentially constant and independent of the length of the specimen (Jansen and Shah 1997; Lee and William 1997).

Using these concepts, concrete material models assigned to distributed-plasticity fiber sections are modified to ensure that all concrete fibers dissipate a constant amount of material energy during crushing. Energy is independent of the characteristic length associated with the fiber section. This is analogous to previously suggested models for simulating tension damage in continuum-based finite element models (Bazant and Oh, 1983).

For implementation a constant value of crushing energy, G_{fc}, is assumed for the concrete and the area under the post-peak portion of the compressive stress-displacement response is set equal to this value. This is shown in Figure 3.3 and defined in Equation 3.1.

$$G_{fc} = h \int \sigma \, \mathrm{d}\epsilon_i \tag{3.1}$$

Equation 3.1 designates a length, h, over which normal strains are simulated and which convert axial strain to displacement. For implementation in DBBC and FBBC elements, the length over which axial strains are simulated is the characteristic length assigned to each individual fiber section by the numerical integration rule used to determine element response. Designating this length as L_{IP} and substituting into Equation 3.1 yields Equation 3.2.

$$\frac{G_{fc}}{L_{IP}} = \int \sigma \, \mathrm{d}\epsilon_i \tag{3.2}$$

Equation 3.2 equates the area under the post-peak portion of the concrete compressive stress-strain curve with the ratio of the crushing energy and the characteristic length associated with fiber section 'i'. For the Concrete02 uniaxial model, this process results in determining a crushing strain (ϵ_{20}) for each fiber section location such that the hatched area in Figure 3.3 is constant. Thus, different post-peak material model softening parameters are assigned to different fiber sections, with post-peak softening parameters assigned based on the fiber section characteristic length.

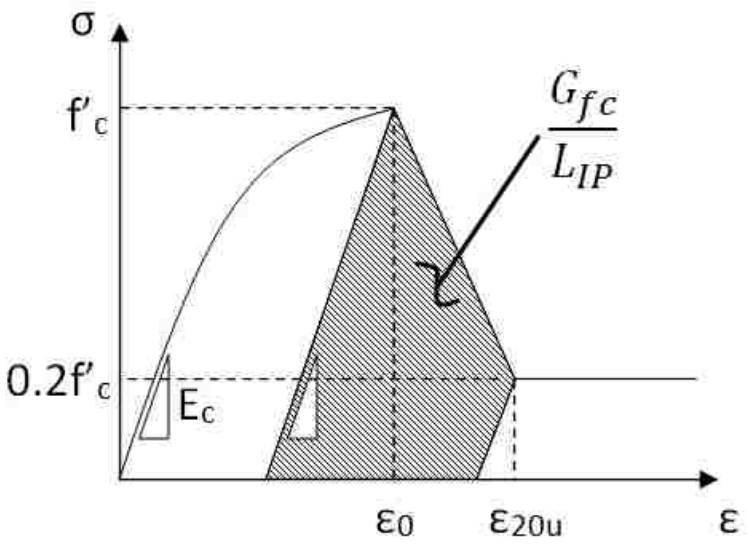

Figure 3.3: Crushing Energy (Yassin Model)

Recommended values for concrete crushing energy based on experimental studies (Jansen and Shah 1997, Nakamura and Higai 1999) can be found in the literature and are discussed further in Section 3.3.4. Cross-section regions experiencing enhanced ductility due to transverse confining reinforcement would be expected to exhibit enhanced crushing energy. Crushing energy for confined fiber section regions is discussed further in Section 3.3.5.

The regularization approach was applied by Coleman and Spacone (2001) to a confined column section tested by Tanaka (1990) as reported by Taylor et al. (1997). The axially and laterally loaded column was modeled using a single FBBC element and meshes with 4,5 and 6 fiber sections. Bilinear steel response with 1% hardening was used for the reinforcement and the concrete material response was modeled using a Park-Kent model with material regularization. Unconfined fibers were assigned a crushing energy of 25 N/mm based on recommendations by Jansen and Shah (1997) and the confined core was assigned a value six times larger than this (150 N/mm) to account for the enhanced response provided by the transverse reinforcement.

Results presented by Spacone and Coleman (Figure 3.4) show the proposed material regularization procedure significantly reduced the mesh dependent softening response and enabled objective numerical simulation of the post-peak response.

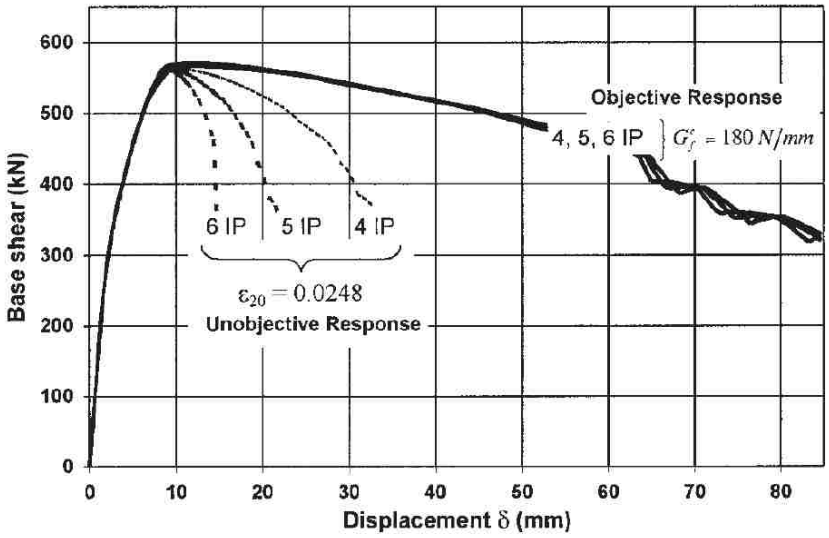

Figure 3.4: Objective vs Non-Objective Response (Coleman and Spacone, 2001)

3.2.3 Fiber Section Models

Fiber section models use a discretized grid of material fibers to represent the wall cross-section geometry (a sample discretized wall fiber section is shown in Figure 3.5). In general, fiber section model response is determined as follows:

1. The kinematic assumption that plane sections remain plane and perpendicular to the neutral axis during bending. Strain profiles across critical wall sections are known to not remain plane (Adebar and Bohl (2011), Birely (2012)) even for slender walls. However previous research indicates that fiber section models utilizing plane-section kinematics, but accounting for shearing deformations, are sufficiently accurate to allow prediction of wall systems responding primarily in flexure. For example, from a study of 60 experimentally tests walls (both squat and slender;planar and barbell),

Oyen (2006) demonstrated 'plane section' fiber models could simulate observed wall strength within an average error 6% and a coefficient of variation of 0.16.

2. Using OpenSees force-based distributed-plasticity elements, shear strains can be aggregated to the fiber section response to account for shearing strains. This aggregation does not change the plane section kinematic assumption, however the use of aggregation does allow plane sections to no longer remain perpendicular to the element neutral axis.

3. Uniaxial (1D) material models are used to define fiber section stress-strain response. For nonlinear analysis of concrete walls it is important that selected models reasonably capture cyclic material behavior.

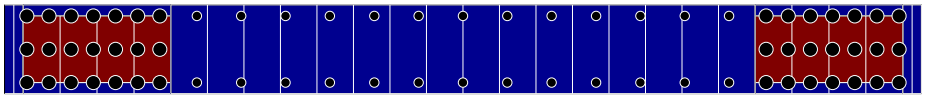

Figure 3.5: Sample Wall Fiber Section

3.2.3.1 Concrete Constitutive Models

Two uniaxial concrete material models commonly used for nonlinear analysis of reinforced concrete components are discussed in the following section. These models are:

- Yassin Model (Cyclic Hognestad/Modified Park-Kent)
- Chang and Mander Model

The Yassin model is a cyclic implementation of the Kent and Park (1971) model as extended by Scott, Park and Priestley (1982) in compression. The tensile response is linear until cracking with a linear softening branch to account for energy dissipation after initial cracking (tension softening).

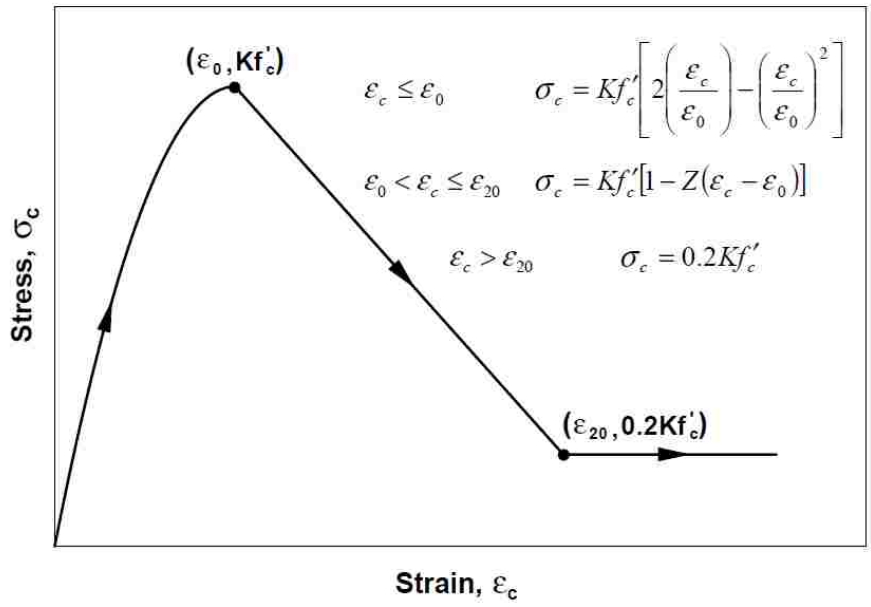

Figure 3.6: Yassin/Modified Park-Kent Monotonic Envelope (Orakcal, 2006)

The monotonic compression envelope (Figure 3.6) contains a initial parabolic region, a linear softening region and an ultimate stress plateau. The impact of confinement provided by transverse reinforcement is modeled by determining an effective confinement factor, K, that is used to adjust the strength and strain capacity of the compression response as shown in Figure 3.6. The effective confinement factor, K, can be determined using any of several available 1D confinement models (Scott, Park and Priestely, 1982; Razvi and Saatcioglu, 1992; Mander et al., 1988).

For cyclic implementation, Yassin assigned bilinear unloading and linear reloading branches for unloading from and reloading to the monotonic compression envelope, respectively (Figure 3.7). These hysteretic rules account for stiffness degredation in both unloading and reloading and assume tensile response occurs immediately after complete unloading in compression occurs. Sudden crack closure is assumed; this can be seen by noting the sudden change in stiffness upon reloading in compression from tension (Figure 3.7). Tensile strength and post-cracking softening can controlled.

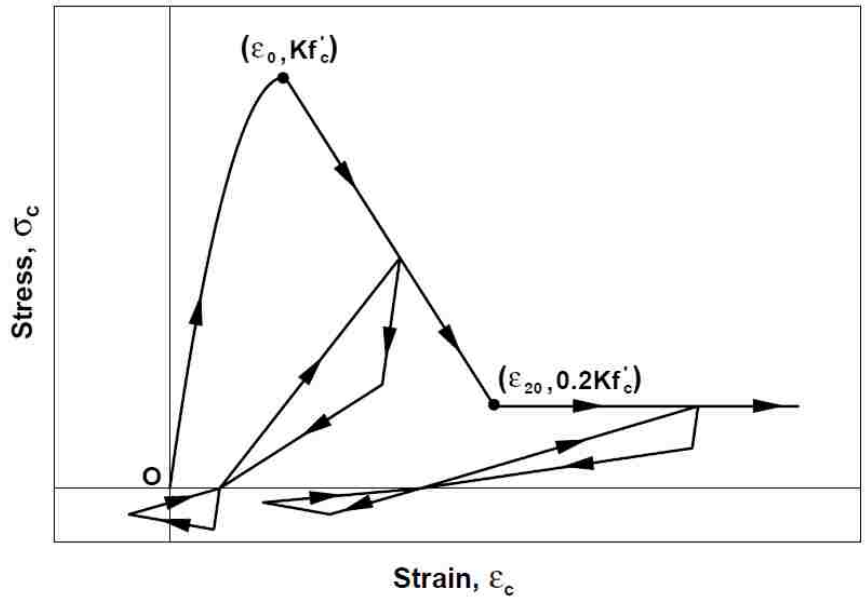

Figure 3.7: Yassin/Modified Park-Kent Cyclic Response (Orakcal, 2006)

The Chang and Mander (1994) model simulates monotonic and hysteretic response of confined and unconfined concrete, using more advanced loading and unloading rules than the Yassin cyclic implementation. The model was defined by Change and Mander using non-dimensional parameters that enable a generalized definition of material behavior. Monotonic envelopes (Figure 3.8) for both tension and compression are similar in form with an initial nonlinear response curve based on Popovics' equation (1973) followed by a straight line branch. For this model, confinement effects are modeled using the generalized confinement models developed by Mander et al. (1988).

For cyclic implementation, smooth 'connecting' curves define unloading and reloading between tension and compression and smooth 'transition' curves define partial unloading and reloading between the connecting curves. Additionally, the smooth connecting curves simulate gradual crack closure when reloading to compression from tension (Figure 3.9).

Numerical implementation of the Chang and Mander model was done independently by Wallace and Orakcal (2006) and Waugh (2009). Both research groups have noted numerical instabilities exist with the original model and have proposed modified rules.

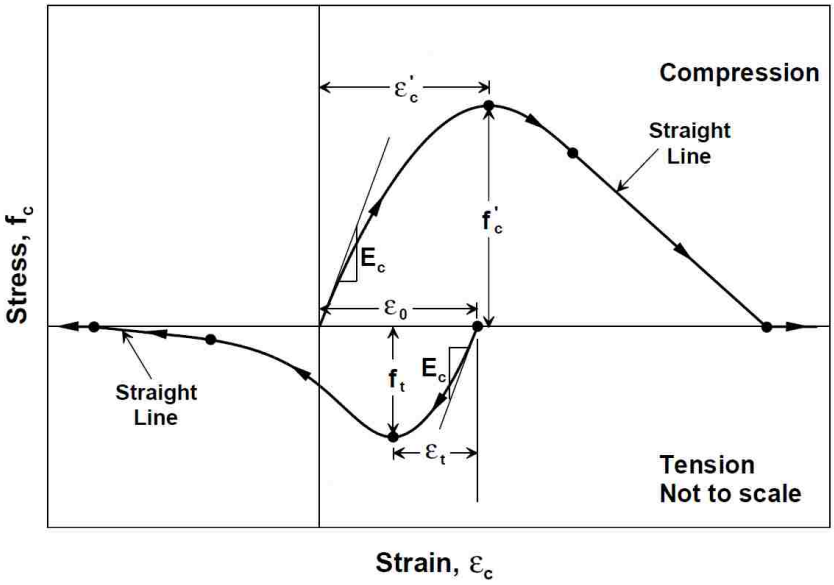

Figure 3.8: Chang and Mander Monotonic Envelopes (Orakcal, 2006)

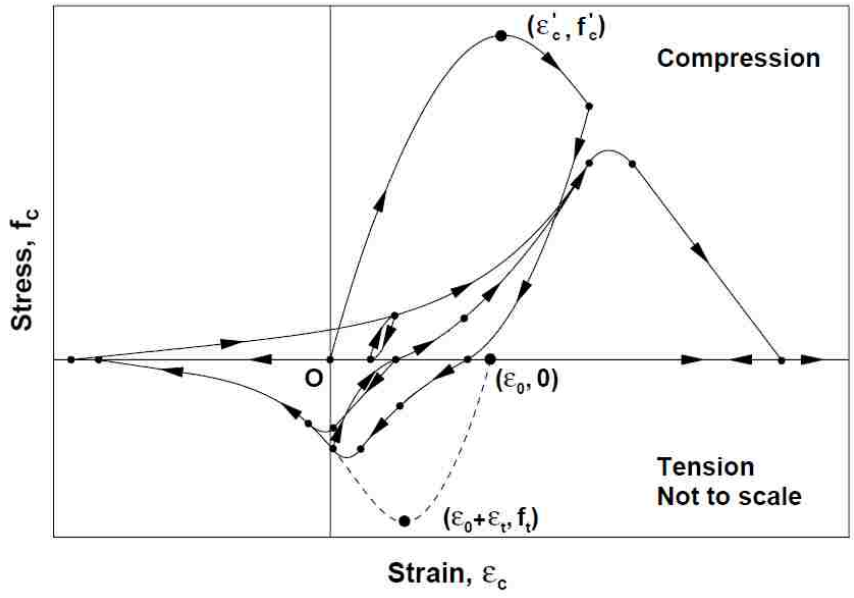

Figure 3.9: Chang and Mander Hysteretic Curves (Orakcal, 2006)

3.2.3.2 Reinforcing Steel Constitutive Models

Cyclic reinforcing steel behavior is commonly modeled using the Menegotto-Pinto-Filippou (1983) which includes isotropic strain hardening (Figure 3.10). This model represents steel behavior as a series of curved transitions between asymptotes defined by linear elastic and strain hardening properties. The curved transition allows for the representation of the Bauschinger effect. Model input parameters allow for control of cyclic stiffness deterioration.

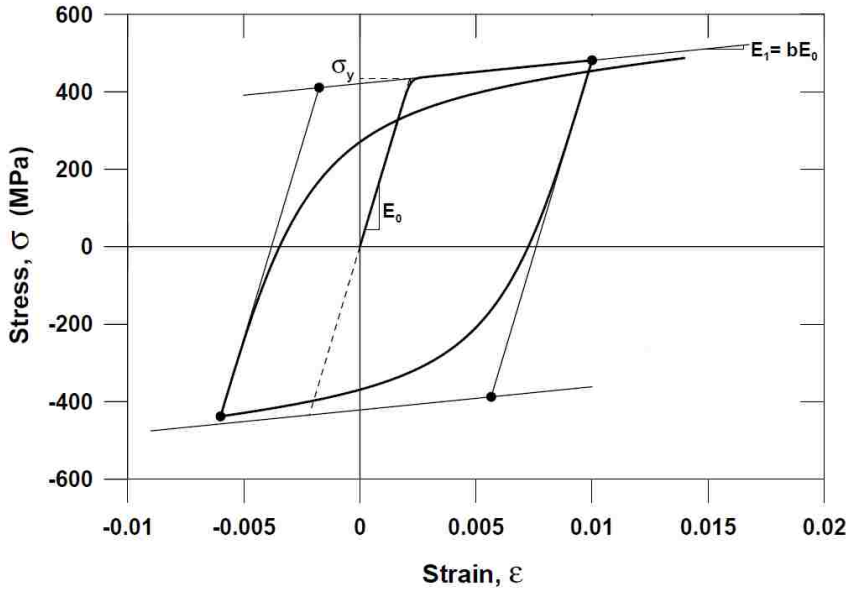

Figure 3.10: Menegotto-Pinto-Filippou Model (Orakcal, 2006)

3.3 Simulating Wall Response Using Regularized Fiber-Type Distributed-Plasticity Beam Column Elements

As discussed in Section 2.5, numerical wall models developed using 'basic' fiber-type distributed-plasticity beam-column elements can not accurately simulate drift capacity and the onset of loss of lateral load carrying capacity for wall specimens that exhibited softening due to concrete crushing prior to failure. This softening behavior, while uncommon for

many other types of structural components, was shown to be a prominent failure mode for many recently tested slender wall specimens (Table 2.1). This failure mode cannot be predicted accurately using the basic models because of severe mesh-dependent localization of inelastic deformation.

Section 3.3 presents a method for regularizing the fiber section material models that significantly reduces the observed mesh dependency and enables accurate simulation of deteriorating inelastic flexural response of ductile walls. The regularization method, definitions of post-yield material energy and calibration of material energy values are presented in Section 3.3.1. Simulation results using regularized models are presented and discussed in Section 3.4.

3.3.1 Regularization of Material Models to Limit Mesh Sensitivity

To limit mesh sensitivity in continuum analyses of materials that exhibit softening, material response is regularized using dissipated energy and a mesh-dependent length. For example, for plain concrete responding in tension, concrete fracture energy, G_f, (CEB-FIP, 1990) is combined with a mesh-dependent characteristic length to regularize the post-peak stress-strain response and thereby limit mesh sensitivity (CEB-FIP, 2008). Coleman and Spacone (2001) extended this approach to the fiber-type beam column element, recommending that for reinforced concrete components that exhibit a softening moment-curvature response at the section level, concrete material response be regularized in compression. Regularization of concrete tensile response is not addressed by Coleman and Spacone because concrete tensile softening does not produce section softening and, thus, localization of section curvatures and material strains.

Figure 3.11(a)-(c) shows stress-strain response envelopes for unconfined and confined concrete loaded in tension and compression as well as the definitions of the concrete fracture energy, G_f, unconfined crushing energy, G_{fc}, and confined crushing energy, G_{fcc}. In Figure 3.11, L_{IP} is the characteristic length of the fiber section (i.e. integration point) for which the material model is used. Given energy dissipation values G_f, G_{fc} and G_{fcc} as well as L_{IP}, the stress-strain response envelopes can be defined using Figure 3.11.

For concrete tensile response, any of several experimental procedures and empirical models may be used to determine concrete fracture energy, G_f (CEB-FIP, 1990). For concrete response in compression, there are no current standard practices for experimental testing to determine G_{fc} or G_{fcc} and few empirical models are found in the literature. Two studies addressing crushing energy are: Jansen and Shah (1997) who recommend a value of 25 N/mm for normalweight concrete, and Nakamura and Higai (1999) who define crushing energy for unconfined concrete to be a function of compressive strength such that normalweight concrete has G_{fc} = 80 N/mm.

Coleman and Spacone (2001) employed the G_{fc} value recommended by Jansen and Shah for unconfined concrete and recommend a value of $G_{fcc} = 6G_{fc}$ for confined concrete; however, these values are not verified through comparison of simulated and measured response for typical reinforced concrete components.

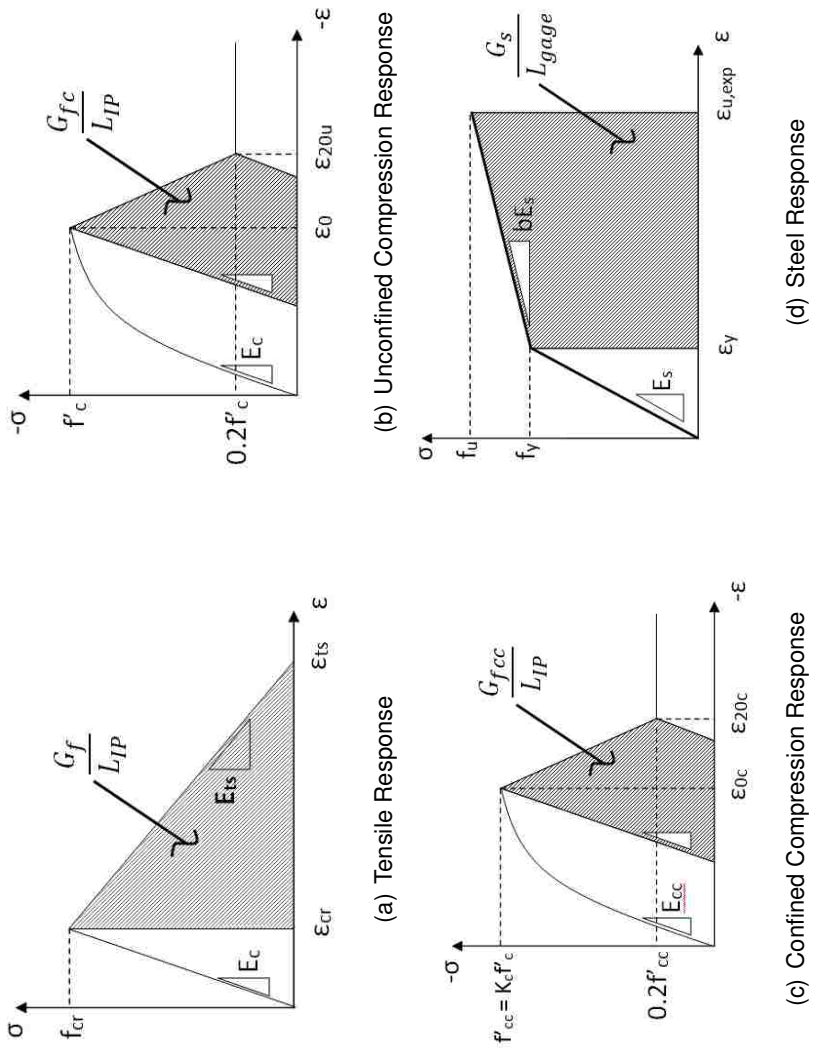

Figure 3.11: Material Energy Definitions

Steel exhibits a hardening-type response. Thus, no localization of deformation would be expected in a fiber-type beam-column element model of a steel beam or column; instead material hardening would ensure distributed yielding along the length of the beam-column element. However, for a reinforced concrete wall in which concrete crushing results in softening of a critical section, concrete and reinforcing steel deformations localize at a single critical section. Thus, steel strain demands at the critical section are affected by mesh refinement and regularization of the steel material response is required to achieve mesh objective results. Figure 3.11(d) shows the regularized stress strain envelope for reinforcing steel with post-yield response defined by a hardening energy, G_s.

Given the hardening energy, G_s, yield and ultimate strength of the reinforcing steel, and L_{IP}, a post-yield hardening modulus can be defined. Only one documented study by Chiaramonte (2011) addressing regularization of steel response for fiber section distributed-plasticity elements was found in the literature; Coleman and Spacone (2001) do not address regularization of steel response.

3.3.2 Limiting Mesh Sensitivity for RC Wall Section

As a preliminary study of material regularization, analyses were conducted for the two wall specimens from Table 2.1 constructed entirely of unconfined concrete, WSH4 tested by Dazio et al. and WR0 tested by Oh, et al. A model employing a single force-based element and intra-element meshes of 5, 7 and 9 fiber sections. Preliminary energy values were employed in these analyses (G_t = 75 N/m, G_{fc} = 30 N/mm, G_s = 15000 N/mm) and analyses were conducted with various combinations of material regularization. Figure 3.12 shows the results of these analyses. Figures 3.12(a) and (b) show simulated results for three levels of mesh refinement with no material regularization. Figures 3.12(c) and (d) show results for concrete material regularization in tension and compression with no regularization of reinforcing steel. Figures 3.12(e) and (f) show results for concrete material regularization in compression but not tension and steel material regularization. On the basis of the results shown in Figure 3.12 it was concluded that

1. For basic models, mesh refinement results in increasingly rapid strength loss once

peak strength is attained. Denser meshes with more fiber sections predict extremely brittle response with essentially zero post-peak ductility.

2. Regularization of concrete tensile response is unnecessary. Concrete tension response has a significant impact on section response at small curvatures, however the impact of tension softening occurs much earlier than section softening begins and has minimal impact on element softening response.

3. Regularization of concrete compression response and reinforcing steel response in compression and tension is necessary to limit mesh sensitivity.

3.3.3 Determination of a Steel Post-Yield Energy

Regularization of the steel material response is motivated by the fact that distributed-plasticity beam-column element softening is controlled by softening at the fiber section level. Softening at the fiber section level does not occur once softening begins at a single fiber, rather it is a function of the softening concrete response, the amount and distribution of reinforcement, and the hardening parameters assigned to the reinforcing material. Because both steel and concrete strains are affected by inelastic damage localization within the element, regularization of both the concrete and steel material models are required to limit mesh dependency within the softening model.

To determine a post-yield energy for reinforcing steel, the approach often employed for continuum analysis of unconfined concrete responding in compression (Spacone and Coleman, 2001) was adopted. Specifically, post-yield energy was defined equal to the area under the experimentally determined post-yield stress-strain envelope (Figure 3.11(d)) multiplied by the length over which inelastic deformation localizes, which was assumed equal to the gage length, L_{gage}, used in the laboratory. Thus,

$$G_s = \frac{1}{2}(\epsilon_{u,exp} - \epsilon_y)(f_u + f_y)L_{gage} \tag{3.3}$$

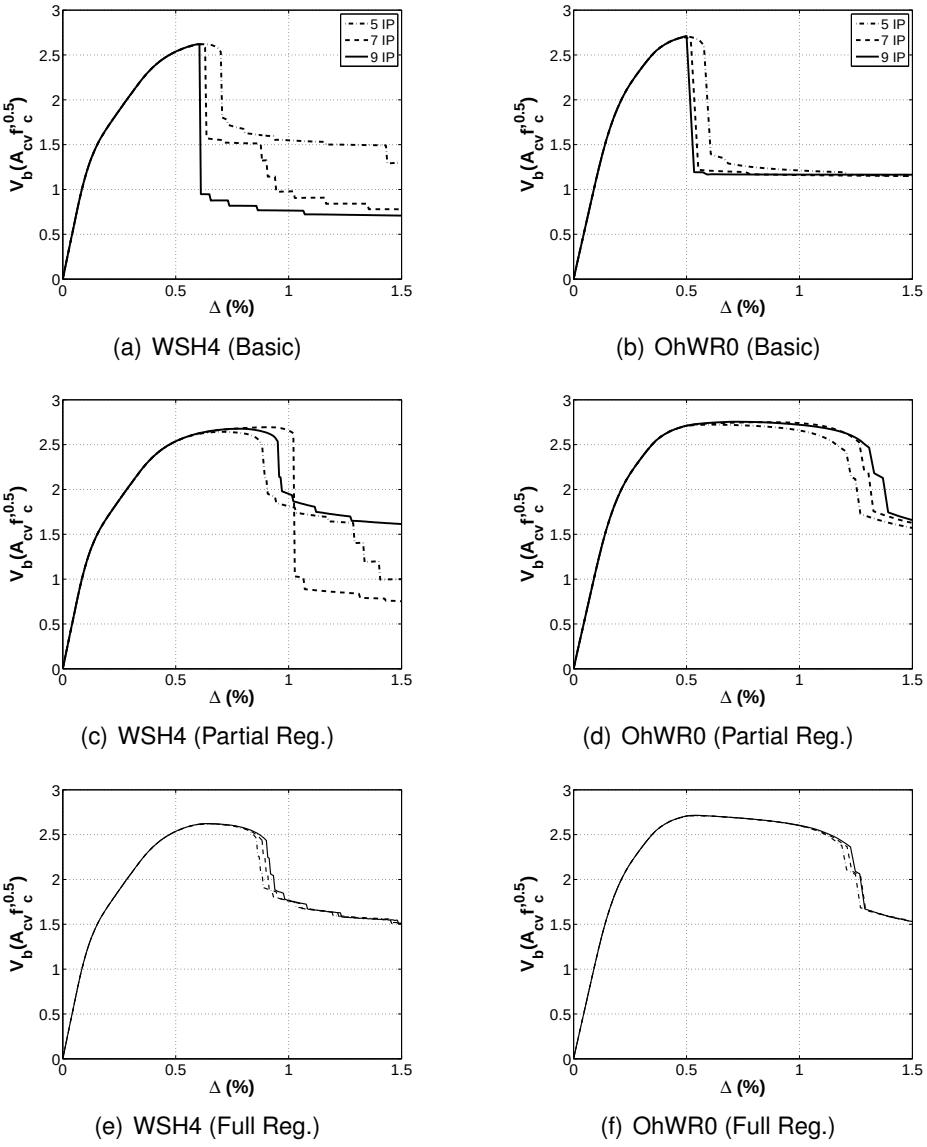

(a) WSH4 (Basic)

(b) OhWR0 (Basic)

(c) WSH4 (Partial Reg.)

(d) OhWR0 (Partial Reg.)

(e) WSH4 (Full Reg.)

(f) OhWR0 (Full Reg.)

Figure 3.12: Regularization Response Comparison

where $\epsilon_{u,exp}$ is the rupture strain of the bar and f_u is the tensile strength of the bar, as determined from laboratory testing and all other parameters are as previously defined. Equation 3.3 was generated assuming the bar strength at rupture is equal to the tensile strength of the steel. This approximation is a simplification of measured reinforcing steel data for which engineering stress typically reduces prior to rupture. Using Equation 3.3 and Figure 3.11(d), the strain at ultimate strength, ϵ_u, used in defining the regularized model can be calculated as:

$$\epsilon_u = \epsilon_y + (\epsilon_{u,exp} - \epsilon_y)\frac{L_{gage}}{L_{IP}} \tag{3.4}$$

where all variables are as previously defined. Thus, as the mesh becomes more highly refined and L_{IP} is reduced, the hardening modulus for the reinforcing steel is also reduced and larger strains are required to achieve a given post-yield stress level. It should be noted that these definitions ignore the curved transition defined by the Menegotto-Pinto model between the initial and post-yielding hardening slopes; however, this is a minor simplification and was determined to have minimal impact on numerical results (Figure 3.12(e) and (f)).

Complicating the proposed method for steel regularization is the fact that not all published specimen results include the gage lengths used to determined reported reinforcing steel material properties. However, sensitivity studies performed on specimens experiencing crushing failures suggest results are not particularly sensitive to reasonable variations in the gage length used to regularize steel response. Analyses of crushing specimens were performed considering gage lengths between 4 and 30 inches. Over this range of gage lengths, simulated system response quantities (stiffness, peak strength, drift capacity) varied by less than 5%. If gage length was not reported, a length of 8 inches was used for numerical modeling of wall specimens. The length (8 in.) is the gage length required per ASTM A370 (*Methods for Testing Steel Reinforcing Bars*).

3.3.4 Determination of Unconfined Concrete Crushing Energy

In this section, laboratory specimen test results are used to develop crushing energy recommendations for wall specimens constructed without confining reinforcement. The recommendations developed in this section are demonstrated to provide accurate simulation of experimentally observed drift capacity for two unconfined wall specimens.

The material regularization approach suggested by Coleman and Spacone (2001) was employed with the Yassin (Concrete02) model for compression. For this material model, only modification to the strain value, ϵ_{20u}, associated with reaching the ultimate compressive stress plateau (Figure 3.6) was required. The modified strain value was determined for each fiber section location by substituting the Yassin model softening stress-strain response into Equation 3.2. This substitution yields Equation 3.5, which was then used for calculating the required strain value at each fiber section location.

$$\epsilon_{20u} = \frac{G_{fc}}{0.6 f_p L_{IP}} - \frac{0.8 f_p}{E_0} + \epsilon_p \tag{3.5}$$

where, f_p is the peak compressive strength of the unconfined concrete, ϵ_p is the strain associated with the peak compressive stress, and E_0 is the initial concrete modulus.

The experimental values of crushing energy determined by Jansen and Shah (20-30 N/mm) were evaluated using data for the two walls in Table 2.1 constructed entirely of unconfined concrete. Load-displacement results generated using a single force-based element w/5 integration points (i.e. - 5 fiber sections) were compared with measured results (Figure 3.13).

The simulated results accurately simulate strength and stiffness of the tested specimens, but do not accurately simulate the observed drift capacity. For the WSH4 specimen, simulated peak strength is 5$\%$ lower the measured peak strength and simulated yield stiffness is 13$\%$ higher than the calculated yield stiffness. Simulated drift capacity for the WSH4 specimen is approximately 56$\%$ of the measured drift capacity. For the WR0 specimen, simulated peak strength is 8$\%$ lower the measured peak strength and simulated yield stiffness is 10$\%$ lower than the calculated yield stiffness. Simulated drift capacity for the WSH4 specimen is approximately 58$\%$ of the measured drift capacity. These results indi-

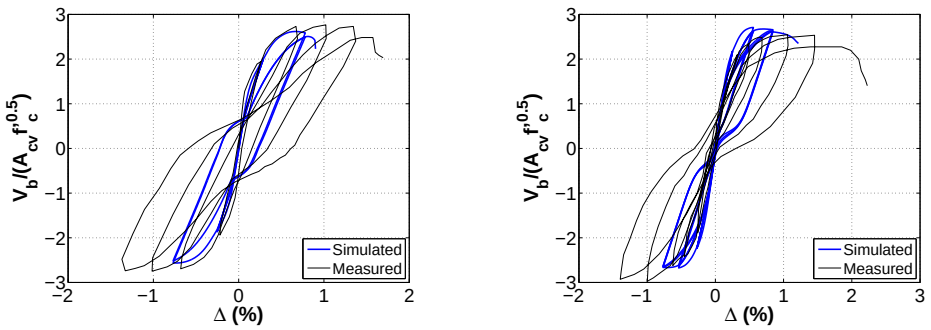

(a) WSH4 (Dazio, et al.) (b) WR0 (Oh, et al.)

Figure 3.13: Unconfined Wall Response, G_{fc} = 30 N/mm

cate that a crushing energy significantly larger than the 20-30 N/mm determined by Jansen and Shah for plain concrete is required to accurately simulate the observed response of walls constructed with unconfined concrete. The significant increase in crushing energy required to accurately simulate the observed drift capacity of these walls is attributed to the crushing resistance provided by the longitudinal reinforcement, which was not present in the cylinder test results reported by Jansen and Shah.

A study was performed to evaluate the relationship between G_{fc} and cyclic drift capacity, Δ_u, for the two unconfined specimens. Crushing energy, G_{fc}, was varied from 30 N/mm to 100 N/mm and Δ_u for each G_{fc} for each wall was recorded. Results of this study are presented in Figure 3.14. The data in Figure 3.14 show

- Increasing the selected value of crushing energy (G_{fc}) increases the simulated drift capacity for both specimens.

- 80 N/mm is required to accurately simulate the drift capacity of the DazioWSH4 specimen.

- 65 N/mm is required to accurately simulate drift capacity of the OhWR0 specimen.

- G_{fc} is a function of compressive strength, f'$_c$.

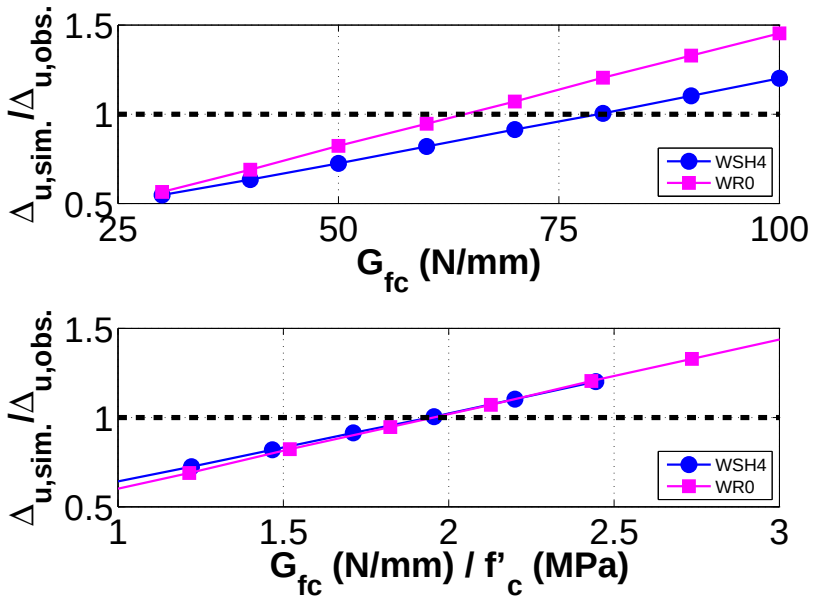

Figure 3.14: Unconfined Material Energy Calibration

In Figure 3.14 the G_{fc} values were normalized by the uniaxial compressive strength (40.9 MPa (5930 psi) for DazioWSH4; 32.9 MPa (4770 psi) for OhWR0). The data presented in Figure 3.14 indicates a normalized crushing energy of approximately 2.0 is appropriate for determining an appropriate crushing energy for unconfined wall cross sections:

$$G_{fc} = 2f'_c(N/mm) \tag{3.6}$$

where f'_c is the compressive strength of the concrete in MPa. Using Equation 3.6, the improved wall simulations shown in Figure 3.15(a) and (b) are achieved.

3.3.5 Determination of Confined Concrete Crushing Energy

To determine an appropriate crushing energy for confined concrete in walls, load-displacement data for the cyclically loaded slender wall specimens with well confined boundary element regions and failing due to flexural compression (CB Failure Mode) listed in Table 2.1 were

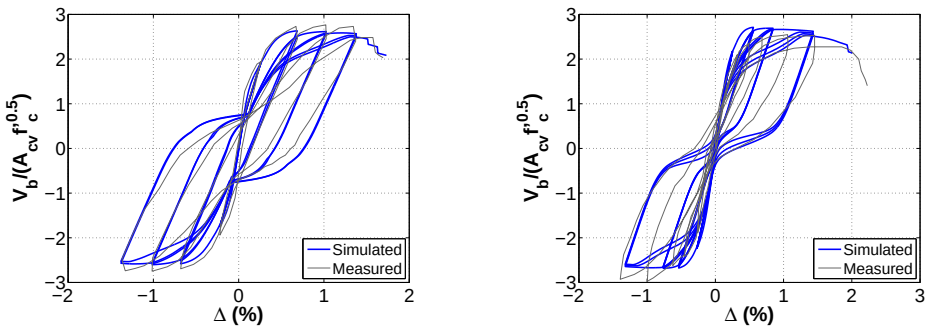

(a) WSH4 (G_{fc} = 80 N/mm) (b) WR0 (G_{fc} = 65 N/mm)

Figure 3.15: Unconfined Wall Response w/Calibrated Regularization Model

used. Table 3.1 lists the specimens that were included in the calibration efforts discussed in this section.

Table 3.1: Confined Energy Calibration Dataset

Specimen ID	Author	Failure Mode
WSH6	Dazio et al.	CB
W1	Liu	CB
PW2	Lowes et al.	CB
PW3	Lowes et al.	CB
PW4	Lowes et al.	CB
RW2	Thomsen et al.	CB
S6	Vallenas et al.	CB
WR20	Oh et al.	CB
WR10	Oh et al.	CB

3.3.5.1 Simulations Without Enhanced Crushing Energy

Wall boundary elements are detailed with confining reinforcement at critical locations to enhance ductility. Figure 3.16 shows the ratio of simulated to measured drift capacity for the confined wall specimens from Table 3.1, where simulated drift capacities were determined using the proposed crushing energy for **unconfined concrete** (Equation 3.6).

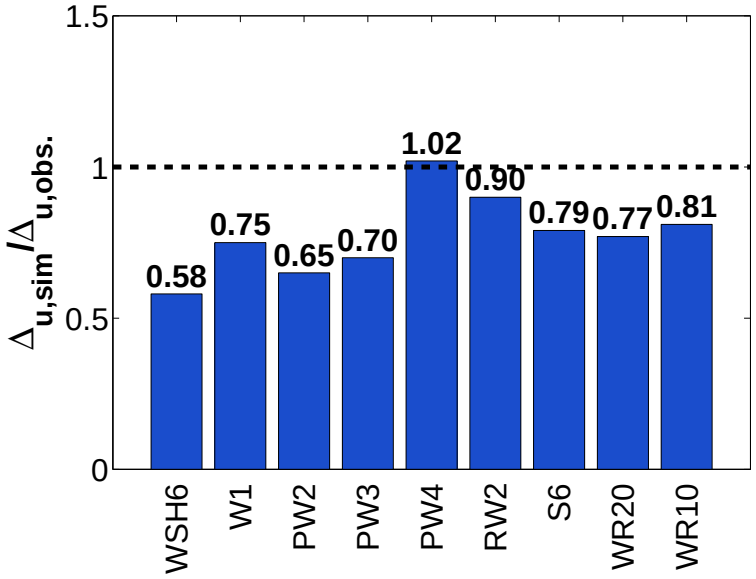

Figure 3.16: Simulated Wall Response, G_{fc} (Equation 3.6)

For all specimens, besides the PW4 specimen tested by Lowes et al., use of Equation 3.6 to determine the cushing energy for confined boundary element regions results in underprediction of observed drift capacity. For the PW4 specimen, drift capacity is overpredicted even when all concrete fibers are assumed to exhibit unconfined response. This result is not consistent with those for the other specimens tested by Lowes et al. The reason for this result is not known. However concrete near the PW4 wall base was observed to be poorly consolidated and necessitated concrete repair prior to the test. Poor quality concrete in this critical region, where failure initiated, may have reduced the ductility of this specimen.

3.3.5.2 Enhanced (Confined) Crushing Energy

An enhanced crushing energy for concrete in confined wall regions was determined using the following methodology:

1. The optimal value of enhanced crushing energy resulting in accurate simulation of drift capacity was determined for each specimen.

2. Relationships between design parameters expected to affect wall and boundary element performance and the optimal crushing energy enhancement were considered.

Wall simulations were performed in which the confined crushing energy was defined as follows. This relationship assumes confining reinforcement scales the unconfined compressive energy (from Equation 3.6) by an enhancement factor, K_c. The enhancement factor, K_c, could be expected to be a function of the parameters that determine how effectively the provided transverse steel confines concrete such as the transverse reinforcing ratio, transverse steel spacing, transverse steel configuration and could also be a function of wall geometry, shear demands and axial load.

$$G_{fcc} = K_c G_{fc} \tag{3.7}$$

Results of this study are shown in Figure 3.17. These results indicate that the K_c value required to accurately predict drift capacity ranges between 1.0 and 2.5. Figure 3.17 shows the ratio of simulated to observed drift capacity versus K_c = G_{fcc}/G_{fc} with data grouped by boundary element confinement configuration. In all cases, except the PW4 specimen, an increase in crushing energy relative to unconfined concrete was required to accurately simulate drift capacity. The data in Figure 3.17 show that, with the exception of PW4, walls with rectangular boundary elements and crossties restraining all longitudinal reinforcement have the largest Kc (average Kc = 2.30) with confinement providing a significant enhancement of concrete post-peak strain capacity while a wall with a rectangular boundary element with no crossties has the smallest Kc (Kc = 1.15) with confinement providing minimal enhancement of concrete post-peak strain capacity. Walls with square boundary elements fall in the middle of this range with an average Kc of 1.45.

With the objective of developing a model for G_{fcc} in terms of boundary element detailing, K_c = G_{fcc}/G_{fc} was plotted versus various design parameters that could be expected to influence boundary element or wall performance. However, the plotted data did not indicate strong correlation between K_c and the design parameters considered. It was concluded that the data set was too small to support development of a predictive model.

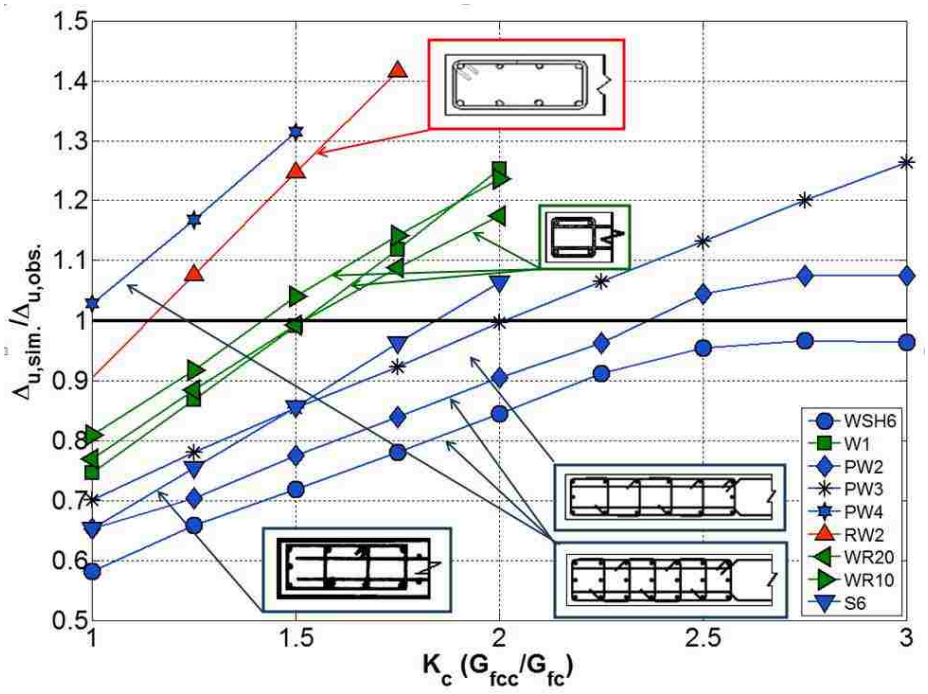

Figure 3.17: Confined Crushing Energy Calibration Study

Thus,

$$G_{fcc} = 1.70 G_{fc} \tag{3.8}$$

was used for all subsequent analyses, where 1.70 is the average value required to accurately predict observed drift capacity for all of the wall specimens shown in Figure 3.17 except for WSH4.

3.3.6 Determination of Crushing Energy for Use with Displacement-Based Distributed-Plasticity Beam Column Elements

Initially, it was assumed that the concrete crushing energies developed for use with the force-based beam column element would be appropriate for use also with the displacement-based element. However, use of Equations 3.6 and 3.8 with the displacement-based element led to significant overprediction of drift capacity. To determine the cause of this, pushover analyses were conducted on wall specimen WSH4 using the displacement- and

force-based element models. Results of these analyses showed that in highly meshed displacement-based elements, significant inelastic deformation developed in multiple sections at the base of the wall prior to strength loss. However, once the critical section softened, deformation localized to the element containing the critical section while other elements and sections unloaded. Thus, the mesh regularization procedure described previously in which inelastic deformation was assumed to localize appears appropriate for the displacement-based element.

Results showed also that despite the fact that 32 displacement-based elements were used in the model, at the onset of strength loss in the critical section, axial load in the bottom section was 170% of the applied axial load while axial load at the next higher section was 30% less than the applied axial load (Figure 3.18(a) and (b)). This variation in axial load increased the strength of the base section and decreased the strength of the next higher section such that the higher section with the lower axial load became the critical section and failed (Figure 3.18(c) and (d)). The reduced axial load at the second section resulted also in this section having a higher curvature capacity than the section subjected to the true axial load in the force-based model. Thus, the model employing the displacement-based elements predicted a larger drift capacity than the model employing the forced-based elements. Similar analyses of other walls yielded similar results and it was concluded that use of the displacement-based element would require use of different crushing energies due to the section response variations permitted by the displacement-based element formulation.

Crushing energies for unconfined and confined concrete for use with the displacement-based element were determined using exactly the same process as was used (Sections 3.3.4 and 3.3.5) with the force-based element. Unconfined concrete crushing energy was determined using data for specimens WSH4 and WR0; confined concrete crushing energy was determined using data from the remaining nine rectangular wall specimens exhibiting strength loss due to flexural compression and constructed with well-confined boundary element regions. The resulting energies determined for use with displacement-based element specimen models are:

$$G_{fc,DBE} = 0.56 f'_c (N/mm) \tag{3.9}$$

$$G_{fcc,DBE} = 1.70 G_{fc,DBE} \tag{3.10}$$

The crushing energy for unconfined concrete is significantly lower than that recommended for use with the force-based element; this offsets the fact that for the displacement-based element the axial load at the critical section will be lower than the actual applied load and, thus, greater section curvature ductility will be predicted using these elements. The ratio of the crushing energy for confined to unconfined concrete is the same as for the force-based elements.

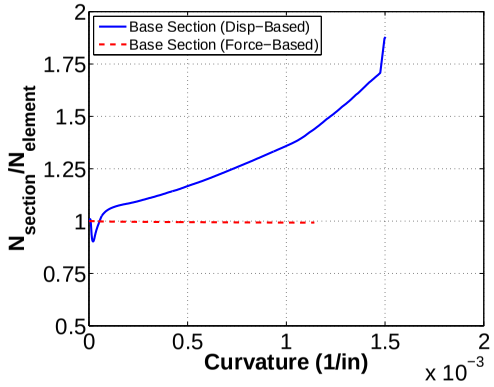

(a) Normalized Axial Response (Base Section)

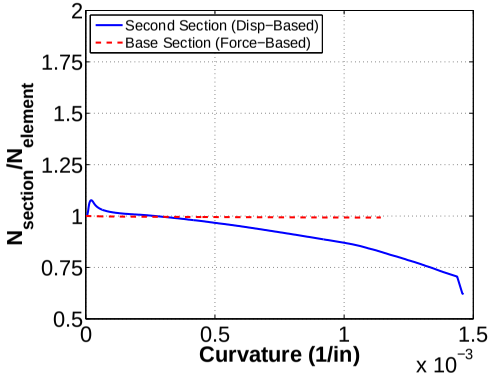

(b) Normalized Axial Response (Second Section)

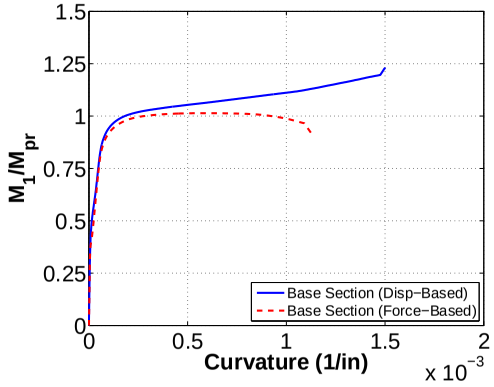

(c) Normalized Flexural Response (Base Section)

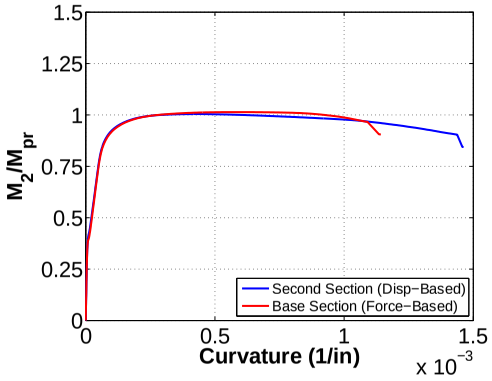

(d) Normalized Flexural Response (Second Section)

Figure 3.18: Displacement-Based Element Section Variations

3.3.7 Summary of Modeling Recommendations

The recommended material energy values for reinforcing steel, concrete response in tension, confined and unconfined concrete response in compression are summarized in Table 3.2.

Table 3.2: Material Energy/Regularization Recommendations

Material	Force-Based Element	Displacement-Based Element
Reinforcing Steel	Equation 3.3 / 3.4	Equation 3.3 / 3.4
Concrete (Tension)	Not Required	Not Required
Concrete (Compression, Unconfined)	G_{fc} = 2f'$_c$ (N/mm)	G_{fc} = 0.56f'$_c$ (N/mm)
Concrete (Compression, Confined)	G_{fcc} = 1.70G_{fc}	G_{fcc} = 1.70G_{fc}

3.4 Wall Simulation Results

Using the modeling recommendations developed in Sections 3.3.3 to 3.3.6 and summarized in Table 3.2, wall simulations were performed for the axially and cyclically loaded planar wall specimens. The purpose of these simulations was to demonstrate that use of regularized models, using the recommended values for material energy, significantly reduces the mesh dependency previously observed for softening systems and accurately simulates loss of flexural strength for slender, ductile walls. All simulated cyclic load displacement history results referenced in this section are provided in Appendix A.

To assess modeling recommendations, several levels of mesh refinement were considered using both force-based and displacement-based elements. For force-based elements, a three element mesh was held constant and intra-element meshes consisting of 3, 5 and 7 fiber sections along each element were considered. For assessment of displacement-based element models, element meshes of 6, 12 and 18 elements were used. All displacement-based element models were assigned five fiber sections along each element length. Results of the mesh studies performed are provided in Tables 3.5 to 3.7 and Figure 3.19.

Mesh refinement results in Tables 3.5 to 3.7 allow comparison of simulated response quantities considering increasingly dense meshes. Response quantities compared were:

1. Model stiffness as determined by the secant stiffness to yield. System yield was defined as the point in the load-displacement response when the theoretical yield moment was achieved at the wall base.

2. Peak strength in terms of maximum base shear strength achieved.

3. Ultimate drift. Ultimate drift was defined as the drift level at which the lateral load carrying capacity of the wall dropped to 80% of the historic maximum, for drift demands in excess of historic drift demands.

For each specimen and each model, simulated response quantities were compared with measured quantities.

The data in Tables 3.5 to 3.7 show that for planar concrete walls subjected to cyclic loading:

1. Peak base shear strength of all walls was accurately simulated by all force-based element meshes considered. The mean simulated to observed peak strength ratio was 0.94 with a coefficient of variation of 0.04 for compression controlled wall specimens and 0.99 with a coefficient of variation of 0.06 for tension controlled specimens. Displacement-based element meshes exhibited minor mesh dependency due to the intra-element axial load variation discussed previously. Mean simulated to observed strength ratios for the 18-element displacement-based element mesh were similar to those determined using force-based element models.

2. Secant stiffness to yield for walls failing due to flexural compression (CB) and flexural tension (BR) was accurately simulated by all force-based element meshes considered. The mean simulated to observed yield stiffness ratio was 1.02 with a coefficient of variation of 0.10 for compression controlled wall specimens and 1.02 with

a coefficient of variation of 0.09 for tension controlled specimens. Simulated to observed stiffness ratios determined using displacement-based element meshes were essentially identical to those determined using force-based element models.

3. Drift capacity of walls failing due to flexural compression (CB) was accurately simulated by force-based element models using different fiber section meshes. The mean simulated to observed drift capacity ratio for models using three fiber sections was 0.96 with a coefficient of variation of 0.14. The mean simulated to observed drift capacity ratio for models using seven fiber sections was 1.02 with a coefficient of variation of 0.17. These data demonstrate the effects of mesh dependency on the softening response have been significantly reduced using material regularization and the calibrated energy values yield accurate simulation results.

4. For specimens failing due to tension rupture prior to significant buckling, simulated to observed drift capacity ratios were slightly overestimated and mesh dependency, although significantly reduced, was observed. Specifically, for three fiber section force-based models, the mean simulated to observed drift capacity ratio was 1.04 with a coefficient of variation of 0.04. For seven fiber section force-based models, the mean simulated to observed drift capacity ratio was 1.18 with a coefficient of variation of 0.03.

5. For specimens failing due to tension rupture after significant buckling (BR), simulated to observed drift capacity ratios were slightly overestimated and mesh dependency, although significantly reduced, was observed. Specifically, for three fiber section force-based models, the mean simulated to observed drift capacity ratio was 1.06 with a coefficient of variation of 0.29. For seven fiber section force-based models, the mean simulated to observed drift capacity ratio was 1.11 with a coefficient of variation of 0.23.

6. The overestimated drift capacity for the specimens observed to fail due to bar rupture is most likely due to fact that strength deterioration of reinforcing steel due to buckling

was not accounted for in the current model.

7. The increased mesh dependency for the rupture specimens is likely due to the fact that failure of the specimens was not purely a compression (i.e. - softening) failure. This is confirmed by noting that simulation results limited by rupture exhibited more mesh dependency than those limited by crushing(Table 3.4). Similar trends were identified for displacement-based element models.

8. Even for specimens observed to failure due to bar rupture, the regularized model provides signficant improvement over the unregularized model for simulating the observed drift capacity for these specimens. For all specimens observed to fail due to bar rupture, the mean simulated to observed drift capacity ratio for five fiber section force-based element models was 1.07 with a coefficient of variation of 0.25. For the same mesh, mean simulated to observed drift capacity ratio for the unregularized specimen models was 1.62 with a coefficient of variation of 0.57. This observation is further investigated in Section 3.5.

Figure 3.19 presents simulated to observed drift capacity results for both the basic and regularized modeling approaches. These data show both the increased accuracy and smaller variations in error determined using the regularized model. For crushing specimens the coefficient of variation was reduced to approximately 0.15 using regularized models compared to a coefficient of variation of approximately 0.60 for the basic modeling. Although mean values presented for the basic models appear to converge and provide accurate simulation of drift capacity, the mean values are misleading due to the large variability (represented by the plotted error bars in Figure 3.19) of the unregularized model results. Comparison of the tabulated simulated results data in Tables 3.5 to 3.7 and Chapter 2 confirm the improved accuracy of the regularized model.

Figure 2.9 provides cyclic load displacement results for four specimens exhibiting different failure modes. Figures 2.9(a) and (d) present load displacement curves for two specimens observed to fail due to crushing/buckling, Figure 2.9(b) presents the load displacement curve for a specimen observed to fail by rupture (prior to buckling) and Figure 2.9(c)

presents the load displacement curve for a specimen observed to fail by rupture (after significant buckling). These results demonstrate the improved accuracy and reduced mesh dependency when material regularization is used. The simulated drift capacity varies little for the three levels of mesh refinement presented and the simulated drift capacity compares well for the observed drift capacity for three of the specimens. Drift capacity for specimen WSH6 (Figure 2.9(d)) was underpredicted because the average confined crushing energy value determined considering all confined wall specimens was used. Unregularized load displacement plots for these specimens is provided in Chapter 2.

3.4.1 Determination of Failure Mode Using Regularized Wall Models

Regularization of material response provides a means of limiting mesh sensitivity and enabling accurate simulation of drift capacity for walls, and other reinforced concrete components, for which material softening produces section softening and, ultimately, component strength loss. However, material regularization does limit the manner in which simulated material response data can be used to assess component performance. Specifically, simulated concrete and steel strain data cannot be directly compared with material test data. A maximum simulated concrete compressive strain of -0.003 mm/mm or a maximum reinforcing steel tensile strain of 0.2 mm/mm are essentially rendered meaningless by material regularization. However, simulated concrete and steel stress-strain data can be evaluated in relative terms to assess performance.

The regularized concrete strain resulting in a 80$\%$ loss in compressive strength at the critical fiber section was used to define a strain limit characterizing concrete crushing and a maximum steel tensile strain equal to 100$\%$ of the regularized rupture strain was used to define a strain limit characterizing steel rupture.

For each specimen model, the minimum extreme fiber concrete compressive strain and the maximum extreme fiber steel strains strains were determined at the load step for which the simulated drift capacity was reached. The peak strain values were then compared to the strain limit values. Compressive strain to strain limit ratios in excess of 1.0 identified simulated crushing failures. Tensile strain to tensile strain limit ratios in excess

of 1.0 identified simulated rupture failures. For all specimens observed in the laboratory to exhibit crushing failures (CB), the identified simulated failure mode was also identified as crushing. However, for specimens observed in the laboratory to exhibit bar rupture failure after significant buckling, simulated failure for 1 of the 5 specimens was identified as rupture and simulated failure for 4 of the specimens was identified as crushing. For one of the two specimens observed to fail due to bar rupture prior to buckling, simulated failure due to bar rupture was correctly identified.

Table 3.3: Regularized Model Mesh Study Results (Rupture Failures)

Specimen	Author	Force-Based											
		Stiffness Ratio			Strength Ratio			Drift Ratio			Simulated Failure Mode		
		3 IP	5 IP	7 IP	3 IP	5 IP	7 IP	3 IP	5 IP	7 IP	3 IP	5 IP	7 IP
WSH1	Dazio, et al.	1.03	1.02	1.02	0.97	0.98	0.98	1.07	1.17	1.20	Ruptured	Ruptured	Ruptured
PW1	Lowes et al.	1.06	1.06	1.06	1.01	1.01	1.00	1.01	1.05	1.15	Crushed	Crushed	Crushed
	Mean	1.05	1.04	1.04	0.99	1.00	0.99	1.04	1.11	1.18	–	–	–
	COV	0.02	0.02	0.03	0.03	0.02	0.02	0.04	0.08	0.03	–	–	–

Table 3.4: Regularized Model Mesh Study Results (BR Failures)

Specimen	Author	Force-Based											
		Stiffness Ratio			Strength Ratio			Drift Ratio			Simulated Failure Mode		
		3 IP	5 IP	7 IP	3 IP	5 IP	7 IP	3 IP	5 IP	7 IP	3 IP	5 IP	7 IP
WSH2	Dazio, et al.	1.02	1.02	1.01	0.93	0.92	0.91	0.93	1.15	1.27	Ruptured	Ruptured	Ruptured
WSH3	Dazio, et al.	0.98	0.98	0.98	0.93	0.93	0.93	0.89	1.00	1.00	Crushed	Crushed	Crushed
WSH5	Dazio, et al.	0.84	0.84	0.84	0.92	0.93	0.93	0.83	0.72	0.72	Crushed	Crushed	Crushed
W2	Liu	1.08	1.11	1.10	1.05	1.03	1.02	1.58	1.37	1.37	Crushed	Crushed	Crushed
RW1	Thomsen, et al.	1.12	1.12	1.12	0.97	0.95	0.94	1.06	1.17	1.17	Crushed	Crushed	Crushed
	Mean	1.01	1.01	1.01	0.96	0.95	0.95	1.06	1.08	1.11	–	–	–
	COV	0.11	0.11	0.11	0.06	0.05	0.05	0.29	0.22	0.23	–	–	–

Table 3.5: Regularized Model Mesh Study Results (CB Failures)

Specimen	Author	Force-Based											
		Stiffness Ratio			Strength Ratio			Drift Ratio			Simulated Failure Mode		
		3 IP	5 IP	7 IP	3 IP	5 IP	7 IP	3 IP	5 IP	7 IP	3 IP	5 IP	7 IP
WSH4	Dazio, et al.	0.96	0.96	0.96	0.95	0.95	0.95	1.05	1.05	1.13	Crushed	Crushed	Crushed
WSH6	Dazio, et al.	0.95	0.95	0.95	0.91	0.92	0.92	0.80	0.70	0.70	Crushed	Crushed	Crushed
W1	Liu	1.16	1.17	1.18	1.02	1.01	1.02	1.00	1.00	1.00	Crushed	Crushed	Crushed
PW2	Lowes et al.	1.06	1.06	1.06	0.97	0.96	0.96	0.82	0.87	0.92	Crushed	Crushed	Crushed
PW3	Lowes et al.	0.95	0.95	0.95	0.93	0.93	0.93	0.95	1.00	1.08	Crushed	Crushed	Crushed
RW2	Thomsen, et al.	1.14	1.15	1.15	0.90	0.88	0.87	1.13	1.21	1.32	Crushed	Crushed	Crushed
S5	Vallenas, et al.	0.87	0.87	0.87	0.98	0.97	0.97	0.70	0.86	1.05	Crushed	Crushed	Crushed
S6	Vallenas, et al.	0.91	0.91	0.91	1.03	1.00	0.99	1.16	1.23	1.30	Crushed	Crushed	Crushed
WR20	Oh, et al.	1.02	1.03	1.03	0.89	0.90	0.90	0.99	0.90	0.83	Crushed	Crushed	Crushed
WR10	Oh, et al.	1.05	1.08	1.07	0.92	0.93	0.93	1.01	0.99	0.96	Crushed	Crushed	Crushed
WR0	Oh, et al.	1.09	1.11	1.11	0.91	0.92	0.92	0.94	0.90	0.88	Crushed	Crushed	Crushed
	Mean	1.01	1.02	1.02	0.95	0.94	0.94	0.96	0.97	1.02	–	–	–
	COV	0.09	0.09	0.10	0.04	0.04	0.04	0.14	0.14	0.17	–	–	–

Table 3.6: Regularized Model Mesh Study Results (Rupture Failures)

Specimen	Author	Displacement-Based											
		Stiffness Ratio			Strength Ratio			Drift Ratio			Simulated Failure Mode		
		6 EL	12 EL	18 EL	6 EL	12 EL	18 EL	6 EL	12 EL	18 EL	6 EL	12 EL	18 EL
WSH1	Dazio, et al.	1.00	0.99	0.99	1.03	1.00	0.99	1.20	1.20	1.20	Ruptured	Ruptured	Ruptured
PW1	Lowes et al.	0.99	0.99	0.99	1.02	0.99	0.99	1.39	1.37	1.38	Crushed	Crushed	Crushed
	Mean	1.00	0.99	0.99	1.03	1.00	0.99	1.30	1.29	1.29	–	–	–
	COV	0.01	0.01	0.00	0.01	0.01	0.01	0.10	0.09	0.10	–	–	–

Table 3.7: Regularized Model Mesh Study Results (BR Failures)

Specimen	Author	Displacement-Based											
		Stiffness Ratio			Strength Ratio			Drift Ratio			Simulated Failure Mode		
		6 EL	12 EL	18 EL	6 EL	12 EL	18 EL	6 EL	12 EL	18 EL	6 EL	12 EL	18 EL
WSH2	Dazio, et al.	0.99	0.99	0.99	0.95	0.91	0.90	1.44	1.44	1.44	Ruptured	Ruptured	Ruptured
WSH3	Dazio, et al.	0.95	0.95	0.95	0.96	0.93	0.93	1.15	1.09	1.05	Crushed	Crushed	Crushed
WSH5	Dazio, et al.	0.81	0.81	0.81	0.97	0.95	0.94	0.95	0.86	0.84	Crushed	Crushed	Crushed
W2	Liu	1.15	1.11	1.10	1.06	1.03	1.02	1.72	1.72	1.72	Crushed	Crushed	Crushed
RW1	Thomsen, et al.	1.10	1.09	1.09	0.98	0.95	0.94	1.22	1.17	1.17	Crushed	Crushed	Crushed
	Mean	1.00	0.99	0.99	0.98	0.95	0.96	1.30	1.26	1.24	–	–	–
	COV	0.13	0.12	0.12	0.04	0.05	0.05	0.23	0.26	0.28	–	–	–

Table 3.8: Regularized Model Mesh Study Results (CB Failures)

Specimen	Author	Displacement-Based											
		Stiffness Ratio			Strength Ratio			Drift Ratio			Simulated Failure Mode		
		6 EL	12 EL	18 EL	6 EL	12 EL	18 EL	6 EL	12 EL	18 EL	6 EL	12 EL	18 EL
WSH4	Dazio, et al.	0.97	0.97	0.97	0.99	0.97	0.96	1.08	1.03	1.06	Crushed	Crushed	Crushed
WSH6	Dazio, et al.	0.89	0.89	0.89	0.94	0.92	0.92	0.96	0.85	0.84	Crushed	Crushed	Crushed
W1	Liu	1.20	1.17	1.17	1.05	1.02	1.01	1.15	1.15	1.15	Crushed	Crushed	Crushed
PW2	Lowes et al.	1.00	1.00	1.00	0.99	0.97	0.96	1.13	1.08	1.08	Crushed	Crushed	Crushed
PW3	Lowes et al.	0.87	0.87	0.87	0.95	0.92	0.92	1.41	1.26	1.26	Crushed	Crushed	Crushed
RW2	Thomsen, et al.	1.14	1.13	1.12	0.91	0.88	0.87	1.33	1.33	1.33	Crushed	Crushed	Crushed
S5	Vallenas, et al.	0.84	0.84	0.84	0.98	0.93	0.92	0.82	0.81	0.83	Crushed	Crushed	Crushed
S6	Vallenas, et al.	0.88	0.88	0.88	1.02	0.98	0.96	1.32	1.36	1.43	Crushed	Crushed	Crushed
WR20	Oh, et al.	1.01	1.01	1.01	0.94	0.91	0.91	0.99	0.99	0.97	Crushed	Crushed	Crushed
WR10	Oh, et al.	1.10	1.05	1.05	0.96	0.94	0.93	1.04	1.02	1.02	Crushed	Crushed	Crushed
WR0	Oh, et al.	1.16	1.15	1.11	0.96	0.94	0.93	0.95	0.95	0.95	Crushed	Crushed	Crushed
	Mean	1.01	1.00	1.00	0.97	0.94	0.93	1.11	1.07	1.08	–	–	–
	COV	0.12	0.12	0.11	0.04	0.04	0.04	0.17	0.17	0.18	–	–	–

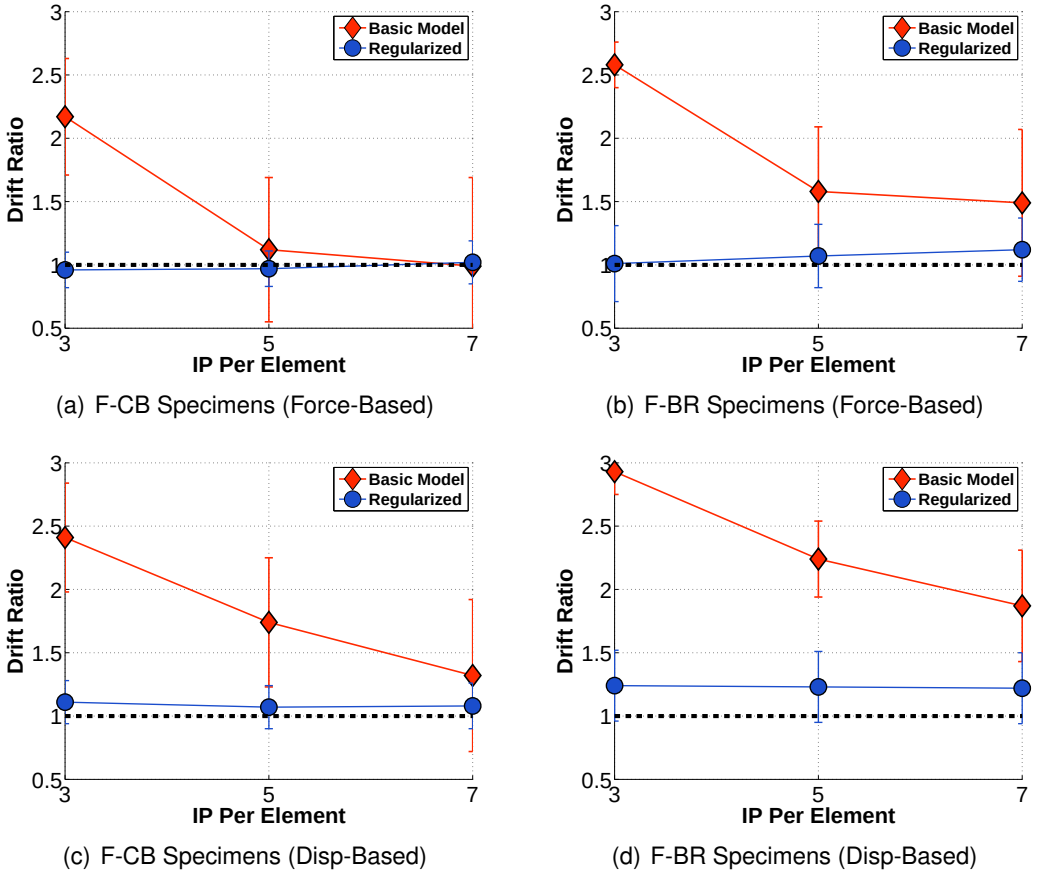

(a) F-CB Specimens (Force-Based)

(b) F-BR Specimens (Force-Based)

(c) F-CB Specimens (Disp-Based)

(d) F-BR Specimens (Disp-Based)

Figure 3.19: Mean Simulation Results (Basic vs Regularized Models)

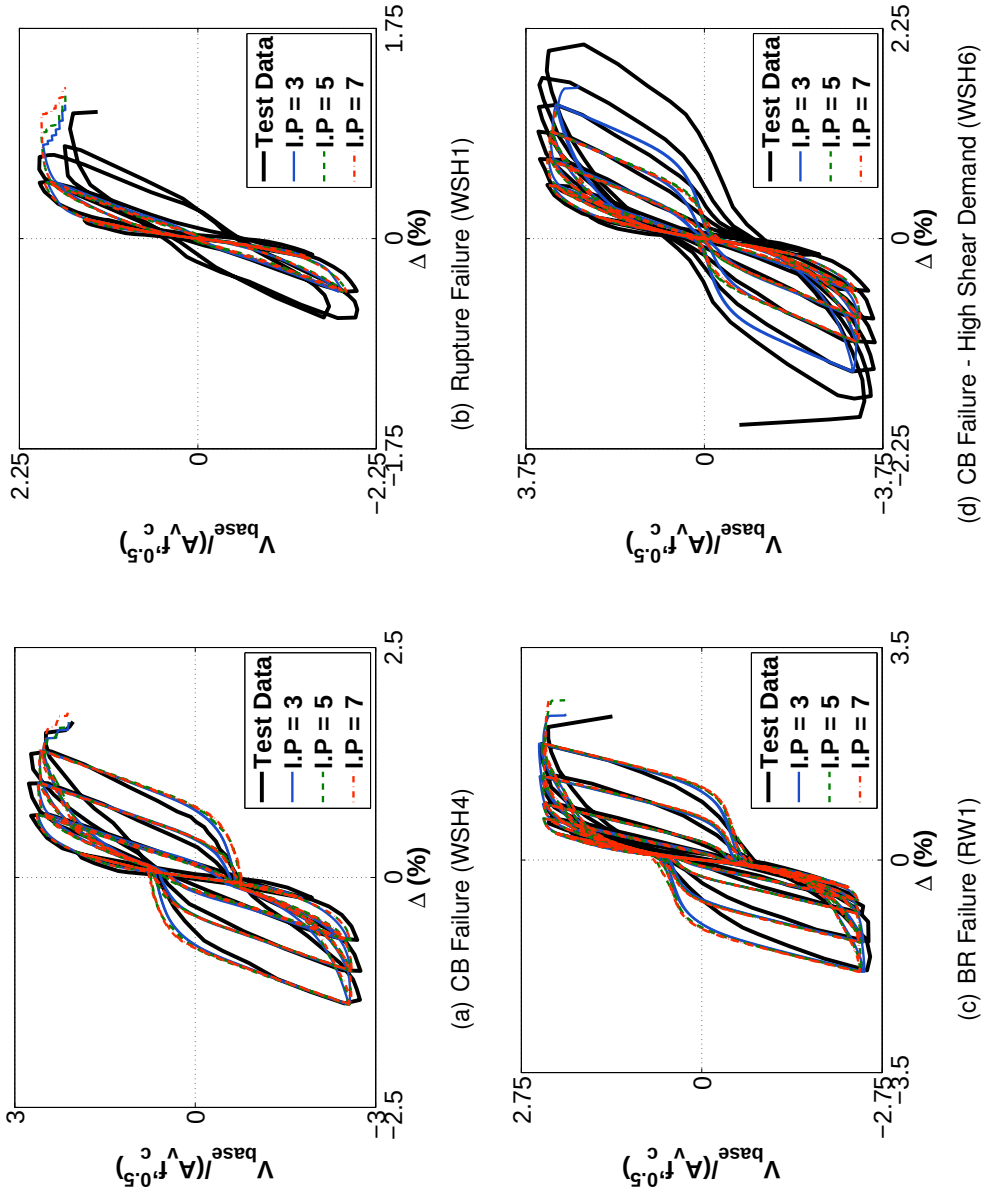

(a) CB Failure (WSH4) (b) Rupture Failure (WSH1)

(c) BR Failure (RW1) (d) CB Failure - High Shear Demand (WSH6)

Figure 3.20: Specimen Load Displacement Curves

3.5 Impact of Regularization for Hardening Sections

This section presents numerical simulation results for two planar wall specimens tested by Oesterle et al (1975) for which loss of lateral load-carrying capacity could not be accurately simulated using the regularized line element modeling recommendations presented in Section 3.3. Investigation of these specimens using moment-curvature analysis suggests that the regularization method, which assumes critical wall section moment-curvature softens prior to failure, is not appropriate for wall sections exhibiting hardening response until tensile failure occurs. Comparison between moment-curvature response determined for the two Oesterle specimens and moment-curvature response determined for the 19 specimens for which regularization was successful identified two methods for determining when regularization should be used.

3.5.1 Oesterle Specimens

The two specimen simulations discussed in this section are planar specimens, R1 and R2, tested by Oesterle et al (1975). Loading and response parameters for these specimens are presented in Table 2.1; detailed description of the specimen test setup, experimental results and parameters used for numerical modeling are provided in Appendix A.

3.5.2 Simulation Results

Comparison between simulated and observed wall response quantities are provided in Table 3.9 for both regularized and unregularized models. Response quantities compared were 1) Model stiffness as determined by the secant stiffness to yield. System yield was defined as the point in the load-displacement response when the theoretical yield moment was achieved at the wall base, 2) Peak strength in terms of maximum base shear strength achieved and 3) Ultimate drift which was defined as the drift level at which the lateral load carrying capacity of the wall dropped to 80% of the historic maximum, for drift demands in excess of historic drift demands. Simulated load-displacement curves for all specimen models are provided in Figures 3.21 through Figure 3.24. Figures 3.21 and 3.22 provide

unregularized simulation results; regularized simulation results are provided in Figures 3.23 and 3.24.

Data from Table 3.9 demonstrate:

1. Wall yield drift is reasonably well simulated for the two specimens. The R1 model was determined to be approximately 6% more flexible than the observed specimen response, the R2 model was determined to be approximately 12% stiffer than the observed response. Regularization of the models had no impact on the simulated yield drift.

2. Peak strength of both specimens was overestimated by the simulations. Peak strength of specimen R1 was overestimated by approximately 5% using unregularized models and 8% for the regularized models. Peak strength of specimen R2 was overestimated by approximately 10% for both unregularized and regularized models. Comparison between simulated and observed load-displacement response identifies that simulated overstrength occurs because the simulations do not accurately simulate specimen failure and continue to harden and gain strength at drift levels in excess of the observed drift capacity.

3. Specimen drift capacity is overestimated by all specimen models and all specimen models simulate a hardening response until failure due to fracture of boundary element reinforcing occurs. For unregularized models, the simulated drift capacity was determined to be 6.7% and 7.7% for specimens R1 and R2, respectively, with little difference in simulated drift capacity determined for 5- and 7-fiber section models. For regularized models, the simulated drift capacity did not converge and simulated drift capacity was found to increase as the number of fiber sections used to model the specimens was increased. This behavior is contrary to results found for the 19 specimens discussed in Section 3.4, where it was found that using material regularization reduced mesh dependency and improved drift capacity simulation accuracy.

Table 3.9: Line Element Simulation Results

Specimen	Author	Basic (Unregularized)									Regularized								
		Stiffness Ratio			Strength Ratio			Drift Ratio			Stiffness Ratio			Strength Ratio			Drift Ratio		
		3 IP	5 IP	7 IP	3 IP	5 IP	7 IP	3 IP	5 IP	7 IP	3 IP	5 IP	7 IP	3 IP	5 IP	7 IP	3 IP	5 IP	7 IP
R1	Oesterle, et al.	1.06	1.06	1.06	1.04	1.05	1.05	3.13	2.66	2.62	1.06	1.06	1.06	1.09	1.08	1.06	1.67	2.54	3.10
R2	Oesterle, et al.	0.88	0.88	0.88	1.10	1.11	1.10	2.45	2.39	2.38	0.88	0.88	0.88	1.13	1.11	1.09	1.41	2.09	2.47

The simulation results determined for the R1 and R2 specimens indicate that the proposed material regularization is not appropriate for all concrete sections, and the inclusion of regulazation for some sections may introduce a mesh dependency that would not be present in the unregularized model.

Error in using material regularization appears to arise when critical section response does not lose strength gradually due to deteriorating compression response, but instead hardens until steel fracture occurs. For the hardening case, no localization of damage occurs prior to failure and regularization is not needed to maintain objectivity in the numerical model.

Differences between hardening and softening section models response was investigated by comparing regularized moment-curvuture response results for the two Oesterle specimens with regularized moment-curvature response results for the 19 specimens modeled in Section 3.4. Figure 3.25(a) presents strength loss data for the 21 specimens determined using cyclic moment-curvature results and regularization relationships from Chapter 3 using an assumed characterstic length equal to 5% of the total specimen height. Figure 3.25(a) plots the ratio between the flexural strength just prior to failure and the maximum flexural strength for each specimen, where failure was quantified as a 20% reduction in flexural strength relative to the historic maximum. For the 19 specimens modeled in Section 3.4, flexural strength ratios less than 1.0 were calculated. This indicates that these sections deteriorated in strength prior to reaching the defined failure criteria (Figure 3.25(b)). For the two Oesterle specimens, strength ratios equal to 1.0 were calculated. This which confirms the hardening section response determined for these wall sections.

These results suggest that determination of whether regularization is appropriate for a given concrete section can be performed by moment-curvature analyses using regularized material models. If regularized section response is determined to exhibit softening (i.e. - gradual strength loss prior to failure), then regularization should be included for line element wall simulations. If hardening section response (i.e. - no strength loss prior to tensile failure) is determined, then unregularized material models should be used for line element wall simulations.

An alternative strain-based criteria for determining if regularization should be included

is suggested in Figure 3.26. Figure 3.26 presents tensile strain, ϵ_t, for the extreme layer of tension reinforcement at nominal flexural strength for the 21 wall sections. Tensile strain at nominal was calculated by moment curvature analysis using unregularized material models. Nominal flexural strength was defined per ACI Section 10.2. The data presented in Figure 3.26 demonstrates that the two Oesterle specimens, R1 and R2, exhibit a significantly higher tensile strain at nominal flexural strength than the other 19 specimens. All 19 softening sections were calculated to have an extreme fiber tensile strain, ϵ_t, less than 0.04 when the extreme compression fiber strain reached -0.003. The R1 and R2 specimens were calculated to have ϵ_t at nominal flexural strength greater than 0.06.

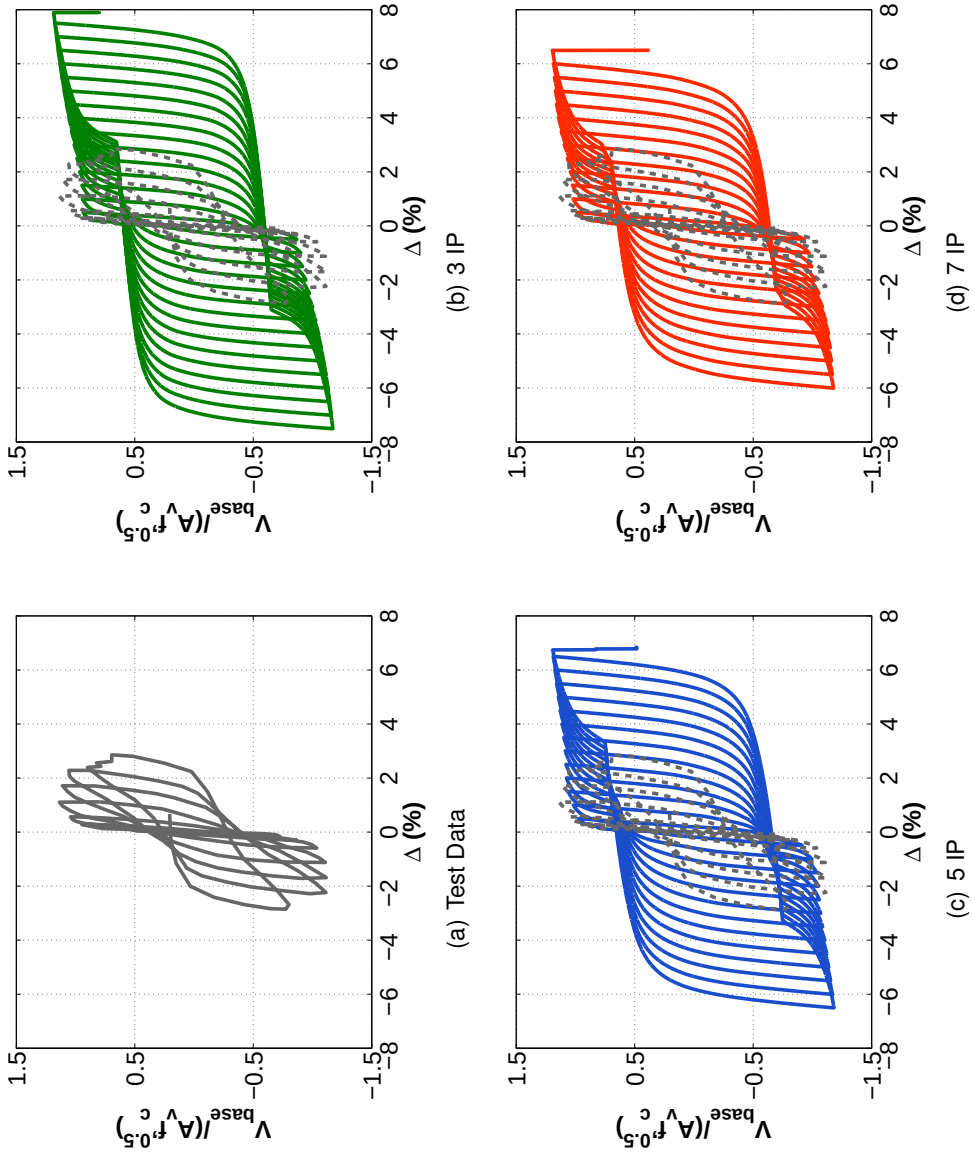

Figure 3.21: Specimen R1: Basic Models

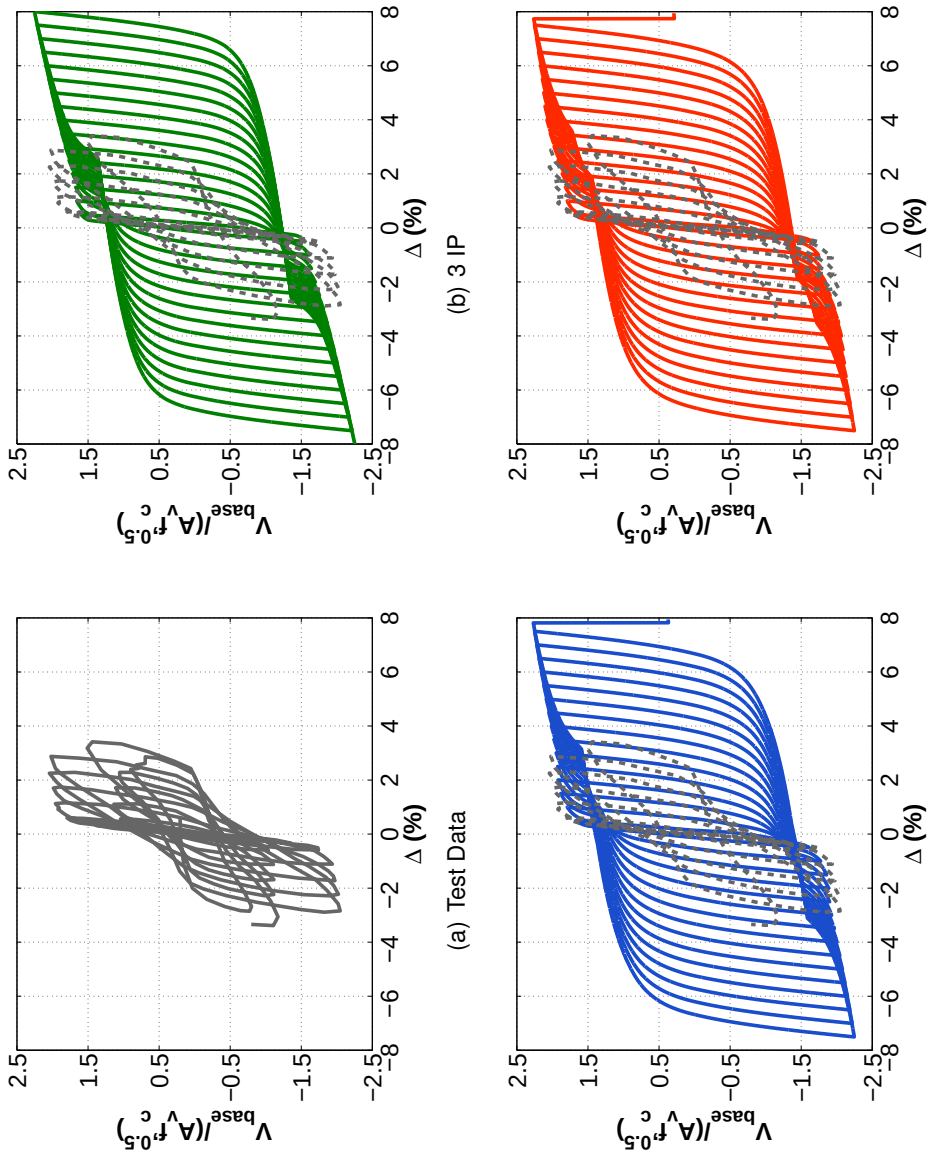

Figure 3.22: Specimen R2: Basic Models

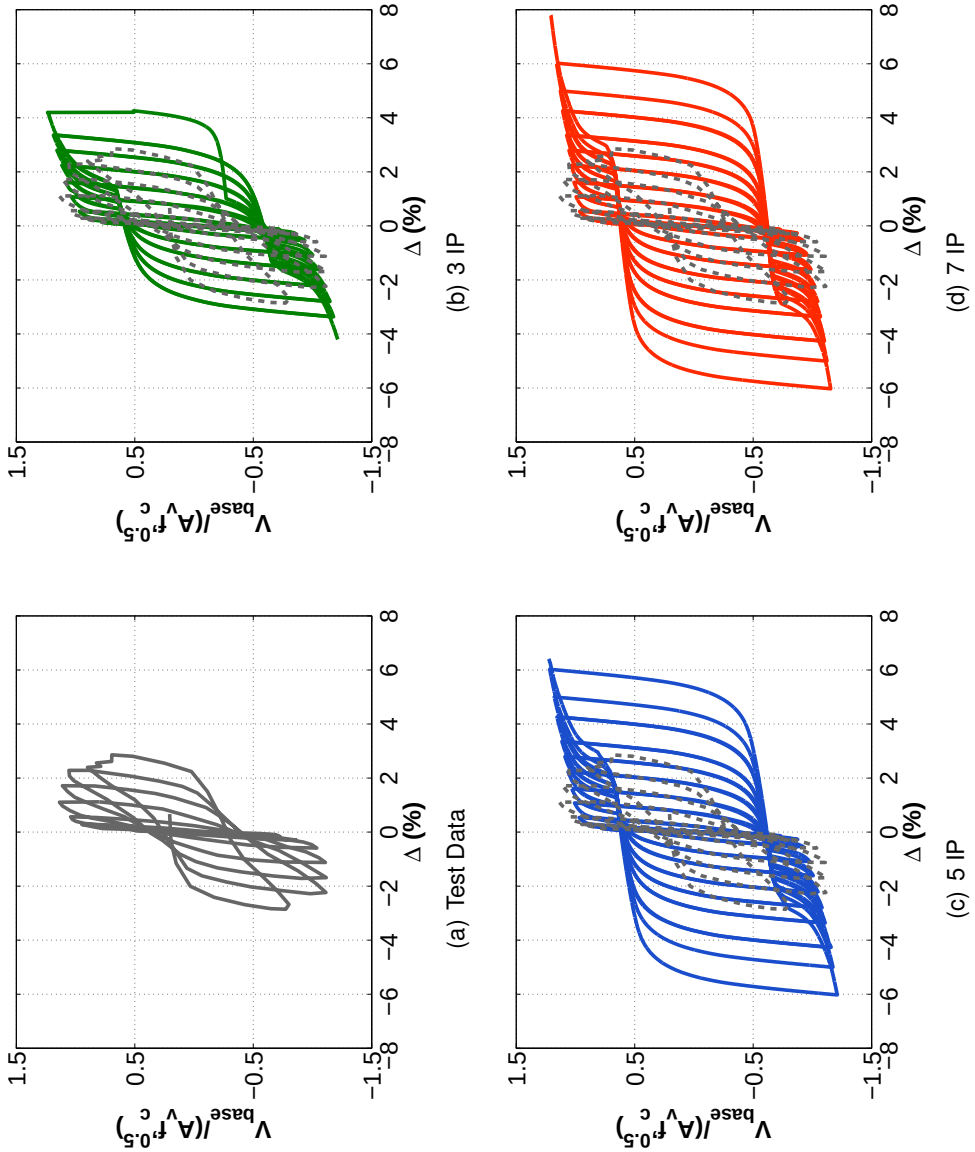

Figure 3.23: Specimen R1: Regularized Models

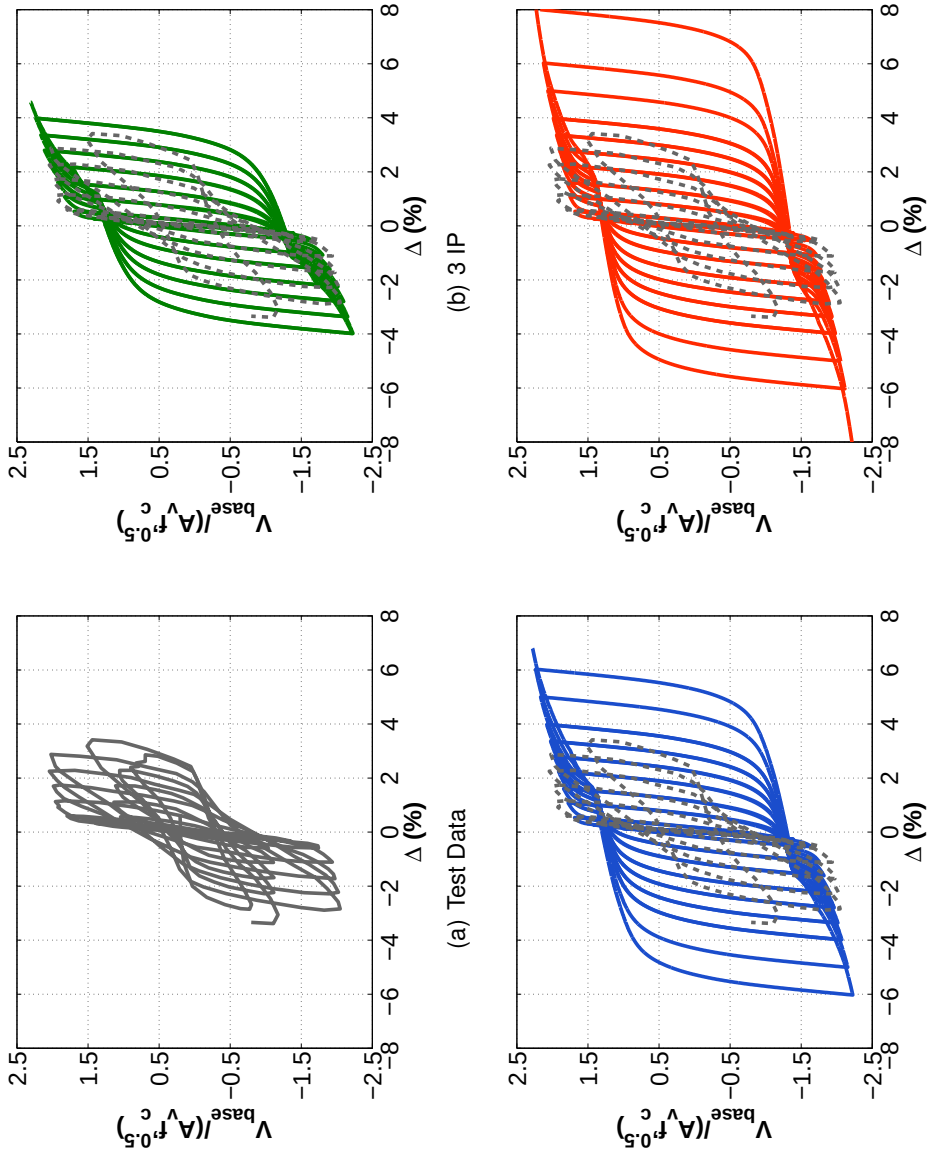

Figure 3.24: Specimen R2: Regularized Models

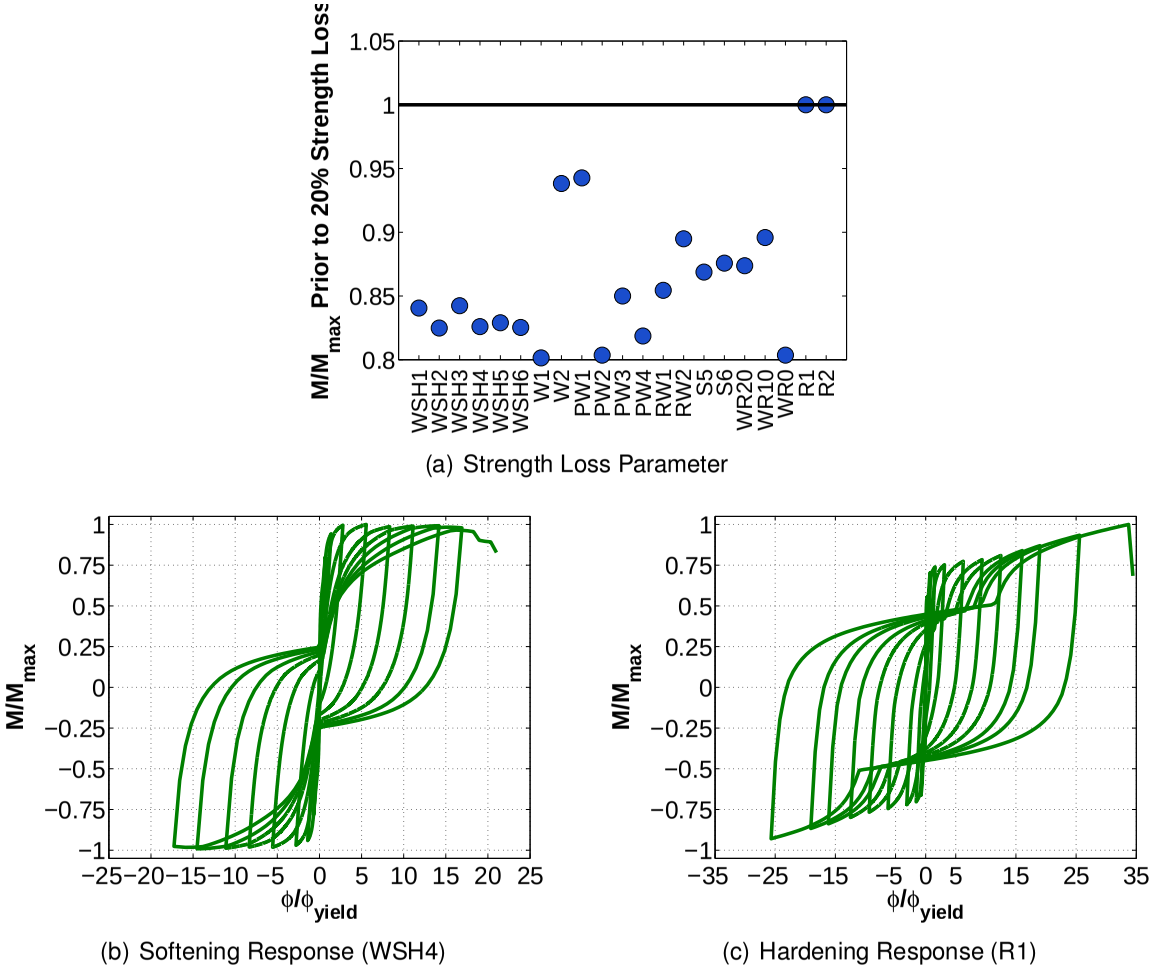

(a) Strength Loss Parameter

(b) Softening Response (WSH4)

(c) Hardening Response (R1)

Figure 3.25: Strength Loss Comparison

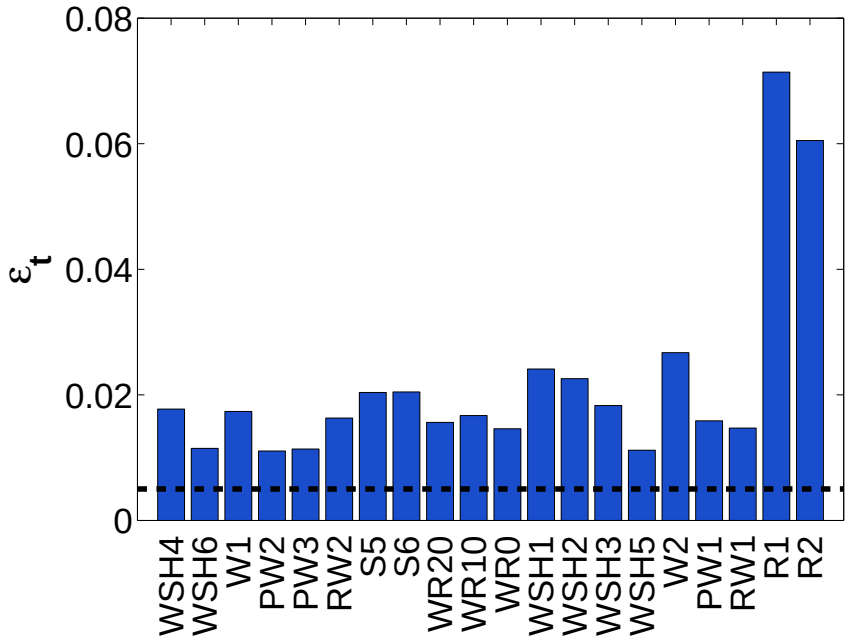

Figure 3.26: Planar Specimen Tensile Strain at Nominal

3.6 Simulation of Non-planar Wall Specimens

This section describes the modeling of six c-shaped wall specimens tested both uni- and bi-directionally using both unregularized and regularized line element models. The objective of this study was to determine whether the modeling recommendations developed using planar wall test data in Section 3.3 can provide accurate simulation of walls constructed using alternate cross-section shapes. Results of this study demonstrate that 1) modeling recommendations developed in Section 3.3 can be used to accurately simulate nonlinear response of the six c-shaped walls and 2) unregularized line element models significantly underestimated observed drift capacity for the c-shaped wall specimens.

3.6.1 Experimental Programs

Results of recent C-shaped wall specimens tests performed by Lowes et al (2012), Fardis et al (2004) and Beyer et al (2007) were used to assess the material regularization recommendations. Loading parameters and experimental results for these specimens are presented in Table A.5 and Table A.6. Detailed description of the experimental programs, specimen test setups, and additional parameters used for numerical modeling are provided in Appendix A. For refernce, the a construction drawing for the UW1 c-shape specimen tested by Lowes et al is provided in Figure 3.27. Parameters listed in Tables A.5 and A.6 are defined as follows:

- l_w = horizontal length of wall parallel to the web.
- t = wall thickness.
- b_f = total flange thickess (i.e. - wall width perpendicular to web).
- H = specimen height.
- $\rho_{be,1}$ = longitudinal reinforcement ratio for flange tip boundary element.
- $\rho_{be,2}$ = longitudinal reinforcement ratio for web to flange intersecting boundary element.
- ρ_v = longitudinal reinforcement ratio outside of boundary element regions.
- $\rho_{v,all}$ = total gross longitudinal reinforcement ratio
- $\rho_{vol,1}$ = volumetric reinforcement ratio for flange tip boundary element.
- $\rho_{vol,2}$ = volumetric reinforcement ratio for web to flange intersecting boundary element.
- $\rho_{t,w}$ = transverse reinforcement ratio in wall web.

- $\rho_{t,f}$ = transerse reinforcement ratio in wall flanges.

- Loading Direction = designated direction of applied lateral load. Loading applied parallel to the wall web is x-direction loading. Z-direction loading is applied perpendicular to the wall web, with +z loading applying a bending moment to the wall base which applies compression to the flange tips and -z loading applying a bending moment to the wall base which applies compression to the wall web.

- $M_b/(V_b l_w)$ = effective lateral loading ratio, where M_b/V_b is the ratio of base moment to base shear.

- M_y = yield moment strength for the base section determined by moment-curvature analysis, defined by first yield of the extreme tension steel layer. Calculated using reported material strengths but without strain hardening.

- M_n = nominal moment strength for the base section determined by moment-curvature analysis, defined by extreme compression fiber strain reaching a strain value of -0.003. Calculated using reported material strengths but without strain hardening.

- $M_{b,max}$ = maximum base moment resisted by the wall.

- $V_{n,pr}$ = nominal shear strength of the wall section per ACI 318 (2011). Calculated using reported material strengths.

- $V_{b,max}$ = maximum base shear resisted by the wall.

- Δ_y = specimen yield drift. Calculated as the drift associated with the base moment reaching M_y.

- Δ_u = specimen drift capacity. Defined as the drift at which the lateral load carrying capacity of the wall dropped to 80% of the historic maximum, for drift demands in excess of historic drift demands.

- Failure Mode = CB for specimens failing due to crushing and buckling of the compression zone or BR for specimens failing due to steel rupture after significant buckling.

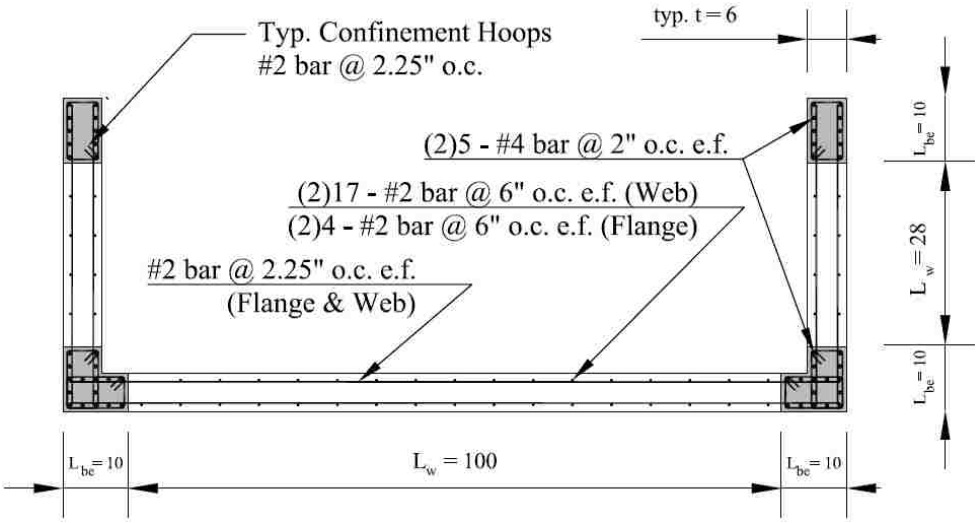

Figure 3.27: UW1 Wall Section

Table 3.10: Core Wall Specimen Section Data

ID	Geometry				Longitudinal Steel				Transverse Steel			
	l_w	t	b_f	H	$\rho_{be,1}$	$\rho_{be,2}$	ρ_v	$\rho_{v,all}$	$\rho_{vol,1}$	$\rho_{vol,2}$	$\rho_{t,w}$	$\rho_{t,f}$
	in.	in.	in.	in.	%	%	%	%	%	%	%	%
UW1	120.0	6.00	48.0	144.0	3.33	3.81	0.27	1.05	1.44	1.63	0.74	0.74
W1	59.1	9.84	49.2	141.7	1.21	0.81	0.17	0.56	0.90	0.90	0.54	0.32
W2	59.1	9.84	49.2	141.7	1.21	0.81	0.17	0.56	0.90	0.90	0.54	0.32
W3	59.1	9.84	49.2	141.7	1.21	0.81	0.17	0.56	0.90	0.90	0.54	0.32
TUA	51.2	5.91	41.3	104.3	2.11	0.84	0.25	0.71	2.28	1.05	0.30	0.30
TUB	51.2	3.94	41.3	104.3	2.26	1.13	0.38	0.97	2.52	1.23	0.45	0.45

Table 3.11: Core Wall Specimen Experimental Results

ID	Loading		Flexural Data				Shear Data				Drift Data		Failure Mode
	Dir.	$\frac{M_b}{V_b l_w}$	M_y	M_n	$M_{b,max}$	$\frac{M_{b,max}}{M_n}$	$V_{n,pr}$	$V_{b,max}$	v_{max}	$\frac{V_{b,max}}{V_{n,pr}}$	Δ_y	Δ_u	Type
			kip-ft	kip-ft	kip-ft		kip	kip			%	%	
UW1	± X	2.84	4530	5580	6190	1.11	431.0	218.0	4.0	0.51	0.34	1.86	CB
W1	± X	2.60	1930	2280	2610	1.14	315.0	204.0	6.0	0.65	0.30	3.00	BR
W2	+Z	3.12	1700	1950	2190	1.12	362.0	171.0	3.0	0.47	0.26	3.00	CB
W2	-Z	3.12	1450	1750	2020	1.15	362.0	156.8	2.8	0.44	0.33	3.00	CB
W3	± X	2.60	1930	2260	2430	1.08	311.0	192.3	6.0	0.61	0.43	2.00	BR
W3	+Z	3.12	1680	1910	1590	0.83	318.0	123.9	2.3	0.39	–	2.00	BR
W3	-Z	3.12	1440	1720	1920	1.12	318.0	149.6	2.8	0.47	0.34	2.00	BR
TUA	± X	2.58	980	1120	1120	1.00	133.0	105.1	3.2	0.79	0.40	3.50	BR
TUA	+Z	2.81	785	920	970	1.05	214.0	100.0	1.9	0.47	0.23	3.50	BR
TUA	-Z	2.81	725	850	850	1.00	214.0	87.9	1.7	0.41	0.35	3.50	BR
TUB	± X	2.58	950	1080	1130	1.05	104.0	102.7	5.7	0.99	0.36	3.00	CB
TUB	+Z	2.81	780	900	920	1.02	168.0	96.5	3.3	0.57	0.33	3.00	CB
TUB	-Z	2.81	640	750	790	1.05	168.0	81.9	2.8	0.49	0.35	3.00	CB

3.6.2 Nonlinear Models

To assess the modeling recommendations developed using planar wall data in Section 3.3, line element models using force-based distributed-plasticity elements were developed for the 6 c-shaped specimens.

Each specimen was modeled as a single vertical cantilever with a fixed base; three distributed-plasticity elements were used for each specimen model. Fiber section models were created for each specimen using fiber dimensions of approximately 1 inch by 1 inch. Regularized material properties were defined using the recommendations for force-based elements listed in Table 3.2. A linear shear stiffness using a reduced shear modulus, G_{eff} equal to 10% of the elastic shear modulus, G_c, was aggregated at the section level to account for shearing deformations.

For bi-directionally loaded specimens, a more advanced control algorithm than used previously for uni-directionally loaded planar specimens was developed. Analyses were performed using the generalized displacement control integrator available in OpenSees; cyclic displacement histories for each specimen were developed to match the drift history applied to the specimen. To ensure applied displacement components exactly matched the experimental tests, highly stiff truss elements oriented orthogonal to the desired direction of motion were systematically created and removed as necessary to match the drift history. The truss elements were used to ensure displacement only in the desired direction was enforced. Moderate numerical difficulties were encountered using this approach and the use of a penalty constraint handler was required to achieve a complete solution for all the specimen models. A penalty factor of 1e8 was found to be sufficient to advance the nonlinear solution without compromising solution accuracy. A global solution tolerance of 1e-6 and an intra-element tolerance of 1e-6 were maintained throughout nonlinear solution. The Newton-Raphson solution method was used at the beginning of each analysis; when non-convergence was detected, the solver was changed based on a solution algorithm developed by the author.

Prior to completing simulations for all specimens, a mesh sensitivity study was performed using the three uni-directional U-shaped specimens (UW1, W1, W2) to confirm pre-

vious findings that line element models which do not use regularization can not accurately simulate response of walls and that the use of regularization limits the observed mesh dependency. Results of the mesh sensitivity study are presented in Section 3.6.2.1. Simulation results for the three bi-directionally loaded specimens are provided in Section 3.6.2.2.

3.6.2.1 Mesh Refinement Study

A mesh refinement study was performed to compare simulation results for both basic (i.e. -unregularized) and regularized line element models. Because force-based elements were used, the number of intra-element fiber sections was increased rather than the number of elements. For the study, meshes of five and seven intra-element fiber sections were considered; three elements were used for every model. Only the three specimens tested uni-directionally (UW1, W1, W2) were considered for the mesh study.

For each specimen, simulated response quantities were compared with values determined by laboratory testing. Comparison of simulated to measured quantities are provided in Table 3.12; simulated and measured load-displacement plots are provided in Figure 3.28. Comparison results presented in Table 3.12 are defined as follows:

- $\frac{\Delta_{y,sim}}{\Delta_{y,obs}}$ = ratio of simulated to observed yield drift. Yield drift was defined as the drift corresponding to the specimen achieving the theoretical yield moment at the wall base.

- $\frac{V_{bm,sim}}{V_{bm,obs}}$ = ratio of simulated to observed maximum base shear strength.

- $\frac{\Delta_{u,sim}}{\Delta_{u,obs}}$ = ratio of simulated to observed drift capacity. Drift capacity was defined as the drift level at which the lateral load carrying capacity of the wall dropped to 80$\%$ of the historic maximum, for drift demands in excess of historic drift demands.

Table 3.12: Core Wall Mesh Study Results

Specimen	Direction	Basic Models						Regularized Models					
		$\frac{\Delta_{y,sim}}{\Delta_{y,obs}}$		$\frac{V_{bm,sim}}{V_{bm,obs}}$		$\frac{\Delta_{u,sim}}{\Delta_{u,obs}}$		$\frac{\Delta_{y,sim}}{\Delta_{y,obs}}$		$\frac{V_{bm,sim}}{V_{bm,obs}}$		$\frac{\Delta_{u,sim}}{\Delta_{u,obs}}$	
		5 IP	7 IP	5 IP	7 IP	5 IP	7 IP	5 IP	7 IP	5 IP	7 IP	5 IP	7 IP
UW1	$\pm$ X	1.03	1.03	1.00	1.01	0.66	0.61	1.03	1.03	0.97	0.97	0.89	0.90
W1	$\pm$ X	0.79	0.79	0.90	0.90	0.50	0.33	0.79	0.79	0.90	0.90	1.24	1.26
W2	+Z	0.80	0.80	0.93	0.93	0.25	0.21	0.80	0.80	0.92	0.92	0.90	0.96
W2	-Z	–	–	–	–	–	–	0.91	0.91	0.87	0.87	0.90	0.96

Results of the mesh study are similar to results previously discussed for planar wall line element models in Section 3.3. Model stiffness and strength were essentially unaffected by the selected mesh and both basic and regularized model accuracy was found to be essentially identical when considering strength and stiffness response quantities.

Drift capacity and strength deterioration was not accurately simulated using unregularized models. For specimen UW1 (Figure 3.28(a)), the unregularized models simulated tensile rupture to occur between 1.35% and 1.50% drift, compared to the experimental failure mode of compression crushing that occurred at 2.2% drift. The increased intra-element mesh of 7 fiber sections simulated a reduced drift capacity of 1.35% compared to a simulated drift capacity of 1.50% determined using the 5-section mesh. This response is consistent with results determined for planar wall specimen simulation results which exhibited increasingly brittle response because of localization effects as the selected mesh density was increased.

Localization effects were significantly more pronounced for W1 and W2 specimens (Figure 3.28(b) and (c)). The W1 specimen was observed to fail due to bar rupture at a drift of 3%, however simulated crushing failures at drifts of 1.48% and 0.96% were determined using 5- and 7-section elements, respectively. The W2 specimen was observed to fail due to concrete crushing at a drift of 3%, however simulated crushing failures at drift levels of 0.76% and 0.63% were determined using 5- and 7-section elements.

Drift capacity was simulated much more accurately using regularized models. For the UW1 specimen, the 5-section mesh simulated a rupture failure at a drift of 1.96% while loading to the ultimate drift capacity of 2.2%. For the 7-section model, the ultimate drift capacity of 2.2% was reached, but rupture failure occurred at a drift of -2.03%, reached after

completing one-half cycle at 2.2% drift. These results identify that some mesh dependency remain even for the regularized model. The 7-section model simulated a more ductile response than the 5-section model although the magnitude of the drift capacity, 1.96% for the 5-section model and 2.03% for the 7-section model, was approximately equal.

For the W1 specimen, both models simulated crushing failures at a drift level of approximately 3.8% which is 26% larger than the observed drift capacity of 3%. For the W2 specimens, both models correctly simulated crushing failure in the +z-direction. Modest mesh dependency was determined for this specimen, with drift capacity of 2.68% and the 2.90% for the 5- and 7-section models. Both values are within 10% of the 3% drift capacity observed for the W2 specimen.

Results for these specimens demonstrates that 1) unregularized wall models significantly underestimate the observed drift capacity for the three uni-directionally loaded c-shaped wall specimens and 2) regularization recommendations from Section 3.3 allowed improved simulation of drift capacity for the specimens. To extend the study of c-shaped walls, simulations were performed for the three bi-directionally loaded specimens using regularized line element models. Results for these analyses are discussed in Section 3.6.2.2.

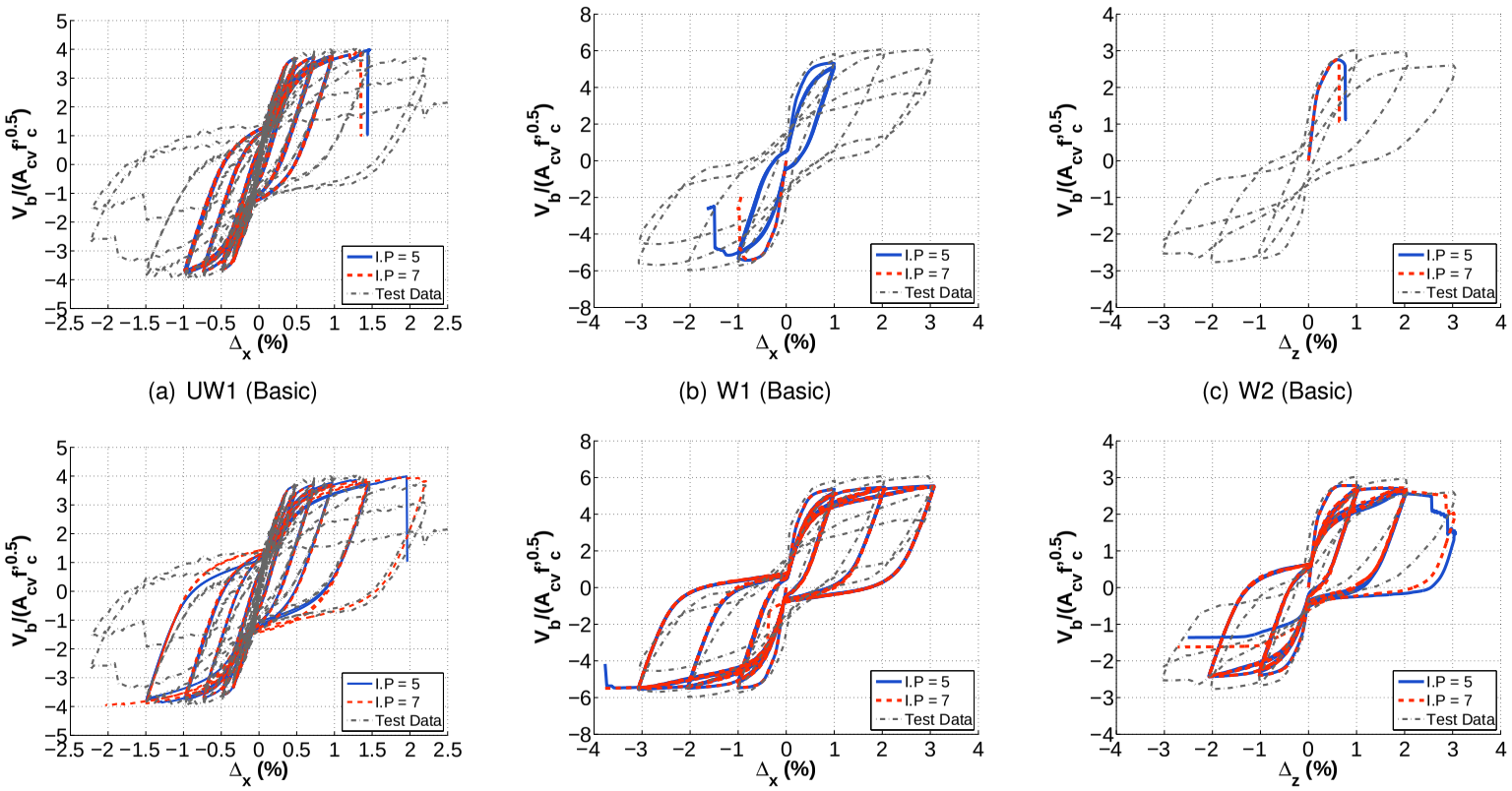

(a) UW1 (Basic) (b) W1 (Basic) (c) W2 (Basic)

(d) UW1 (Regularized) (e) W1 (Regularized) (f) W2 (Regularized)

Figure 3.28: Mesh Refinement Study Results

3.6.2.2 Bi-Directional Simulation Results

Simulated to observed response quantity comparisons for the three bi-directionally loaded specimens (W3, TUA, TUB) are provided in Table C.1; load-displacement histories for the specimens are provided in Figures 3.29 to 3.31. Specimen W3 was observed to fail in the laboratory after sustaining two cycles at 2% drift but failed due to bar rupture after completing the second cycle. For the specimen model, rupture failure was simulated just as the first excursion to 2% in the -z-direction achieved the target drift. After rupture, the specimen was loaded to a target drift of 2% in the +x-direction but a crushing failure was simulated at 1.6% prior to reaching the target drift. For this specimen the simulation underestimated the actual ductility of the specimen, although the peak drift achieved prior to failure was accurately determined. For specimen W3, strength was underestimated by approximately 6% for all loading directions. Yield drift was accurately simulated in the z-direction but the model was too flexible in the x-direction for which yield drift was overestimated by 15%.

Specimen TUA was observed to fail due to rupture of previously buckled bars at a drift of 3.5% in the -z-direction. For the specimen model, rupture failure was simulated at a drift of 3.85% while loading to a target drift of 4.00% in the -z-direction. Ductility of the TUA specimen was overestimated by the simulation, most likely due to the inability of the current model to simulate deterioration of steel strain capacity due to the previous buckling. Strength of the simulation in the x-direction and -z-direction was approximately 5% greater than the observed strength while strength in the +z-direction was accurately simulated. Model stiffness simulation was accurate (yield drift ratio = 1.03) for the x-direction and -z-direction. Simulated stiffness was approximately 10% high for the +z-direction.

Specimen TUB was observed to fail was due to crushing of unconfined concrete adjacent to the well-confined flange-web intersection during diagonal loading after achieving a drift of 3.08% in the -z-direction. For the specimen model, rupture failure was simulated at a drift of 3.40% while loading to a target drift of 3.50% in the -z-direction. Thus, the simulated results overestimated the ductility of this specimen although the peak simulated drift capacity was only modestly overestimated (ratio of peak simulated to peak observed drift capacity = 1.10). Strength of the simulation in the x-direction was approximately 5%

greater than the observed strength while strength in both the +z- and -z-directions was accurately simulated. Simulated model stiffness was accurate (yield drift ratio = 1.03) for the x-direction; simulated stiffness was approximately 10% too flexible for both the +z- and -z-directions.

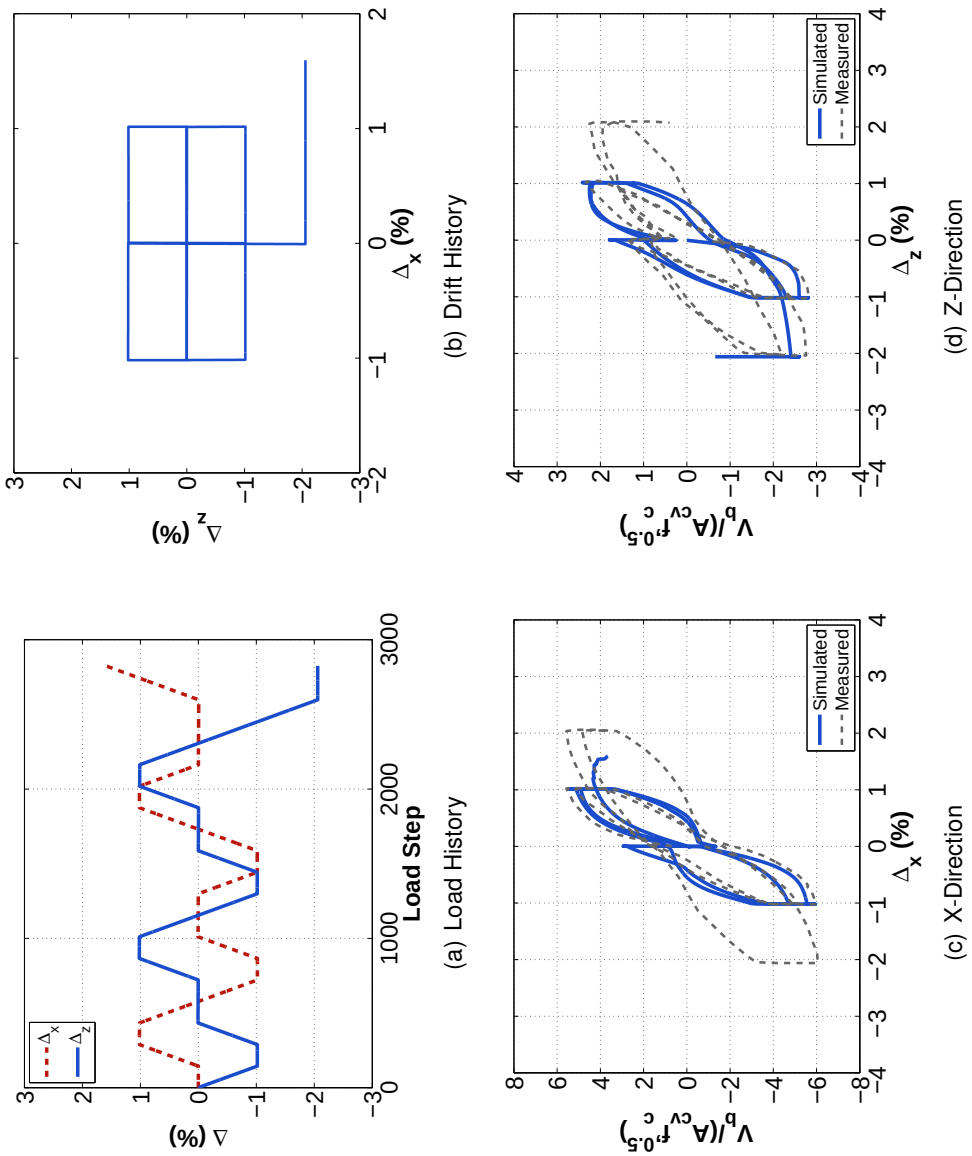

Figure 3.29: W3 Simulation Results

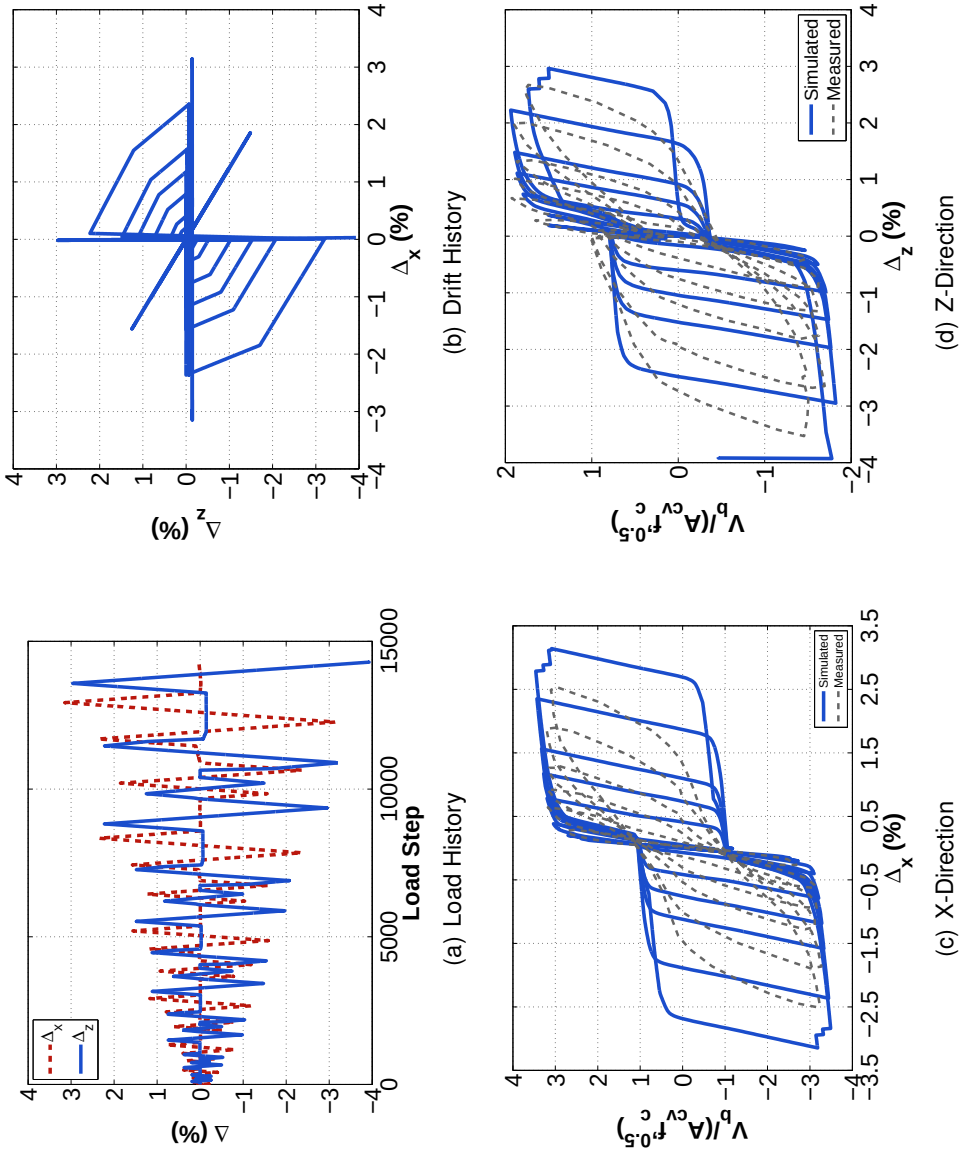

Figure 3.30: TUA Simulation Results

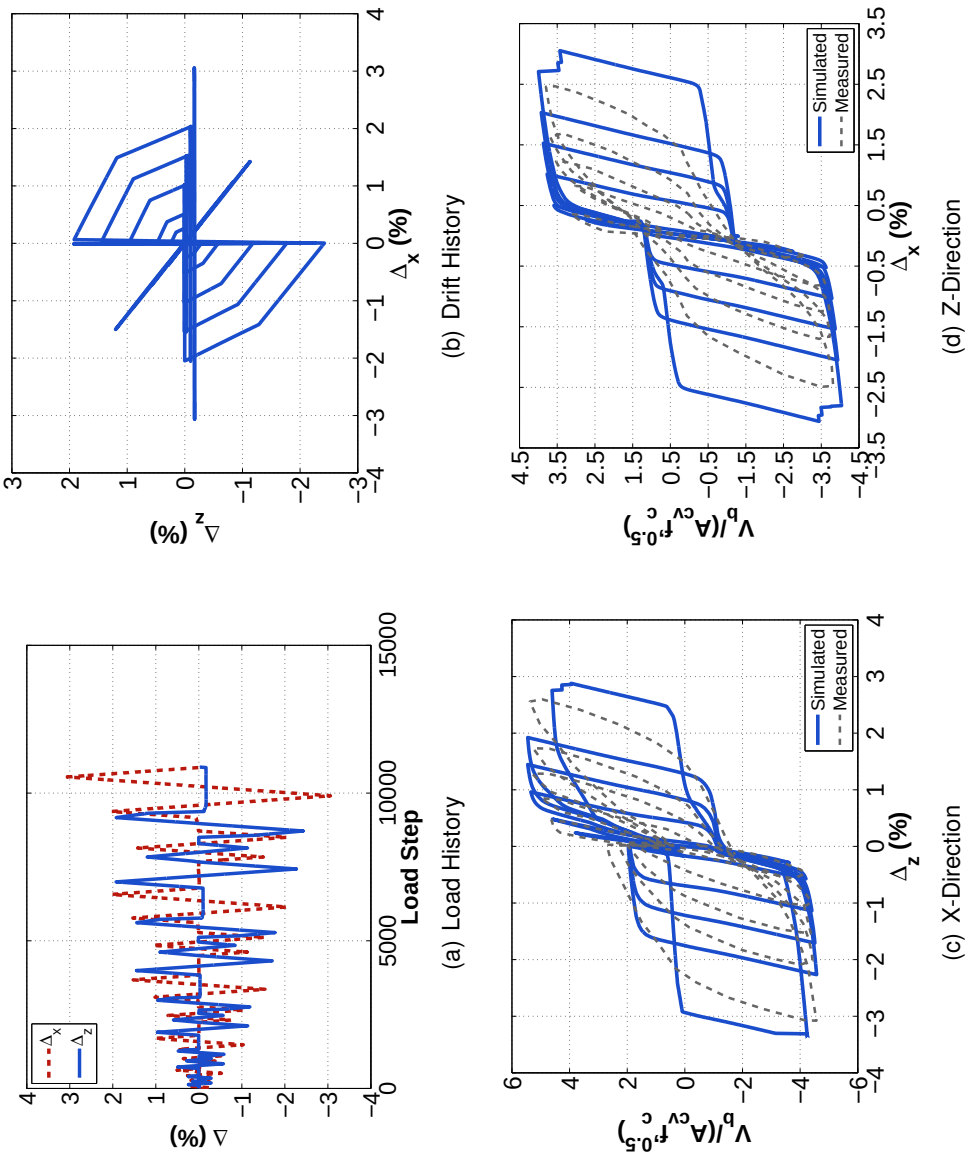

Figure 3.31: TUB Simulation Results

Table 3.13: Core Wall Specimen Simulation Results

Specimen	Direction	Regularized Models			
		$\frac{\Delta_{y,sim}}{\Delta_{y,obs}}$	$\frac{V_{bm,sim}}{V_{bm,obs}}$	$\frac{\Delta_{u,sim}}{\Delta_{u,obs}}$	Failure Mode
UW1	$\pm$ X	0.97	0.97	0.89	Ruptured
W1	$\pm$ X	1.26	0.90	1.24	Crushed
W2	+Z	1.25	0.92	0.90	Crushed
W2	-Z	1.10	0.87	0.90	Crushed
W3	$\pm$ X	1.16	0.93	–	Ruptured
W3	+Z	–	1.06	–	Ruptured
W3	-Z	1.00	0.92	1.00	Ruptured
TUA	$\pm$ X	0.97	1.05	–	Ruptured
TUA	+Z	0.91	1.00	–	Ruptured
TUA	-Z	0.97	1.07	1.10	Ruptured
TUB	$\pm$ X	0.98	1.06	–	Ruptured
TUB	+Z	1.10	1.03	–	Ruptured
TUB	-Z	1.09	1.00	1.10	Ruptured
	Mean	1.07	0.97	0.99	
	COV	0.11	0.07	0.17	

3.6.2.3 Summary and Conclusions

Simulations for six core wall specimens tested both uni- and bi-directionally were performed using regularized line element models. While not all observed specimen behavior could be captured by the simplified models, the recommended regularization relationships presented in Section 3.3 were determined to provide reasonably accurate simulation results for core wall specimens. Comparisons between mean results for the 19 planar wall specimens simulated in Section 3.4 and the mean response quantity results for the six core wall specimens identify 1) simulated to observed yield drift ratios are larger for core wall simulations than planar wall specimens (1.07 vs. 1.01), 2) no clear trends between simulated to observed yield drift and specimen loading direction was found, 3) peak simulated strength was nearly as accurate for core wall specimens as planar wall specimens (0.97 vs 0.99)

and 4) drift ratios for core walls and planar walls were found to have approximately equal mean values and coefficients of varation.

3.7 Conclusions

Modeling recommendations were developed with the objective of providing accurate simulation of the stiffness, strength and drift capacity of slender walls dissipating energy primarily through flexural yielding and failing due to flexural deterioration in either tension (rupture; rupture after significant buckling) or compression (crushing; buckling and crushing).

Results presented in this chapter demonstrate that regularized fiber section models, where uniaxial material models are modified through the use of material dependent post-yield energy relationships, can be used with distributed-plasticity beam column elements to both significantly reduce the observed mesh dependency and accurately simulate flexural deterioration of softening wall specimens. Relationships for determining post-yield material energy for steel reinforcing, unconfined concrete and confined concrete were determined using a set of 12 recently tested slender wall specimens observed to fail due to flexural compression. These relationships were validated by applying the modeling recommendations to additional slender wall specimens observed to fail due to flexural tension. For compression controlled specimens, the modeling recommendations enabled accurate simulation of complete cyclic response including ultimate drift capacity, and mesh dependency was significantly reduced. For tension controlled specimens, the modeling recommendations adequately simulated stiffness and strength charactersitics but modestly overestimated drift capacity. For both planar and c-shaped walls specimens tested in the laboratory and observed to fail in flexure, the recommended modeling approach permitted significantly improved simulation of flexural response and accurate simulation of specimen drift capacity.

Chapter 4

FEMA P695 COLLAPSE ASSESSMENT OF CORE WALLED BUILDINGS USING REGULARIZED BEAM COLUMN ELEMENT MODELS

4.1 Introduction

In Chapter 3, regularized distributed-plasticity beam-column elements were shown to provide accurate simulation of the cyclic response of slender, planar walls responding in flexure. Also in Chapter 3, the regularized beam-column elements were shown to provide adequate simulation of c-shaped walls loaded both uni- and bi-directionally. In this chapter, the regularized beam-column element modeling recommendations are used to assess seismic performance of a series of idealized buildings for which slender walls resist 100$\%$ of the design earthquake; hereafter these buildings are referred to as walled buildings.

Walled buildings ranging in height between 16 and 30 stories are designed and assessed using the 'Quantification of Building Seismic Performance Factors' methodology developed as part of the Applied Technology Council ATC-63 project and adopted by FEMA (2009). The methodology is based on the prevailing seismic design philosophy in which limited inelastic structural response under design-level and larger seismic events is considered acceptable. The level of inelastic response permitted is system specific and depends on the ability of the lateral system under consideration to sustain inelastic deformations without significant deterioration of lateral strength. Current US Code prescribes different seismic performance factors, R and C_d, to different systems based on their perceived ability to sustain inelastic deformations (ASCE, 2010). For slender walls expected to dissipate energy primarily through flexural yielding, current US Code (ASCE, 2010) prescribes R and C_d values between 5 and 6; however, these force reduction factors have not been well quantified by numerical simulation (SEAOC, 2008). The 'Quantification of Building Seismic Performance Factors' presented by ATC/FEMA, which links the results of numerical simulations to collapse risk, is a rational method but has not yet been used extensively to quantify

parameters for existing systems. The method was utilized previously by Gogus and Wallace (2011) to assess walled buildings up to 12 stories in height using distributed-plasticity beam-column elements. Results presented by Gogus and Wallace (2011) suggest the existing performance factors for walls are adequate. However the wall designs developed by Gogus and Wallace were, without clear justification, provided with shear capacity well in excess of current ASCE/ACI requirements. Additionally, the numerical modeling approach used by Gogus and Wallace 1) did not include material regularization and 2) was not extensively validated using all available test data.

This chapter summarizes the performance evaluation of wall buildings ranging between 16 and 30 stories in height using collapse risk assessment per FEMA P695, with regularized beam-column element modeling recommendations from Chapter 3 used to simulate wall response. Background on the FEMA P695 methodology is provided in Section 4.2. Design of the walled buildings and performance evaluation results are presented in Section 4.3.

4.2 Background on FEMA P695 Methodology

Results presented in this chapter evaluate seismic performance of core wall buildings using the FEMA P695 methodology developed as part of the Applied Technology Council ATC-63 project (Kircher and Heintz, 2008). Prior to discussing the building designs and application of the methodology, a brief summary of the P695 methodology is provided in this section.

The objective of the methodology is to provide a rational basis for establishing seismic performance factors (e.g. R, C_d) for newly proposed seismic lateral force resisting systems and for evaluating current design provisions for established seismic lateral force resisting systems (Haselton et al. 2008). Seismic performance factors determined using the methodology are intended to ensure equivalent safety against collapse for buildings with different seismic lateral force resisting systems. Safety against collapse is determined, for a seismic lateral force resisting system, by 1) developing a series of building designs that comply with proposed seismic design guidelines and reasonably represent all salient features of the system being considered, 2) performing nonlinear response history simulations

of the designed buildings using simulation tools capable of identifying system collapse and, 3) ensuring that an acceptably low probability of collapse is achieved when the system is subjected to Maximum Considered Earthquake (MCE) ground motions. For the investigation discussed in this chapter, ASCE 7 (2010) and ACI 318 (2011) were used for building design and nonlinear numerical simulations were performed using the regularized beam column element modeling approach developed in Chapter 3.

Collapse probability is determined by evaluating 'collapse capacity' for the multiple building designs using inelastic time history analysis (ITHA). Per P695, collapse capacity for a building design is determined using a prescribed set of ground motions that are scaled relative to the MCE. Collapse capacity is quantified in terms of a collapse margin ratio (CMR) that is the ratio between the ground motion intensity that causes collapse for over half the ground motion record set, $\hat{S}_{CT}$, and the MCE intensity, S_{MT}. Acceptable collapse safety is determined in terms of an adjusted collapse margin ratio (ACMR), which adjusts the CMR to account for spectral shape variations expected for extreme (rare) seismic events and probabilistic assessment considering uncertainties in design, simulation and building idealization (Deierlein et al. 2008).

4.3 Collapse Assessment of Long Period Core Wall Buildings

The FEMA P695 methodology was used to assess collapse risk for a series of tall walled buildings having fundamental periods, T_1, greater than 1.5 seconds. The walled buildings were designed using a single slender core wall as the lateral seismic force resisting system. The objective of the evaluation was to assess whether slender walls designed using current US seismic design standards can achieve an adequate margin of safety against collapse when exposed to MCE ground motions. Building designs ranging from 16 to 30 stories in height were developed; earthquake loads were determined as prescribed by ASCE 7 (2010), and ACI 318 (2011) was used to determine wall strength and detailing requirements. To completely explore the design demands prescribed by ASCE 7, both the equivalent lateral force (ELF) method and the modal response spectrum analysis (MRSA) method were used to design the buildings. Sections 4.3.1 to 4.3.3 provide details on the

performance groups, design methodology, and development of the nonlinear models used to perform ITHA. Details of the ground motion records and ground motion scaling are provided in Section 4.3.4. Presentation and discussion of P695 evaluation results are provided in Section 4.3.5.

4.3.1 Performance Groups

To assess performance of long period walled buildings, two performance groups (Table 4.1) were developed, each consisting of four walled buildings ranging between 16 and 30 stories in height. Two performance groups were defined to assess the impact of the two basic design methodologies available for determining the magnitude and distribution of earthquake design forces for walls prescribed by ASCE 7:

1. PG-1 walls were designed using the MRSA procedures outlined in Section 12.9 of ASCE 7-10

2. PG-2 walls were designed using the ELF procedure outlined in Section 12.8.1 of ASCE 7-10

Table 4.1: Long Period Performance Groups

Group No.	Basic Config.	Gravity Load	Design Method	Seismic Group	Period Domain	No. of Archetypes
PG-1	Core Wall	0.1f'$_c$A$_g$	MRSA	SCD D$_{max}$	Long	4
PG-2	Core Wall	0.1f'$_c$A$_g$	ELF	SCD D$_{max}$	Long	4

For both performance groups, a simple symmetric (regular) building geometry with a constant 100ft x 100ft building footprint was used. The lateral force system was assumed to consist of a single core wall comprising two wall webs in the loading (direction '1' in Figure 4.1). A 12 ft story height was used for all stories. For these buildings, only seismic loads applied in loading direction '1', parallel to the wall webs, was considered. For all walls,

a minimum thickness of 12 inches was considered for design, and all flexural reinforcement was assumed equally distributed across the section.

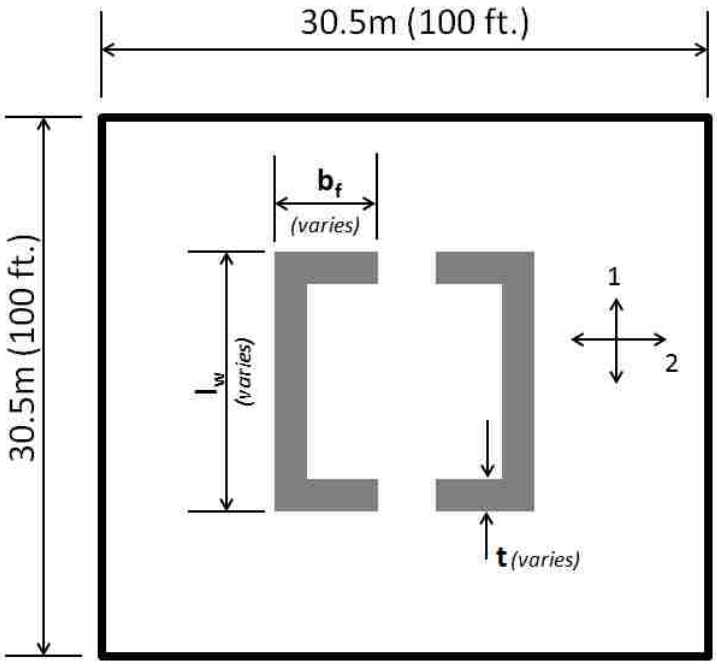

Figure 4.1: Plan View of Walled Building and Walls (NTS)

A factored gravity load of 190 psf and a seismic weight 170 psf were assumed to be distributed equally to each floor, with the exception that the roof level gravity load and seismic weight was reduced by 50%. All seismic weight was assigned to the lateral system and no lateral stiffness contribution from the gravity framing was considered. Intensity of wall axial stress due to gravity load was assumed to be $0.1f'_cA_g$ at the base of the wall. Gravity load carried by the gravity system was applied to the seismic system as a p-delta loading. Accidental torsion and building irregularity were not considered in design or analysis of the walled buildings.

Because 24- and 30-story building designs exceeded the 240 ft. maximum height limit for torsionally regular systems prescribed by ASCE/SEI, additional design guidelines were referenced that include additional design guidelines for taller buildings:

- 'Guidelines for Performance-Based Design of Tall Buildings, PEER 2010/05' (TBI Guidelines Working Group 2010)

- 'Seismic Design of Cast-in Place Concrete Special Walls and Coupling Beams, NIST GCR-917-11' (NIST 2011)

4.3.2 Wall Design

The design process used for wall sizing and reinforcement selection was

1. Select building height, N.

2. Determine base shear demand, V_u, and base moment demand, M_u, using either MRSA (PG-1) or ELF (PG-2), minimum base shear requirements and a force reduction factor, R = 6. For MRSA designs, base shear demand was scaled to 100% of the base shear demand determined by ELF analysis.

3. Select wall length, l_w, and thickness, t, such that 1) base shear demand, $V_u/(A_{cv}f'_c{}^{0.5})$ was approximately 2-3$\sqrt{f'_c(psi)}$ (NIST, 2011) and 2) cross-section aspect ratios, l_w/t, were kept around 16 (Mohr, 2007).

4. Select length of core wall flanges such that nominal design flexural strength, ϕM_n, provided at the wall base exceeded the base moment demand, M_u, with a targeted longitudinal reinforcing ratio of 1.0%.

For ELF designs, large base moment demands led to required longitudinal reinforcing ratios in excess of the target ratio of 1.0%. To maintain reasonable levels of reinforcement in these walls, increased wall area was provided. This reduced the design shear demand, $V_u/(A_{cv}f'_c{}^{0.5})$, below 2.0 for the ELF wall designs.

Table 4.2 provides a summary of the wall designs; quantities in Table 4.2 are defined as follows:

- PG = Performance Group; either PG-1 for MRSA designs or PG-2 for ELF designs.

- N = Number of stories
- T_1 = Calculated fundamental period using effective stiffness values of $0.5E_cI_g$, $1.0G_cA_{cv}$ and $1.0E_cA_g$.
- C_uT_a = ASCE 7 upper period limit.
- l_w = horizontal wall length.
- t = wall web and flange thickness.
- b_f = wall flange width for each of the 2 c-shaped walls comprising the core wall.
- Δ = design story drift.
- ρ = provided longitudinal reinforcement ratio.
- Ω_o = Flexural overstrength provided at the wall base, defined as M_{pr}/M_u where M_{pr} is the probable flexural strength including expected material strengths and strain hardening and M_u is the design base moment demand.
- v_u = Design level base shear demand, $V_u/(A_{cv}f'_c{}^{0.5})$.
- ρ_t = provided transverse reinforcement ratio.
- $\phi V_n/V_u$ = ratio of nominal wall shear capacity, ϕV_n, to design base shear demand, V_u, where V_n is the nominal shear strength computed per ACI 318 (2011) using design concrete and steel strengths and ϕ is taken as 0.60.
- $\phi V_{n,pr}/V_u$ = ratio of expected nominal wall shear capacity, $\phi V_{n,pr}$, to design base shear demand, V_u, where $V_{n,pr}$ is the expected nominal shear strength computed per ACI 318 (2011) using expected concrete and steel strengths and ϕ is taken as 0.60.

Table 4.2: Wall Design Data

	General								Flexural Design				Shear Design		
	Wall ID	N (Stories)	T_1 sec.	$C_u T_a$ sec.	l_w ft	t in	b_f in	Δ %	$\phi M_n/M_u$	ρ %	Ω_o	v_u	ρ_t %	$\phi V_n/V_u$	$\phi V_{n,pr}/V_u$
PG-1	MRSA1	16	3.35	1.44	25	18	48	1.58	1.00	1.00	1.34	2.38	0.25	1.07	1.24
PG-1	MRSA2	20	4.40	1.71	25	18	84	1.67	1.02	1.00	1.47	2.56	0.27	1.02	1.18
PG-1	MRSA3	24	5.58	1.96	25	18	120	1.76	1.02	1.00	1.48	2.67	0.29	1.06	1.22
PG-1	MRSA4	30	7.42	2.31	25	18	180	1.88	1.01	1.00	1.52	2.89	0.33	1.07	1.24
PG-2	ELF1	16	2.03	1.44	32	24	60	1.73	1.01	0.75	1.43	1.39	0.25	1.80	2.08
PG-2	ELF2	20	2.87	1.71	32	24	84	2.11	1.01	1.00	1.41	1.50	0.25	1.68	1.94
PG-2	ELF3	24	3.67	1.96	32	24	120	2.19	1.03	1.20	1.50	1.56	0.25	1.61	1.86
PG-2	ELF4	30	4.92	2.31	32	24	180	2.30	1.00	1.40	1.53	1.69	0.25	1.49	1.72

4.3.2.1 Design Level Seismic Demand

Design level seismic demands were based on the 5% damped design spectrum specified in Section 11.4.5 of ASCE 7-10, using spectral ordinates of S_{DS} = 1.00g and S_{D1} = 0.6g consistent with a P695 D_{max} design category. The D_{max} spectral ordinates are recommended in FEMA P695 (2010) for use in estimating maximum demands for Seismic Design Category D and site class D soil conditions. This design spectrum is shown in Figure 4.2.

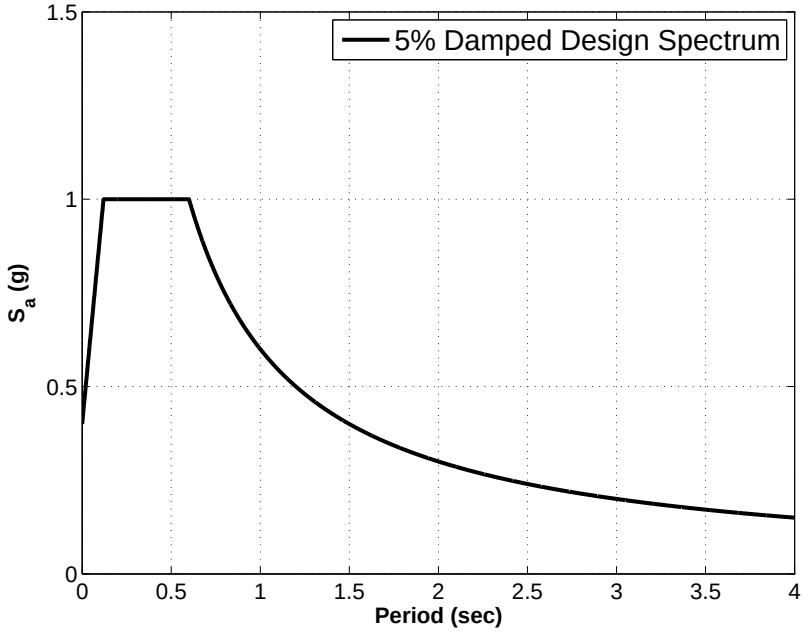

Figure 4.2: Design Spectrum Comparison

4.3.2.2 Flexural Design Method

Flexural reinforcement for the walls was selected such that provided design flexural strength, ϕM_n, was equal to or greater than calculated base moment seismic demands. Design concrete compressive strength was taken as 5000 psi and design yield strength of flexural re-

inforcement was taken as 60000 psi. Provided flexural capacity to demand ratios, ϕM$_n$/M$_u$, ranged between 1.00 and 1.03 for the designed walls. For the evaluation results presented in this chapter, the flexural reinforcement required at the base section was assumed to remain constant, without bar curtailment, up the entire wall height. The impact of alternate bar cutoff configurations is addressed in Chapter 7.

Flexural reinforcement for all walls was uniformly distributed along the cross-section in two curtains and both flange and web regions of the walls were detailed to satisfy boundary element detailing requirements specified by ACI 318 (2011) Section 21.9.6. Core wall webs were detailed to satisy boundary element requirements because these regions are expected to sustain large compressive demands when the core wall is loaded laterally as a coupled wall in the loading direction perpendicular to the core wall web.

4.3.2.3 Shear Design Method

Transverse reinforcement was provided to satisfy shear strength requirements per Section 21.9.4.1 of ACI 318 (2011). Provided shear capacity to demand ratios, ϕV$_n$/V$_u$ for MRSA walls ranged between 1.02 and 1.07. For ELF wall designs, larger wall areas were required meet flexural demands and this resulted in larger provided wall shear areas. Larger shear areas and minimum transverse steel ratios resulted in shear capacity to demand ratios between 1.49 and 1.80 for ELF wall designs.

4.3.2.4 Calculated Story Drift

For both ELF and MRSA wall designs, maximum story drifts were calculated using ASCE 7 procedures and elastic analysis results. Amplification of drifts calculated under design level load patterns were increased by C$_d$ to estimate inelastic drift demands. Amplified drift demands, Δ, were calculated using a C$_d$ value of 5.0, as specified by ASCE 7 for special reinforced concrete shear walls.

4.3.3 Nonlinear Model Details

All nonlinear wall modeling was performed using the open-source OpenSees software platform (Mazzoni et al, 2006). Each walled building was modeled using a combination of elastic zero-length elements, elastic beam elements and nonlinear force-based fiber section distributed-plasticity elements. Each story of the wall comprised three elastic zero-length elements in parallel below a FBBC element. One zero-length elastic element represented the shear flexibility of the story. The other two zero-length elements were given large (essentially rigid) stiffness values and were included solely to transfer axial force and bending moment in the wall in parallel with the shear element. Seismic mass was lumped at each story level. Axial load was applied at each story to generate a gravity load axial stress of $0.1f'_cA_g$ at the wall base. The base of the wall was fixed against translation and rotation, and no foundation flexibility was considered.

P-delta effects were included by adding a leaning column to the wall model. Nonlinear geometry was simulated using the co-rotational tranformation available in OpenSees. The leaning column was modeled using an elastic beam element with a pinned (free to rotate) base. The elastic stiffness of the leaning column was very small (several orders of magnitude below that of the cracked wall stiffness) to ensure negligible lateral stiffness was provided the column. At each floor level, the leaning column was linked to the wall using horizontal truss elements. Further details of the nonlinear model used for inelastic time history analyses are provided in the following sections.

4.3.3.1 Expected Material Properties

Expected material properties were used to define fiber section material models. Expected yield strength of reinforcement was increased by 17% from 60000 psi to 70200 psi based on material strength recommendations by PEER (TBI, 2010). Ultimate strength of reinforcement was taken as 105 ksi with rupture assumed to occur at a tensile strain of 20%. Expected unconfined uniaxial concrete compressive strength, f'_c, was increased by 30% from 5000 psi to 6500 psi based on material strength recommendations by PEER (TB1, 2010).

4.3.3.2 Flexural Response Model

Wall flexural response was modeled using force-based distributed-plasticity beam-column elements with fiber fiber-section (i.e integration points) along the length of each element. Concrete and steel material response was regularized as described in Chapter 3. Fiber section models were discretized using a fiber length of approximately one inch. For each building model, c-shaped walls were combined into a single fiber section to permit the use of a single beam-column element per story to represent the core wall.

The OpenSees 'Concrete02' uniaxial material model was used to model both confined and unconfined concrete fibers. Strength enhancement of confined concrete fibers was determined using the model developed by Saatcioglu and Razvi (1992). For both fibers, the strain at peak strength was determined such that the initial material modulus, E_c, was equal to $57000\sqrt{f'_c}$ (psi). Concrete tensile strength was taken as $4\sqrt{f'_c}$ (Wong and Vecchio, 2006) with a tension softening slope taken as $E_c/20$ per recommendations by the material model developers (Yassin, 1994). The strain associated with 80% strength loss, ϵ_{20}, was determined using regularized crushing energy data developed in Chapter 3. For unconfined fibers, ϵ_{20u} was determined using the expression for recommended crushing energy provided in Table 3.2. For confined fibers, confined crushing energy was taken as 230% greater than the value used for unconfined crushing energy. This value for confined crushing energy is moderately higher than the recommended increase of 170% suggested in Table 3.2. A larger increase was used because all designed boundary element were detailed such that multiple cross-ties were provided along the entire flange width. With this confinement configuration, Figure 3.17 suggests an increase in crushing energy of approximately 230% can be achieved.

The OpenSees 'Steel02' uniaixal material model was used to model flexural reinforcing steel fibers. Regularized material model parameters were defined using expected material property values provided in the previous section and equations 3.3 and 3.4.

4.3.3.3 Shear Response

A reduced effective linear shear stiffness of $0.1G_cA_v$ was determined to be appropriate for modeling statically loaded wall specimens with aspect ratios between 1.5 and 3.0 experiencing significant flexural distress over a large portion of their height using distributed plasticity fiber section elements (Chapter 3). However, because the walled buildings designed in this section represent dynamically loaded buildings ranging in aspect ratio between 3.5 and 10, it is unclear whether the previously validated shear model is appropriate. Particularly, it is unlikely that upon initial loading the entire wall will possess a shear stiffness that is significantly lower than the elastic value. For these reasons, an elastic shear stiffness taken equal to the gross, elastic value (G_cA_v) was used to model shear stiffness of the walls. Alternate shear response models were also considered; comparison of ITHA results considering different shear response models are discussed in Chapter 7.

4.3.3.4 Rayleigh Damping

Rayleigh damping was used to model the effects of non-hysteretic damping. Rayleigh damping coefficients were assigned such that 2% damping was achieved at periods corresponding to $1.5T_1$ and T_2, where T_1 and T_2 are the first two building periods as determined by modal analysis using effective flexural and shear stiffness values of $0.5E_cI_g$ and G_cA_v, respectively. A period larger than T_1 was used in an attempt to reduce overdamping first mode response when period elongation occurs. Anchoring to T_2 provides a viscous damping ratio of around 4.5% of critical for the third mode with increasing damping values for higher modes (Figure 4.3.). This was deemed acceptable as the current study considers buildings of 16 to 30 stories, and it was verified that higher modes (> 3) had minimal impact on the predicted response. For response at periods between $1.5T_1$ and T_2, the provided Rayleigh damping curve is less than 2%. This period range affects the first mode (prior to significant period elongation) and the second mode (after period elongation occurs).

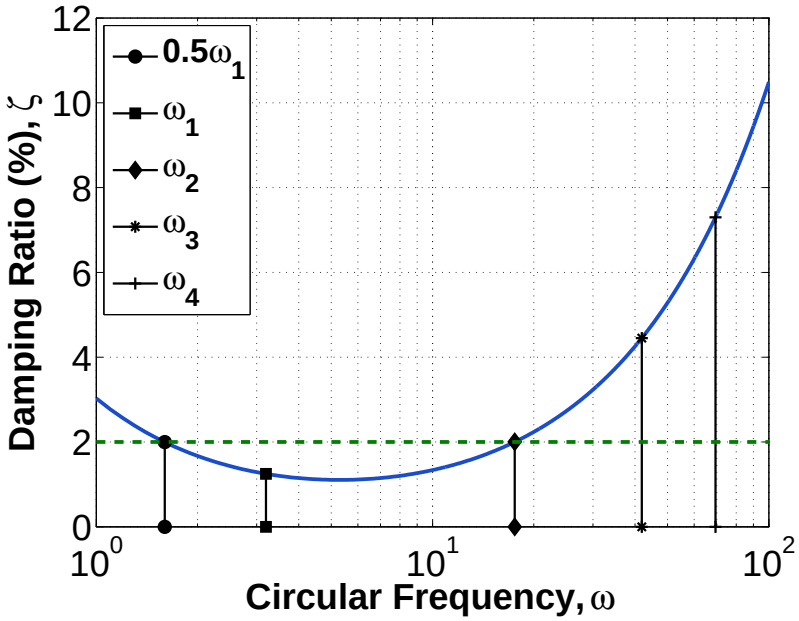

Figure 4.3: Rayleigh Damping Curve (All Walls)

4.3.3.5 Dynamic Solution Technique

For each input ground motion, dynamic solution progressed using a constant time step of 0.002 seconds. Ground motion input data reported at a time step larger than 0.002 seconds were linearly interpolated to yield acceleration ordinates at intermediate time values. Prior to dynamic solution, all gravity loads were applied to the model and held constant throught the analysis. Time stepping was performed using the Hilber-Hughes-Taylor (HHT) method with a specified numerical damping, α, factor of 0.7. A value of 0.7 was selected to maximize the numerical damping of spurious higher modes effects while maintaining second order accuracy during time integration. Nonlinear solution for each time step was initially attempted using the Newton-Raphson algorithm, with global convergence tolerance on the Relative Energy Increment assigned a value of 1e-5 and FBBC element internal convergence tolerance assigned a value of 1e-8. If convergence was not achieved during a time step, a solution strategy developed by the author modified solution parameters (nonlinear solver, monitored convergence quantity, time step) until convergence was achieved.

4.3.4 Ground Motion Input

The 44 recorded accleration records comprising the P695 'Far-Field' record set, which includes 22 ground motion pairs recorded at sites located at least 10 kilometers from the fault rupture location, event magnitudes between 6.7 and 7.9, were used to perform ITHA of the core wall buildings.

4.3.4.1 Ground Motion Scaling

Ground motion scaling of the far-field record set was performed by anchoring the median spectrum of the record set to the ASCE 7-10 MCE spectrum. Per P695 requirements, the median spectrum of the record set was anchored to the ASCE MCE spectrum at the code-based upper period limit, $C_u T_a$. The median spectrum scaled to match the ASCE MCE spectrum at $C_u T_a$ defines the MCE intensity for the record set. P695 performance evaluation is accomplished primarily through the establishment of the collapse margin ratio (CMR). The CMR is the seismic intensity level, above or below the MCE level, for which half the ground motion records initiate building collapse. Seismic intensity, relative to the MCE intensity for the record set, is measured at the code-based period limit, $C_u T_a$. Thus, P695 evaluation requires evaluating structural performance at increasing ground motion intensity levels until over 50$\%$ of the scaled records initiate collapse of the building model.

Plots showing the MCE level for the record set for the 4 building heights evaluated are shown in Figure 4.4. For each building height, only one MCE level spectrum is calculated because the anchoring period, $C_u T_a$, defined for walled buildings is determined solely by building height.

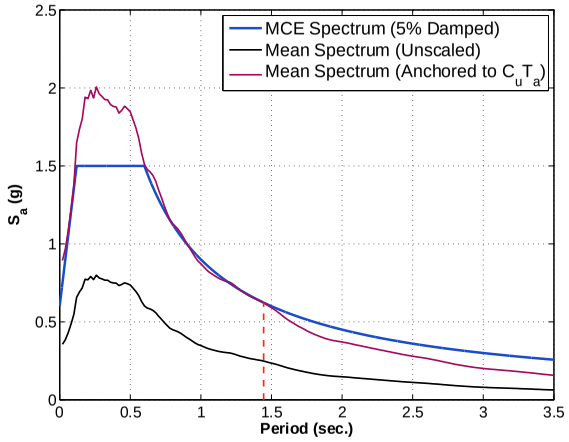

(a) 16-story Buildings

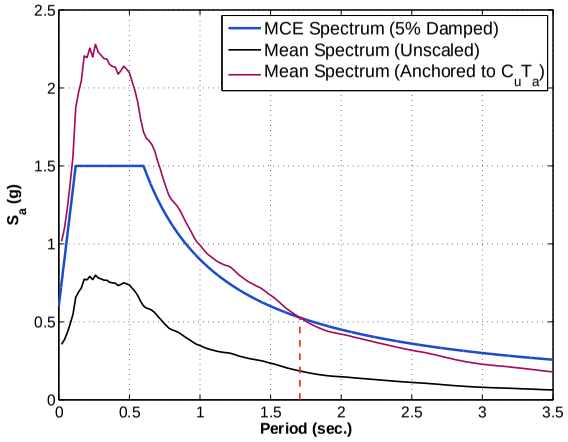

(b) 20-story Buildings

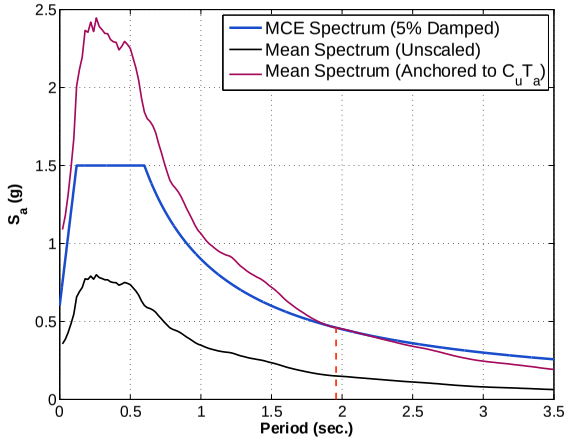

(c) 24-story Buildings

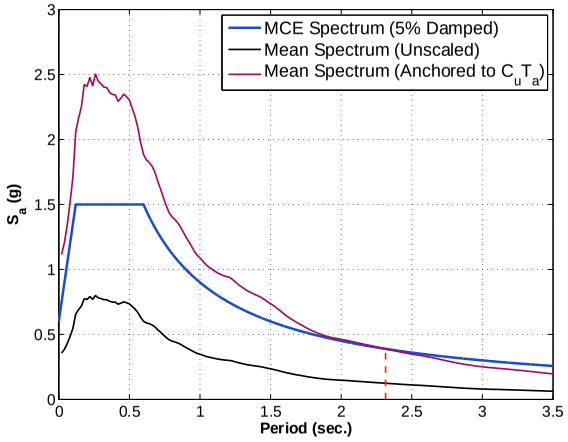

(d) 30-story Buildings

Figure 4.4: P695 Ground Motion Scaling Results (N = 16,20,24 and 30)

4.3.5 P695 Evaluation Results

Results of P695 evaluation for the selected wall designs are presented in this section. Sections 4.3.5.1 and 4.3.5.2 address the simulated and non-simulated collapse criteria used in the evaluation. Section 4.3.5.3 provides performance evaluation results for the core wall buildings.

4.3.5.1 Simulated Collapse Criteria

The regularized beam-column element used to model the core walls was shown in Chapter 3 to be capable of directly simulating flexural failure for wall sections. Thus, loss of lateral strength due to flexural failure can be detected by the numerical model. Ground motions causing deterioration of the hysteretic flexural model sufficient to reduce flexural strength below 80$\%$ of the peak capacity were considered to 'initiate flexural failure' of the core walls. Quantification of flexural damage during nonlinear analysis is discussed in greater detail in Chapter 7.

4.3.5.2 Nonsimulated Collapse Criteria

Two nonsimulated collapse criteria were used to assess system behavior which could not be simulated directly by the numerical simulations:

Shear Failure A shear failure was initiated if shear force in the wall determined by inelastic time history analysis, V_{ITHA}, was larger than the provided shear strength. Wall strength was taken as, $V_{n,pr}$, the expected nominal strength defined by ACI 318 (2011) calculated using expected material strength and a strength reduction factor, ϕ = 1.0. A shear failure was assumped to represent initiation of lateral strength loss for the wall; this constitutes 'collapse' per P695.

Gravity System Collapse Story drift was imposed as a non-simulated collapse criterion to to capture the limited drift capacity of the gravity systems. Here is was assumed that

loss of gravity load carrying capacity would initiate at 5$\%$ story drift; this constitutes failure per P695.

4.3.5.3 Median System Collapse Results

Collapse margin ratios (CMRs) and calculated collapse probabilities for the core wall buildings are presented in Table 4.3. For all core buildings, non-simulated shear failure initiated building collapse prior to flexural failure or gravity system collapse. Plots showing the relationship between increasing ground motion amplitude, with respect to the MCE, and inelastic shear demand to expected capacity ratios, $V_{ITHA}/V_{n,pr}$, are provided in Figure 4.5.

CMRs represent the ratio between the ground motion intensity at which 50$\%$ of the acceleration records cause collapse, $\hat{S}_{CT}$, and the MCE level ground motion intensity, S_{MT}. To determine collapse probability, a collapse fragility is defined by the P695 methdology for each building using the calculated CMR value and 1) an estimated level of uncertainty accounting for the robustness of the design guidelines, experimental data and numerical simualation tools used to determine the CMR and 2) a beneficial adjustment to the calculated CMR accounting for spectral shape variations expected for rare seismic events.

Quantification of uncertainty requires an estimation of the uncertainty in the design procedures, available test data, and numerical models used to determine the CMR values. For the core wall buildings, system uncertainty was assigned quality ratings of 'B' (good) to define the level of uncertainty present in the 1) design guidelines available for walls, 2) available test data and 3) the regularized beam column model used to simulate wall response. With quality ratings of B assigned, P695 defines the total uncertainty for the core system, β_{TOT} = 0.525.

Per the P695 methodology, collapse fragility is defined assuming a lognormal cumulative distribution function with a mean value equal to the calculated CMR value, and a dispersion or standard deviation, σ = β_{TOT}. A collapse fragility for one building (ELF1) is shown in Figure 4.6, where CMR, S_{CT}/S_{MT}, is plotted vs collapse probability, $P_{collapse}$. Finally, collapse probability was determined by multiplying the CMR by the spectral shape factor, SSF, and determining the $P_{collapse}$ corresponding to the MCE (S_{CT}/S_{MT} = 1.0). For

example, the adjusted collapse probability for the ELF1 building design was determined to be approximately 78%.

Comments on Collapse Results CMRs for all core wall buildings were controlled by the shear failure criterion. For all core walls, ACMR values less than 1.0 were determined, indicating the building designs could not sustain MCE level seismic shear demands without significant risk of shear failure. Collapse probabilities for 7 of the 8 designs were determined to exceed 90%, and all collapse probability values were determined to be greater than 75%. Additionally, for 7 of the 8 designs, ACMR values were less than 0.67, which indicates the building designs could not sustain design level seismic shear demands without significant risk of shear failure. Figure 4.5 compares the relationship between shear demand and seismic intensity for walls designed using MRSA and ELF methods. The results show that both design methods yielded shear designs insufficient to resist MCE shear demands.

Table 4.3: Core Wall Building P695 Evaluation Results

ID	Design Summary								P695 Results			
	N (Stories)	Envelope (Flexure)	R	$C_u T_a$ (Sec.)	S_{MT} (g)	μ_T	β_{TOT}	SSF	S_{CT} (g)	CMR	ACMR	Collapse Prob.
MRSA1	16	Constant	6	1.44	0.63g	7.3	0.525	1.56	0.20g	0.32	0.50	90%
MRSA2	20	Constant	6	1.71	0.53g	5.7	0.525	1.49	0.15g	0.29	0.43	95%
MRSA3	24	Constant	6	1.96	0.46g	5.2	0.525	1.47	0.13g	0.27	0.40	96%
MRSA4	30	Constant	6	2.31	0.39g	5.0	0.525	1.46	0.11g	0.29	0.42	95%
ELF1	16	Constant	6	1.44	0.63g	10.0	0.525	1.59	0.26g	0.42	0.67	78%
ELF2	20	Constant	6	1.71	0.53g	8.9	0.525	1.61	0.17g	0.32	0.52	90%
ELF3	24	Constant	6	1.96	0.46g	8.1	0.525	1.61	0.13g	0.27	0.43	94%
ELF4	30	Constant	6	2.31	0.39g	7.4	0.525	1.58	0.10g	0.25	0.40	96%

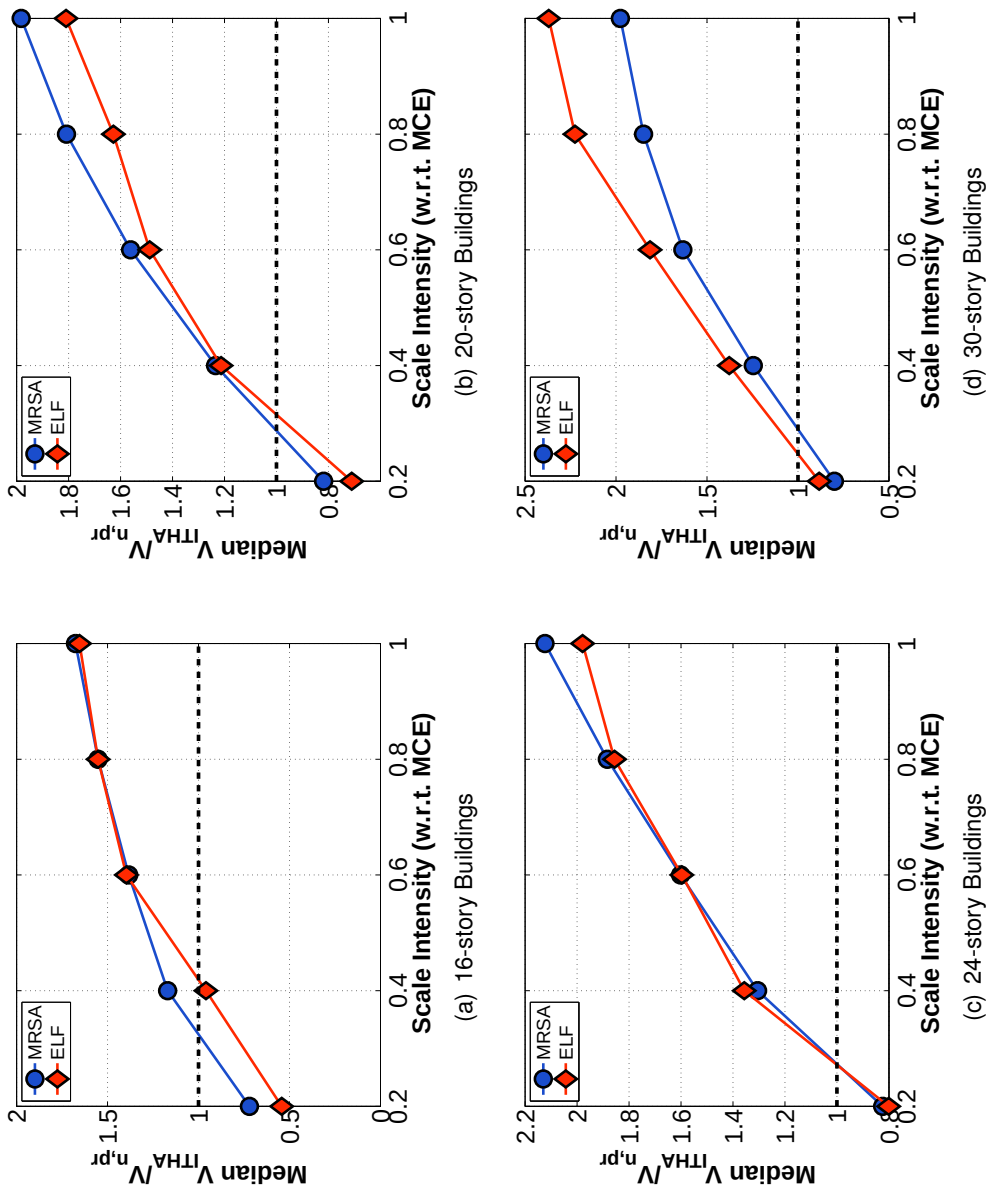

Figure 4.5: P695 Shear Demand Evaluation

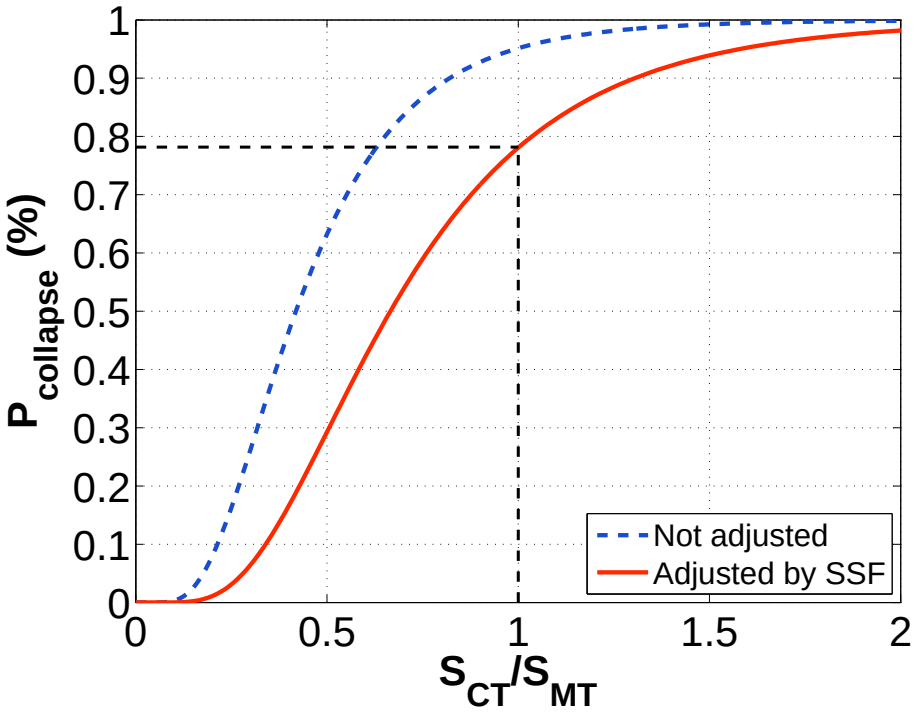

Figure 4.6: Calculated Collapse Fragility (ELF1 Building)

4.4 Conclusions

In this chapter, regularized beam column elements were used to perform numerical simulation of core wall buildings designed in accordance with current US seismic design procedures (ASCE 7-2010 and ACI 318-2011). The objective of the simulations was to evaluate the current design procedure for slender walls and evaluate whether slender walls designed using current US seismic design standards can achieve adequate margins of safety against collapse at the Code defined maximum considered earthquake (2% probability of exceedence in 50 years). P695 was employed to accomplish the evaluation. Eight buildings were designed and analyzed using incremental dynamic analysis considering a suite of 44 ground motion records scaled to the maximum considered earthquake.

IDA results show that for all buildings, the collapse risk was controlled by 'shear failure'.

For the suite of 44 ground motion records, median shear demand exceeded provided wall shear capacity for seismic intensity levels lower than the design level earthquake. These results suggest that slender walls designed using current US code-based shear demands may be unable to achieve the expected ductile flexural response and could be limited in ductility by shear failure.

Chapter 5

EVALUATION OF CURRENT METHODS FOR ESTIMATING SEISMIC SHEAR DEMANDS

5.1 Introduction

Prevailing ductile design philosophy for concrete walls consists of ensuring shear demands that develop within walls during a seismic event do not exceed the provided shear capacity. To ensure such a design objective is met, a capacity design approach is necessary. For walls responding inelastically in flexure, capacity design procedures that account for:

1. The increase in shear demand associated with the development of the probable flexural strength, rather than the design flexural strength, at the wall base.

2. The observation that all modal load patterns are not equally affected by the selected force reduction factor, R.

are required to limit shear demands.

The need for such procedures was first identified by Blakeley et al. (1975) and currently, many national building codes throughout the world recognize the need for capacity design to ensure ductile response of slender walls. However, current building code documents in the US which directly address new construction of such walls (ASCE 7 (2010);ACI 318 (2011)) do not, as of their current editions, require a capacity design approach nor do they supply the designer with recommendations to be used for capacity design of slender walls. Walled buildings designed using current US building code documents were investigated in Chapter 4. This evaluation demonstrated that the current US seismic design requirements for walls do not adequately limit shear demands developing in slender walls responding inelastically in flexure to acceptable levels. These results suggest current US design procedures may be inadequate to ensure shear demands do not inhibit the forma-

tion of a ductile flexural mechanism and highlight the need for inclusion of capacity design requirements for walled buildings in US building codes.

The remainder of this chapter summarizes existing capacity design procedures for limiting shear demands in walls responding inelastically in flexure. Several existing capacity design procedures are evaluated using inelastic time history analysis (ITHA) and it is demonstrated that existing procedures do not accurately estimate design-level shear demands predicted by ITHA for 64 walled buildings designed considering a range of building heights, initial fundamental periods and force reduction factors (R). The results presented in this chapter motivate the development of an improved procedure for limiting shear demands in walled buildings presented in Chapter 6.

A background of wall shear capacity design and review of existing shear capacity design recommendations used in other national building code and design practice documents are presented in Section 5.2. Section 5.3 details a development of a suite of wall designs that are then analyzed to assess the existing design recommendations. Details of the ITHA and the numerical model development are presented in Section 5.4. Assessment of the existing recommendations are provided in Section 5.5.

5.2 Existing Shear Capacity Design Methods for Slender Walls

The need to capacity design slender walls for shear was first demonstrated by Blakeley, et al. (1975) who performed ITHA of cantilevered walls using inelastic beam column elements and noted that walls were predicted to develop significantly higher dynamic shear demands than would be predicted using elastic modal response spectrum analysis (MRSA) demands reduced by a seismic force reduction factor. The amplification of shear forces observed by Blakeley was attributed primarily to two modes of behavior present in the nonlinear simulation but not accounted for by elastic MRSA:

1. Provided (i.e. - probable) flexural capacity at the wall base in excess of the minimum required nominal design strength. The additional flexural capacity, subsequently referred to in this thesis as flexural overstrength, reduces the effective force reduction realized during a seismic event. The increase in shear forces due to flexural over-

strength is demonstrated in Figure 5.1. In Figure 5.1, elastic shear force and bending moment envelopes determined to develop due to ground motion acceleration input, $a_g(t)$, are denoted as V_E and M_E, respectively. For design, the elastic force envelopes are each reduced by a force reduction factor, R, which yields the design envelopes denoted by subscript 'u' in Figure 5.1(a). The required design flexural strength at the wall base can then be determined such that the design nominal strength, ϕM_n, equals or slightly exceeds the reduced demand, M_u. As shown in Figure 5.1(b), excess flexural capacity provided at the wall base decreases the internal force reduction. If the probable moment, M_{pr}, is defined as an overstrength factor, Ω_o, multiplied by the provided nominal strength, M_n, then the effective force reduction can be estimated more accurately as R/Ω_o rather than R.

2. Flexural yielding does not reduce shear demands from all modal load patterns equally. Wall yielding which does not reduce shear contributions from all modal load patterns equally allows for larger shear forces to develop than are suggested by elastic MRSA. This behavior is demonstrated in Figure 5.2, where for brevity only the first two modal load patterns are considered. In Figure 5.2(a), both the first and second mode load patterns are assumed to be reduced by an identical force reduction factor, R. In this case, the effective loading height of the reduced seismic demands and the elastic seismic demands remains constant and only the magnitude of the demands changes. However, if yielding induces a larger reduction in first mode shear demands than second mode shear demands, the effective loading height for the system can change significantly. This is demonstrated in Figure 5.2(b), where the first mode is assumed to reduce by R, however the second mode load pattern is assumed to remain essentially unaffected by flexural yielding. In this case, the second mode load pattern contributes more significantly to system response and the effective loading height is lowered because the resultant force location for the second mode is significantly lower than that of the first mode load pattern. The lower effective height allows a higher shear force to develop when the flexural strength at the wall base is reached. This increase in shear force due to the impact of flexural yielding on modal response

contributions is subsequently referred to in this thesis as dynamic amplification.

All current wall shear capacity design recommendations included in national building codes and design practice documents account for flexural overstrength by increasing shear demands by either multiplying the reduced demands by an overstrength factor, Ω_o, or using an effective force reduction factor, R/Ω_o. Both methods for including flexural overstrength are nearly identical and do not introduce significant variability between the existing methods.

Dynamic amplification effects are accounted for in the existing recommendations by either performing elastic MRSA, reducing elastic shear contribution for one or more modes of vibration and combining the reduced load patterns or by using a simplified design equation. Available simplified design equations are intended to accurately estimate the expected dynamic amplification through the calculation of a dynamic amplification factor, typically designed in the literature as ω_v, which increases the reduced design shear demand determined by either elastic MRSA or equivalent static loading.

The remainder of this section presents a summary of shear capacity design recommendations for slender walls designed to yield in flexure. Capacity design shear envelopes proposed by 1)Eibl et al (1988), 2) New Zealand Standard (NZS) 3101 (2006), 3) Structural Engineering Association of California (SEAOC) (2008) and 4) Priestley et al. (2007) are discussed. Prior to discussing the individual design recommendations, comparative capacity design shear force envelopes for the four methods are presented in Figure 5.3 to demonstrate the significant variability between the existing recommendations. In Figure 5.3, capacity design envelopes for each of the four methods are compared to seismic design envelopes determined by reducing elastic MRSA shear demands by the same force reduction factor used to determine reduced flexural demands, as is permitted by ASCE 7 (2010). The use of the capacity design envelopes increase the design base shear by a factor of between 2.0 (SEAOC) and 4.5 (Priestley) for the walled building considered. Comparison plots were created considering a 16-story building designed using a force reduction factor, R = 4, and assuming a flexural overstrength factor, Ω_o = 1.50.

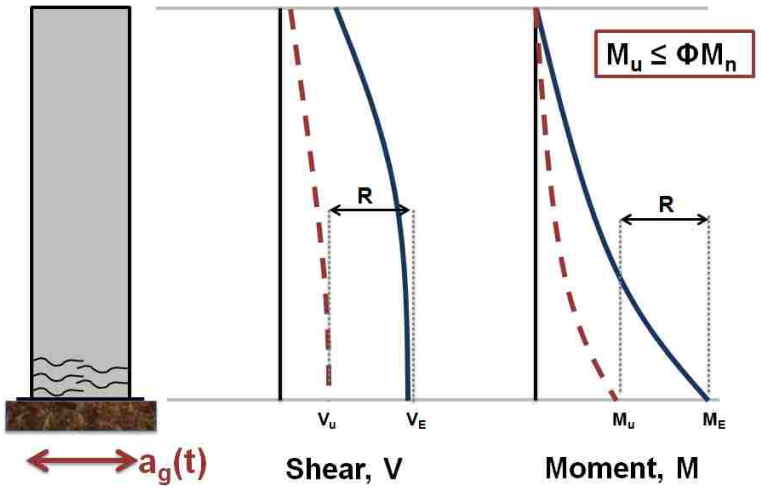

(a) Reduced Forces

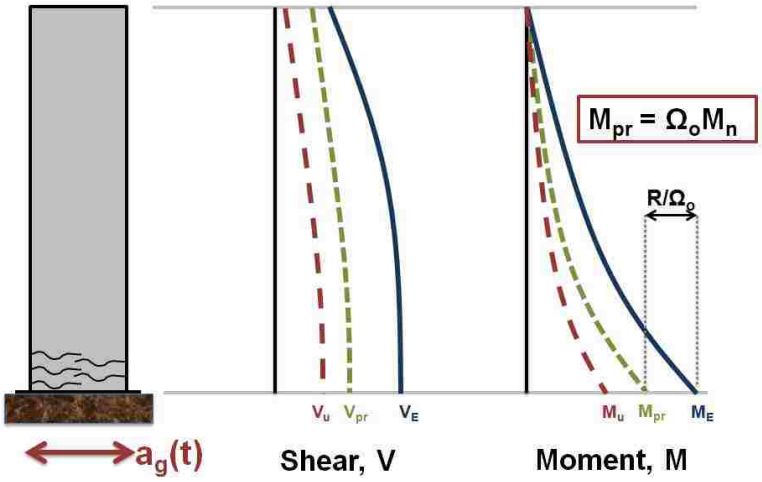

(b) Force Increase (Overstrength)

Figure 5.1: Impact of Flexural Overstrength

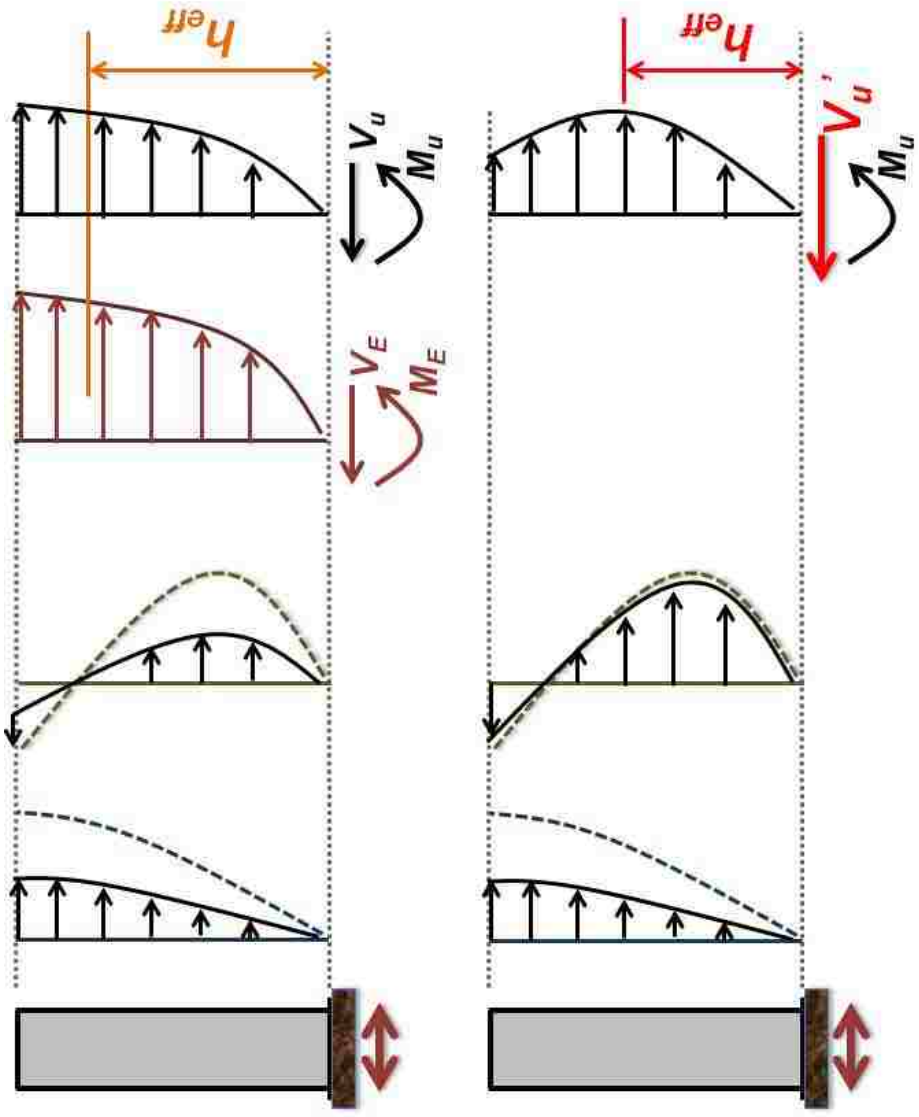

Figure 5.2: Impact of Dynamic Amplification

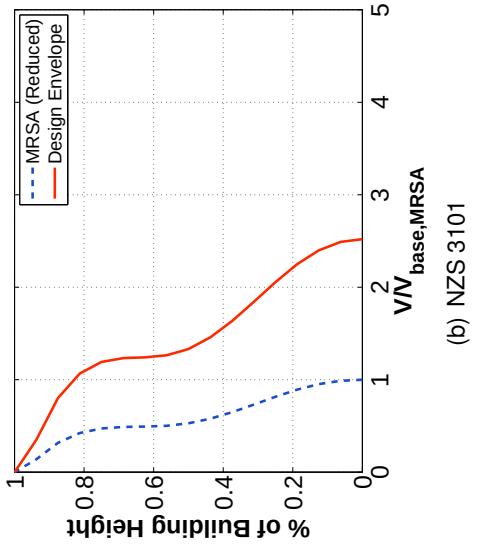

(a) Eibl et al.

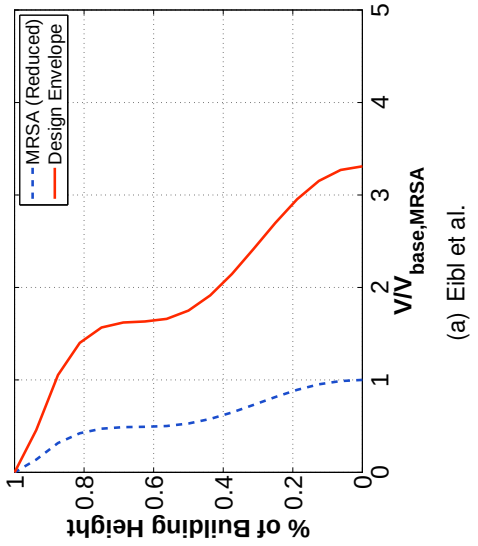

(b) NZS 3101

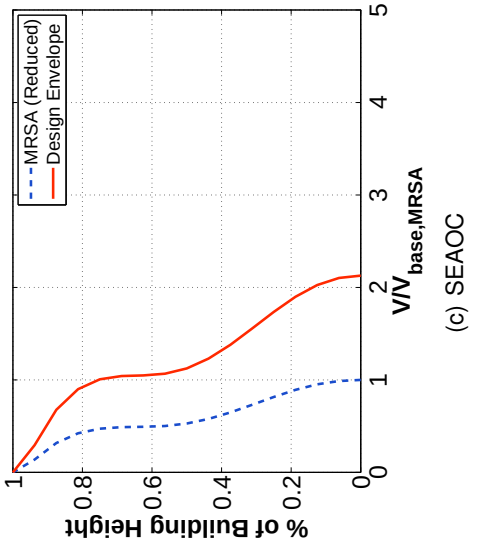

(c) SEAOC

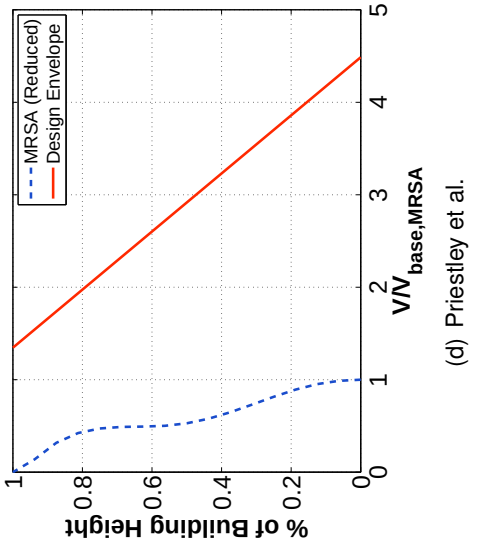

(d) Priestley et al.

Figure 5.3: Capacity Design Envelopes for Shear Design

5.2.1 Eibl MRSA Method

Parametric ITHA studies performed for walled buildings between one and five stories in height and considering various force reduction factors and initial fundamental period values by Eibl and Keintzel (1988) suggest wall flexural yielding primarily affects only the first mode load pattern while higher mode demands remain essentially as predicted from elastic MRSA. Based on this behavior, Eibl et al proposed a modified MRSA method where the first mode shear contribution is capped such that the first mode base shear contribution does not exceed the the base shear associated with development of the probable flexural strength at the wall base. Design shear demands are then determined by modal combination of the capped first mode shear contribution and the elastic higher mode shear force contributions. The Eibl MRSA method can be defined as:

$$V_u' = \sqrt{V_{1D,i}^2 + V_{2E,i}^2 + V_{3E,i}^2 + ...} \tag{5.1}$$

where $V_{1D,i}$ is the capped first mode shear contribution at story 'i' and $V_{jE,i}$ is the 'jth' mode elastic shear contribution at story 'i'.

5.2.2 NZS 3101 (2006)

The NZS 3101 standard suggests the following expression for determining the capacity design shear envelope:

$$V_u' = \omega_v \Omega_o V_E \tag{5.2}$$

where ω_v represents a simplified relationship for estimating the effects of dynamic amplification based on the work of Blakeley et al (1975) and Ω_o is the flexural overstrength provided at the wall base. The simplified dynamic amplification factor, subsequently incorporated into design practice recommendations published by Paulay and Priestely (1992) is defined solely in terms of the number of building stories, n_t, and is presented as:

$$\omega_v = 0.9 + \frac{n_t}{10} \tag{5.3}$$

for buildings with no more than six stories and

$$\omega_v = 1.3 + \frac{n_t}{30} \leq 1.8 \tag{5.4}$$

for buildings greater than 6 stories in height.

5.2.3 CSA A23.3-04 (R10)

Canadian Standard Association (CSA) A23 addresses capacity design for shear and accounts for both flexural overstrength and dynamic amplification due to higher mode effects. Flexural overstrength is accounted for by using the overstrength shear envelope defined as:

$$V_p = V_f \frac{M_p}{M_f} \tag{5.5}$$

where M_p is the expected flexural capacity in the hinge region and M_f is the factored moment resistance at a height of $0.5l_w$ + $0.1h_w$ above the base; which is taken as the height of the plastic hinge region for flexural detailing. V_f is the design shear demand profile without consideration of flexural overstrength. The calculated V_p envelope does not need to exceed the elastic shear envelope determined using a force reduction factor, R_d, of one.

Section 21.6.9.1 of CSA A23 states that ductile wall shear design shall 'account for the magnification of the shear due to the inelastic effects of higher modes', however no design equations or guidance are referenced or provided to assist the designer.

5.2.4 ASCE 7-10/ACI 318-11

Currently, ASCE 7 and ACI 318 documents recommend, but do not require, the inclusion of flexural overstrength in determining capacity design shear for slender walls. Accounting for dynamic amplification effects are neither recommended nor required.

5.2.5 SEAOC Seismic Design Recommendations

SEAOC (2008) recommendations include a capacity design methodology for walls that accounts for both flexural overstrength and dynamic amplification of shear forces. The capacity design equation defining the base shear demand is:

$$V_u' = \omega_v \frac{M_{pr}}{M_u} V_u \tag{5.6}$$

where ω_v is the inelastic dynamic amplification factor, M_{pr} is the expected flexural strength at the wall base and M_u and V_u are design level base force demands. For walls designed using an equivalent lateral force (ELF) distribution, the relationship proposed by Paulay and Priestley (Equations 5.3 and 5.4) is to be used for determining the dynamic amplification factor, ω_v. For walls designed using a MRSA or linear response history analysis an alternate expression for ω_v is given as:

$$\omega_v = 1.2 + \frac{N}{50} \geq 1.5 \tag{5.7}$$

where N is the number of stories.

5.2.6 NEHRP Seismic Design Technical Brief No. 6

A technical brief regarding best practices for seismic design of walls was published by the National Earthquake Hazards Reduction Program (NEHRP) in 2011. The published brief recommends a shear capacity design procedure for walls identical to those recom-

mended by SEAOC (2008). In addition to capacity design recommendations, the briefing suggests that factored wall shear demands (including flexural overstrength) not exceed approximately $3\sqrt{f_c}A_{cv}$ to $5\sqrt{f_c}A_{cv}$ to ensure excess shear demands do not limit flexural ductility capacity.

5.2.7 Priestley, Calvi and Kowalski

Priestley et al. (2007) found the dynamic amplification relationship developed by Blakeley (1975) and presented in Paulay and Priestley (1992) provided an unconservative estimate of the shear demands determined from ITHA for wall designs ranging in heights from 2 to 20 stories. To address this identified unconservatism, Priestely developed a simplified linear envelope, based on the MRSA method developed by Eibl, to conservatively estimate shear demands in slender walls. The design envelope is defined by a capacity design base shear value, V_u' and a design value, V_n^o, related to the base shear value, prescribed at the top of the wall.

The design base shear value is given by:

$$V_u' = \Omega_o \omega_v V_u \tag{5.8}$$

where V_u is the base shear demand without considering flexural overstrength or dynamic amplification and ω_v is calculated as:

$$\omega_v = 1 + \frac{\mu_\Delta}{\Omega_o} C_{2,T} \tag{5.9}$$

where μ_Δ is the displacement ductility factor and

$$C_{2,T} = 0.067 + 0.4(T_i - 0.5) \leq 1.15 \tag{5.10}$$

and T_i is the elastic wall fundamental period. The prescribed capacity design shear

force at the top of the wall is given as:

$$V_n^o = C_3 V_u' \tag{5.11}$$

where

$$C_3 = 0.9 - 0.3T_i \geq 0.3 \tag{5.12}$$

5.2.8 Summary of Capacity Design Recommendations

Current shear capacity design recommendations are based on parameter studies performed using ITHA and simplified numerical models. The NZS 3101 and SEAOC recommendations are based on the initial numerical results developed by Blakeley and present simplified dynamic amplification design equations which depend only on the number of building stories. Recent studies of these simplified dynamic amplification recommendations performed by Ghosh (1992) and Krawinkler (1994) have demonstrated these equations can significantly underpredict the amount of amplification predicted by ITHA and that simplified relationships which depend solely on building height are inadequate to accurately estimate shear demands for a wide range of building parameters. Additionally, the design envelope developed by Priestley, and based on Eibl's MRSA method, was demonstrated by Priestely et al (2007) to provide a more accurate estimation of expected dynamic amplification than the simplified relationship developed by Blakeley. Experimental results reported by Eberhard and Sozen (1993) and Ghorbani-renani (2009) confirm shear demands larger than those associated with achieving the base flexural strength with a first mode loading pattern can develop in walls.

In the following sections the capacity design recommendations presented in this section are investigated by comparing peak shear demands determined by ITHA for 64 walled buildings designed considering a range of building heights, force reduction factors and

initial fundamental periods to the amplified dynamic shear forces predicted by the existing capacity design procedures.

5.3 Walled Building Design

Previous research results presented in Chapter 4 demonstrate that shear demand in slender walls is underestimated if design shear demands are determined by reducing elastic MRSA shear demands by the same force reduction factor, R, that is use to determine reduced flexural demands. To investigate shear demand in flexural walls, 64 simplified walled buildings were designed and analyzed using regularized distributed-plasticity beam column elements (Chapter 3) and artificially generated synthetic ground motion records. The buildings ranged in height from 6 to 24 stories. For each building height considered, buildings were designed considering several different force reduction R factors and sized to target a range of initial periods (T_1). These parameters (R and T_1) have been identified by previous researchers as the parameters that most significantly impact predicted shear demand in walls (Boivin and Paultre, 2010).

Prior to discussing the selected parameter ranges for R and T_1, it is importance to discuss the distinction between theoretical R values and code-based R values defined for structural wall systems by ASCE 7 (2010). Code-based R values, prescribed as R = 5 or 6 for walls by the ASCE 7 standard, are designated throughout Chapters 5, 6 and 7 of this thesis as R_{ASCE}. This designation is used to distinguish between a theoretical force reduction factor, R, that is used to directly reduce elastic MRSA force demands and a code-base force reduction factor, R_{ASCE}, that is used to determine design level earthquake demands per ASCE 7. R and R_{ASCE} are not directly comparable because elastic MRSA permitted by ASCE 7 requires 1) the code-based period limit, C_uT_a, be used to determine first mode MRSA contribution if the calculated fundamental period, T_1 exceeds C_uT_a and 2) shear and moment demands calculated using MRSA and the code-based force reduction factor, R_{ASCE}, must be increased by a scale factor, V/V_t, where V is the reduced elastic base shear calculated using a first-mode ELF load pattern and V_t is the reduced elastic base shear calculated using MRSA. These two modifications to the elastic MRSA procedure

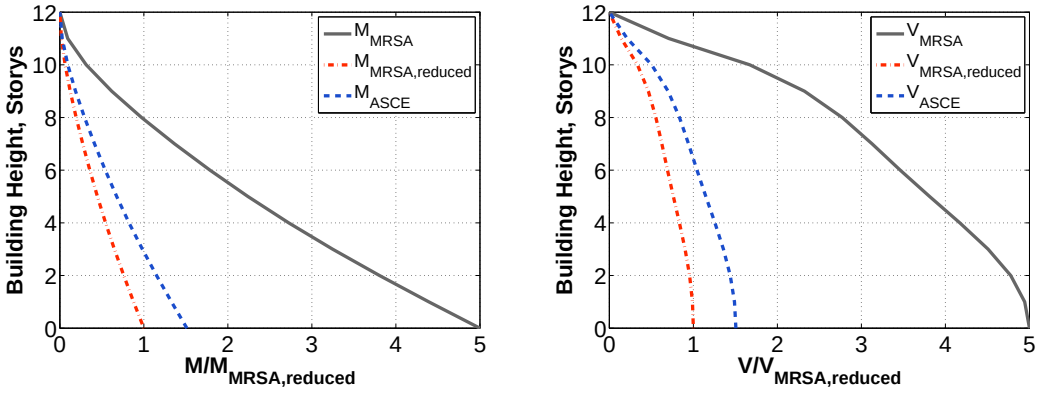

(a) Moment Demand (b) Shear Demand

Figure 5.4: Force Reduction Comparison

increase earthquake demands specified by ASCE 7 above the values that would be calculated by reducing elastic MRSA shear demands by a theoretical force reduction factor,R, equal in magnitude to R_{ASCE}.

To demonstrate the difference between R and R_{ASCE}, Figure 5.4(a) and (b) present determination of reduced earthquake moment and shear forces for a 12-story walled building considering both R = 5 and R_{ASCE} = 5. For R = 5, elastic force demands calculated from MRSA are reduced by a factor of 5 with no further adjustment of the reduced demands; reduced force envelopes are labeled as $M_{MRSA,reduced}$ and $V_{MRSA,reduced}$ in Figure 5.4 for moment and shear, respectively. For R_{ASCE} = 5, use of period limit, C_uT_a, in MRSA and ELF scaling requirements lead to calculated reduced moment and shear demands that are 50% larger than calculated using R = 5. Thus, the force reduction realized by the ASCE design procedure is not as large as suggested by the R_{ASCE} = 5. For the 12-story wall considered in Figure 5.4, the force reduction realized by R_{ASCE} = 5 is in fact approximately 3.3 ($\approx$ 5.0/1.5) or in other words, for this building R_{ASCE} = 5 is effectively equal to a theoretical force reduction, R = 3.3, determined by elastic MRSA. Similar studies performed as part of the current research suggest that R_{ASCE} = 5 and 6 are generally comparable to R = 3 and 4 for walled buildings, respectively.

Wall Design and ITHA analysis results presented in this section were performed to

study amplification of shear force demands in slender walls yielding in flexure; for these studies assessment of flexural performance was not specifically addressed. Assessment of flexural performance of both capacity designed and code-based designed slender walls is discussed extensively in Chapter 7. For the current study regarding shear demand in slender walls yielding in flexure, the primary goals were:

1. Assess shear demands predicted to develop in walled buildings when subjected to design level seismic events.

2. Compare simulated shear demands under earthquake loading with shear demands defined by capacity design equations currently available in the literature.

3. Identify limitations of existing capacity design equations and develop an improved capacity design procedure for slender walls.

The assessment of shear demands in walled buildings and the comparison of dynamic shear demands with existing capacity design shear recommendations are discussed in this chapter. An improved capacity design method for estimating shear demands in walled buildings is developed and validated in Chapter 6. Design methods, nonlinear modeling, and analysis of the walled buildings are described in the following sections.

5.3.1 Simplified Walled Building Configuration

A simple symmetric (regular) building geometry was used for this phase of the study to assess shear demand in walled buildings. All of the buildings had a building footprint of 100ft x 100ft. The buildings ranged between 6 and 24 stories.

The lateral force system was assumed to consist of two walls in each direction, and a 12 ft story height was used for all stories. For building heights of 12 stories or less, wall sections were planar (rectangular) in cross-section (Figure 5.5(a)). For buildings greater than 12 stories, a core wall configuration consisting of two coupled c-shaped walls was used (Figure 5.5(b)); for these walls only earthquake loads applied parallel to the wall webs (loading direction ‘1’ in Figure 5.5) were considered. For all walls, a minimum thickness of

12 inches was considered for design and all flexural reinforcement was assumed equally distributed across the section.

A factored gravity load of 190 psf and a seismic weight of 170 psf were assumed to be distributed equally to each floor, with the exception that the roof level gravity load and roof level seismic weight were reduced by 50%. All seismic weight was assigned to the lateral system; any lateral stiffness provided by the gravity frame was neglected. Intensity of wall axial stress due to gravity load was assumed to be $0.1f'_cA_g$ at the base of the wall. Gravity load carried by the gravity system was considered to apply to the seismic system as a p-delta loading. Accidental torsion and building irregularity were not considered in design or analysis of the walled buildings. A summary of the designed walls is provided in Table 5.1.

Design parameters presented in Table 5.1 are defined as follows:

- N = number of stories.
- R = force reduction factor.
- W = total seismic weight.
- T_1 = calculated fundamental period using effective flexural stiffness, $0.5E_cI_g$ and $1.0G_cA_g$.
- l_w = horizontal wall length.
- t = wall (web and flange) thickness.
- b_f = core wall flange width. One-half the total provided core width.
- C_s = design base shear coefficient, calculated as V_b/W where V_b is the elastic MRSA base shear divided by R and W is the total seismic weight.
- ρ = longitudinal reinforcement ratio.

- v_u = design base shear demand, calculated as $V_b/(A_{cv}(f'_c)^{0.5})$, where A_{cv} is the wall web area and f'_c is the design concrete compressive strength.

- Δ = design story drift.

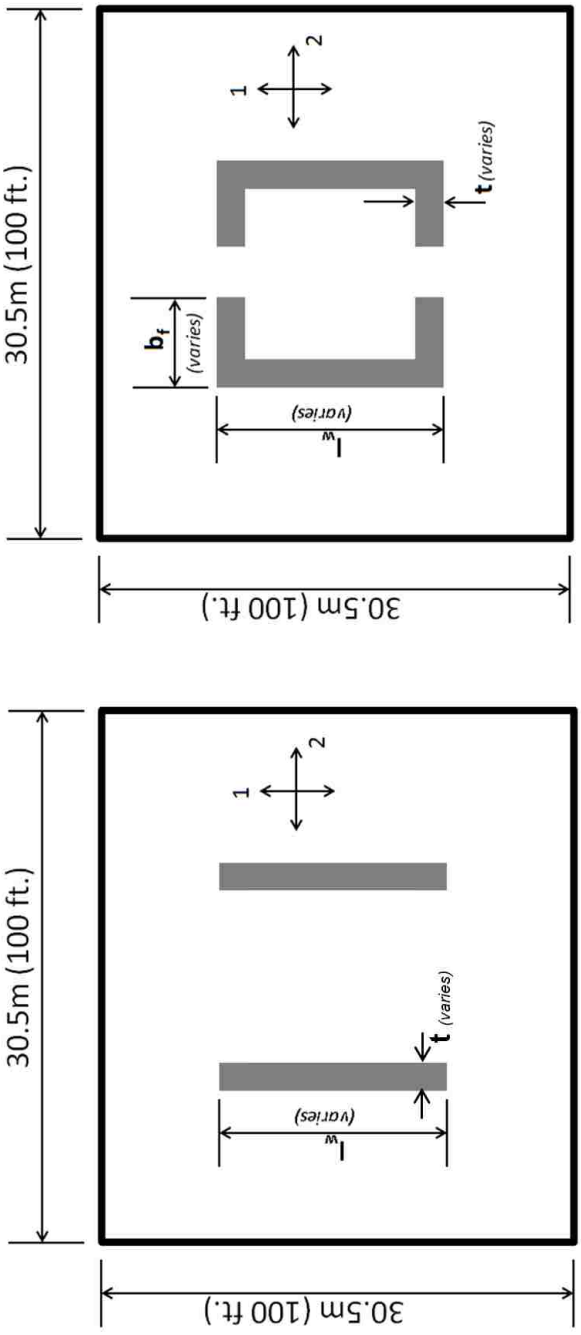

(a) $N \leq 12$ (b) $N \geq 16$

Figure 5.5: Simplified Building Plan

Table 5.1: Shear Demand Study Wall Designs

Shape[1]	N (Stories)	R	W[2] (kip)	T_1	Design Summary l_w ft	t in	b_f ft	C_s	ρ %	v_u[3]	Δ %
R		2						0.26-0.43	2.9-8.3	4.8-6.7	
R	6	3	9350	0.08N,0.10N,0.13N,0.18N	18-27	12-18	–	0.18-0.28	1.4-4.3	3.2-4.5	0.72-2.00
R		4						0.13-0.21	.67-2.6	2.4-3.4	
R		2						0.22-0.42	2.9-5.6	4.4-5.5	
R	8	3	12750	0.07N,0.09N,0.14N,0.18N	24-33	14-22	–	0.14-0.28	1.4-3.0	2.9-3.7	0.76-1.96
R		4						0.11-0.21	.72-1.8	2.2-2.8	
R		2						0.16-0.29	2.4-5.0	3.3-4.9	
R	12	3	19550	0.08N,0.09N,0.13N,0.21N	24-39	16-26	–	0.11-0.16	.98-2.7	2.2-3.3	0.85-2.28
R		4						0.08-0.14	.46-1.6	1.6-2.5	
C		2						0.15-0.23	1.6-4.9	3.8-6.1	
C	16	3	26350	0.08N,0.10N,0.15N,0.20N	24-36	16-26	5-10	0.10-0.15	.77-2.4	2.5-4.0	0.89-2.29
C		4						0.07-0.10	1.0-1.6	2.4-3.0	
C		2						0.14-0.19	1.4-3.5	3.3-5.6	
C	20	3	33150	0.08N,0.10N,0.15N,0.20N	27-38	18-30	6-12.5	0.09-0.13	.67-2.2	2.2-3.7	0.89-2.24
C		4						0.07-0.08	.91-1.1	2.2-2.8	
C		2						0.12-0.18	1.2-3.2	3.5-4.7	
C	24	3	39950	0.08N,0.10N,0.15N,0.20N	30-38	20-32	6-20	0.08-0.11	.71-2.0	2.5-3.1	0.87-2.25
C		4						0.06	1.0	2.3	

[1] R = Rectangular Cross-Section; C = Core Cross-Section; [2] Total Seismic Weight; [3] v_u = Design Shear Demand ($\sqrt{f'_c(psi)}$)

5.3.2 Wall Design

Building designs were developed and analyzed to study dynamic shear response of yielding walls considering a wide range of design parameters. The primary design parameters varied were building height, fundamental period and force reduction factor. The design process used for wall sizing and reinforcement selection was:

1. Select building height, N.
2. Select target value for fundamental period, T_1.
3. Size cross-section dimensions to achieve the desired fundamental period.
4. Determine elastic earthquake demands using MRSA.
5. Select force reduction factor, R.
6. Reduce elastic demands by R and calculate seismic design level base moment.
7. Determine distributed reinforcement ratio required to satisfy flexural strength requirements per ACI 318-11 Sections 21.9 and 10.2.

Further explanation on the design process and selected parameter ranges are discussed in Section 5.3.3.

5.3.3 Wall Sizing

For each design, wall cross-section geometry was selected to achieve a target fundamental period. Fundamental periods were calculated using modal analysis assuming effective stiffness values of $0.5E_cI_g$ (flexural), $1.0A_gE_c$ (axial) and $1.0G_cA_v$ (shear). Initial calculations demonstrated that axial and shear stiffness had minimal impact on the calculated fundamental period and a closed form equation (Young and Budynas, 2002) considering

flexural deformations only was used to simplify the calculation of building period. For a cantilevered wall with uniformly distributed mass and an effective flexural stiffness of $0.5E_cI_g$, the fundamental period can be approximated as:

$$T_1 \approx 0.13\sqrt{\frac{PN^4H^3}{EI_g}} \tag{5.13}$$

where P is the lumped story weight, N is the number of stories, H is story height and E_c is the modulus of elasticity of concrete. In the current study, E_c was calculated to be 4600 ksi per ACI 318 (2011) Section 8.5, assuming normalweight concrete and an expected concrete strength of 6500 psi. Equation 5.13 was used to determine the gross moment of inertia of wall required to achieve the target period.

5.3.3.1 Planar Walls

The cross section geometry was calculated using a cross-section aspect ratio (l_w/t) equal to 18. This value was deemed consistent with west coast building construction per comparison with a previously developed west coast US building inventory compiled by Mohr (2007). With the selected aspect ratio, a unique cross-section geometry required to achieve the target period was determined using Equation 5.13

5.3.3.2 Core Walls

A given aspect ratio was not sufficient to uniquely define a core wall section, because both the flange length, b_f, and the wall length, l_w, can be varied independently to achieve a targeted moment of inertia. For the designed core wall sections, selected cross-section aspect ratios were between 14 and 18 while maintaining a longitudinal reinforcing ratios greater than 0.75%.

5.3.4 Selected Period Range

The ASCE 7-10 empirical period limit, $C_u T_a$, ranges from 0.08N to 0.14N for walled buildings designed for various seismic design categories (ASCE, 2010). This range was expanded to include slightly longer fundamental periods and the total period range considered by the current study was from 0.08N to 0.20N.

5.3.5 Selected Force Reduction Factor Range

MRSA was performed to determine elastic flexural demands. For MRSA analysis, all translational modes were considered and the square-root-sum-of-squares (SRSS) rule was used to combine modal response. This method has been noted by others to be appropriate for MRSA of cantilevered walls (Priestely et al., 2007). Elastic MRSA demands were reduced by a selected force reduction factor, R, for each design. Force reduction factors of 2, 3 and 4 were selected to determine the impact of force reduction on the dynamic shear response. A maximum force reduction factor of 4 was considered because this value was found to be comparable to the maximum force reduction R_{ASCE} = 6 allowed for wall design by ASCE 7 (Figure 5.4).

5.3.6 Design Level Seismic Demand

Initially, design level demands were determined using the 5% damped design spectrum specified in Section 11.4.5 of ASCE 7-10. Spectral ordinates for a Maximum Considered Event (MCE) were defined assuming S_{MS} = 1.50g and S_{M1} = 0.9g. MCE spectral coefficients were reduced to 1.0g and 0.6g for S_{DS} and S_{D1}, respectively per ASCE 7-10 to define the Design Basis Earthquake (DBE). This design spectrum is shown in Figure 5.6.

As will be discussed in greater detail in Section 5.4.6, the 5% damped design spectrum was initially used for design because the expectation was that use of 2% Rayleigh damping combined with hysteretic energy dissipation during ITHA would reduce overall building response to the point that a 5% damped spectrum would provide accurate prediction of

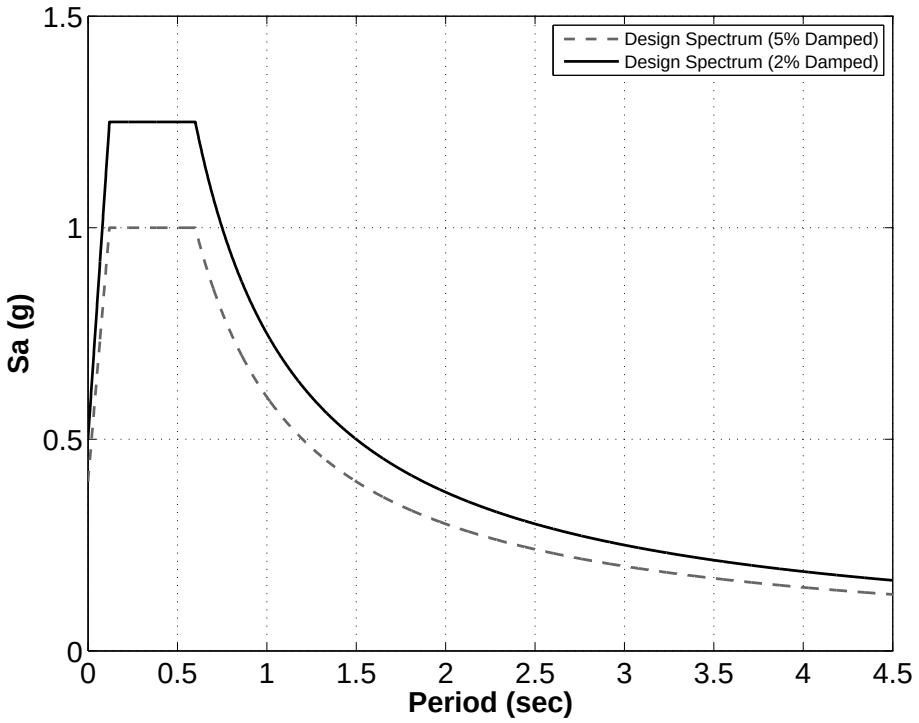

Figure 5.6: Design Spectrum Comparison

earthquake demands. However, nonlinear analysis results showed shear demands that generally exceeded shear demands predicted using the 5% damped spectrum and a force reduction factor R = 1. This was considered to indicate a problem with the design process as the elastic response could be considered an upper bound to the shear demand because inelastic response will limit the demands associated with at least one modal load pattern.

The discrepancy in predicted and simulated shear demand was attributed to the difference between the 5% damping assumed by the design spectrum and the actual energy dissipation resulting from Rayleigh damping and hysteretic response present in the nonlinear model. Because Rayleigh damping coefficients used in nonlinear modeling were selected to maintain around 2% damping for the first few modes, the 5% damped design spectrum was scaled to represent a 2% damped spectrum and the 2% damped spectrum was used to redesign the walled buildings. The 5% damped design acceleration response spectrum was increased by a scale factor of 1.25 to account for the reduced damping, as

recommended by Naeim and Kircher (2001). As noted by Naeim and Kircher, this scale factor is consistent with previous recommendations developed by Newmark and Hall (1982) and NEHRP (1997). Figure 5.6 shows the 2$\%$ damped spectrum used for design. Table 5.1 presents design parameters for the redesigned walls (2$\%$ damped design spectrum).

5.3.7 Flexural Design Method

Flexural design demands were determined using elastic MRSA, the 2$\%$ damped design acceleration spectrum shown in Figure 5.6, and three different levels of force reduction. Flexural reinforcement for the wall was selected such that provided design flexural strength (ϕM$_n$) was equal to or greater than the elastic MRSA base moment reduced by force reduction factor R, M$_u$=M$_{MRSA}$/R. Design concrete compressive strength was taken as 5000 psi and design yield strength of flexural reinforcement was taken as 60000 psi. Provided flexural demand to capacity ratio (ϕM$_n$/M$_u$) ranged between 1.00 and 1.14 with a mean value of 1.06 for the 64 completed designs. The flexural reinforcement required at the base section was assumed to remain constant, without bar curtailment, up the entire wall height. The impact of alternate bar cutoff configurations was also considered; these designs are discussed further in Chapter 7.

For longer period walls designed with R = 2, the wall size required to achieve the target period coupled with the high flexural demands led to the selection of reinforcing ratios ($>$ 5$\%$ in some cases) which exceed practical design limits. However, because these wall designs were intended only to populate as wide of a range of wall designs as possible, such large reinforcing ratios were considered acceptable for the current study. Flexural reinforcement for all walls was uniformly distributed along the cross-section in two curtains. Wall ends were designed to satisfy confining reinforcement requirements per Section 21.9.6 of ACI 318-11. Core walls webs were designed as boundary elements per ACI 318 Section 21.9.6 because these regions would be expected to sustain large compressive demands when loaded as a coupled wall in the perpendicular direction.

5.3.8 Shear Design Method

Shear demand was not considered in the wall sizing process. Design level shear demands were calculated by reducing elastic MRSA demands by various force reduction factors. Calculated design shear demands were between $1.6\sqrt{f'c(psi)}$ and $6.7\sqrt{f'_c(psi)}$ with a mean value of $3.5\sqrt{f'_c(psi)}$. For longer period walls designed with R = 2, the wall size required to achieve the target period led to design shear demands which exceed current recommended design limits (NEHRP, 2011). However, as the goal of the current study was to assess the differences between design shear demands and shear demands predicted by ITHA, no redesign was performed. For this same reason, selection of shear reinforcement and calculation of design shear strength was not performed for these building designs.

5.3.9 Calculated Story Drift

Maximum peak story drifts were calculated using modal response spectrum analysis and the selected force reduction (R) factor. Amplification of drifts calculated under design level load patterns were increased by C_d to estimate inelastic drift demands. Amplified drift demands (Δ) were calculated assuming C_d values equal to R.

5.4 Nonlinear Model Devlopment and ITHA Parameters

All nonlinear wall modeling was performed using the open-source OpenSees software platform (Mazzoni et al, 2006). Each walled building was modeled using a combination of elastic zero-length elements, elastic beam elements and nonlinear force-based fiber beam column (FBBC) elements. The only nonlinear elements in the model were used to model the response of the wall system and both wall webs were combined into a single fiber section so that only one nonlinear element was required per story. Each story of the wall was comprised of three elastic zero-length elements in parallel below a FBBC element. One zero-length elastic element represented the shearing deformation occurring in the story. The other two elements were given large (essentially rigid) stiffness values and were included solely to transfer axial force and bending moment in the wall in parallel with the shear element. Seismic mass was lumped at each story level as was the required axial

load necessary to generate a gravity load axial stress of $0.1f'_cA_g$ at the wall base. The base of the wall was considered fixed and no foundation flexibility was considered.

P-delta effects were considered by adding a leaning column to the wall model and using the co-rotational formulation (de Souza, 2000) to simulate nonlinear geometry. The leaning column was modeled using an elastic beam element with a pinned (free to rotate) base. The elastic stiffness of the leaning column was set extremely low (more than several orders of magnitude below that of the cracked wall stiffness) to ensure negligible lateral stiffness was attributed to the column. At each floor level, the leaning column was linked to the wall using horizontal truss elements. Further details of the nonlinear model used for ITHA are provided in the following sections.

5.4.1 Expected Material Properties

Expected material properties were used to define fiber section material models. Expected yield strength of reinforcement was increased by 17% from 60000 psi to 70200 psi based on material strength recommendations suggested by PEER (2010). Ultimate strength of reinforcement was taken as 105 ksi with rupture assumed to occur at a tensile strain of 20%. Expected unconfined uniaxial concrete compressive strength (f'_c) was increased by 30% from 5000 psi to 6500 psi based on material strength recommendations suggested by PEER (2010).

5.4.2 Flexural Response Model

Wall flexural response was modeled using five integration point force based distributed-plasticity beam column elements with full material regularization (Chapter 3). For planar wall sections, fiber sections used a fiber length such that 32 fibers represented the boundary element length with a similar length used to discretize the web region. For flanged core walls, a fiber length of 1 inch was used, which discretized the flange area into layers ranging between 16 and 30 fibers. For each building model, both resisting wall webs were combined into a single fiber section to permit the use of a single line element per story to represent the building lateral system.

OpenSees' 'Concrete02' uniaxial material model was used to model both confined and unconfined concrete fibers. Strength enhancement of confined concrete fibers was determined using the model developed by Saatcioglu and Razvi (1992). For both fibers, the strain at peak strength was determined such that the initial material modulus (E_c) was equal to $57000\sqrt{f'_c}$(psi). Concrete tensile strength was taken as $4\sqrt{f'_c}$ (Wong and Vecchio, 2006) with a tension softening slope taken as $E_c/20$. The strain associated with 80% strength loss (ϵ_{20}) was determined using regularized crushing energy data developed in Chapter 3. For unconfined fibers, ϵ_{20u} was determined using the expression for recommended crushing energy provided in Table 3.2. For confined fibers, confined crushing energy was taken as 230% greater than the value used for unconfined crushing energy. This value for confined crushing energy is moderately higher than the recommended increase of 170% suggested in Table 3.2. A larger increase was used because all boundary element lengths were 2-4 times the wall thickness and detailed such that each bar was laterally supported by cross-ties. With this confinement configuration, Figure 3.17 suggests an increase in crushing energy around 230% can be achieved.

OpenSees' 'Steel02' uniaixal material model was used to model flexural reinforcing steel fibers. Regularized material model parameters were defined using expected material property values provided in the previous section and equations 3.3 and 3.4.

5.4.3 Shear Response

A reduced effective linear shear stiffness of $0.1G_cA_v$ was determined to be appropriate for modeling statically loaded wall specimens with aspect ratios between 1.5 and 3.0 experiencing significant flexural distress over a large portion of their height using distributed plasticity fiber section elements (Chapter 3). However, because the walled buildings designed in this section represent dynamically loaded buildings ranging in aspect ratio between 3.5 and 10, it is unclear whether the previously validated shear model is appropriate. Particularly, it is unlikely that upon initial loading the entire wall will possess a shear stiffness that is significantly lower than the elastic value. For these reasons, an elastic shear stiffness taken equal to the gross, elastic value (G_cA_v) was used to model shear stiffness of the

walls. Alternate shear response models were also considered; comparison of ITHA results considering different shear response models are discussed in Chapter 7.

5.4.4 Rayleigh Damping

Rayleigh damping, which is the only damping option available within OpenSees, was used to model the effects of non-hysteretic damping. Rayleigh damping coefficients were assigned such that 2% damping was anchored at periods corresponding to $1.5T_1$ and T_2 where T_1 and T_2 are the first two building periods as determined by modal analysis ($0.5E_c I_g/G_c A_v$). A period longer than T_1 was used to reduce overdamping the first mode response as period elongation occurs. Anchoring to T_2 provides a viscous damping ratio of around 4.5% of critical for the third mode with increasing damping values for higher modes (Figure 5.7). This was deemed acceptable because the current study considers a maximum building height of 24 stories and it was verified that modes higher than the second had minimal impact on the predicted response. For response at periods between $1.5T_1$ and T_2 the provided Rayleigh damping curve is less than 2%. This period range affects the first mode (prior to significant period elongation) and the second mode (after period elongation occurs).

5.4.5 Dynamic Solution Technique

For each input ground motion, dynamic solution progressed using a constant time step of 0.002 seconds. Prior to dynamic solution, all gravity loads were applied to the model and held constant throught the analysis. Time stepping was performed using the Hilber-Hughes-Taylor (HHT) method with a specified numerical damping (α) factor of 0.7. A value of 0.7 was selected to maximize the numerical damping of spurious higher modes effects while maintaining second order accuracy during time integration. Nonlinear solution for each time step was initially attempted using the Newton-Raphson algorithm, with global convergence tolerance on the Relative Energy Increment assigned a value of 1e-5 and FBBC element internal convergence tolerance assigned a value of 1e-8. If convergence

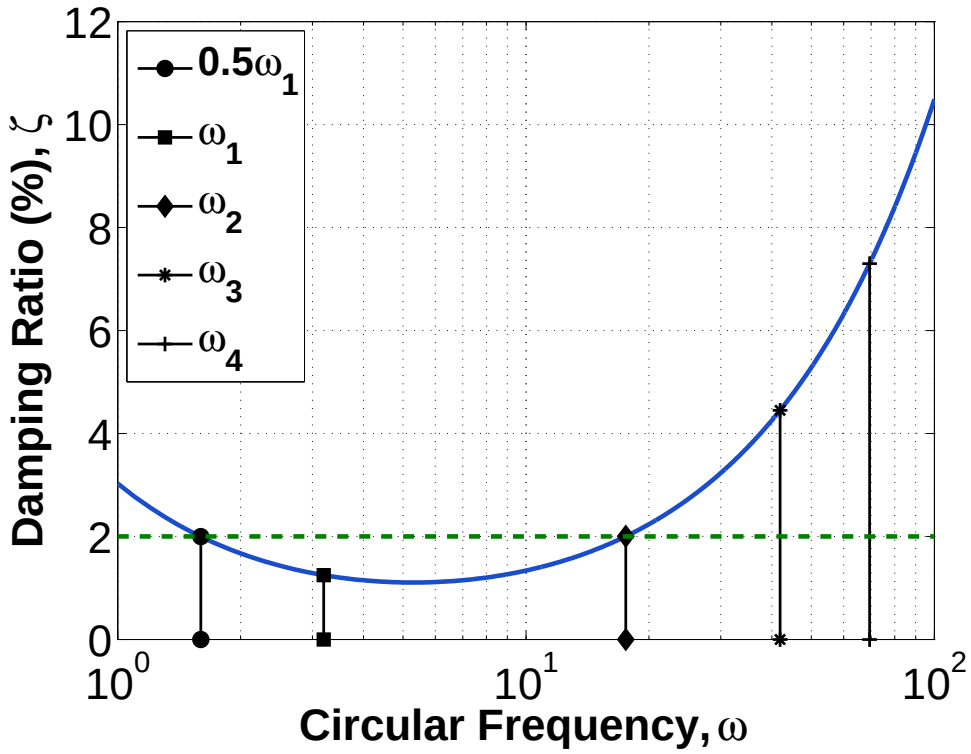

Figure 5.7: Rayleigh Damping Curve (All Walls)

was not achieved during a time step, a solution strategy developed by the author modified solution parameters (nonlinear solver, monitored convergence quantity, time step) until convergence was achieved.

5.4.6 Ground Motion Input

The input design level ground motions comprised seven artificial acceleration time histories. Synthetic motions were used for this study to better match the acceleration response spectrum used for design over the wide of range of periods representative of walled buildings ranging between 6 and 24 stories in height. All synthetic motions were generated using the SIMQKE-1 program developed by Vanmarcke et al. (1976, 1990) and available for download from NISEE/PEER. Synthetic motions were generated using recommendations provided by Tola (2010).

Initially, a set of seven synthetic ground motions was created to match the ASCE 7-10 5% damped design spectrum described previously in Section 5.3.6. Although Rayleigh damping was specified as 2% of critical, the 5% damped target spectrum was used in anticipation of additional hysteretic damping provided by inelastic flexural wall response. Comparison between the target 5% damped spectrum and the geometric mean spectrum of the 7 synthetic ground motion suite is shown in Figure 5.8. Excellent representation of the spectral shape throughout the entire period range shown was achieved by the the suite of artifical records.

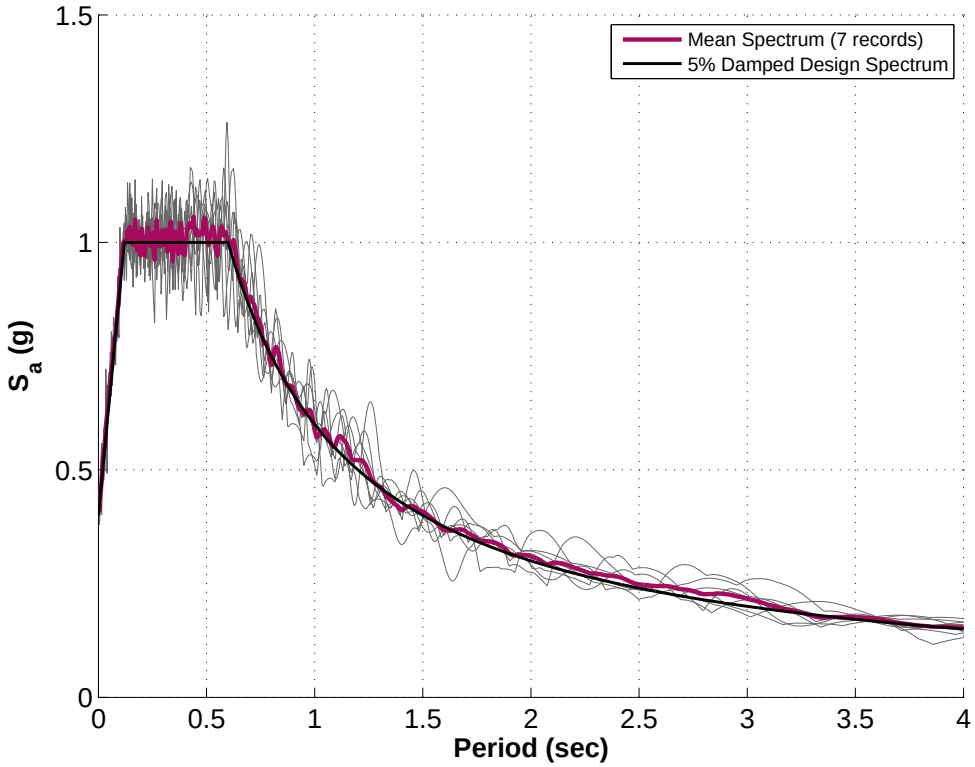

Figure 5.8: 5% Damped Spectrum Comparison

5.4.6.1 Shear Demands Using 5% Damped Design Spectrum

After completing ITHA for the building models, the peak nonlinear base shear demand predicted for each building, V_{ITHA}, was compared to the base shear demand for each building calculated using elastic MRSA, the 5% damped design spectrum, and a force reduction R = 1. Comparison between inelastic and elastic peak base shear demands are plotted in Figure 5.9. This comparison indicates for building heights greater than 6 stories, V_{ITHA} exceeds $V_{elastic}$ in a significant number of the designs (for this study, ITHA were completed only for building heights up to 16 stories). This behavior is unrealistic because the elastic response should provide an upper bound to the shear demand due to flexural yielding occurring in the nonlinear model. Flexural yielding limits the response of at least one modal load pattern and would be expected to lead to decreased shear demands compared to the elastic case.

The discrepancy in predicted demand was attributed to the difference between the 5% damping value used to generate the synthetic ground motions and the amount of damping present in the nonlinear model. Rayleigh damping coefficients for the models were assigned targeting a value of 2% of critical for the first two modal load patterns. Use of a 5% damped design spectra was thought to be justified due to additional hysteretic damping expected to be supplied by inelastic flexural wall response. The presented results suggest the realized hysteretic damping within the model does not supply sufficient hysteretic damping to warrant usage of a 5% damped spectrum. As this phenomenon is mitigated for six story walls and increases in severity with wall height, it is suspected that the discrepancy arises from reduced hysteretic damping occurring in the second mode. Sufficient hysteretic damping to warrant usage of a 5% damped design spectrum occurs in shorter walls; however taller walls, for which the second mode plays an increasingly important role, do not appear to dissipate significant hysteretic energy in the second mode using the current modeling and design approach.

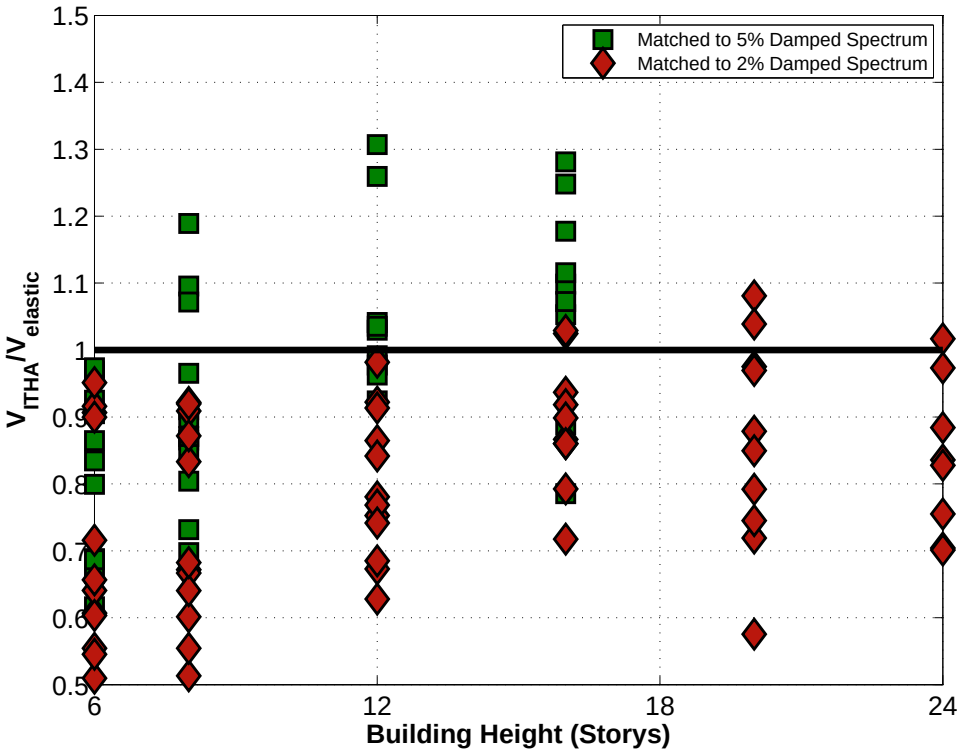

Figure 5.9: ITHA Base Shear Comparison

5.4.6.2 Shear Demands Using 2% Damped Design Spectrum

To further study the identified increase in dynamic shear response, the 5% damped design spectrum was scaled to represent a 2% damped spectrum and the 2% damped spectrum was used to redesign all walled buildings (Figure 5.10). The 5% damped design acceleration response spectrum was increased by a scale factor of 1.25 to account for the reduced damping, as recommended by Naeim and Kircher (2001). Design data for walls redesigned using the 2% damped design spectrum are provided in Table 5.1.

ITHA was performed for the redesigned wall and inelastic and elastic base shear demands were compared (Figure 5.9). These results show that when the 2% critically damped spectrum is used for design, inelastic base shear demand is typically less than elastic de-

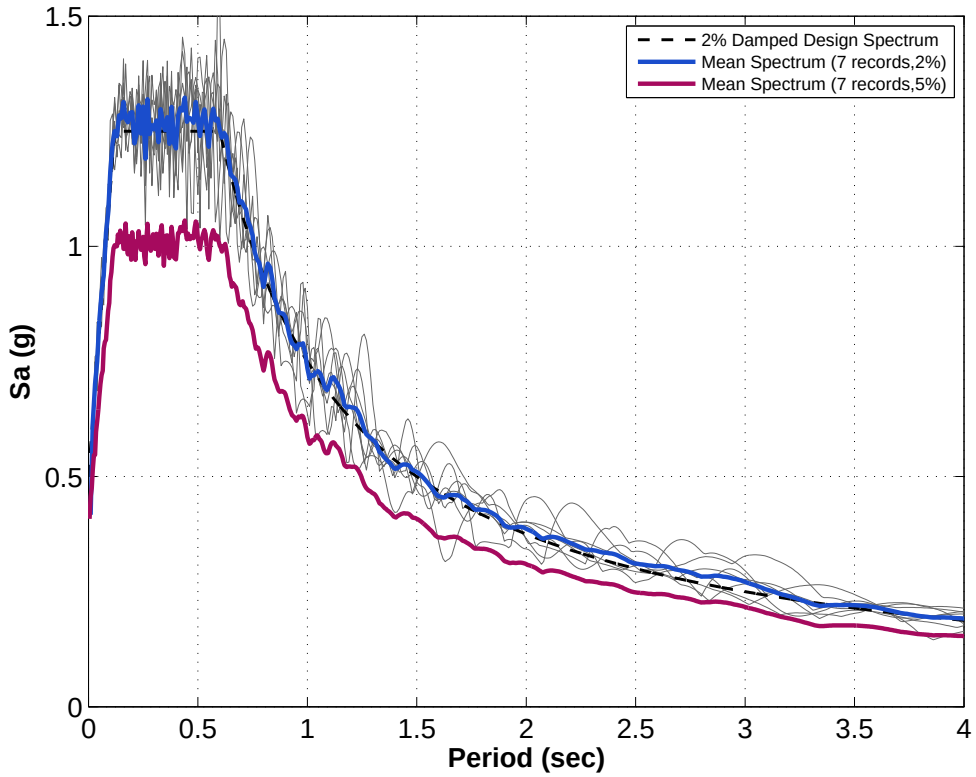

Figure 5.10: 2% Damped Design Spectrum Comparison

mands for all building heights. A small number of walled buildings have inelastic shear demands that are greater than the elastic demands, however the maximum increase in demand for the redesigned walls is approximately 10% compared with a maximum increase of 30% for walls designed using the 5% damped strectrum. This modest increase in inelastic shear demand was attributed to the fact that Rayleigh damping coefficients were computed to achieve 2% of critical damping at periods of $1.5T_1$ and T_2. Between these periods, Rayleigh damping falls below 2% (Figure 5.7). Reduced damping in this period range affects the first mode prior to significant period elongation and the second mode during period elongation. Damping of less than 2% in the first two modes could be expected to lead to inelastic demands which slightly exceed elastic demands if 2% of critical damping is used for elastic analyses.

5.5 Evaluation of Existing Recommendations for Estimating Design Level Shear Demands in Flexural Walls

5.5.1 Design Level Base Shear Demands

Using the 2% damped design spectrum, a peak base shear demand for each building determined by ITHA, V_{ITHA}, were determined and compared with the design base shear demand, V_u (Figure 5.11). For this comparison, V_{ITHA} was defined as the median peak shear demand determined from ITHA using the suite of synthetic ground motion records. Design demand, V_u was defined as the SRSS base shear calculated using the 2% damped design spectrum, elastic MRSA and a selected force reduction factor, R. The plotted data demonstrates that shear demands determined from ITHA for all building designs exceed the calculated design level base shear demand, typically by more than a factor of 2.0 for walls designed with force reduction factors of 3 or 4. These results are consistent with finding by Blakeley (1975) and Eibl (1988) which previously identified that shear demands for yielding walls are unconservatively predicted by reducing elastic MRSA shear forces by the same force reduction factor used for flexure. These results suggest that wall shear demands determined by ASCE 7 procedures using R_{ASCE} = 5 or 6, which can be compared with ITHA demands predicted for walls designed using R = 3 or 4, can significantly underestimate design level shear demands that develop in yielding walls. For example, for all buildings designed using a force reduction factor, R = 4, the mean ratio of V_{ITHA} to V_u was calculated to be 2.59 with a coefficient or variation, COV = 0.15. Shear demand ratios presented in Figure 5.11 also demonstrate:

1. Predicted shear demands exceed reduced elastic demands more significantly when higher force reduction factors are used. Mean shear demand ratios of 1.88, 2.28 and 2.59 were determined for buildings designed using force reduction factors of 2, 3 and 4, respectively. The increase in shear demand can be attributed to increasing dynamic amplification occurring as the amount of inelastic flexural response increases.

2. Shear amplification was determined to be largest for 12- and 16-story buildings. Less amplification was determined for shorter (6- and 8-story) and taller (20- and 24-story)

walled buildings.

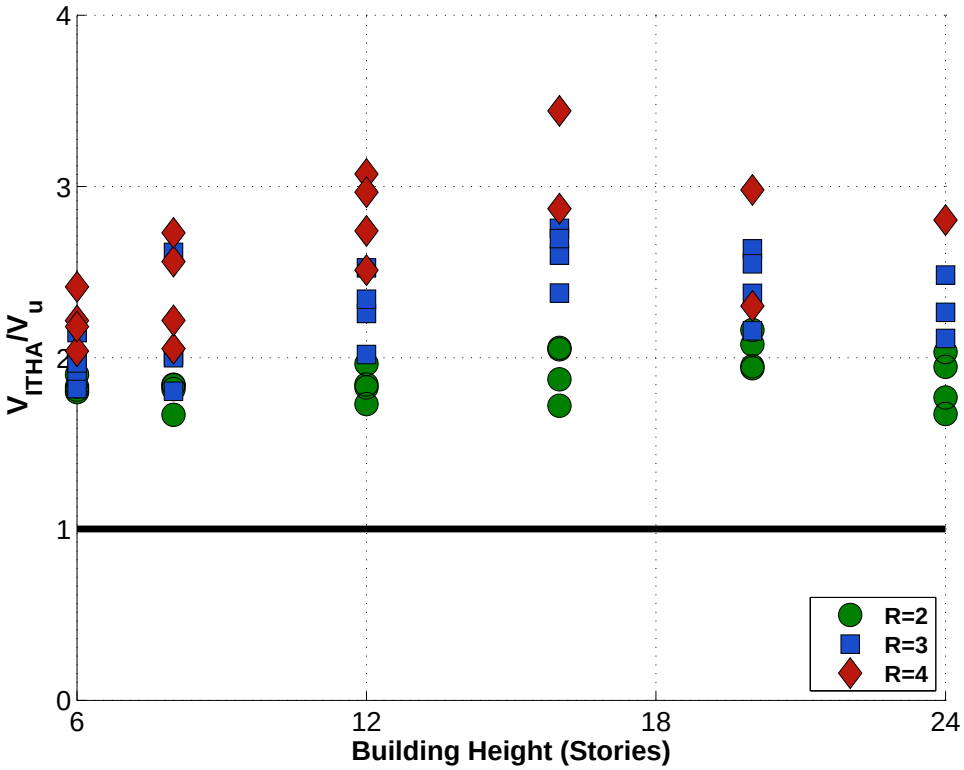

Figure 5.11: Fully Reduced Shear Comparison

As discussed in Section 5.2, flexural overstrength and dynamic amplification effects both contribute to the amplification of dynamic shear forces in walls. To determine the relative contribution of these effects, V_{ITHA} can be related to V_u by the following amplification equation:

$$V_{ITHA} = \omega_v \Omega_o V_u \tag{5.14}$$

Where Ω_o accounts for flexural overstrength provided at the wall base and ω_v accounts for the impact of dynamic amplification.

5.5.1.1 Impact of Flexural Overstrength

Flexural overstrength can be calculated for the building designs by defining a flexural overstrength factor, Ω_o, that is equal to the ratio of the calculated probable moment capacity, M_{pr}, provided at the wall base to the reduced elastic base moment demand, M_u. Calculated flexural overstrength factors for the wall designs are plotted in Figure 5.12(a). For data presented in Figure 5.12(a), M_{pr} is calculated as the peak flexural capacity predicted by moment-curvature of the base section using expected material strength, strain hardening and a ϕ-factor = 1.0. Calculated overstrength factors range from 1.25 to 1.65 with an average value of 1.42 (COV = 0.07). Overstrength factors are essentially unaffected by the selected force reduction factor. Mean overstrength factors of 1.43, 1.42 and 1.43 were calculated for buildings designed using force reduction factors of 2, 3 and 4, respectively. This could be expected because the same flexural design approach was used for all building designs.

61 of the 64 calculated overstrength factors exceed the overstrength factor of 1.25 suggested by ACI 318-11. However, the calculated mean overstrength value of 1.42 is similar to expected overstrength values suggested for wall sections by NEHRP (2011) and Priestley, et al. (2007).

5.5.1.2 Impact of Dynamic Amplification

The calculated dynamic amplification factor, ω_v, for the buildings is plotted in Figure 5.12(b). As suggested by Figure 5.11, dynamic amplification contributes significantly to the shear amplification and becomes increasingly pronounced as larger force reduction factors are used for design. Mean dynamic amplification factors of 1.32, 1.62 and 1.81 were determined for buildings designed using force reduction factors of 2, 3 and 4. Additionally, larger dynamic amplification factors were determined for 12- and 16-story buildings, with decreasing amplification determined for both shorter and taller buildings.

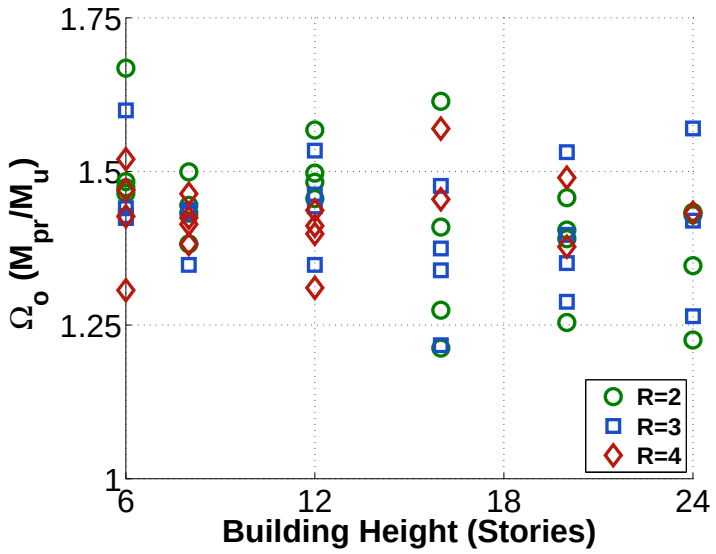

(a) Flexural Overstrength

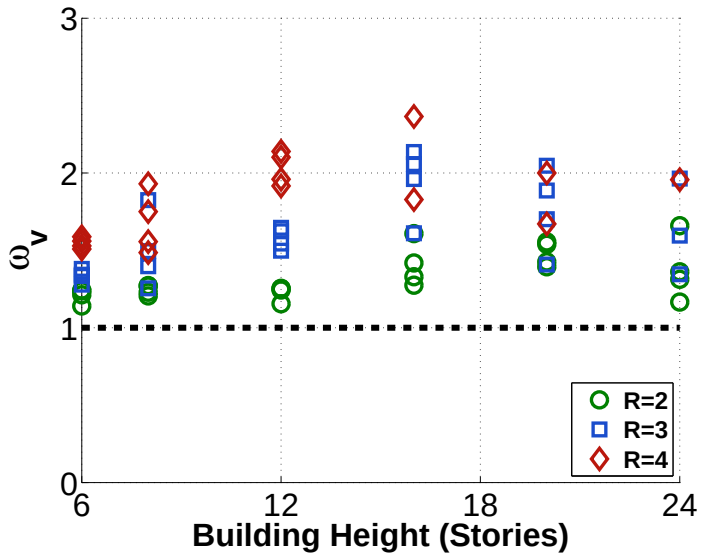

(b) Dynamic Amplification

Figure 5.12: Shear Amplification Components

5.5.1.3 Implications for Design

The median ω_v for walled buildings designed with R values of 3.0 and 4.0 is 1.70 (COV = 0.17). Median values of $\omega_v\Omega_o$ for walled buildings designed with R values of 3.0 and 4.0 is 2.40 (COV = 0.17). These results suggest that ignoring dynamic amplification of shear and flexural overstrength in seismic design of walled buildings may lead to significantly unconservative estimates of peak shear demand under design level seismic events.

5.5.2 Demand Comparison using Existing Capacity Design Equations

The dynamic amplification data plotted in Figure 5.12(b) were used to evaluate the existing dynamic amplification equations previously presented in Section 5.2. For the NZS 3101, SEAOC and Priestely methods, calculated dynamic amplification factors for each building design were calculated and directly compared to the data plotted in Figure 5.12(b). For the Eibl MRSA method, the dynamic amplification factor for each building was calculated as:

$$\omega_v = \frac{V_u'}{\Omega_o V_u} \tag{5.15}$$

and the calculated amplification factors were compared to the data plotted in Figure 5.12(b). For the Priestley method, the displacement ductility factor, μ_Δ, was replaced by the force reduction factor, R. Comparison of the calculated dynamic amplification factors with the amplification predicted by ITHA are provided in Figures 5.13 and 5.14. Figure 5.13 presents dynamic amplification comparison for the NZS and SEAOC methods, both of which are based on work by Blakeley and for which the calculated dynamic amplification factor is determined as a function of number of building stories only. Figure 5.14 presents dynamic amplification comparison for the Eibl MRSA and the simplified version of Eibl's method developed by Priestley.

Data in Figures 5.13 and 5.14 are presented as ratios between the predictive dynamic amplification factor for each capacity design method, ω_v, to the dynamic amplification effect determined by ITHA, ω_{ITHA}. Ratios near 1.0 indicate the predictive method accurately

estimate the dynamic amplification predicted by the numerical simulation. Ratios less than 1.0 indicate the predictive method underestimated the amount of dynamic amplification determined by inelastic analysis.

5.5.2.1 Amplification Based on Building Height

Data presented in Figure 5.13 demonstrates that the simplified methods that only use building height to estimate dynamic amplification effects become increasingly unconservative as the force reduction factor used for design increases. Mean dynamic amplification ratios for the buildings were determined to be 1.09 (COV = 0.08), 0.90 (COV = 0.13) and 0.79 (COV = 0.11) for buildings designed using force reduction factors of 2, 3 and 4, respectively. These results demonstrate these existing methods do not accurately predict the amount of dynamic amplification predicted by the numerical simulations for the range of building design parameters considered in the current study.

5.5.2.2 Amplification Based on MRSA

Data presented in Figure 5.14 suggest the Eibl MRSA method and the Priestley method provide improved prediction of dynamic amplification for 6- and 8-story buildings but become less accurate as building height increases above 8 stories. For the Eibl MRSA method, mean dynamic amplification ratios were determined to be 0.90 (0.09), 0.96 (0.17) and 1.01 (0.21) for buildings designed using force reduction factors of 2, 3 and 4, respectively. The minimum and maximum amplification ratios calculated for the Eibl method were 0.79 and 1.58 indicating this method does not accurately predict the numerical simulation results for the entire range of building designs. For buildings less than 12 stories in height, the Priestely method, which is a simplification of the Eibl MRSA method, predicts results similar to the Eibl method. For building heights of 12 stories or greater, the Priestley method becomes increasingly conservative and subject to large variability. For the Priestely method, mean dynamic amplification ratios were determined to be 1.18 (0.22), 1.14 (0.28) and 1.10 (0.35) for buildings designed using force reduction factors of 2, 3 and 4, respectively.

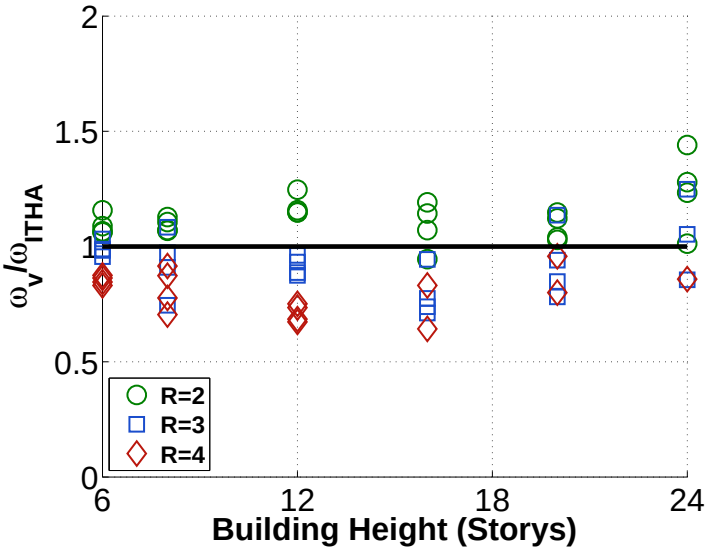

(a) NZS 3101

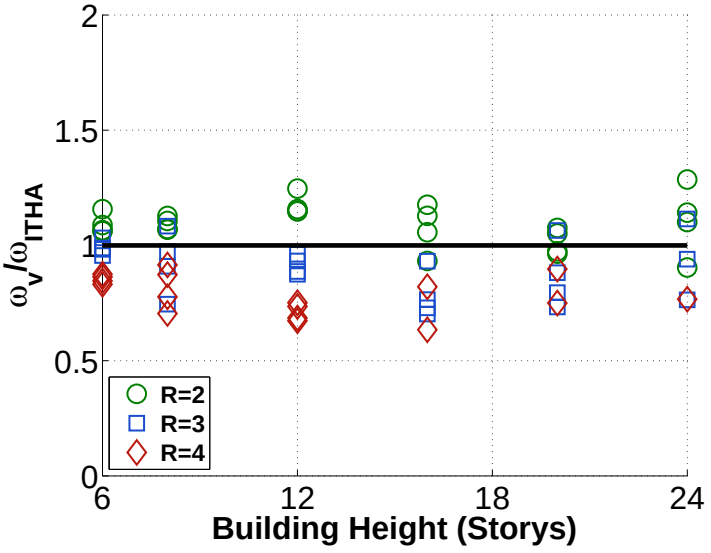

(b) SEAOC

Figure 5.13: Building Story-Based Dynamic Amplification

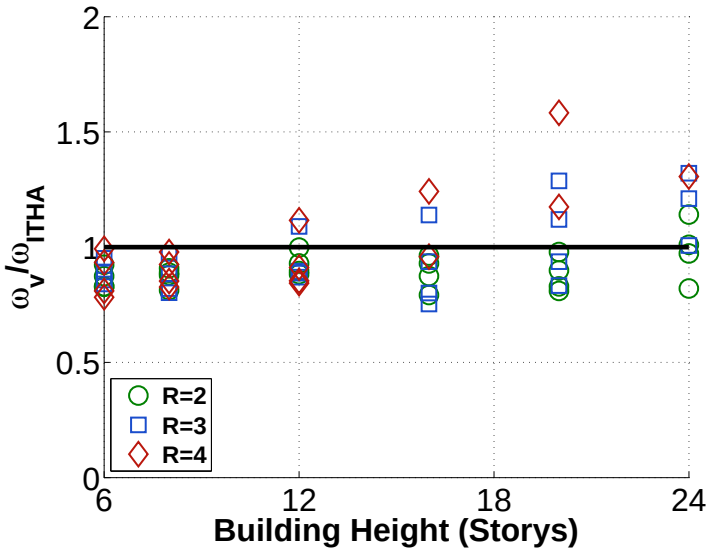

(a) Eibl MRSA

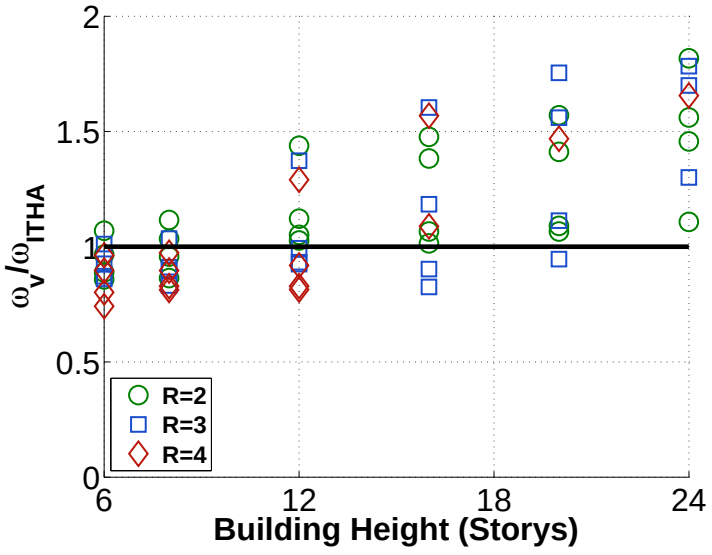

(b) Priestley

Figure 5.14: MRSA-Based Dynamic Amplification

5.6 Conclusions

In this chapter, existing shear capacity design recommendations for walls designed to exhibit flexural yielding during significant seismic events were presented and evaluating using regularized line element models. Evaluation was completed by designing and analyzing a suite of 64 buildings and comparing the dynamic shear demands predicted by inelastic time history analysis to the dynamic amplification predicted using recommendations from the existing literature. Results of the time history analysis demonstrate the significant impact that both flexural overstrength and dynamic amplification of modal response can have on the predicted shear demands. Comparison between time history analysis results and the predictive equations demonstrates that none of the presented current methods accurately predict shear amplification for the entire suite of designs. Of the existing methods, the Eibl MRSA most accurately predicts amplification for the entire suite of designs. The simplified Priestely method is similar in accuracy for building heights less than 12 stories but becomes increasing conservative as building height increases. The NZS 3101 and SEAOC recommendations are significantly unconservative for building designed using a force reduction factor greater than three. The development of an improved method for estimating shear amplification in walled buildings, based on Eibl's MRSA method, is presented and validated in Chapter 6.

Chapter 6

AN IMPROVED METHOD FOR ESTIMATING SEISMIC SHEAR DEMANDS

6.1 Introduction

In Chapter 5, the accuracy of existing methods for estimating the effects of dynamic amplification in slender walls designed to exhibit flexural yielding during a design level seismic event were investigated. Existing amplification recommendations were evaluated by comparing dynamic amplification factors determined by the existing predictive equations and inelastic time history analysis results generated for a suite of 64 building designs using regularized line element models. The building designs were developed considering a range of building heights, initial fundamental period values and several different levels of seismic force reduction. Results of this investigation identified that existing dynamic amplificaion recommendations do not accurately predict the shear amplification determined by numerical simulation for the entire range of building design parameters considered.

In this chapter, an improved method for estimating the dynamic shear demands in slender walls is presented. The method is based on the capped MRSA method previously presented by Eibl (1988). Eibl's method, which was based on the observation that wall yielding primarily reduced first mode shear demands while higher mode loading patterns remained essentially elastic, was demonstrated in Chapter 5 to provide accurate estimation of dynamic shear demands for buildings less than 12 stories tall but became increasingly inaccurate with increasing building height. The modified MRSA method presented in this chapter eliminates the inaccuracy in predicting shear demands for taller buildings and is demonstrated to accurately predict shear demands for the entire building suite developed in Chapter 5. A new suite of wall designs that were capacity designed using the modified MRSA method was developed and ITHA was performed for this new suite of walls considering both design base earthquake (DBE) and maximum considered earthquake (MCE) synthetic ground motion input. ITHA results for the capacity designed buildings demon-

strate that the proposed modified MRSA method successfully limits shear demands for both DBE and MCE seismic events.

Section 6.2 presents development details for the modified MRSA method. Details of the wall designs, numerical models and ITHA results are provided in Section 6.3. In Section 6.3, shear demand-to-capacity ratios for walls designed using the modified MRSA approach and the current US design approach required by ASCE 7 (2010) and ACI 318 (2011) are compared. The presented comparison further demonstrates that the current US seismic design approach significantly underestimates the dynamic shear demands predicted to develop in yielding walls.

6.2 A Modified MRSA Method for Estimating Seismic Shear Demand

Data presented in Chapter 5 demonstrates that existing dynamic amplification equations do not accurately predict shear amplification over a wide range of building heights, initial periods and force reduction factors. To address this problem, a modified MRSA method for predicting dynamic shear amplification in walled buildings was developed.

6.2.1 Development of the Modified MRSA Method

The basis for the modified MRSA method is the capped MRSA method proposed by Eibl et al (1988). Comparison of dynamic amplification estimated using Eibl's MRSA method to dynamic amplification predicted by ITHA (Figure 5.14(a)) demonstrated that Eibl's method is accurate for walled buildings 12 stories or less in height, regardless of the building period or selected force reduction factor. For buildings taller than 12 stories, reduced accuracy was demonstrated, with higher levels of conservatism provided for buildings designs using larger force reduction factors.

To study the loss of accuracy and increased variability in predicting shear demands for taller buildings, the dynamic amplification comparison data from Figure 5.14(a) was replotted versus initial building fundamental period, T_1, in Figure 6.1(a). The data presented in Figure 6.1(a) demonstrates that:

1. Increasingly overpredicted dynamic amplification occurs beginning at a T_1 value of approximately 2.0 seconds.

2. Increased dispersion in the amplification ratio appears to begin at a value of approximately 2.0 seconds. To highlight this, an approximated trend line is overlayed on the amplification comparison data in Figure 6.1(b). The added trend line highlights the increased variability in the predicted amplification for building periods greater than 2.0 seconds.

To further investigate the observed period dependency, the ratio between the first and second mode elastic MRSA base shear contributions, V_{1e}/V_{2e}, was determined and plotted versus T_1. These data are presented in Figure 6.2. These data show that the second mode base shear contribution, V_{2e}, exceeds the first mode base shear contribution, V_{1e}, for buildings designed such that the fundamental period, T_1, is greater than approximately 2.0 seconds. These data combined with the data from Figure 6.1(a) suggest that the Eibl MRSA method tends to overestimate dynamic amplification when second mode elastic base shear contributions exceed the first mode elastic base shear contribution. For the walled buildings designed in Chapter 5, V_{2e} begins to exceed V_{1e} at $T_1 \approx 2.0$ seconds; why the transition occurs at $T_1 \approx 2.0$ seconds for the walls designed in Chapter 5 is addressed subsequently.

6.2.1.1 Modified MRSA Method

On the basis of the above discussion, a modified MRSA method was developed where the effective force reduction factor, R/Ω_o is applied to reduce elastic MRSA shear response for the mode contributing most significantly to base shear demand. The intent of this modification is to eliminate the identified trend that the Eibl MRSA method overpredicts dynamic amplification for walls in which second mode elastic base shear contribution exceeds the first most elastic base shear contribution. MRSA analysis using this approach was performed for the 64 buildings designed and previously discussed in Chapter 5. Dynamic

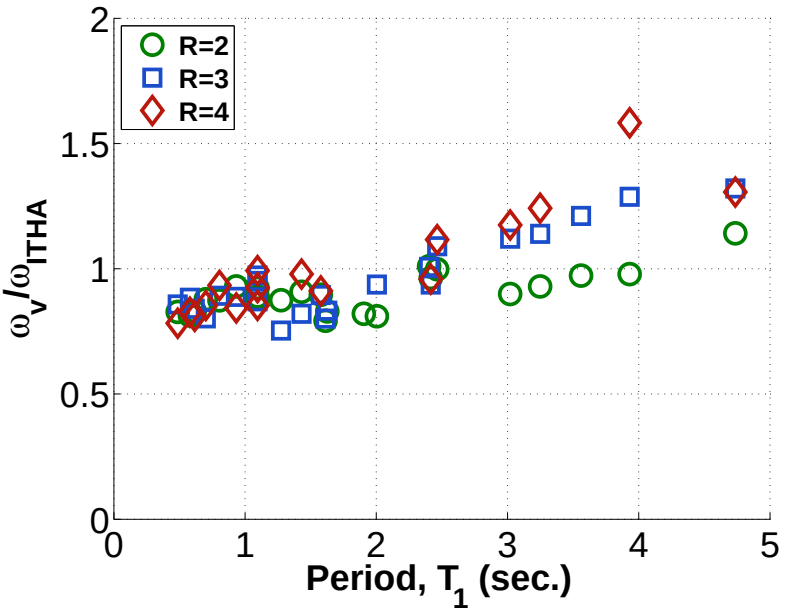

(a) Eibl MRSA Results

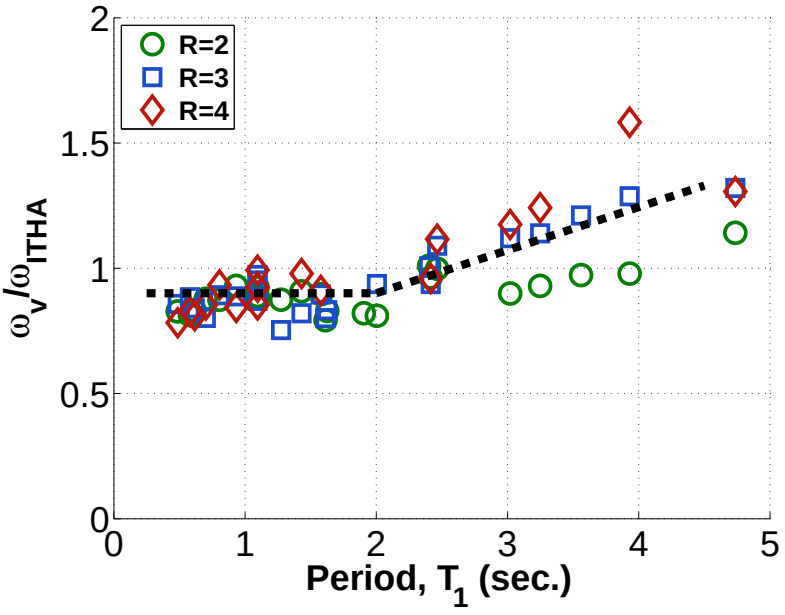

(b) MRSA Results Trend

Figure 6.1: Eibl MRSA Comparison Results

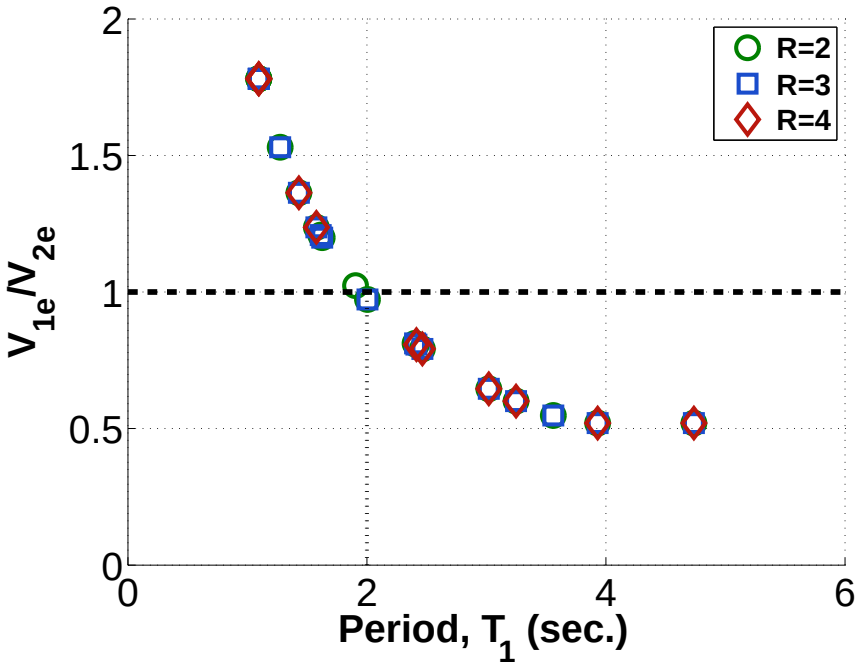

Figure 6.2: Elastic Modal Contribution to Base Shear

amplification factors from the analysis were calculated using Equation 5.15 and compared to the dynamic amplification determined by ITHA, ω_{ITHA}. Comparison of dynamic amplification factors are presented in Figure 6.3(a).

The data in Figure 6.3(a) show the suggested MRSA approach significantly reduces the variability in predicted dynamic amplification for taller buildings and that the accuracy of the suggested MRSA approach is unaffected by the selected initial period or force reduction factor. Mean amplification factor ratios of 0.88, 0.87 and 0.88 were determined for buildings designed using force reduction factors of 2, 3 and 4, respectively. The results also demonstrate that the suggested MRSA method underestimates shear amplification by approximately 10% for the 64 building suite that was analyzed. This underestimation of demand is likely due to one or more of the following:

1. 2% damping was used to generate the synthetic ground motion records used to analyze the walled buildings, however the Rayleigh damping curve used for ITHA pre-

scribes less than 2% damping for period values between 1.5T_1 and T_2. (Figure 5.7)

2. The simplification of assuming a single modal load pattern is reduced by the effective force reduction factor, R/Ω_o.

3. Approximations inherent in using MRSA to determine peak response quantities instead of a time history analysis

To account for these errors, dynamic amplification factors calculated by modified MRSA were increased by 10%. Results for the proposed modified MRSA method, including the 10% increase in demand, are shown in Figure 6.3(b). Use of the modified MRSA method for determined capacity design shear demands for yielding walls can be summarized as:

1. Perform elastic MRSA using appropriate effective stiffness values and determine elastic base shear contributions from each mode.

2. Determine the mode that contributes most to elastic base shear demand. Reduce this elastic base shear contribution by an effective force reduction factor,R/Ω_o, where R is the force reduction factor used for flexural design and Ω_o is the provided flexural overstrength at the wall base.

3. Combine the modal base shear contributions using an appropriate modal combination rule.

4. Increase the SRSS shear envelope value by 10% to account for the sources of error discussed above.

Using the modified MRSA method, mean amplification factor ratios of 0.96, 0.97 and 0.98 were determined for buildings designed using force reduction factors of 2, 3 and 4, respectively. These results suggest the proposed method can be used to accurately estimate dynamic amplification for buildings designed using various force reduction factors.

The mean amplification ratio for the entire building suite is 0.97 with a coefficient of variation of 0.07. The minimum amplification ratio calculated using the modified MRSA method was 0.83 and the maximum ratio calculated was 1.16.

6.2.1.2 Characteristics of the Modified MRSA Methodology

A study of modal load patterns for cantilevered walls was performed to determine the building fundamental period at which the second mode elastic MRSA base shear contribution, V_{2e}, will be larger than the first mode elastic MRSA base shear contribution, V_{1e}. Assuming uniformly distributed seismic mass and an ASCE 7-10 design spectral shape, it can be shown that the transition fundamental period, indicating second mode elastic base shear contribution is larger than first mode elastic base shear contribution, is:

$$T_{lim} \approx 3.25 \frac{S_{D1}}{S_{DS}} \tag{6.1}$$

Thus, if the calculated building period, T_1, is less than T_{lim}, the first mode elastic base shear contribution will exceed the second mode contribution. If T_1 is greater than T_{lim}, the second mode elastic base shear contribution will be larger. For buildings significantly taller than 24 stories, alternate period limits could be derived to determine when modes higher than the second mode are largest, however such limits are not presented in this thesis.

The derivation of Equation 6.1 is as follows. From MRSA, elastic shear contributions can be defined as:

$$V_{ie} = r_{vi} S_i \tag{6.2}$$

Where V_{ie} is the elastic base shear contribution due to modal load pattern 'i', r_{vi} is the modal static response contribution to base shear from the i^{th} modal load pattern (Chopra, 2001) and S_i is the spectral acceleration corresponding to the i^{th} modal period.

For cantilevered walls greater than four stories in height with equal floor heights and

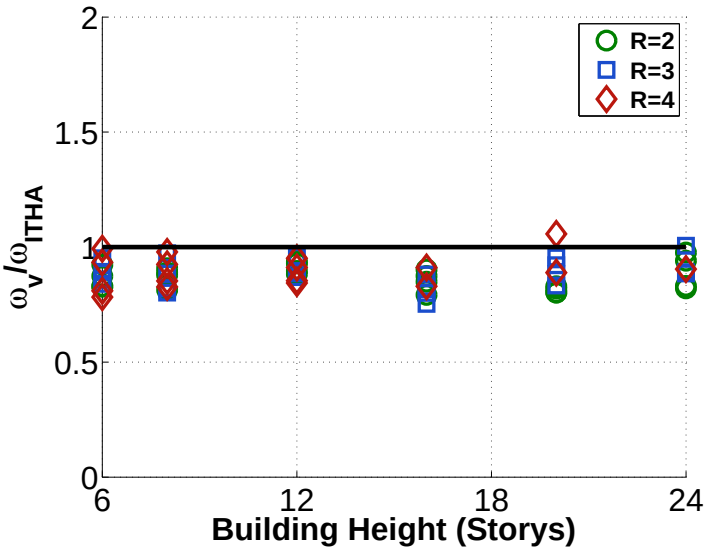

(a) MRSA Results

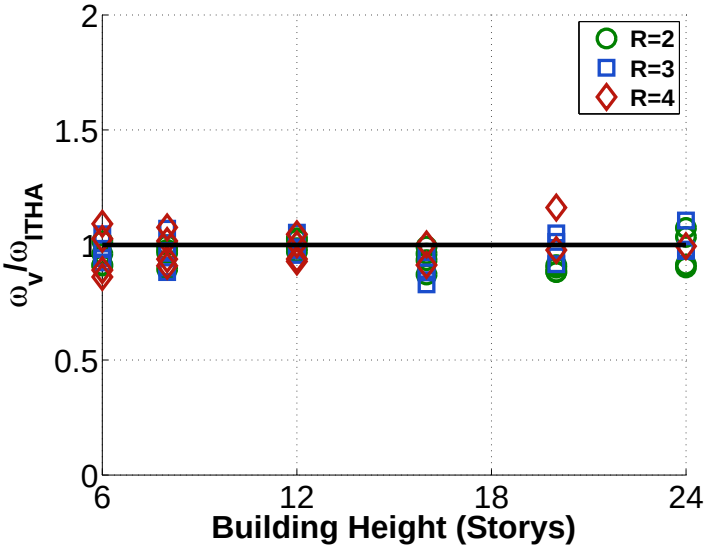

(b) Modified MRSA Method Results

Figure 6.3: Proposed Shear Amplification Results

uniformly distributed seismic weight, the modal static response contribution to base shear for the first and second modes can be approximated as:

$$r_{v1} \approx \frac{W}{620} \tag{6.3}$$

and

$$r_{v2} \approx \frac{r_{v1}}{3.25} \tag{6.4}$$

where W is the total seismic weight in kips. These expressions, which are validated in Appendix C, can be used to write the ratio of the elastic MRSA base shear contributions from the first and second mode as:

$$\frac{V_{2e}}{V_{1e}} = \frac{r_{v2}S_2}{r_{v1}S_1} = \frac{r_{v1}S_2}{3.25r_{v1}S_1} = \frac{S_2}{3.25S_1} \tag{6.5}$$

which implies:

$$V_{2e} > V_{1e} \text{ if } S_2 > 3.25S_1 \tag{6.6}$$

Thus, the second mode elastic base shear contribution exceeds the first mode contribution if S_2 is approximately 3.25 times greater than S_1. For an ASCE 7-10 shaped spectrum, this is only possible if T_1 is greater than the transition period, $T_s = S_{D1}/S_{DS}$. If T_1 is greater than T_s, then S_1 is defined by ASCE as:

$$S_1 = \frac{S_{D1}}{T_1} \tag{6.7}$$

Solving this equation for the period required to create a ratio between S_2 and S_1 greater

than 3.25 yields the transition period value provided in Equation 6.1. For this calculation, it was noted that the relationship between T_1 and T_2 for cantilevered walls can reasonably be approximated (Young and Budynas, 2002) as:

$$T_2 \approx \frac{T_1}{6.25} \tag{6.8}$$

and thus when T_{lim} is reached:

$$T_2 \approx 0.52 \frac{S_{D1}}{S_{DS}} \tag{6.9}$$

which corresponds to a spectral acceleration value of S_{DS} for all seismic design categories defined by ASCE 7-10. Thus, for walled buildings calculated to have $T_1 < T_{lim}$, the modified MRSA method should be used to reduce elastic first mode shear response. For the walled buildings used in this section to assess dynamic amplification, the ratio of S_{D1}/S_{DS} = 0.75g/1.25g = 0.60, thus for these buildings $T_{lim} \approx$ 1.95 seconds. This calculated transition period value is consistent with Figure 6.2, which shows that second mode elastic base shear contribution begins to exceed the first mode contribution at a fundamental period, $T_1 \approx$ 2.0 seconds.

6.2.1.3 Simplification of the Proposed Methodology

Based on static modal contribution factors, elastic MRSA and the ASCE 7 design spectrum shape, a simplified design equation was developed to allow determination of the modified MRSA base shear demand without requiring the designer to perform a complete MRSA. The simplified equation presented in this section is appropriate for analysis of walls for which the flexural overstrength and fundamental period have already been determined.

The only simplification required is to truncate the MRSA to include the first two modes of response. The simplified equation accounts for the slight unconservatism involved with truncating third mode response. For walls significantly taller than 24 stories, third mode

response will be more significant and the simplified equation presented in this section can become unconservative.

The simplified equation, with the truncated modal response can be writen as:

$$V_u' \approx \frac{W}{530}\sqrt{(\frac{S_1}{\hat{R}_1})^2 + 0.10(\frac{S_2}{\hat{R}_2})^2} \tag{6.10}$$

where

$$\text{for } T_1 < 3.25\frac{S_{D1}}{S_{DS}} \text{ , } \hat{R}_1 = \frac{R}{\Omega_o} \text{ and } \hat{R}_2 = 1 \tag{6.11}$$

and

$$\text{for } T_1 > 3.25\frac{S_{D1}}{S_{DS}} \text{ , } \hat{R}_1 = 1 \text{ and } \hat{R}_2 = \frac{R}{\Omega_o} \tag{6.12}$$

6.2.1.4 Simplified Equation for Preliminary Design

When beginning preliminary design, the wall size (and fundamental period) may not be known. For this case, a further simplified equation was developed to estimate the shear demand for preliminary design; for this equation, preliminary shear demands are estimated using 1) peak short period spectral acceleration from the design spectrum, S_{DS}, 2) total seismic weight, W and 3) the number of stories, N. For development of this equation, R = 3, Ω_o = 1.5 and T_1 = 0.1N were assumed. The use of the simplified design equation provides means to estimate the wall area required to resist base shear demands; shear for design should be verified using the modified MRSA method or Equation 6.10 once the wall is sized and flexural design is complete.

Shear demand used for preliminary design, in kips, may be estimated as:

$$V'_u \approx \frac{S_{DS}W}{530}(0.25 + \frac{2}{N}) \tag{6.13}$$

or, in terms of a base shear coefficient similar to the C_s value used by ASCE 7-10:

$$C'_s \approx \frac{S_{DS}}{530}(0.25 + \frac{2}{N}) \tag{6.14}$$

These equations are intended to be used for buildings ranging between six and thirty stories in height. Comparison between the approximate capacity designed base shear coefficients (C_s') and base shear coefficients calculated using ASCE 7-10 equations 12.8-2, 12.8-3 and 12.8-4 are provided in Figure 6.4. For comparison, an R_{ASCE} of 5 and a period of 0.1N were used to calculate code-based base shear coefficients ,C_s. Figure 6.4 demonstrates the significant increase in base shear demand when using the capacity design modified MRSA method instead of the current ASCE 7 seismic design procedure.

6.2.1.5 Proposed Design Process for Capacity Design of Shear in Slender Walls

A flow chart describing the proposed design process for wall sizing using the modified MRSA method to capacity design for shear is provided in this section. This process is intended to support design of slender shear walls by directly accounting for the increase in base shear demands associated with dynamic amplification and flexural overstrength.

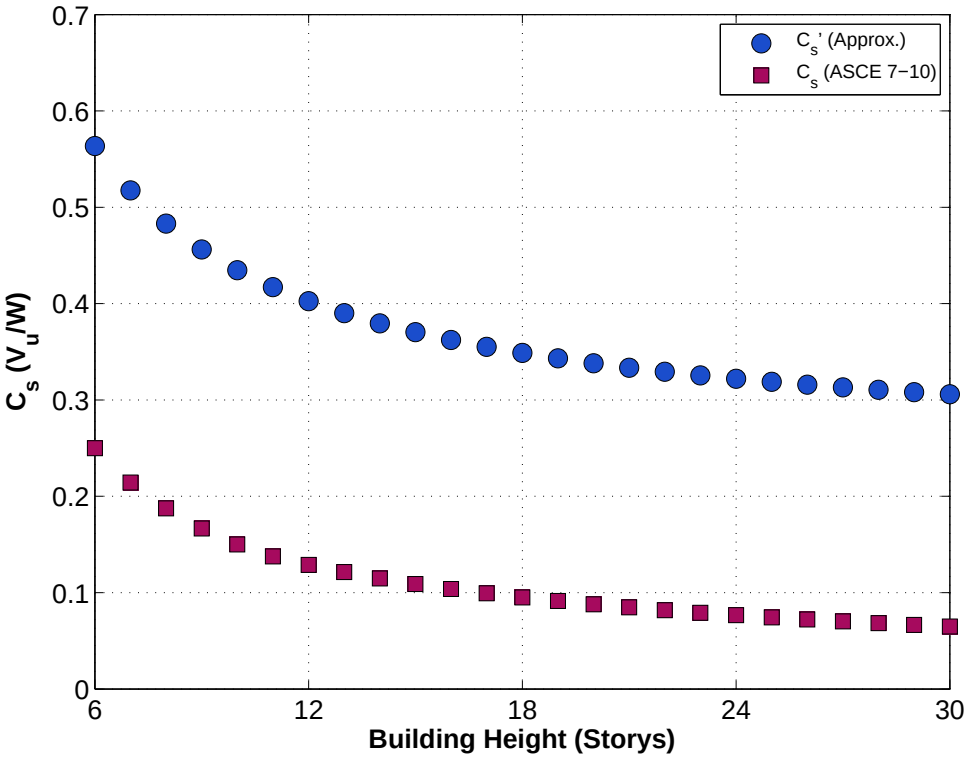

Figure 6.4: Base Shear Coefficient Comparison

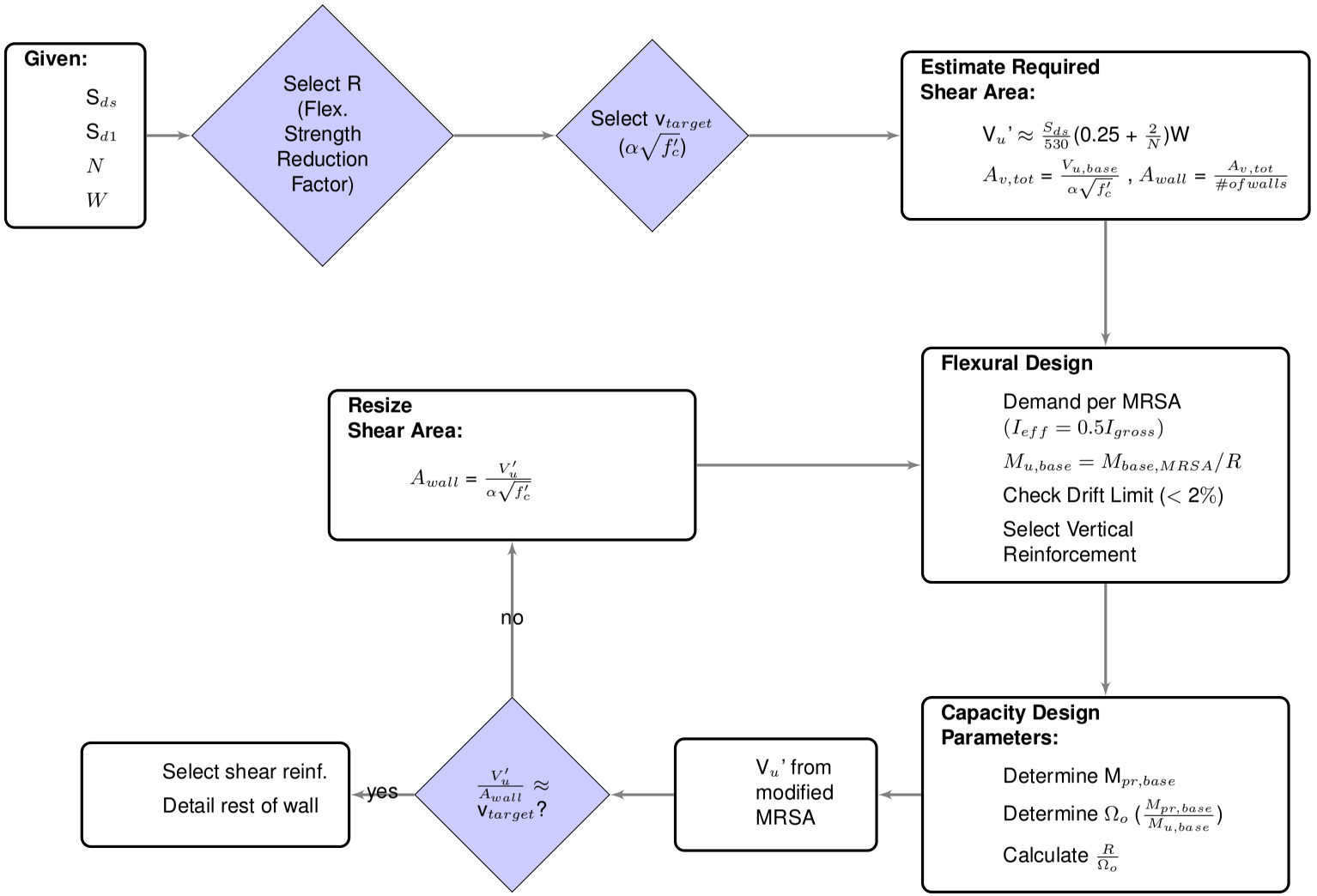
Given:
S_{ds}
S_{d1}
N
W
Select R (Flex. Strength Reduction Factor)
Select v_{target} ($\alpha\sqrt{f'_c}$)
Estimate Required Shear Area:
$V_u' \approx \frac{S_{ds}}{530}(0.25 + \frac{2}{N})W$
$A_{v,tot} = \frac{V_{u,base}}{\alpha\sqrt{f'_c}}$, $A_{wall} = \frac{A_{v,tot}}{\#ofwalls}$
Flexural Design
Demand per MRSA ($I_{eff} = 0.5I_{gross}$)
$M_{u,base} = M_{base,MRSA}/R$
Check Drift Limit ($< 2\%$)
Select Vertical Reinforcement
Capacity Design Parameters:
Determine $M_{pr,base}$
Determine Ω_o ($\frac{M_{pr,base}}{M_{u,base}}$)
Calculate $\frac{R}{\Omega_o}$
V_u' from modified MRSA
$\frac{V_u'}{A_{wall}} \approx v_{target}$?
yes
Select shear reinf.
Detail rest of wall
no
Resize Shear Area:
$A_{wall} = \frac{V_u'}{\alpha\sqrt{f'_c}}$

6.3 Assessment of the Modified MRSA method Using Synthetic Ground Motions

In this section, the adequacy of the modified MRSA method for capacity designing against excessive shear demand in slender walls is investigated. The assessment results presented in this section demonstrate that walls that are capacity designed for shear using the modified MRSA method developed shear demands at or below the provided shear capacity when subjected to both DBE and MCE ground motion records.

To complete this assessment, 27 walled buildings were designed and analyzed using inelastic time history analysis. The walls designed and analyzed in this section were designed using two different methodologies:

1. Buildings designed using force reduction factors of R = 2, 3 and 4 were capacity designed for shear using the modified MRSA method.

2. Buildings designed using code-based force reduction factors of R_{ASCE} = 5 or 6 were designed using seismic loading defined by ASCE 7 (2010).

The code-based building designs discussed in this section differ from the wall designs developed in Chapter 5 because the code-based walls designed in this section were sized to limit design level shear demands based on recommendations provided by NEHRP (2011).

Both the modified MRSA method and the current US code-based design methodologies were investigated to facilitate comparison between shear demand-to-capacity ratios predicted to develop in walls designed using different seismic design procedures. Design methods, nonlinear modeling and analysis of the designed walled buildings are described in the following sections. A summary of pertinent design parameters for the wall designs are provided in Table 6.1. Design parameters presented in Table 6.1 are defined as follows:

- Shape = geometry of the wall cross-section. R = rectangular (planar); C = core (flanged).

- N = number of building stories.

- R = force reduction factor. Code-based walls were designed using force reduction factors of R_{ASCE} = 5 and 6. For these walls, the theoretical force reduction factor, R, provided by the design is presented in parantheses after the R_{ASCE} value used for design. Theoretical force reduction, R, is determined as the ratio between the elastic MRSA base moment demand and the base moment demand specified by ASCE 7.

- T_1 = calculated fundamental period using effective flexural stiffness, $0.5E_cI_g$.

- l_w = horizontal wall length.

- t = wall (web and/or flange) thickness.

- b_f = core wall flange width. One-half the total provided core width.

- Δ = design story drift.

- ρ = longitudinal reinforcement ratio.

- Ω_o = flexural overstrength provided at the base of the wall, calculated as M_{pr}/M_u, where M_{pr} is the expected flexural strength considering expected material strength, strain hardening and a strength reduction factor, ϕ = 1.0. M_u is the base moment earthquake demand determined using elastic MRSA and theoretical force reduction factor, R.

- R/Ω_o = the ratio between the force reduction factor, R, and the flexural overstrength, Ω_o.

- μ_ϕ = provided curvature ductility capacity at the wall base.

- v_u = design base shear demand, calculated as $V_b/(A_{cv}(f'_c)^{0.5})$, where A_{cv} is the wall web area and f'_c is the design concrete compressive strength.

- ρ_t = transverse reinforcement ratio

- $\phi V_n/V_u$ = ratio of design shear strength of the wall calculated using ACI 318 (2011) Equation 21-7 to the design shear demand.

- $\phi V_{n,pr}/V_u$ = ratio of expected design shear strength of the wall calculated using ACI 318 (2011) Equation 21-7 and using expected material strengths to the design shear demand.

Table 6.1: Wall Design Data

	General							Flexural Design				Shear Design			
Shape[1]	N	R	T_1	l_w	t	b_f	Δ	ρ	Ω_o[2]	R/Ω_o	μ_ϕ	v_u[3]	ρ_t	$\phi V_n/V_u$	$\phi V_{n,pr}/V_u$
	(Stories)		sec.	ft	in	in	%	%					%		
R	6	2	0.38	336	26	–	0.45	1.20	1.27	1.37	15	5.38	0.68	1.08	1.26
R	6	3	0.49	312	20	–	0.72	1.27	1.38	1.99	15	5.52	0.73	1.09	1.30
R	6	4	0.58	288	18	–	1.02	1.41	1.49	2.44	14	5.82	0.69	1.01	1.18
R	6	5 (3.4)	0.62	288	16	–	1.12	1.95	1.53	2.20	13	3.59	0.48	1.02	1.18
R	6	6 (4.0)	0.62	288	16	–	1.12	1.59	1.62	2.49	14	2.99	0.36	1.01	1.17
R	8	2	0.47	432	26	–	0.49	1.50	1.37	1.28	20	5.95	0.85	1.01	1.35
R	8	3	0.64	384	20	–	0.87	1.56	1.40	1.94	20	6.02	0.73	1.00	1.19
R	8	4	0.82	324	20	–	1.12	1.00	1.37	2.72	23	5.22	0.63	1.05	1.22
R	8	5 (3.4)	0.84	320	20	–	1.14	1.56	1.61	2.11	20	2.64	0.31	1.05	1.22
R	8	6 (4.1)	0.84	320	20	–	1.14	1.00	1.50	2.72	23	2.21	0.26	1.14	1.32
R	12	2	0.83	504	26	–	0.76	2.00	1.31	1.29	19	5.99	0.85	1.00	1.34
R	12	3	1.20	432	20	–	1.09	1.56	1.47	1.84	20	5.93	0.73	1.01	1.21
R	12	4	1.43	384	20	–	1.31	1.00	1.48	2.54	23	5.74	0.73	1.05	1.25
R	12	5 (3.3)	1.35	400	20	–	1.41	1.27	1.51	2.16	21	2.02	0.26	1.25	1.44
R	12	6 (3.6)	1.45	380	20	–	1.64	1.00	1.43	2.54	23	1.95	0.26	1.29	1.49
C	16	2	1.13	480	30	96	0.77	1.41	1.20	1.29	23	5.89	0.73	1.02	1.22
C	16	3	1.45	480	22	60	0.99	1.15	1.42	1.81	22	6.08	0.80	0.99	1.26
C	16	5 (3.1)	1.93	384	18	84	1.74	1.41	1.67	1.84	27	2.80	0.32	1.00	1.16
C	16	6 (3.5)	2.02	384	16	84	1.92	1.25	1.69	2.09	31	2.62	0.31	1.06	1.23

Table 6.1: Wall Design Data

	General							Flexural Design				Shear Design			
Shape[1]	N	R	T_1	l_w	t	b_f	Δ	ρ	Ω_o[2]	R/Ω_o	μ_ϕ	v_u[3]	ρ_t	$\phi V_n/V_u$	$\phi V_{n,pr}/V_u$
	(Stories)		sec.	ft	in	in	%	%					%		
C	20	2	1.63	480	34	108	0.89	1.53	1.27	1.14	21	5.83	0.86	1.03	1.40
C	20	3	2.03	480	26	72	1.12	0.98	1.39	1.82	24	5.83	0.85	1.03	1.37
C	20	5 (2.9)	2.61	402	20	96	2.17	1.27	1.61	1.82	30	2.56	0.28	1.03	1.19
C	20	6 (3.4)	2.72	402	18	96	2.36	1.11	1.62	2.10	38	2.37	0.28	1.10	1.27
C	24	2	2.26	480	34	120	0.75	1.53	1.30	1.14	27	5.90	0.86	1.02	1.38
C	24	3	2.69	480	26	96	1.25	0.98	1.41	1.78	19	5.92	0.85	1.01	1.35
C	24	5 (3.0)	3.14	432	20	126	2.28	1.27	1.73	1.75	38	2.50	0.26	1.00	1.16
C	24	6 (3.5)	3.28	432	18	126	2.50	1.11	1.72	2.04	45	2.32	0.28	1.13	1.30

[1] R = Rectangular Cross-Section; C = Core Cross-Section

[2] Ω_o = M_{pr}/M_u

[3] v_u = Design Shear Demand ($\sqrt{f'_c(psi)}$)

6.3.1 Simplified Walled Building Configuration

The simplified walled building configuration described in Chapter 5 was maintained for the designs presented in this section.

6.3.2 Wall Design Methodology

The following sections describe the difference between the design methodology used for capacity designed and code-based walls.

6.3.2.1 Capacity-Based Designs (R = 2, 3 or 4)

Flexural demands were determined by elastic MRSA, the calculated fundamental period, T_1, and the force reduction factor, R. Capacity designed shear demands were determined using the modified MRSA method. Wall sizing was determined by limiting the base shear demand determined by modified MRSA to approximately $6\sqrt{f'_c}$(psi)A_v, where f'$_c$ is the design compressive concrete strength and A_v is the web area of the wall. $6\sqrt{f'_c}A_v$ is the maximum demand permitted by ACI 318-11 assuming a design shear strength of ϕV_n, with ϕ taken as 0.75 and V_n taken as $8\sqrt{f'_c}A_v$. A ϕ-factor of 0.75 is permitted by Section 9.3 of ACI 318-11 when flexural overstrength is accounted for in the design.

6.3.2.2 Code-Based Designs (R_{ASCE} = 5 or 6)

Walls designed using a code-based force reduction factor, R_{ASCE}, of 5 or 6 were designed in accordance with ASCE 7-10, which modifies elastic MRSA by imposing a period limit, C_uT_a, on the fundamental period used to determine first mode demand contribution. Additionally, MRSA demands must be increased to meet base shear demands determined assuming a first-mode dominant equivalent lateral seismic force distribution. Wall sizing was determined by limiting design level shear demand to less than $4\sqrt{f'_c}$(psi)A_v (NEHRP, 2011) and targeting a fundamental period between 0.10N-0.15N. For some designs, the calculated design story drift exceeded the allowable drift limit of 2% for walls per Table

12.12-1 of ASCE 7-10. For these cases, walls were not redesigned to achieve the required drift limit.

6.3.2.3 Design Level Seismic Demand

The 2% damped design spectrum discussed in Chapter 5 was used to determine design level demands for the walled buildings. Justification for using a 2% damped design spectrum instead of the commonly used 5% damped design spectrum is discussed in Chapter 5.

6.3.2.4 Flexural Design Method

Flexural design of all walled buildings was performed using the methods discussed in Chapter 5. As with walls designed in Chapter 5, planar wall cross-sections were used for building heights shorter than 16 stories; core (flanged) configurations were used for 16 stories or taller walled buildings.

6.3.2.5 Shear Design Method

Shear reinforcement was selected to satisfy strength requirements per Section 21.9.4 of ACI 318-11. Nominal shear strength was limited to $8\sqrt{f'_c}$(psi)A_v per Section 21.9.4.4. For capacity designed walls, a ϕ-factor of 0.75 was used for shear design (ACI 318-11 Section 9.3.2.3). For code-based designs, flexural overstrength was not considered and a ϕ-factor of 0.60 was used for shear design (ACI 318-11 Section 9.3.4(e)). Probable shear strength, V_{pr} was determined using expected material property values for concrete and reinforcing steel. Expected material strength values for concrete and reinforcing steel are discussed in Chapter 5.

6.3.2.6 Calculated Story Drift

For capacity designed walls, maximum story drifts were calculated using MRSA, the selected force reduction factor R and a deflection amplification factor, C_d, taken equal to the

force reduction factor, R. For code-based designs, C_d = 5 was used per Table 12.2-1 of ASCE 7-10 for 'special reinforced concrete shear walls'.

6.3.2.7 Flexural Design Envelope

For preliminary investigation of the 27 building designs the design section provided at the wall base was assumed to remain constant up the entire wall height. Alternate flexural design envelopes were considered and assessment of flexural performance of the designed walls is discussed in Chapter 7. Wall cross-section dimensions and reinforcing ratios provided in Table 6.1 correspond to the design section required to resist design forces at the wall base.

6.3.3 Nonlinear Modeling and Dynamic Solution Technique

The nonlinear modeling approach used to generate ITHA results presented in this section is identical to the modeling approach discussed in detail in Chapter 5.

6.3.4 Ground Motion Input

The seven synthetic ground motions introduced in Chapter 5 were used as input ground motions for the ITHA results presented in this section. For design level demands the synthetic ground motions were used directly. For maximum considered earthquake (MCE) demands, the synthetic ground motions were scaled by a factor of 1.50.

6.3.5 Assessment of Seismic Shear Demand in Walls

Sections 6.3.5.1 and 6.3.5.2 present results, determined using ITHA, that assess shear demand-capacity ratios for walled buildings capacity designed for shear using the modified MRSA method. Demand-capacity ratios for walls subjected to design level ground motion records are discussed in Section 6.3.5.1; demand-capacity ratios for walls subjected to maximum considered earthquake ground motion records are discussed in Section 6.3.5.2.

The data presented in these sections confirm that shear demands in walls designed using the modified MRSA method remain below the provided shear capacitites for all force reduction factors and building heights considered, and considering both DBE and MCE ground motion records. For comparison purposes, shear demand-capacity ratios are also presented for buildings designed to resist shear demands calculated using current US seismic design procedures. For buildings designed to resist code-based shear demands, seismic shear demands exceed the provided wall shear capacity for both design design basis and maximum considered seismic input.

6.3.5.1 Buildings Subjected to Design Level Seismic Demands

For each of the 27 walled buildings, ITHA was performed using a suite of 7 synthetic ground motion records scaled to the 2% damped design level (10% probability of exceedence in 50 years) spectrum. For each building, a maximum shear demand, V_{ITHA}, was defined. V_{ITHA} was defined as the median peak base shear demand determined for the 7 ground motion record set. The seismic base shear demand, V_{ITHA}, was then compared to the probable design shear strength, $\phi V_{n,pr}$, of the building. Shear demand-to-capacity ratios, calculated as $V_{ITHA}/\phi V_{n,pr}$, are provided in Figure 6.5. For each building height considered, shear demand-to-capacity ratios are plotted in order of increasing force reduction factors used for design. Force reduction factors of 2.0, 3.0 and 4.0 correspond to buildings capacity designed for shear using the modified MRSA method. Force reduction factors in between 3.0 and 4.0 and greater than 4.0 correspond to buildings designed using code-based force reduction factors, R_{ASCE}, of 5 and 6, respectively. Code-based force reduction factors, R_{ASCE}, were converted to theoretical force reduction factors, R, for presentation in Figure 6.5.

For capacity designed walls (R = 2, 3 or 4), median demand to capacity ratios were determined to be less than 1.0 for all building heights. A mimimum demand-to-capacity ratio of 0.79 was calculated for the 8-story building designed using a force reduction factor, R = 4. A maximum demand-to-capacity ratio of 0.96 was calculated for the 24-story building designed using a force reduction factor, R = 3. As discussed previously, these

results further confirm the modified MRSA adequately estimates seismic shear demands independent of the selected force reduction factor.

For code-based designs, median ratios exceed 1.50 for all buildings heights (minimum ratio of 1.60; maximum ratio of 2.90). These results demonstrate that shear demands prescribed by current ASCE 7 design procedures significantly underestimate seismic shear demand predicted to develop in slender walls. For buildings designed to satisfy current US design requirements, the provided design shear strength is significantly exceeded when subjected to ground motion records scaled to represent the design level seismic event.

6.3.5.2 Buildings Subjected to Maximum Considered Seismic Demands

For each of the 27 walled buildings, ITHA was performed using a suite of 7 synthetic ground motion records scaled to the 2% damped maximum considered earthquake (2% probability of exceedence in 50 years) spectrum. For each building, a maximum shear demand, V_{ITHA}, was defined. V_{ITHA} was defined as the median peak base shear demand determined for the 7 ground motion record set. The seismic base shear demand, V_{ITHA}, was then compared to the probable shear strength, $V_{n,pr}$, of the building. A ϕ-factor of 1.0 was used to define the probable building shear strength. Shear demand-to-capacity ratios, calculated as $V_{ITHA}/V_{n,pr}$, are provided in Figure 6.6. For each building height considered, shear demand-to-capacity ratios are plotted in order of increasing force reduction factors used for design. Force reduction factors of 2.0, 3.0 and 4.0 correspond to buildings capacity designed for shear using the modified MRSA method. Force reduction factors in between 3.0 and 4.0 and greater than 4.0 correspond to buildings designed using code-based force reduction factors, R_{ASCE}, of 5 and 6, respectively. Code-based force reduction factors, R_{ASCE}, were converted to theoretical force reduction factors, R, for presentation in Figure 6.5.

For capacity designed walls (R = 2, 3 or 4), median demand to capacity ratios were determined to be less than 1.0 for all building heights. A mimimum demand-to-capacity ratio of 0.76 was calculated for the 6-story building designed using a force reduction factor, R = 2. A maximum demand-to-capacity ratio of 0.95 was calculated for the 12-story building

designed using a force reduction factor, R = 3.

It is of interest to note that although the development of the modified MRSA method did not directly address seismic demands at ground motion intensity levels higher than the design level, the calculated demand-to-capacity ratios calculated for the MCE motions suggest that the methodology is adequate for controlling shear at increased seismic intensity levels. One reason for this is that shear capacity at the MCE has been taken as V_n with a ϕ-factor of 1.0 which increases the capacity by 33$\%$ (1/0.75). A second reason for this is that although shear amplification does increase with seismic intensity, the increase is limited by further development of inelastic flexural response in multiple modes. This flexural yielding further limits shear demands imposed by multiple modal load patterns and limits base shear amplification.

For code-based designs, median ratios exceed 1.0 for all buildings heights (minimum ratio of 1.17; maximum ratio of 2.03). The decrease in demand-to-capacity ratios for these buildings at the MCE level compared to the DBE level can be attributed to the large difference between the probable design strength, calculated using a ϕ-factor of 0.60, and the probable shear strength, calculated using a ϕ-factor of 1.0.

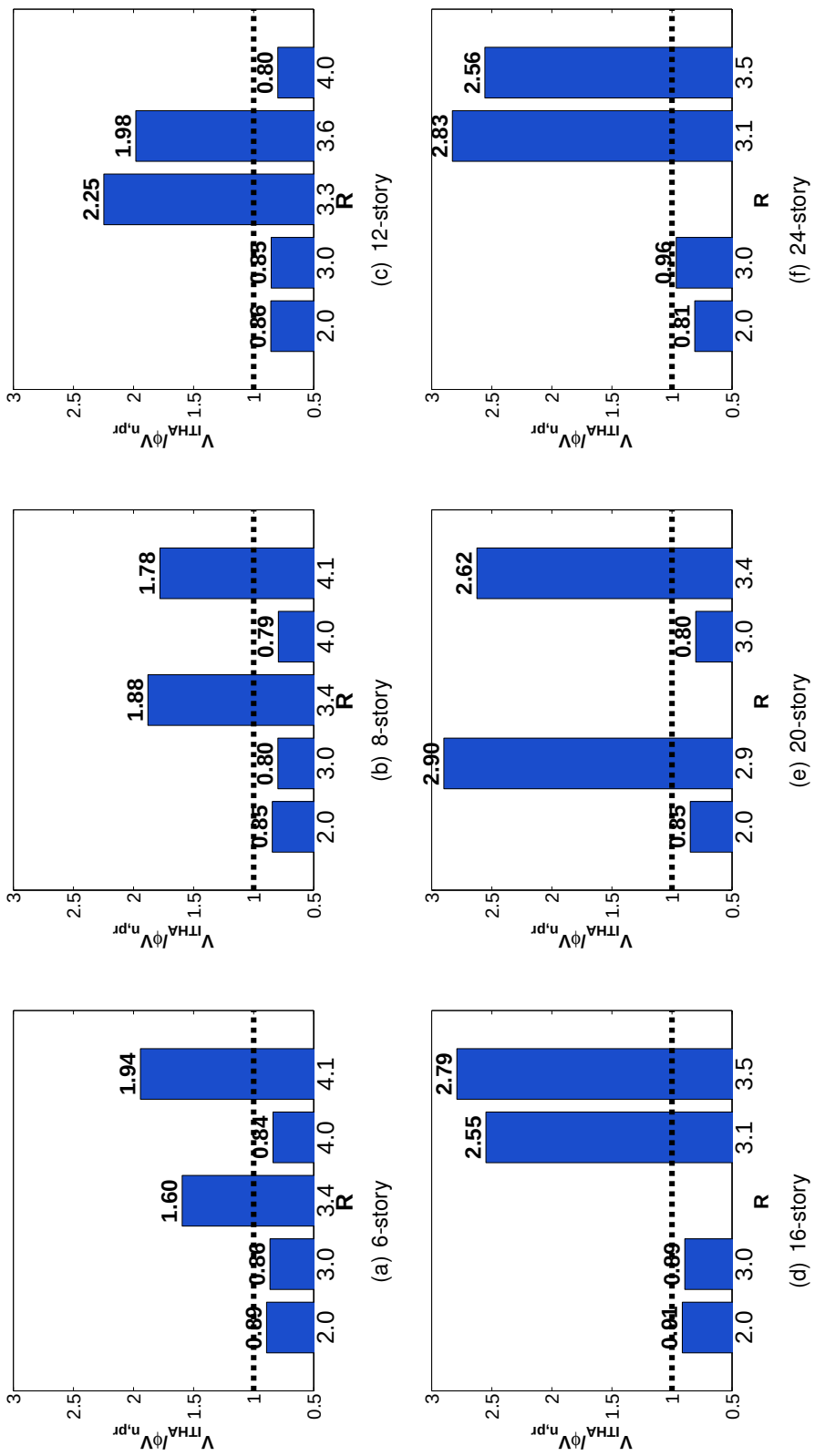

Figure 6.5: Design Level (10% in 50) Shear Demand/Capacity Ratio

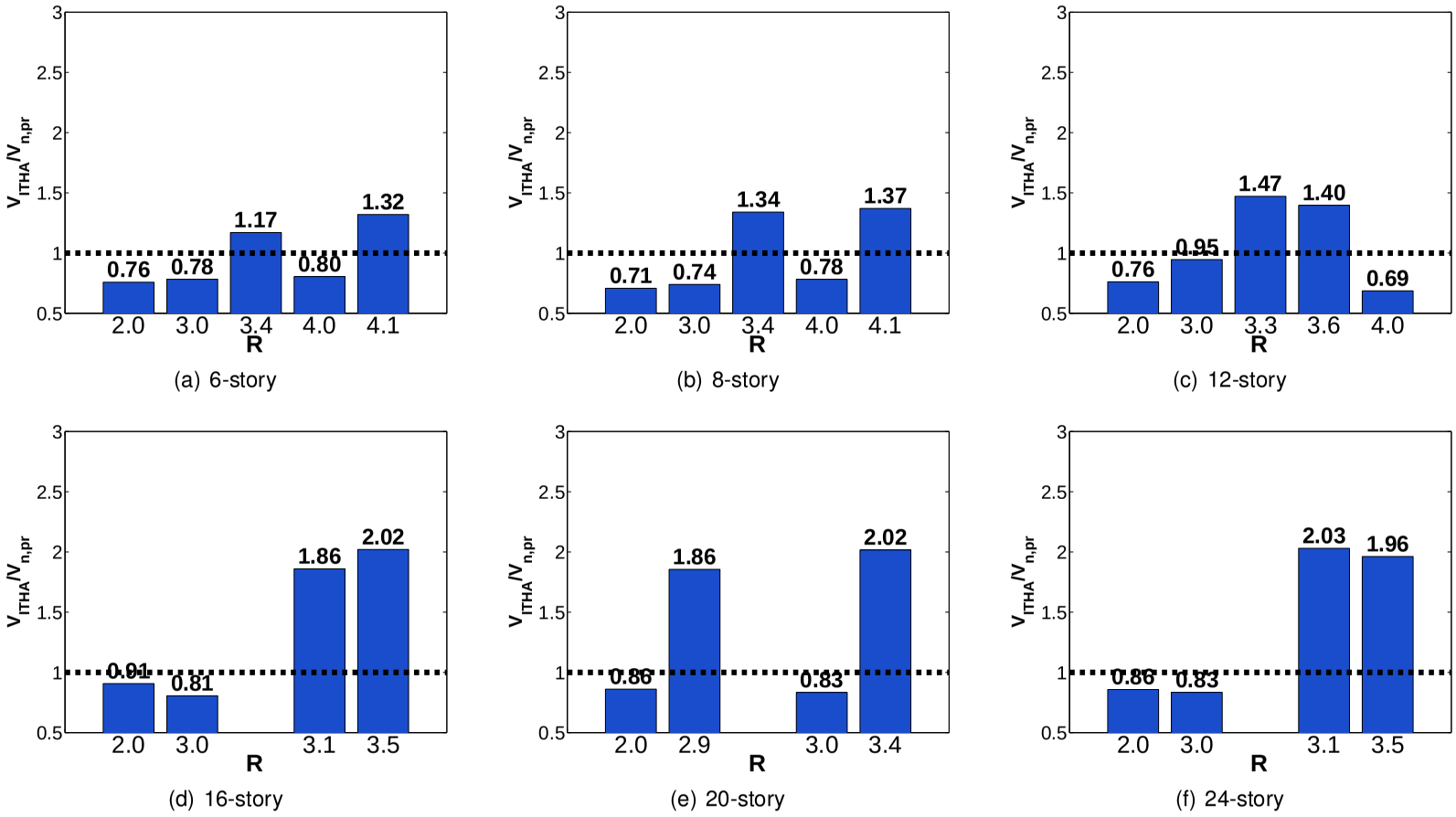

Figure 6.6: MCE Level (2% in 50) Shear Demand/Capacity Ratio

6.4 Conclusions

In this chapter, a modified MRSA method was developed to improve existing shear capacity design recommendations for walled buildings. The modified MRSA method developed was a modification to the first mode capped MRSA method developed by Eibl (1988) and was demonstrated in this chapter to accurately predict seismic shear demands for the 64 walls designed and analyzed in Chapter 5. Once development of the modified MRSA method was complete, a series of 20+ buildings were designed to verify the adequacy of the proposed shear capacity design method and to compare shear demand-to-capacity ratios calculated for both buildings capacity designed for shear using the modified MRSA method and for buildings designed to resist shear forces specified by current US building code seismic design procedures. ITHA results for walls capacity designed for shear using the modified MRSA method demonstrated that the proposed method adequately estimates shear demands expected to develop in slender walls subjected to both design level and maximum earthquake ground shaking. ITHA results for code-based designed walls further demonstrate that current US building code seismic design procedures, which do not require a capacity design approach for shear demands, underestimate seismic shear demands for buildings subjected to both design level and maximum considering earthquake ground motions.

Chapter 7

RECOMMENDATIONS FOR FLEXURAL DESIGN ENVELOPES AND FORCE REDUCTION (R) FACTORS

7.1 Introduction

Prevailing ductile design philosophy for concrete walls consists of constraining inelastic response to flexural yielding at the wall base while maintaining shear force demands at or below nominal design strengths. To ensure such design objectives are met a capacity design approach is necessary. Specifically, capacity design should be used to ensure:

1. Seismic shear demands remain less than provided shear capacity to prevent shear failure from limiting ductile wall response.

2. Ductility demands in regions of inelasticity are less than the provided ductility capacity.

3. Provided flexural strengths at sections above the wall base are sufficient to constrain inelastic curvature demand to the wall base.

Currently, many national building codes throughout the world recognize the need for capacity design to ensure ductile response of slender walls. However, current code documents in the US which directly address new construction of such walls (ASCE 7 (2010);ACI 318 (2011)) do not, as of their current editions, require a capacity design approach nor do they supply the designer with recommendations to be used for capacity design of slender walls.

In Chapters 5 and 6, shear capacity design of walls was discussed extensively. In Chapter 5, ITHA results were used to demonstrate that existing shear capacity design recommendations do not provide accurate prediction of seismic shear demands expected to develop in slender walls. In Chapter 6, a modified MRSA method was developed that

adequately predicted seismic shear demands and was demonstrated to adequately capacity design slender walls for shear for walled buildings subjected to both design basis earthquake (DBE) and maximum considered earthquake (MCE) synthetic ground motion records.

Capacity design recommendations developed in Chapter 6 do not quantify flexural performance of slender walls during seismic events. In this chapter the flexural performance of slender walls is evaluated and design recommendations are presented. Flexural performance was evaluated using the regularized line element models developed in Chapter 3. As demonstrated in Chapter 3, such models can be used to simulate flexural ductility and loss of lateral load-carrying capacity for both planar and c-shaped walls. The ability to simulate wall inelastic flexural ductility capacity allows for the determination of an appropriate level of force reduction that limits flexural damage to acceptable levels during a maximum considered earthquake event. In addition to the determination of recommendation force reduction factors, R, for slender walls, several different flexural design evelopes specified in existing building code documents and design practice documents were evaluated. Such envelopes dictate the curtailment of flexural strength above the wall base, with the intention of ensuring inelastic flexural demands remain at expected hinge locations.

A review of existing flexural design recommendations used in various building code and design practice documents are presented in Section 7.2. Section 7.3 provides assessment of flexural performance for a set of 20+ buildings designed using a range of building heights and flexural force reduction factors. Wall assessment results presented in Section 7.3 consist of ITHA results generated by subjecting nonlinear models to a suite of seven synthetic ground motion records scaled to represent both DBE and MCE seismic demands. Finally, Section 7.4 provides additional flexural performance assessment using the formalized collapse assessment procedure defined by the FEMA P695 (ATC, 2008) methodology. Use of the P695 methodology allows for systematic evaluation of appropriate force reduction factors for slender walls subjected to suites of recorded, rather than synthetic, ground motions.

7.2 Existing Flexural Design Procedures for Slender Walls

This section presents a summary of capacity design procedures proposed for ensuring designed wall sections can adequately resist the expected inelastical flexural deformations and that flexural yielding remains near the wall base. In this section flexural design envelopes recommended by 1) New Zealand Standard 3101 (NZS 3101, 2006) 2) Canadian Standard A23.3 (CSA A23.3, R2010) 3) Structural Engineers Association of California (SEAOC, 2008) and Priestley, Calvi and Kowalski (Priestley et al, 2008) are discussed. Prior to discussing the existing seismic design procedures, qualitative comparison of the methods are presented in Figure 7.1. In Figure 7.1, design envelopes for the four methods are compared to seismic demand envelopes determined by reducing elastic seismic flexural demands, calculated using MRSA, by a force reduction factor, R. Profile plots shown in Figure 7.1 were created considering a 16-story building designed using a force reduction factor, R = 4, and assuming 1) nominal flexural wall strength at the base, $M_{n,base}$, exceeds the base moment demand, $M_{b,MRSA}$, by 10%, and 2) expected flexural overstrength at the wall base, $M_{b,pr}/M_{b,MRSA}$, is 1.50. The envelope plots identify that proposed flexural design envelopes differ in shape, with similar bilinear envelopes predicted by the NZS 3101/Priestley procedures and the CSA A23.3/SEAOC procedures.

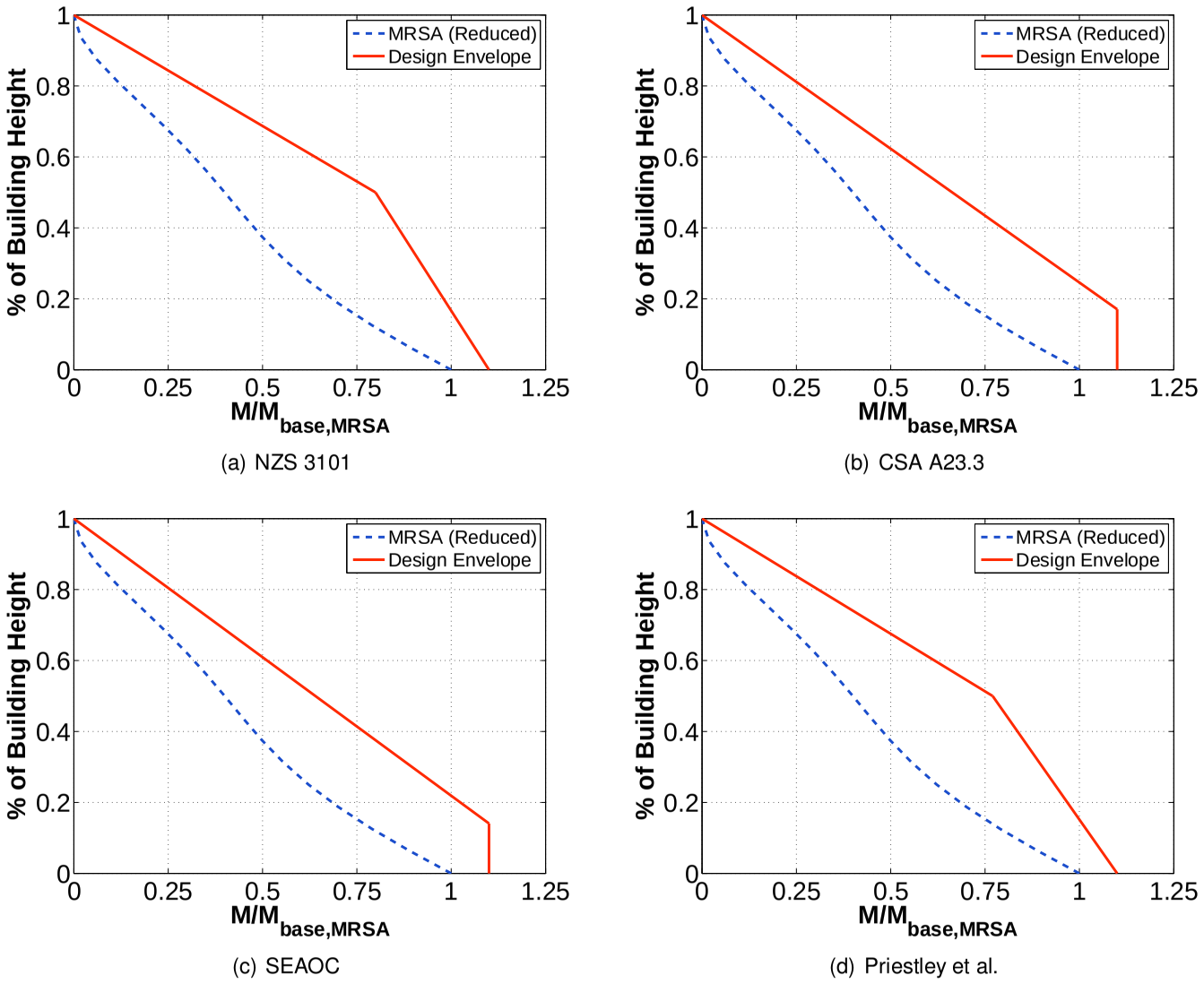

(a) NZS 3101

(b) CSA A23.3

(c) SEAOC

(d) Priestley et al.

Figure 7.1: Existing Recommended Flexural Design Envelopes

7.2.1 NZS 3101(2006)

The New Zealand NZS3101 standard requires that slender walls be capacity designed to dissipate energy solely through flexural yielding at the wall base. Flexural demands are defined by a design envelope that is anchored to the wall strength provided at the wall base and amplified demands above the base to ensure inelastic response concentrates at the base of the wall. To ensure adequate ductility at the wall base, the base section is required to have adequate curvature ductility to enable the wall to achieve a design roof drift displacement demand. System ductility is assessed by a structural ductility factor, μ, that is calculated as 5/β for slender walls, where β is a value between 1.0 and 2.0 depending on the wall aspect ratio. For slender walls having an aspect ratio greater than 3.0, β is equal to 1.0 and the system ductility factor is equal to 5.0. Displacement demands calculated using elastic methods are increased by μ to account for inelastic flexural deformations. To be classified as a ductile slender wall, the provided curvature ductility capacity in the plastic hinge must exceed the inelastic ductility demand, where inelastic ductility demand is determined using the inelastic system displacements and an assumed plastic hinge length. For walls, the plastic hinge length is to be taken as the minimum of 1) 50$\%$ of the wall length and 2) 15$\%$ of the shear span assuming a first mode loading pattern. To ensure the provided plastic hinge section is adequate, the maximum usable curvature ductility for ductile wall sections is taken as 16. Plastic hinge ductile detailing is required to extend to a height, h_p, vertically above the wall base where h_p is taken as the larger of the horizontal wall length, l_w, and 0.17M_b/V_b, where M_b and V_b are the design moment and shear earthquake forces at the wall base.

The procedure for determining the capacity design envelope for flexure is as follows:

1. Determine the provided nominal flexural strength at the wall base, M_b.

2. Determine the design moment at mid-height (either by modal response spectrum analysis or equivalent lateral force analysis), $M_{H/2}$.

3. Determine the adjusted mid-height design moment by:

$$\tilde{M}_{H/2} = \frac{M_{H/2}}{0.85}(1 + \frac{n_t - 1}{4}) \leq 2M_{H/2} \tag{7.1}$$

where n_t is the building height, in stories.

4. The unshifted capacity design envelope is bi-linear with lines connecting M_b, the base moment, with $\tilde{M}_{H/2}$ and mid-height and zero at the top of the wall. The adjusted mid-height design moment accounts for higher mode effects in taller walls.

5. The final flexural capacity design envelope is tri-linear and determined by extending the base moment demand, M_b to a height l_w and shifting the remainder of the envlope up a distance such that the adjusted mid-height moment demand $\tilde{M}_{H/2}$ occurs at a height of H/2+ l_w, where l_w is the horizontal wall length.

7.2.2 CSA A23.3-04(R10)

The Canadian Standard CSA A23.3 requires regular ductile walls to be detailed assuming energy dissipation during a seismic event is limited to inelastic flexural response at the wall base. For flexural design, a force reduction factor R_d of either 3.5 or 4.0 is used. However, for sections within the plastic hinge region, provided flexural reinforcement ratios must meet or exceed a minimum ratio. Boivin and Paultre (2012) show that this minimum ratio potentially increases flexural capacity well above design values calculated using MRSA and a R_d value of 3.5 or 4.0. Within the hinge region, the design flexural section must provide inelastic rotation capacity, θ_{ic}, that exceeds the inelastic rotation demand, θ_{id}. Per CSA Equation 21-11, θ_{ic} is calculated

$$\theta_{ic} = (\frac{\epsilon_{cu} l_w}{2c} - 0.002) \leq 0.025 \tag{7.2}$$

where ϵ_{cu} is the usable concrete compressive strain, l_w is the horizontal wall length and c is the neutral axis depth when the extreme compressive strain, ϵ_{cu}, is reached. For de-

sign, the ϵ_{cu} value used to calculate the provided ductility capacity is to be taken as 0.0035 unless closely spaced transverse ties are used to effectively confine the boundary element core. The volume and spacing of transverse reinforcement required can be adjusted to provide the strain capacity required to achieve the design deformation.

Recasting the provided section rotational capacity in terms of a provided curvature ductility is useful for comparing the CSA design equations with other design methodologies such as NZS 3103. This can be accomplished by comparing the CSA equations θ_{ic} and θ_{id}, which suggest a plastic hinge length of l_w links wall displacements to wall rotations. Using this plastic hinge length value permits calculation of the inelastic curvature capacity of the wall section, ϕ_{ic} as:

$$\phi_{ic} = (\frac{\epsilon_{cu} l_w}{2c l_w} - \frac{0.002}{lw}) \leq \frac{0.025}{l_w} \tag{7.3}$$

which can be interpreted as an equation of the form:

$$\phi_i = \phi_{tot} - \phi_y \text{ or } \phi_{tot} = \phi_y + \phi_i \tag{7.4}$$

which suggests the yield curvature can be approximated as

$$\phi_{yield} = \frac{0.002}{l_w} \tag{7.5}$$

Thus, the upper limit for usable curvature ductility allowed by the CSA code for wall sections can be calculated to be:

$$\mu_\phi = \frac{\phi_i}{\phi_y} = \frac{0.025/l_w}{0.002/l_w} = 12.5 \tag{7.6}$$

This value is less than that the maximum usable curvature ductility of 16 suggested by

the NZS 3103 design standard.

Plastic hinge ductile detailing is required to extend to a height, h_p, vertically above the wall base where h_p is taken as $0.5l_w + 0.1h_w$, where l_w is the horizontal wall length and h_w is the total wall height. To complete the design envelope for flexure, all sections above the plastic hinge region are required to be capacity designed by increasing the design demands by the factor M_r/M_f, where M_r is the factored moment resistance in the plastic hinge region and M_f is the design demand at the top of the plastic hinge region, h_p.

7.2.3 ASCE 7-10/ACI 318-11

ASCE 7-10 and ACI 318-11 provide requirements for seismic design of walls in the United States, however definition of a capacity designed flexural envelope to be used to ensure yielding is limited to the wall base is not addressed. Force reduction factors R = 5 or 6 are used for ductile (special) reinforced concrete shear walls per ASCE 7-10. An R value of 5 is used for 'bearing wall' building systems which are defined as building systems with gravity frame connections not detailed as ductile moment connections. An R value of 6 is used for 'building frame' systems which provide a full space frame gravity system in addition to primary walls. In building frame systems, although full moment resisting connections are provided, walls are to be proportioned for 100% of the lateral seismic force resistance (NEHRP, 2010). Within the plastic hinge region at the base of the wall, a displacement-based procedure is used to determine detailing requirements to ensure ductile response. Boundary element detailing requirements are dictated by the design displacements, which are determined by elastic analysis using MRSA or equivalent lateral force (ELF) analysis. Elastic displacements, determined using seismic forces reduced by R, are increased by the modification factor, C_d, which accounts for the amplification in elastic displacements due to inelastic response. For both 'bearing wall' and 'building frame' systems, a C_d value of 5.0 is prescribed by ASCE 7-10.

Detailing requirements are provided in Chapter 21 of ACI 318-11. Walls calculated to experience larger curvature demands in the plastic hinge region are required to meet more stringent 'special' boundary element detailing requirements. Special boundary elements

are required for walls calculated to have neutral axis depths, c, under design level seismic loads greater than:

$$c \geq \frac{l_w}{600\frac{\delta_u}{h_w}} \tag{7.7}$$

Where δ_u/h_w is the design roof drift (elastic roof drift amplified by C_d). The neutral axis depth limit in Equation 7.7 ensures special detailing is provided for designs in which concrete compressive strains exceed -0.003 under design displacement demands. In contrast to other code (e.g.- NZS 3101 and CSA A23.3), ACI 318-11 does not impose ductility limits or require calculation of the provided curvature ductility for the critical section. Special boundary element detailing is required to extend vertically to a height h_p above the wall base, where h_p is calculated as the minimum of:

1. The horizontal wall length, l_w.

2. 25$\%$ of the effective shear span. The effective shear span is taken as M_u/V_u, where M_u and V_u are design actions calculated using the load combination which maximizes the effective shear span.

Neither ACI 318-11 nor ASCE 7-10 specify a capacity design envelope for flexural sections above the plastic hinge region, thus flexural deamnds used for design are determined directly from MRSA or ELF analyses. Numerical results from inelastic finite element analyses indicate that walls designed using MRSA envelopes may be subjected to significant inelastic deformation over the entire wall height (Blakeley et al., 1975;Pangiotou and Restrepo, 2009). These results are inconsistent with the detailing requirements prescribed by ACI, and current provisions do not alert the designer to the possibility of inelastic flexural response occurring well above the base hinge region.

7.2.4 SEAOC Seismic Design Recommendations

The Structural Engineers Association of California (SEAOC) has published additional design recommendations for slender walls in Article 9.01.010 (2008) and the Structural/Seismic Design Manual (2006). The SEAOC capacity design recommendations for walls attempt to limit the inelastic flexural damage to the single plastic hinge location assumed using the ASCE/ACI design procedure. The SEAOC recommendations have not been adopted by ACI or ASCE and it is unclear how widespread the use of thse recommendations is in the United States. Recommendations for design of slender walls responding in flexure comprise:

1. Use of the capacity design envelope for flexure proposed by Paulay and Priestley (1992) is suggested. This envelope consists of a linear moment diagram between the nominal flexural strength provided at the wall base and a point of inflection at the top of the wall. The entire envlope is then shifted up by the horizontal wall length, l_w, to account for tension shift due to inclined flexural cracking.

2. Owing to the historic nature of the current force modification factors in ASCE 7-10, rational study of the R-values currently in use for ductile walls and the detailing provisions are recommended.

7.2.5 NEHRP Seismic Design Technical Brief No. 6

A technical brief regarding best practices for seismic design of walls was published by the National Earthquake Hazards Reduction Program (NEHRP) in 2011. The published brief recommends the use of the flexural design envelope proposed by Paulay and Priestley (1992).

7.2.6 Priestley, Calvi and Kowalski

To support development of their direct displacement-based design methodology, Priestley et al. (2007) performed ITHA for walls of various heights designed using two possible flexural design envelopes:

1. A linearly decreasing envelope between the nominal strength provided at the wall base and an assumed inflection point at the top of the wall.

2. Flexural demands determined directly from MRSA and reduced by a force modification factor (μ for displacement-based design or R for force-based design).

ITHA results confirmed these envelopes are insufficient to adequately limit inelastic flexural response to the base hinge region. To address this, two envelopes were proposed that provide better estimates of the required flexural capacity along the wall height to ensure inelastic demands remain concentrated within the well detailed hinge region at the base of the wall. The first envelope is determined using the modified MRSA proposed by Eibl and Keintzel (1988) and the second is a simpler, more conservative envelope that does not require MRSA.

7.2.7 Eibl MRSA Method

The modified MRSA envelope is based on work by Eibl and Keintzel that suggests inelastic response primarily limits first mode demands while higher mode demands remain, essentially, as predicted from elastic MRSA. Based on this behavior, the first mode moment profile is capped such that the base moment is equal to the expected flexural capacity at the wall base. Design moments are then determined by modal combination of the capped first mode moment profile and the elastic higher mode moment profiles. The modified modal response spectrum as presented by Priestely et al. (2007) is:

$$M_{MMS,i} = \sqrt{M_{1D,i}^2 + M_{2E,i}^2 + M_{3E,i}^2 + ...} \tag{7.8}$$

where $M_{1D,i}$ is the capped first mode moment contribution at story 'i' and $M_{jE,i}$ is the 'jth' model elastic moment contribution at story 'i'. Using this method, the capacity design envelope for flexure can be determined by:

1. A linearly decreasing envelope from the provided flexural capacity at the base to $M_{MMS,H/2}$ at mid-height.

2. Use of modified modal response spectrum analysis to determined $M_{MMS,i}$ at stories above mid-height.

7.2.8 Priestley, Calvi and Kowalski

A simplified bilinear relationship was proposed by Priestley et al. (2007) to conservatively estimate flexural demands for walls yielding in flexure. To define the bilinear relationship, an overstrength mid-height moment, $M^o_{H/2}$ is defined as:

$$M^o_{H/2} = C_{1,T}\Omega_o M_{base} \tag{7.9}$$

where $\Omega_o M_{base}$ is the provided flexural capacity (including material overstrength and strain hardening) at the wall base and $C_{1,T}$ is defined as:

$$C_{1,T} = 0.4 + 0.075T_i(\frac{\mu}{\Omega_o} - 1) \geq 0.4 \tag{7.10}$$

where T_i is the elastic first mode period calculated for the wall and μ is the wall ductility factor (or force reduction factor, R, for force-based design). The bilinear envelope is constructed as a linearly decreasing envelope between the provided flexural capacity at the base and $M^o_{H/2}$ from the wall base to mid-height, and a second linearly decreasing envelope between $M^o_{H/2}$ and zero from mid-height to the top of the wall.

7.3 Assessment of Flexural Performance Using Synthetic Ground Motions

Flexural performance of walled buildings was assessed by performing ITHA of the walled buildings designed and discussed in Chapter 6. This suite of walled buildings designed in Chapter 6 consists of 27 building designs. A summary of pertinent design parameters for

these wall designs are provided in Table 6.1. A summary of the design procedures used to develop the designs summarized in Table 6.1 are provided in Section 6.3.

7.3.1 Provided Section Curvature Ductility Capacity

One aspect of the wall design not addressed in Chapter 6 is an esimation of the expected curvature ductility of the designed wall cross-sections. To estimate the provided section ductility, moment-curvature analyses were performed to ensure the wall cross-sections were designed and detailed sufficiently to achieve an appropriate level of ductile response. To verify the calculated wall curvature ductility values for the designed wall sections are similar to values generally expected for ductile wall sections, moment-curvature analysis results for the designed walls were compared to simplified estimated curvature ductility values expected for well detailed walls developed by Priestley and Kowalski (1998) for ductile planar walls and Priestley et al. (2007) for flanged walls. The values recommended by Priestley et al. were determined based on the results of parameter studies performed on various wall sections using moment-curvature analysis.

7.3.1.1 Planar Wall Designs

By studying sectional response of planar wall sections considering a wide range of expected axial load levels, reinforcement ratios and reinforcement distributions, Priestley and Kowalski (1998) suggest relationships for estimating yield level and ultimate (survival-level) wall section curvature. Survival level curvature values were determined by increasing tension and compression strain limits (taken as 0.06 for tension and -0.018 for compression) assumed to signify the onset of significant flexural damage by 30-50$\%$. For planar walls with uniformly distributed longitudinal reinforcement, yield curvature for planar wall sections was found to be adequately estimated as:

$$\phi_y \approx \frac{2.25\epsilon_y}{l_w} \tag{7.11}$$

Where, ϵ_y is the reinforcing yield strain and l_w is the horizontal wall length.

An estimated lower bound on the expected ultimate curvature is given as:

$$\phi_u \approx \frac{90}{1000 l_w} \tag{7.12}$$

The ratio of these values provides an estimate of the expected curvature ductility which is calculated to be:

$$\mu_\phi \approx 16.5 \tag{7.13}$$

It should be noted that μ_ϕ is independent of wall geometry.

A comparison between the suggested values and the values calculated for the designed wall sections are provided in Figure 7.2(a) and Figure 7.2(b), respectively.

7.3.1.2 Flanged Wall Designs

Comparing curvature parameters developed in a similar manner by Priestley, Calvi and Kowalski (2007) to the curvature parameters determined by Priestley and Kowalski (1998) suggests a similar expression for estimating yield curvature for flanged walls:

$$\phi_y \approx \frac{2.00 \epsilon_y}{l_w} \tag{7.14}$$

7.3.1.3 Comments on Designed Wall Section Ductility

As shown in Figure 7.2(a), the yield curvatures calculated for the designed wall sections compare well to the suggested values from the literature. Ultimate ductility values exceed the suggested lower bound value for all designed buildings greater than 6 stories; the ultimate ductility capacity of the 6-story building designs were determined to be slightly lower

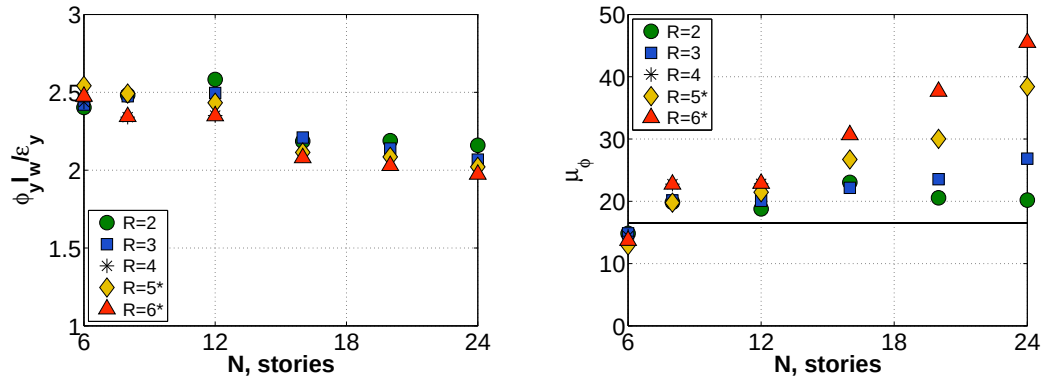

(a) Yield Curvature (b) Curvature Ductility

Figure 7.2: Design Section Moment Curvature Capacity Results

(14 vs 16.5) than the suggested lower bound value. Curvature ductility of the code-based flanged wall designs (R_{ASCE} = 5,6) were significantly larger than the capacity designed walls (R=2,3). This is due to the smaller design shear demands used to design the code-based sections. The smaller design shear led to a reduction in web area (wall length and web thickness). Variations in curvature ductility for flanged walls suggest that the design cross-section geometry for flanged walls may be of significance for increasing ductility capacity of flanged walls.

These comparisons indicate that the designed wall sections possess flexural ductility characteristics similar to those generally expected for well-detailed ductile walls.

7.3.2 Material Regularization

Inclusion of material regularization enables accurate simulation of flexural failure for wall sections limited by exhaustion of the compression capacity of the well-confined boundary element. Such sections have been demonstrated (Chapter 3) to exhibit a softening response prior to strength loss. As strength loss occurs, localized softening response leads to mesh-dependent predictions of structural response unless material regularization is included.

However, reguarization is not appropriate for hardening sections that do not exhibit crit-

ical section softening prior to failure but instead harden until significant strength loss is initiated by rupture of longitudinal reinforcement. For each wall design, to assess whether regularization was appropriate for the designed cross section, moment curvature analyses were performed and the failure mechanism (crushing or steel rupture) was identified. Section analyses were performed using expected material properties. The Saatcioglu and Razvi (1992) confinement model was used to estimate strength and strain enhancement within the well-confined boundary element region. For each analysis, curvature demand was imposed until a strength loss of 20$\%$ was achieved. Fiber strains were then post-processed to determine if strength loss was due to crushing of the compression zone or rupture of the flexural reinforcement.

To assess whether failure of the section was due to crushing or rupture, a crushing damage index was defined. The crushing damage ratio (CDR) was defined as :

$$CDR = \frac{\epsilon_c}{\epsilon_{20}} \tag{7.15}$$

Where ϵ_c is the strain in the extreme fiber of the confined boundary element and ϵ_{20} is the strain at 80$\%$ compressive strength loss as determined using the Saatcioglu and Razvi confinement model.

The CDR for the designed wall sections is plotted in Figure 7.3. Sections reaching CDR $>$ 1.0 are expected to fail due to exhaustion of the ductility capacity of the boundary element. Sections experiencing a 20$\%$ strength loss prior to reaching CDR = 1.0 are expected to fail due to rupture of tensile reinforcement. Presented results suggest that all designed specimens except the 24-story/R$_{ASCE}$ = 6 design are expected to fail due to crushing. For these sections, full material regularization was deemed appropriate and was included in the nonlinear model. For the 24-story/R$_{ASCE}$ = 6 design, tension (rupture) failure was expected and material regularization was not included in the model.

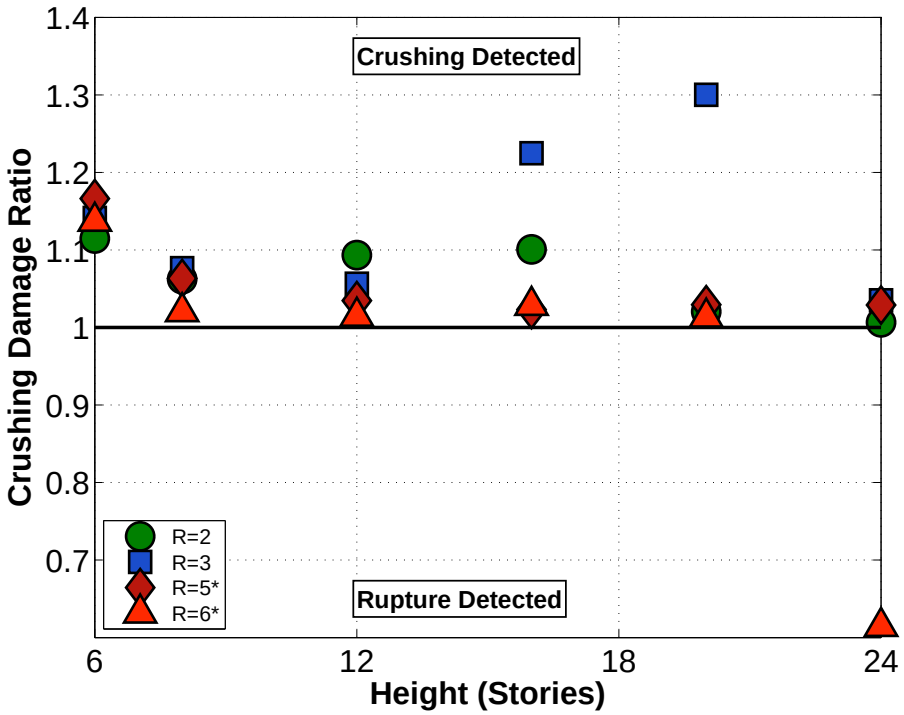

Figure 7.3: Crushing Damage at 20% Section Strength Loss

7.3.3 Flexural Design Envelope

For preliminary investigation of the 27 building designs the design section provided at the wall base was assumed to remain constant up the entire wall height. Alternate flexural design envelopes were considered and discussed further in Section 7.3.4.4. Wall cross-section dimensions and reinforcing ratios provided in Table 6.1 correspond to the design section required to resist design forces at the wall base.

7.3.4 Assessment of Flexural Response/Force Reduction Factor

Results presented in Chapter 3 show that the fiber beam column element models, with regularized material response, provide accurate prediction of the drift capacity of walls exhibiting flexural strength deterioration prior to failure. The ability to simulate loss of lateral load carrying capacity in flexure allows for rational assessment of the reliability of well-

detailed slender walls designed using 1) different levels of force reduction and 2) different envelopes for flexural design. For assessment of flexural response, flexure damage predicted by ITHA, using both design and MCE level sythetic ground motion record sets, were determined for all the designed buildings. For these ITHA, the designed wall base size and strength were maintained as constant along the entire wall height. To assess the impact of various flexural design envelopes, three of the wall buildings were subjected to additional ITHA considering reductions in wall size and bar curtailment along the wall height. ITHA results for the 'constant' wall designs are presented in Sections 7.3.4.2 and 7.3.4.3. The impact of alternative flexural design envelopes are provided in Section 7.3.4.4. Specific information on how flexual damage was defined is provided in Section 7.3.4.1.

7.3.4.1 Criteria to Quantify Flexural Damage

To quantify flexural damage in the nonlinear models, a crushing damage ratio,CDR, and a tensile (rupture) damage ratio, TDR, were used. These ratios are:

$$CDR = \frac{\epsilon_c}{\epsilon_{20c}} \tag{7.16}$$

$$TDR = \frac{\epsilon_s}{\epsilon'_u} \tag{7.17}$$

where ϵ_c is the extreme compression fiber strain in the wall boundary element, ϵ_{20c} is the regularized confined crushing strain, ϵ_s is the extreme tension reinforcing steel strain and ϵ'_u is the regularized rupture strain. The CDR is a nondimensional measure of the strain demand placed on the confined boundary element. CDR values approaching one indicate increased crushing damage within the boundary element, values greater than one indicate the boundary element has crushed and longitudinal reinforcement buckling has occurred (Figure 7.4(a)). TDR values approaching one indicate the reinforcing steel strain is approaching the ultimate strain value. Values of one or greater indicate the extreme layer

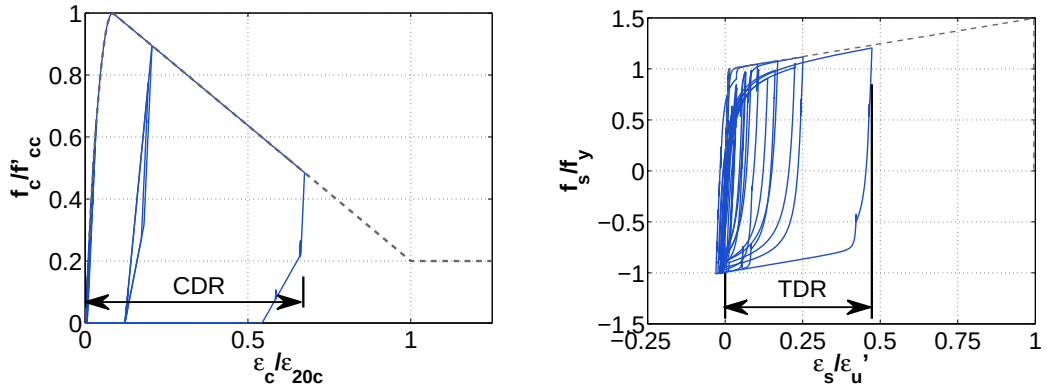

(a) Crushing Damage (CDR) (b) Tensile (Rupture) Damage (TDR)

Figure 7.4: Flexural Damage Ratio Definition

of reinforcing steel has ruptured (Figure 7.4(b)).

An additional damage parameter was introduced to assess spalling damage under design level earthquake demands. Spalling damage was defined as:

$$SDR = \frac{\epsilon_c}{\epsilon_{85c}} \tag{7.18}$$

Where ϵ_{85c} is the compressive strain associated with a 15% loss in peak compressive strength. Spalling damage ratios approaching one suggest higher liklihood of concrete spalling during a given seismic event.

During postprocessing of nonlinear models, extreme fiber damage ratios were calculated at every time step during the dynamic excitation at all fiber section locations within the wall model. Reported damage values provided here are the peak damage ratios for the structure, which is to say the maximum damage ratios determined from all fiber sections used to mesh the walled building model.

Use of CDR/TDR is demonstrated in Figure 7.5, where results from 3 ITHA of the 8-story/R_{ASCE} = 5 walled building are shown. Figure 7.5 provides the base section moment curvature response due to 3 of the 7 synthetic ground motions scaled to the match the MCE. In Figure 7.5(a), flexural demands due to GM6 were determined to be modest (CDR

= 0.44); the resulting hysteretic flexural response shows moderate curvature demands and no loss of strength. Flexural demands due to GM4 (Figure 7.5(b)) were determined to be significantly more severe (CDR = 0.94); with large curvature demands resulting in initation of strength loss at the wall base. Finally, flexural failure was identified for the building subjected to GM2 (Figure 7.5(c)); flexural damage was determined to be extremely severe (CDR = 5.74) with significant crushing and deterioration of the flexural response.

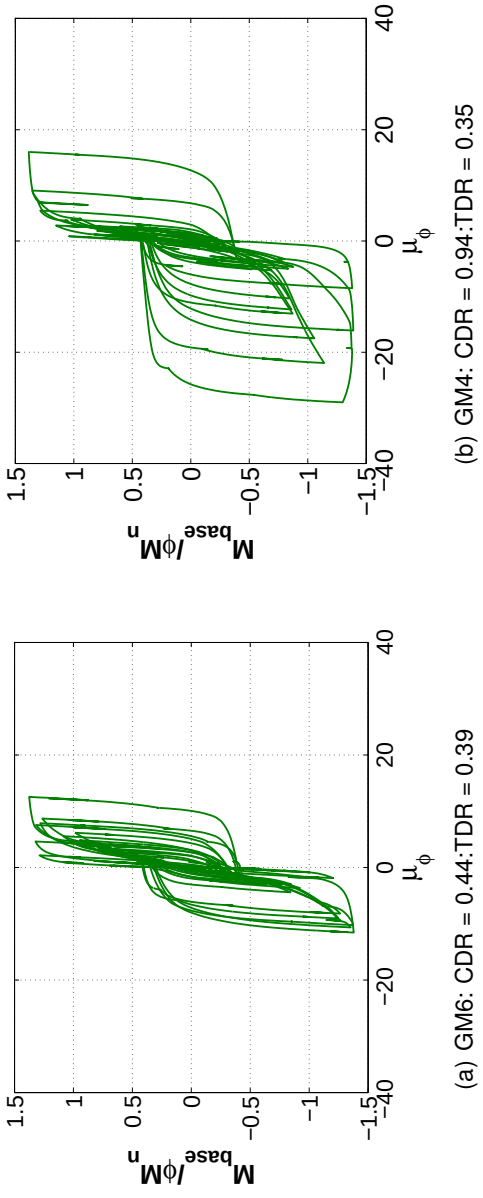

(a) GM6: CDR = 0.44:TDR = 0.39

(b) GM4: CDR = 0.94:TDR = 0.35

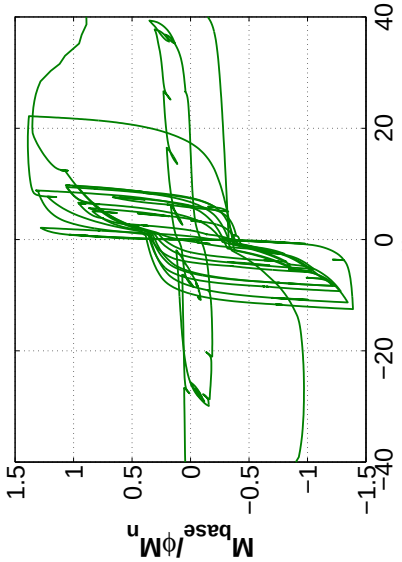

(c) GM2: CDR = 5.74:TDR = 1.54

Figure 7.5: MCE Level (2% in 50) Damage Comparison (8-story/R$_{ASCE}$ = 5)

7.3.4.2 Predicted Flexural Damage: Design Level Event

Flexural damage ratios considering the design level seismic event (10% probability in 50 years) were determined for each building and the median results from the seven synthetic ground motions are provided in Table 7.1. The results shown in Table 7.1 are for the baseline wall designs for which the base section design (geometry and reinforcing ratio) is maintained up the entire wall height. For all baseline designs, peak damage ratios were largest at the wall base. These results indicate:

1. Predicted flexural damage for planar wall buildings increases as the force reduction factor increases, with mean CDR values of 0.27, 0.31 and 0.37 determined for buildings subjected to design level ground motions using R = 2, 3 and 4, respectively.

2. Code-based planar walls designed using R_{ASCE} incur mean CDR values of 0.35 and 0.43 for designs using R_{ASCE} = 5 and 6, respectively. These data suggest that the actual force reduction realized for walls designed using R_{ASCE} = 5 is similar to a wall designed using a theoretical force reduction factor, R $\approx$ 3.5. This is consistent with the theoretical R values determined for these designs presented in Table 6.1. Similarly, for walls designed using R_{ASCE} = 6, the realized force reduction is similar to that which could be expected using a theoretical R = 4.5, which is higher than suggested using calculated R values presented in Table 6.1.

3. Predicted flexural damage for core wall buildings subjected to design level ground motions is significantly lower than predicted for planar wall buildings. Mean flexural damage ratios of 0.17 and 0.32 were determined for core wall buildings subjected to design level ground motions using R = 2 and 3. Mean design level damage ratios of 0.37 and 0.42 were determined for code-based core walled buildings designed using R_{ASCE} = 5 and 6, respectively.

4. Mean spalling damage for planar wall buildings increased with an increase in force reduction factor. Mean SDR values of 0.49, 0.64, and 0.97 were determined using

R = 2, 3 and 4, respectively. Spalling damage for core wall building was lower with mean SDR values of 0.30 and 0.37 for R = 2 and 3.

5. Spalling damage, SDR $>$ 1.0, were predicted for 12-story buildings designed using force reduction factors, R $>$ 4.

Table 7.1: ITHA Flexural Damage

Shape	Design N (Stories)	R	10% Probability in 50 years(Design Level) Spalling SDR	Crushing CDR	Tension TDR	2% Probability in 50 years (MCE) Spalling SDR	Crushing CDR	Tension TDR
R	6	2	0.43	0.23	0.17	0.81	0.33	0.31
R	6	3	0.70	0.31	0.26	1.57	0.48	0.42
R	6	4	0.69	0.33	0.29	2.33	0.72	0.48
R	6	5[1]	0.91	0.36	0.26	1.67	0.52	0.36
R	6	6[1]	0.72	0.32	0.25	3.77	1.18	0.58
R	8	2	0.57	0.31	0.24	0.79	0.37	0.33
R	8	3	0.61	0.33	0.26	1.49	0.46	0.40
R	8	4	0.86	0.35	0.34	24.8	7.69	1.51
R	8	5[1]	0.84	0.37	0.31	3.02	0.94	0.54
R	8	6[1]	0.95	0.35	0.37	3.01	0.93	0.62
R	12	2	0.48	0.27	0.16	0.98	0.43	0.34
R	12	3	0.60	0.32	0.25	2.52	0.79	0.45
R	12	4	1.35	0.42	0.40	22.2	6.88	1.51
R	12	5[1]	0.59	0.31	0.27	33.4	10.4	1.94
R	12	6[1]	2.00	0.62	0.52	20.2	6.27	0.66
R	16	2	0.32	0.18	0.15	0.40	0.22	0.28
R	16	3	0.44	0.23	0.32	1.09	0.34	0.46
R	16	5[1]	0.38	0.20	0.33	0.58	0.27	0.58
R	16	6[1]	0.38	0.20	0.33	0.74	0.27	0.69
R	20	2	0.27	0.16	0.11	0.47	0.25	0.38
R	20	3	0.29	0.21	0.27	1.26	0.39	0.66
R	20	5[1]	0.41	0.22	0.44	0.62	0.27	0.66
R	20	6[1]	0.37	0.19	0.43	0.70	0.28	0.85
R	24	2	0.30	0.18	0.15	0.40	0.22	0.29
R	24	3	0.39	0.20	0.38	0.62	0.27	0.62
R	24	5[1]	0.32	0.17	0.35	0.56	0.25	0.72
R	24	6[1]	0.35	0.18	0.51	0.58	0.24	0.86

[1] R_{ASCE} = 5 or 6

7.3.4.3 Predicted Flexural Damage: Maximum Considered Event

Flexural damage ratios considering the maximum considered event (2% probability in 50 years) were determined for each building design. The median results from the seven synthetic ground motions are provided in Table 7.1. The results shown in Table 7.1 are for the baseline wall designs, with the base section geometry and reinforcing ratio maintained up the entire wall height. For all baseline designs, peak damage ratios were largest at the wall base. The results indicate:

1. For planar walls, a force reduction factor between 3 and 4 would be required if a performance objective of CDR = 1.0 was deemed acceptable for the MCE. Data suggests the required force reduction factor to meet this objective is building height dependent, with R $\approx$ 4.2 required for 6-story buildings and R $\approx$ 3.0 required for the 8- and 12-story buildings.

2. For capacity designed core walls, a force reduction factor greater than 4 could be acceptable if a performance objective of CDR = 1.0 was deemed acceptable for the MCE.

3. For core walled buildings, predicted tensile damage typically exceed compression damage, TDS $>$ CDR, when subjected to MCE ground motions. This is contrary to moment-curvature results which suggested the designed wall sections were compression-controlled.

These results suggest that planar walls designed with force reduction factors, R $>$ 3, could be expected to sustain significant flexural damage when subjected to MCE ground motions. Particularly at risk are mid-rise (8 to 12-story) planar walls, which were determined to have crushing damage greater than or near to 1.0 for all designs utilizing a force reduction factor R $>$ 3.

Force Reduction Factor Comparison In Figure 7.6, the flexural damage ratio for each building is plotted versus an effective force reduction factor defined as R/Ω_o. The flexural

damage ratio is plotted in Figure 7.6 alongside the force reduction factor used in design. When flexural damage is plotted against the effective force reduction, it can be verified that R_{ASCE} = 5 imposes an actual force reduction in between the force reductions realized by R = 3 and R = 4 designs. Similary for the flanged walls, the code-based R_{ASCE} = 5 provides nearly the same level of force reduction as the MRSA based R = 3 design.

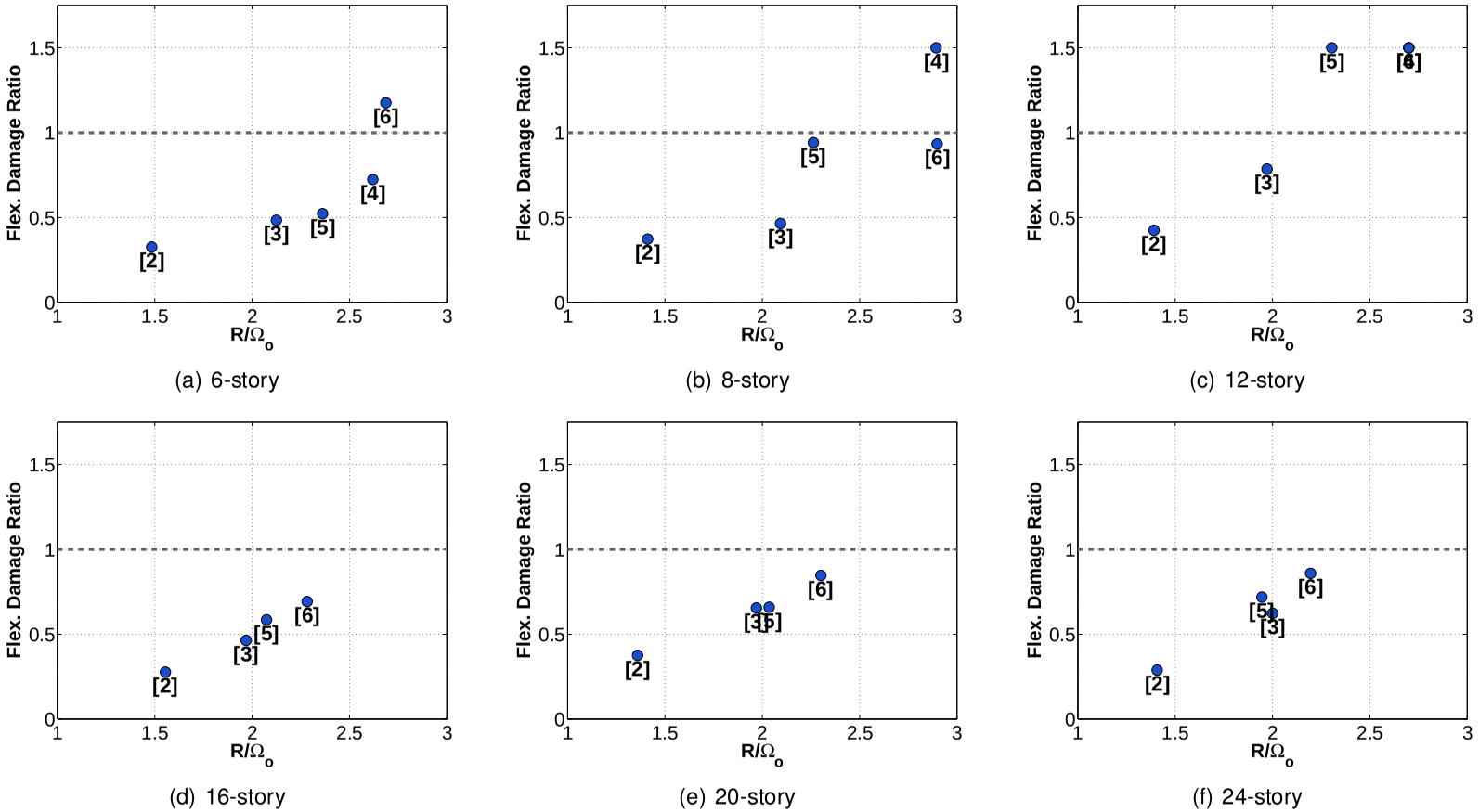

(a) 6-story (b) 8-story (c) 12-story

(d) 16-story (e) 20-story (f) 24-story

Figure 7.6: MCE Level (2% in 50) Flexural Failure versus Effective Force Reduction (Labeled with theoretical R-factor)

7.3.4.4 Impact of Bar Curtailment

Because reduced flexural and shear demands are expected at story levels above the base, economical wall designs typically reduce the wall area and strength provided at story heights where design demands are significantly lower than those required at the wall base. Several flexural design envelopes have been proposed in the literature for reducing wall flexural capacity for walls designed to yield during earthquake loading (Section 5.2). Using ITHA, several flexural envelopes from the literature were investigated to assess the impact that the selected flexural design envelope has on inelastic wall response. These envelopes considered in the current study are:

1. Constant. The flexural reinforcement and wall size required at the wall base are held constant along the entire wall height.

2. MRSA Envelope. The flexural reinforcement and wall size are varied to yield design resistance, ϕM$_n$, greater than or equal to the demands predicted by reducing elastic MRSA results by a force reduction factor, R.

3. Paulay/Priestley Envelope. The flexural reinforcement and wall size are varied to yield design resistance , ϕM$_n$, greater than or equal to the demands corresponding to the design moment envelope recommended by Paulay and Priestley (1992) and SEAOC (2006).

4. Dual Hinge Detailing. The flexural resistance is significantly weakened just above mid-height to ensure inelastic flexural demands concentrate at the wall base and the 'second hinge' location. Flexural capacity provided at the second hinge location are determined using recommendations of Panagiotou and Restrepo (2009).

To evaluate the impact of these design envelopes, three walled buildings were re-designed at sections above the wall base using each of the three altrenate design evelopes. For this study, 6, 12 and 20-story buildings designed using a force reduction factor R = 3 were considered. Each design was modified such that the provided design flexural

strength along the wall height exceeded the demand designated by the particular design envelope while maintaining the same design section at the wall base. For the dual hinge design, the base section geometry and reinforcing ratio was assumed to remain constant outside of the second hinge region. Plots of the design envelopes and provided flexural strength for all nine design configurations are provided in Figure 7.7.

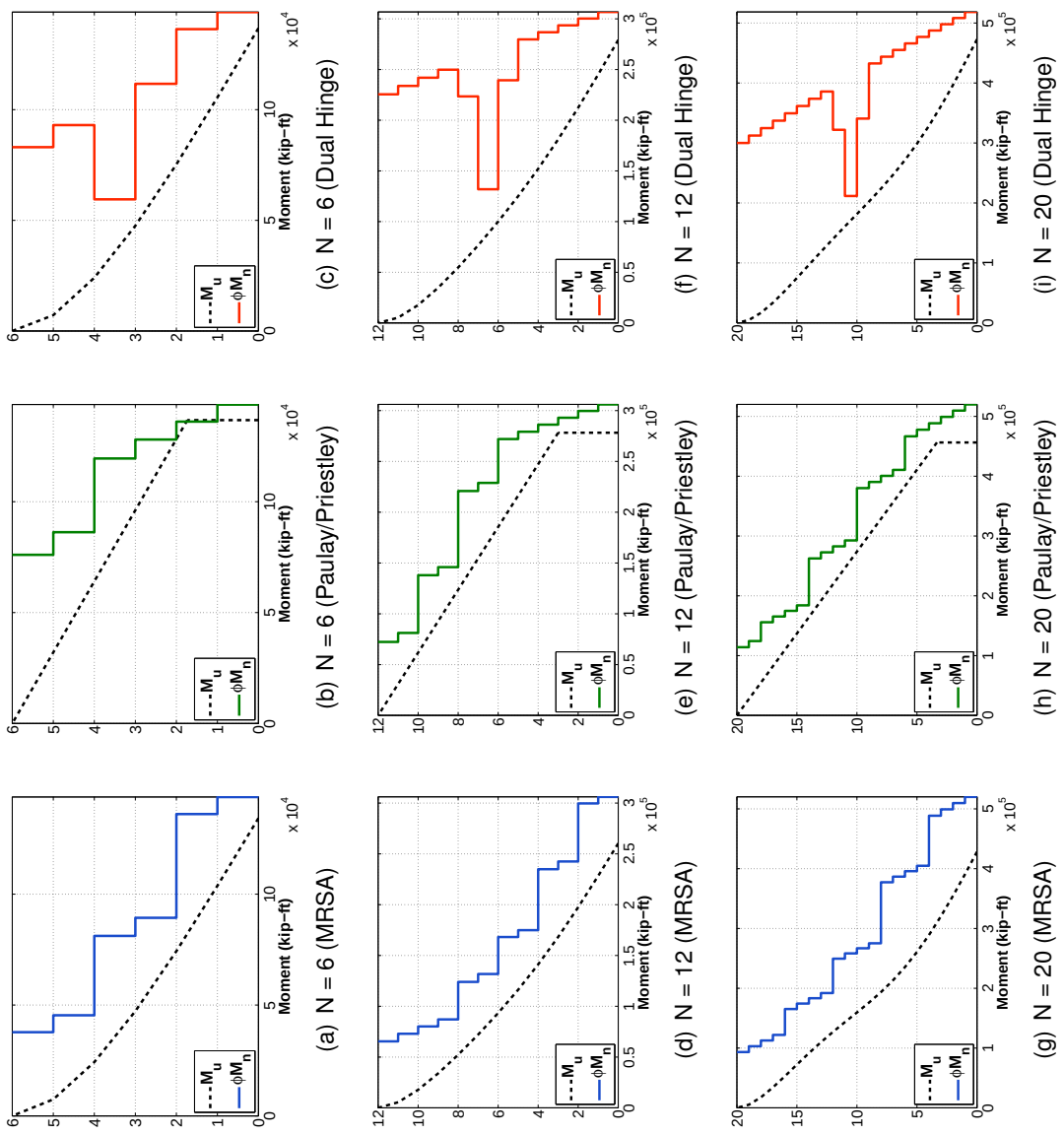

Figure 7.7: Demand Envelopes for Alternate Curtailment Methods

Flexural Damage The impact of the selected design envelope on flexural damage was determined using ITHA by subjecting each building to a set of 7 synthetic ground motion records scaled to match both design level and MCE earthquake demands. Flexural damage for the buildings quantified in terms of previously defined compression and tension damage ratios, CDR and TDR, for both design and MCE loading, is presented in Figure 7.8. At the design level, peak flexural damage (crushing/rupture) ratios were found to be insignificantly affected by the chosen detailing configuration. At the design level, flexural damage ratios for the buildings was essentially unaffected by the detailing, and flexural damage ratios of approximately 0.30 were predicted for all buildings. When subjected to MCE ground motions, flexural damage ratios were found to be more sensitive to the selected detailing configuration. Flexural damage was determined to be maximum for the constant reinforcing configuration (mean of 0.55 for the 3 building heights considered), however trends between the alternative detailing configurations were not found to be consistent across the entire range of building heights considered. For the 6 and 20-story walls, the impact of alternate detailing configurations were modest with the MRSA envelope design calculated to sustain the lowest flexural damage ratio (0.48 for the 6-story building; 0.39 for the 20-story building). For the 12-story wall, all alternate detailing configurations reduced flexural damage; flexural detailing per MRSA reduced the predicted damage ratio from 0.79 for the constant detailing to 0.65. Paulay/Priestley and Dual Hinge detailing both reduced flexural damage predicted for the 12-story wall to approximately 0.50.

Further insight into the impact of the selected design flexural envelope can be gained by considering the flexural damage profile plots for each design configuration presented in Figure 7.9. The profile plots present the median story ductility demand determined for each building design. Dark, medium and light regions are plotted corresponding to predicted story ductility. Dark regions correspond to story ductility greater than 1.5. Medium regions are used for stories in which ductility demand is between one and 1.5. Lighter regions are used for stories with predict ductility demands less than one (i.e. - elastic wall regions). These plots indicate significant differences in the predicted spread of inelastic flexure response are predicted by the different flexural design methods. Profiles plotted in Figure 7.9 indicate:

1. Buildings detailed using elastic MRSA demands reduced by a force reduction factor R were predicted to experience inelastic flexural response over a significant portion of the building height. While curvature demands are predicted to be largest at the base, curvature ductility demands between three and four are predicted at multiple story levels above the base.

2. The Paulay/Priestley design envelope generally limits inelastic flexural response to the wall base. Some inelastic flexural response was identified in the upper stories of the 20 story building, however predicted ductility demands at these stories remained modest (below 1.50).

3. The Dual Hinge method limits inelastic flexural response to the wall base and the second hinge location. Flexural demands at the base exceed those at the weakened midspan hinge location for 6 and 12-story buildings. For the 20-story building, the second hinge demands exceed those at the base.

These results suggest that direct use of the MRSA moment envelope can lead to significant inelastic flexural response over a large portion of the wall height. This could be undesirable from a design perspective because ductile detailing for these inelastic demands may require a significant portion of the wall to be confined with closely spaced transverse hoops. It should be noted that use of the MRSA method for estimating flexural demands is the approach typically taken and current ACI 318 (2011) requirements do not require special confinement to extend a distance above the wall base equal to the minimum of 1) the wall length or 2) 25% of the effective shear span. The current ACI 318 code does not alert the designer to the fact that inelastic flexural response may occur over a significant portion of the wall height.

The results suggest that Paulay/Priestley and Dual Hinge detailing can sufficiently limit inelastic response to the base (Paulay/Priestley) or base and second hinge (Dual Hinge) for the range of building heights considered in this study. However, for the Dual Hinge designs, reinforcement was assumed to remain constant between the hinge locations. This may be

uneconomical and the inelastic response along the wall considering different variation in flexural strengths between the hinges warrants further study.

Shear Demands The data in Figure 7.8 suggests that some reduction in MCE level seismic shear demand can be realized by considering more realistic bar curtailment configurations. The reduction in base shear demand is due to the fact that reduced flexural capacity over the wall height generally increases inelastic flexural response. This increased flexural response causes yielding in multiple modal load patterns thus limiting the peak base shear demand. The reduction in seismic wall shear for buildings subjected to design level ground motions was found to be less significant because inelastic flexural demands were not large enough to significantly limit the modal load patterns.

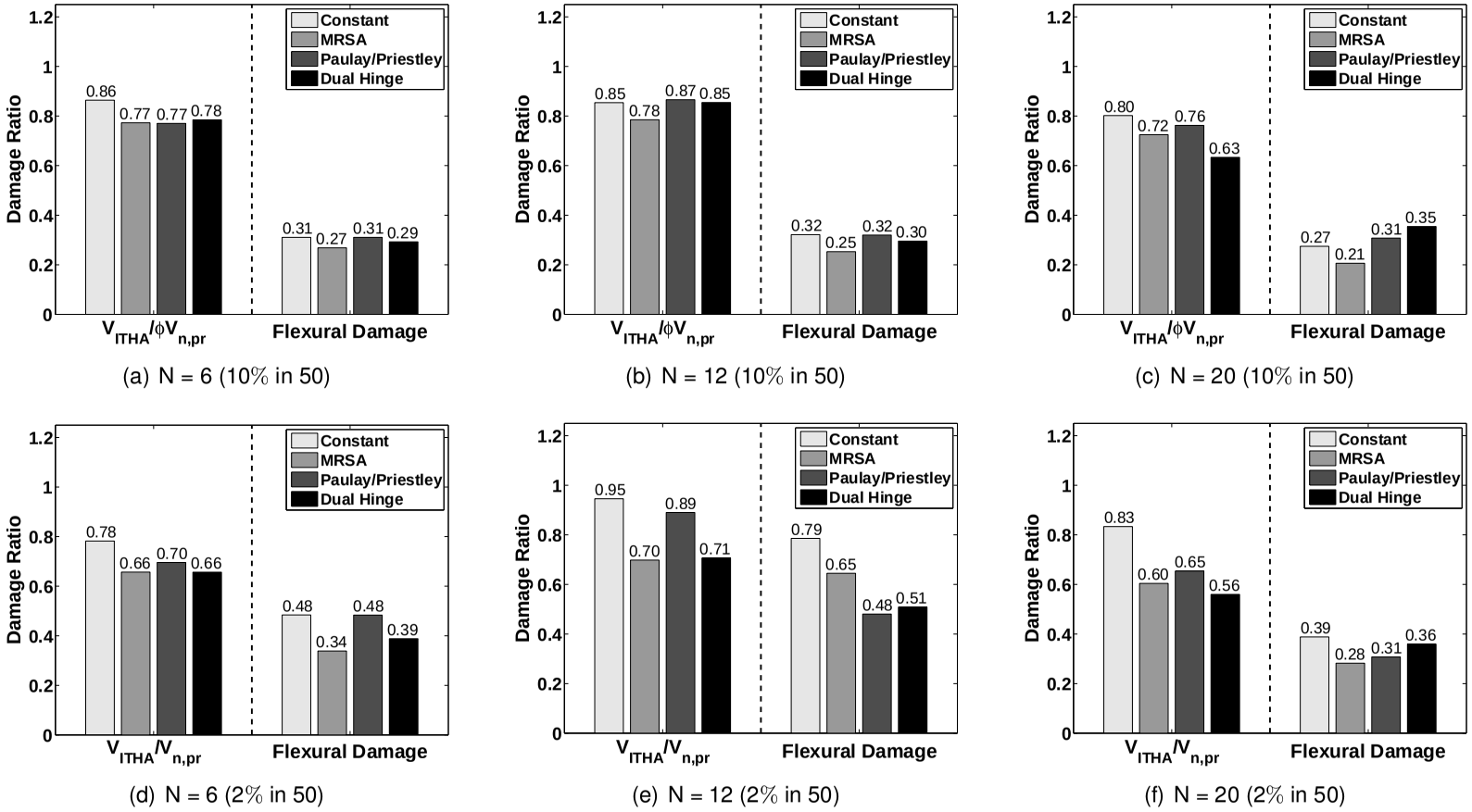

Figure 7.8: Predicted Damage Ratios for Alternate Detailing Methods

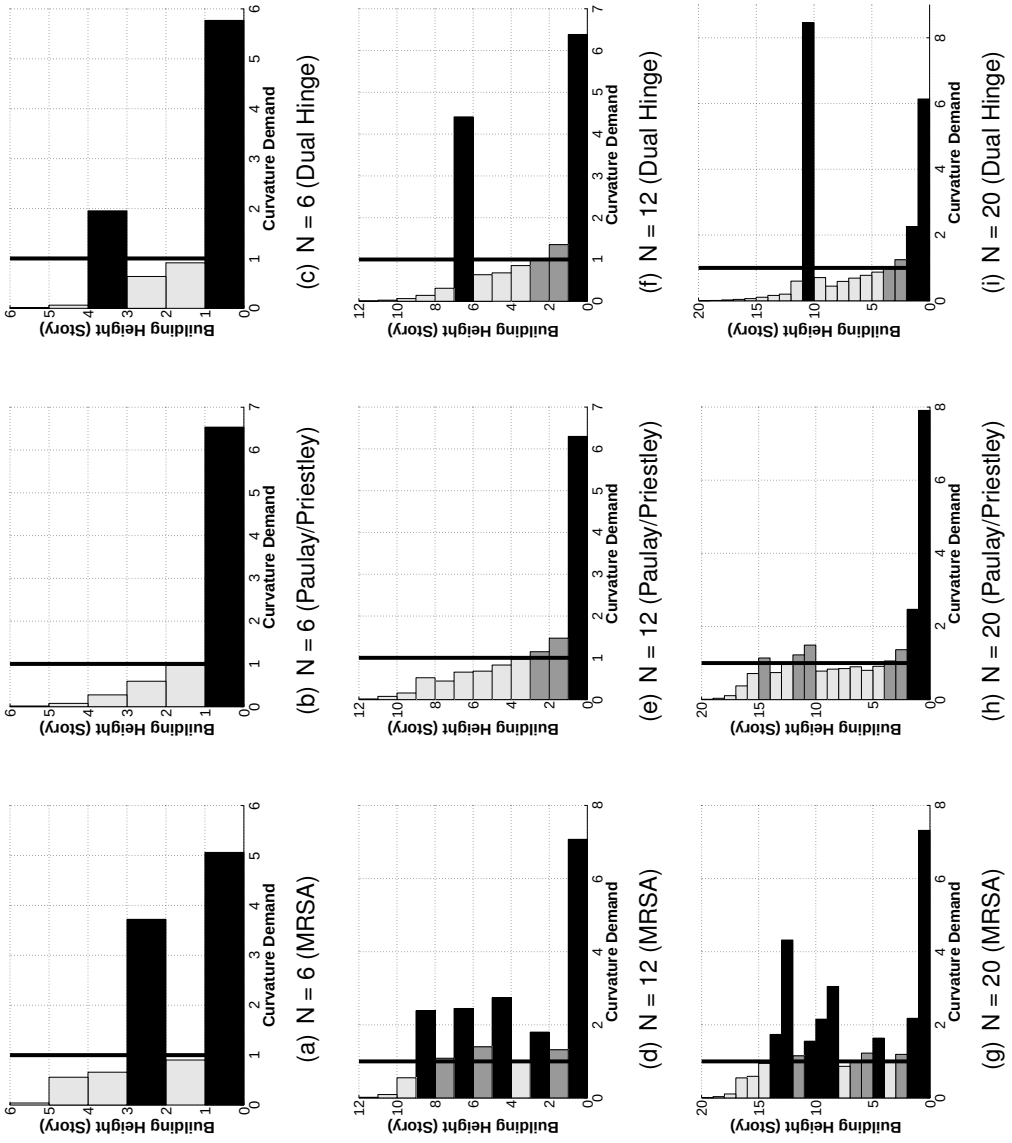

Figure 7.9: Curvature Demand Profiles for Alternate Detailing Methods

7.3.4.5 Conclusions Regarding Flexural Damage

Data for ITHA of walled buildings designed using different flexural demand envelopes suggest the following:

1. Flexural damage predicted at the MCE level strongly depends on the selected force reduction factor R. For mid-rise planar walls, an R-value no larger than three is required to achieve median flexural damage ratios less than 1.0 for the MCE. For taller core walls, an increased R-value may be justifiable.

2. Comparison of effective force reduction factors, R/Ω_o, suggests that an ASCE 7 Code-based force reduction factors, R_{ASCE}, values of 5 or 6 are comparable to theoretical force reduction factors, R, between 3 and 4.

3. The spread of inelastic flexural response over the wall height is highly dependent on the moment envelope assumed for design. MRSA-based envelopes are insufficient to prevent inelastic flexural response from spreading across a large region of the wall height. Both the Paulay/Priestley and Dual Hinge detailing methods limited inelastic response to expected hinge locations.

The results presented in this section provide an initial estimate of force reduction factors required for well-detailed walled buildings considering MCE-level performance objectives. However, these results were based on ITHA performed using a small set of artificially generated synthetic ground acceleration records. To overcome this limitation, a subset of the buildings developed in this section were re-evaluated using the FEMA P695 'Quantification of Building Seismic Performance Factors' (ATC, 2008) methodology. This framework accounts for potentially important variations in structural performance, modeling limitations and ground motion variability not accounted for in the results presented thus far and does so in a standard methodology that is currently being used to validate other seismic lateral force resisting systems. Performance analysis of walled buildings using the P695 methodology is discussed in Section 7.4.

7.3.5 Assessing Model Sensitivity

Results presented in this section were developed using regularized beam-column elements to predict shear and flexural damage for slender walls subjected to both design and MCE ground motion record sets. In Chapter 3, this simple modeling approach was shown to provide accurate and precise simulation of strength, secant stiffness to yield and drift capacity of statically loaded laboratory-tested wall specimens. As similar experimental data is not available for dynamically loaded large scale full-size buildings, the modeling approach can not be directly validated for such systems. However, to address some modeling uncertainty two significant modeling parameters were further studied to assess the sensitivity of the reported results to variations in these parameters. The parameters are:

1. Modeled shear response

2. Calibrated crushing energy

7.3.5.1 Shear Deformations

In Chapter 3, results indicated that models employing a shear stiffness equal to the elastic, gross-section stiffness ($G_c A_{cv} \approx 0.4 E_c A_{cv}$) predicted significantly stiffer wall response than observed during laboratory testing. Using data from multiple tests, a reduced effective stiffness ($0.042 E_c A_{cv}$) was validated to enable accurate simulation of yield displacement. This stiffness was determined using data from reduced scale specimens and the assumption of such a low reduced shear stiffness may not be appropriate for use over the entire height of full-scale walled building components throughout the entire time history analysis. In lieu of a more advanced model, the gross elastic shear stiffness was used to generate ITHA results for full-scale walled building designs.

To assess model sensitivity to the selected shear model, inelastic time history results generated using the elastic shear model were were compared with results generated using an advanced, nonlinear hysteretic shear force-displacement model developed by Lowes and Birely (2012). The shear force backbone model (Figure 7.10) consists of a trilinear curve. The definition of the trilinear curve is:

1. An initial elastic shear stiffness of $0.4E_cA_v$ prior to shear cracking.

2. A cracked shear stiffness of $0.16E_cA_v$ beginning at a shear force demand of $1.5\sqrt{f'_c}A_v$.

3. A shear stiffness of $0.04E_cA_v$ corresponding to shear reinforcement yield beginning at a shear force demand of $0.6V_{n,pr}$.

The backbone definition and pinched hysteretic response were determined using experimental data processed and analyzed by Birely (2012).

Damage ratios determined from inelastic time history analyses using both shear models are compared in Figure 7.11. Analyses were conducted for 6, 8, 12 and 20-story capacity designed buildings using R = 3 (Table 6.1) considering both the design and MCE level ground motion records.

Impact on Base Shear Demands Base shear demand to capacity ratios for the walled buildings at both the design and MCE levels are shown in Figure 7.11. For all building heights considered, replacement of the linear shear model with the advanced tri-linear shear model had minimal impact on the design level shear demand. For the 8-story building, inclusion of the nonlinear shear model slightly increased design level base shear demand to capacity ratio (from 0.80 to 0.83). For the 20-story building, design level shear demand to capacity ratio decreased from 0.80 to 0.69 when the nonlinear shear model was included. Larger impact was observed at the MCE level, particularly for the 12-story walled building where use of the nonlinear shear model decreased MCE demand to capacity ratio from 0.95 to 0.73.

Impact on Flexural Demands Flexural damage ratios at the design level were essentially unaffected by the inclusion of the nonlinear shear response model. At the MCE level, flexural demand ratios were significantly reduced for the 12-story building model (from 79% to 50%) but reductions were less significant for other building heights (from 39% to 31% for the 20-story building) and an increase in damage was predicted for the 8-story building (from 46% to 51%).

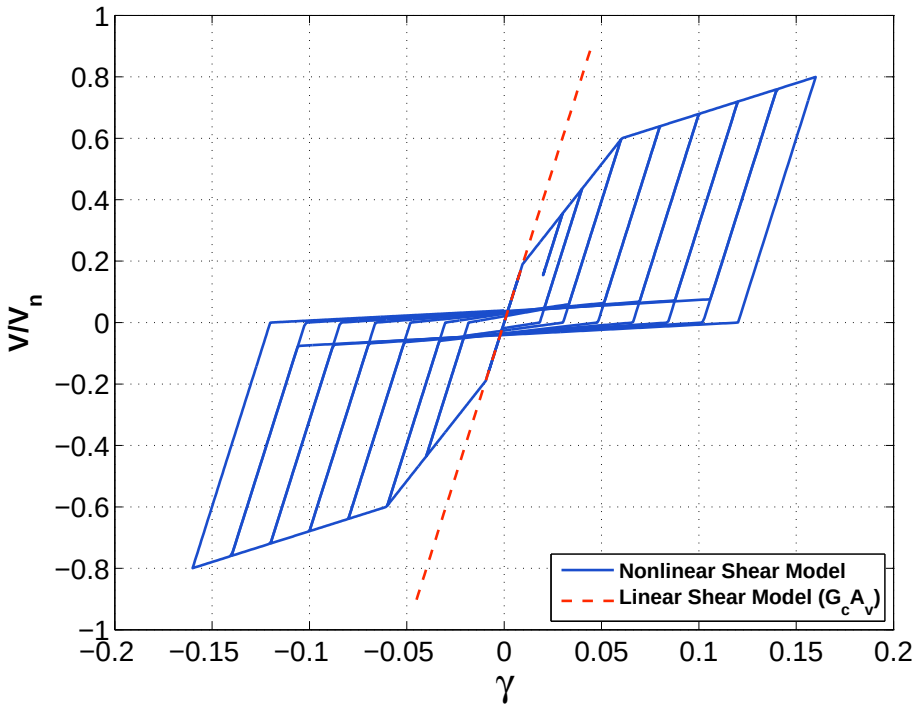

Figure 7.10: Shear Model Comparison

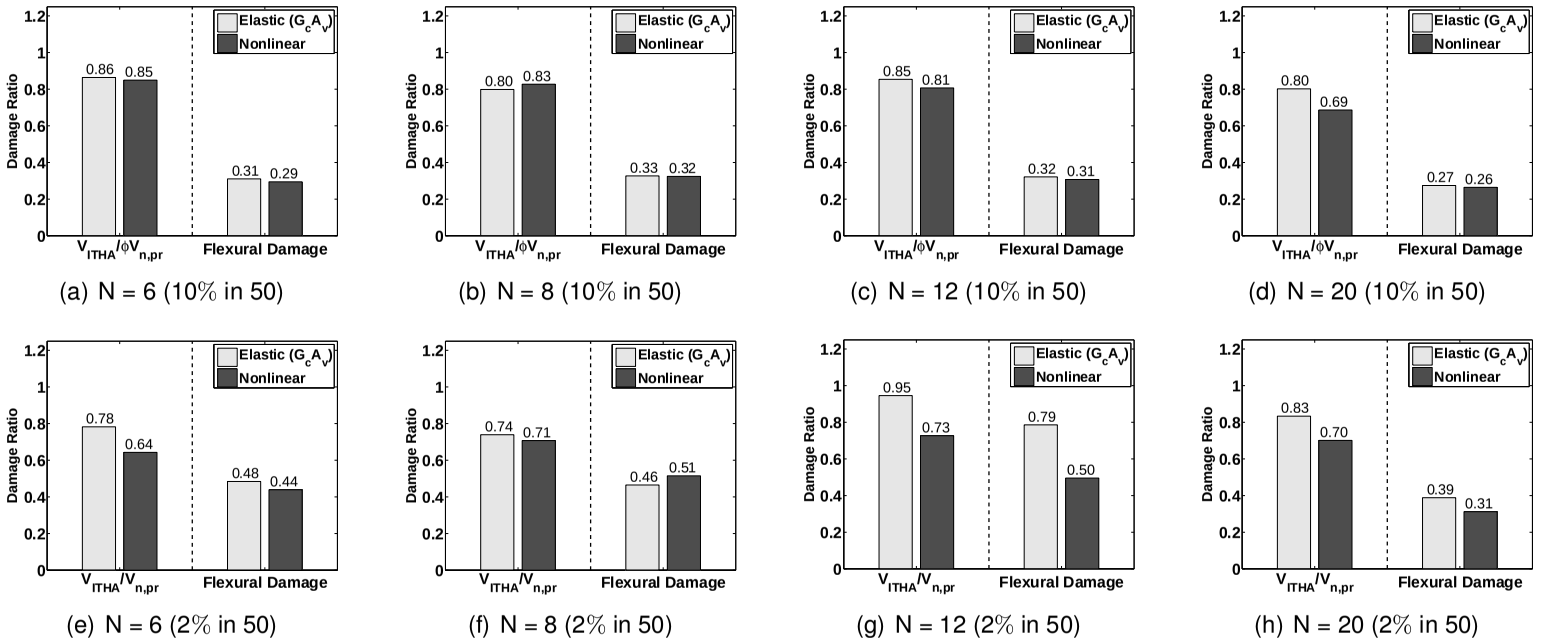

Figure 7.11: Predicted Damage Ratios for Alternate Shear Component Models

7.3.5.2 Crushing Energy

In Chapter 3 it was shown that regularization of the concrete compressive softening response is necessary for accurate simulation of drift capacity for wall specimens limited in drift capacity by deteriorating flexural response. Regularization required the introduction of a material energy for unconfined concrete and an enhanced material energy for well-confined concrete regions (boundary element). Recommended material energy values were detemined using data from previous wall tests of both well confined and completely unconfined wall sections. However, only 12 tests were found in which response was flexural and failure was due to concrete crushing and buckling of longitudinal reinforcement. Given the small size of this dataset, it is appropriate to consider the recommended material energy values (G_{fc}, G_{fcc}) highly uncertain and to assess the sensitivity of the analysis results to the assumed crushing energy values used for wall modeling.

To study this sensitivity analyses were conducted in which the the assumed value of confined crushing energy (Chapter 6) was both increased and reduced by 25% and 50%. Damage results for these analyses are presented in Figure 7.12. Analyses were conducted considering MCE level ground motions and building heights of 6, 12 and 20-story capacity designed walls (Table 6.1).

Impact on Base Shear Demands The data in Figure 7.12 show that for the MCE, base shear demands are not particularly sensitive to variation in the assumed crushing energy value. For the 12-story building, essentially no variation was determined in base shear demand to capacity ratio for the entire range of crushing energy values considered. For 6 and 20-story buildings, a 15% decrease in base shear demand to capacity ratio was determined both for increased and decreased values of crushing energy.

Impact on Flexural Demands The data in Figure 7.12 show that for the MCE, flexural damage ratios are very sensitive to the variation in the assumed crushing energy. Results shown in Figure 7.12 indicate that selecting a crushing energy value less than the calibrated value dramatically increases the flexural damage predicted for buildings sub-

jected to MCE ground motions. A 25% increase in the crushing energy reduced crushing damage predicted for the 6 and 20-story buildings by 20% and 13%, respectively. For the 12-story building, a larger reduction in damage (35%) was predicted. Flexural damage results were fairly insensitive to crushing energy enhancements beyond 25%. This was due to the excessively enhanced compressive response transitioning the section failure mode to a tension controlled (rupture) response. Once section response transitioned to a tension rupture failure mode, further increase of the compressive capacity did not affect the results.

These results suggest that flexural damage results determined using regularized beam column models are quite sensitive to the crushing energy relationships used to regularize element response. Further experimental investigation of confined wall boundary element configurations would be useful to further validate the material energy relationships proposed in Chapter 3.

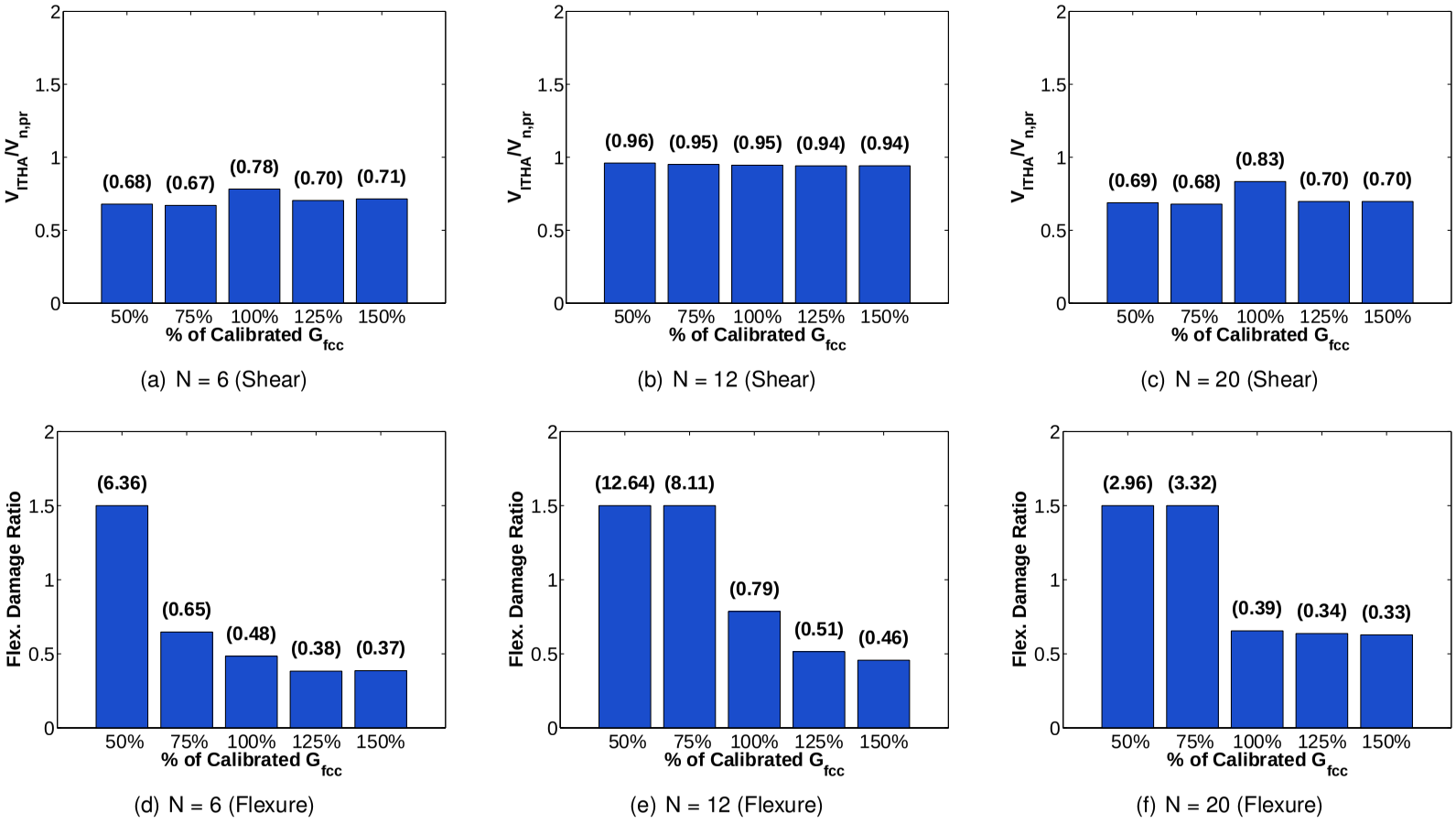

Figure 7.12: Damage Sensitivity to Confined Crushing Energy Value (2% in 50 event)

7.4 Assessment of Force Reduction Factors for Walled Buildings

In this section, FEMA P695 methodology is used to determine force reduction factors for slender walled buildings such that a target collapse probability for buildings subjected to MCE level ground motions can be achieved. The FEMA methodology provides a rational methodology for linking numerical simulation results to collapse probability. Additionally, the methodology assesses performance using a suite of 44 recorded ground motion records which account for time history variability that may have been insufficiently captured by the synthetic ground motion records used extensively in Section 7.3.

Results presented in Section 7.3 indicate that force reduction factors less than those currently allowed by ASCE 7 may be required to reduce MCE level flexural damage. This conclusion was reached by comparing the expected flexural damage for walls designed using both 1) theoretical force reduction factors of R = 2, 3 and 4 and 2) code-based force reduction factors, R_{ASCE} = 5 and 6. Flexural damage was determined using ITHA and the regularized fiber beam column element model developed in Chapter 3. Design of the analyzed walls were performed using two approaches, 1) A capacity design approach using the modified MRSA (Chapter 6) for shear design and elastic MRSA reduced by the force reduction factor of R = 2, 3 and 4 for flexural design and 2) code-based approach in which design demands were determined per ASCE 7-10. Performance assessment in Chapter 6 demonstrated the capacity design approach was successful in suppressing shear failure for buildings subjected to both design and MCE level ground motions records while the code-based designs were identified to be unconservative with respect to shear design. Flexural performance assessment indicated $R < 3$ is required to limit flexural damage in mid-rise planar walls while higher values may be justified for core walls. To develop recommended force reduction factors for well-detailed slender walls, the 'Quantification of Building Seismic Performance Factors' framework developed by FEMA (2009) was used. In comparison with the performance assessment presented in Section 7.3, FEMA P695 methodology employs:

1. Recorded ground motion records instead of artificially generated synthetic ground

motion records. The P695 far field ground motion set consists of 44 recorded time history records considering different magnitudes, site distances and fault types. This accounts for record variability that is unlikely to be captured properly by synthetic ground motions.

2. Probabilistic collapse fragilities used to link structural damage identified by the numerical model directly to collapse probability while accounting for uncertainties in available design requirements, test data and the numerical modeling approach.

This section extends the performance evaluation of Section 7.3 by conducting a P695 evaluation for nine of the previously designed walled buildings. Section 7.4.1 discusses the designs selected for evaluation. Section 7.4.2 provides details on the ground motion record set and ground motion scaling. Section 7.4.3 discusses results of the P695 evaluation and provides recommended force reduction factors for well detailed concrete walled buildings.

7.4.1 Selected Walled Building Design Configurations

Section 7.3 describes the development and design of 27 walled building configurations developed considering a range of building heights (6 to 24 stories) and force reduction factors (2 to 4). Performance evaluation of these designs using synthetic ground motions suggest a force reduction factor, R, of less than three is required to limit flexural damage at the MCE level for mid-rise planar walls and a value larger than three may be appropriate for core wall designs. These results were used to select a reduced set of wall designs to evaluate using the P695 methodology. Specifically, designs for R = 3 (capacity designed) and R_{ASCE} = 6 (code-based designed) were considered.

Building Heights Evaluated The 27 buildings assessed in Section 7.3 included building heights of 6, 8, 12, 16, 20 and 24 stories. For the P695 evaluation, only 6, 12 and 20 story buildings were assessed.

Force Reduction Factors Evaluated Preliminary performance evaluation results presented in Section 7.3 suggests force reduction factor values R $\approx$ 3 may be appropriate for

mid-rise capacity designed planar walls and values of R $>$ 3 may be appropriate for taller capacity designed core walls. To evaluate these results, 6, 12 and 20-story buildings from Section 7.3 designed using a force reduction factor, R = 3, were used for P695 evaluation. For evaluation of code-based wall designs, buildings designed using force reduction factor, R_{ASCE}, of 6 were evaluated.

Flexural Design Envelopes Both flexural envelopes suggested by 1) SEAOC and 2) Panagiotou and Restrepo (Dual Hinge) were evaluated.

7.4.2 Input Ground Motion Records

The FEMA P695 44 record far-field ground motion record set was used as ground motion input for evaluation. Per the P695 methodology, the MCE for the record set was determined by anchoring the record set mean spectra to the ASCE MCE spectrum at the code-based building fundamental period, $C_u T_a$. For evaluation of the walled buildings, the record set was anchored to a 2% damped MCE spectrum instead of the standard 5% damped spectrum, based on review of preliminary ITHA results discussed in Chapter 5. The use of a 2% damped spectrum is a deviation from the 5% damped spectrum specified for use by the P695 methodology. Figures showing the MCE level scaled mean spectrum for the record set for the three building heights evaluated are shown in Figure 7.13. For each building height, only one MCE level mean spectrum is calculated because the anchoring period specified for walled buildings, $C_u T_a$, is only a function of building height. P695 performance evaluation is quantified primarily through the establishment of the collapse margin ratio (CMR). The CMR represents the seismic intensity level, above or below the MCE level, for which half the ground motion records initiate building collapse. Complete P695 evaluation requires evaluating performance at increasing intensity levels until over 50% of the scaled records initiate collapse of the building model. Once 50% of the scaled records initiate collapse the P695 evaluation can be considered complete.

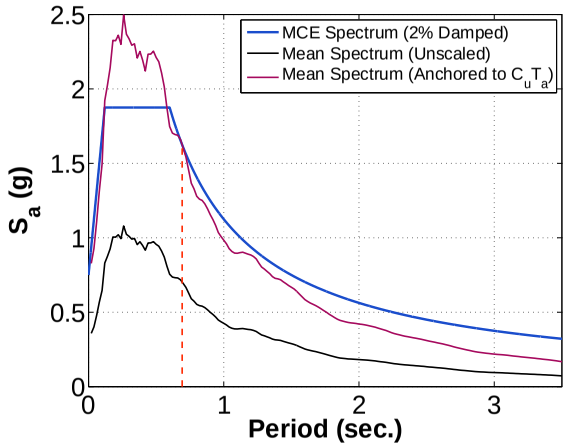

(a) N = 6

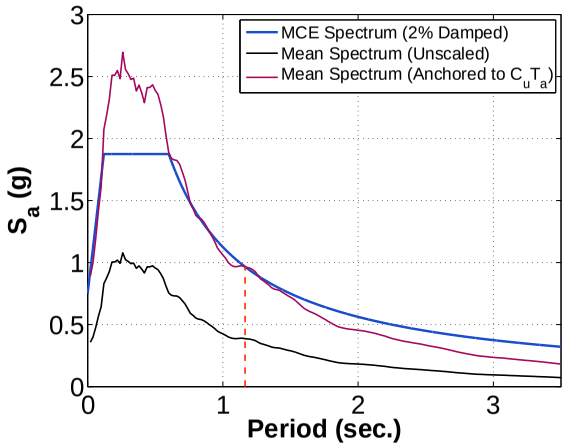

(b) N = 12

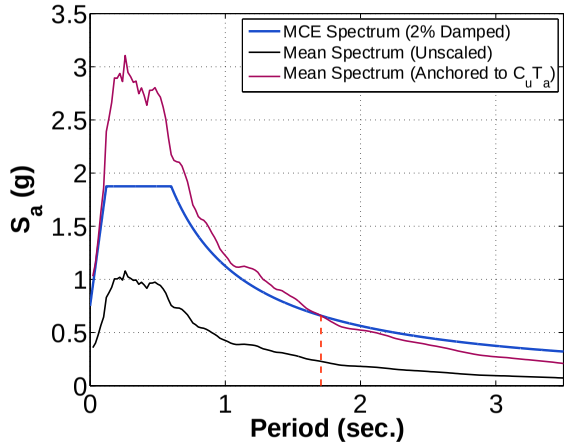

(c) N = 20

Figure 7.13: P695 Ground Motion Scaling Results

7.4.3 P695 Evaluation Results

Results of P695 evaluation for the selected wall designs are presented in this section. Sections 7.4.3.1 and 7.4.3.2 address the simulated and non-simulated collapse criteria used in the evaluation. Sections 7.4.3.3 to 7.4.3.4 provide evaluation results, including comparison between shear demands predicted using synthetic and actual ground records and recommended force reduction factors for walls.

7.4.3.1 Simulated Collapse Criteria

The fully regularized fiber beam column element was shown in Chapter 3 to be capable of directly simulating flexural failure for wall sections. Thus, loss of lateral strength due to flexural failure can be detected by the numerical model. Ground motions causing deterioration of the hysteretic flexural model sufficient to reduce flexural strength below 80$\%$ of the peak capacity were considered to initiate flexural failure. This collapse criteria is comparable to the flexural damage ratio introduced in Section 7.3.

7.4.3.2 Nonsimulated Collapse Criteria

Two nonsimulated collapse criteria were used to assess system behavior which could not be captured by the numerical model

Shear Failure A shear failure non-simulated collapse criteria was initiated if wall shear force determined by inelastic time history analysis, V_{ITHA}, was determined to be larger than the provided shear strength. Wall strength was taken as, $V_{n,pr}$, the expected nominal strength defined by ACI 318 (2011) calculated using expected material strength and a strength reduction factor, ϕ = 1.0.

Gravity System Collapse A story drift limit was introduced as a non-simulated collapse criteria to impose a deformation limit between the lateral force resisting wall and the non-ductile gravity system. A limiting value of 5$\%$ story drift was used to estimate the deformation capacity of the unmodeled gravity system.

7.4.3.3 Median System Collapse Results

Collapse margin ratios (CMRs) and calculated collapse probabilities for the buildings are presented in Table 7.2. CMRs represent the ratio between the ground motion intensity at which 50% of the acceleration records cause collapse, $\hat{S}_{CT}$, and the MCE level ground motion intensity, S_{MT}. To determine collapse probability, a collapse fragility was defined for each building using the calculated CMR value and 1) an estimated level of uncertainty accounting for the robustness of the design guidelines, experimental data and numerical simualation tools used to determine the CMR and 2) a beneficial adjustment to the calculated CMR accounting for spectral shape variations expected for rare seismic events. Collapse fragility for each building was determined using the calculated CMR and a system uncertainty, β_{TOT}, value of 0.525. System uncertainty was determined by selecting quality ratings of 'B' (good) to define the level of uncertainty present in the 1) design guidelines available for walls, 2) available test data and 3) the regularized beam column model used to simulate wall response. Per the P695 methodology, collapse fragility is defined assuming a lognormal cumulative distribution function with a mean value, μ = CMR, and a dispersion or standard deviation, $\sigma = \beta_{TOT}$. Finally, collapse probability was determined by adjusting the CMR by the spectral shape factor, SSF, and determining the $P_{collapse}$ corresponding to the MCE (S_{CT}/S_{MT} = 1.0). CMRs, adjusted CMRS (ACMR = CMR * SSF) and calculated collapse probabilities for the walled buildings are presented in Table 7.2. Plots showing the relationship between increased ground motion amplitude and system damage are provided in Figure 7.14.

Comments on Capacity Designed Walls CMRs for the 6, 12 and 20-story capacity designed walls were limited by flexural failure directly detected by the numerical model. At a ground motion amplification sufficient to cause 50% of the ground motions to cause flexural failure, the number of motions causing shear failures were 5%, 25% and 20% for the 6, 12 and 20 story buildings, respectively. This suggests the proposed capacity design methodology adequately suppressed shear failure prior to achieving the desired flexural mechanism. The calculated collapse probabilities for the capacity designed walls were

approximately 30% for the 6 and 12-story walls and approximately 9% for the 20-story wall. If a collapse probability of 10%-20% is desired, these values suggest a lower force reduction factor (R $<$ 3) is necessary for mid-rise planar walls and a larger force reduction factor (R $>$ 3) for core walls may be sufficient.

Data show that the use of the Paulay/Priestley flexural envelope vs. the Dual Hinge design method for flexural design has minimal impact on the calculated collapse probability. For the 6-story building, use of the Dual Hinge method rather than the Paulay/Priestley envelope resulted in a slightly lower probability of collapse (27% vs. 32%). Use of both methods resulted in collapse probabilities of approximately 30% for the 12-story wall. For the 20-story wall, the use of the Paulay/Priestley design envelope resulted in a slightly lower probability of collapse (9% vs 12%) than did the use of the Dual Hinge Method.

With ACMRs determined for a force reduction factor of R = 3, collapse results were extrapolated to estimate the R factor required to achieve a 20% collapse probability. To perform this extrapolation, the following linearized relationship between force reduction and ACMR was used:

$$\tilde{R}_{20} \approx R\frac{ACMR}{ACMR_{20}} \tag{7.19}$$

Where $ACMR_{20}$ is the ACMR required to achieve a 20% collapse probability per Table 7.3 of FEMA P695. Linearized force reduction values were found to be reasonably approximated as R = 2.5 for mid-rise planar walls and R = 3.5 for core walls.

Comments on Code Based Designed Walls The shear failure non-simulated collapse criteria limited the calculated CMR for all code-based designed buildings. For these buildings, CMRs less than 1.0 were determined, indicating the design could not sustain MCE level seismic demands without significant risk of shear failure. For further comparison between the selected force reduction factors used in design, performance evaluation of the code-based designs without including the shear failure non-simulated collapse criteria was also determined.

With the shear failure non-simulated collapse criteria removed, increased collapse probabilities compared to the capacity designed walls with R = 3 were calculated. Collapse probabilities of 36%, 38% and 25% were determined for the 6, 12 and 20-story designs, respectively. Linearized estimated force reduction factors required to reduce collapse probability to 20% were found to be between approximately R = 3 for 6 and 20-story walls and approximately R = 2.5 for the 12-story wall.

Table 7.2: p695 Results

	Design Summary							P695 Results				
Shape[1]	N (Stories)	Envelope	R	C_uT_a (Sec.)	S_{MT} (g)	Ω_o	μ_T	S_{CT} (g)	CMR	ACMR	Collapse Prob.	$\tilde{R}_{20}$
R	6	Paulay/Priestley	3	0.69	1.63g	1.38	4.3	1.60g	0.98	1.23	32%	2.42
R	6	Paulay/Priestley	6	0.69	1.63g	1.62	4.0	–	<1.0	–	>60%	–
R	6[2]	Paulay/Priestley	6	0.69	1.63g	1.62	4.0	1.47g	0.90	1.13	36%	2.91
R	6	Dual Hinge	3	0.69	1.63g	1.38	4.3	1.76g	1.08	1.36	27%	2.68
R	12	Paulay/Priestley	3	1.16	0.97g	1.52	3.4	0.97g	1.00	1.30	29%	2.56
R	12	Paulay/Priestley	6	1.16	0.97g	1.43	4.0	–	<1.0	–	>60%	–
R	12[2]	Paulay/Priestley	6	1.16	0.97g	1.43	4.0	0.80g	0.82	1.09	38%	2.54
R	12	Dual Hinge	3	1.16	0.97g	1.52	3.4	0.94g	0.97	1.26	31%	2.49
C	20	Paulay/Priestley	3	1.71	0.66g	1.38	5.6	0.87g	1.32	1.97	9.1%	3.89
C	20	Paulay/Priestley	6	1.71	0.66g	1.62	4.0	–	<1.0	–	>60%	–
C	20[2]	Paulay/Priestley	6	1.71	0.66g	1.62	4.0	0.64g	0.97	1.40	25%	3.04
C	20	Dual Hinge	3	1.71	0.66g	1.38	4.3	0.81g	1.22	1.82	12%	3.60

[1] R = Rectangular Cross-Section; C = Core Cross-Section

[2] Shear Failure Non-Simulated Criteria Ignored

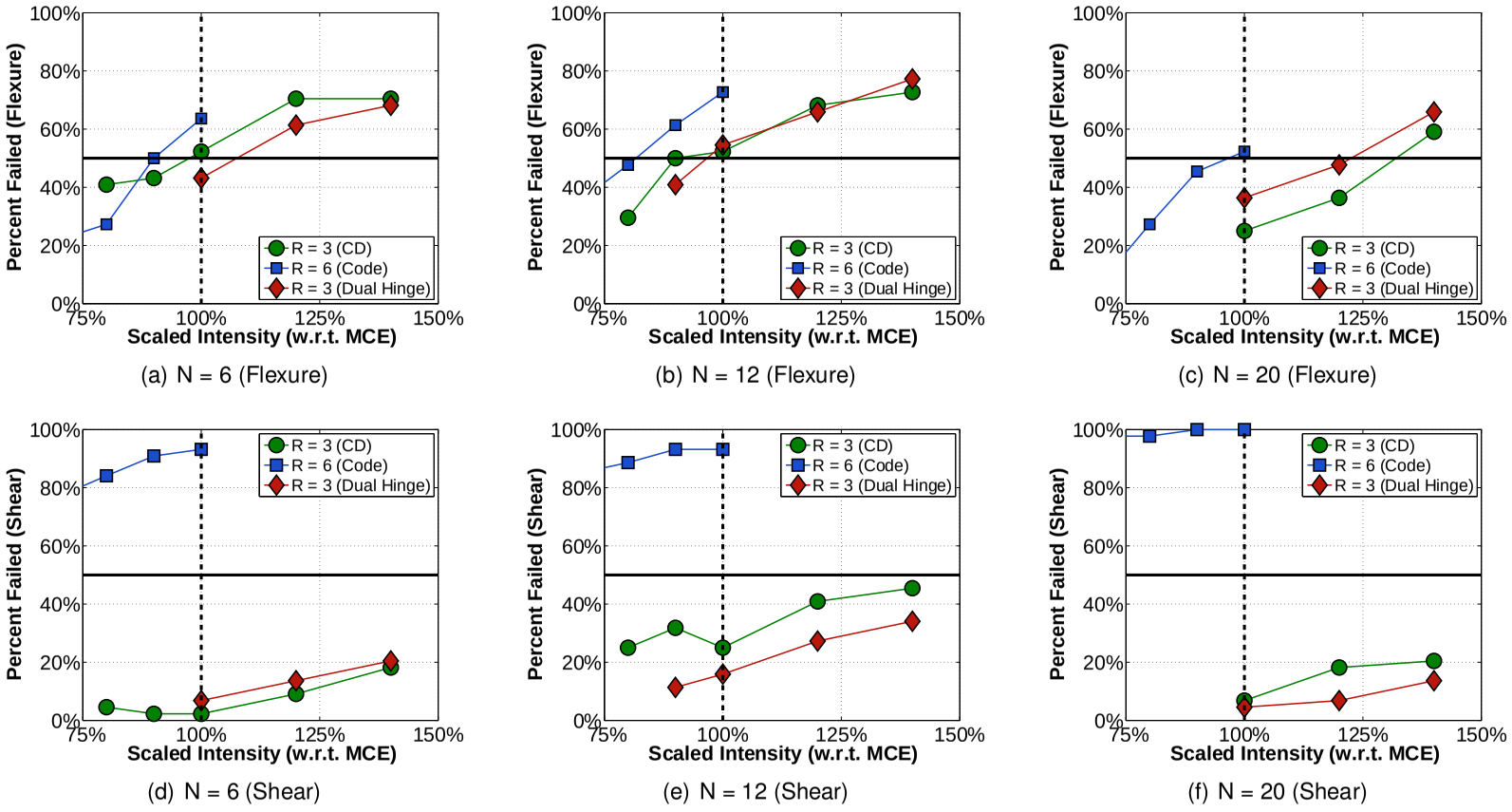

(a) N = 6 (Flexure) (b) N = 12 (Flexure) (c) N = 20 (Flexure)

(d) N = 6 (Shear) (e) N = 12 (Shear) (f) N = 20 (Shear)

Figure 7.14: P695 Results Comparison

7.4.3.4 Comments on Shear Demand

Table 7.3 compares MCE base shear demand-capacity ratios using the P695 ground motion set with the ratios determined using the set of 7 synthetic records and reported in Chapter 6. Comparison of the median shear demand-capacity ratios shows that the synthetic motion set and the large suite of scaled ground motions result in very similar median shear demand-capacity ratios. Minimum and maximum demand capacity ratios confirm the increased variability in demands resulting from the use of the large suite of P695 records.

Table 7.3: $V_{ITHA}/V_{n,pr}$ Comparison (MCE Intensity)

	Design			7 Synthetic Motions			44 P695 Recorded Motions		
Shape[1]	N (Stories)	Envelope	R	Median	Max.	Min.	Median	Max.	Min.
R	6	Paulay/Priestley	3	0.70	0.74	0.63	0.72	1.02	0.38
R	6	Paulay/Priestley	6	1.32	1.45	1.14	1.38	2.41	0.92
R	12	Paulay/Priestley	3	0.89	1.12	0.76	0.89	1.31	0.42
R	12	Paulay/Priestley	6	1.40	1.57	1.07	1.58	2.13	0.74
C	20	Paulay/Priestley	3	0.65	0.79	0.63	0.72	1.75	0.46
C	20	Paulay/Priestley	6	2.02	2.20	1.82	2.00	2.80	1.14

[1] R = Rectangular Cross-Section; C = Core Cross-Section

7.5 Conclusions

Results of the P695 evaluation suggest the following force reduction factors for well detailed concrete walls:

1. Force reduction factor R = 2.5 for planar walls

2. Force reduction factor R = 3.5 for flanged core walls

These recommended force reduction factors represent theoretical force reduction factors, R, which are to be used directly with elastic MRSA to determine reduced design

flexural demands. These recommended force reduction factors are not directly comparable with R_{ASCE} force reduction factors of 5 or 6, which imply a larger force reduction than is realized in the design, due to code period limits and consideration of ELF static load patterns. Comparisons between force reductions realized using both theoretical R values and R_{ASCE} values throughout this chapter suggest that current R_{ASCE} = 5 and 6 are comparable to theoretical R = 3 and 4, respectively. Thus recommended theoretical force reduction factors of 2.5 and 3.5 for planar and core walls could be expected to be similar to recommended R_{ASCE} values of 4 and 5.

Flexural performance evaluation also demonstrated that flexural design envelopes based on reduced elastic MRSA demands can develop significant inelastic flexural response distributed over a large portion of the building height. The use of alternate flexural design envelopes such as the Paulay and Priestley envelope or the Dual Hinge design method were demonstrated to localize inelastical flexural response to expected hinge locations. Additionally, P695 results demonstrated the modified MRSA shear equation was sufficient to suppress shear failure for the capacity designed walled buildings.

Chapter 8

SUMMARY, CONCLUSIONS AND RECOMMENDATIONS FOR FUTURE WORK

Reinforced concrete walls are a commonly used seismic lateral force system throughout the western United States. Because walls are expected to respond inelastically in large earthquakes, numerical simulation tools are needed that are capable of accurately simulating nonlinear response. Computationally efficient fiber-type beam-column elements and less efficient 2-D plane stress elements are commonly used by practitioners to simulate nonlinear wall response, however such models have not been validated using an extensive dataset of available laboratory tested wall specimen data. A recommended nonlinear wall modeling approach shown to improve simulation accuracy for a range of wall specimens is required to improve predictions of building seismic demands and to improve seismic design procedures for walls.

The primary objectives of the research presented in this thesis were:

1. To evaluate existing tools for simulating the nonlinear response of concrete walls.

2. To develop modeling recommendations that provide accurate simulation of cyclic response, including loss of lateral strength for slender walls responding primarily in flexure.

3. To evaluate US seismic design procedures for walls by conducting inelastic time history analyses (ITHA) using the above modeling recommendations.

4. To develop improved seismic design procedures that ensure that slender walls develop the desired flexural response mechanism and can sustain expected inelastic flexural deformations.

The recommended modeling approach was developed using fiber-type distributed-plasticity

beam-column elements. Such elements are computationally efficient enough to be considered for design office applications and are currently available for use within the open-source OpenSees software platform. The recommended modeling approach was used to evaluate seismic shear and moment demands in walls. Inelastic wall analysis results suggest that elastic design methods used by current US building codes unconservatively envelope wall seismic force demands.

8.1 Research Summary

Evaluation of Conventional Modeling Approaches Two conventional nonlinear wall simulation tools were evaluated to determine the accuracy with which these tools simulate inelastic wall response. Fiber-section based distributed-plasticity beam column element models available in the OpenSees program and 2-D VecTor2 plane stress element models were evaluated. Model performance was evaluated by comparing simulation results with results from 21 slender wall tests taken from the literature.

Evaluation of the simulation results identified that both tools can be used to adequately simulate strength and initial stiffness of walls. However neither modeling approach yielded accurate simulation of deteriorating flexural response and loss of lateral wall strength. Mesh studies performed identified that model softening due to strength loss in compression led to localization of inelastic deformations. Localization of compressive damage contributed significantly to inaccurate drift capacity simulation for the specimen models.

The OpenSees Concrete02 material model, which allows the user to specify a concrete compressive post-peak softening slope, provided an opportunity to improve the OpenSees line element models by using material regularization.

Development of a Regularized Beam-Column Element for Simulating the Response of Flexural Walls Using an approach to material regularization for line element models previously developed by Coleman and Spacone (2001), material energy recommendations were developed. Specifically, material energies for use in regularization were developed for reinforcing steel, concrete tension, unconfined concrete compression and confined con-

crete compression material response.

The proposed recommendations were developed using test data for unconfined and confined concrete walls, and were demonstrated to provide accurate simulation for planar wall specimens. The recommendations were applied to simulate the response of c-shaped walls by comparing simulated and measured response for 6 uni- and bi-directionally loaded c-shaped walls.

Evaluation of Squat Wall Simulation Models The VecTor2 program, which uses 2-D plane stress elements with Modified Compression Field Theory-based constitutive models, were use to evaluate numerical simulation of 13 squat wall specimens. The squat wall specimens exhibited shear failures that could not accurately be identified by fiber section flexural line element models. Squat wall strength was accurately simulated by VecTor2 plane stress element models. Specimen stiffness and drift capacity were not accurately simulated. Simulated drift capacity for the squat wall simulations was mesh dependent; however, advancement of the VecTor2 models was limited by the closed-source nature of the software and could not be accomplished by the current research.

Shear Demand in Long Period Core Wall Buildings The regularized beam column element and inelastic time history analysis (ITHA) were used to assess current US seismic design procedures for slender walls. Eight core wall buildings ranging from 16 to 30 stories in height were designed using current US design standards. These designs were assessed using ITHA and the FEMA P695 methodology. Results showed that current US design standards specify unconservative shear demands for use in design and that shear demands in walls designed using current US standards may exceed provided design shear strength under the design level seismic event. Unacceptable collapse probability values were determined for the core wall building using the FEMA P695 methodology. For P695 evaluation, it was assumed that shear failure occurs when the seismic shear demand, V_u, exceeds the probable nominal shear capacity, $V_{n,pr}$, calculated per ACI 318-11 Equation 21-7.

Evaluation of Current Shear Capacity Design Recommendations To assess existing capacity design recommendations for shear in slender walled buildings, 60+ walled buildings ranging from 6 to 24 stories were designed and analyzed using ITHA. Buildings were subjected to a suite of seven synthetic ground motions generated to match a 2% damped ASCE 7 (2010) design spectrum. A 2% damped design spectrum was used because preliminary analysis results indicated that hysteretic damping in higher modes was not sufficient to warrant use of the typical 5% damped spectrum. It was found that current recommendations used in other parts of the world do not accurately predict maximum base shear demands for walled buildings designed using a wide range of building heights, initial fundamental periods and designed using a range of force reduction factors.

Development of an Improved Method for Estimating Seismic Shear Demands A modified MRSA method was developed for determining shear demand for design; this method was based on Eibl's (1988) capped MRSA method. The modified MRSA method was shown to improve accuracy and precision in predicting seismic shear demands in slender walls. To validate the method, the modified MRSA method was used to design a set of 25+ walled buildings ranging in height from 6 to 24 stories and designed using a range of force reduction, R, factors. Evaluation of shear demands confirmed that walls designed using the modified MRSA method were successfully capacity protected from seismic shear demands predicted to develop for both design level and maximum considered earthquake level ground motion records. Similar walls designed using current code-based elastic MRSA procedures were determined to develop shear demands in excess of the provided shear capacity when subjected to design level ground motion records.

Flexural Design Recommendations for Slender Walls Recommended force reduction factors for slender walls were determined using regularized line element models capable of simulating loss of lateral strength for slender walls. For building heights between 6 and 24 stories, walls were designed using several force reduction factors. For each design, building models were developed and ITHA was performed using a set of synthetic ground motion records scaled to represent the maximum considered earthquake. ITHA using

synthetic records provided an initial estimate of the maximum level force reduction that could be employed in wall design without walls exhibiting flexural failure for MCE ground motions.

Using the estimated force reduction factors, 6-, 12- and 20-story building models were subjected to the FEMA P695 methodology to develop force reduction factors that account for record-to-record ground motion variability and model uncertainty. Using P695 procedures, theoretical force reduction factors of R = 2.5 and 3.5 were determined for planar and core wall building, respectively, to limit risk of loss of lateral strength to 20% for the MCE. These theoretical force reduction factors were determined to be comparable to code-based force reduction factors of R_{ASCE} = 4.0 and 5.0. For planar walls, the recommended code-based force reduction factor of 4.0 is less than the current values of 5.0 and 6.0 allowed by ASCE 7 (2010).

8.2 Conclusions

8.2.1 Evaluation of Current Modeling Tools and Numerical Simulation Methods

Both line element and continuum element models evaluation accurately simulated strength and stiffness of flexural walls. Wall simulation tools that do not regularize concrete compressive response do not accurately simulate deteriorating flexural strength and loss of lateral strength for flexural walls.

Plane stress elements using Modified Compression Field Theory-based constitutive models can provide accurate simulation of squat wall strength. Squat wall stiffness and drift capacity were not accurately simulated by the VecTor2 models.

8.2.1.1 Best Practices for Modeling Walled Building Using Line Elements

Type of Element The force-based distributed-plasticity element should be used instead of the displacement-based distributed-plasticity element. The force-based element allows for computationally efficient simulation of wall response. The displacement-based element is susceptible to uncontrolled variation of axial load at intra-element fiber sections; such

variations introduce variability in the simulated response that does not occur using force-based elements.

Number of Integration Points A minimum of 5 integration points should be used with the force-based beam-column element.

Material Regularization For concrete wall sections experiencing gradual strength loss prior to failure, fiber section material models for reinforcing steel, unconfined concrete compression and confined concrete compression should be regularized. Material regularization recommendations demonstrated to accurate simulate both planar and c-shaped wall specimen response are provided in Chapter 3. For wall sections experiencing hardening response prior to tensile failure, material regularization should not be used.

8.2.2 Current US Code-Based Wall Design

Current US wall seismic design procedures were determined to significantly underestimate the seismic shear demands determined to develop in walls using inelastic time history analysis. The use of shear design procedures that account for flexural overstrength and dynamic amplification of higher mode response can be used to capacity protect walls against high shear demands. Capacity design procedures for walls have been adopted by national building code documents in Canada and New Zealand.

8.2.2.1 Best Practices for Demand Evaluation of Walled Buildings

Flexural Overstrength To adequately capacity design slender walls for shear, accurate estimation of the provided probable flexural wall strength should be included. Flexural design performed for over 80 wall designs suggest an appropriate flexural overstrength factor, Ω_o, for wall sections of approximately 1.40 - 1.50. This suggested flexural overstrength factor was calculated by moment-curvature analysis using recommendations for expected steel and concrete strengths provided by PEER (2010) and accounting for strain hardening of reinforcement.

Higher Mode Effects Dynamic amplification of shear forces occurs for slender walls because force reduction caused by flexural yielding does not reduce elastic shear demands from all modes equally. For walls less than 12 stories, flexural yielding at the wall base primarily reduces first mode shear force demands while higher mode shear demands remain essentially elastic. The higher reduction in first mode shear demands relative to higher mode demands reduces the effective loading height and allows higher shear forces to develop after wall yielding occurs. For taller walls, the reduction in modal demands are not limited to the first mode and seismic shear demands are more difficult to predict. The modified MRSA method developed in Chapter 6 was developed to improve accuracy in predicting seismic shear demands for walls of varying height.

Force Reduction Factor Inelastic time history analysis performed using regularized line element models suggests that force reduction factor values for walls that limit flexural damage for walled buildings subjected to MCE ground motions may depend on both building height and the provided wall cross-section. For walled buildings less than 14 stories designed using planar walls, smaller force reduction values than currently allowed by ASCE 7 (2010) are required to limit flexural damage. For buildings taller than 14 stories designed using core wall cross-sections, current ASCE force reduction factors were determined to be adequate. An investigation of planar walls taller than 14 stories and core walls shorter than 14 stories was not performed as part of the current research. This investigation should be performed in the future to clarify whether the identified trends are affected more significantly by building height or provided cross-section ductility.

Approximation of Moment Demands To ensure inelastic flexural demands are constrained to expected plastic hinge regions, flexural design envelopes such as those recommended by Paulay and Priestley (1992) or Panagiotou and Restrepo (2009) should be used. Designing flexural strength and bar cutoff locations based on MRSA or ELF load distributions can lead to significant levels of inelastic flexural deformation developing uniformly over large portions of the wall height. Such demands could result in premature flexural failure or result in flexural failure at lower earthquake demand levels unless ductile detailing is

provided over a significant portion of the wall.

8.2.3 Future Work

Compression Regularization for Continuum Elements The implementation of crushing regularization into commercially available continuum-based finite element programs should be investigated and material energy relationship developed in Chapter 3 should be assessed in the context of continuum element modeling. Continuum element programs allow removal of limiting assumptions (plane sections, 1-dimensional material models) inherent in currently available beam column element implementations and thus are more robust for handling wall configurations where flexural response may not dominate component response (squat walls, coupling beams). For these shear critical components, component deformation capacity may very well be compression-controlled and as demonstrated in Chapter 2, without regularization of material behavior, simulated softening response will be dependent on the critical element size.

Impact of Wall Cross-Section Shape Recommended force reduction factors for walled buildings were determined to be dependent on cross-section shape; recommended force reduction factors for planar walls were smaller than recommended force reduction factors for core walls. It is suspected this dependence is strongly related to the higher curvature ductility capacity of core wall sections, which is influenced by the smaller neutral axis depth within the concrete flange. However for the current research, buildings less than 14 stories were designed using planar walls and buildings taller than 14 stories were designed using core walls. Further investigations considering both taller planar wall buildings and shorter core wall buildings should be performed to further identify the full impact of the selected wall cross-section shape.

Quantifying Shear Capacity of Wall Sections The results discussed in this thesis focus on improving simulation techniques and improving seismic design procedures such that design earthquake demands are more accurately quantified. Equally important is the

advancement of techniques for accurately estimating the shear capacity of wall sections. In particular, research advancing the understanding of how shear capacity of wall sections is affected by increasing inelastic flexural demands would be especially useful. Recommended capacity design procedures discussed in this thesis assume shear demands should remain below nominal shear strength values defined by ACI 318 (2011). If ACI strength values provide excess conservatism, as suggested by recent tests by Massone et al (2006), the recommended capacity design recommendations may be unnecessarily onerous.

Seismic Shear Demands and Force Reduction Factors for Coupled Walls The research presented in this thesis addresses only uncoupled, isolated walls. For core walled buildings, only seismic loading parallel to the core web was considered. Coupled concrete walls are also commonly used as seismic force resisting elements. The proposed regularization approach should be extended to evaluate the performance and existing capacity design recommendations for coupled wall systems.

REFERENCES

ACI, *Building Code Requirements for Structural Concrete (ACI 318-08) and Commentary (ACI 318R-08)*, American Concrete Institute, Committe 318, Farmington Hills, MI, 2008.

——, *Building Code Requirements for Structural Concrete (ACI 318-11) and Commentary (ACI 318-11)*, American Concrete Institute, Committe 318, Farmington Hills, MI, 2011.

P. Adebar, A. Ibrahim, and M. Bryson, "Test of high-rise core wall: Effective stiffness for seismic analysis," *ACI Structural Journal*, vol. 104, no. 5, pp. 549–559, 2007.

J. Almeida, S. Das, and R. Pinho, "Adaptive force-based frame element for regularized softening response," *Computers and Structures*, vol. 102-103, pp. 1–13, 2012.

ASCE, *Minimum Design Loads for Buildings and Other Structures*, A. S. of Civil Engineers, Ed. Reston, VA: ASCE/SEI 7-10, 2010.

ATC, "Modeling and acceptance criteria for seismic design and analysis of tall buildings," Prepared by Applied Technology Council for the Pacific Earthquake Engineering Research Center, Redwood City, California, Tech. Rep. Report No. PEER/ATC-72-1, 2010.

F. Barda, J. Hanson, and W. Corley, "Shear strength of low-rise walls with boundary elements," Research and Development Bulletin, American Concrete Institute, Detroit, MI, Tech. Rep. Bulletin RD043.01D, 1976.

Z. Bazant and B. Oh, "Crack band theory for fracture of concrete," *Materials and Structures*, vol. 16, pp. 155–177, 1983.

——, "Microplane model for progressive fracture of concrete and rock," *ASCE Journal of Engineering Mechanics*, vol. 111, pp. 559–582, 1985.

Z. Bazant and J. Ozbolt, "Nonlocal microplane model for fracture, damage and size effect

in structures," *ASCE Journal of Engineering Mechanics*, vol. 116, no. 11, pp. 2484–2504, 1990.

Z. Bazant and P. Prat, "Measurement of mode III fracture energy of concrete," *Nuclear Energy and Design*, vol. 106, pp. 1–8, 1988.

E. Bentz, "Sectional analysis of reinforced concrete members," Ph.D. dissertation, Dept. of Civil Engineering, University of Toronto, Toronto, ON, 2000.

M. Berry, "Performance modeling strategies for modern reinforced concrete bridge columns," Ph.D. dissertation, Dept. of Civil and Environmental Engineering, University of Washington, Seattle, WA, 2006.

M. Berry, D. Lehman, and L. Lowes, "Lumped-plasticity models for performance simulation of bridge columns," *ACI Structural Journal*, vol. 105, no. 3, pp. 270–279, 2008.

K. Beyer, A. Dazio, and M. Priestley, "Quasi-static cyclic tests of two U-shaped reinforced concrete walls," *Journal of Earthquake Engineering*, vol. 12, pp. 1023–1053, 2011.

——, "Shear deformations of slender reinforced concrete walls under seismic loading," *ACI Structural Journal*, vol. 108, no. 2, pp. 167–177, 2011.

A. Birely, "Seismic performance of slender reinforced concrete walls," Ph.D. dissertation, Dept. of Civil and Environmental Engineering, University of Washington, Seattle, WA, 2012.

R. Blakeley, R. Cooney, and L. Megget, "Seismic shear loading at flexural capacity in cantilever wall structures," *Bulletin of the New Zealand Society for Earthquake Engineering*, vol. 8, no. 4, pp. 278–290, 1975.

A. Bohl and P. Adebar, "Plastic hinge lengths in high-rise concrete shear walls," *ACI Structural Journal*, vol. 108, no. 2, pp. 148–157, 2011.

Y. Boivin and P. Paultre, "Seismic performance of a 12-story ductile concrete shear wall system designed according to 2005 nation building code of canada and 2004 canadian

standard association standardA23.3," *Canadian Journal of Civil Engineering*, vol. 37, no. 1, pp. 1–16, 2010.

——, "Seismic force demand on ductile reinforced concrete shear walls subjected to western north american ground motions: Part 1 - parametric study," *Canadian Journal of Civil Engineering*, vol. 39, no. 7, pp. 723–737, 2012.

——, "Seismic force demand on ductile reinforced concrete shear walls subjected to western north american ground motions: Part 2 - new capacity design methods," *Canadian Journal of Civil Engineering*, vol. 39, no. 7, pp. 738–750, 2012.

B. Brueggen, "Performance of T-shaped reinforced concrete structural walls under multi-directional loading," Ph.D. dissertation, Dept. of Civil Engineering, University of Minnesota, Minneapolis, MN, 2009.

R. Budynas and W. Young, *Roark's Formulas for Stress and Strain*, McGraw-Hill, Ed. Singapore: ISBN 0-07-072542-X, 2002.

V. Calugaru and M. Panagiotou, "Response of tall cantilever wall buildings to strong pulse type seismic excitation," *Earthquake Engineering and Structural Dynamics*, vol. 41, pp. 1301–1318, 2012.

A. Cardenas and D. Magura, "Strength of high rise shear walls - rectangular cross section," American Concrete Institute, Farmington Hills, MI, Tech. Rep. SP-36, 1973.

F. Charney, "Unintended consequences of modeling damping in structures," *ASCE Journal of Structural Engineering*, vol. 134, no. 4, pp. 581–592, 2008.

A. Chopra, *Dynamics of Structures: Theory and Applications to Earthquake, 2nd Edition*, Prentice-Hall, Ed. Upper Saddle River, NJ: ISBN 0-13-086973-2, 2001.

J. Coleman and E. Spacone, "Localization issued in force-based frame elements," *ASCE Journal of Structural Engineering*, vol. 127, no. 11, pp. 1257–1265, 2001.

CSA, *Design of Concrete Structures*, C. S. Association, Ed. Toronto, Ontario: CSA A23.3-04, 2009.

A. Dazio, K. Beyer, and H. Bachmann, “Quasi-static cyclic tests and plastic hinge analysis of rc structural walls,” *Engineering Structures*, vol. 31, no. 7, pp. 1556–1571, 2009.

R. de Souza, “Force-based finite element for large displacement inelastic analysis of frames,” Ph.D. dissertation, Dept. of Civil and Environmental Engineering, University of California, Berkeley, Berkeley, CA, 2000.

G. Deirlein, A. Liel, C. Haselton, and C. Kircher, “ATC-63 methodology for evaluating seismic collapse safety of archetype buildings,” in *Proceedings, ASCE-SEI Structures Congress*, 2008.

M. Eberhard and M. Sozen, “Behavior-based method to determine design shear in earthquake resistant walls,” *ASCE Journal of Structural Engineering*, vol. 119, no. 2, pp. 619–640, 1993.

Eibl and E. Keintzel, “Seismic design shear forces in RC cantilever shear wall structures,” *European Earthquake Engineering*, vol. 3, pp. 7–16, 1990.

V. et al., *SIMQKE-I Simulation of Earthquake Ground Motions*. Department of Civil Engineering, Massachusetts Institute of Technology, Cambridge, MA, 1976, 1990.

FEMA, “Quantification of building seismic performance factors,” Federal Emergency Management Agency, Washington, D.C., Tech. Rep. No. FEMA P-695, 2009.

F. Filippou and A. Issa, “Nonlinear analysis of reinforced concrete frames under cyclic load reversals,” Earthquake Engineering Research Center, Berkeley, CA, Tech. Rep. No. UCB/EERC-88/12, 1988.

F. Filippou and A. Saritas, “A beam finite element for shear-critical RC beams,” American Concrete Institute, Farmington Hills, MI, Tech. Rep. SP-237-19, 2006.

F. Filippou, E. Popov, and V. Bertero, “Effects of bond deterioration on hysteretic behavior of reinforced concrete joints,” Earthquake Engineering Research Center, University of California, Berkeley, CA, Berkeley, CA, Tech. Rep. EERC 83-19, 1983.

I. Ghorbanirenani, “Experimental and numerical investigations of higher mode effects on seismic inelastic response of reinforced concrete shear walls,” Ph.D. dissertation, Dept. of Civil Engineering, Ecole Polytechnique de Montreal, Montreal, QC, 2010.

S. Ghosh, *Required Shear Strength of Earthquake-Resistant Reinforced Concrete Shear-walls*, P. Fajfar and H. Krawinkler, Eds. London, UK: Elsevier, 1992.

R. Goel and A. Chopra, “Evaluation of modal and FEMA pushover analysis: Sac buildings,” *Earthquake Spectra*, vol. 20, no. 1, pp. 225–254, 2004.

——, “Period formulas for concrete shear wall buildings,” *ASCE Journal of Structural Engineering*, vol. 124, no. 4, pp. 426–433, 1998.

A. Gogus, “Structural wall systems - nonlinear modeling and collapse assessment of shear walls and slab-column frames,” Ph.D. dissertation, Dept. of Civil and Environmental Engineering, University of California, Los Angeles, Los Angeles, CA, 2010.

C. Gulec, “Performance-based assessment and design of squat reinforced concrete shear walls,” Ph.D. dissertation, Dept. of Civil, Structural and Environmental Engineering, The State University of New York at Buffalo, Buffalo, NY, 2009.

C. Hart, “Cracking of reinforced concrete structural walls subjected to cyclic loading,” Ph.D. dissertation, Dept. of Civil and Environmental Engineering, University of Iliinois at Urbana-Champaign, Urbana-Champaign, IL, 2012.

C. Haselton, “Assessing seismic collapse safety of modern reinforced concrete moment frame buildings,” Ph.D. dissertation, Dept. of Civil and Environmental Engineering, Stanford University, Palo Alto, CA, 2006.

C. Haselton, A. Liel, G. Deierlein, B. Dean, and J. Chou, “Seismic collapse safety of reinforced concrete buildings I: Assessment of ductile moment frames,” *ASCE Journal of Structural Engineering*, vol. 137, no. 4, pp. 481–491, 2011.

ICC, *International Building Code*, I. C. Conference, Ed. Country Club Hills, IL: IBC 2006, 2006.

N. Ile and J. Reynouard, “Behavior of U-shaped walls subjected to uniaxial and biaxial cyclic lateral loading,” *Journal of Earthquake Engineering*, vol. 9, no. 1, pp. 67–94, 2005.

D. Jansen and S. Shah, “Effect of length on compressive strain softening of concrete,” *ASCE Journal of Engineering Mechanics*, vol. 123, no. 1, pp. 25–35, 1997.

H. Jiang and Y. Kurama, “Analytical modeling of medium-rise reinforced concrete shear walls,” *ACI Structural Journal*, vol. 107, no. 4, pp. 400–410, 2010.

H. Krawinkler, “Importance of good nonlinear analysis,” *The Structural Design of Tall and Special Buildings*, vol. 15, no. 5, pp. 515–531, 2006.

H. Krawinkler and F. Zareian, “Prediction of collapse - how realistic and practical is it, and what can we learn from it?” *The Structural Design of Tall and Special Buildings*, vol. 16, no. 5, pp. 633–653, 2007.

H. Kupfer and K. Gerstle, “Behavior of concrete under biaxial stresses,” *ASCE Journal of Engineering Mechanics*, vol. 99, no. EM4, pp. 853–866, 1973.

H. Kupfer, H. Hilsdorf, and H. Rusch, “Behavior of concrete under biaxial stress,” *ACI Journal*, vol. 87, no. 2, pp. 656–666, 1969.

Y. Lee and K. William, “Mechanical properties of concrete in uniaxial compression,” *ACI Material Journal*, vol. 94, no. 6, pp. 457–471, 1997.

I. Lefas, “Behavior of reinforced concrete structural walls and its implication for ultimate limit state design,” Ph.D. dissertation, Dept. of Civil Engineering, University of London, London, UK, 1988.

I. Lefas and M. Kotsovos, “Strength and deformation characteristics of reinforced concrete walls under load reversals,” *ACI Structural Journal*, vol. 87, no. 6, pp. 716–726, 1990.

I. Lefas, M. Kotsovos, and N. Ambraseys, “Behavior of reinforced concrete structural walls: Strength, deformation characteristics and failure mechanisms,” *ACI Structural Journal*, vol. 87, no. 1, pp. 23–31, 1990.

H. Liu, “Effect of concrete strength on the response of ductile shear walls,” MS thesis, Dept. of Civil Engineering and Applied Mechanics,McGill University, Montreal, QC, 2004.

J. Mander, M. Priestley, and R. Park, “Observed stress-strain behavior of confined concrete,” *ASCE Journal of Structural Engineering*, vol. 114, no. 8, pp. 1827–1849, 1988.

——, “Theoretical stress-strain model for confined concrete,” *ASCE Journal of Structural Engineering*, vol. 114, no. 8, pp. 1804–1826, 1988.

L. Massone, “RC wall shear-flexure interaction: Analytical and experimental results,” Ph.D. dissertation, Dept. of Civil and Environmental Engineering, University of California, Los Angeles, Los Angeles, CA, 2006.

L. Massone and J. Wallace, “Load-deformation response of slender reinforced concrete walls,” *ACI Structural Journal*, vol. 101, no. 1, pp. 101–113, 2004.

L. Massone, K. Orakcal, and J. Wallace, “Modeling of squat structural walls controlled by shear,” *ACI Structural Journal*, vol. 106, no. 5, pp. 646–655, 2009.

S. Mazzoni, F. McKenna, and G. Fenves, *Open System for Earthquake Engineering Simulation Users Manual*. Berkeley, CA, 2010.

D. Mohr, “Nonlinear analysis and performance based design methods for reinforced concrete coupled shear walls,” MS thesis, Dept. of Civil and Environmental Engineering, University of Washington, Seattle, WA, 2007.

F. Naeim and C. Kircher, “On the damping adjustment factor for earthquake response spectra,” *ASCE Journal of Structural Engineering*, vol. 81, no. 6, pp. 1590–1607, 2001.

H. Nakamura and T. Higai, *Compressive Fracture Energy and Fracture Zone Length of Concrete*, A. S. of Civil Engineers, Ed. Reston, VA: ASCE, 2001.

A. Neuenhofer and F. Filippou, “Evaluation of nonlinear frame finite element models,” *ASCE Journal of Structural Engineering*, vol. 123, no. 7, pp. 958–966, 1997.

——, “Geometrically nonlinear flexibility-based frame finite element,” *ASCE Journal of Structural Engineering*, vol. 124, no. 6, pp. 704–711, 1998.

Newmark and Hall, *Earthquake Spectra and Design*, E. E. R. Institute, Ed. California, USA: EERI, 1982.

NIST, "Evaluation of the FEMA P-695 methodology for quantification of building seismic performance factors," NEHRP Consultants Joint Venture for the National Institute of Standards and Technology, Gaithersburg, MD, Tech. Rep. No. GCR 10-917-8, 2010.

——, "Seismic design of cast-in-place concrete special structural walls and coupling beams," NEHRP Consultants Joint Venture for the National Institute of Standards and Technology, Gaithersburg, MD, Tech. Rep. No. GCR 11-917-11, 2011.

——, "NEHRP seismic design technical brief no. 6: Seismic design of cast-in-place concrete special structural walls and coupling beams," The National Earthquake Hazards Reduction Program, Redwood City, California, Tech. Rep. NIST GCR 11-917-11, 2011.

NZS, *Concrete Structures Standard, Part 1: The Design of Concrete Structures: Part 2: Commentary on the Design of Concrete Structures*, S. N. Zealand, Ed. Wellington, New Zealand: NZS 3103, 2006.

R. Oesterle, A. Aristizabal-Ochoa, J. Carpenter, H. Russell, and W. Corley, "Earthquake resistant structural walls - tests of isolated walls," Portland Cement Association/National Science Foundation, Washington, D.C., Tech. Rep. No. NSF/RA-760815, 1976.

Y. Oh, S. Han, and L. Lee, "Effect of boundary element details on the seismic deformation capacity of structural walls," *Earthquake Engineering & Structural Dynamics*, vol. 31, no. 8, 2002.

K. Orakcal and J. Wallace, "Flexural modeling of reinforced concrete walls - experimental verification," *ACI Structural Journal*, vol. 103, no. 2, pp. 196–206, 2006.

K. Orakcal, J. Wallace, and J. Conte, "Flexural modeling of reinforced concrete walls - model attributes," *ACI Structural Journal*, vol. 101, no. 5, pp. 688–698, 2004.

K. Orakcal, M. L.M., and W. J.W., "Analytical modeling of reinforced concrete walls for pre-

dicting flexural and coupled shear-flexural responses," Pacific Earthquake Engineering Research Center, Berkeley, CA, Tech. Rep. No. 2006/07, 2006.

K. Orakcal, L. Massone, and J. Wallace, "Shear strength of lightly reinforced wall piers and spandrels," *ACI Structural Journal*, vol. 106, no. 4, pp. 455–465, 2009.

C. Osses-Hernandez, "Advancements on the disturbed stress field model," MS thesis, Dept. of Civil and Environmental Engineering, University of Washington, Seattle, WA, 2007.

P. Oyen, "Evaluation of analytical tools for determining the seismic response of reinforced concrete shear walls," MS thesis, Dept. of Civil and Environmental Engineering, University of Washington, Seattle, WA, 2006.

J. Ozbolt and Z. Bazant, "Microplane model for cyclic triaxial behavior of concrete," *ASCE Journal of Engineering Mechanics*, vol. 118, no. 7, pp. 1365–1386, 1992.

D. Palermo and F. Vecchio, "Behavior and analysis of reinforced concrete walls subjected to reversed cyclic loading," Department of Civil Engineering, University of Toronto, Toronto, ON, Tech. Rep. ISBN 0-7727-7553-02, Publication No. 2002-01, 2002.

——, "Simulation of cyclically loaded concrete structures based on the finite-element method," *ASCE Journal of Structural Engineering*, vol. 133, no. 5, pp. 728–738, 2007.

——, "Compression field modeling of reinforced concrete subjected to reverse loading: Verification," *ACI Structural Journal*, vol. 101, no. 2, pp. 155–164, 2004.

M. Panagiotou and J. Restrepo, "Dual-plastic hinge design concept for reducing higher-mode effects on high-rise cantilever wall buildings," *Earthquake Engineering & Structural Dynamics*, vol. 38, no. 12, 2009.

——, "Lessons learnt from the ucsd full-scale shake table testing on a 7-story residential building slice," in *Proceedings, 2007 Structural Engineers Association of California Convention*, 2007, pp. 57–74.

M. Panneton, P. Leger, and R. Trembley, “Inelastic analysis of a reinforced concrete shear wall building according to the National Building Code of Canada 2005,” *Canadian Journal of Civil Engineering*, vol. 33, no. 7, pp. 854–871, 2006.

R. Park, M. Priestley, and W. Gill, “Ductility of square-confined concrete columns,” *Journal of the Structural Division*, vol. 108, pp. 125–137, 1982.

T. Paulay and M. Priestley, *Seismic Design of Reinforced Concrete and Masonry Buildings*, W. Interscience, Ed. United States of America: ISBN 0-471-54915-0, 1992.

PEER, Berkeley, CA, Tech. Rep.

M. Petrangeli, “Fiber element for cyclic bending and shear of rc structures II: Verification,” *Journal of Engineering Mechanics*, vol. 125, no. 9, pp. 1002–1009, 1999.

K. Pilakoutas, “Earthquake resistant design of reinforced concrete walls,” Ph.D. dissertation, Civil Engineering Department, Imperial College of Science Technology and Medicine, University of London, London, UK, 1990.

K. Pilakoutas and A. Elnashi, “Cyclic behavior of reinforced concrete cantilever walls, part I: Experimental results,” *ACI Structural Journal*, vol. 92, no. 3, pp. 271–281, 1995.

——, “Cyclic behavior of reinforced concrete cantilever walls, part II: Discussion and theoretical comparisons,” *ACI Structural Journal*, vol. 92, no. 4, pp. 425–433, 1995.

S. Popovics, “A numerical approach to the complete stress-strain curve of concrete,” *Cement and Concrete Research*, vol. 3, no. 5, pp. 583–599, 1973.

M. Priestley and A. Amaris, “Dynamic amplification of seismic moments and shear forces in cantilever walls,” Rose School, University of Pavia, Pavia, Italy, Tech. Rep. Report No. ROSE-2002/01, 2002.

M. Priestley and M. Kowalsky, “Aspects of drift and ductility capacity of rectangular cantilever structural walls,” *Bulletin of the New Zealand Society for Earthquake Engineering*, vol. 31, no. 2, pp. 73–85, 1998.

M. Priestley, G. Calvi, and M. Kowalsky, *Displacement-Based Seismic Design of Structures*, I. Press, Ed. Pavia, Italy: ISBN 978-88-6198-000-6, 2007.

K. Rejec, T. Isakovic, and M. Fischinger, "Seismic shear force magnification in RC cantilever structural walls designed according to Eurocode 8," *Bulletin of Earthquake Engineering*, vol. 10, no. 2, 2011.

F. Richart, A. Brandtzaeg, and R. Brown, "A study of the failure of concrete under combined compressive stresses," University of Illinois Engineering Experimental Station, Urbana, IL, Tech. Rep. Bulletin No. 185, 1928.

J. Rocks, "Large scale testing of low aspect ratio reinforced concrete walls," MS thesis, Dept. of Civil, Structural and Environmental Engineering, The State University of New York at Buffalo, Buffalo, NY, 2011.

M. Rodriguez, J. Restrepo, and A. Carr, "Earthquake-induced floor horizontal accelerations in buildings," *Earthquake Engineering and Structural Dynamics*, vol. 31, pp. 693–718, 2002.

M. Saatcioglu and S. Razvi, "Strength and ductility of confined concrete," *ASCE Journal of Structural Engineering*, vol. 81, no. 6, pp. 1590–1607, 1992.

——, "Confinement of reinforced concrete columns with welded wire fabric," *ACI Structural Journal*, vol. 86, no. 5, pp. 615–623, 1986.

T. Salonikios, A. Kappos, I. Tegos, and G. Penelis, "Cyclic load behavior of low-slenderness reinforced concrete walls: Design basis and test results," *ACI Structural Journal*, vol. 79, no. 1, pp. 13–27, 1996.

A. Saritas, "Mixed formulation frame element for shear critical steel and reinforced concrete members," Ph.D. dissertation, Dept. of Civil and Environmental Engineering, University of California, Berkeley, Berkeley, CA, 2006.

B. Scott, R. Park, and M. Priestley, "Stress-strain behavior of concrete confined by overlapping hoops at low and high strain rates," *ACI Journal*, vol. 79, no. 1, pp. 13–27, 1982.

M. Scott and G. Fenves, “Plastic hinge integration methods for force-based beam-column elements,” *ASCE Journal of Structural Engineering*, vol. 132, no. 2, pp. 244–252, 2006.

SEAOC, *IBC Structural/Seismic Design Manual Volume 3: Building Design Examples for Steel and Concrete*, ICC, Ed. Sacramento, CA: ICC, 2006.

——, “Reinforced concrete structures,” Structural Engineers Association of California, Sacramento, CA, Tech. Rep. Article 9.01.010, 2008.

M. Seckin, “Hysteretic behaviour of cast-in-place exterior beam-column-slab subassemblies,” Ph.D. dissertation, Dept. of Civil Engineering, University of Toronto, Toronto, ON, 1981.

K. Shiu, A. Aristizabal-Ochoa, A. Fiorato, and W. Corley, “Earthquake resistant structural walls - tests of walls with and without openings,” National Science Foundation, Washington, D.C., Tech. Rep., 1981.

E. Spacone, F. Taucer, and F. Filippou, “A fiber beam-column element for seismic response analysis of reinforced concrete structures,” Earthquake Engineering Research Center, Berkeley, CA, Tech. Rep. No. UCB/EERC-91/17, 1991.

E. Spacone, V. Ciampi, and F. Filippou, “A beam element for seismic damage analysis,” Earthquake Engineering Research Center, Berkeley, CA, Tech. Rep. No. UCB/EERC-92/07, 1992.

A. Synge., T. Paulay, and M. Priestley, “Ductility of squat shear walls,” Department of Civil Engineering, University of Canterbury, Christchurch, New Zealand, Tech. Rep. Report No. 80-8, 1980.

H. Tanaka and R. Park, “Effect of lateral confining reinforcement on the ductile behavior of reinforced concrete columns,” Department of Civil Engineering, University of Canterbury, Christchurch, New Zealand, Tech. Rep. Report No. 90-2, 1990.

A. Tasnimi, “Strength and deformation of mid-rise shear walls under load reversal,” *Engineering Structures*, vol. 22, pp. 311–322, 2000.

J. Thomsen IV and J. Wallace, “Displacement-based design of RC structural walls: An experimental investigation of walls with rectangular and t-shaped cross sections,” Department of Civil Engineering, Clarkson University, Potsdam, NY, Tech. Rep. No. CU/CEE-95/06, 1995.

——, “Displacement-based design of slender reinforced concrete structural walls - experimental verification,” *ASCE Journal of Structural Engineering*, vol. 130, no. 4, pp. 618–630, 2004.

A. Tola, “Development of a comprehensive linear response history analysis procedure for seismic load analysis,” MS thesis, Dept. of Civil and Environmental Engineering, Virginia Polytechnic University, Blacksburg, VA, 2010.

R. Trembley, P. Leger, and Tu, “Inelastic seismic response of concrete shear walls considering p-delta effects,” *Canadian Journal of Civil Engineering*, vol. 28, no. 4, pp. 640–655, 2001.

J. Turgeon, “The seismic performance of coupled reinforced concrete walls,” MS thesis, Dept. of Civil and Environmental Engineering, University of Washington, Seattle, WA, 2011.

J. Vallenas, B. V.V., and E. Popov, “Hysteretic behavior of reinforced concrete structural walls,” Earthquake Engineering Research Center, Berkeley, CA, Tech. Rep. No. UCB/EERC-79/20, 1979.

F. Vecchio, “Finite element modeling of concrete expansion and confinement,” *ASCE Journal of Structural Engineering*, vol. 118, no. 9, pp. 2390–2406, 1992.

——, “Disturbed stress field model for reinforced concrete: Formulation,” *ASCE Journal of Structural Engineering*, vol. 126, no. 9, pp. 1070–1077, 2000.

F. Vecchio and M. Collins, “The modified compression-field theory for reinforced concrete elements subjected to shear,” *ACI Journal*, vol. 83, no. 2, pp. 219–231, 1986.

——, “Response of reinforced concrete to in-plane shear and normal stresses,” Department of Civil Engineering, University of Toronto, Toronto, Ontario, Tech. Rep. No. 82-03, 1982.

——, “Compression response of cracked reinforced concrete,” *ASCE Journal of Structural Engineering*, vol. 119, no. 12, pp. 3590–3610, 1993.

F. Vecchio, D. Lai, W. Shim, and J. Ng, “Disturbed stress field model for reinforced concrete: Validation,” *ASCE Journal of Structural Engineering*, vol. 127, no. 4, pp. 350–358, 2001.

A. Vulcano, V. Bertero, and V. Colotti, “Analytical modeling of RC structural walls,” in *Proceedings*, 1988, pp. 41–46.

J. Waugh, “Nonlinear analysis of T-shaped concrete walls subjected to mulit-directional displacements,” Ph.D. dissertation, Dept. of Civil and Environmental Engineering, Iowa State University, Ames, IA, 2009.

S. Wiradinata, “Behavior of squat walls subjected to load reversals,” MS thesis, Dept. of Civil Engineering, University of Toronto, Tononto, ON, 1985.

Wong and Vecchio, *VecTor2 and FormWorks Users Manual*. University of Toronto, 2006.

J. Wright and J. MacGregor, *Reinforced Concrete Mechanics and Design, 6th Edition*, P. Education, Ed. Upper Saddle River, NJ: ISBN 978-0-13-217652-1, 2012.

M. Yassin, “Nonlinear analysis of prestressed concrete structures under monotonic and cyclic loads,” Ph.D. dissertation, Dept. of Civil and Environmental Engineering, University of California, Berkeley, Berkeley, CA, 1994.

Y. Zhang and Z. Wang, “Seismic behavior of reinforced concrete shear walls subjected to high axial loading,” *ACI Structural Journal*, vol. 97, no. 5, pp. 739–750, 2000.

Chapter 9

REFERENCES

Appendix A

SPECIMEN TEST PROGRAMS

This Appendix provides a summary of the wall specimen tests reviewed and used to assess the ability of current finite elements to simulate wall behavior. As the research contained in this thesis is focused on modeling of slender walls which respond primarily in flexure, only specimens which exhibited flexural failure modes were considered for model evaluation and regularization recommendations presented in Chapters 2 and 3, respectively. In addition to exhibiting flexural failure, three additional criteria were imposed on the specimen dataset: 1) Specimens were at least 3 inches thick to ensure wall thickness would not adversely affect response, 2) sufficient data were available in the literature to fully define a numerical model and 3) sufficient data were provided in the literature to enable evaluation of simulation results. The thickness requirement was imposed because review of thin specimen data (Lefas et al, Pilakoutas et al) identified that thin walls can exhibit a splitting type failure in which vertical cracks form parallel to longitudinal reinforcement in the compression zone leading to strength deterioration and specimen failure (Figure A.1). This type of failure was only identified for specimens less than 3.0 inches thick. For specimen modeling, the data deemed necessary included concrete compressive strength, reinforcing steel data, specimen geometry, reinforcing layout and test specimen boundary conditions. For simulation results evaluation, data deemed necessary included global load-displacement response as well as discussion of the observed failure mode. A complete list of the wall specimen tests reviewed for the current research is provided in Table A.1. Experimental programs which did not meet one or more of the flexural specimen requirements are indicated by a shaded box in Table A.1.

Table A.1: Previous Wall Specimen Tests

Author	Specimens	Data				
		Shape	$M_b/(V_b l_w)$	Failure Mode	Thickness (in.)	Specimen Data
Dazio et al.	WSH1-WSH5	R	2.28	Flexure	5.91	Yes
Dazio et al.	WSH6	R	2.26	Flexure	5.91	Yes
Liu	W1, W2	R	3.13	Flexure	7.87	Yes
Lowes et al.	PW1	R	2.84	Flexure	6.00	Yes
Lowes et al.	PW2-PW4	R	2.00	Flexure	6.00	Yes
Oesterle et al.	R1, R2	R	2.35	Flexure	4.00	Yes
Oh et al.	WR20, WR10, WR0	R	2.00	Flexure	7.87	Yes
Thomsen et al.	RW1, RW2	R	3.13	Flexure	4.00	Yes
Vallenas et al.	S5, S6	R	1.60	Flexure	4.49	Yes
Lowes et al.	UW1	C	2.84	Flexure	6.00	Yes
Fardis et al.	W1-W3	C	2.60	Flexure	9.84	Yes
Beyer et al.	TUA	C	2.58	Flexure	5.91	Yes
Beyer et al.	TUB	C	2.58	Flexure	3.94	Yes
Cardenas et al.	SW1-SW3,SW6	R	2.00	Flexure	3.00	No
Cardenas et al.	SW4, SW5	R	1.00	Shear	3.00	No
Barda et al.	B1-B6	F	0.50	Shear	4.00	Yes
Barda et al.	B7	F	0.25	Shear	4.00	Yes
Barda et al.	B8	F	1.00	Shear	4.00	Yes
Lefas et al.	SW11-SW17	R	1.10	Shear	2.76	Yes
Lefas et al.	SW21-SW26	R	2.11	Flexure	2.76	Yes
Lefas et al.	SW31-SW33	R	2.11	Flexure	2.76	Yes
Massone et al.	WP5-WP9	R	0.44	Shear	6.00	Yes
Oesterle et al.	B1-B9	B	2.35	Shear	4.00	Yes
Palermo et al.	DP1-2	F	0.81	Shear	2.95	Yes
Pilakoutas et al.	SW4-SW9	R	2.36	Flexure/Shear	2.36	Yes
Synge et al.	W1, W2	R	0.57	Shear	3.94	Yes
Synge et al.	W3, W4	F	0.57	Shear	3.94	Yes
Tasnimi	T1-T4	R	2.20	Flexure	1.97	Yes
Whittaker et al.	SW1	R	0.94	Shear	0.94	Yes
Whittaker et al.	SW2-SW4	R	0.54	Shear	0.94	Yes
Whittaker et al.	SW5-SW7	R	0.33	Shear	0.94	Yes
Wiradinata et al.	W1	R	0.58	Shear	3.94	Yes
Wiradinata et al.	W2	R	0.33	Shear	3.94	Yes

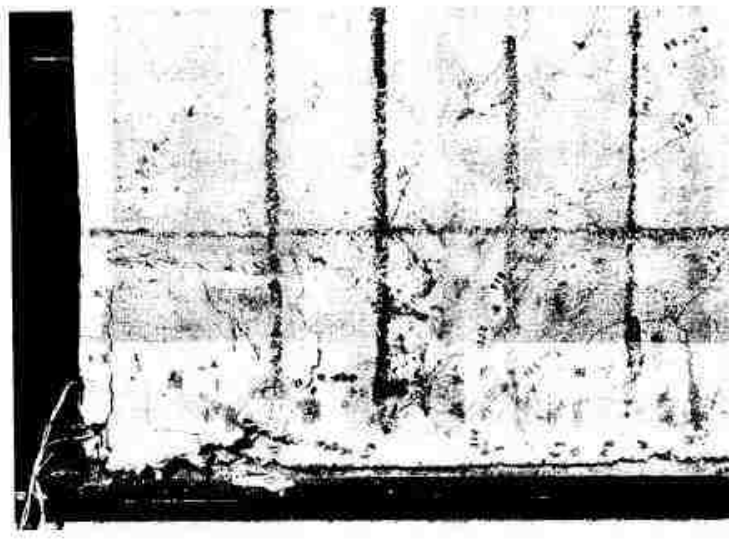

Figure A.1: Splitting Failure Mode (Lefas et al. 1990)

A.1 Slender Planar Wall Test Programs

A brief summary of the tested slender wall specimens and experimental results are described in this section. Prior to discussion of the experimental programs, Table A.2 provides geometric and reinforcing steel quantities for the tested specimens, Table A.3 provides a summary of pertinent experimental results and response quantities for the specimens and Table A.4 provides material and loading data used to develop finite element simulations. Parameters listed in Table A.2 to Table A.4 are defined as follows:

- l_w = horizontal length of wall parallel to the web.
- t = wall thickness.
- H = specimen height.
- h_{eff} = effective loading height (i.e. - shear span).
- ρ_{be} = longitudinal reinforcement ratio for at wall end.

- ρ_v = longitudinal reinforcement ratio in wall web.
- $\rho_{v,all}$ = total gross longitudinal reinforcement ratio
- ρ_{vol} = volumetric reinforcement ratio for wall end region.
- ρ_t = transverse reinforcement ratio in wall web.
- $M_b/(V_b l_w)$ = effective lateral loading ratio, where M_b/V_b is the ratio of base moment to base shear.
- M_y = yield moment strength for the base section determined by moment-curvature analysis, defined by first yield of the extreme tension steel layer. Calculated using reported material strengths but without strain hardening.
- M_n = nominal moment strength for the base section determined by moment-curvature analysis, defined by extreme compression fiber strain reaching a strain value of -0.003. Calculated using reported material strengths but without strain hardening.
- $M_{b,max}$ = maximum base moment resisted by the wall.
- $V_{n,pr}$ = nominal shear strength of the wall section per ACI 318 (2011). Calculated using reported material strengths.
- $V_{b,max}$ = maximum base shear resisted by the wall.
- Δ_y = specimen yield drift. Calculated as the drift associated with the base moment reaching M_y.
- Δ_u = specimen drift capacity. Defined as the drift at which the lateral load carrying capacity of the wall dropped to 80% of the historic maximum, for drift demands in excess of historic drift demands.
- f'_c = compressive concrete strength.

- $f_{y,be}$ = yield strength of longitudinal boundary element reinforcing steel.
- $E_{s,be}$ = Elastic modulus of longitudinal boundary element reinforcing steel.
- $f_{u,be}$ = ultimate strength of longitudinal boundary element reinforcing steel.
- $\epsilon_{u,be}$ = rupture strain of longitudinal boundary element reinforcing steel.
- $f_{y,v}$ = yield strength of longitudinal web reinforcing steel.
- $E_{s,v}$ = Elastic modulus of longitudinal web reinforcing steel.
- $f_{u,v}$ = ultimate strength of longitudinal web reinforcing steel.
- $\epsilon_{u,v}$ = rupture strain of longitudinal web reinforcing steel.
- Axial Load = axial load, including self-weight, applied to the specimen.

Specimen results for the 21 slender wall specimens from Table A.1 are discussed in this section.

Table A.2: Wall Specimen Data Summary

ID	Author	Geometry				Reinforcing Steel				
		l_w	t	H	h_{eff}	ρ_{be}	ρ_v	$\rho_{v,all}$	ρ_{vol}	ρ_t
		in.	in.	in.	in.	%	%	%	%	%
WSH1	Dazio, et al.	78.7	5.91	158.7	179.5	1.57	0.30	0.56	1.01	0.25
WSH2	Dazio, et al.	78.7	5.91	158.7	179.5	1.57	0.30	0.56	1.01	0.25
WSH3	Dazio, et al.	78.7	5.91	158.7	179.5	1.74	0.54	0.85	0.96	0.25
WSH4	Dazio, et al.	78.7	5.91	158.7	179.5	1.74	0.54	0.85	0.00	0.25
WSH5	Dazio, et al.	78.7	5.91	158.7	179.5	0.77	0.27	0.40	0.75	0.25
WSH6	Dazio, et al.	78.7	5.91	158.7	177.9	1.74	0.54	0.85	1.44	0.25
W1	Liu	47.2	7.78	147.6	147.6	3.07	0.34	1.24	2.26	0.40
W2	Liu	47.2	7.78	147.6	147.6	3.07	0.34	1.24	2.26	0.47
PW1	Lowes, et al.	120.0	6.00	144.0	340.8	3.50	0.28	1.35	1.24	0.28
PW2	Lowes, et al.	120.0	6.00	144.0	249.6	3.50	0.28	1.35	1.24	0.28
PW3	Lowes, et al.	120.0	6.00	144.0	240.0	1.86	1.57	1.68	1.37	0.28
PW4	Lowes, et al.	120.0	6.00	144.0	240.0	3.50	0.28	1.35	1.24	0.28
RW1	Thomsen, et al.	48.0	4.00	144.0	150.0	2.95	0.33	1.15	0.78	0.33
RW2	Thomsen, et al.	48.0	4.00	144.0	150.0	2.95	0.33	1.15	1.17	0.33
S5	Vallenas, et al.	95.0	4.49	120.0	151.6	5.66	0.55	1.73	0.84	0.55
S6	Vallenas, et al.	95.0	4.49	120.0	151.6	5.66	0.55	1.73	0.84	0.55
WR20	Oh, et al.	59.1	7.87	78.7	118.1	1.27	0.32	0.62	1.43	0.28
WR10	Oh, et al.	59.1	7.87	78.7	118.1	1.27	0.32	0.62	2.85	0.36
WR0	Oh, et al,	59.1	7.87	78.7	118.1	1.27	0.32	0.62	0.00	0.28
R1	Oesterle, et al,	75.0	4.00	176.0	180.0	1.47	0.28	0.49	0.80	0.31
R2	Oesterle, et al,	75.0	4.00	176.0	180.0	4.00	0.28	1.00	4.41	0.31

Table A.3: Specimen Experimental Results

ID	Author	Loading	Flexural Data				Shear Data				Drift Data		Failure Mode
		$\frac{M_b}{V_b l_w}$	M_y	M_n	$M_{b,max}$	$\frac{M_{b,max}}{M_n}$	$V_{n,pr}$	$V_{b,max}$	v_{max}	$\frac{V_{b,max}}{V_{n,pr}}$	Δ_y	Δ_u	
			kip-ft	kip-ft	kip-ft		kip	kip			%	%	
WSH1	Dazio, et al.	2.28	930	1100	1130	1.03	173.5	75.5	2.01	0.44	0.24	1.04	BR
WSH2	Dazio, et al.	2.28	960	1085	1210	1.12	153.0	80.9	2.27	0.53	0.27	1.75	BR
WSH3	Dazio, et al.	2.28	1140	1390	1530	1.10	152.6	102.4	2.92	0.67	0.32	2.07	BR
WSH4	Dazio, et al.	2.28	1130	1400	1480	1.06	159.2	99.2	2.77	0.62	0.29	1.60	CB
WSH5	Dazio, et al.	2.28	1210	1350	1460	1.08	156.9	97.4	2.81	0.62	0.20	1.52	BR
WSH6	Dazio, et al.	2.26	1530	1810	2010	1.11	163.2	135.4	3.58	0.83	0.31	2.04	CB
W1	Liu	3.13	615	740	725	0.98	149.9	58.8	2.31	0.39	0.64	2.98	CB
W2	Liu	3.13	650	790	765	0.97	190.7	62.1	1.67	0.33	0.55	2.91	BR
PW1	Lowes, et al.	2.84	4260	4930	5190	1.22	256.8	182.8	3.51	0.71	0.38	1.53	BR
PW2	Lowes, et al.	2.08	4880	5590	6080	1.25	262.7	292.2	5.31	1.11	0.45	1.50	CB
PW3	Lowes, et al.	2.00	2960	3880	4480	1.51	254.2	224.1	4.41	0.88	0.24	1.22	CB
PW4	Lowes, et al.	2.00	3660	4290	4360	1.19	246.7	217.9	4.63	0.88	0.40	1.01	CB
RW1	Thomsen, et al.	3.13	330	390	420	1.07	67.2	33.4	2.57	0.50	0.48	2.26	BR
RW2	Thomsen, et al.	3.13	330	385	450	1.16	68.1	35.7	2.65	0.52	0.55	2.35	CB
S5	Vallenas, et al.	1.60	1880	2200	2600	1.18	232.8	205.5	6.81	0.88	0.31	1.47	CB
S6	Vallenas, et al.	1.60	1880	2200	2450	1.12	233.0	194.3	6.42	0.83	0.32	1.65	CB
WR20	Oh, et al.	2.00	790	875	970	1.11	130.1	98.3	3.00	0.76	0.35	2.82	CB
WR10	Oh, et al.	2.00	795	880	950	1.08	150.5	96.7	2.87	0.64	0.47	2.82	CB
WR0	Oh, et al.	2.00	790	870	940	1.08	128.9	95.4	2.97	0.74	0.52	2.14	CB
R1	Oesterle, et al.	2.40	295	350	410	1.17	118.7	27.5	1.1	0.23	0.17	2.52	BR
R2	Oesterle, et al.	2.40	510	615	755	1.23	121.4	50.4	2.0	0.42	0.33	3.25	BR

Table A.4: Specimen Simulation Parameters

ID	Material									Loading
	f'_c	$f_{y,be}$	$E_{s,be}$	$f_{u,be}$	$\epsilon_{u,be}$	$f_{y,v}$	$E_{s,v}$	$f_{u,v}$	$\epsilon_{u,v}$	Axial Load
	psi	ksi	ksi	ksi	mm/mm	ksi	ksi	ksi	mm/mm	kips
WSH1	6526	79.4	29000	89.9	0.05	84.6	29000	87.1	0.02	166.3
WSH2	5874	84.6	29000	108.4	0.08	70.3	29000	77.5	0.06	171.3
WSH3	5685	87.2	29000	105.2	0.08	82.6	29000	101.6	0.07	168.3
WSH4	5932	83.5	29000	97.9	0.07	84.7	29000	103.6	0.08	173.3
WSH5	5555	84.7	29000	103.6	0.08	75.3	29000	81.0	0.05	354.2
WSH6	6613	83.5	29000	97.9	0.07	84.7	29000	103.6	0.08	349.7
W1	4801	66.4	29000	91.4	0.18	67.4	29000	84.2	0.17	135.0
W2	10245	66.4	29000	91.4	0.18	67.4	29000	84.2	0.17	135.0
PW1	5231	84.0	29000	100.8	0.12	75.7	29000	77.0	0.06	373.0
PW2	5843	84.0	29000	100.8	0.12	75.7	29000	77.0	0.06	560.0
PW3	4980	51.3	29000	77.9	0.20	51.3	29000	77.9	0.20	374.0
PW4	4272	67.1	29000	109.5	0.12	75.7	29000	77.0	0.06	374.0
RW1	4580	63.0	29000	93.0	0.10	65.0	29000	85.0	0.08	92.4
RW2	4925	63.0	29000	93.0	0.10	65.0	29000	85.0	0.08	87.4
S5	5004	69.9	29000	99.6	0.15	73.5	29000	105.9	0.12	103.0
S6	5033	69.9	29000	99.6	0.15	73.5	29000	105.9	0.12	103.0
WR20	4960	65.1	29000	89.5	0.15	49.6	29000	64.5	0.18	240.0
WR10	5250	65.1	29000	89.5	0.15	49.6	29000	64.5	0.18	240.0
WR0	4772	65.1	29000	89.5	0.15	49.6	29000	64.5	0.18	240.0
R1	6490	74.2	29000.	111.0	0.18	75.7	29000.	101.5	0.18	0.0
R2	6735	65.3	29000.	102.7	0.18	77.6	29000.	100.2	0.18	0.0

A.1.1 Dazio et al.

Dazio, et al. tested a series of six 1/2-scale structural walls specimens. The purpose of the experimental program was to investigate the performance of wall designs typical for moderate areas of seismicity in Central Europe. The focus of the investigation was on the mechanical properties and amount of reinforcement and also the applied axial load. The specimens were intended to represent the lower portion of a structural wall located within a six-story reference building. The specimen height was taken as 45% of the building height;

this height equated to the lowest shear span (considering higher mode effects) determined through analytical studies. Lateral loading was applied by actuators located a distance of 179.5 inches above the wall base for specimens WSH1-WSH5, the actuator height was slightly lowered to 178.0 inches for specimen WSH6 (Figure A.2). All specimens were tested cyclically, with two cycles of full load reversal applied at increasing drift demand levels. For drift demands less than or equal to the theoretical yield drift, Δ_y, loading demands were force-controlled. Once the specimen drift reached Δ_y, subsequent cycles were displacement-controlled and the target drift was increased in magnitude by Δ_y. Axial load was applied to all specimens using unbonded post-tensioning; axial load was applied as load step 1 (i.e. - prior to lateral loading) and was held constant throughout the lateral loading protocol. The main differences beween specimens was 1) the amount of provided longitudinal reinforcement, 2) mechanical properties of reinforcement and 3) the applied axial load. All specimens had concentrated boundary element reinforcement at the wall ends, and all specimens except WSH4 were constructed with closely spaced transverse confining reinforcement. WSH1 and WSH2 were constructed with low-ductility reinforcing to assess the impact of such steel on wall performance. Strains at failure for the steel used for WSH1 were approximately half the value as for the other wall specimens. Construction details of the individual specimen wall cross-sections are provided in Figure A.3 and Figure A.4.

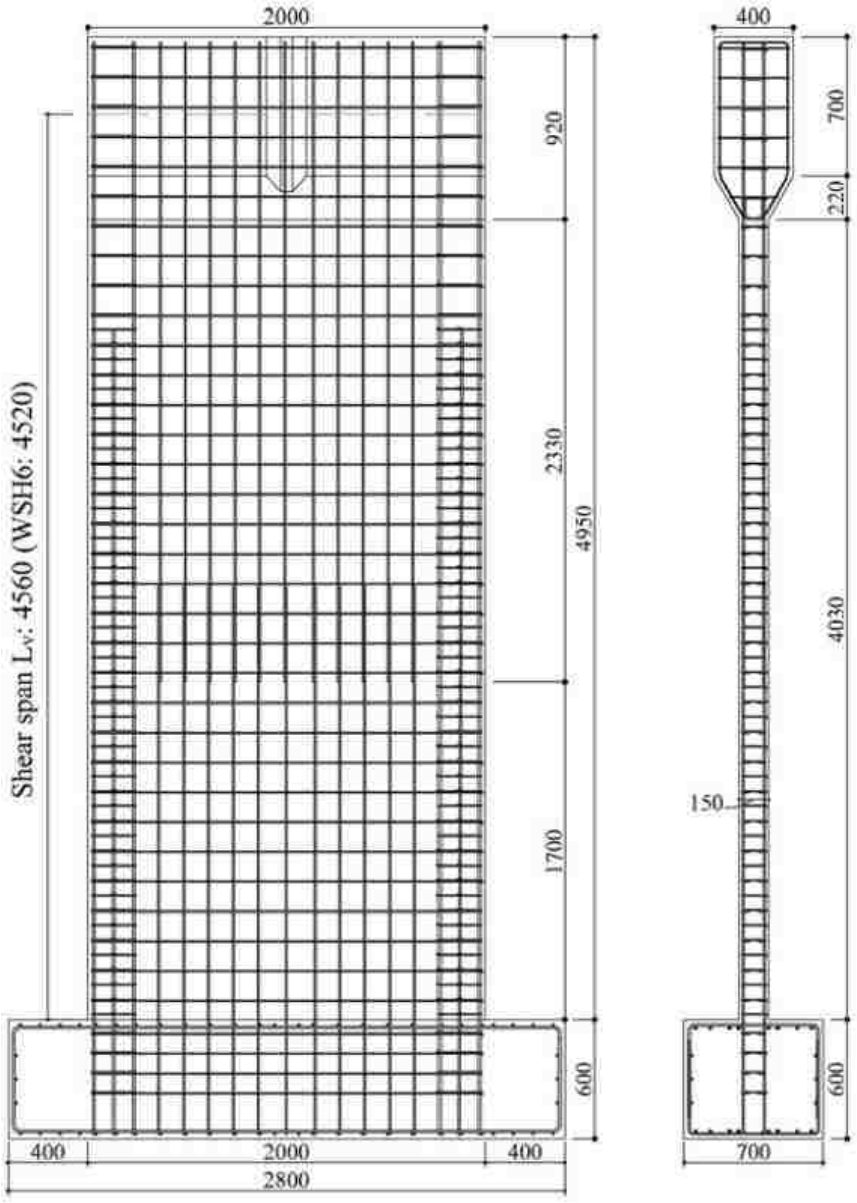

Figure A.2: Dazio Specimen Geometry (dimensions in mm) (Dazio et al., 2007)

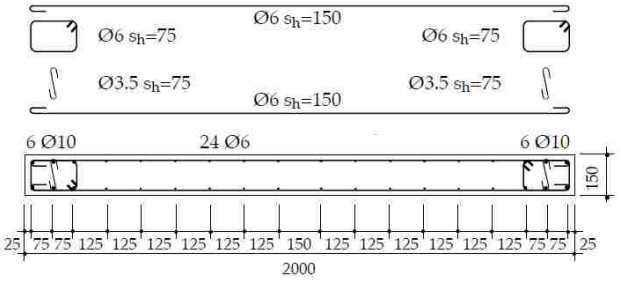

(a) WSH1

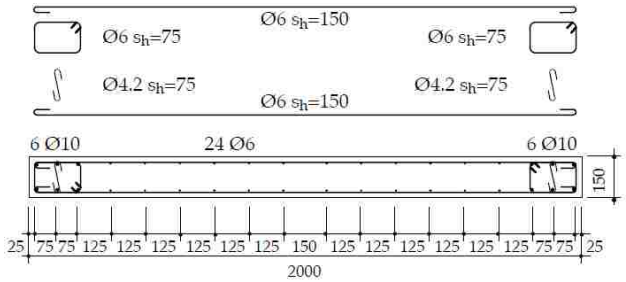

(b) WSH2

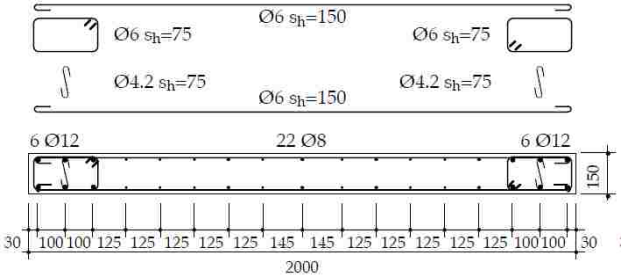

(c) WSH3

Figure A.3: Dazio et al. Specimen Sections (dimensions in mm) (Dazio et al., 2007)

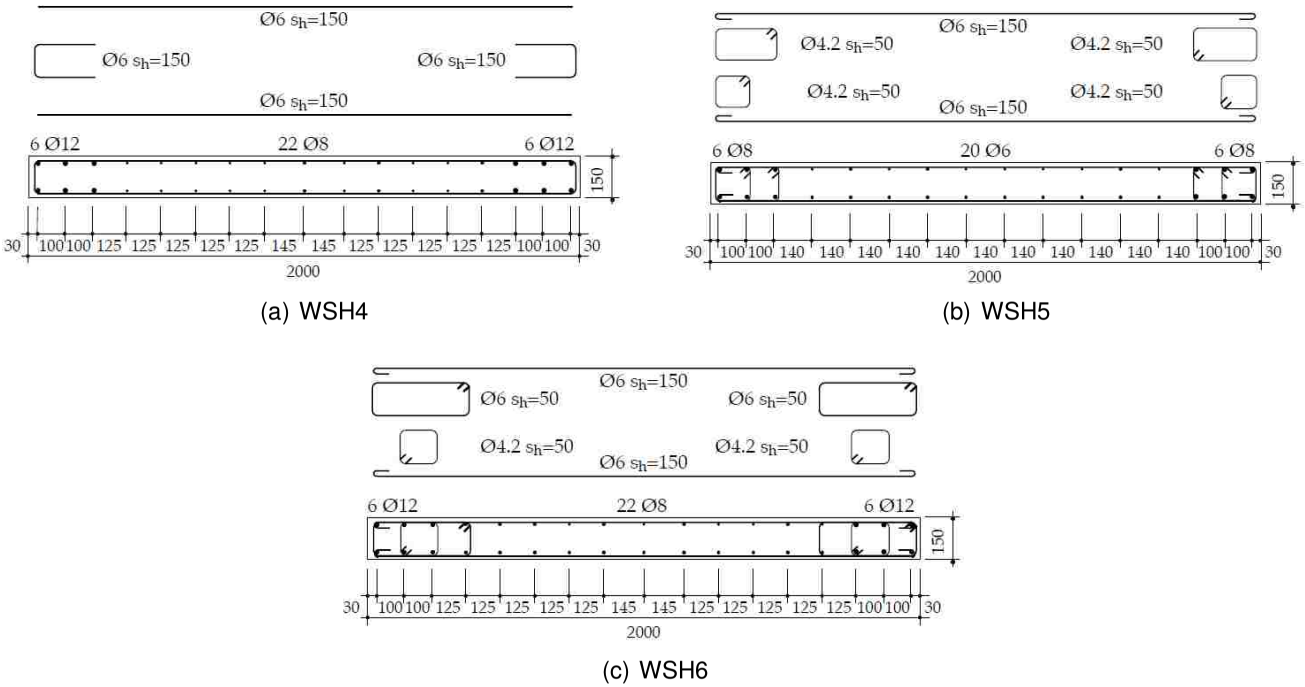

Figure A.4: Dazio et al. Specimen Sections (dimensions in mm) (Dazio et al., 2007)

Specimen WSH1 achieved peak strength at a lateral drift of 1.04%. The maximum specimen strength was 75.5 kips, which corresponded to a shear stress demand, v_{max}, of $2.01\sqrt{f'_c(psi)}A_{cv}$ and a shear demand to capacity ratio, $V_{b,max}/V_{n,pr}$ of 0.44 using reported material strengths (f'_c = 6530 psi and f_{yt} = 84600 psi) and ACI 318 (2011) Equation 21-7. Based on strain gauge measurement, first yield of the specimen occurred at a drift of 0.18% and a shear stress demand of $1.5\sqrt{f'_c}A_{cv}$. WSH1 failed due to rupture of longitudinal reinforcement. Rupture of the vertical web reinforcement occurred at a drift of 0.68% followed by rupture of boundary element steel at a drift of 1.04%. Rupture of the boundary element steel decreased the specimen resistance to below 80% of the historic maximum and testing was ended.

Specimen WSH2 achieved peak strength at a lateral drift of 1.38%. The maximum specimen strength was 80.9 kips, which corresponded to a shear stress demand of $2.27\sqrt{f'_c}A_{cv}$ and a shear demand to capacity ratio of 0.53 (f'_c = 5870 psi and f_{yt} = 70300 psi). Based on strain gauge measurement, first yield of the specimen was reported at a drift of 0.17% and a shear stress demand of $1.6\sqrt{f'_c}A_{cv}$. WSH2 failed due to rupture of boundary element longitudinal reinforcement which occurred after significant buckling. Rupture of several vertical web bars occurred at a drift of 1.16% follwed by buckling and rupture of boundary element steel which occurred at a drift of 1.38%.

Specimen WSH3, which used reinforcing steel with mechanical properties similar to those specified for full-size ductile Central European wall design, achieved peak strength at a lateral drift of 2.03%. The maximum specimen strength was 102.4 kips, which corresponded to a shear stress demand of $2.92\sqrt{f'_c}A_{cv}$ and a shear demand to capacity ratio of 0.67 (f'_c = 5690 psi and f_{yt} = 70900 psi). Based on strain gauge measurement, first yield of the specimen was reported at a drift of 0.25% and a shear stress demand of $1.9\sqrt{f'_c}A_{cv}$. This specimen failed due to rupture of boundary element longitudinal reinforcement which occurred after significant buckling.

Specimen WSH4 was nearly identical to WSH3 in terms of reinforcement layout and mechanical properties except WSH4 contained no transverse hoops within the end boundary element wall region. Specimen WSH4 achieved peak strength of 99.2 kips at a lateral drift of 1.35%. This strength corresponded to a shear stress demand of $2.77\sqrt{f'_c}A_{cv}$ and

a shear demand to capacity ratio of 0.62 (f'$_c$ = 5930 psi and f$_{yt}$ = 75300 psi). Failure of specimen WSH4 was a compressive-type failure caused by crushing of the concrete at the compressive toe of the wall. Upon spalling of the toe, it was observed that reinforcement buckled immediately due to the lack of confinement ties.

Specimen WSH5 was designed to have a flexural capacity equal to WSH3, however, since WSH5 was tested under a higher axial load demand than WSH3, WSH5 was constructed using a lower amount of longitudinal reinforcement than was used to construct WSH3. Specimen WSH5 achieved peak strength of 97.4 kips at a lateral drift of 1.36$\%$. This strength corresponded to a shear stress demand of 2.81$\sqrt{f'_c}$A$_{cv}$ and a shear demand to capacity ratio of 0.62 (f'$_c$ = 5560 psi and f$_{yt}$ = 75300 psi). WSH5 failed due to rupture of boundary element longitudinal reinforcement which occurred after significant buckling. Concrete spalling at the wall base led to exposure of web and boundary element vertical bars. At 1.01$\%$ drift, all vertical web bars had fractured. Further loading led to buckling and fracture of boundary element reinforcement. Fracture of longitudinal boundary element reinforcement reduced specimen strength to below 80$\%$ of the historic maximum load and testing was ended.

Specimen WSH6 was designed to have the highest flexural capacity as this specimen was tested under the higher axial load demand used to test specimen WSH5 and contained the same amount of longitudinal reinforcement as specimen WSH3. Specimen WSH5 achieved peak strength of 135.4 kips at a lateral drift of 1.71$\%$. This strength corresponded to a shear stress demand of 3.58$\sqrt{f'_c}$A$_{cv}$ and a shear demand to capacity ratio of 0.83 (f'$_c$ = 6610 psi and f$_{yt}$ = 75300 psi). Based on strain gauge measurement, first yield of the specimen was reported at a lateral drift of 0.22$\%$ and a shear stress demand of 2.4$\sqrt{f'_c}$A$_{cv}$. Failure of specimen WSH6 was due to crushing of the boundary element concrete which occurred after several of the closely spaced confining hoops had fractured.

Experimental load-displacement plots for the six specimens tested by Dazio, et al. are provided in Figures A.5 and A.6.

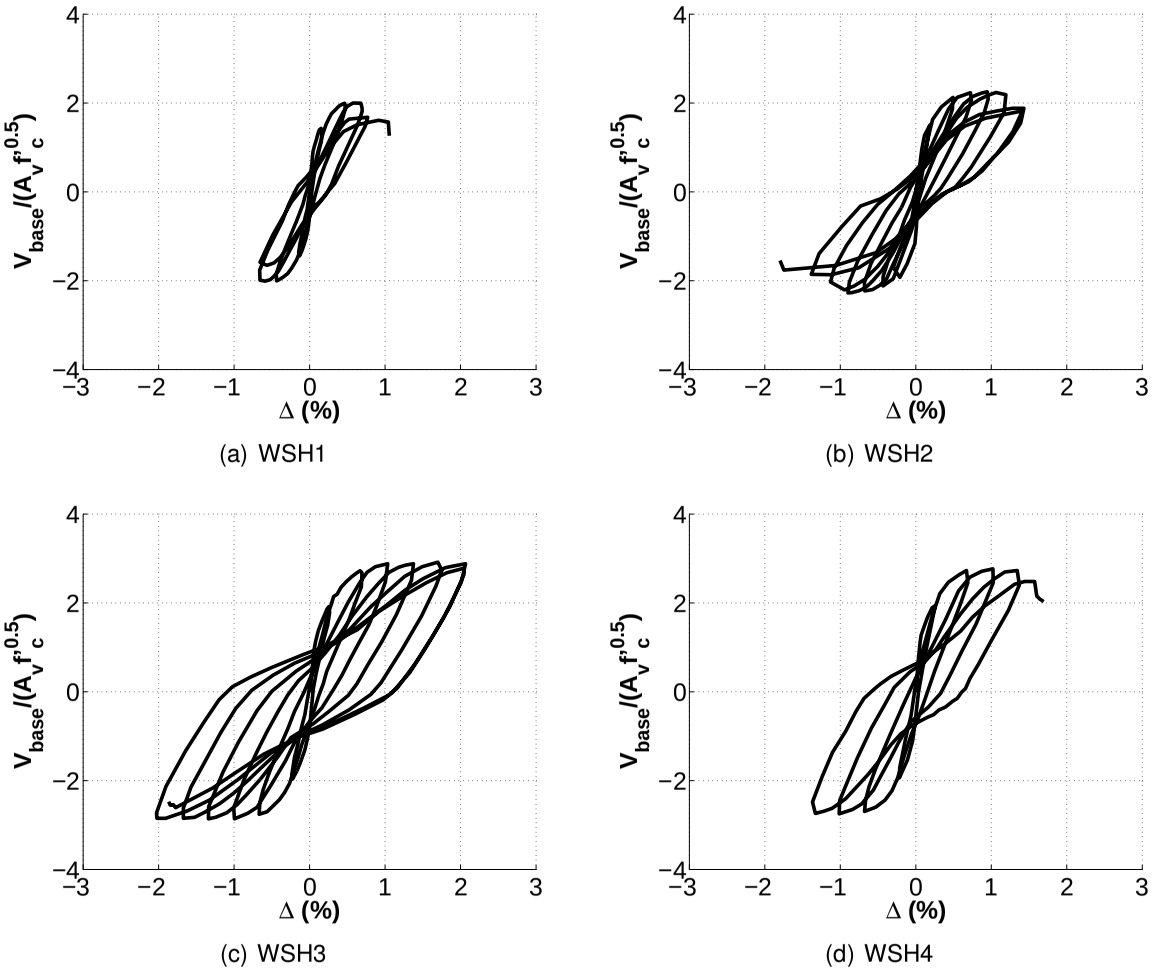

Figure A.5: Dazio et al. Test Results

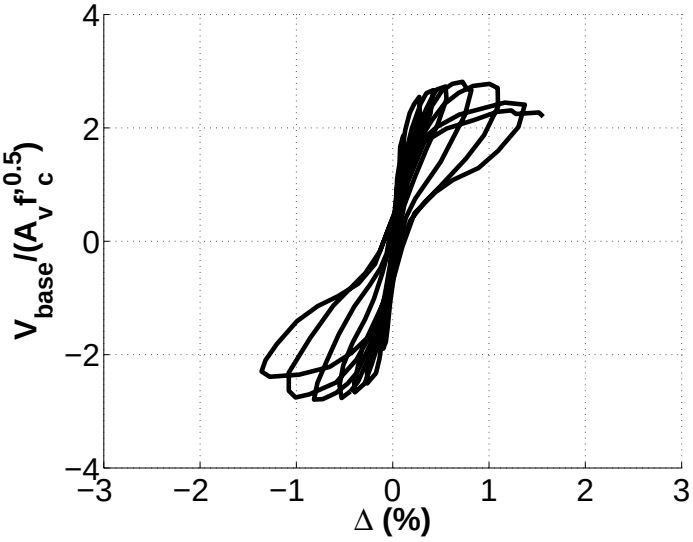

(a) WSH5

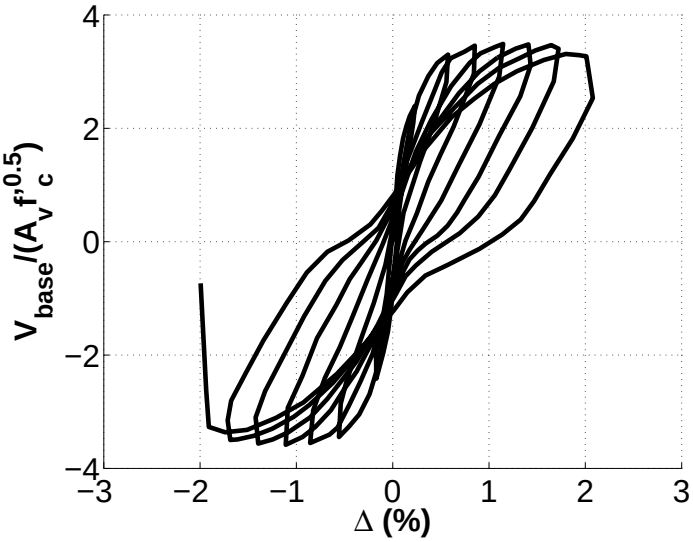

(b) WSH6

Figure A.6: Dazio et al. Test Results

A.1.2 Liu

Liu tested two rectangular walls to investigate the effect of concrete compressive strength on the response of cyclically tested shear walls. The walls were designed with heavier reinforcement concentrated at the wall ends and boundary element transverse confining reinforcement was designed in accordance with the 2004 A23.3 Canadian design standard. The walls were tested in a horizontal position and lateral loading was applied by actuators located a distance of approximately 148 inches from the wall base (Figure A.7). Both specimens were tested cyclically, with three full load reversals applied at each target drift level. Cycles were force controlled until the calculated yield drift, Δ_y was reached; beyond yield, cycles were displacement controlled with target drift levels between 1.25Δ_y and 4.00Δ_y. Axial load was applied to both specimens as load step 1 (i.e. - prior to lateral loading) and was held constant throughout the lateral loading protocol. Details of the wall cross-section are provided in Figure A.8.

Specimen W1 achieved peak strength at a drift of 1.9$\%$. The maximum specimen strength was 58.8 kips, which corresponded to a shear stress demand, v_{max}, of 2.31$\sqrt{f'_c}A_{cv}$ and a shear demand to capacity ratio, $V_{b,max}/V_{n,pr}$ of 0.39 using reported material strengths (f'_c = 4800 psi and f_{yt} = 67300 psi) and ACI 318 (2011) Equation 21-7. Failure of specimen W1 was compressive flexural failure due to combined crushing and buckling of boundary element longitudinal reinforcement. Bar buckling, caused by considerable spalling of cover concrete, was first observed at a drift of 2.6$\%$. Futher loading led to severe buckling and concrete crushing; which led to a pronounced decrease in load carrying capacity of the specimen.

Specimen W2 achieved peak strength at a drift of 1.6$\%$. The maximum specimen strength was 62.1 kips, which corresponded to a shear stress demand of 1.67$\sqrt{f'_c}A_{cv}$ and a shear demand to capacity ratio of 0.33 (f'_c = 10250 psi and f_{yt} = 67300 psi). Failure of W2 was due to rupture of longitudinal boundary element reinforcement after significant

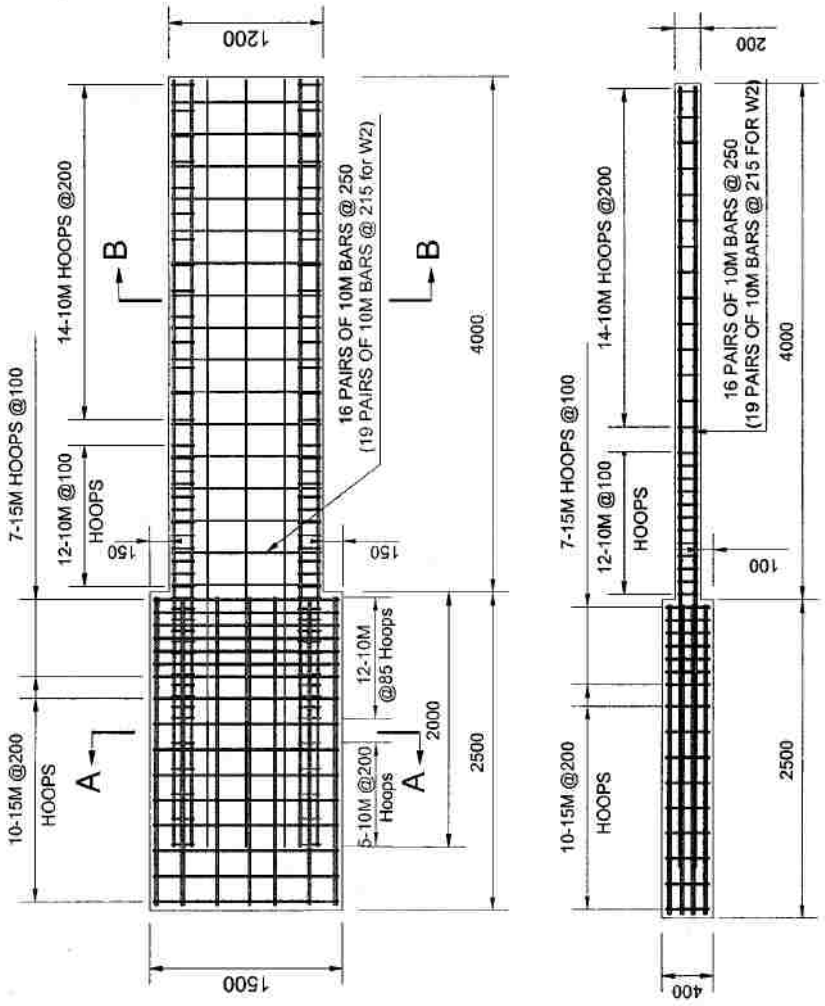

Figure A.7: Liu Specimen Geometry (dimensions in mm) (Liu 2004)

buckling of the reinforcement had been observed. Bar buckling, caused by considerable spalling of cover concrete, was first observed at a drfit of 2.9% drift.

Experimental load-displacement plots for the W1 and W2 specimens are provided in Figure A.9.

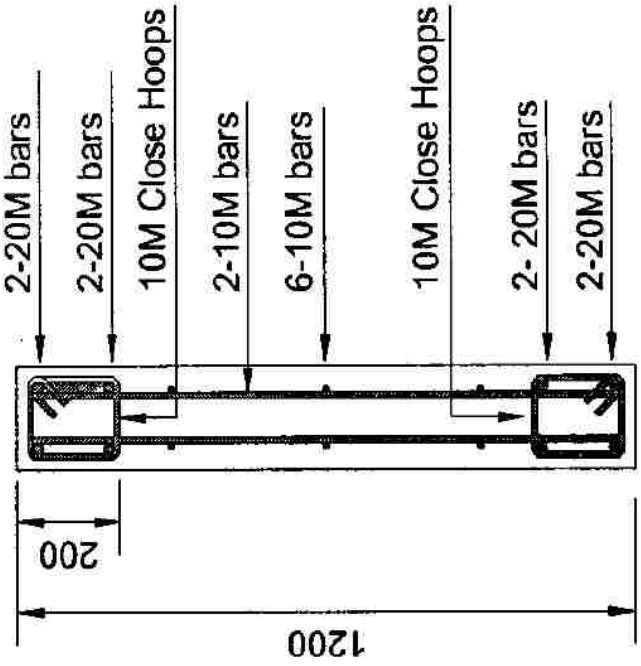

Figure A.8: Liu Specimen Base Section (dimensions in mm) (Liu 2004)

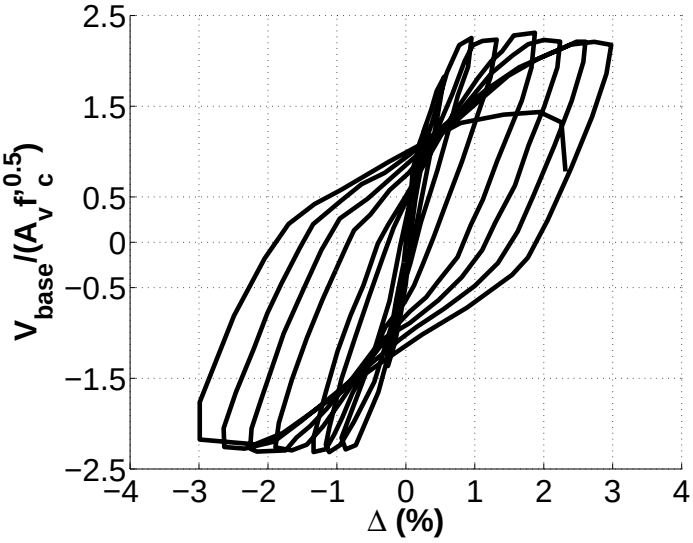

(a) WSH5

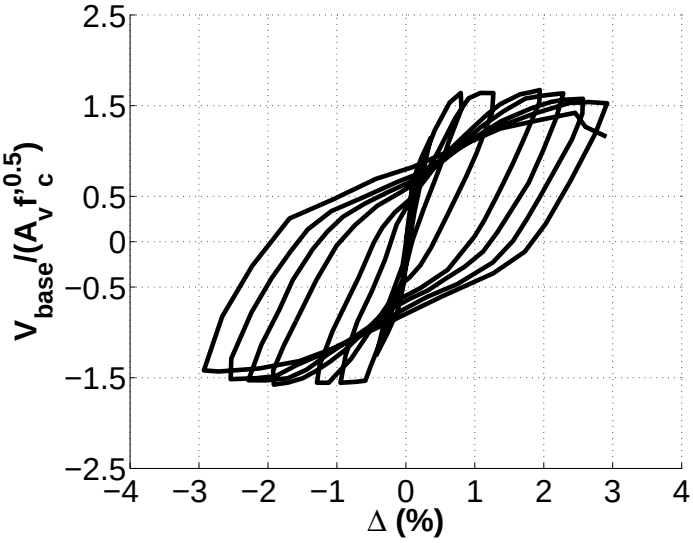

(b) WSH6

Figure A.9: Liu et al. Test Results

A.1.3 Lowes et al.

Lowes, et al. tested a series of four 1/3-scale large scale structural wall specimens with construction details representative of modern mid-rise buildings used along the west coast of the United States. Specimen construction was based on a prototype design of a structural wall providing the primary lateral force resisting system for a 10-story building; test specimens were constructed to represent the first three stories of the prototype building (Figure A.10). Loading applied to the top of the wall consisted of applied shear and in-plane moment as well as an axial compression held constant throughout the test. Applied shear, moment and axial forces were controlled by six degree-of-freedom Loading and Boundary Condition Boxes (LBCBs) uniquely available at the NEES University of Illinois testing facility. The relationship between the applied shear and bending moment applied to the top of the specimen was such that a constant effective loading height equal to either 71% or 50% of the 10-story building height was maintained throughout the experiment. An effective height of 0.71H was determined to be consistent with the ASCE 7 (2005) equivalent static load pattern for a 10-story walled building and was used to test specimend PW1. A lower effective height of 0.50H consistent with a uniform lateral load distribution applied to the building was used for specimens PW2, PW3 and PW4 to study the effects of increased shear demand on wall response. Lateral loads were applied cyclically with three full load reversals performed at increasing target drift levels. The design of the specimens was in accordance with ACI 318-05 building code requirements. Specimens PW1,PW2 and PW4 had heavier steel concentrated in boundary elements at each wall end with code-minimum vertical steel in the web. Specimen PW3 had a uniform distribution of vertical steel across the wall section, with a lower reinforcement ratio in the boundary element and a higher reinforcement ratio in the web than the other three specimens. All specimens had rectangular confinement hoops around the seven rows of bars nearest the wall edge with cross-ties providing support to interior longitudinal boundary element bars (Figures A.11 and A.12). To understand the effect of placing bar splices in the expected plastic hinge region, specimens PW1-PW3 each contain a lap splice. A detailed account of the design of the wall specimens is provided by Birely (2012).

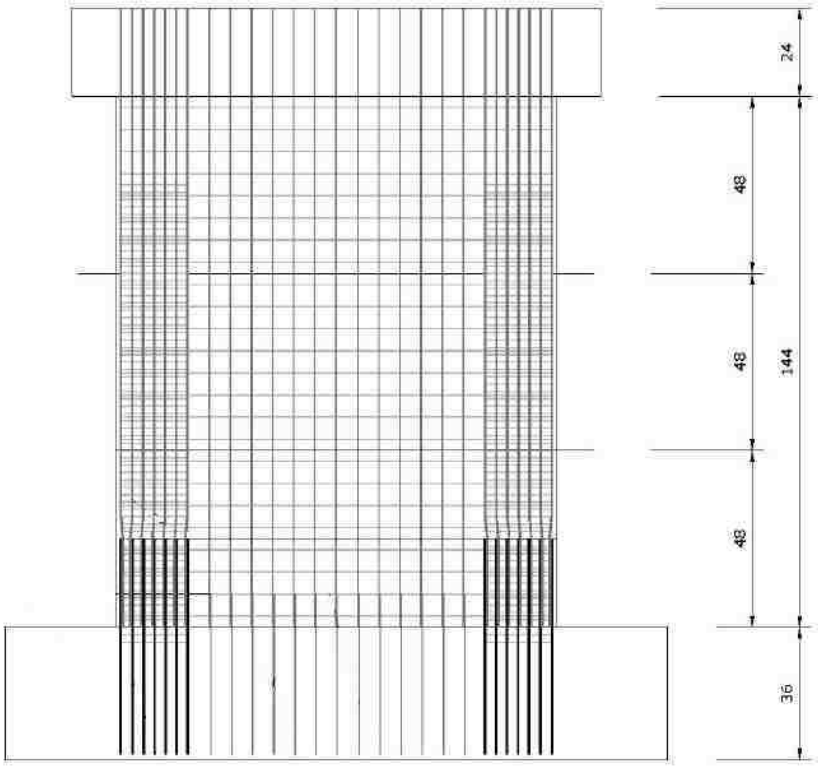

Figure A.10: Lowes et al. Specimen Geometry

Specimen PW1 achieved peak strength at a drift of 1.3%. The maximum specimen strength was 182.8 kips, which corresponded to a shear stress demand, v_{max}, of 3.51$\sqrt{f'_c}A_{cv}$ and a shear demand to capacity ratio, $V_{b,max}/V_{n,pr}$ of 0.71 using reported material strengths (f'_c = 5230 psi and f_{yt} = 75700 psi) and ACI 318 (2011) Equation 21-7. The PW1 specimen lost lateral load-carrying capacity during the second loading cycle targeting a peak drift of 1.5%. Specimen failure was due to fracture of longitudinal boundary element reinforcement at the wall-foundation interface. Per strain gauge data, first yield of the extreme longitudi-

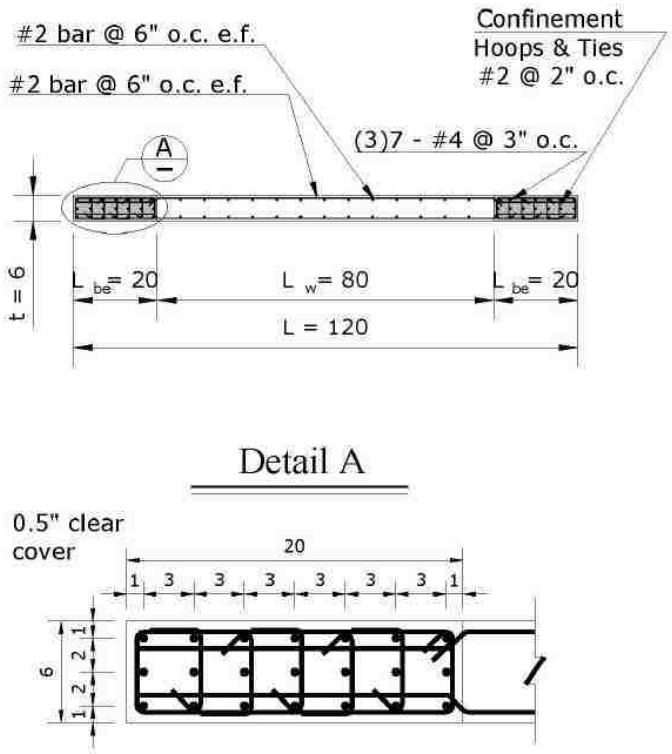

Figure A.11: Lowes et al. PW1, PW2, PW4 Specimen Base Section

nal boundary element reinforcing occurred at a drift of 0.30%; first compression yielding of longitudinal reinforcing occurred at 0.64%.

Specimen PW2 achieved peak strength at a drfit of 1.0%. The maximum specimen strength was 292.2 kips, which corresponded to a maximum shear stress demand of $5.31\sqrt{f'_c}A_{cv}$ and a shear demand to capacity ratio of 1.11 (f'$_c$ = 5840 psi and f_{yt} = 75700 psi). PW2 failed due to crushing of boundary element concrete during the first excursion to 1.5% drift. Using strain gauge measurements, tensile yield of the extreme longitudinal boundary element reinforcing occurred at a drift of 0.42%; compression yielding of longitudinal reinforcing occurred at 0.20%.

Specimen PW3 achieved peak strength at a drift of 1.0%. The maximum specimen strength was 224.1 kips, which corresponded to a maximum shear stress demand of $4.41\sqrt{f'_c}A_{cv}$ and a shear demand to capacity ratio of 0.88 (f'$_c$ = 4980 psi and f_{yt} = 75700

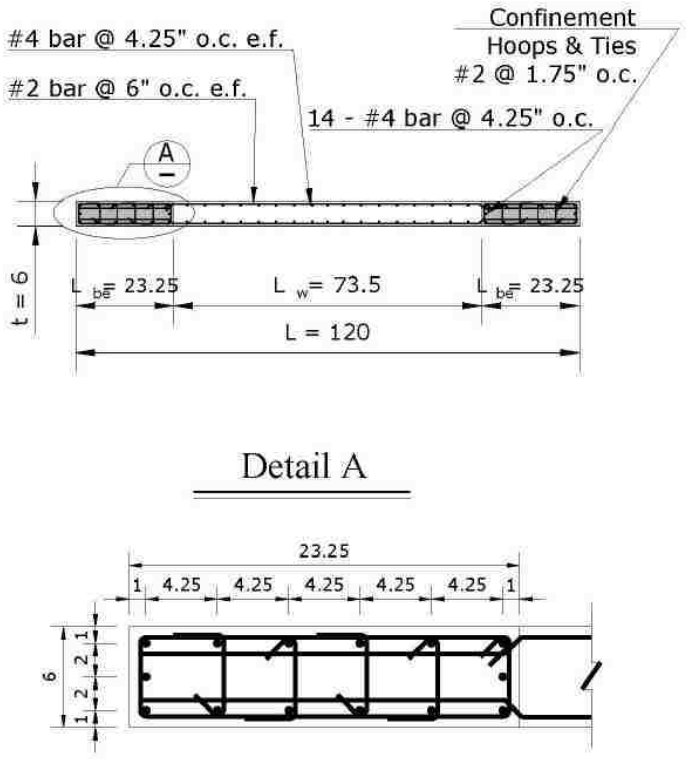

Figure A.12: Lowes et al. PW3 Specimen Base Section

psi). Failure of PW3 occurred due to crushing of boundary element concrete at a drift of 1.25% during the first cycle of loading to a target drift of 1.5%. Spalling of concrete at the boundary element initiated at a drift of 0.52%; crushing damage and bar buckling initiated at a drift of 1.0%. Using strain gauge measurements, tensile yield of the extreme longitudinal steel occurred at a drift of 0.17%; compression yielding of longitudinal reinforcing occurred at 0.32%.

Specimen PW4 achieved peak strength at 0.9% drift. The maximum specimen strength was 217.9 kips, which corresponded to a maximum shear stress demand of $4.63\sqrt{f'_c}A_{cv}$ and a shear demand to capacity ratio of 0.88 (f'_c = 4270 psi and f_{yt} = 75700 psi). Failure of PW4 occurred due to crushing of boundary element concrete during the second loading cycle to 1.0% drift. Spalling of boundary element concrete began at a drift of 0.50%; crushing damage and longitudinal bar buckling was observed to initiated at 0.75% drift.

Compression yield of longitudinal steel was measured to occur prior to tension yielding. Compression yielding of longitudinal steel occurred at 0.19% drift; first tension yield occurred at 0.30% drift.

Experimental load-displacement plots for PW1-PW4 are provided in Figure A.13.

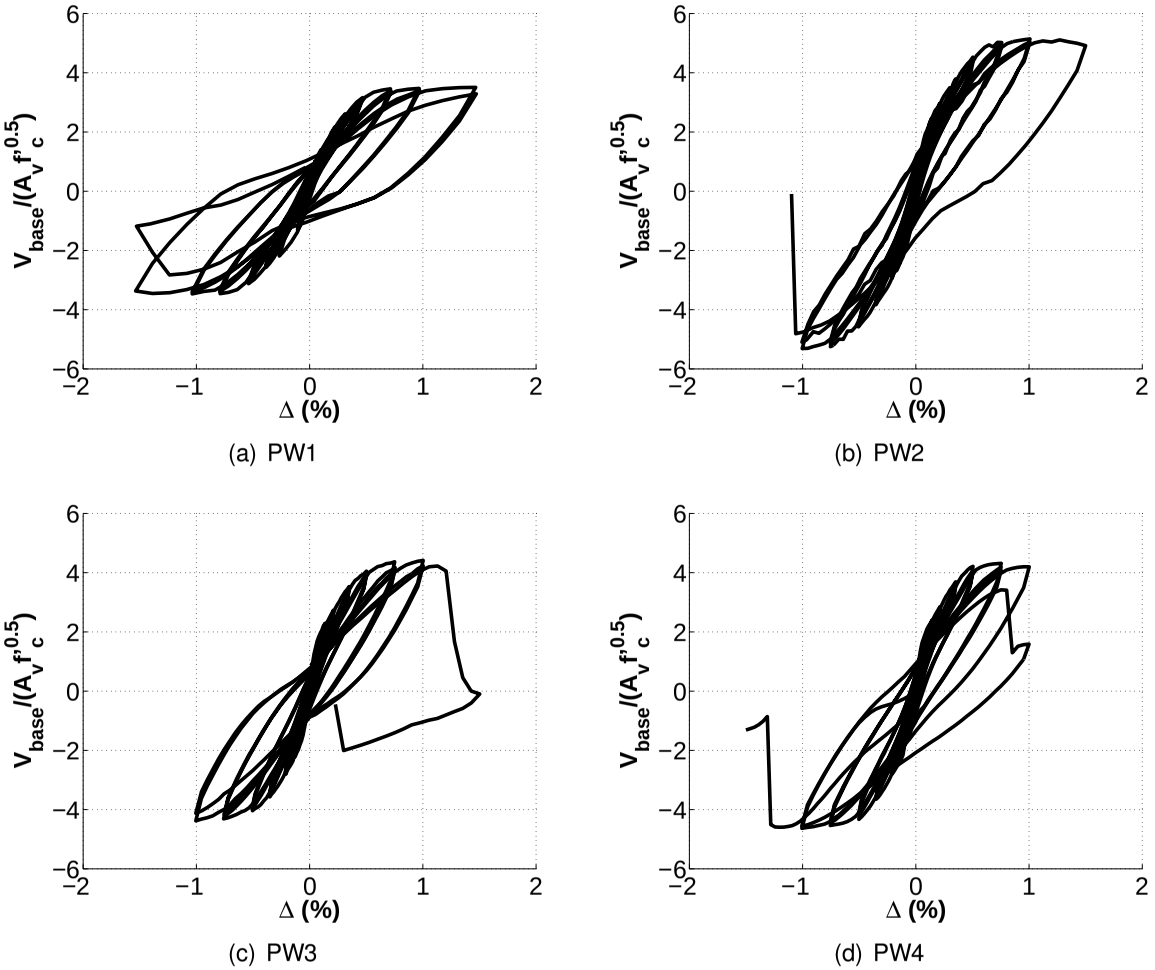

Figure A.13: Lowes et al. Test Results

A.1.4 Thompsen et al.

Thomsen and Wallace tested two 1/4-scale rectangular wall specimens to assess the impact of spacing and configuration of reinforcement on structural wall performance and to verify the displacement-based design methodology developed by Wallace (1994, 1995). Both specimens represent the lower four stories of a six story prototype building. Lateral load was applied as a single concentrated force located 150 inches above the wall base (Figure A.14), with the loading height selected to be consistent with the resultant force location for a triangular loading pattern on the 6-story prototype building. Lateral load was applied cyclically, with two complete load reversals at each target drift level. Prior to lateral loading, an axial load demand of $0.08A_g f'_c$ was applied to the specimens and was maintained constant through specimen testing. Heavily reinforced and well-confined boundary elements were provided at each end of the wall (Figure A.15). Detailing of the boundary elements was performed in accordance with displacement-based design recommendations developed by Wallace (1994, 1995). Specimen RW1 and RW2 boundary elements were detailed with approximately the same amount of volumetric reinforcing, however RW2 transverse hoops were spaced at 2 inches ($5.33d_b$) compared to the 3 inch spacing ($8d_b$) used for RW1.

Specimen RW1 achieved peak strength at a drift of 2.0%. The maximum specimen strength was 33.4 kips, which corresponded to a shear stress demand, v_{max}, of $2.57\sqrt{f'_c}A_{cv}$ and a shear demand to capacity ratio, $V_{b,max}/V_{n,pr}$ of 0.50 using reported material strengths (f'_c = 4580 psi and f_{yt} = 65000 psi) and ACI 318 (2011) Equation 21-7. First yield of the specimen was reported at a drift of 0.75% with a shear stress demand of $2.3\sqrt{f'_c}A_{cv}$. Failure of the specimen was due to rupture of longitudinal reinforcement after significant bar buckling had occurred. Minor buckling of reinforcing was first observed during the first loading cycle to 2.0% drift. During subsequent cycles, the buckling became more pronounced and fracture occurred during the first excursion targeting a peak drift of 2.5%.

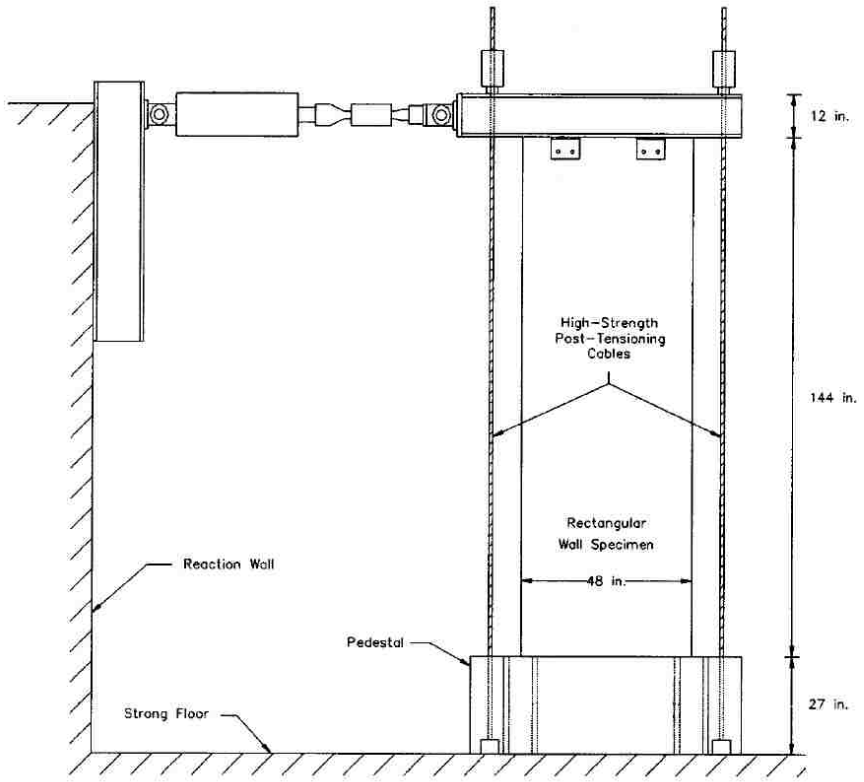

Figure A.14: Thomsen et al. Specimen Geometry (Thomsen et al., 2004)

Spalling and minor crushing at the wall base was observed to occur during the first cycle to 1.00% drift.

Specimen RW2 achieved peak strength at a drift of 2.4%. The maximum specimen strength was 35.7 kips, which corresponded to a shear stress demand of $2.65\sqrt{f'_c}A_{cv}$ and a shear demand to capacity ratio of 0.52 (f'_c = 4580 psi and f_{yt} = 65000 psi) and ACI 318 (2011). Failure of the specimen was due to buckling and crushing of the compressive boundary element, which occurred after two cycles were complete targeting 2.5% drift. At 2.5% drift, significant spalling of the concrete boundary element occurred, which led to buckling of two of the boundary element reinforcing bars. The second excursion at this drift level led to buckling of six additional boundary element bars. It was noted that core concrete crushing had begun. Testing was stopped after two cycles at 2.5% drift because

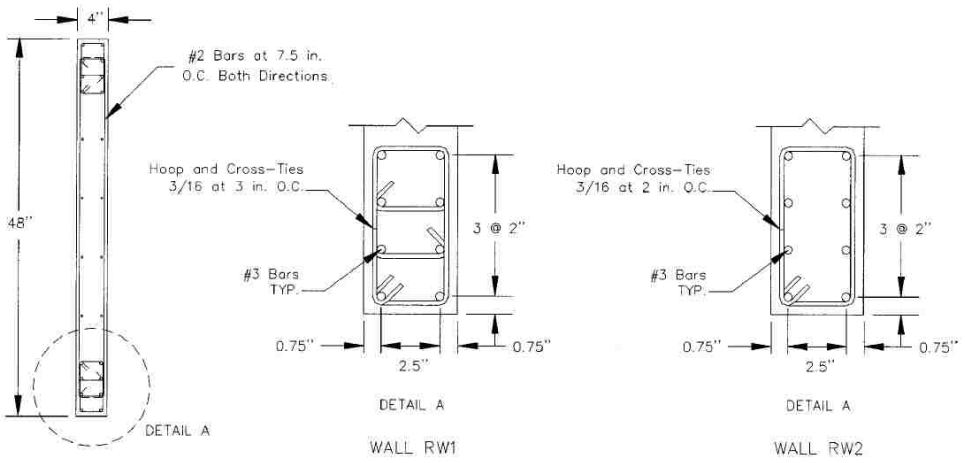

Figure A.15: Thomsen et al. Specimen Base Section (Thomsen et al., 2004)

the specimen appeared to be on the verge of collapse.

Experimental load-displacement plots for RW1 and RW2 are provided in Figure A.16.

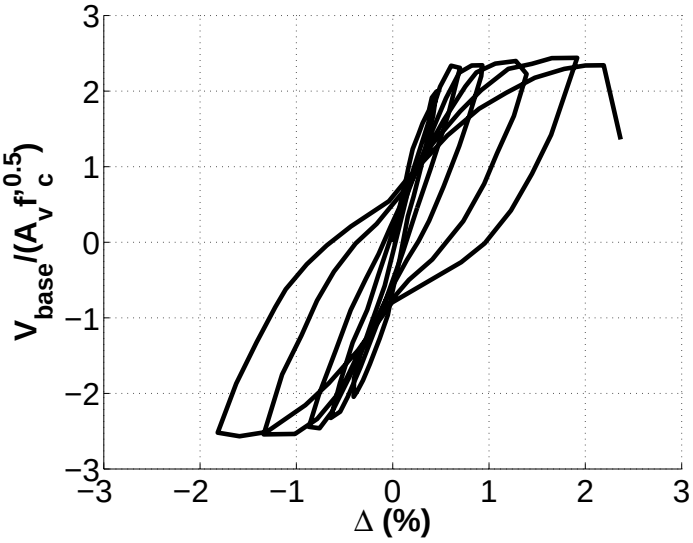

(a) RW1

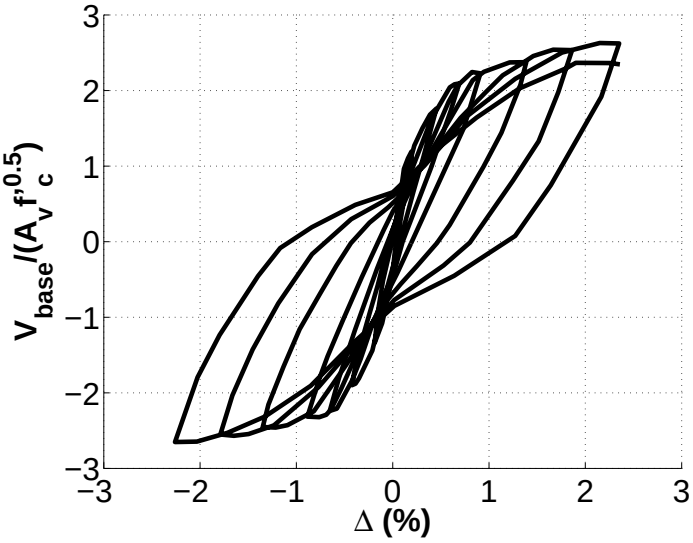

(b) RW2

Figure A.16: Thomsen et al. Test Results

A.1.5 Vallenas et al.

Vallenas, et al. tested two 1/3-scale planar walls representing the lower three stories of a seven-story prototype walled building. Loading applied to the top of each specimen consisted of an applied shear force and in-plane momenet as well as an axial compression force which remained constant through the lateral loading protocol. The effective loading height of 152 inches was selected based on dynamic analysis of the prototype building (Figure A.17). Each specimen was subjected to a different load history. Specimen S5 was loaded essentially monotonically, with drift cycles only performed in the elastic range (0.08$\%$ drift) and after significant flexural yielding has occurred (1.10$\%$). Specimen S6 was loading cyclically with three full load reversals applied at increasing target drift levels. Prior to lateral loading, an axial load demand of 0.08$A_g f'_c$ was applied to each specimen and was maintained constant throughout specimen testing. Both specimens were designed using identical cross-section configurations (Figure A.18). Heavily reinforced and well-confined boundary element regions were provided at each wall end.

Specimen S5 achieved peak strength at a drift of 2.5$\%$. The maximum specimen strength was 205.5 kips, which corresponded to a shear stress demand, v_{max}, of 6.81$\sqrt{f'_c}A_{cv}$ and a shear demand to capacity ratio, $V_{b,max}/V_{n,pr}$ of 0.88 using reported material strengths (f'_c = 5000 psi and f_{yt} = 73530 psi) and ACI 318 (2011) Equation 21-7. Failure of the specimen was due to crushing and buckling of the compression boundary element occurring after rupture of confining reinforcement. Hoop rupture reduced the wall capacity to 81$\%$ of peak strength; further loading led to buckling of several boundary element reinforcing bars, which reduced the wall capacity to 32$\%$ of peak strength. First yield of the specimen was reported a drift of 0.40$\%$ with a shear stress demand of 6.9$\sqrt{f'_c}A_{cv}$.

Specimen S6 achieved peak strength a drift of 0.83$\%$. The maximum specimen strength was 194.3 kips, which corresponded to a shear stress demand of 6.42$\sqrt{f'_c}A_{cv}$ and a shear demand to capacity ratio of 0.83 (f'_c = 5030 psi and f_{yt} = 73530 psi). Failure of the specimen

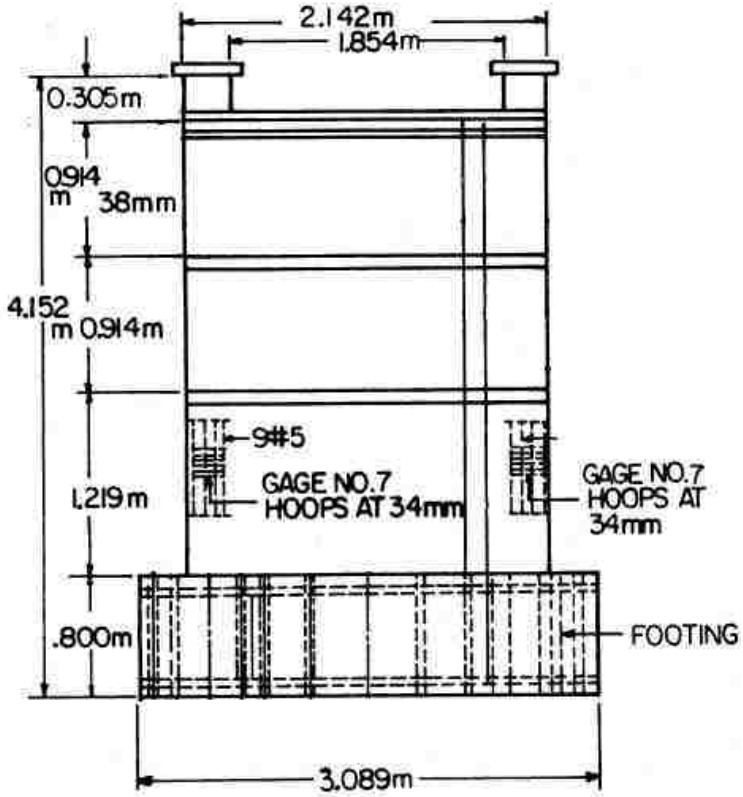

Figure A.17: Vallenas et al. Specimen Geometry (Vallenas et al., 1979)

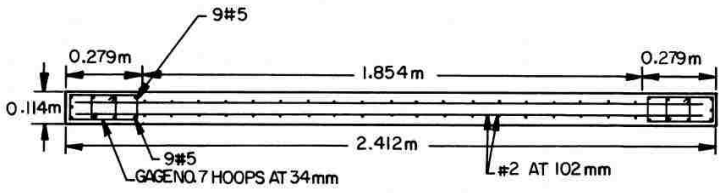

Figure A.18: Vallenas et al. Specimen Base Section (Vallenas et al., 1979)

was due to crushing and buckling of the compression boundary element. First yield of the specimen was reported at a drift of 0.42% with a shear stress demand of $6.1\sqrt{f'_c}$.

Experimental load-displacement plots for S5 and S6 are provided in Figure A.19.

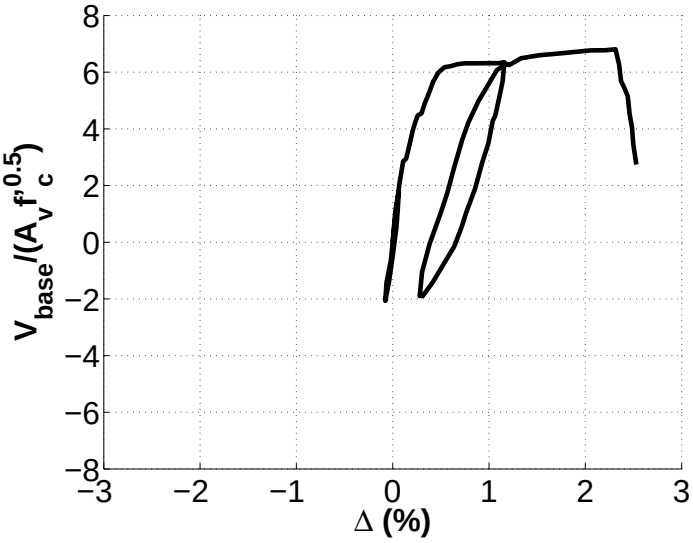

(a) S5

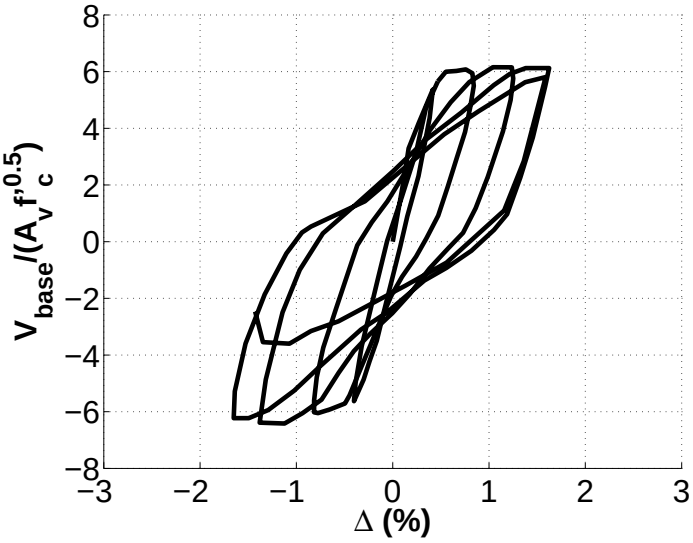

(b) S6

Figure A.19: Vallenas et al. Test Results

A.1.6 Oh et al.

Oh, et al. tested three planar structural walls to study the effects of boundary element confining details on wall response. The primary difference between the three specimens was the spacing of tranverse confining reinforcement in the heavily reinforced boundary element regions provided at the wall ends. Three tie spacings were considered with 1) 7.87 inch (200 mm;) spacing used for the WR20 specimen, 2) 3.94 (100 mm) spacing used for the WR10 specimen and 3) no ties used for the WR0 specimen. The WR20 specimen detailing was considered the baseline specimen because the 200 mm spacing was considered by the authors to be most representative of current Korean building construction practice. Specimens were tested in a vertical position, with lateral loading supplies by actuators located a distance of approximately 79 inches above the wall base (Figure A.20). All specimens were tested cyclically, with three complete load cycles performed at increasing target drift demands. Prior to lateral loading, an axial load demand of $0.10A_g f'_c$ was applied to each specimen and held constant throughout the lateral loading protocol. Besides the variation in transverse confining reinforcement spacing, the longitudinal section detailing was constant for all three specimens (Figure A.21).

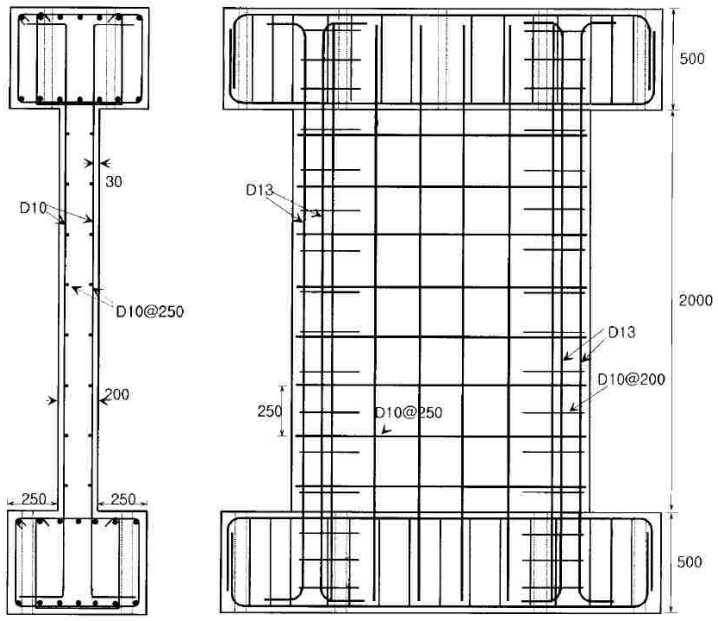

Figure A.20: Oh et al. Specimen Geometry (Oh et al., 2002)

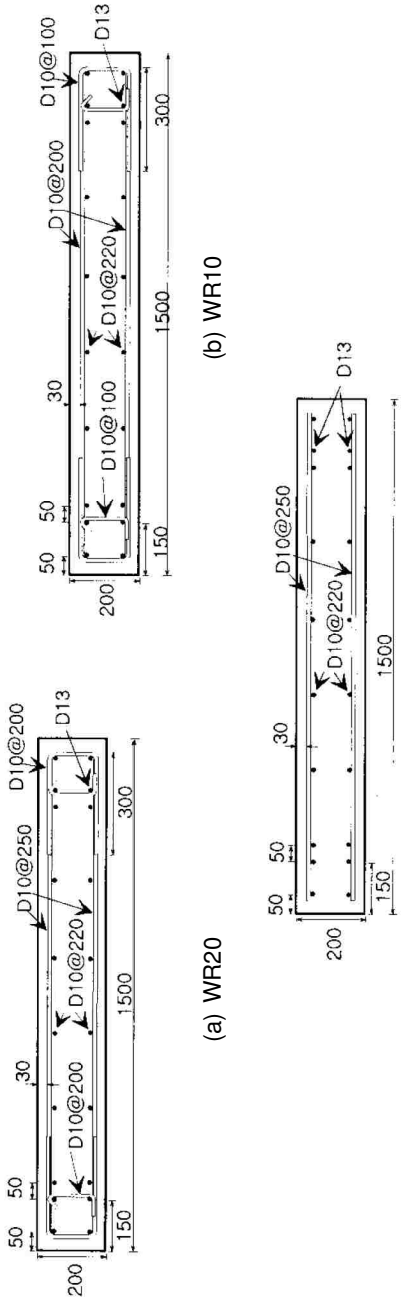

Figure A.21: Oh et al. Specimen Sections (dimensions in mm) (Oh et al., 2002)

Specimen WR20 achieved peak strength at a drift of 1.53%. The maximum specimen strength was 98.3 kips, which corresponded to a shear stress demand, v_{max}, of $3.00\sqrt{f'_c}A_{cv}$ and a shear demand to capacity ratio, $V_{b,max}/V_{n,pr}$ of 0.76 using reported material strengths (f'_c = 4960 psi and f_{yt} = 59600 psi) and ACI 318 (2011) Equation 21-7. The WR20 specimen failed due to crushing and buckling of the boundary element region at a drift of 2.72% during the first excursion to a target drift of 3.0%.

Specimen WR10 achieved peak strength at a drift of 1.92%. The maximum specimen strength was 96.7 kips, which corresponded to a shear stress demand of $2.87\sqrt{f'_c}A_{cv}$ and a shear demand to capacity ratio of 0.64 (f'_c = 5250 psi and f_{yt} = 59600 psi). The WR10 specimen failed due to crushing and buckling of the boundary element region at a drift of 2.70% during the first excursion to a target drift of 3.0%.

Specimen WR0 achieved peak strength at a drift of 1.00%. The maximum specimen strength was 95.4 kips, which corresponded to a shear stress demand of $2.97\sqrt{f'_c}A_{cv}$ and a shear demand to capacity ratio of 0.74 (f'_c = 4770 psi and f_{yt} = 59600 psi). The WR0 specimen failed due to crushing and buckling of the boundary element region at a drift of 2.14% during the first excursion to a target drift of 2.5%. For specimen WR0, which contained no transverse confinement reinforcement, both earlier strength deterioration and reduced drift capacity were observed than for confined specimens, WR10 and WR20/

Experimental load-displacement plots for WR20, WR10 and WR0 are provided in Figure A.22.

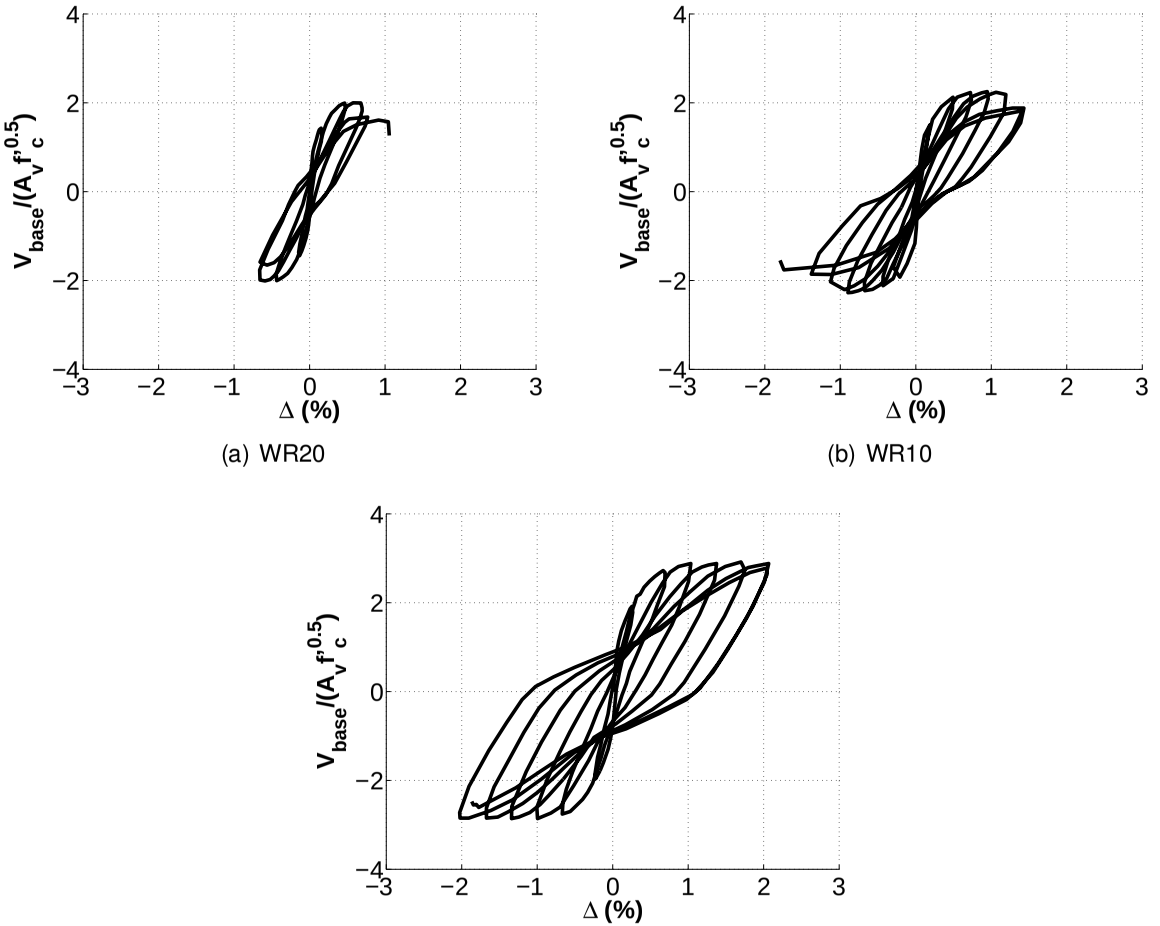

(a) WR20

(b) WR10

(c) WR0

Figure A.22: Oh et al. Test Results

A.1.7 Oesterle et al.

Oesterle, et al. (1976) tested a series of 22 approximately 1/3-scale structural walls over a series of three test phases. Of the 22 walls tested, four were rectangular in cross-section. Of these four, only complete results for two (designated by Oesterle as R1 and R2) of the walls were published. Peak strength values for the remaining two walls (R3 and R4) have been published, but complete experimental results are not available. Specimens R1 and R2 are slender walls with boundary element reinforcement. No axial load was applied to either specimen, and both specimens were tested cyclically, with complete load reversals, until failure. The primary difference between the specimens is the amount of steel provided in the boundary element, which was varied in the experimental program to provide specimen results for a wall expected to develop low shear stress demand (R1) and moderate shear stress demand (R2) when flexural yielding at the wall base occurred. Specimen R1 contains 1.47$\%$ vertical reinforcement ratio in the boundary element and specimen R2 contains 4.00$\%$. Additionally, the boundary element of specimen R2 contained 0.25 inch diamater hoops with cross-ties at 1-1/3 inches on center within the bottom 6 ft of the wall; Specimen R1 contained 0.195 inch diameter hoops at 4 inches on center along the entire wall length. The confinement reinforcmenet provided for specimen R2 was designed to comply with the 1971 ACI Building Code. Cyclic lateral load effects consisted of a single horizontal force applied a distance of 180 inches above the wall base, and three complete cycles were completed at each target drift level. During testing, both specimens were subjected to extensive yielding of horizontal and vertical steel. Yielding of boundary element vertical steel was observed to extend to a distance of 6 ft (41% of the wall height) and 9 ft (60%) above the wall base for specimens R1 and R2, respectively. Peak strains in the vertical reinforcement reached a strain of approximately six times the yield strain prior to failure for both specimens. For both specimens, yielding of horizontal web reinforcement occurred in the same regions where vertical yielding occurred and damage was concentrated in the bottom 3 ft.

Specimen R1 was observed to fail due to rupture of boundary element steel occurring after significant buckling was observed. The maximum specimen strength was 27.5 kips,

which corresponds to a shear stress demand, v_{max}, of $1.1\sqrt{f'_c(psi)}A_{cv}$ and a shear demand to capacity ratio, $V_{b,max}/V_{n,pr}$, of 0.17 when using reported material strengths (f'_c = 6490 psi and f_y = 75700 psi) and ACI 318 (2011) Equation 21-7. The specimen maintained strength at or above 80% of peak strength to a drift level of 2.52%. Concrete spalling withing the bottom 3 ft of the wall led to bar buckling throughout the boundary element. Further inelastic cycles ultimately led to bar fracture and crushing of the boundary element core. The experimentally determined load-displacement curve for specimen R1 is provided in Figure A.23(a).

Specimen R2 was also observed to fail due to rupture of boundary element steel occurring after significant buckling was observed. The maximum specimen strength was 50.4 kips, which corresponds to a shear stress demand, v_{max}, of $2.0\sqrt{f'_c(psi)}A_{cv}$ and a shear demand to capacity ratio, $V_{b,max}/V_{n,pr}$, of 0.33 (f'_c = 6490 psi and f_y = 75700 psi). The specimen maintained strength at or above 80% of peak strength to a drift level of 3.25%. During the second excursion 2.2% drift, it was noted the compression boundary element was bowing outwards with a 3 inch magnitude out-of-plane displacement. At that point the test was stopped and lateral bracing was added to each boundary element. Concrete spalling withing the bottom 3 ft of the wall led to bar buckling throughout the boundary element. During the third excursion to 3.25% drift, a large out-of-plane displacement in the compressive zone occurred and the load carrying capacity decreased to below the 80% failure criteria. Upon inpsection, it was observed that several bars fractured and considerable crushing of the boundary element was reported. The experimentally determined load-displacement curve for specimen R2 is provided in Figure A.23(b).

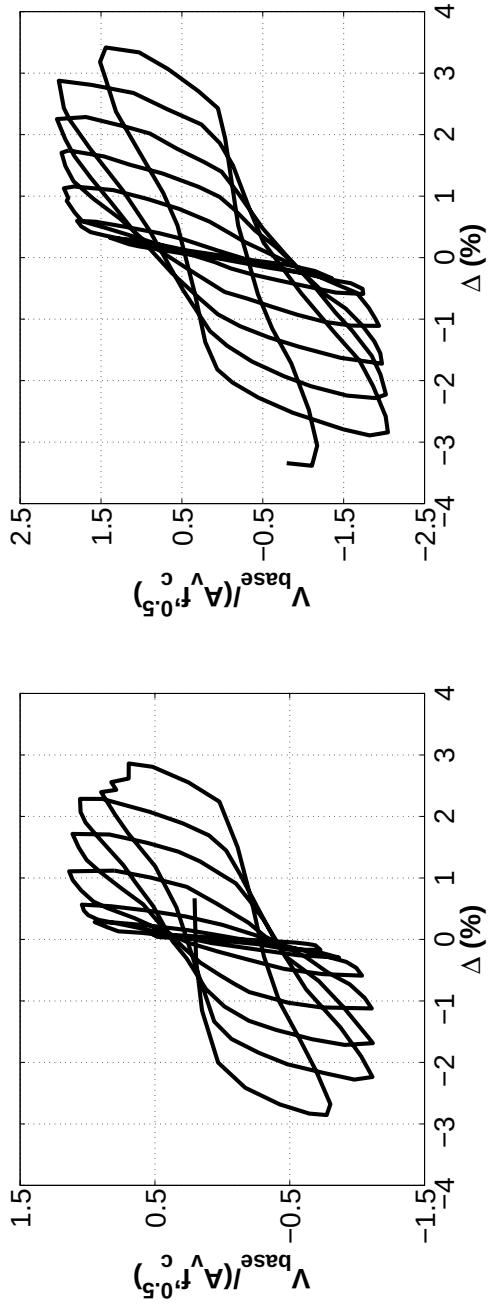

Figure A.23: Specimen Measured Load-Diaplacement Response

A.2 Slender Core Wall Test Programs

A brief summary of the tested specimen and experimental results are described in this section. Prior to discussion of the experimental programs, Table A.5 provides geometric and reinforcing steel quantities for the tested specimens and Table A.6 provides a summary of pertinent experimental results and response quantities for the specimens. Parameters listed in Tables A.5 and A.6 are defined as follows:

- l_w = horizontal length of wall parallel to the web.
- t = wall thickness.
- b_f = total flange thickess (i.e. - wall width perpendicular to web).
- H = specimen height.
- $\rho_{be,1}$ = longitudinal reinforcement ratio for flange tip boundary element.
- $\rho_{be,2}$ = longitudinal reinforcement ratio for web to flange intersecting boundary element.
- ρ_v = longitudinal reinforcement ratio outside of boundary element regions.
- $\rho_{v,all}$ = total gross longitudinal reinforcement ratio
- $\rho_{vol,1}$ = volumetric reinforcement ratio for flange tip boundary element.
- $\rho_{vol,2}$ = volumetric reinforcement ratio for web to flange intersecting boundary element.
- $\rho_{t,w}$ = transverse reinforcement ratio in wall web.
- $\rho_{t,f}$ = transerse reinforcement ratio in wall flanges.

- Loading Direction = designated direction of applied lateral load. Loading applied parallel to the wall web is x-direction loading. Z-direction loading is applied perpendicular to the wall web, with +z loading applying a bending moment to the wall base which applies compression to the flange tips and -z loading applying a bending moment to the wall base which applies compression to the wall web.

- $M_b/(V_b l_w)$ = effective lateral loading ratio, where M_b/V_b is the ratio of base moment to base shear.

- M_y = yield moment strength for the base section determined by moment-curvature analysis, defined by first yield of the extreme tension steel layer. Calculated using reported material strengths but without strain hardening.

- M_n = nominal moment strength for the base section determined by moment-curvature analysis, defined by extreme compression fiber strain reaching a strain value of -0.003. Calculated using reported material strengths but without strain hardening.

- $M_{b,max}$ = maximum base moment resisted by the wall.

- $V_{n,pr}$ = nominal shear strength of the wall section per ACI 318 (2011). Calculated using reported material strengths.

- $V_{b,max}$ = maximum base shear resisted by the wall.

- Δ_y = specimen yield drift. Calculated as the drift associated with the base moment reaching M_y.

- Δ_u = specimen drift capacity. Defined as the drift at which the lateral load carrying capacity of the wall dropped to 80% of the historic maximum, for drift demands in excess of historic drift demands.

- Failure Mode = CB for specimens failing due to crushing and buckling of the compression zone or BR for specimens failing due to steel rupture after significant buckling.

Table A.5: Core Wall Specimen Section Data

ID	Geometry				Longitudinal Steel				Transverse Steel			
	l_w	t	b_f	H	$\rho_{be,1}$	$\rho_{be,2}$	ρ_v	$\rho_{v,all}$	$\rho_{vol,1}$	$\rho_{vol,2}$	$\rho_{t,w}$	$\rho_{t,f}$
	in.	in.	in.	in.	%	%	%	%	%	%	%	%
UW1	120.0	6.00	48.0	144.0	3.33	3.81	0.27	1.05	1.44	1.63	0.74	0.74
W1	59.1	9.84	49.2	141.7	1.21	0.81	0.17	0.56	0.90	0.90	0.54	0.32
W2	59.1	9.84	49.2	141.7	1.21	0.81	0.17	0.56	0.90	0.90	0.54	0.32
W3	59.1	9.84	49.2	141.7	1.21	0.81	0.17	0.56	0.90	0.90	0.54	0.32
TUA	51.2	5.91	41.3	104.3	2.11	0.84	0.25	0.71	2.28	1.05	0.30	0.30
TUB	51.2	3.94	41.3	104.3	2.26	1.13	0.38	0.97	2.52	1.23	0.45	0.45

Table A.6: Core Wall Specimen Experimental Results

ID	Loading		Flexural Data				Shear Data				Drift Data		Failure Mode
	Dir.	$\frac{M_b}{V_b l_w}$	M_y	M_n	$M_{b,max}$	$\frac{M_{b,max}}{M_n}$	$V_{n,pr}$	$V_{b,max}$	v_{max}	$\frac{V_{b,max}}{V_{n,pr}}$	Δ_y	Δ_u	Type
			kip-ft	kip-ft	kip-ft		kip	kip			%	%	
UW1	± X	2.84	4530	5580	6190	1.11	431.0	218.0	4.0	0.51	0.34	1.86	CB
W1	± X	2.60	1930	2280	2610	1.14	315.0	204.0	6.0	0.65	0.30	3.00	BR
W2	+Z	3.12	1700	1950	2190	1.12	362.0	171.0	3.0	0.47	0.26	3.00	CB
W2	-Z	3.12	1450	1750	2020	1.15	362.0	156.8	2.8	0.44	0.33	3.00	CB
W3	± X	2.60	1930	2260	2430	1.08	311.0	192.3	6.0	0.61	0.43	2.00	BR
W3	+Z	3.12	1680	1910	1590	0.83	318.0	123.9	2.3	0.39	–	2.00	BR
W3	-Z	3.12	1440	1720	1920	1.12	318.0	149.6	2.8	0.47	0.34	2.00	BR
TUA	± X	2.58	980	1120	1120	1.00	133.0	105.1	3.2	0.79	0.40	3.50	BR
TUA	+Z	2.81	785	920	970	1.05	214.0	100.0	1.9	0.47	0.23	3.50	BR
TUA	-Z	2.81	725	850	850	1.00	214.0	87.9	1.7	0.41	0.35	3.50	BR
TUB	± X	2.58	950	1080	1130	1.05	104.0	102.7	5.7	0.99	0.36	3.00	CB
TUB	+Z	2.81	780	900	920	1.02	168.0	96.5	3.3	0.57	0.33	3.00	CB
TUB	-Z	2.81	640	750	790	1.05	168.0	81.9	2.8	0.49	0.35	3.00	CB

Table A.7: Core Wall Specimen Simulation Parameters

ID	Material									Loading
	f'_c	$f_{y,be}$	$E_{s,be}$	$f_{u,be}$	$\epsilon_{u,be}$	$f_{y,v}$	$E_{s,v}$	$f_{u,v}$	$\epsilon_{u,v}$	Axial Load
	psi	ksi	ksi	ksi	mm/mm	ksi	ksi	ksi	mm/mm	kips
UW1	5600	63.7	29000.	91.3	0.15	75.7	29000.	82.0	0.06	305.0
W1	3440	74.8	29000.	89.5	0.25	76.1	29000.	89.5	0.24	450.0
W2	3440	74.8	29000.	89.5	0.25	76.1	29000.	89.5	0.24	450.0
W3	3020	74.8	29000.	89.5	0.25	76.1	29000.	89.5	0.24	450.0
TUA	11300	70.8	29000.	86.3	0.13	75.1	29000.	98.8	0.08	175.4
TUB	7930	68.3	29000.	83.2	0.13	75.1	29000.	98.8	0.08	175.4

A.2.1 Lowes et al.

As a continuation of a large experimental test program undertaken by researchers at the Universities of Washington, Illinois and California undertaken to investigate seismic performance of modern, code-compliant walls, three U-shaped wall specimens were to be tested at the University of Iliinois beginning in May 2012. The objective of these tests was to assess performance of cyclically loaded, core wall sections with the single U-shaped specimen representing one-half of a core wall system. The impact of the loading protocol on cyclic performance was the primary variable studied by the experimental program; specimen UW1 was loaded uni-directionally in the plane of the core web and specimens UW2 and UW3 were loaded bi-directionally in both the web and flange directions. Because this experimental test program is currently in progress, only experimental results exist for the UW1 specimen at this time.

UW1 is a 1/3-scale wall specimen representing one-half of a building core wall. UW1 was scaled from a 10-story building prototype design and the specimen height of 144 inches, represents the lower three stories of the prototype building. To represent earthquake forces due to loaded mass above the bottom three stories, axial, shear and bending moment forces were applied to the top of the specimen using six degree of freedom Loading and Boundary Condition Boxes (LBCBs) uniquely available at the NEES University of Illinois testing facility. A fixed load pattern representative of an ASCE 7 (2010) equivalent

lateral force pattern was used to load the specimen laterally. For the 10-story prototype building, the fixed static load pattern was calculated to have an effective height (i.e. - the ratio of base moment, M_u, to base shear, V_u, equal to 0.71H, where H is prototype building height. This effective height was used to determine the constant ratio of moment to shear that was applied to the top of the specimen to achieve the same M_u/V_u ratio as the prototype building (Figure A.24). Through the cyclic loading protocol, applied axial load remained constant at an axial stress demand ratio of $0.05A_g f'_c$, where f'_c is the design concrete compression strength of 5000 psi and A_g is the gross cross-sectional area of the specimen, which is shown in Figure A.25. The UW1 section was constructed to have a web depth and flange width of 120 inches and 48 inches, respectively. Specimen thickness was six inches for both the web and the flanges. Heavily reinforced boundary elements with closely spaced confined ties were used at the flange tips and the wall corners. Distributed longitudinal and transverse reinforcement were provided in the web and flange regions outside of the well-confined boundary elements. Reinforcement ratios and other calculated cross-section design quantities for specimen UW1 are provided in Table A.5; a summary of measured response quantities and calculated strength parameters are provided in Table A.6. Loading of the specimen was quasi-static, with two complete cycles performed at increasing levels of lateral drift until loss of lateral load-carrying capacity was achieved. Failure of the UW1 specimen was due to crushing of unconfined concrete near the web to flange intersection at a drift of 1.86$\%$ while attempting to achieve a target drift of 2.25$\%$ in the negative direction. At a drift of 1.86$\%$, wall resistance reduced to 62$\%$ of the historic maximum. The maximum strength of UW1 was 218 kips, which corresponds to a maximum shear stress demand, v_{max} of $4\sqrt{f'_c(psi)}A_{cv}$ and a maximum shear demand to capacity ratio, $V_{u,max}/V_{n,pr}$, of 0.51 when using reported material strengths (f'_c = 5600 psi and f_y = 75700 psi) and ACI 318 (2011) equation 21-7. Yield drift for the specimen, calculated as the drift corresponding to the base moment reaching the theoretical yield moment, was determined to be 0.34$\%$. The experimentally determined load-displacement curve for specimen UW1 is provided in Figure A.26.

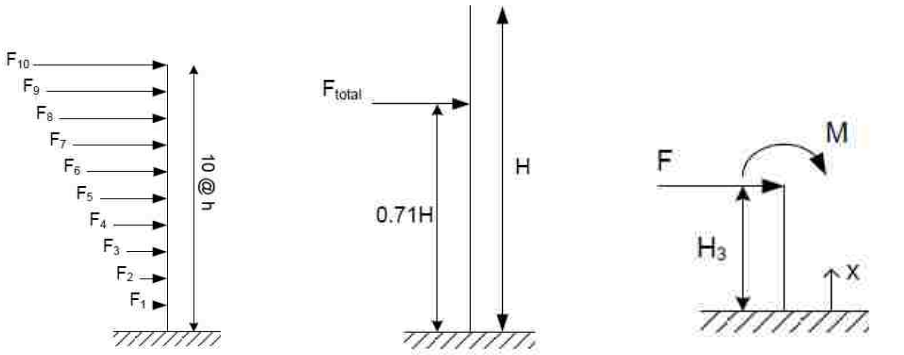

(a) 10-Story Prototype (Floor Loads)

(b) 10-Story Prototype (Effective Loads)

(c) 3-Story Specimen Loads

Figure A.24: UW1 Load Pattern

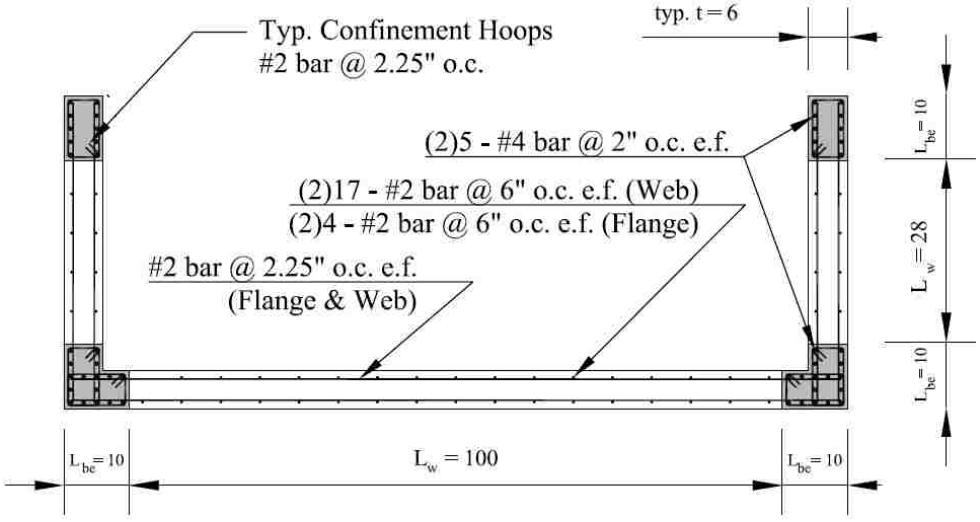

Figure A.25: UW1 Wall Section

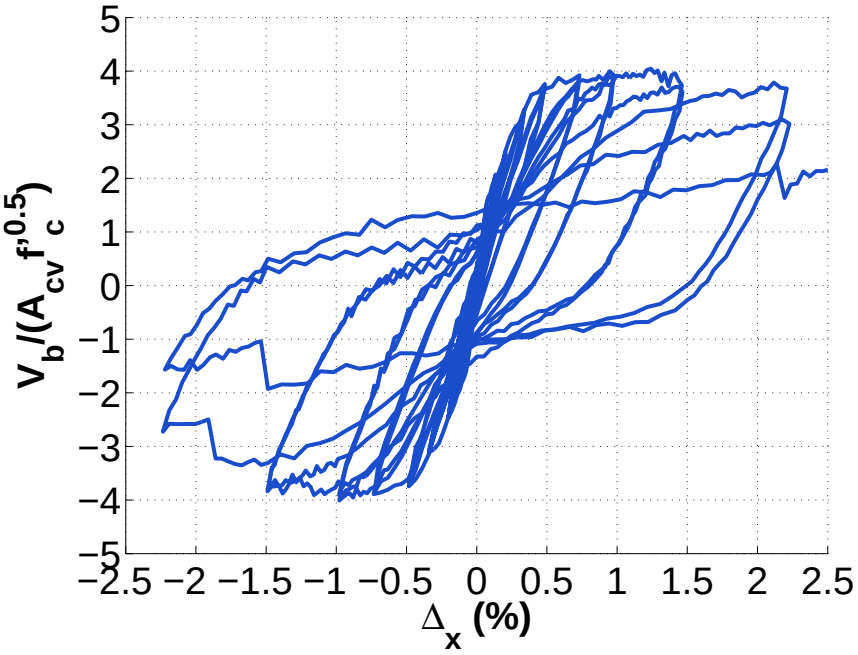

Figure A.26: UW1 Experimental Load-Displacement Response

A.2.2 Fardis et al.

Ile and Reynouard (2004) provide description of three U-shaped wall specimens designed and detailed by Fardis (Reynouard and Fardis, 2001) and tested by Pegon et al. (2000). The three specimens were designed and detailed to be identical, however each specimen was subjected to a unique loading protocol with 1) Specimen W1 loaded cyclically in the direction parallel to the wall web , 2) Specimen W2 loaded cyclically in the direction perpendicular to the wall web and 3) Specimen W3 loaded biaxially with cyclic excursions both parallel and orthogonal to the plane of the web. Load histories for the three specimens are provided in Figure A.27. Loading for all three specimens was quasi-static; three complete load cycles were performed at increasing levels of lateral drift for specimens W1 and W2, a complete square cloverleaf pattern was performed at increasing levels of lateral drift for specimen W3. The specimens represented a full size core surrounding, on three sides, a small elevator shaft. Design and detailing of the specimens were performed according to a proposed draft version of 2001 Eurocode 8 (EC8) provisions. Per EC8 provisions,

confined boundary elements were provided at the flange tips as well as at flange to web intersections. Each specimen was detailed with identical confining reinforcement consisting of 0.31 inch hoops with cross-ties at 3.5 inches on center. Lateral loading was applied as a single concentrated force located a distance of 153.5 inches above the wall base. Lateral load was applied by two horizontal pistons, which were displacement-controlled to ensure no twist of the specimen occurred. Through the cyclic loading protocol, applied axial load remained constant at an axial stress demand ratio of $0.10A_g f'_c$, where f'_c is the design concrete compression strength of 3300 psi and A_g is the gross cross-sectional area of the specimen, which is shown in Figure A.28. The three specimens section were constructed to have a web depth and flange width of 59 inches and 49.2 inches, respectively; Specimen thickness was 9.8 inches for both the web and the flanges. Heavily reinforced boundary elements with closely spaced confined ties were used at the flange tips and the wall corners. Distributed longitudinal and transverse reinforcement were provided in the web and flange regions outside of the well-confined boundary elements. Reinforcement ratios and other calculated cross-section design quantities for specimens W1-W3 are provided in Table A.5; a summary of measured response quantities and calculated strength parameters are provided in Table A.6.

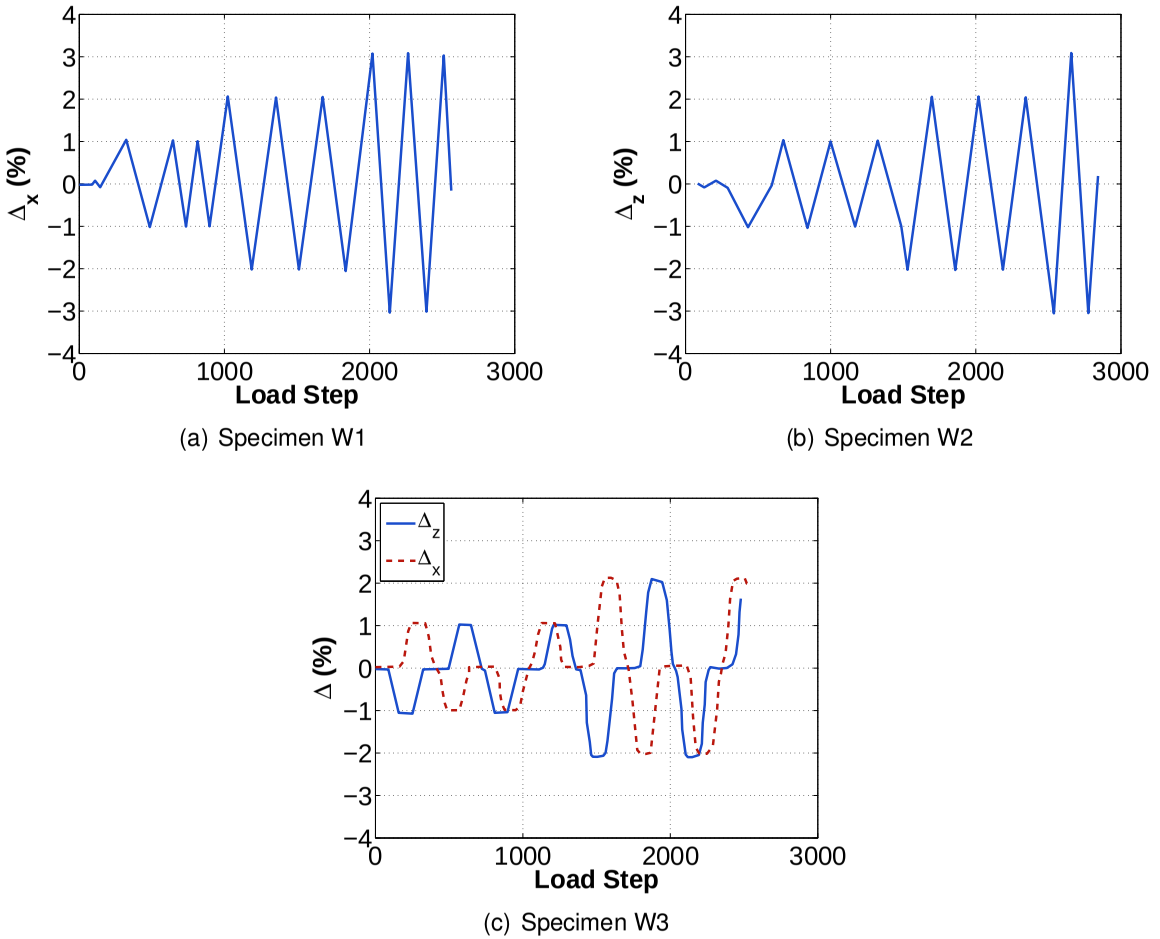

(a) Specimen W1

(b) Specimen W2

(c) Specimen W3

Figure A.27: Fardis specimen drift history

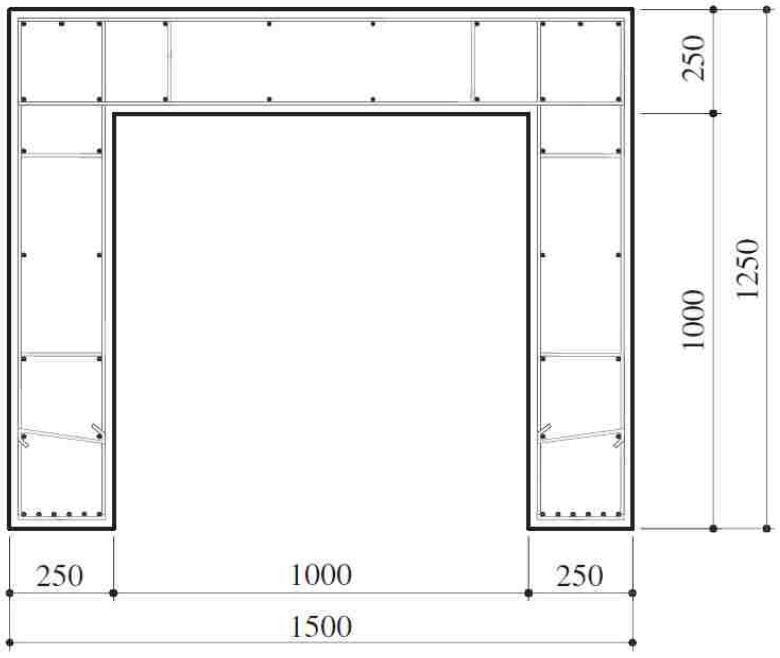

Figure A.28: W1-W3 Section (dimensions in mm) (Beyer et al, 2007)

Failure of the W1 specimen was due to rupture of flange and web longitudinal reinforcement occurring during load reversal after significant buckling of reinforcement was observed. Deterioration of wall resistance occurred during second and third excursions to 3% drift. After two complete cycles severe buckling of longitudinal reinforcement and hoop rupture was observed. During the third cycle, specimen failure in both +x and -x loading directions was observed. The maximum specimen strength was approximately 204 kips; achieved in both +x and -x loading directions. This peak load corresponds to a maximum shear stress demand, v_{max} of $6.0\sqrt{f'_c(psi)}A_{cv}$ and a maximum shear demand to capacity ratio, $V_{u,max}/V_{n,pr}$, of 0.65 when using reported material strengths (f'_c = 3440 psi and f_y = 80800 psi) and ACI 318 (2011) equation 21-7. Yield drift for the specimen, calculated as the drift corresponding to the base moment reaching the theoretical yield moment, was determined to be 0.30%. The experimentally determined load-displacement curve for specimen W1 is provided in Figure A.29(a).

Failure of the W2 specimen was due to deterioration of the confined boundary element in the flange tips. In the +z loading direction, strength deterioration was observed during the first excursion to 2% (1% strength deterioration) and became more pronounced during the first excursion to 3% drift (15% loss of strength). During the first excursion to 3% drift in the +z loading direction, significant crushing on the flange tips was observed accompanied by significant buckling of boundary element reinforcement. Upon reloading to 3% drift in the -z direction, rupture of the previously buckling reinforcement occurred. Reinforcement rupture reduced wall resistance to approximately 75% of the historic maximum strength in the -z direction and the specimen was considered to have failed. The maximum specimen strength was 171 kips, achieved in the +z loading direction. This peak load corresponds to a maximum shear stress demand, v_{max} of $3.0\sqrt{f'_c(psi)}A_{cv}$ and a maximum shear demand to capacity ratio, $V_{u,max}/V_{n,pr}$, of 0.47 when using reported material strengths (f'_c = 3440 psi and f_y = 80800 psi) and ACI 318 (2011) equation 21-7. The maximum resistance achieved by specimen W2 in the -z loading direction was 156 kips, which corresponds to a maximum shear stress demand, v_{max} of $2.8\sqrt{f'_c(psi)}A_{cv}$ and a maximum shear demand to capacity ratio, $V_{u,max}/V_{n,pr}$, of 0.43. Yield drift for the specimen was determined to be 1) 0.26% in the +z loading direction and 2) 0.33% in the -z loading direction. The experimentally determined load-displacement curve for specimen W2 is provided in Figure A.29(b).

Failure of the W3 specimen, in both the x- and z-directions was due to rupture of longitudinal reinforcement occurring during load reversal after significant buckling of reinforcement was observed. For the bi-directionally loaded W3 specimen, strength deterioration was observed for every cycle initially preceded by loading in the orthogonal direction. Significant strength loss was observed in both directions during the second loading cycle to 2% drift. During the second loading cycle to 2% drift, significant crushing of flange tip concrete and longitudinal reinforcement buckling was observed. Failure in the z-direction occurred during the second loading cycle to 2% drift at a drift level of 2% in the +z direction. Failure in the x-direction occurred during the second loading cycle to 2% drift at a drift level of 2% in the +x direction. The maximum specimen strength in the x-direction was 190 kips; peak strength in the z-direction was 150 kips. For the z-direction, this peak load corresponds to a maximum shear stress demand, v_{max} of $2.8\sqrt{f'_c(psi)}A_{cv}$ and a maximum shear demand

to capacity ratio, $V_{u,max}/V_{n,pr}$, of 0.47 when using reported material strengths (f'_c = 3020 psi and f_y = 80800 psi) and ACI 318 (2011) equation 21-7. For the x-direction, the peak load corresponds to a maximum shear stress demand, v_{max} of $6.0\sqrt{f'_c(psi)}A_{cv}$ and a maximum shear demand to capacity ratio, $V_{u,max}/V_{n,pr}$, of 0.61. Yield drift for the specimen was determined to be 1) 0.43% for x-direction loading and 2) 0.34% for z-direction loading. The experimentally determined load-displacement curves for specimen W3 is provided in Figure A.29(c) and Figure A.29(d) for x-direction and z-direction loading, respectively.

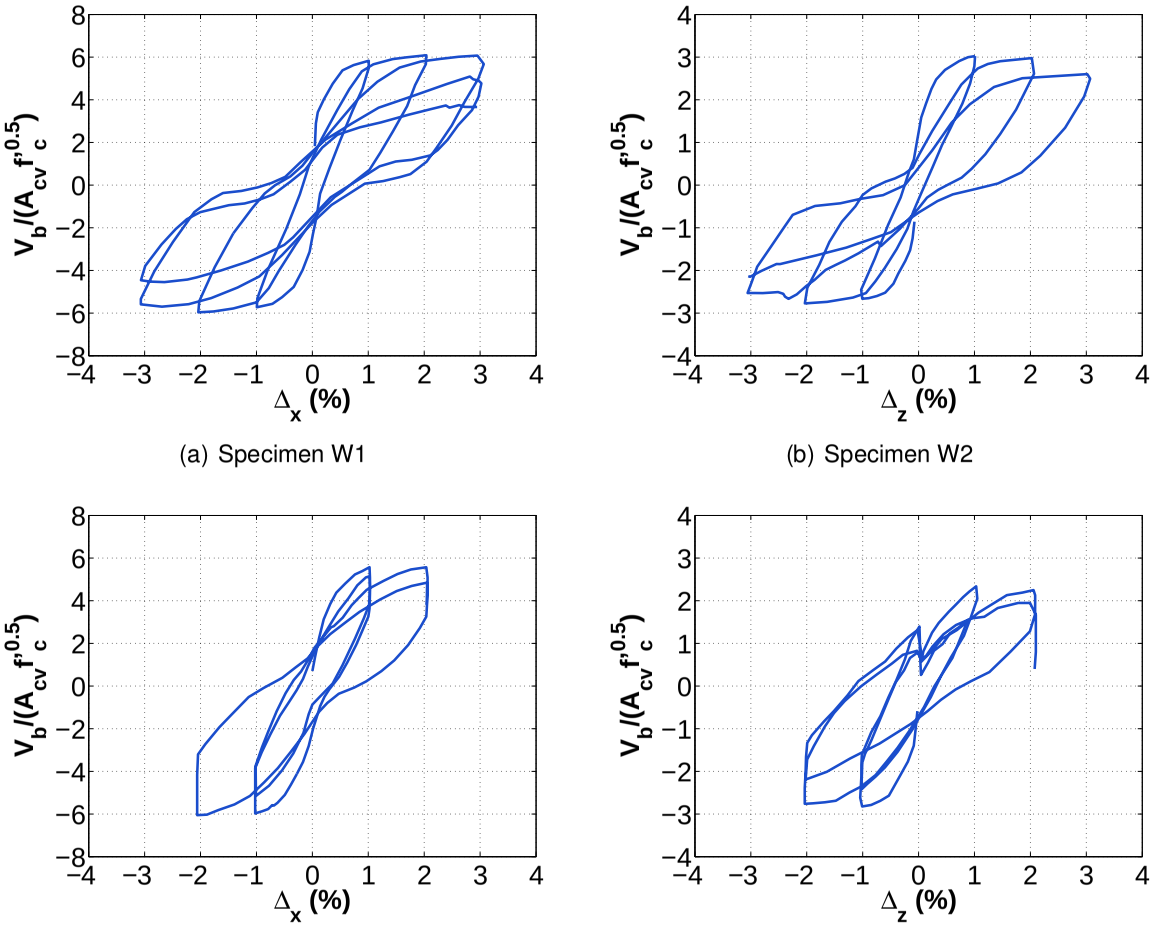

(a) Specimen W1

(b) Specimen W2

(c) Specimen W3 (X-dir)

(d) Specimen W3 (Z-dir)

Figure A.29: W1, W2, W3 Experimental Load-Displacement Response

A.2.3 Beyer et al.

Beyer et al. (2007) testing two U-shaped wall specimens to extend the existing literature on bi-directionally loaded U-shaped walls. Two half-scale specimens of different wall thickness were tested to further assess failure modes, deformation contributions and deformation capacity of U-shaped walls. Both specimens were loading bi-directionally, using a target drift history comprising a fan-shaped sweep in one diagonal direction followed by a complete cyclic excusion in the opposite diagonal direction (Figure A.27). For each target drift level, diagonal sweeps were preceded by full drift cycles displacing the wall 1) parallel to the wall web and 2) perpendicular to the wall web. Bi-directional cycles were force-controlled until estimated yield forces were developed; all subsequent cycles were displacement-controlled and loading for both specimens was quasi-static. Lateral loading was applied using three actuators, with two actuators loading the wall flanges and a single actuator loading the wall web. The height of the acuators loading the specimen was different for the two principal directions. For loading parallel to the wall web, an effective shear span ratio, $M_b/(V_b l_w)$, where M_b is the base moment, V_b is the base shear and l_w is the horizontal length of the wall in the direction being considered, of 2.58 was used. For loading perpendicular to the wall web, an effective shear span ratio of 2.81 was used. Different shear span ratios were used based on inelastic time history analyses (ITHA) performed using a 6-story prototype building and ground motion records applied to both principal building directions. An effective shear span ratio of 2.81 was used for all diagonal excursions. Throughout the cyclic loading protocol, applied axial load remained constant at an axial stress demand ratio of $0.02A_g f'_c$ and $0.04A_g f'_c$ for specimens TUA and TUB, respectively. Both specimens section were constructed to have a web depth and flange width of 51.2 inches and 41.3 inches; wall thickess was varied for the specimens with the thickness of TUA being 5.9 inches and the thickness of TUB being 3.9 inches. Heavily reinforced boundary elements with closely spaced confined ties were used at the flange tips and the wall corners (Figure A.31). Distributed longitudinal and transverse reinforcement were provided in the web and flange regions outside of the well-confined boundary elements. Reinforcement ratios and other calculated cross-section design quantities for specimens TUA and TUB are pro-

vided in Table A.5; a summary of measured response quantities and calculated strength parameters are provided in Table A.6.

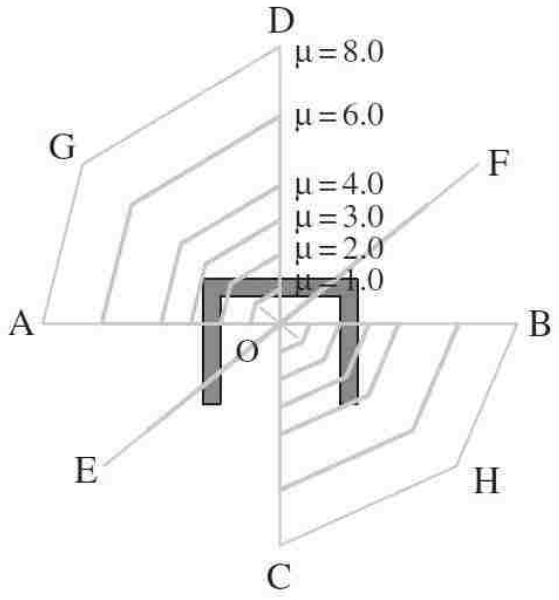

Figure A.30: TUA/TUB Loading Protocol (Beyer et al, 2007)

Failure of the TUA specimen was due to rupture of flange and web longitudinal reinforcement occurring during load reversal after significant buckling of reinforcement was observed. The first ruptures occurred in the distributed flange reinforcement while loading in the +x-direction to a target drift of 2.5%. The distributed flange reinforcement which fractured were bars which had previously been observed to have sustained significant buckling. Three boundary element longitudinal bars, which had previously buckled during diagonal loading, ruptured when loading was reversed to target a drift of 3.5% in this -z-direction. After fracture of boundary element steel occurred, one final diagonal excursion reduced wall resistance to approximately 70% of the historic peak strength and tested was concluded. The maximum specimen strength was approximately 102 kips; achieved in both +x and

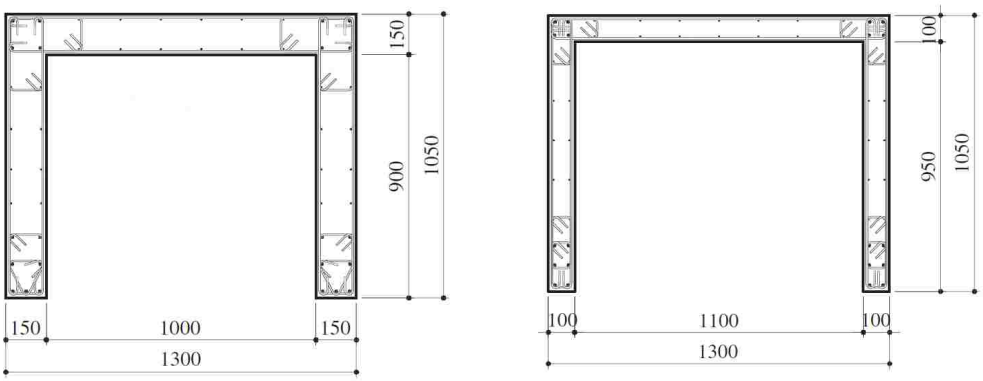

(a) Specimen TUA (b) Specimen TUB

Figure A.31: Beyer Specimens (dimensions in mm) (Beyer et al, 2007)

-x loading directions. This peak load corresponds to a maximum shear stress demand, v_{max} of $3.2\sqrt{f'_c(psi)}A_{cv}$ and a maximum shear demand to capacity ratio, $V_{u,max}/V_{n,pr}$, of 0.77 when using reported material strengths (f'_c = 11300 psi and f_y = 75100 psi) and ACI 318 (2011) equation 21-7. Peak strength was 100 kips in the +z-direction and 88 kips in the -z-direction. For +z-direciton loading, peak strength corresponds to a maximum shear stress demand, v_{max} of $1.9\sqrt{f'_c(psi)}A_{cv}$ and a maximum shear demand to capacity ratio, $V_{u,max}/V_{n,pr}$, of 0.47. Yield drift for the specimen, calculated as the drift corresponding to the base moment reaching the theoretical yield moment, was determined to be 1) 0.40% for x-direction loading, 2) 0.23% for +z-direction loading and 3) 0.35% for -z-direction loading. The experimentally determined load-displacement curve for specimen TUA is provided in Figure A.32(a).

Failure of the TUB specimen was due to crushing of unconfined concrete adjacent to the well-confined flange-web intersection while loaded diagonally. Failure occurred during the fan-shaped diagonal loading pattern at a drift of 3%. Crushing was accompanied by significant spalling and wall thickness loss in the unconfined wall region. No rupture of longitudinal reinforcement was observed although buckling was observed for flange tip boundary element reinforcing during previous diagonal loading at 3% drift. The maximum specimen strength was approximately 103 kips; achieved in both +x and -x loading directions. This

peak load corresponds to a maximum shear stress demand, v_{max} of $5.7\sqrt{f'_c(psi)}A_{cv}$ and a maximum shear demand to capacity ratio, $V_{u,max}/V_{n,pr}$, of 0.99 using reported strength values of f'_c = 7930 psi and f_y = 75100 psi. Peak strength was 95 kips in the +z-direction and 82 kips in the -z-direction. For +z-direciton loading, peak strength corresponds to a maximum shear stress demand, v_{max} of $3.3\sqrt{f'_c(psi)}A_{cv}$ and a maximum shear demand to capacity ratio, $V_{u,max}/V_{n,pr}$, of 0.57. Yield drift for the specimen was calculated to be 1) 0.36% for x-direction loading, 2) 0.33% for +z-direction loading and 3) 0.35% for -z-direction loading. The experimentally determined load-displacement curve for specimen TUB is provided in Figure A.32(a).

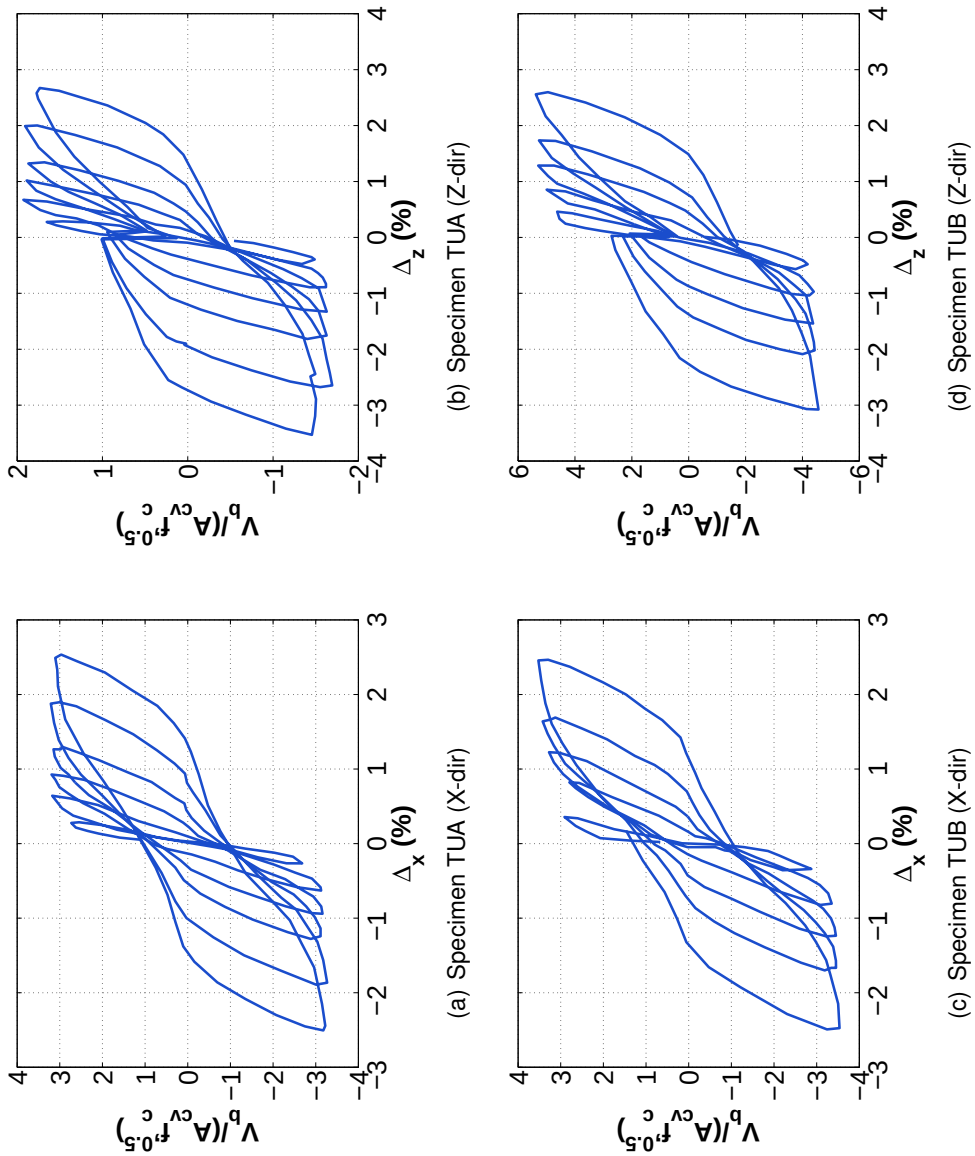

(a) Specimen TUA (X-dir)

(b) Specimen TUA (Z-dir)

(c) Specimen TUB (X-dir)

(d) Specimen TUB (Z-dir)

Figure A.32: TUA, TUB Experimental Load-Displacement Response

A.3 Squat Wall Test Programs

A brief summary of the tested specimens and experimental results are described in this section. Prior to discussion of the experimental programs, Table A.8 provides geometric and reinforcing steel quantities for the tested specimens and Table A.9 provides a summary of pertinent experimental results and response quantities for the specimens. Parameters listed in Tables A.8 and A.9 are defined as follows:

The experimental specimens meeting the assigned defintion of 'squat' are the 13 wall specimens tested by Massone et. al (2006) and Whittaker et al. (2012).

- l_w = horizontal length of wall parallel to the web.
- t = wall thickness.
- H = specimen height.
- h_{eff} = effective loading height (i.e. - shear span).
- ρ_{be} = longitudinal reinforcement ratio for at wall end.
- ρ_v = longitudinal reinforcement ratio in wall web.
- $\rho_{v,all}$ = total gross longitudinal reinforcement ratio
- ρ_{vol} = volumetric reinforcement ratio for wall end region.
- ρ_t = transverse reinforcement ratio in wall web.
- $M_b/(V_b l_w)$ = effective lateral loading ratio, where M_b/V_b is the ratio of base moment to base shear.
- M_y = yield moment strength for the base section determined by moment-curvature analysis, defined by first yield of the extreme tension steel layer. Calculated using reported material strengths but without strain hardening.

- M_n = nominal moment strength for the base section determined by moment-curvature analysis, defined by extreme compression fiber strain reaching a strain value of -0.003. Calculated using reported material strengths but without strain hardening.

- $M_{b,max}$ = maximum base moment resisted by the wall.

- $V_{n,pr}$ = nominal shear strength of the wall section per ACI 318 (2011). Calculated using reported material strengths.

- $V_{b,max}$ = maximum base shear resisted by the wall.

- $\Delta_{0.75}$ = drift quantity used to compare simulated and observed wall stiffness. Calculated as the drift associated with the base shear reaching 75$\%$ of the peak observed value.

- Δ_u = specimen drift capacity. Defined as the drift at which the lateral load carrying capacity of the wall dropped to 80$\%$ of the historic maximum, for drift demands in excess of historic drift demands.

Table A.8: Squat Wall Specimen Section Data

ID	Geometry				Reinforcing Steel				
	l_w	t	H	h_{eff}	ρ_{be}	ρ_v	$\rho_{v,all}$	ρ_{vol}	ρ_t
	in.	in.	in.	in.	%	%	%	%	%
SW1	120.0	8.00	130.0	112.8	0.67	0.67	0.67	–	0.67
SW2	120.0	8.00	82.0	64.8	1.00	1.00	1.00	–	1.00
SW3	120.0	8.00	82.0	64.8	0.67	0.67	0.67	–	0.67
SW4	120.0	8.00	82.0	64.8	0.33	0.33	0.33	–	0.33
SW5	120.0	8.00	57.0	39.6	1.00	1.00	1.00	–	1.00
SW6	120.0	8.00	57.0	39.6	0.67	0.67	0.67	–	0.67
SW7	120.0	8.00	57.0	39.6	0.33	0.33	0.33	–	0.33
WP5	54.0	6.00	48.0	24.0	1.36	0.26	0.45	–	0.28
WP6	54.0	6.00	48.0	24.0	1.36	0.26	0.45	–	0.28
WP7	54.0	6.00	48.0	24.0	1.36	0.26	0.45	–	0.28
WP8	54.0	6.00	48.0	24.0	1.36	0.26	0.45	–	0.28
WP9	54.0	6.00	48.0	24.0	1.36	0.26	0.45	–	0.28

Table A.9: Squat Wall Specimen Experimental Results

ID	Loading	Flexural Data				Shear Data				Drift Data		Failure Mode
	$\frac{M_b}{V_b l_w}$	M_y	M_n	$M_{b,max}$	$\frac{M_{b,max}}{M_n}$	$V_{n,pr}$	$V_{b,max}$	v_{max}	$\frac{V_{b,max}}{V_{n,pr}}$	$\Delta_{0.75}$	Δ_u	
		kip-ft	kip-ft	kip-ft		kip	kip			%	%	
SW1	0.94	1380	1950	2350	1.21	460.8	249.7	4.3	0.54	0.57	2.10	Sliding
SW2	0.54	1910	2760	3070	1.11	642.6	568.5	7.1	0.88	0.42	1.81	Crushing/Sliding
SW3	0.54	1430	1910	2510	1.31	659.6	464.8	5.5	0.70	0.43	2.71	Sliding
SW4	0.54	860	1050	1220	1.16	400.0	225.9	3.6	0.56	0.13	1.37	Sliding
SW5	0.33	1900	2800	2400	0.86	503.6	725.9	11.5	1.44	0.46	1.15	Sliding
SW6	0.33	1370	1930	1870	0.97	473.4	567.1	9.6	1.20	0.33	1.96	Sliding
SW7	0.33	830	1040	1040	1.00	386.0	314.4	5.5	0.81	0.20	0.75	Sliding
WP5	0.44	390	440	360	0.82	118.0	179.6	8.7	1.52	0.18	0.71	Diagonal Crushing
WP6	0.44	420	465	382	0.82	121.4	191.2	8.7	1.58	0.20	0.94	Diagonal Crushing
WP7	0.44	305	340	295	0.87	121.9	147.3	6.7	1.21	0.14	0.68	Diagonal Crushing
WP8	0.44	305	340	320	0.93	122.0	158.6	7.2	1.30	0.17	0.85	Diagonal Crushing
WP9	0.44	175	190	180	0.96	119.8	90.8	4.3	0.76	0.15	1.29	Diagonal Crushing

A.3.1 Whittaker et al.

Whittaker et al tested a series of seven large-size low-rise structural wall specimens (Rocks, 2011). The purpose of the experimental program was to increase understanding of expected peak strength and hysteretic performance of squat wall systems designed using construction details commonly specified for new construction of buildings and safety-related nuclear structures. Each wall specimen was loaded cyclically with complete load reversals until significant loss of lateral load-carrying capacity was observed. No external gravity load was applied to the specimens; lateral loading was applied to the specimens by a single actuator. The two primary design parameters addressed in the experimental program were aspect ratio and reinforcing steel ratio. Three aspect ratios were considered: 1) an aspect ratio of 0.94 for specimen SW1, 2) aspect ratios of 0.54 for specimens SW2-SW4 and 3) aspect ratios of 0.33 for specimens SW5-SW7. Each specimen was constructed using two curtains of uniformly distributed No. 4 bars for both longitudinal and transverse reinforcement. All reinforcing steel was uniformly distributed throughout the specimens and no transverse confining reinforcing was used at the wall ends (Figure A.33). Three reinforcing ratios were used, 1) ρ = 1.00$\%$ for specimens SW2 and SW5, 2) ρ = 0.67$\%$ for specimens SW1, SW3 and SW6 and 3) ρ = 0.33$\%$ for specimens SW4 and SW7. A summary of measured response quantities and calculated strength parameters for the seven specimens are provided in Table A.9.

Specimen SW1 was the only specimen constructed with an aspect ratio of 0.94 and achieved peak strength at an imposed drift of 1.30$\%$. The maximum specimen strength was 249.7 kips, which corresponds to a shear stress demand, v_{max}, of $4.3\sqrt{f'_c(psi)}A_{cv}$ and a shear demand to capacity ratio, $V_{b,max}/V_{n,pr}$, of 0.54 when using reported material strengths (f'_c = 3600 psi and f_y = 67300 psi) and ACI 318 (2011) Equation 21-7. The specimen maintained strength at or above 80$\%$ of peak strength to a drift level of 2.4$\%$. After completing drift cycles at this level, specimen strength fell to 57$\%$ of peak strength when loaded to a target drift of 3$\%$. Diagonal shear and flexural cracks were observed throughout

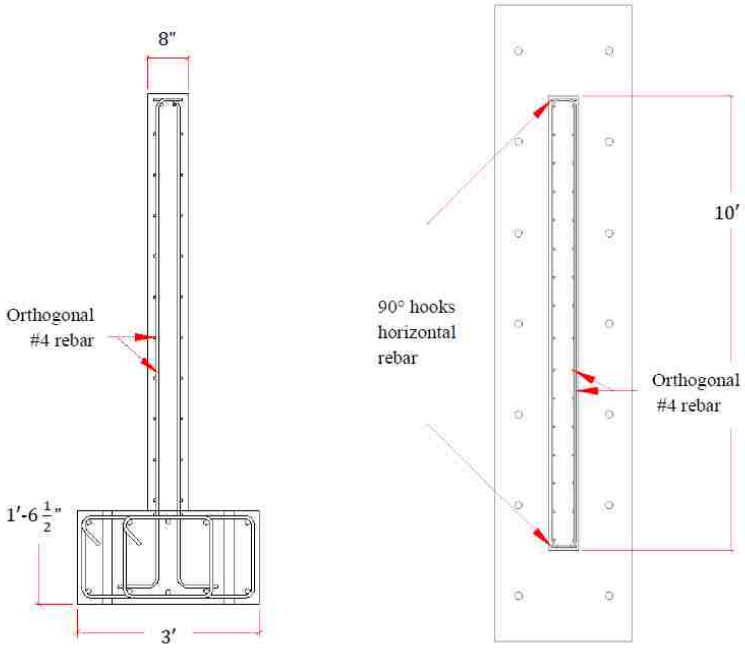

Figure A.33: Whittaker Specimen Details (Rocks, 2011)

the experiment and specimen failure was due to significant sliding along a horizontal crack roughly 10 inches above the wall base. The experimentally determined load-displacement curves for specimen SW1 is provided in Figure A.36(a).

Specimen SW2, which was loaded at an aspect ratio of 0.54 and contained 1.00% horizontal and vertical reinforcement, achieved peak strength at an imposed drift of 1.25%. The maximum specimen strength was 568.5 kips, which corresponds to a shear stress demand, v_{max}, of $7.1\sqrt{f'_c(psi)}A_{cv}$ and a shear demand to capacity ratio, $V_{b,max}/V_{n,pr}$, of 0.88 (f'_c = 7000 psi and f_y = 63000 psi). The specimen maintained strength at or above 80% of peak strength to a drift level of 1.81%. Failure of the specimen was due to compressive failure of the specimen. Crushing of the wall toe, signficant spalling and buckling of vertical reinforcement was observed. The experimentally determined load-displacement curves for specimen SW2 is provided in Figure A.36(b).

Specimen SW3, which was loaded at an aspect ratio of 0.54 and contained 0.67% horizontal and vertical reinforcement, achieved peak strength at an imposed drift of 2.10%. The maximum specimen strength was 464.8 kips, which corresponds to a shear stress demand, v_{max}, of $5.5\sqrt{f'_c(psi)}A_{cv}$ and a shear demand to capacity ratio, $V_{b,max}/V_{n,pr}$, of 0.70 (f'_c = 7800 psi and f_y = 63000 psi). The specimen maintained strength at or above 80% of peak strength to a drift level of 2.71%. Failure of the specimen was ultimately caused by sliding at the base, however signficant spalling of cover concrete, toe crushing and vertical reinforcement buckling were observed as well. The experimentally determined load-displacement curves for specimen SW3 is provided in Figure A.36(c).

Specimen SW4, which was loaded at an aspect ratio of 0.54 and contained 0.33% horizontal and vertical reinforcement, achieved peak strength at an imposed drift of 1.08%. The maximum specimen strength was 225.9 kips, which corresponds to a shear stress demand, v_{max}, of $3.6\sqrt{f'_c(psi)}A_{cv}$ and a shear demand to capacity ratio, $V_{b,max}/V_{n,pr}$, of 0.56 (f'_c = 4200 psi and f_y = 67300 psi). The specimen maintained strength at or above 80% of peak strength to a drift level of 1.37%. Similar to specimen SW3, the primary mode of failure was base sliding, however significant damage of the compression zone was observed prior to failure. The experimentally determined load-displacement curves for specimen SW4 is provided in Figure A.36(d).

Specimen SW5, which was loaded at an aspect ratio of 0.33 and contained 1.00% horizontal and vertical reinforcement, achieved peak strength at an imposed drift of 0.95%. The maximum specimen strength was 725.9 kips, which corresponds to a shear stress demand, v_{max}, of $11.5\sqrt{f'_c(psi)}A_{cv}$ and a shear demand to capacity ratio, $V_{b,max}/V_{n,pr}$, of 1.44 (f'_c = 4300 psi and f_y = 67300 psi). The specimen maintained strength at or above 80% of peak strength to a drift level of 1.15%. Failure of specimen SW5 was due to a sliding shear crack that formed roughly 7 inches above the base of the specimen. Significant diagonal shear cracks were observed prior to specimen failure. The experimentally determined load-displacement curves for specimen SW5 is provided in Figure A.37(a).

Specimen SW6, which was loaded at an aspect ratio of 0.33 and contained 0.67% horizontal and vertical reinforcement, achieved peak strength at an imposed drift of 0.81%. The maximum specimen strength was 567.1 kips, which corresponds to a shear stress

demand, v_{max}, of $9.6\sqrt{f'_c(psi)}A_{cv}$ and a shear demand to capacity ratio, $V_{b,max}/V_{n,pr}$, of 1.20 (f'_c = 3800 psi and f_y = 67300 psi). The specimen maintained strength at or above 80% of peak strength to a drift level of 1.96%. Failure of specimen SW6 was due to a sliding shear crack at the base of the specimen. Significant diagonal shear cracks were observed prior to specimen failure. The experimentally determined load-displacement curves for specimen SW6 is provided in Figure A.37(b).

Specimen SW7, which was loaded at an aspect ratio of 0.33 and contained 0.33% horizontal and vertical reinforcement, achieved peak strength at an imposed drift of 0.44%. The maximum specimen strength was 314.4 kips, which corresponds to a shear stress demand, v_{max}, of $5.5\sqrt{f'_c(psi)}A_{cv}$ and a shear demand to capacity ratio, $V_{b,max}/V_{n,pr}$, of 0.81 (f'_c = 3600 psi and f_y = 67300 psi). The specimen maintained strength at or above 80% of peak strength to a drift level of 0.75%. Failure of specimen SW7 was due to a sliding shear crack at the base of the specimen. Significant diagonal shear cracks were observed prior to specimen failure. The experimentally determined load-displacement curves for specimen SW7 is provided in Figure A.37(c).

A.3.2 Massone et al.

Massone, Orakcal and Wallace tested six 3/4-scale wall pier specimens detailed to mimic construction features commonly used in hospital construction during the 1960s and 1970s. The intent of the experimental program was to assess lateral load behavior of such specimens in order to aid in assessing performance and rehabilitation. The wall pier specimens were intended to represent vertical wall segments in between openings with stiff spandrel beams spanning the top and bottom of the pier (Orackal, Massone and Wallace 2009). To simulate these boundary conditions, wall specimen rotations were prevented at the top and bottom of the specimen and lateral loads were applied to induce reverse curvature bending. To facilitate this internal load distribution, an L-shaped steel loading frame was used to apply lateral load at specimen midheight(Figure A.34). Axial load was applied to the specimen through the use of two vertical actuators, with one actuator located on each side of the test specimen. Additional control of the actuators ensured a zero rotation boundary condi-

tion along the top of the specimen. The geometric aspect ratio of the wall piers was 0.89 but the application of lateral load at specimen midheight reduces the shear span aspect ratio, $M_b/(V_b l_w)$, to one half of this value, or 0.44. Loading consisted of cyclic lateral loading (with full load reversal) with increasing target drift levels. Three complete cycles were performed at low drift levels (less than 0.80%), two cycles were performed thereafter. Each wall pier specimen (Figure A.35) was 48 inches tall, 54 inches wide and 6 inches thick. Vertical reinforcement consisted of a single curtain of distributed No. 4 bars (at 13 inches on center), with a pair of No. 4 bars provided at each wall end; no confining reinforcement was provided. Horizontal reinforcement consisted of a single curtain of No. 4 bars spaced at 12 inches on center, and hooks were not provided at either bar end. The only design parameter intentionally varied between specimen tests was the applied axial load ratio with three axial load demands considered: 1) zero axial load for specimens WP9 and 10, 2) $0.05A_g f'_c$ for specimens WP7 and WP8 and 3) $0.10A_g f'_c$ for WP5 and WP6. Calculated reinforcement ratios for the specimens are provided in Table A.8; a summary of measured response quantities and calculated strength parameters are provided in Table A.9.

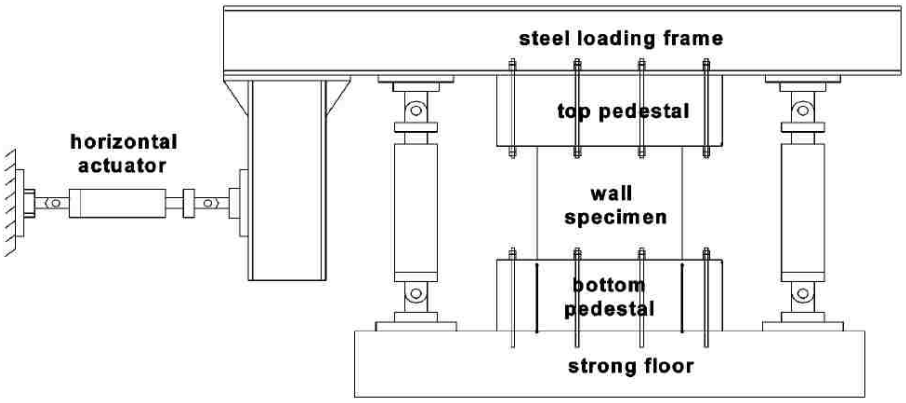

Figure A.34: Massone Specimen Loading Frame

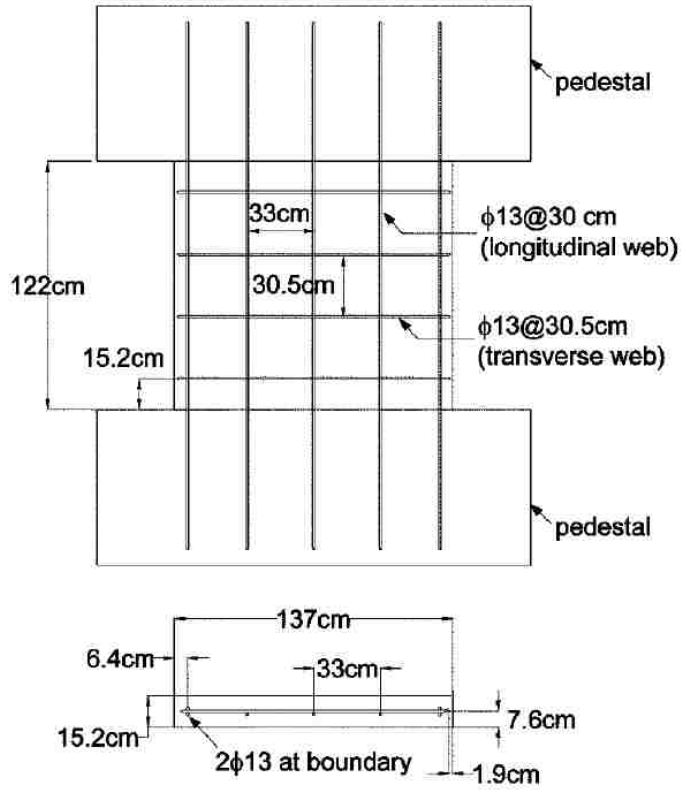

Figure A.35: Massone Wall Pier (WP) Specimen (dimensions in cm) (Orakcal et al.,2009)

Specimen WP5 was tested under an applied axial load of 133 kips, or 10% of the gross axial capacity and achieved peak strength at an imposed drift of 0.41%. The maximum specimen strength was 118.0 kips, which corresponds to a shear stress demand, v_{max}, of $8.7\sqrt{f'_c(psi)}A_{cv}$ and a shear demand to capacity ratio, $V_{b,max}/V_{n,pr}$, of 1.52 when using reported material strengths (f'_c = 4100 psi and f_y = 61500 psi) and ACI 318 (2011) Equation 21-7. Failure of the specimen was due to a diagonal crushing shear failure. First cracking was observed when a single diagonal crack (approx. 45 degrees) formed at 0.20% drift, first yielding (vertical and horizontal) occurred at a drift level of 0.40%. At 0.60% drift, a diagonal crack spanning from corner to corner of the specimen began to widen and sliding along this crack was observed. This sliding behavior led to complete loss of lateral specimen strength. Upon load reversal, strength gain was minimal and concrete crushing was observed near

midheight of the specimen. The experimentally determined load-displacement curve for specimen WP5 is provided in Figure A.37(d).

Specimen WP6 was tested under an applied axial load of 147 kips, or 10% of the gross axial capacity and achieved peak strength at an imposed drift of 0.63%. The maximum specimen strength was 121.4 kips, which corresponds to a shear stress demand, v_{max}, of $8.7\sqrt{f'_c(psi)}A_{cv}$ and a shear demand to capacity ratio, $V_{b,max}/V_{n,pr}$, of 1.58 when using reported material strengths (f'_c = 4550 psi) and ACI 318 (2011) Equation 21-7. Failure of the specimen was due to a diagonal crushing shear failure. First cracking was observed when a single diagonal crack (approx. 45 degrees) formed at 0.20% drift, first yielding (vertical and horizontal) occurred at a drift level of 0.40%. At 0.80% drift, primary diagonal crack spanning from corner to corner of the specimen began to widen. After completing load cycles at this drift level, the target drift was increased. When specimen drift reached 0.94% drift, the primary diagonal crack widened significantly and substantial strength loss occurred. The experimentally determined load-displacement curve for specimen WP6 is provided in Figure A.38(a).

Specimen WP7 was tested under an applied axial load of 75 kips, or 5% of the gross axial capacity and achieved peak strength at an imposed drift of 0.67%. The maximum specimen strength was 121.9 kips, which corresponds to a shear stress demand, v_{max}, of $6.7\sqrt{f'_c(psi)}A_{cv}$ and a shear demand to capacity ratio, $V_{b,max}/V_{n,pr}$, of 1.21 when using reported material strengths (f'_c = 4640 psi) and ACI 318 (2011) Equation 21-7. Failure of the specimen was due to a diagonal crushing shear failure. First cracking was observed when a single diagonal crack (approx. 45 degrees) formed at 0.20% drift, first yielding (both vertical and horizontal) occurred at a drift level of 0.30%. At 0.80% drift, concrete crushing at specimen midheight began and widening of primary diagonal cracks occurred. The experimentally determined load-displacement curve for specimen WP7 is provided in Figure A.38(b).

Specimen WP8 was also tested under an applied axial load of 75 kips and achieved peak strength at an imposed drift of 0.81%. The maximum specimen strength was 122.0 kips, which corresponds to a shear stress demand, v_{max}, of $7.2\sqrt{f'_c(psi)}A_{cv}$ and a shear demand to capacity ratio, $V_{b,max}/V_{n,pr}$, of 1.30 when using reported material strengths (f'_c

= 4640 psi) and ACI 318 (2011) Equation 21-7. Failure of the specimen was due to a diagonal crushing shear failure. First cracking was observed when a single diagonal crack (approx. 45 degrees) formed at 0.20% drift, first yielding (vertical only) occurred at a drift level of 0.30%. First horizontal yield was observed at the next drift level (0.40%). At 0.80% drift, concrete crushing at specimen midheight began and sliding was observed along the primary diagonal crack. This sliding behavior led to complete loss of lateral specimen strength upon reversal of load. After failure occurred, all concrete was removed and it was noted that significant kinking of vertical web reinforcement had occurred along the location of the primary diagonal crack. The experimentally determined load-displacement curve for specimen WP8 is provided in Figure A.38(c).

Specimen WP9 was tested without externally applied gravity load and achieved peak strength at an imposed drift of 0.72%. The maximum specimen strength was 119.8 kips, which corresponds to a shear stress demand, v_{max}, of $4.3\sqrt{f'_c(psi)}A_{cv}$ and a shear demand to capacity ratio, $V_{b,max}/V_{n,pr}$, of 0.76 when using reported material strengths (f'_c = 4030 psi and f_y = 61500 psi) and ACI 318 (2011) Equation 21-7. Failure of the specimen was due to a diagonal crushing shear failure. Yielding of vertical reinforcement occurred at a drift level of 0.20% and horizontal reinforcement was observed to yield one cycle later, at 0.30% drift. As loading continued, existing diagonal cracks continued to widen, however few new cracks were observed to form. As cracks widened, sliding along diagonal cracks and strength loss under reversing load were observed. At 1.6% drift, concrete spalling at midheight was observed and vertical cracks at wall boundaring increased in length. As loading continues, crushing at midheight spread to the wall edges and large triangular wedged of concrete spall from the specimen. The experimentally determined load-displacement curve for specimen WP9 is provided in Figure A.38(d).

Specimen WP10 was constructed to be similar to WP10 with no externally applied gravity load. However, this specimen was accidentally loading in tension prior to testing. Measured specimen response indicates a modestly weaker and significantly more flexible response for this specimen than for the WP9 specimen. Due to the difficulty in correctly simulating the accidentally cracked initial conditions, simulation of WP10 was not performed.

A.3.3 Wiradinata et al.

Wiradinata tested two low-rise structural walls (W1 and W2) to assess the performance of squat walls with varying aspect ratios. Specimen W1 had an aspect ratio of 0.5 and specimen W2 had an aspect ratio of 0.25. Each wall had a boundary element at each end and orthogonal layers of web reinforcement. No axial load was applied to either specimen, and lateral loading was applied cyclically (with complete load reversals) until failure.

Table A.10: Summary of Specimen Variation

Wall Specimen	Aspect Ratio (h_w/l_w)
W1	0.50
W2	0.25

Specimen W1 achieved peak strength at a lateral displacement of 0.31 inches (0.78% drift). The nominal shear stress in the wall at peak strength was $6.9\sqrt{f'_c}$. First yield of the specimen was reported at a lateral displacement of 0.08 inches (0.19% drift) at a shear stress level of $5.7\sqrt{f'_c}$. Failure of specimen W1 was a flexural type of failure. Although large diagonal cracks formed, ultimately failure was caused by crushing of the compressive toe of the wall. The specimen was able to reach a displacement capacity of approximately 0.38 inches (0.96% drift) before failure occurred. Removal of base slip deformations yields an observed drift capacity of 0.70%.

Reported strain gage data indicates minimal yielding of the horizontal reinforcement occurred during testing. Vertical steel yielding was reported to extend the entire height of the wall. Reported vertical reinforcement stresses indicate the inelastic strains remained on the yield plateau ($\epsilon \leq 7\epsilon_y$).

Specimen W2 achieved peak strength at a lateral displacement of 0.08 inches (0.42% drift). The nominal shear stress in the wall at peak strength was $8.9\sqrt{f'_c}$. First yield of the specimen was reported at a lateral displacement of 0.06 inches (0.30% drift) at a shear stress level of $8.7\sqrt{f'_c}$. Failure of specimen W2 was a shear type of failure. Extensive crushing of concrete occurred after horizontal reinforcement had yielded; the calculated

flexural capacity of the specimen was not reached during the test. The specimen was able to reach a displacement capacity of approximately 0.43 inches (2.3% drift) before failure occurred. Removal of base slip deformations yields an observed drift capacity of 0.25%.

Reported strain gage data indicates extensive yielding of the horizontal reinforcement occurred during testing. Vertical steel yielding was minimal and limited to the extreme reinforcing bar at each end.

A.3.4 Synge et al.

Synge, at al. tested four 1/2-scale low-rise structural walls; two of which were rectangular in cross section. Of the two planar walls, one specimen (W1) contained typical orthogonally distributed web reinforcement. The other planar wall (W2) contained both orthtogonally distributed web reinforcement and diagonal reinforcement. The intent of the diagonal reinforcement was to study the effect that diagonal reinforcement has on sliding strength. As no other walls in the experimental database include diagonal reinforcement, only wall specimen W1 is included in the experimental database.

Specimen W1 is a low-rise wall with boundary element reinforcement. No axial load was applied to the specimen, and lateral loading was applied cyclically (with complete load reversals) until failure.

Specimen W1 achieved peak strength at a lateral displacement of 0.36 inches (0.60% drift). The nominal shear stress in the wall at peak strength was $6.1\sqrt{f'_c}$. First yield of the specimen was reported at a lateral displacement of 0.09 inches (0.15% drift) at a shear stress level of $3.7\sqrt{f'_c}$. Behavior of specimen W1 was predominantly flexural, but failure of the specimen was a flexure-shear type failure. Crushing of the compression toe and yielding of vertical steel was reported, thus indicated a flexural hinge at the base of the wall. However, ultimately failure was caused by loss of shear carrying capacity in the compressive zone which led to a sliding failure at the wall base. The specimen was able to reach a displacement capacity of approximately 0.51 inches (0.86% drift) before the sliding failure occurred.

Reported strain gage data indicates no yielding of the horizontal reinforcement occurred

during testing. Vertical steel yielding was reported to extend to a height of approximately 3.3 ft (68% of the wall height) above the wall base. Peak strains in the vertical reinforcement reached a strain of approximately ten times the yield strain prior to failure of the specimen.

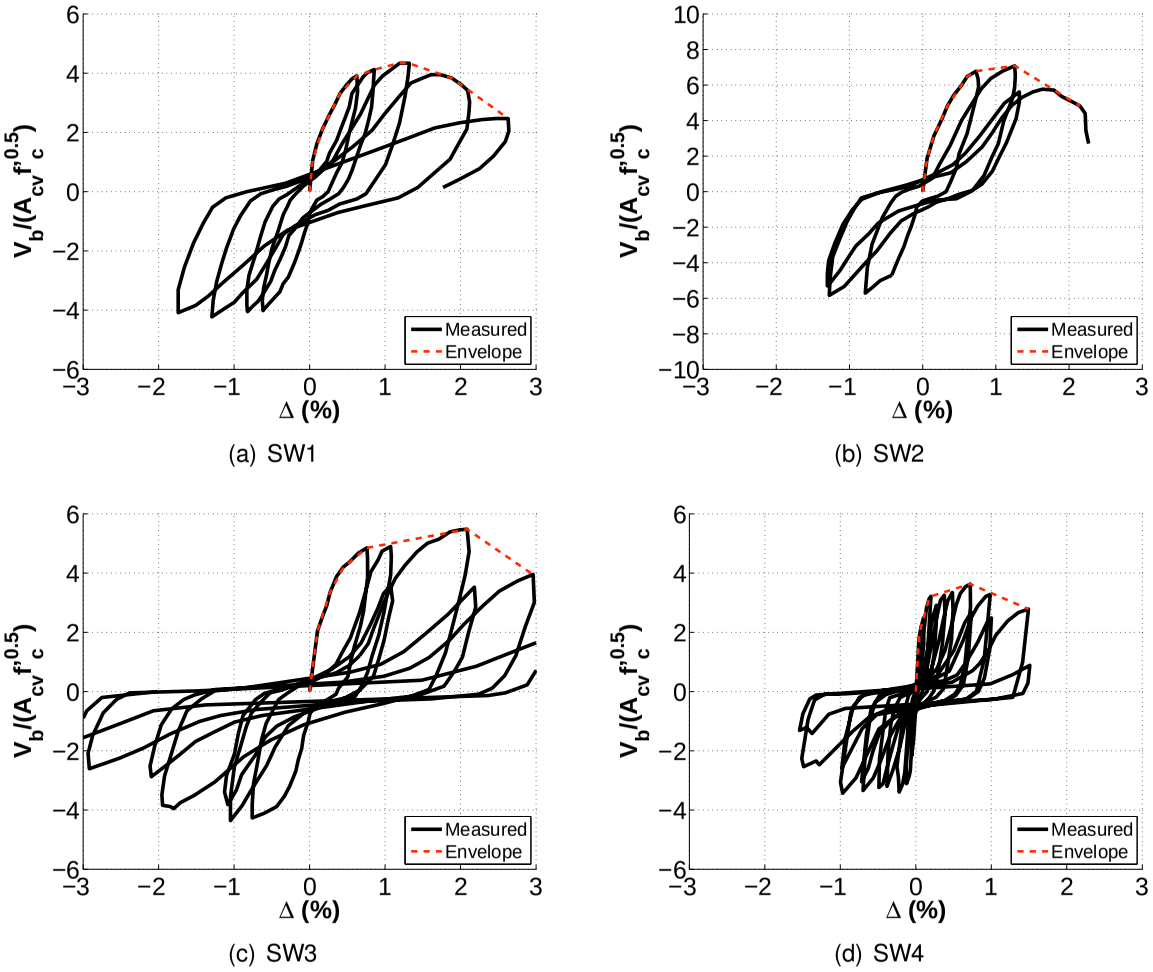

Figure A.36: Squat Wall Test Results

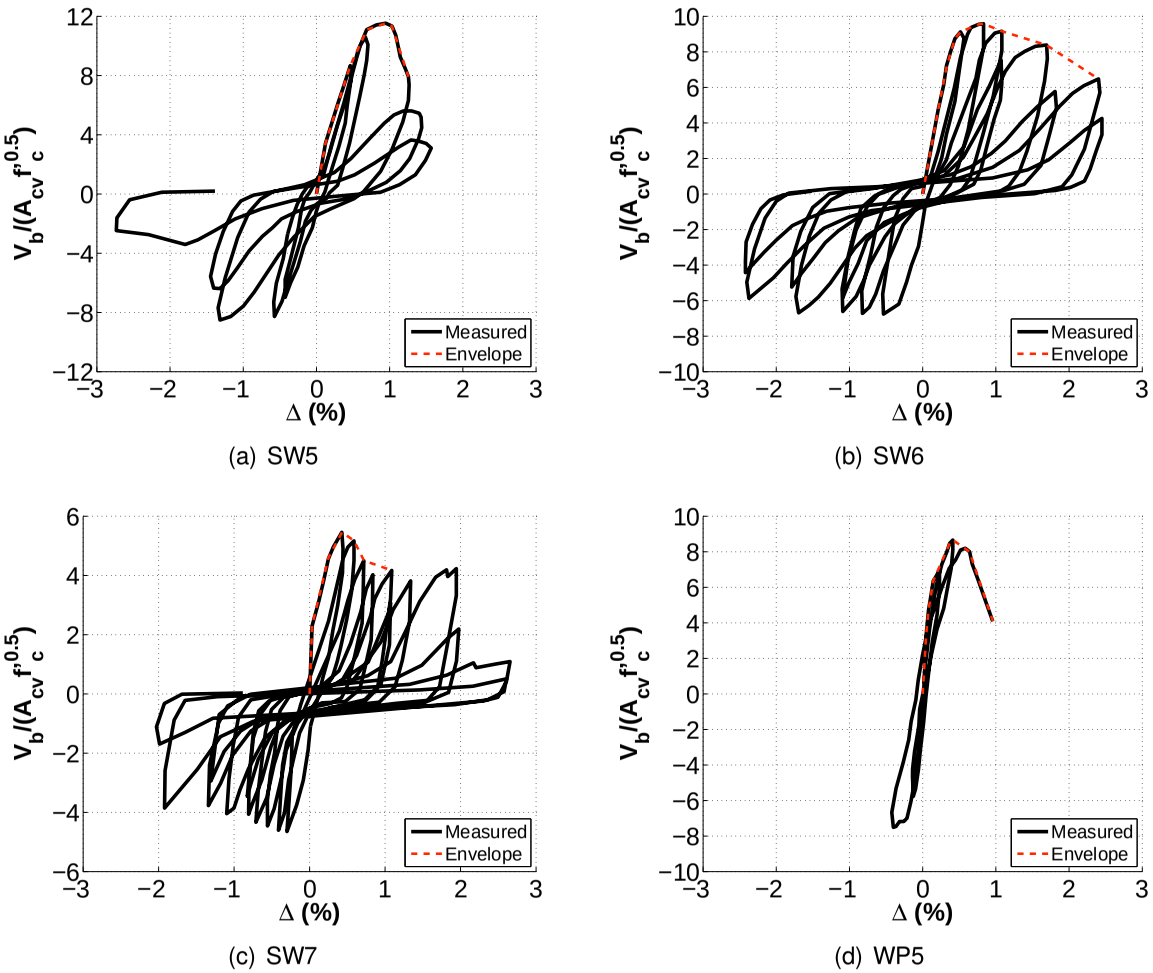

Figure A.37: Squat Wall Test Results

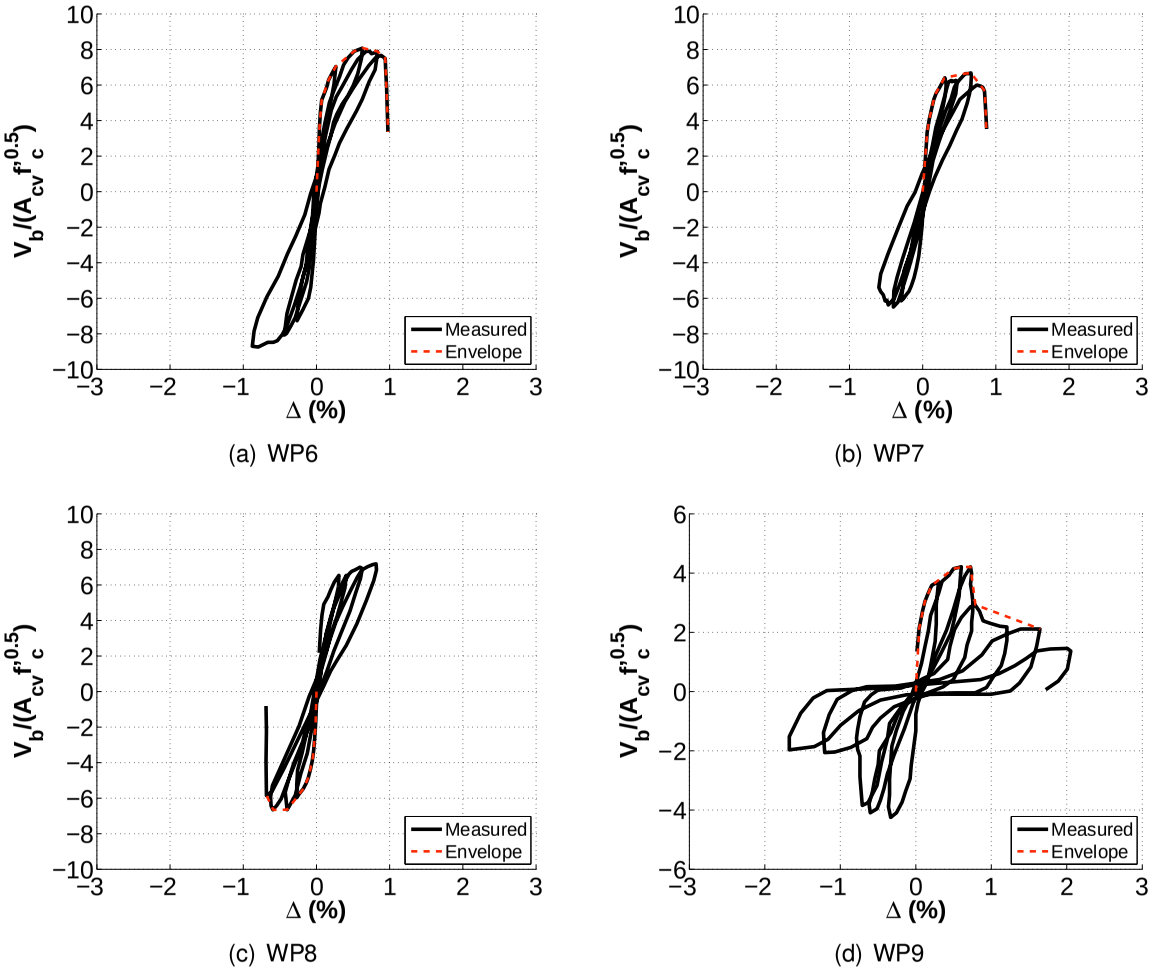

(a) WP6 (b) WP7

(c) WP8 (d) WP9

Figure A.38: Squat Wall Test Results

A.4 Specimen Modeling Considerations

A single numerical modeling approach that has been extensively validated to consistently and accurately predict failure across a large range of wall configurations (e.g. -squat/slender; planar/flanged) does not exist at this time. It is suspected that such a model would require a sophisticated finite element model capable of simulating (at a minimum) three-dimensional cyclic concrete material response, spalling and activation of confining reinforcement, bar buckling and bond deterioration. The development of such a model could be possible, however the practical applications of such a complex and computationally demanding model may be limited. Instead, most wall simulation research has advanced through the use of simplified models capable of representing some (but not all) aspects of performance.

Model simplification can limit the ability of a selected modeling approach to simulate all possible failure modes observed for the entire range of tested specimens. To address this, Figure A.39 provides reported specimen failure data plotted against shear span and shear demand-to-capacity (SDC) ratio. Plotted data include the database specimens from Table A.3 as well as an expanded database of squat, planar walls failing in shear reported by Gulec (2010). This data allows for some general observations regarding model simplifications for various wall configurations:

1. Wall specimens loaded with shear span aspect ratios greater than 1.50 and SDCs less than 1 typically exhibit flexual failures.

2. Wall specimens loaded with shear span aspect ratios greater than 1.50 and SDCs greater than 1 may exhibit web crushing shear failures (although the specimen data for this quadrant are sparse).

3. Wall specimens loaded with shear span aspect ratios less than 1.0 typically exhibit shear failures.

4. Wall specimens loaded with shear span ratios between 1.0 and 1.50 are observed to fail in both flexure and shear modes.

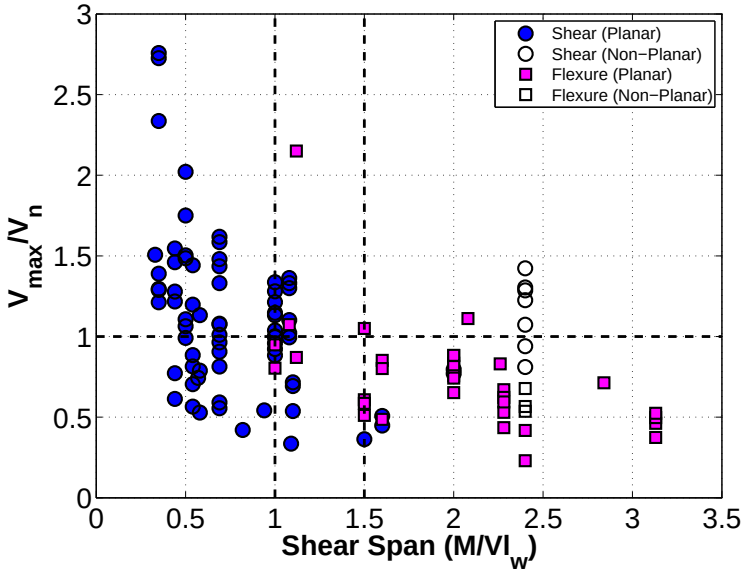

Figure A.39: Reported Specimen Failures

This data can be used to develop a decision matrix (Fig A.40) for numerical simulation of the tested specimens. For specimens expected to exhibit flexural failures, an acceptable modeling approach should be capable of simulating inelastic flexural response and simulating the failure modes associated with such a response (i.e. - crushing/buckling of concrete, rupture of longitudinal reinforcement). Such flexural models are less important for walls expected to fail in shear, and modeling of such specimens should include the effects of inelastic shear response and all possible shear failure modes (i.e. - diagonal crushing, transverse reinforcement yielding, sliding strength).

A.4.1 West Coast Building Inventory

Table A.11 compares design parameter statistics for the 21 slender wall specimens and an inventory of wall designs from recent walled building designs throughout the west coast of the United States (Mohr, 2007). The building inventory database includes 18 wall systems in high seismic regions of California and Washington. The inventory walls ranged between six and 30 stories in height, have rectangular and flanged cross-sections and were de-

	$M/(Vl_w) < 1$	$1 < M/(Vl_w) < 1.5$	$M/(Vl_w) > 1.5$
$V_{max}/V_n < 1$	✓Nonlinear Shear Response ✓Shear Failure Modes	✓Nonlinear Shear/Flexure ✓Shear Failure Modes ✓Flexural Failure Modes	✓Nonlinear Flexural Response ✓Flexural Failure Modes
$V_{max}/V_n > 1$	✓Nonlinear Shear Response ✓Shear Failure Modes	✓Nonlinear Shear/Flexure ✓Shear Failure Modes ✓Flexural Failure Modes	✓Nonlinear Flexural Response ✓Flexural Failure Modes ✓Web Crushing Shear

Figure A.40: Model Simulation Decision Matrix

signed between 1995 and 2005 (using design codes prevalent at the time of design).

Comparing the parameters in Table A.11 suggests that specimen database designs are representative of current wall design practices. The range of design parameters used for construction of the wall specimens adequately span the range of design parameters determined for actual wall designs. The average values of the parameters compare well for aspect ratio, longitudinal reinforcing ratio and transverse reinforcing ratio.

Table A.11: Specimen Design Parameter Statistics

Parameter	Group	Min.	Max.	Mean
l_w/t	Specimen Database	7.5	21.2	14.1
	Bldg. Inventory	4.9	20.3	12.8
l_{be}/l_w	Specimen Database	0.10	0.19	0.13
	Bldg. Inventory	0.10	0.31	0.19
ρ_{be} (%)	Specimen Database	0.77	5.7	2.3
	Bldg. Inventory	2.1	4.1	3.1
ρ_v (%)	Specimen Database	0.23	1.57	0.45
	Bldg. Inventory	0.25	1.00	0.48
ρ_t (%)	Specimen Database	0.25	1.00	0.39
	Bldg. Inventory	0.25	1.38	0.45
$\rho_{t,be}$ (%)	Database	0.25	1.90	0.70
	Bldg. Inventory	0.52	1.18	0.86

Appendix B

LINE ELEMENT MODEL STUDIES

B.1 Fiber Section Model Discretization Study

Moment curvature results were generated to determine a rule for estimating a reasonable number of concrete material fibers to accurately simulate flexural response of planar wall cross-sections. Considerable computational cost can be unduly incurred by selected an unnecessarily dense grid of fibers. Reducing the number of fibers to an optimal level can lead to considerable computational savings, particularly for collapse assessment applications require structures be analyzed using large suites of ground motion records scaled to multiple intensity levels.

The discretization study was performed considering the planar wall specimen database referenced extensively in Chapter 2. For each specimen, multiple discretizations along the wall length were considered and differences between the predicted moment-curvature results were compared by visual inspection of the plotted data.

Each fiber mesh was defined in terms of the number of fibers defined across the well confined end boundary element, n_f. The specimen boundary element length and the selected value for n_f defined a fiber thickness for the analysis and this fiber length was used to determined the number of equal thickness fibers used to discretize the unconfined wall web. For all analyses, a single fiber was consider in the wall thickness direction because only curvatures in the plane of the were considered.

Moment curvature plots for the planar specimens are shown in Figures B.1 to B.3. Plotted results shown two discretization levels, n_f equal to 2 and n_f equal to 8. These data shown that even crudely discretized concrete fiber meshes can reasonably simulate cyclic section response of wall cross-sections. However, for a few sections, the softening cyclic response can not accurately be determined for coarse meshes (RW1 (Thomsen and Wallace); WR20 (Oh et al.)). Thus, it is recommended that a maximum fiber thickness be used such that 8 fibers are provided across the length of the boundary element for planar wall cross-sections. This maximum thickness was found to capture the fully cyclic response of the specimen cross-sections and further discretization minimally impacted the simulated results.

Using the minimum recommended value of 8 fibers across the boundary element length,

the total number of fibers along the wall section can be calculated to be:

$$n_f \approx \frac{8}{\beta} \tag{B.1}$$

where β is the ratio of the boundary element length to the wall length.

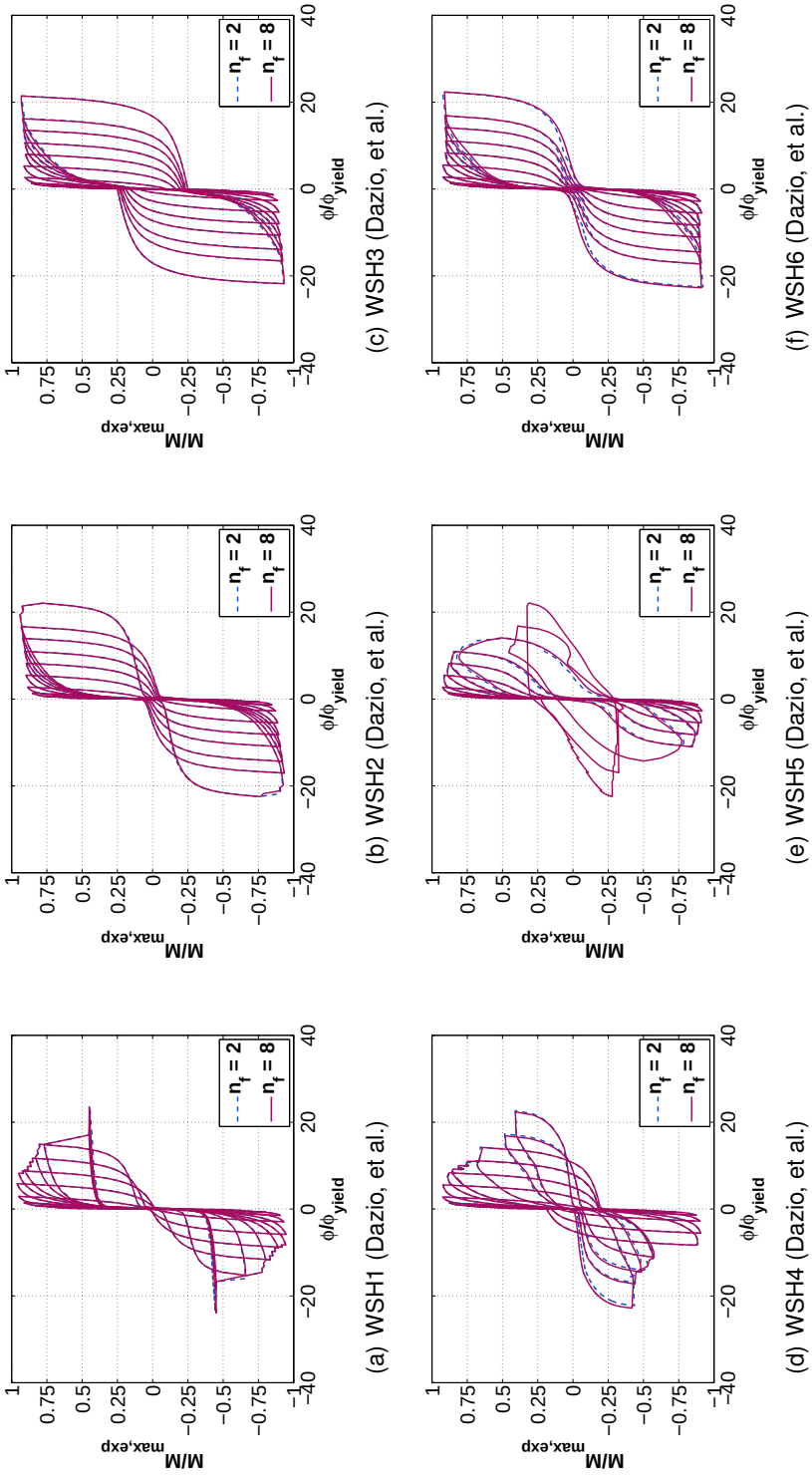

(a) WSH1 (Dazio, et al.)

(b) WSH2 (Dazio, et al.)

(c) WSH3 (Dazio, et al.)

(d) WSH4 (Dazio, et al.)

(e) WSH5 (Dazio, et al.)

(f) WSH6 (Dazio, et al.)

Figure B.1: Fiber-Section Response

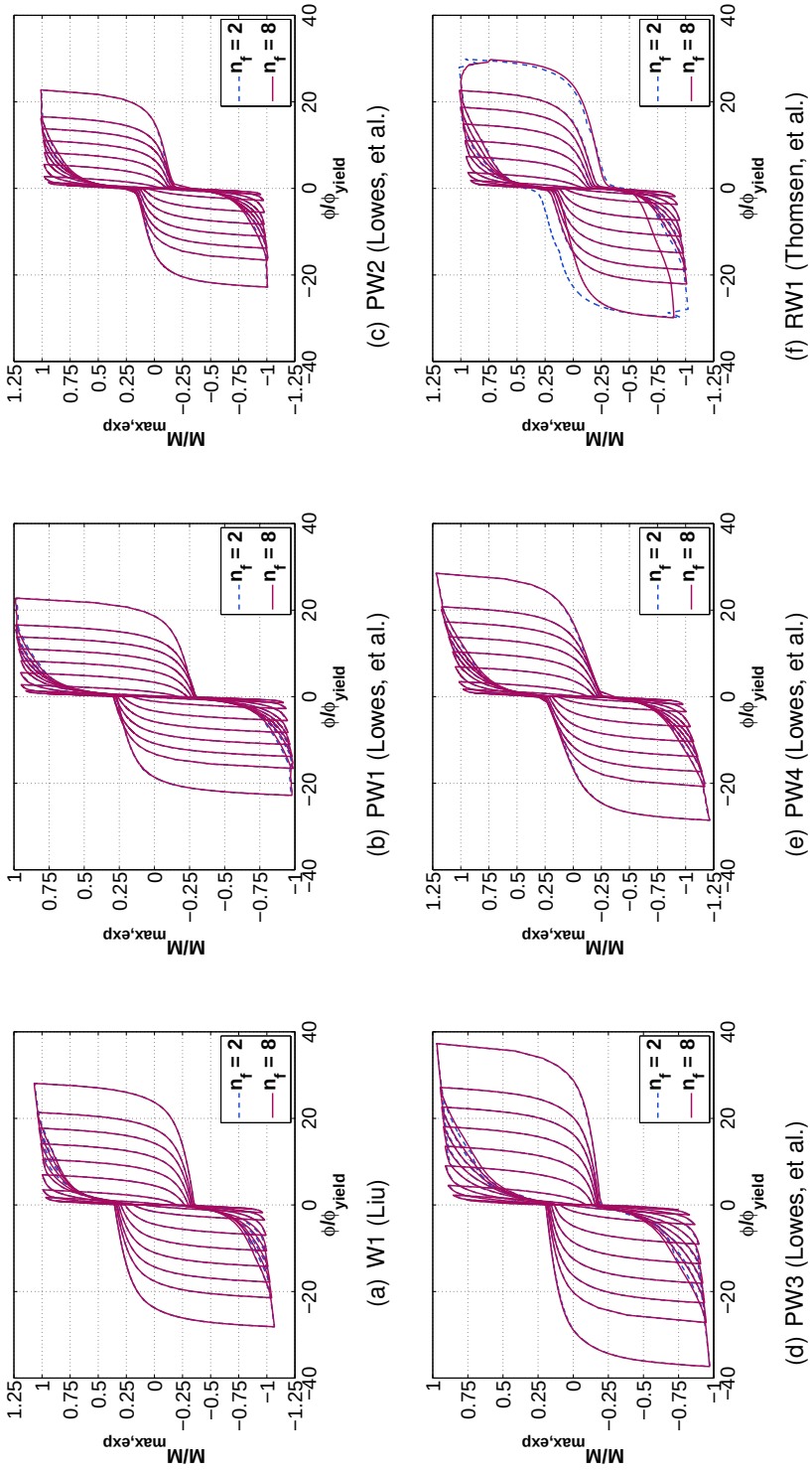

(a) W1 (Liu) (b) PW1 (Lowes, et al.) (c) PW2 (Lowes, et al.)

(d) PW3 (Lowes, et al.) (e) PW4 (Lowes, et al.) (f) RW1 (Thomsen, et al.)

Figure B.2: Fiber-Section Response

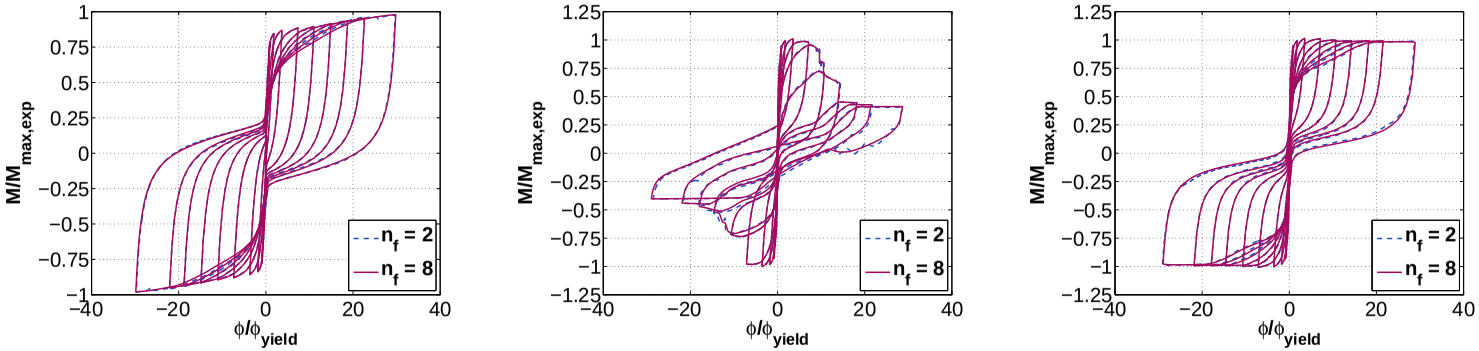

(a) RW1 (Thomsen, et al.) (b) WR0 (Oh, et al.) (c) WR10 (Oh, et al.)

(d) WR20 (Oh, et al.) (e) S5 (Vallenas, et al.) (f) S6 (Vallenas, et al.)

Figure B.3: Fiber-Section Response

B.2 Basic Line Element Specimen Load-Displacement Results

This section provides simulation results for the slender wall specimens using basic (unregularized) force-based and displacement-based distributed-plasticity line element models. Force-based element results are provided in Section B.2.1; displacement-based element results are provided in Section B.2.2.

B.2.1 Force-Based Beam Column Element Results

Table B.1: Basic Model Mesh Refinement Results

Specimen	Author	Displacement-Based									Force-Based					
		Stiffness Ratio			Strength Ratio			Drift Ratio			Stiffness Ratio		Strength Ratio		Drift Ratio	
		2 EL	4 EL	8 EL	2 EL	4 EL	8 EL	2 EL	4 EL	8 EL	3 IP	5 IP	3 IP	5 IP	3 IP	5 IP
WSH1	Dazio, et al.	1.02	1.02	1.01	1.17	1.05	1.01	3.80	2.42	1.40	0.98	0.98	0.97	1.00	3.25	1.38
WSH2	Dazio, et al.	1.02	1.01	1.00	1.15	1.04	1.01	3.27	2.45	1.43	1.00	0.99	0.94	0.99	3.05	1.16
WSH3	Dazio, et al.	1.02	1.01	1.00	1.17	1.05	1.01	3.21	2.22	1.41	1.03	0.99	0.96	0.99	3.37	1.28
WSH4	Dazio, et al.	1.02	1.01	1.00	1.19	1.08	1.03	3.50	2.49	1.52	1.02	0.99	0.99	1.00	2.90	1.31
WSH5	Dazio, et al.	1.07	1.00	1.00	1.19	1.07	1.02	3.66	2.42	1.57	0.97	1.01	0.99	1.00	3.52	1.41
WSH6	Dazio, et al.	1.04	1.00	1.00	1.18	1.05	1.02	3.10	2.25	1.46	0.99	1.00	0.97	1.00	3.95	1.46
W1	Liu	1.03	1.01	1.00	1.21	1.05	1.01	1.85	1.77	1.23	1.01	1.00	0.94	1.01	1.63	0.99
W2	Liu	1.04	1.00	1.00	1.17	1.04	1.00	1.52	1.52	1.25	1.01	1.00	0.92	1.01	1.30	0.95
PW1	Lowes et al.	1.01	1.00	1.00	1.08	1.03	1.01	2.99	1.88	1.28	1.00	1.00	0.99	1.00	1.85	1.09
PW2	Lowes et al.	1.01	1.00	1.00	1.10	1.04	1.01	3.63	2.18	1.37	1.00	1.00	0.98	1.00	2.32	1.12
PW3	Lowes et al.	1.01	1.00	1.00	1.09	1.03	1.01	2.14	1.57	1.20	1.00	1.00	0.98	1.00	1.74	1.04
PW4	Lowes et al.	1.01	1.00	1.00	1.10	1.04	1.01	2.45	1.52	1.16	1.00	1.00	0.99	1.00	1.24	1.03
RW1	Thomsen, et al.	1.03	1.01	1.00	1.17	1.03	1.01	2.39	1.92	1.34	1.00	1.00	0.93	1.00	2.50	1.01
RW2	Thomsen, et al.	1.03	1.01	1.00	1.15	1.03	1.01	1.93	1.81	1.28	1.00	1.00	0.92	1.01	2.23	1.00
S5	Vallenas, et al.	1.01	1.00	1.00	1.09	1.04	1.02	2.00	1.47	1.16	1.00	1.00	0.99	0.99	1.23	1.01
S6	Vallenas, et al.	1.01	1.00	1.00	1.09	1.04	1.01	2.01	1.47	1.18	1.00	1.00	0.99	1.00	1.23	1.00
WR20	Oh, et al.	1.04	1.02	1.00	1.15	1.05	1.01	3.63	2.53	1.51	0.98	0.99	0.99	1.00	3.98	1.51
WR10	Oh, et al.	1.04	1.03	1.00	1.14	1.05	1.01	3.34	2.35	1.67	0.97	0.99	0.98	1.00	4.01	1.71
WR0	Oh, et al.	1.04	1.02	1.00	1.15	1.05	1.02	3.49	2.27	1.42	0.98	0.99	0.99	1.00	2.72	1.25
	Mean	1.02	1.00	1.00	1.14	1.05	1.01	2.84	2.02	1.36	1.00	1.00	0.97	1.00	2.53	1.20
	COV	0.01	0.01	0.00	0.04	0.01	0.01	0.26	0.19	0.11	0.02	0.01	0.03	0.00	0.39	0.18

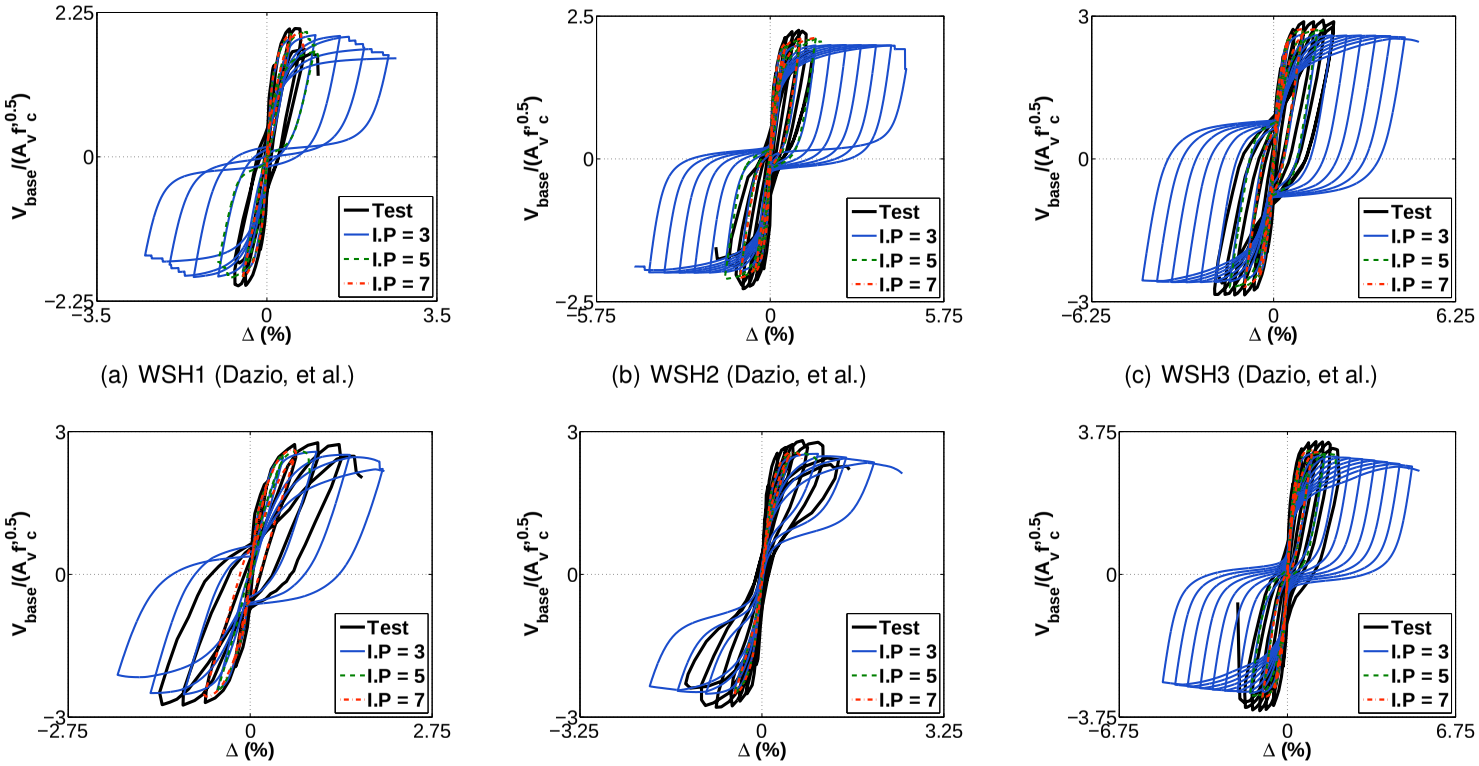

(a) WSH1 (Dazio, et al.) (b) WSH2 (Dazio, et al.) (c) WSH3 (Dazio, et al.)

(d) WSH4 (Dazio, et al.) (e) WSH5 (Dazio, et al.) (f) WSH6 (Dazio, et al.)

Figure B.4: Force-Based Beam Column Element Basic Modeling: Mesh Refinement Study

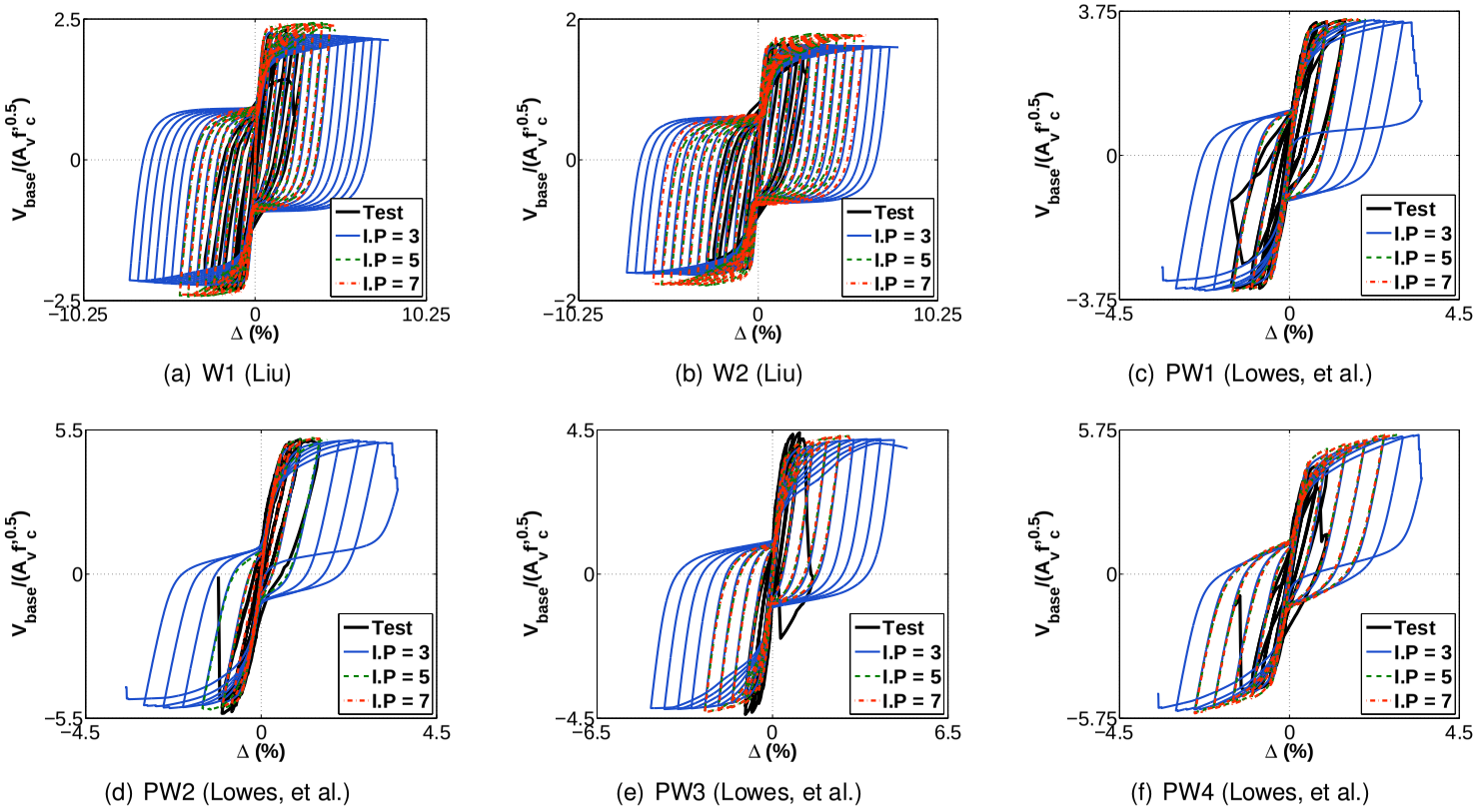

(a) W1 (Liu) (b) W2 (Liu) (c) PW1 (Lowes, et al.)

(d) PW2 (Lowes, et al.) (e) PW3 (Lowes, et al.) (f) PW4 (Lowes, et al.)

Figure B.5: Force-Based Beam Column Element Basic Modeling: Mesh Refinement Study

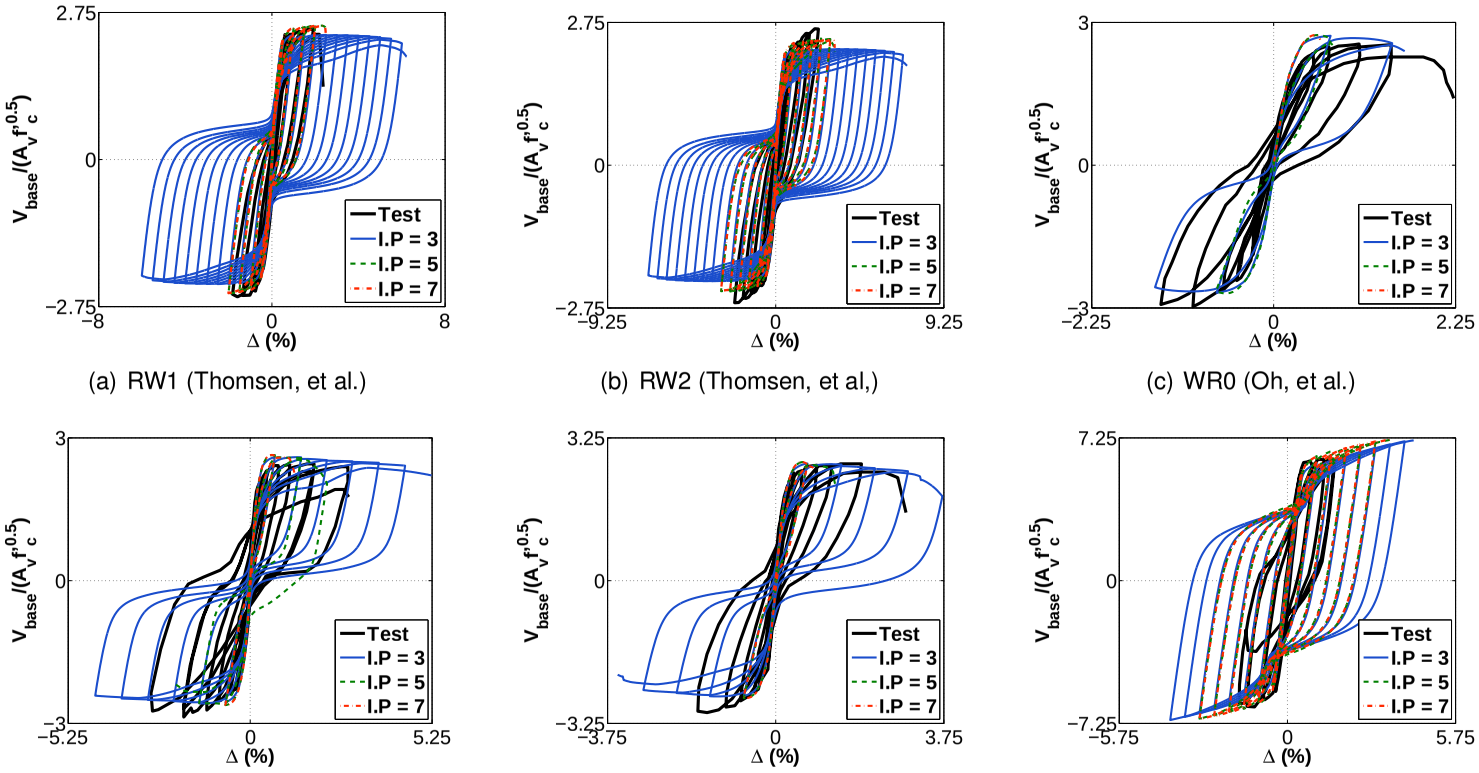

(a) RW1 (Thomsen, et al.)

(b) RW2 (Thomsen, et al,)

(c) WR0 (Oh, et al.)

(d) WR10 (Oh, et al.)

(e) WR20 (Oh, et al.)

(f) S6 (Vallenas, et al.)

Figure B.6: Force-Based Beam Column Element Basic Modeling: Mesh Refinement Study

B.2.2 Displacement-Based Beam Column Element Results

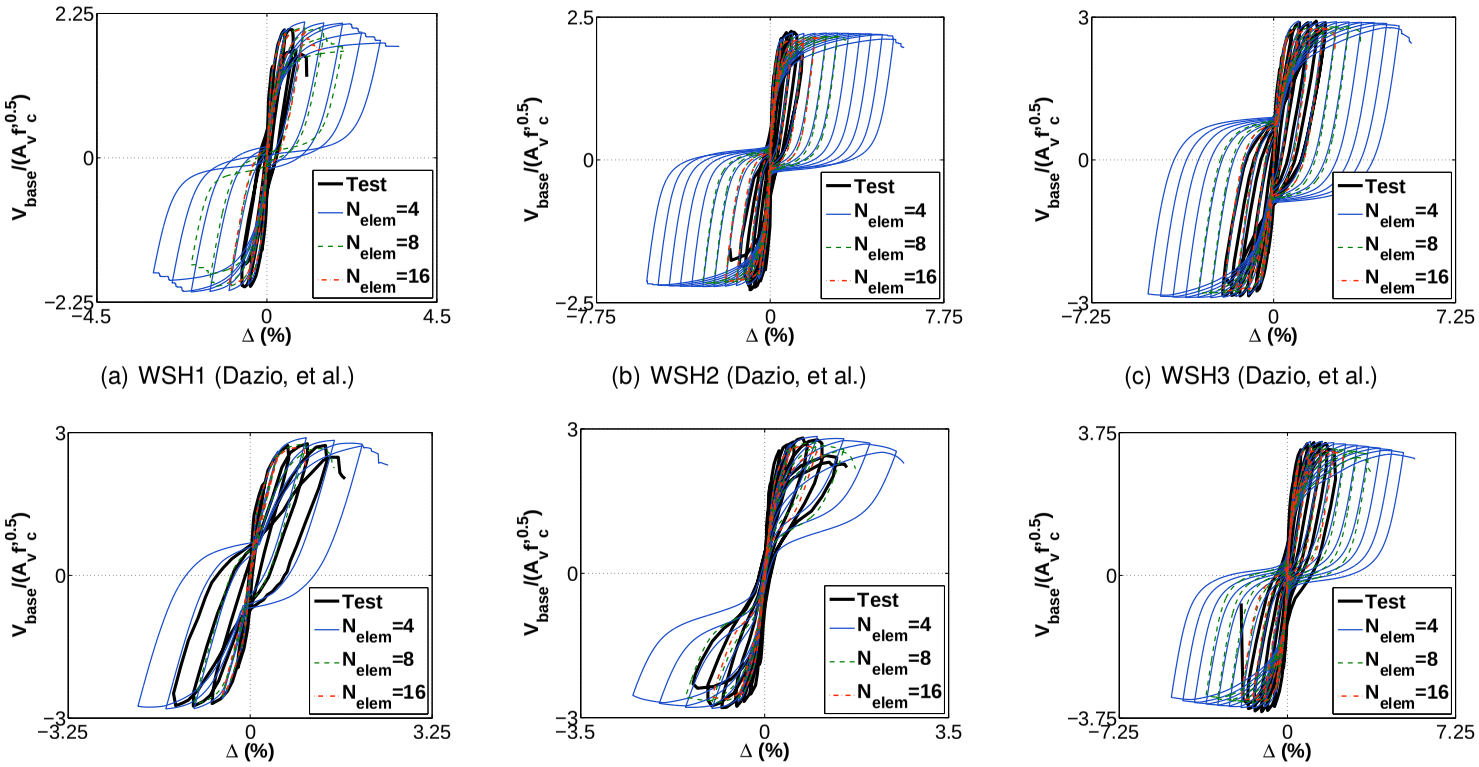

(a) WSH1 (Dazio, et al.)

(b) WSH2 (Dazio, et al.)

(c) WSH3 (Dazio, et al.)

(d) WSH4 (Dazio, et al.)

(e) WSH5 (Dazio, et al.)

(f) WSH6 (Dazio, et al.)

Figure B.7: Displacement-Based Beam Column Element Basic Modeling: Mesh Refinement Study

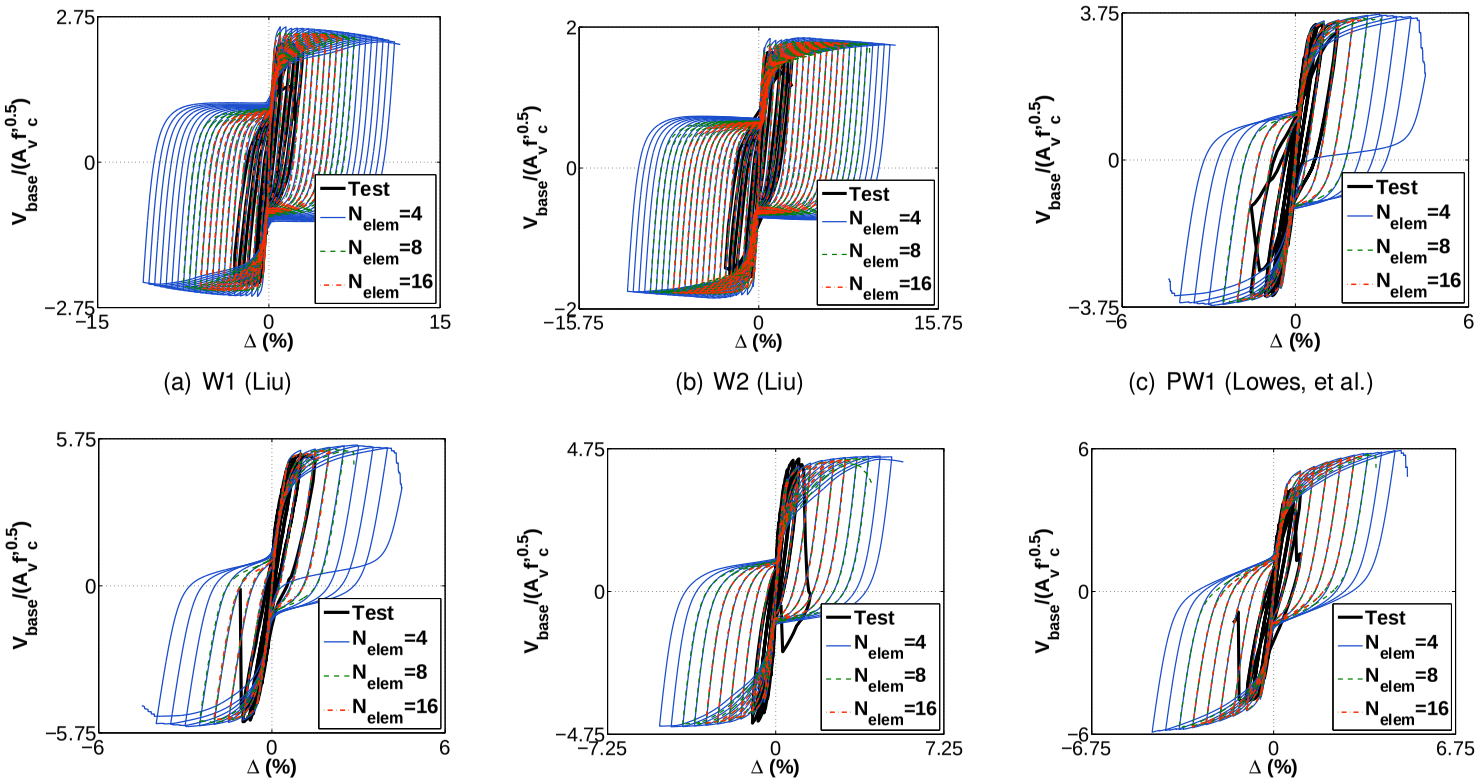

(a) W1 (Liu) (b) W2 (Liu) (c) PW1 (Lowes, et al.)

(d) PW2 (Lowes, et al.) (e) PW3 (Lowes, et al.) (f) PW4 (Lowes, et al.)

Figure B.8: Displacement-Based Beam Column Element Basic Modeling: Mesh Refinement Study

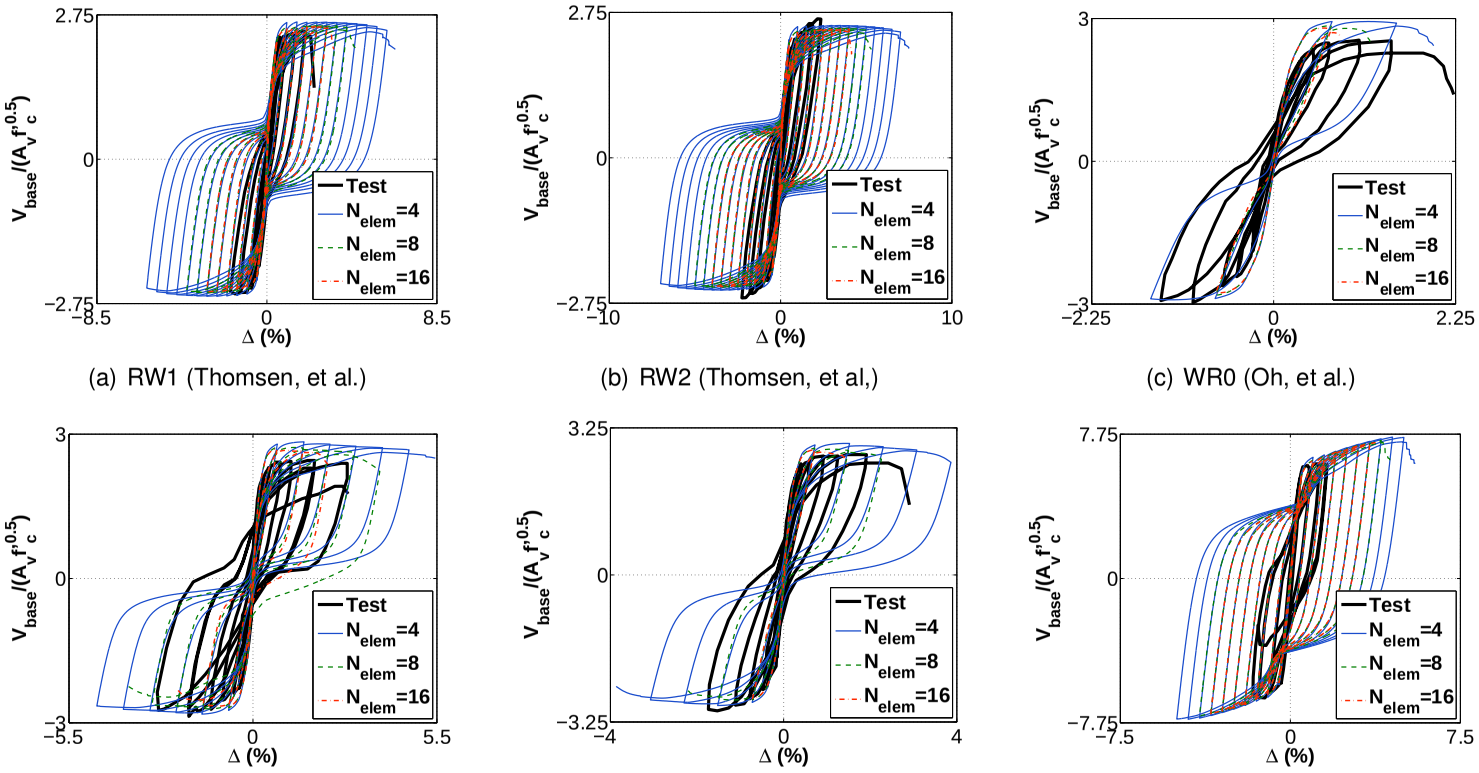

(a) RW1 (Thomsen, et al.)

(b) RW2 (Thomsen, et al,)

(c) WR0 (Oh, et al.)

(d) WR10 (Oh, et al.)

(e) WR20 (Oh, et al.)

(f) S6 (Vallenas, et al.)

Figure B.9: Displacement-Based Beam Column Element Basic Modeling: Mesh Refinement Study

B.3 Regularized Line Element Specimen Load-Displacement Results

This section provides simulation results for the slender wall specimens using basic (unregularized) force-based and displacement-based distributed-plasticity line element models. Force-based element results are provided in Section B.3.1; displacement-based element results are provided in Section B.3.2.

B.3.1 Force-Based Beam Column Element Results

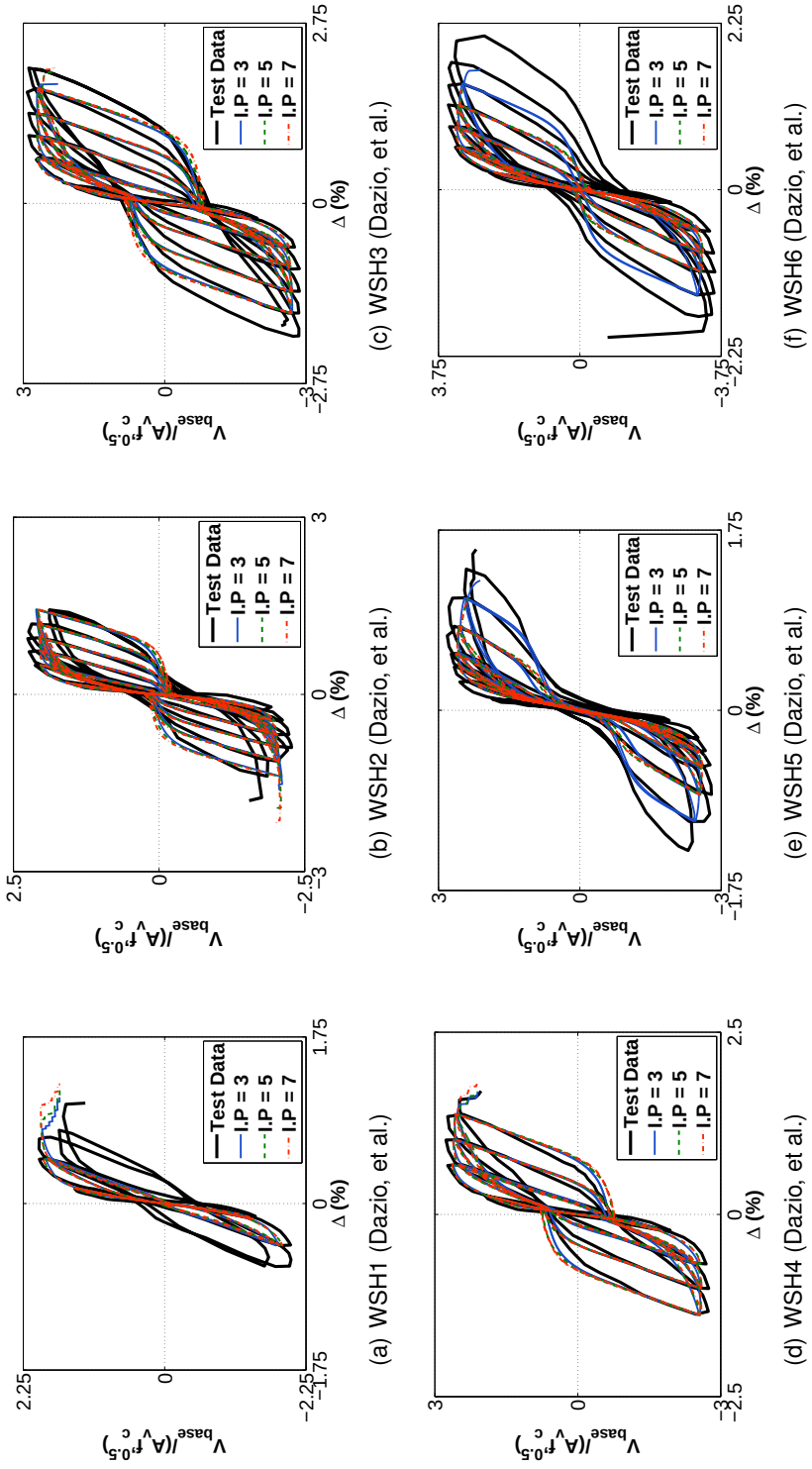

(a) WSH1 (Dazio, et al.) (b) WSH2 (Dazio, et al.) (c) WSH3 (Dazio, et al.)

(d) WSH4 (Dazio, et al.) (e) WSH5 (Dazio, et al.) (f) WSH6 (Dazio, et al.)

Figure B.10: Force-Based Beam Column Element Regularized Modeling: Mesh Refinement Study

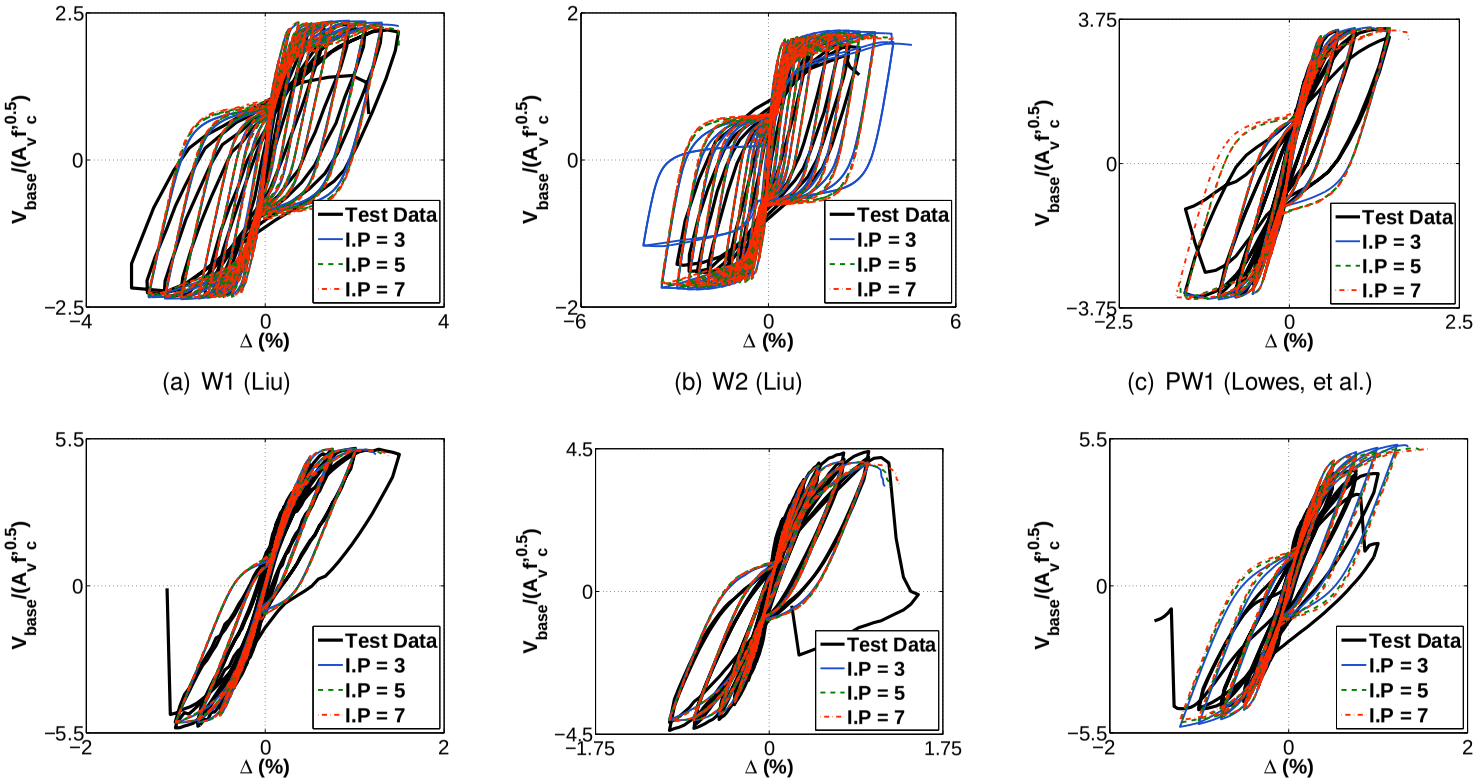

(a) W1 (Liu) (b) W2 (Liu) (c) PW1 (Lowes, et al.)

(d) PW2 (Lowes, et al.) (e) PW3 (Lowes, et al.) (f) PW4 (Lowes, et al.)

Figure B.11: Force-Based Beam Column Element Regularized Modeling: Mesh Refinement Study

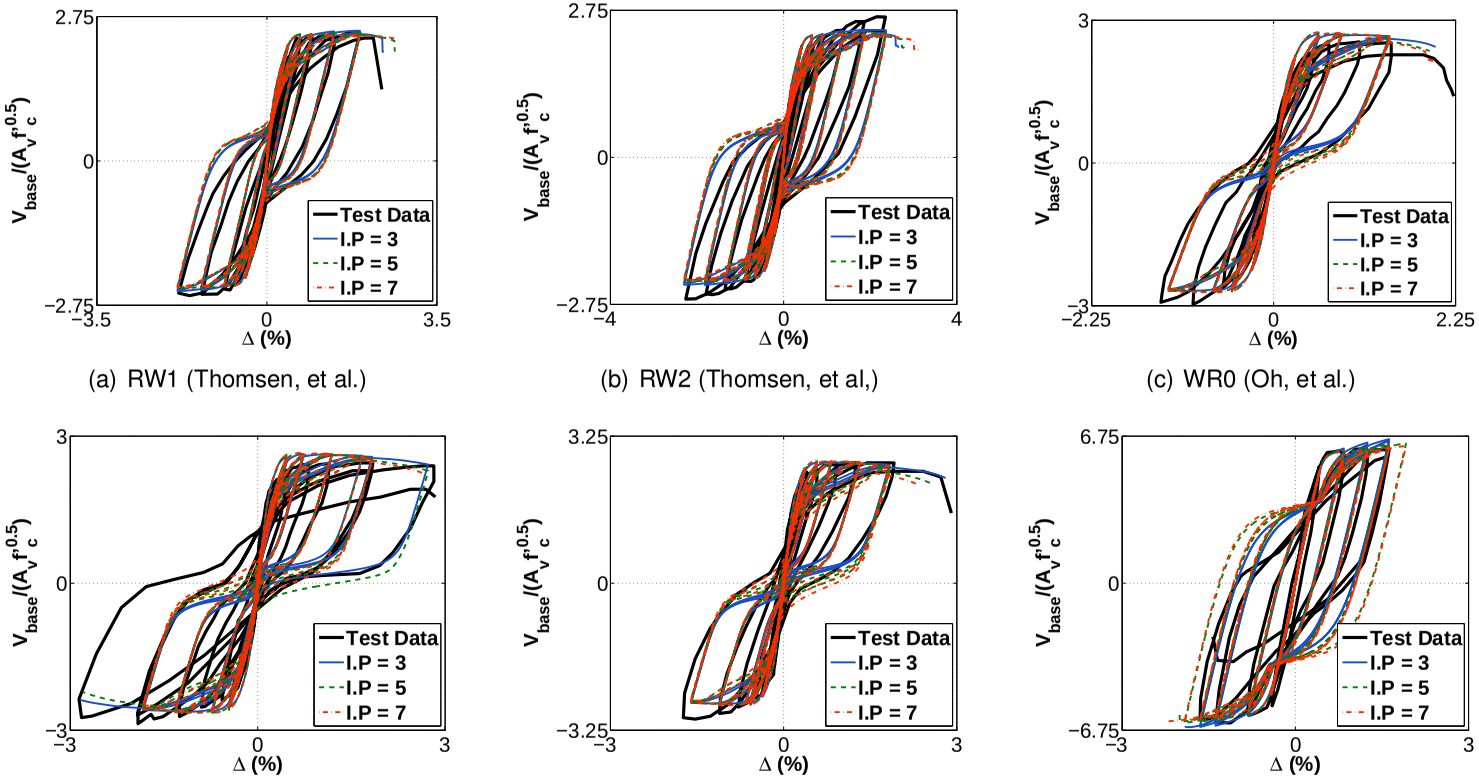

(a) RW1 (Thomsen, et al.) (b) RW2 (Thomsen, et al,) (c) WR0 (Oh, et al.)

(d) WR10 (Oh, et al.) (e) WR20 (Oh, et al.) (f) S6 (Vallenas, et al.)

Figure B.12: Force-Based Beam Column Element Regularized Modeling: Mesh Refinement Study

B.3.2 Displacement-Based Beam Column Element Results

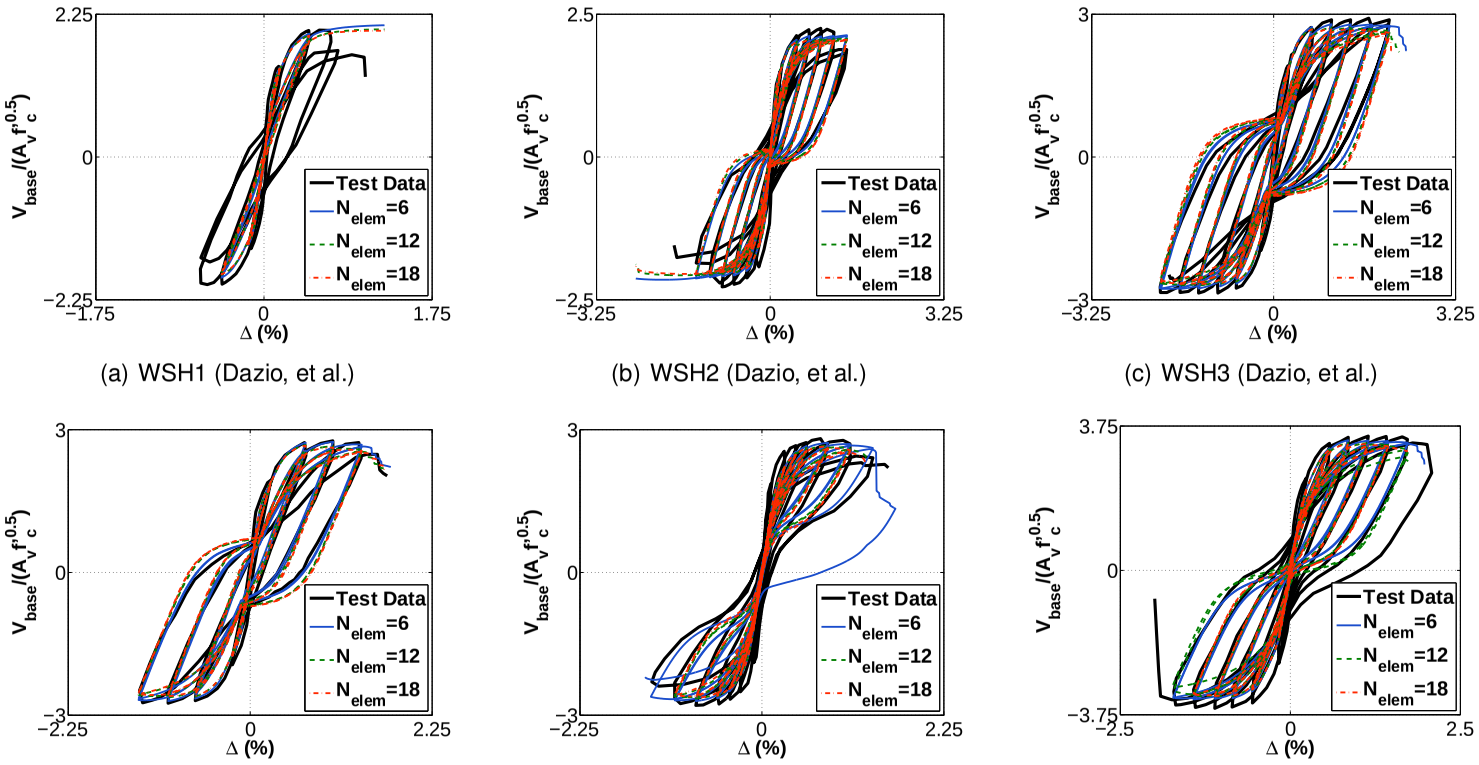

(a) WSH1 (Dazio, et al.) (b) WSH2 (Dazio, et al.) (c) WSH3 (Dazio, et al.)

(d) WSH4 (Dazio, et al.) (e) WSH5 (Dazio, et al.) (f) WSH6 (Dazio, et al.)

Figure B.13: Displacement-Based Beam Column Element Regularized Modeling: Mesh Refinement Study

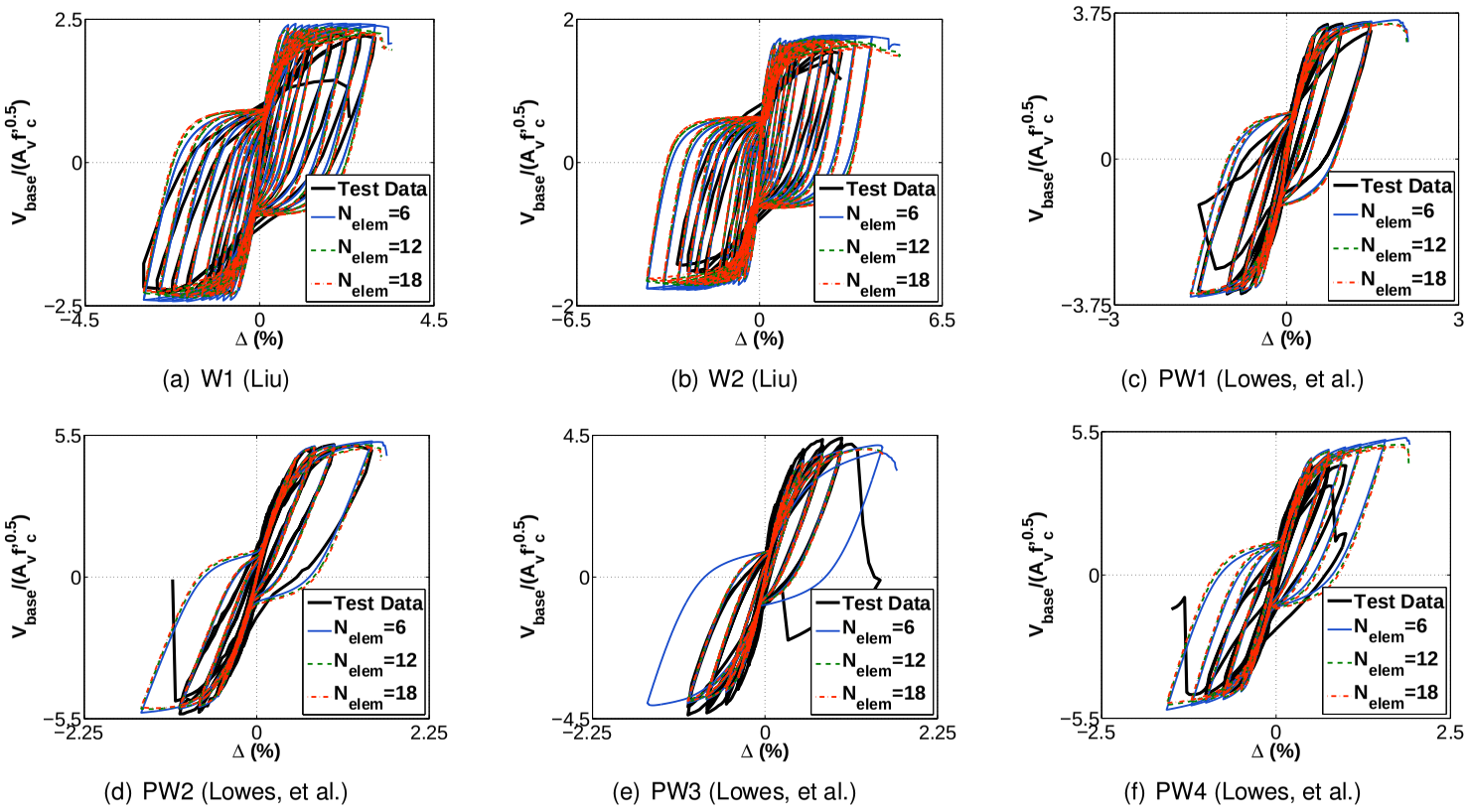

(a) W1 (Liu) (b) W2 (Liu) (c) PW1 (Lowes, et al.)

(d) PW2 (Lowes, et al.) (e) PW3 (Lowes, et al.) (f) PW4 (Lowes, et al.)

Figure B.14: Displacement-Based Beam Column Element Regularized Modeling: Mesh Refinement Study

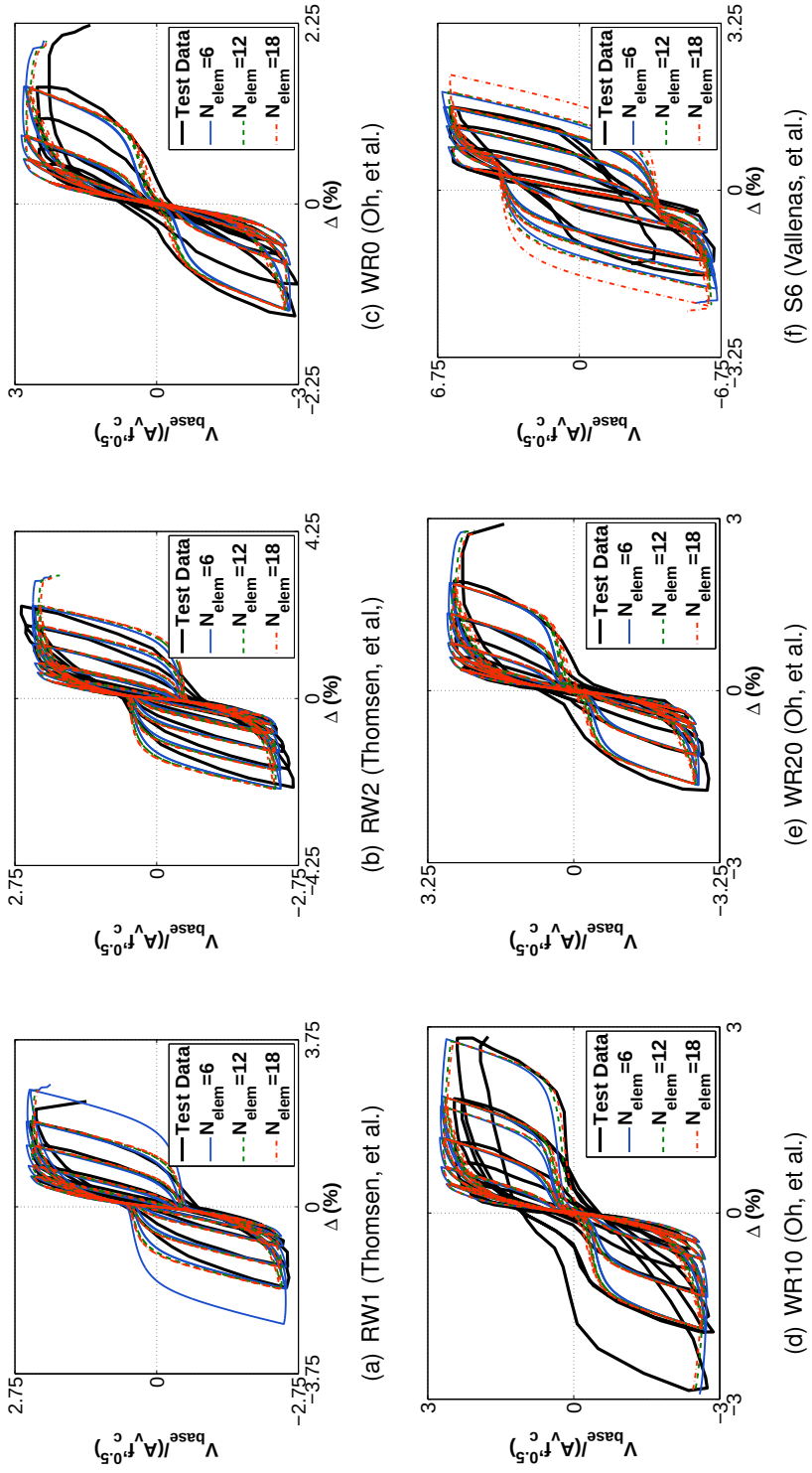

Figure B.15: Displacement-Based Beam Column Element Regularized Modeling: Mesh Refinement Study

Appendix C

VECTOR2 STUDIES

C.1 VecTor2 Squat Wall Results

In Chapter 2, the VecTor2 program was used to model 19 slender wall specimens. Results of this investigation demonstrated that 1) VecTor2 wall models can accurate simulate peak strength of slender walls, 2) slender wall models are approximately 15% stiffer than walls tested in the laboratory and 3) simulated drift capacity depends on the chosen mesh and localized softening effects the rate at which simulated strength is lost. Also in Chapter 2, VecTor2 results were compared to simulation results using computationally cheaper line element models and it was noted that both VecTor2 and distributed-plasticity line elements are equally accurate in predicting strength of slender walls, where response is expected to be dominated by flexure. However, the use of distributed-plasticity line element wall models would be inappropriate for modeling of squat walls that are dominated by shear behavior. For these walls, the use of a continuum analysis may be necessary and there is need to quantify how accurately finite element models in widespread use currently can simulate the response of squat walls. To study this topic, VecTor2 simulations for 12 squat wall specimens, tested as part of two recent experimental programs were performed. The primary goal of this study was to determine, in terms of global wall response quantities such as stiffness and strength, the accuracy for which VecTor2 simulations compare to laboratory test data.

C.1.1 Experimental Programs

A summary of the tested specimens and experimental results are provided in Appendix A. Numerical models were analyzed for the 13 squat wall specimens tested by Massone et. al (2006) and Whittaker et al. (2012).

C.1.2 Nonlinear Models

All specimen models were meshed to represent a single cantilever extending vertically above a fixed base using an orthogonal grid of rectangular plane stress elements. Based on wall modeling recommendations by Palermo and Vecchio (2009), approximately 20 ele-

ments across the horizontal wall width was used to define the continuum mesh. Horizontal and longitudinal reinforcement were modeled as smeared throughout the plane stress element mesh (i.e. - bars were not modeled as discrete elements). Specimen foundation and top reaction blocks were modeled using elastic plane stress elements and the foundation base was assigned full fixity. For specimens tested by Massone et al., lateral loads were applied at specimen midheight by using an L-shaped steel loading frame. The resultant load height reduced the specimen shear span to one-half the specimen height and produced an effective shear span ratio, ($M_b/(V_b l_w)$ = 0.44. To achieve this loading in VecTor2, Massone specimen models required explicit modeling of the steel loading frame(Figure C.1). While the inclusion of addition elements representing the geometry of the L-shaped frame does allow for correct specimen loading, this modeling approach does not enforce a zero-rotation boundary condition at the top of the specimen as was done experimentally. To address this potential modeling shortcoming, a more advanced model was created by the author which explicitly corrected for any rotations occurring at the top of the loading block. However, the difference between the predicted results were negligible and the simpler model was used. For Whittaker specimens, lateral cyclic loads were applied through a steel plate designed to spread the shear load across the entire wall length. For VecTor2 simulation of these specimens, the shear force was applied assuming a uniform load distribution across the wall and the steel loading plate was not modeled. For specimens subjected to axial loading, a uniformly distributed axial stress was applied to the top of the specimen and maintained constant throughout lateral loading. Lateral loading was applied using displacement-control. The average lateral displacement measured across the row of nodes located at the specimen effective height was used to monitor the applied displacement. Only monotonic loading was considered in the current evaluation. Horizontal and vertical fixed boundary conditions were applied to every node located along the base of the foundation block.

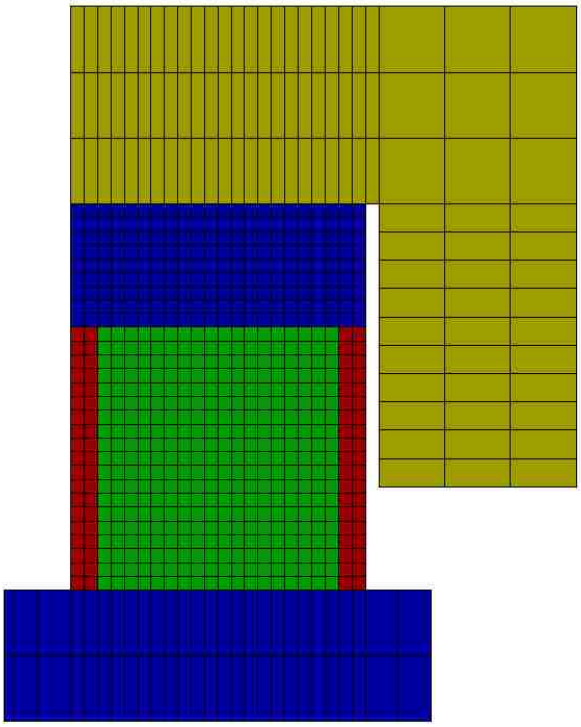

Figure C.1: Massone Specimen Model with L-shaped Frame

C.1.3 Simulation Results

Simulated to observed response quantity comparisons for the specimens are provided in Table C.1; load-displacement histories for the specimens are provided in Figures C.2 to C.4. Data from Table C.1 demonstrate:

1. Squat wall stiffness is poorly simulated by the VecTor2 models. For the seven specimens tested by Whittaker, the mean ratio of simulated $\Delta_{0.75}$ to observed $\Delta_{0.75}$ was 0.45 with coefficient of variation (COV) of 0.21. For the five specimens tested by Massone, the mean ratio was 0.40 with COV = 0.21. Thus, for all 12 specimens, the simulated stiffness was more than twice as stiff as determined experimentally. These results are consistent with investigations of squat walls performed by Palermo (2002), who suggested the inaccurate initial stiffness simulated by VecTor2 was due to the initially cracked state of laboratory tested specimens due to shrinkage.

2. Stiffness ratios simulated by VecTor2 tended to increase with applied axial load ratio. For WP specimens tested under varying axial demand, mean simulated stiffness ratios were 0.27, 0.42 and 0.45 for axial demands of 0.0, 0.05 and 0.10f'$_c$A$_g$, respectively.

3. Stiffness ratios simulated by VecTor2 tended to increase with decreasing aspect ratio. For varying aspect ratio SW specimens, mean simulated stiffness ratios were 0.29, 0.43 and 0.53 were determined for specimen aspect ratios of 0.94, 0.54 and 0.33, respectively.

4. Mean wall strength of the 12 specimens was accurately simulated by VecTor2 (mean strength ratio = 0.95;COV = 0.06). For specimens SW1-SW7, simulated strength was accurately determined for all three specimen aspect ratios with a mean ratio of 0.93, 0.92 and 0.98 determined for specimens tested with aspect ratios of 0.94, 54 and 0.33, respectively. For the WP5 specimens loaded with different axial load ratios, 1) mean strength ratio for specimens loaded with 0.10f'$_c$A$_g$, 0.05f'$_c$A$_g$ and zero axial load ratios were 0.92, 0.94 and 1.06, respectively.

5. VecTor2 simulations significantly underestimated drift capacity both for specimens observed to fail due to sliding and for specimens observed to fail by diagonal crushing. A mean simulated to drift capacity ratio of 0.55 (COV = 0.27) was determined for specimens observed to exhibit sliding failures (SW1-SW7);a mean ratio of 0.62 (COV = 0.45) was found for specimens observed to fail by diagonal compression (WP5-WP7).

6. For all SW specimens, VecTor2 correctly simulated a sliding failure initiated at the wall base (Fig C.5(a)). For 4 of the 5 WP specimens, VecTor2 correctly simulated a diagonal compressive failure (Fig C.5(b)). For WP9, VecTor2 incorrectly simulated a sliding failure instead of the observed diagonal compressive failure.

Table C.1: Core Wall Specimen Simulation Results

Specimen	Monotonic Simulation			Failure Mode	
	$\frac{\Delta_{0.75,sim}}{\Delta_{0.75,obs}}$	$\frac{V_{bm,sim}}{V_{bm,obs}}$	$\frac{\Delta_{u,sim}}{\Delta_{u,obs}}$	Simulated	Observed
SW1	0.29	0.93	0.49	Sliding	Sliding
SW2	0.41	0.97	0.60	Sliding	Sliding
SW3	0.41	0.85	0.42	Sliding	Sliding
SW4	0.46	0.94	0.51	Sliding	Sliding
SW5	0.46	1.00	0.79	Sliding	Sliding
SW6	0.58	0.95	0.36	Sliding	Sliding
SW7	0.55	0.98	0.68	Sliding	Sliding
WP5	0.50	0.91	0.51	Diagonal Crushing	Diagonal Crushing
WP6	0.40	0.93	0.37	Diagonal Crushing	Diagonal Crushing
WP7	0.43	0.97	0.63	Diagonal Crushing	Diagonal Crushing
WP8	0.41	0.90	0.51	Diagonal Crushing	Diagonal Crushing
WP9	0.27	1.06	1.10	Sliding	Diagonal Crushing
Mean	0.43	0.95	0.58		
COV	0.21	0.06	0.36		

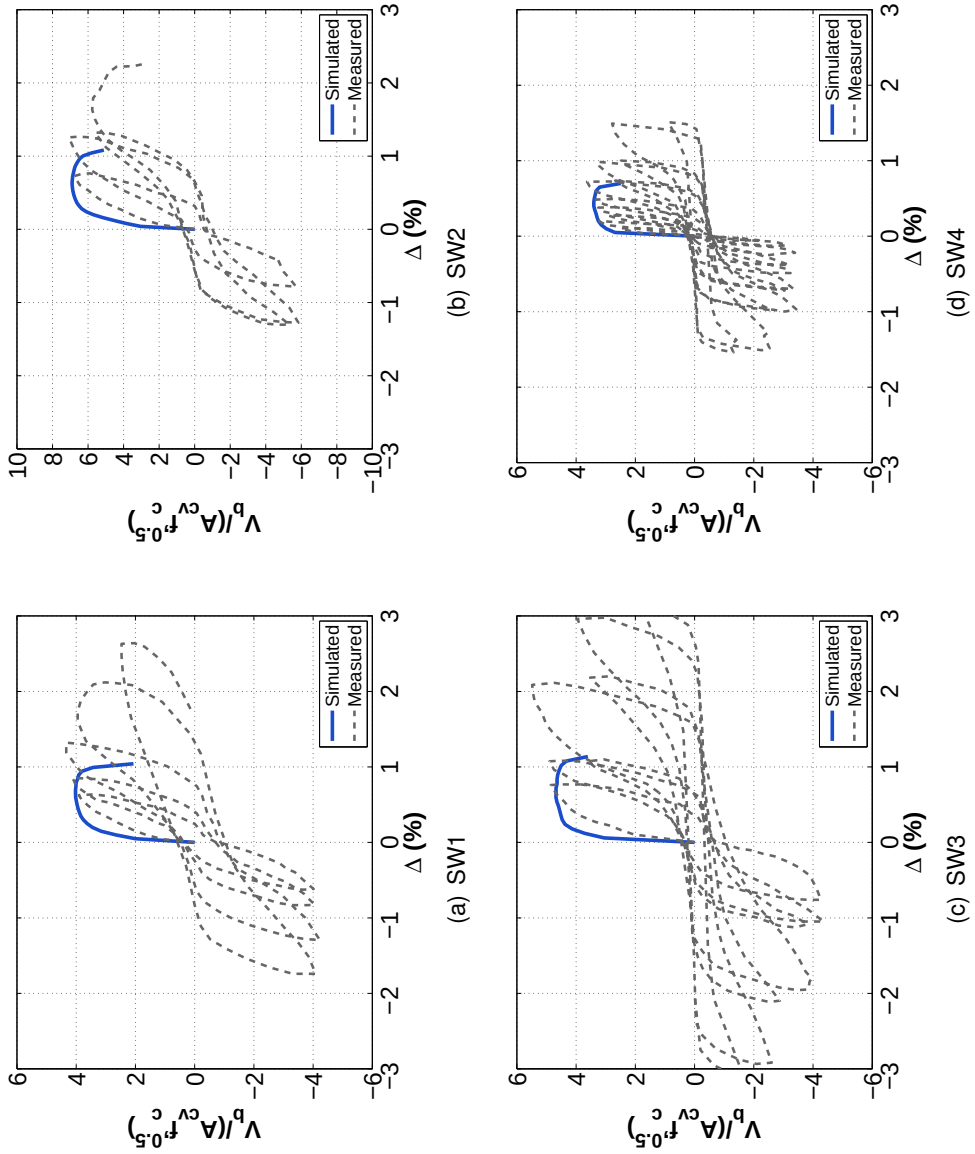

Figure C.2: Squat Wall Specimen Results

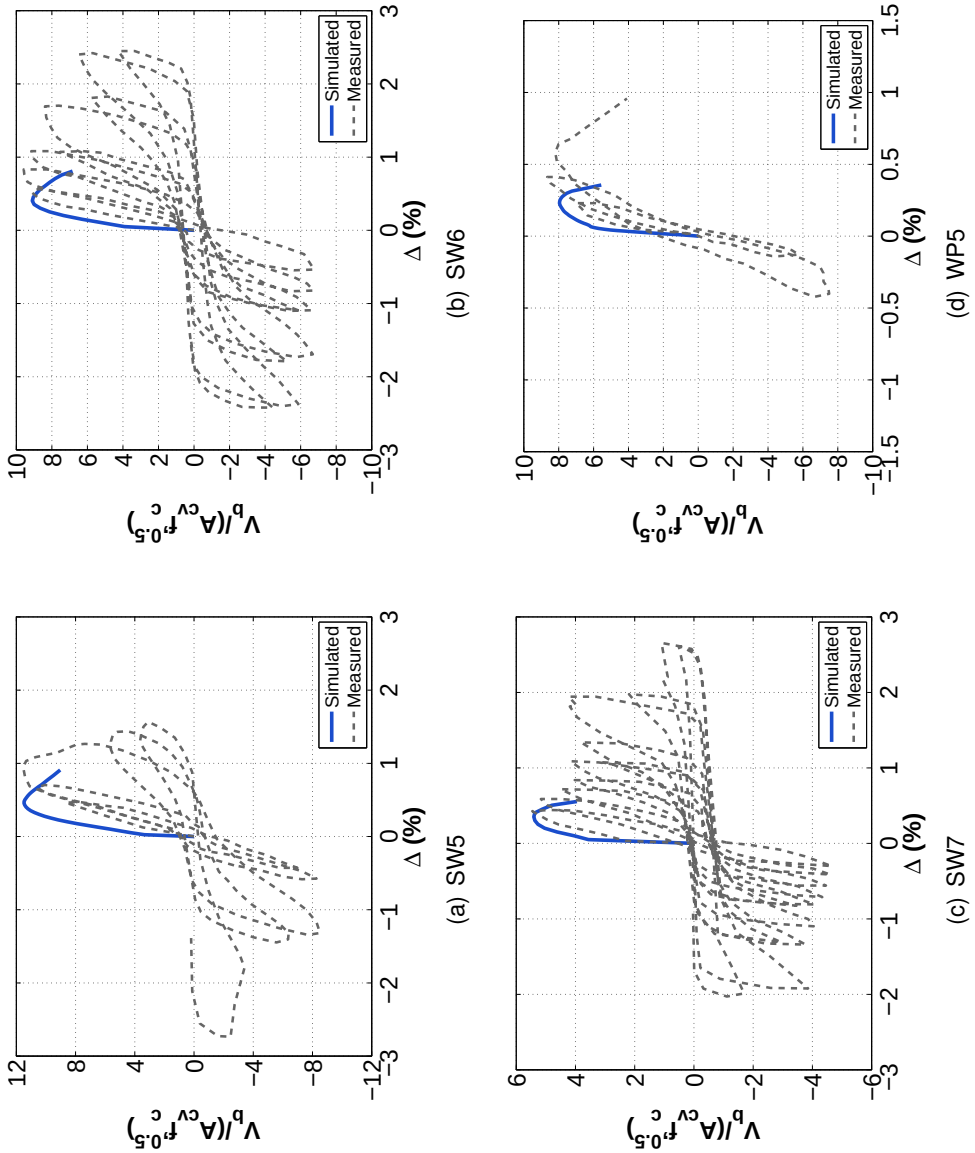

Figure C.3: Squat Wall Specimen Results

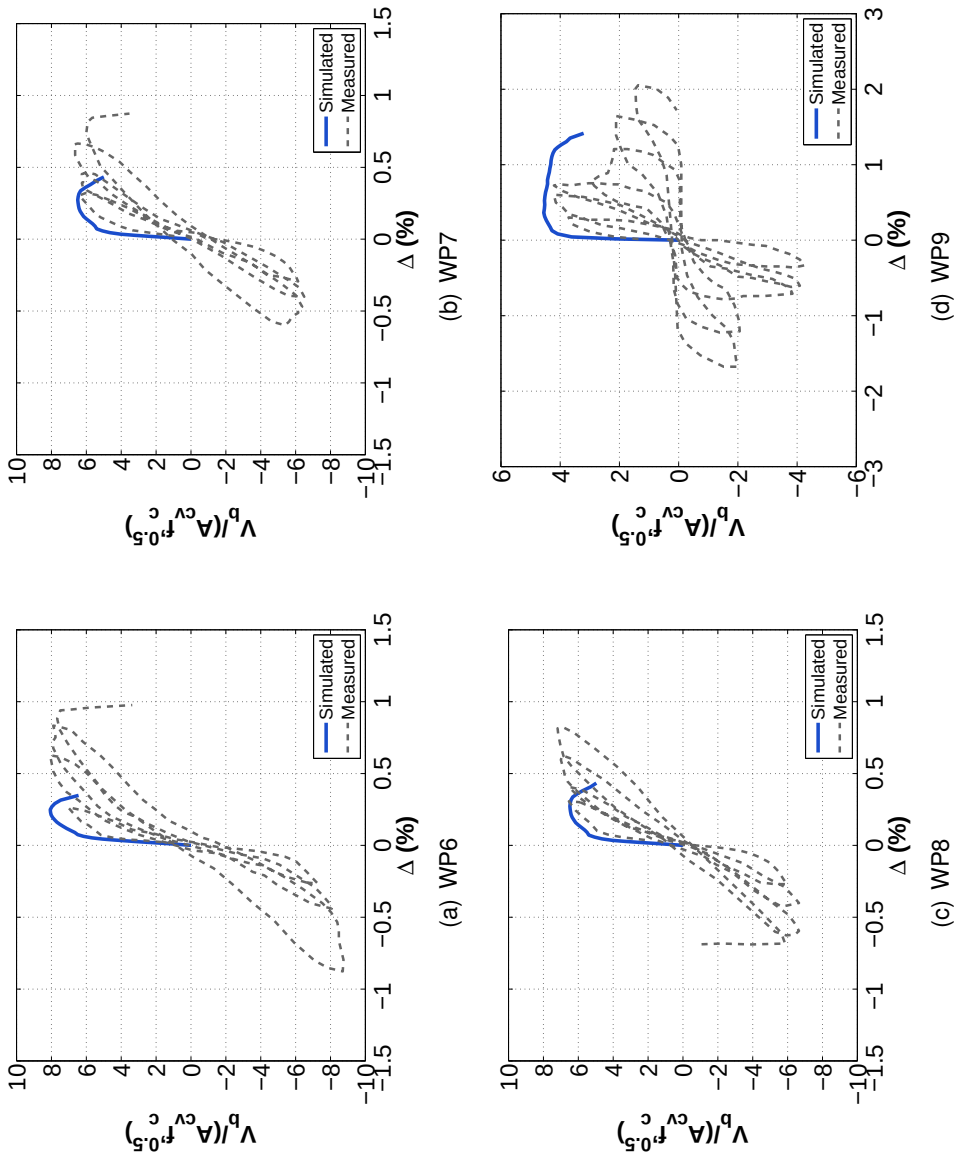

Figure C.4: Squat Wall Specimen Results

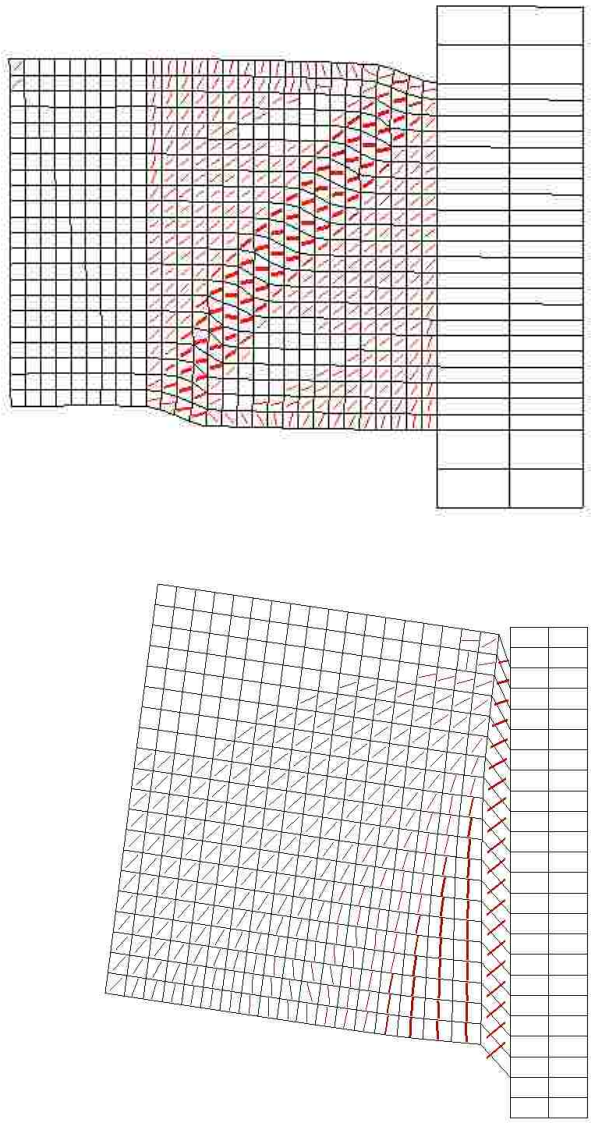

(b) Diagonal Crushing

(a) Sliding

Figure C.5: Failure Mode

Appendix D

WALLED BUILDING ANALYSIS AND DESIGN

D.1 Modal Contribution Relationships for Cantilever Walls

To aid in developing the modified MRSA method presented in Chapter 5, modal static response contributions for base shear and base moment were studied. Studying the static contribution factors identified simplified relationships for determining MRSA base shear and base moment demands for cantilevered walls. The simplified relationships presented in this section allow the analyst to estimate MRSA demands without having to determine the system mode shapes. Simplified relationships presented in this section are limited by the following assumptions: 1) uniformly distributed seismic mass, 2) uniform stiffness along the wall height, 3) symmetric building plan and 4) building height between 6 and 30 stories.

D.1.1 Methods

To study static modal contribution factors for walled buildings, modal analysis of a simplified building configuration was performed considering a large range of seismic weight, wall stiffness and building height. For the simplified building configuration, a square plan area of 100 ft x 100 ft was used and two planar walls were assumed to resist 100% of the seismic loads. Various wall areas were considered by varying both the provided wall thickness and the wall lengths. A minimum wall length of 18 ft and a maximum wall length of 40 ft was considered. For a given wall length, modal analysis was performed for different values of assumed thickness, different values of seismic weight and different building heights. All modal analysis was performed using OpenSees and the parameter study was automated using MATLAB scripts developed by the author. For the parameter study, wall length increments of 2 ft were used and wall thickness increments of 2 inches were used; a minimum thickness 12 inches and a maximum thickness of 28 inches were considered. Seismic weights were varied between 25 psf and 350 psf, in 25 psf increments. Wall buildings were varied between 6 and 30 stories, in two story increments. In total, 19656 modal analyses were performed (12 wall lengths x 9 wall thickness x 13 building heights x 14 story weights).

D.1.2 Static Load Patterns and Modal Contribution Factors

For each modal analysis, static load pattern were determined using the method presented by Chopra (2000). In this method, the total building inertial force vector, s_n, is expanded in an orthogonal basis using the system eigenvectors. This decomposition provides 'n' modal inertial force vectors, s_n, each of which only produce response only in the nth mode of vibration. Using Chopra's notation, s_n can be written:

$$s_n = \Gamma_n [M] \phi_n \tag{D.1}$$

where

$$\Gamma_n = \frac{\{\phi_n\}^T \{M\}}{M_n} \tag{D.2}$$

and

$$M_n = \{\phi_n\}^T [M] \{\phi_n\} \tag{D.3}$$

In Equations D.1- D.3, [M] is the diagonal mass matrix for the building, $\{M\}$ is the vector representation of the diagonal mass matrix and $\{\phi_n\}$ is the nth mode eigenvector. The s_n vectors represent static inertial load vectors associated with each vibration mode. Thus, static base shear contribution factors, r$_{vn}$, and base moment contribution factors, r$_{mn}$, can be defined which determine the contribution of each mode of vibration to the total static response.

$$r_{vn} = \sum_{j=1}^{N} s_{nj} \tag{D.4}$$

and

$$r_{mn} = \sum_{j=1}^{N} s_{nj} h_j \tag{D.5}$$

Where r_{vn} is the static base shear contribution due to mode 'n', r_{mn} is the static base moment contribution due to mode 'n', s_{nj} is the j^{th} story component of s_n, h_j is the height from the wall base to story 'j', and N is the number of stories. r_{vn} and r_{mn} are useful quantities because they 1) provide information on the relative importance of each mode to base response quantities and 2) they can be used directly with modal spectral acceleration quantities to estimate peak demands using modal response spectrum analysis (MRSA). If spectral accelerations associated with each period of vibration are known, base shear and base moment contributions for each mode can be written as:

$$V_{bn} = r_{vn} S_n \tag{D.6}$$

and

$$M_{bn} = r_{mn} S_n \tag{D.7}$$

Where V_{bn} is the base shear contribution from mode 'n', M_{bn} is the base moment contribution from mode 'n' and S_n is the spectral acceleration associated with the n^{th} modal period. With contributions known for each mode, total base shear and moment demands can be determined using any of several common techniques for modal combination (SRSS, CQC). For walled buildings, period spacing is such that SRSS can be used for modal combination.

D.1.3 Base Shear Contribution Factors

Considering results from the 19000+ modal analyses performed using the simplified building configuration, the relationship between first mode base shear contribution factor, r_{v1},

and total seismic weight, W, was found to be essentially linear with constant slope for all building heights, N, and wall areas considered. The linear relationship determined by the study is presented in Figure D.1. Thus, the following relationship was determined for the first mode base shear contribution factor for walled buildings:

$$r_{v1} \approx \frac{W}{620} \tag{D.8}$$

Further investigation of the modal contribution results identified approximately constant relationships between the second and third mode base shear contribution factors and the first mode base shear contribution factor:

$$r_{v2} \approx \frac{r_{v1}}{3.25} \tag{D.9}$$

$$r_{v3} \approx \frac{r_{v1}}{9.25} \tag{D.10}$$

D.1.4 Base Moment Contribution Factors

Similar relationships were found relating the seismic weight to base moment:

$$r_{m1} \approx \frac{WN}{70} \tag{D.11}$$

$$r_{m2} \approx \frac{r_{m1}}{11.25} \tag{D.12}$$

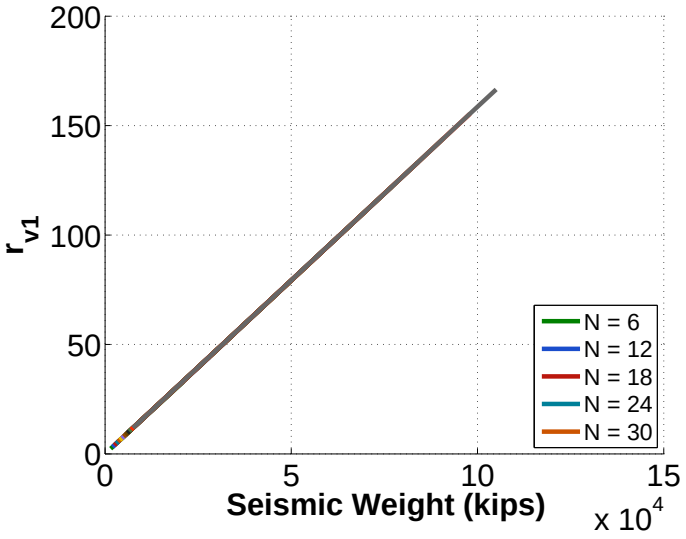

Figure D.1: First Mode Base Shear Contribution

$$r_{m3} \approx \frac{r_{m1}}{53.5} \tag{D.13}$$

VITA

Joshua Pugh was born on May 22, 1978 in Springfield, Illinois to Julian L. and Carolyn R. Pugh. He attended Marquette University in Milwaukee, Wisconsin and graduated in 2001 with a Bachelor of Science in Civil and Environmental Engineering. After graduation, he studied structural engineering at The University of Texas at Austin and received a Master's of Science in Engineering degree in 2003. He practiced structural engineering as a consultant for the oil and gas industry from 2003 to 2008 and is a licensed professional engineer. He began work on his doctorate in 2008.